



UNIVERSITY OF NAIROBI
DEPARTMENT OF CHEMISTRY

**SYNTHESIS, STRUCTURE ELUCIDATION AND REACTIVITY OF
PALLADIUM(II) AND PLATINUM(II) COMPLEXES FOR ANTICANCER
APPLICATIONS**

BY

MBUGUA, SIMON NGIGI

Reg. No. I80/51491/2017

**Thesis Submitted for Examination in Fulfilment of the Requirements for the Award of the
Degree of Doctor of Philosophy in Chemistry of the University of Nairobi.**

2020.

DECLARATION

I declare that this is my original work and has not been submitted elsewhere for examination. Where other people's work has been used, this has properly been acknowledged and referenced in accordance with the University of Nairobi's requirements.

Signature _____ Date _____

Mbugua, Simon Ngigi
Department of Chemistry, School of Physical Sciences
University of Nairobi

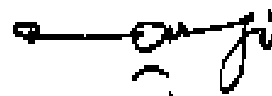
This thesis is submitted for examination with our approval as the research supervisors:

Prof. Lydia W. Njenga

University of Nairobi
P.O Box 30197-00100
Nairobi Kenya
lnjenga@uonbi.ac.ke

Signature

Date



Prof. Shem O. Wandiga

University of Nairobi
P.O Box 30197-00100
Nairobi Kenya
wandigas@uonbi.ac.ke

Signature

Date



Dr. Ruth A. Odhiambo

University of Nairobi
P.O Box 30197-00100
Nairobi Kenya
odhiambor@uonbi.ac.ke

Signature

Date



Prof. Martin O. Onani

Department of Chemistry,
University of Western Cape,
Private bag X17, Bellville 7535
South Africa.
monani@uwc.ac.za

Signature

Date

DEDICATION

This thesis is dedicated to my wife Jane Muthoni and children; Stephen Ngigi and Martin Ngigi for their support especially during my long stays in South Africa.

ACKNOWLEDGEMENT

The support and insightful comments and timely feedback from my supervisors; Prof L. Njenga, Prof S.O. Wandiga, Dr Ruth A. Odhiambo and Prof M.O. Onani were just boundless and is greatly and humbly appreciated. All my friends and colleagues at the Department of Chemistry of the University of Nairobi and University of the Western Cape are all appreciated.

A major part of this research was carried out in the Department of Chemistry, University of the Western Cape, South Africa. The expert supervision and guidance of my host Prof Martin Onani is especially appreciated- those regular departmental presentations and the many lunch-ins and lunch-outs...and that last out-of-town lunch- it was just wonderful! The whole experience was just homely and social, I miss that.

The constructive advice and valuable ideas of Chemistry post doc students at the University of the Western Cape; Dr Eunice Nyawande (JKUAT, Kenya) and Dr Vincent Asanda in our research group are appreciated. Prof M. Meyer and Dr Nicole Sibuyi from the Biotechnology Department of the University of the Western Cape are acknowledged for their comments and active part in bioassay tests. Dr Waryo and Dr Lindsay from Sensor lab are appreciated for their support on electrochemical studies. Prof. L. Rogers from Rutgers University in New York, much appreciated for the great work of solving and refining our crystal structures.

My employer Kisii County is acknowledged for the study leave which enabled me to carry out this work. The Chairman of the Department of Chemistry of the University of Nairobi, Prof Onyari, is acknowledged for his words of encouragement every time I visited his office.

I am especially grateful to my sponsor in this project, the International Science Program, ISP, under the KEN 01 project. This work could not have been possible without their support through a study fellowship to South Africa. The NRF South Africa is acknowledged for their support through our research group at UWC.

All my family members, especially my wife for playing both roles of mother and father during my absence in South Africa, and 'kicking' me out of bed at 3.00am to work on this project, thank you my dearest.

And finally, to God, 'Who is able to do immensely more than we can ever think or imagine', 'in whom all the treasures of wisdom and knowledge are hid'.

ABSTRACT

The objective of the work was to come up with stable metal complexes with bulky ligands coordinated to the metal center and test them in anticancer studies. Literature reports that bulky ligands and trans geometry for palladium and platinum complexes may produce compounds with enhanced anticancer activity but this has not yet been studied.

Palladium and platinum metal centers were chosen for this work due to their prominence and in-depth literature reports on their use in similar anticancer studies. The similarities in the bonding profiles of the +2 oxidation states for these *d8* ions produces 16-electron low spin complexes with similar square planar geometry to the well-known commercially available anticancer drugs which allows their anticancer activity to be compared. However, the differences in their d-orbital energies, ligand substitution kinetics and effective nuclear charge affords interesting contrasts in the resulting compounds.

In this regard, a series of eleven new Palladium(II) and Platinum(II) complexes from four pyrrole-based ligands and four thiosemicarbazide-based ligands; have been synthesized, characterized, and their electronic properties, DNA binding modes and anti-cancer properties studied. The synthesis for all the compounds was performed under mild conditions; reflux in absolute methanol for the ligands and room temperature for the complexes.

Inert procedures were employed in the synthesis and isolation followed by characterization by FTIR, ^1H and ^{13}C NMR, UV-vis, cyclic voltammetry and elemental analysis in addition to x-ray crystallography for 4 ligands and 1 platinum complex. The complexes were found to be of square planar geometry. Yields for the pyrrole-based ligands ranged from 80%- 95% while the thiosemicarbazide ligands yields ranged from 54%-68%. The yields for the complexes ranged from 42%- 98%. These yields were on average lower compared to those of the ligands and were attributed to the steric shielding of the bulky ligands to the metal center making coordination to the metal challenging.

The cyclic voltammograms for the palladium complexes showed irreversible reduction peaks at -0.57V, -1.47 V and -1.7V vs Ag/AgCl which corresponded to the Pd(II)→Pd(I) and Pd(I)→Pd(0) reduction processes. The platinum complexes showed peaks around -0.5 V corresponding to H^+ reduction to H_2 occurring at -0.41V at pH 7 vs Ag/AgCl. The molar conductivities ranged from 4.0-8.8 $\mu\text{S}/\text{cm}$ suggesting neutrality. Solubility studies were carried out by studying their partition coefficients. This gave a range of logP values ranging between 0.6- 1.9927 indicating a more than 20times partitioning for most of the compounds in oil layer compared to the water layer. This indicated the lipophilic nature for these complexes.

Stability study measurements were performed using ^1H NMR in DMSO- d_6 after adding 200 μl of D_2O over a 72h period. Proton scans were conducted at 6h intervals to monitor any changes in peaks. The lack of shift in peaks or any other change in spectra over the test period indicated that the compounds were stable in solution, and therefore could be analysed for bioassay

DNA-binding kinetics were studied by spectroscopy using calf thymus DNA. The complexes were found to bind to DNA through intercalative mode and to induce apoptosis, where one of the platinum complexes showed the highest binding constant of $8.049 \times 10^4 \text{ M}^{-1}$. The compounds showed comparable DNA-binding profiles to some of the available well-known intercalators indicating they can be important candidates in the line of potential DNA intercalators for further work.

The anti-cancer cytotoxicity and apoptosis for the complexes was performed *in vitro*, using human colon, Human Cervical, Human Hepatocellular Carcinoma, breast cancer, human prostate and non-cancer human breast cells, where their activity was correlated with their corresponding structures. The metal center, electronic and steric effects of the different ligands around the metal center effected different rates of ligand substitution, which reflected on the observed cytotoxicity profiles.

This was most notable for two of the palladium complexes, which differed by a -Br in position 5 of thiophene ring of one of them. This caused a remarkable increase in cell viability, from 11% - 48% in cervical cancer cells, and 28% - 78% in prostate cancer cells, a difference of 37% and 50%.

One of the platinum complexes also showed remarkable therapeutic potential as it selectively killed all the cancer cells and not the normal breast cells, and an IC_{50} of $0.2685 \pm 0.0054 \mu M$ against Hepatocellular cell lines, compared to $0.3 \mu M$ for the commercially available *cis*-platin. The selectivity for this particular complex was attributed to its preferential accumulation into cancerous cells since the cells are known to have high levels of sulphur-containing bioligands which afford the preferred soft-soft bonding interactions for platinum. This suggests that it can be a viable candidate for further research as a possible anticancer agent and requires further *in vivo* tests.

TABLE OF CONTENTS

DECLARATION	I
DEDICATION	II
ACKNOWLEDGEMENT	III
ABSTRACT	IV
TABLE OF CONTENTS	VI
LIST OF FIGURES	XIV
LIST OF SCHEMES	XIX
LIST OF TABLES	XXI
LIST OF ABBREVIATIONS	XXII
LIST OF PUBLICATIONS	XXIV
CHAPTER 1	1
INTRODUCTION	1
1.1 PLATINUM GROUP CHEMISTRY: GENERAL BACKGROUND	1
1.1.1 Chemistry of Ruthenium	2
1.1.2 Osmium	4
1.1.3 Rhodium	5
1.1.4 Iridium	6
1.1.5 Palladium	9
1.1.6 Platinum	10
1.2 CANCER	13
1.3 ORGANOMETALLIC COMPLEXES IN CANCER THERAPY: TARGETING DNA	14
1.4 STATEMENT OF THE PROBLEM	18
1.5 AIMS AND OBJECTIVES	18
1.5.1 Objectives of the Study	18

1.5.2	Specific Objectives	19
1.6	JUSTIFICATION OF THE STUDY	19
CHAPTER 2.....		20
LITERATURE REVIEW		20
2.1	METAL-BASED COMPLEXES	20
2.2	BONDING IN METAL COMPLEXES	21
2.3	THE TRANS INFLUENCE/ EFFECT	22
2.4	KINETIC TRANS EFFECT.....	23
2.5	STABILITY AND SPECTRA IN COORDINATION COMPLEXES	24
2.5.1	Stability of Square Planar Complexes	24
2.5.2	Stability of Octahedral Complexes (Cr(CO) ₆)	26
2.5.3	Spectra of Transition Metal Complexes.....	27
2.6	LIGANDS AND LIGAND SUBSTITUTION KINETICS	28
2.6.1	Phosphines Ligands	28
2.6.2	Schiff base Ligands.....	29
2.6.3	Ligand Substitution trends in the Periodic Table	30
2.7	COORDINATION COMPLEXES IN CANCER THERAPY	31
2.7.1	Ferrocene Compounds	31
2.7.2	Titanocene Complexes	32
2.7.3	Ruthenium and Osmium Arene Complexes.....	33
2.7.4	Ruthenium Azopyridine Complexes.....	37
2.7.5	Platinum Complexes	39
2.7.6	Palladium Complexes	43
2.7.7	Palladium(II) Complexes with Mixed Donor Ligand: N, S and O donor ligands.....	44
2.7.8	Complexes from Five Membered Heterocycles: Pyrrole Scaffolds	45

2.7.9	Complexes from Thiosemicarbazone Derivatives.....	47
2.7.10	Complexes from Quinolone Derivatives.....	50
2.8	DNA BINDING TO METAL COMPLEXES.....	50
2.9	BEYOND DNA-TARGETING IN CANCER CHEMOTHERAPY. EMERGING FRONTIERS.....	51
2.9.1	Immunotherapies	53
2.9.2	Natural antioxidants	57
2.9.3	Tumor ablation and magnetic hyperthermia	57
2.9.4	Laser therapy	59
2.9.5	Radiomics and pathomics.....	60
2.9.6	Exosomes	61
CHAPTER 3.....		65
METHODOLOGY.....		65
3.1	SYNTHESIS.....	65
3.2	INSTRUMENTATION	65
3.3	SYNTHESIS OF PYROLE-BASED LIGANDS.....	66
3.3.1	Synthesis of (E)-N-((1H-pyrrol-2-yl) methylene) (phenyl)methanamine (L1).....	66
3.3.2	Synthesis of (E)-N-((1H-pyrrol-2-yl) methylene) (thiophen-2-yl) methanamine (L2) 66	
3.3.3	Synthesis of (E)-N-((1H-pyrrol-2-yl) methylene) (furan-2-yl)methanamine (L3)....	67
3.3.4	Synthesis of (E)-N-((1H-pyrrol-2-yl) methylene) (pyridin-2-yl)methanamine (L4).	67
3.4	SYNTHESIS OF THIOSEMICARBAZIDE-BASED LIGANDS.....	67
3.4.1	Synthesis of (E)-1-((thiophen-2-yl) methylene) thiosemicarbazide (L5)	67
3.4.2	Synthesis of (E)-1-((5-bromothiophen-2-yl)methylene)thiosemicarbazide (L6).....	67
3.4.3	Synthesis of (E)-1-((4-bromothiophen-2-yl)methylene)thiosemicarbazide (L7).....	67
3.4.4	Synthesis of (E)-1-((quinolin-2-yl)methylene)thiosemicarbazide (L8).....	68

3.5	CHARACTERIZATION OF THE LIGANDS	68
3.5.1	Gas Chromatography-Mass Spectroscopy	68
3.5.2	Elemental Analysis	68
3.5.3	UV-Visible Spectroscopy.....	68
3.5.4	Fourier Transform InfraRed Spectroscopy	68
3.5.5	Proton Nuclear Magnetic Resonance Spectroscopy	68
3.5.6	Carbon-13 Nuclear Magnetic Resonance Spectroscopy.....	69
3.5.7	Single Crystal x-ray Crystallography.....	69
3.6	PREPARATION FOR PRECURSOR COMPLEXES.....	69
3.6.1	Preparation of cis-Cyclooctadienepalladium(II) Chloride Precursor	69
3.6.2	Synthesis of cis-dichloro bis-(dimethylsulfoxide) Platinum(II) Precursor	69
3.6.3	Synthesis of cis-dichloro bis-(triphenylphosphine) Platinum(II) Precursor	69
3.7	SYNTHESIS OF THE PYRROLE-BASED COMPLEXES.....	70
3.7.1	Synthesis of trans-Chloridobis[(pyrrolylmethylidene)(benz-2-ylmethyl) amine- κ N] methylPalladium(II) (C1).....	70
3.7.2	Synthesis of Synthesis of trans-Chloridobis[(pyrrolylmethylidene)(thiophen-2-ylmethyl) amine- κ N] methylPalladium(II) (C2)	70
3.7.3	Synthesis of trans-dichloridobis[(pyrrolylmethylidene)(furan-2-ylmethyl) amine- κ N] methylPalladium(II)- (C3).....	70
3.7.4	Synthesis of cis-dichlorido[(pyrrolylmethylidene)(pyridyl-2-ylmethyl) amine N,N] Palladium(II)- (C4)	70
3.7.5	Synthesis of Pt ₂ Cl ₂ (dms ₂) ₂ -L1 (C5)	70
3.7.6	Synthesis of PtCl ₂ (dms ₂)-L1 (C6).....	71
3.8	SYNTHESIS OF THE THIOSEMICARBAZONE-BASED COMPLEXES (C7-C11)	71
3.8.1	Synthesis of L5-PdCl ₂ (C7)	71
3.8.2	Synthesis of L6-PdCl ₂ (C8).....	71

3.8.3	Synthesis of L8-PdClMe (C9)	71
3.8.4	Synthesis of L5-PtCl ₂ (C10).....	71
3.8.5	Synthesis of L7-PtPPh ₃ (C11)	71
3.9	CHARACTERIZATION OF THE COMPLEXES	72
3.9.1	Liquid Chromatography-Mass Spectroscopy Analysis.....	72
3.9.2	Elemental Analysis	72
3.9.3	Electrochemical Properties of the Complexes by Cyclic Voltammetry	72
3.9.4	UV-Visible Spectroscopy.....	72
3.9.5	Fourier Transform Infrared Spectroscopy.....	72
3.9.6	Proton Nuclear Magnetic Resonance Spectroscopy	72
3.9.7	Carbon-13 Nuclear Magnetic Resonance Spectroscopy	73
3.9.8	Single Crystal x-ray Crystallography.....	73
3.9.9	Partition Coefficient: Lipophilicity studies	73
3.9.10	Stability studies.....	74
3.9.11	DNA binding Studies.....	74
3.9.12	Cytotoxicity Assay.....	74
CHAPTER 4	76
RESULTS AND DISCUSSION	76
4.1	BACKGROUND	76
4.2	SYNTHESIS OF THE PYRROLE-BASED LIGANDS (L1-L4)	77
4.3	STRUCTURE CONFIRMATION FOR LIGAND L1	78
4.3.1	Gas Chromatography-Mass Spectroscopy Analysis for L1.....	78
4.3.2	Single Crystal X-ray Structure for L1.....	79
4.4	STRUCTURE CONFIRMATION FOR LIGAND L2.....	80
4.4.1	Gas Chromatography-Mass Spectroscopy for Ligand 2	80

4.4.2	Single Crystal X-ray Structure for L2.....	81
4.5	STRUCTURE CONFIRMATION FOR LIGAND L3.....	83
4.5.1	Gas Chromatography-Mass Spectroscopy for Ligand 3.....	83
4.5.2	Single Crystal X-ray Structure for L3.....	84
4.6	STRUCTURE CONFIRMATION FOR LIGAND L4.....	84
4.6.1	Gas Chromatography-Mass Spectroscopy for Ligand 4.....	84
4.6.2	UV-Visible Spectra for Ligands 1- 4.....	85
4.6.3	Fourier Transform Infrared for L4.....	86
4.6.4	Proton and Carbon-13 Nuclear Magnetic Resonance for Ligand 4.....	87
4.7	SYNTHESIS OF THE THIOSEMICARBAZIDE-BASED LIGANDS (L5-L8).....	89
4.8	STRUCTURE CONFIRMATION FOR THE LIGAND L5-L8.....	90
4.8.1	UV-Visible Spectra for L5- L8.....	90
4.8.2	Single Crystal X-ray Structure for L5.....	91
4.8.3	Fourier Transform InfraRed Spectroscopy for Ligands 5- 8.....	92
4.8.4	Proton and Carbon-13 Nuclear Magnetic Resonance for Ligand 5- 8.....	93
4.8.5	Solubility.....	96
4.9	SYNTHESIS OF THE PRECURSOR COMPLEXES.....	97
4.10	SYNTHESIS OF THE COMPLEXES.....	98
4.10.1	Synthesis of the Pyrrole-based Complexes (C1-C6).....	98
4.10.2	Synthesis of Thiosemicarbazide-based Complexes (C7-C11).....	99
4.11	CHARACTERIZATION AND STRUCTURE CONFIRMATION FOR THE PYRROLE-BASED COMPLEXES.....	100
4.11.1	Liquid Chromatography-Mass Spectroscopy Analysis for the Complexes.....	100
4.11.2	Elemental Analysis for Pyrrole-based Complexes C1- C6.....	100
4.11.3	UV-Visible Spectroscopy for the Pyrrole-based Complexes 1- 6.....	101

4.11.4	Fourier Transform InfraRed Spectroscopy for Pyrrole Complexes 1-6	102
4.11.5	Proton and Carbon-13 Nuclear Magnetic Resonance spectra for the Pyrrole-based Complexes 1- 6	104
4.11.6	Single Crystal X-ray Analysis for Complex 6.....	106
4.12	CHARACTERIZATION AND STRUCTURE CONFIRMATION FOR THE THIOSEMICARBAZIDE-BASED COMPLEXES (C7- C11)	108
4.12.1	UV-Vis Spectroscopy for Thiosemicarbazide Complexes C7-C11	108
4.12.2	Elemental Analysis for Thiosemicarbazide Complexes	110
4.12.3	Fourier Transform InfraRed Spectroscopy for the Thiosemicarbazide Complexes ..	111
4.12.4	Proton and Carbon-13 Nuclear Magnetic Resonance for the Thiosemicarbazide Complexes	112
4.13	CYCLIC VOLTAMMETRY.....	115
4.14	LIPHILICITY STUDIES.....	117
4.14.1	Partition Coefficient.....	117
4.15	STABILITY STUDIES	118
4.16	DNA BINDING KINETICS	119
4.17	DNA BINDING STUDIES FOR PYRROLE-BASED COMPLEXES (C1, C3, C4, C6).....	122
4.18	DNA BINDING STUDIES FOR THIOSEMICARBAZIDE COMPLEXES (C7-C11).....	125
4.19	BIOASSAYS- APOPTOTIC ACTIVITY FOR THE COMPLEXES	128
4.20	IC ₅₀ VALUES FOR THIOSEMICARBAZIDE COMPLEXES	135
CHAPTER 5	136
CONCLUSION AND RECOMMENDATIONS	136
5.1	CONCLUSION	136
5.2	RECOMMENDATIONS.....	137
REFERENCES	139

APPENDICES	169
FTIR SPECTRA DATA	169
PROTON NUCLEAR MAGNETIC RESONANCE SPECTRA FOR THE LIGANDS	174
PROTON NUCLEAR MAGNETIC RESONANCE SPECTRA FOR THE COMPLEXES	177
CARBON-13 NUCLEAR MAGNETIC RESONANCE SPECTRA FOR THE LIGANDS	179
CARBON-13 NUCLEAR MAGNETIC RESONANCE SPECTRA FOR THE COMPLEXES	183
UV/VIS SPECTRA FOR SELECTED LIGANDS AND COMPLEXES	185
PUBLICATIONS	190

LIST OF FIGURES

Figure 1 The general chemical structure of a metal bis-arene complex (M = Ru).....	3
Figure 2 The chemical structures of $[(\eta^6\text{-p-cymene}) \text{Ru}(\eta^6\text{-phenylalanine})]^{2+}$ (a) and $[(\eta^6\text{-p-cymene}) \text{Ru}(\eta^6\text{-H-dopamine})]^{2+}$ (b).....	4
Figure 3 Structure of $[\text{Rh}_2(\text{O}_2\text{CCH}_3)_4]$. L= axial ligand; R= carbon chain of carboxylate groups.6	
Figure 4 pi-backbonding in carbonyls.....	8
Figure 5 The σ -donor Orbitals of Square Planar Complexes	25
Figure 6 Molecular Orbital Energy Diagram for Octahedral Complex	27
Figure 7 Tolman cone angle for phosphine ligands.....	29
Figure 8 General structure of a Schiff base	29
Figure 9 Guanine (G) and Adenine (A) adducts formed by DNA interactions of arene Ru-anticancer Complexes	36
Figure 10 DNA Adducts Formed by Oxaliplatin.....	42
Figure 11 Mechanism of Action of Cancer Vaccines. Administered through injection with adjuvants that activate dendritic cells.	56
Figure 12 Hyperthermia Process complementing traditional cancer therapy. (Prasad <i>et al.</i> , 2018)58	
Figure 13 Structure and Composition of exosomes derived from cancerous Cells.	62
Figure 14 Summary of the number of clinical trials started during the years 2008–2010 (blue) and from 2017 until today (orange) www.clinicaltrials.gov	63
Figure 15 GC-MS peaks for L1	78
Figure 16. The unit Cell for ligand L1 showing the crystal packing.....	79
Figure 17 GC-MS for L2	81
Figure 18 ORTEP Ellipsoids for L2	82
Figure 19 The unit Cell for L2 showing the crystal packing.....	82
Figure 20 GC-MS peaks for L3	83
Figure 21 ORTEP Ellipsoids for L3 at 50% probability.....	84

Figure 22 GC-MS peaks for L4	85
Figure 23 UV-Vis Spectrum for L2	86
Figure 24 ¹ H NMR (a) and ¹³ C NMR (b) spectra for L1	88
Figure 25 ORTEP view for the molecular pair for L5	92
Figure 26 FTIR Spectra for Ligand L6	93
Figure 27 ¹ H NMR spectra (a) and ¹³ C NMR spectra for L7	95
Figure 28 LC-MS for Complex C1	100
Figure 29 UV-vis Spectra for C1	102
Figure 30 FTIR Spectrum for C1	104
Figure 31 ¹ H NMR spectrum for C1	105
Figure 32 Unit cell packing (a) and bond angles (b) for C6	107
Figure 33 UV-Vis Spectrum of C9	109
Figure 34 FTIR Spectra for C9	112
Figure 35 ¹ H NMR Spectra for C7	114
Figure 36 Cyclic Voltammetry for C3 and C4	116
Figure 37 CV Scans for C6 at different scan Rates	117
Figure 38 Partitioning of complexes C1, C3, C7-C11 between water (bottom layer) and n-octanol (top layer)	118
Figure 39 ¹ H-NMR Stability Scans for (a) C7 , (b) C8 , (c) C9 , (d) C6 , (e) C11	119
Figure 40 Dilutions for determination of DNA concentration used. Inset is Absorbance vs Concentration at 260nm	120
Figure 41 DNA-Binding UV-visible absorption spectra for complex C1	122
Figure 42 DNA-Binding UV-visible absorption spectra for complex C3	122
Figure 43 DNA-Binding UV-visible absorption spectra for complex C4	123
Figure 44 DNA-Binding UV-visible absorption spectra for complex C6	123

Figure 45 DNA-Binding UV-visible absorption spectra for complex C7	125
Figure 46 DNA-Binding UV-visible absorption spectra for complex C8	126
Figure 47 DNA-Binding UV-visible absorption spectra for complex C9	126
Figure 48 U DNA-Binding UV-visible absorption spectra for complex C10	127
Figure 49 DNA-Binding UV-visible absorption spectra for complex C11	127
Figure 50 Screening of anti-cancer activity of Pyrrole complexes (C1 , C3 , C4 and C6) against selected human cell lines. The cells were exposed to 100 µg/ml of compounds for 24 h, cell viability was assessed by MTT assay. *indicates statistical significance at p<0.05, ** p<0.01, *** p<0.001	130
Figure 51 Effect of C1 and C7 on cellular morphology. PC-3 and Caco-2 cells were exposed to IC ₅₀ of the organometallic complexes, were observed under inverted contrast microscope at 10× magnification. DMSO was used a positive control.	132
Figure 52 Apoptotic effects of the complexes on human cancer cells after exposure for 24 h. Apoptosis was assessed by Apopercentage assay. *indicates statistical significance at p<0.05, ** p<0.01, *** p<0.001.	133
Figure 53 Percent cell viability for the Thiosemicarbazide-based complexes	134
Figure 54 FTIR Spectra for L1	169
Figure 55 FTIR Spectra for L2	169
Figure 56 FTIR Spectra for L3	169
Figure 57 FTIR Spectra for L4	170
Figure 58 FTIR Spectra for L5	170
Figure 59 FTIR Spectra for L7	170
Figure 60 FTIR Spectra for L8	171
Figure 61 FTIR Spectra for C2	171
Figure 62 FTIR Spectra for C3	171
Figure 63 FTIR Spectra for C4	172

Figure 64 FTIR Spectra for C5	172
Figure 65. FTIR Spectra for C6	172
Figure 66 FTIR Spectra for C7	173
Figure 67 FTIR Spectra for C8	173
Figure 68 FTIR Spectra for C10	173
Figure 69 ¹ H NMR for L1	174
Figure 70 ¹ H NMR for L2	174
Figure 71 ¹ H NMR for L3	175
Figure 72 ¹ H NMR for L4	175
Figure 73 ¹ H NMR for L5	176
Figure 74 ¹ H NMR for L8	176
Figure 75 ¹ H NMR for C7	177
Figure 76 ¹ H NMR for C8	177
Figure 77 ¹ H NMR for C9	178
Figure 78 ¹ H NMR for C6	178
Figure 79 ¹ H NMR for C11	179
Figure 80 ¹³ C NMR for L1	179
Figure 81 ¹³ C NMR for L2	180
Figure 82 ¹³ C-NMR for L3	180
Figure 83 ¹³ C NMR for L4	181
Figure 84 ¹³ C NMR for L5	181
Figure 85 ¹³ C NMR for L7	182
Figure 86 ¹³ C NMR for L8	182
Figure 87 ¹³ C-NMR for C1	183
Figure 88 ¹³ C-NMR for C8	183

Figure 89 ^{13}C -NMR for C9	184
Figure 90 ^{13}C -NMR for C10	184
Figure 91 UV-Vis for L1	185
Figure 92 UV-Vis for L2	185
Figure 93 UV-Vis for L3	185
Figure 94 UV-Vis for L4	186
Figure 95 UV-Vis Spectra for C2	186
Figure 96 UV-Vis Spectra for C3	186
Figure 97 UV-Vis Spectra for C4	187
Figure 98 UV-Vis Spectra for C6	187
Figure 99 UV-Vis Spectra for C7	188
Figure 100 UV-Vis Spectra for C8	188
Figure 101 UV-Vis Spectra for C10	188
Figure 102 UV-Vis Spectra for C11	189

LIST OF SCHEMES

Scheme 1 Reactions with the Vaska's compound.....	7
Scheme 2 Addition of Hydrogen to Vaska's Compound	8
Scheme 3 addition of methyl iodide to Vaska's compound proceeds by a SN ₂ type reaction	8
Scheme 4 Activation step of cis-platin formation.	12
Scheme 5 Nitrate salts of halide-capped platinum (IV) dimers.	12
Scheme 6 Cisplatin aquation and DNA adduct formation on guanidine residues	16
Scheme 7 C-C Coupling using Pd(0) catalyst.....	20
Scheme 8 Synergistic bonding in a pi complex	21
Scheme 9 Hydrolysis of Ru-Z bond in RuII arene complexes.....	35
Scheme 10 Scheme Possible scheme for catalytic activity of ruthenium azopyridine complexes .	39
Scheme 11 Aquation reaction of cisplatin by DNA base	41
Scheme 12 Aquation and DNA adduct formation with cisplatin.....	42
Scheme 13 Synthesis of the Pyrrole-based ligands L1-L4	77
Scheme 14 Reaction Mechanism for the Schiff base formation between the primary amines and the aldehydes	77
Scheme 15 Proposed fragmentation for L1	79
Scheme 16 Proposed Fragmentation Pattern for L2	81
Scheme 17 Proposed Fragmentation Pattern for L3	83
Scheme 18 Proposed Fragmentation Pattern for L4	85
Scheme 19 Synthesis of the Thiosemicarbazide-based ligands L5-L8	90
Scheme 20 Synthetic Routes for the precursor complexes	97
Scheme 21 Synthetic Routes for the precursor complexes	97
Scheme 22 Synthetic Routes for the Pyrrole-based Pd(II) and Pt(II) complexes C1-C6	98
Scheme 23 Synthetic Routes for the Palladium complexes C7-C11	99

Scheme 24 Proposed mechanism for the binding of complexes to DNA.....	121
Scheme 25 The reduction of the MTT by NADH or NADPH in viable cells	129

LIST OF TABLES

Table 1 UV-Vis data for L1-L4	86
Table 2 Electronic spectra for the Ligands L1-L4	88
Table 3 UV-vis Spectral Data for L5-L8	91
Table 4 Electronic spectral data for L5-L8	96
Table 5 LC-MS Data for the pyrrole complexes.....	100
Table 6 Elemental Analysis Data for C1- C6	101
Table 7 UV-Vis Spectra for the Pyrrole-based Complexes	101
Table 8 ¹ H NMR Spectral Data for the Complexes	105
Table 9 Single Crystal data and Structure Refinement Parameters for C6	106
Table 10 UV-Vis Spectra for the Thiosemicarbazone-based Complexes	108
Table 11 Elemental Analysis Data for C7- C11	110
Table 12 ¹ H NMR Spectral Data for C7- C11	114
Table 13 Comparison of Binding constants (K_b) and Gibbs free energy ($-\Delta G$) values for the Pyrrole-based complexes–DNA interactions derived from UV-vis spectrophotometric data with other reported intercalators.....	124
Table 14 Comparison of K_b and $-\Delta G$ values for the thiosemicarbazide complexes–DNA interactions with other reported intercalators.	128
Table 15 IC_{50} values for the ligands and their respective pyrrole complexes	131
Table 16 IC_{50} values for thiosemicarbazide complexes.	135

LIST OF ABBREVIATIONS

ATR	Attenuated Total Reflectance
CD	Cyclodextrin
CDDP	<i>Cis</i> -diaminodichloro Platinum(II)
CE	Counter Electrode
CF	Crystal Field
CNS	Central Nervous System
COD	Cyclo Octadiene
CV	Cyclic Voltammetry
CT-DNA	Calf Thymus- DNA
D/CD	Drug-Cyclodextrin complex
DCM	Dichloromethane
Db	Dibenzylidene acetone
DMF	Dimethyl Formamide
DMSO	Dimethyl Sulfoxide
DNA	Deoxyribonucleic Acid
Fc-diOH	Dihydroxy Ferrocifen
Fc-OH	Hydroxy Ferrocifen
Fc-Tam	Ferrocenyl Tamoxifen
FTIR	Fourier <i>Transform</i> Infrared

HOMO	Highest Occupied Molecular Orbital
KBr	Potassium bromide
LMCT	Ligand to Metal Charge Transfer
LUMO	Lowest Unoccupied Molecular Orbital
MLCT	Metal Ligand Charge Transfer
NADH	Nicotinamide Adenine Dinucleotide
NADPH	Nicotinamide Adenine Dinucleotide Phosphate
NMR	Nuclear Magnetic Resonance
ORTEP	Oak Ridge Thermal Ellipsoid Plot
RE	Reference Electrode
RNA	Ribonucleic Acid
SALC	Symmetry Adapted Linear Combination
UV-VIS	Ultraviolet-Visible
WE	Working Electrode

LIST OF PUBLICATIONS

1. **Mbugua, S. N.**, Sibuyi, N. R., Njenga, L. W., Odhiambo, R. A., Wandiga, S. O., Meyer, M., Lalancette R. A., Onani, M. O. (2020). New Palladium (II) and Platinum (II) Complexes Based on Pyrrole Schiff Bases: Synthesis, Characterization, X-ray Structure, and Anticancer Activity. *ACS omega*, 5(25), 14942-14954.
<https://dx.doi.org/10.1021/acsomega.0c00360>
2. **Simon N. Mbugua**, Nicole R. S. Sibuyi, Lydia W. Njenga, Ruth A Odhiambo Shem O. Wandiga, Mervin Meyer, Roger A. Lalancette, Martin O. Onani, (2020). Synthesis, Characterization and DNA Binding Kinetics of New Pd(II) and Pt(II) Thiosemicarbazone Complexes. Spectral, Structural and Anticancer Evaluation. *Hindawi Journal of Chemistry Volume 2020*
<https://doi.org/10.1155/2020/3863269>
3. **Mbugua, S.N.**, Njenga, L.W., Odhiambo, R.A., Wandiga, S.O., Onani, M.O. (2020). Beyond DNA-targeting in Cancer Chemotherapy. Emerging Frontiers- A Review. *Current Topics in Medicinal Chemistry*. Bentham Science Publishers.
<https://doi.org/10.2174/1568026620666200819160213>

CHAPTER 1

INTRODUCTION

1.1 Platinum Group Chemistry: General Background

The elements from second and third triads of group VIII B (groups 8, 9 and 10) viz. ruthenium, rhodium, palladium, osmium, iridium and platinum are collectively known as the platinum metals since they are found together in platinum bearing minerals (Peng *et al.*, 2017).

The electronic arrangements of the components are Ru ($4d^7 5s^1$); Rh ($4d^8 5s^1$); Pd ($4d^{10}$); Os ($5d^6 6s^2$); Ir ($5d^7 6s^2$) and Pt ($5d^9 6s^1$). All the six components have nearly equivalent nuclear size, which partly explains the similarities behind chemical characteristics (Lazarević *et al.*, 2017). General similarities are seen in their having high ionization potentials and high positive standard electrode potentials for M^{2+}/M couples (Safarzadeh *et al.*, 2018). Notwithstanding, the wide varieties in the science of platinum metals emerge due to variable qualities of the distinctive oxidation states and stereochemistry (Sawama *et al.*, 2018). The normal oxidation states are: Ru, +3 and +4, Rh, +3; Ir, +4 and +3; Pd, +4 and +2; Pt, +4 and +2 (X. Wang, Van Bokhoven, *et al.*, 2020).

There is likewise the natural propensity of the $4d^n$ and $5d^n$ configurations to match their spins (Liberka *et al.*, 2020). All these lead to diamagnetic low spin arrangement of platinum metals. Other than forming the standard sigma-bonding with regular ligands like H_2O , halides, nitrogen and sulphur donor ligands, they likewise readily form a broad spectrum of pi-bonded structures (Shadap *et al.*, 2020). The transition elements have an unparalleled tendency to form coordination compounds with Lewis bases, that is with groups which are able to donate an electron pair. These groups are called ligands. A ligand may be a neutral molecule such as NH_3 , or an ion such as Cl^- or CN^- .

The reason transition elements are good at forming complexes is that they have small, highly charged ions and have vacant or partially filled low energy d-orbitals to accept lone pairs of electrons donated by other groups or ligands (Dezhi Wang, Liu, Wang, *et al.*, 2018). Some metal ions form their most stable complexes with ligands in which the donor atoms are N, O or F. Such metal ions include Group 1 and 2 elements, the first half of the transition elements, the lanthanides and actinides, and the *p*-block elements (Gichumbi & Friedrich, 2018).

These metals are called class-a acceptors, and correspond to 'hard' acids. In contrast the metals Rh, Ir, Pd, Pt, Ag, Au and Hg form their most stable complexes with the heavier elements of Groups V,

VI and VII. These metals are called class-b acceptors, and correspond to 'soft' acids (Mohite *et al.*, 2017). The principle of hard or soft is attributed to the rigidity of the electron cloud surrounding a particular element. A tightly held electron cloud have low polarizability and this makes the element to be classified as hard. Elements with easily polarizable electron cloud are classified as “soft”. Preferred interactions are soft-soft or hard-hard whereby soft metals prefers coordinating to soft donors and vice versa.

The rest of the transition metals, and the heaviest elements in the p-block, form complexes with both types of donors, and are thus 'intermediate' in nature (Nicholls, 2017).

1.1.1 Chemistry of Ruthenium

(Atomic symbol, Ru; Atomic number, 44; Atomic weight, 101.1; Electronic configuration [Kr] 4d⁷5s¹). Ruthenium's capacity to adopt a broad range of oxidation modes (from -2 to +8) and spatial configurations offer special catalytic possibilities and has proven to be valuable for a number of single-electron transfer applications (Hayashi *et al.*, 2020; Medina & Pinter, 2020). The element's most stable oxidation state is +2 and +3. Both of the oxidation states are chemically inert, although +3 state is more inert to a greater degree.

Because of their low ligand substitution kinetics resembling those of the processes that take place inside the cells, together with the metal's capacity to imitate iron in coordinating to particular biological ligands, ruthenium complexes are ideal for use in biological tests (Kanaoujiya *et al.*, 2020; Turan & Buldurun, 2018). One of the important qualities is that the redox ranges of Ru(II), Ru(III) and Ru(IV) are attainable under biochemical environments, with reductants such as glutathione and ascorbate able to reduce Ru(III) and Ru(IV) and Ru(II) oxidation easily caused by molecular oxygen or cytochrome oxidase (R. F. Lee *et al.*, 2017).

Ruthenium red, a cytological stain with the formula [(NH₃)₅Ru-O-Ru(NH₃)₄-O-Ru(NH₃)₅]⁶⁺ was the first ruthenium complex to be used in biology (Trondl *et al.*, 2014). Ever since, several medicinal properties of ruthenium have been uncovered which include antimalarial, antimicrobial, and anti-tumor properties (Kanaoujiya *et al.*, 2020; Smitten *et al.*, 2020; Turan & Buldurun, 2018).

Organometallic ruthenium compounds are most widespread in lower oxidation states and include ligands varying from arenes, allyls, and cyclopentadienyls to carbonyl, nitrido, and cyano groupings (P. Kumar *et al.*, 2014). They occur as mono-or bis-arene complexes, typically both in zero or + 2

oxidation state (P. Kumar *et al.*, 2014). Mono-arene compounds of ruthenium (II) are classified as 'half-sandwich' complexes with a quasi-octahedral 'piano-stool' shape.

As a consequence of the importance in this category of compounds as chemotherapy candidates, detailed research into the impact of differing arene and X, Y, and Z groups on the characteristics of the compounds demonstrates the degree to which exchange rates, configurations, electrochemical behaviour solution chemistry, and biochemistry rely on the ligands. The solution chemistry of Ru compounds is generally reliant on the ligands concerned and are significant in terms of tuning the compounds for medical applications (Sarı *et al.*, 2020).

Ru(II) mono-arene complexes containing three non-equivalent ligands are chiral with a metal stereogenic center (Rao *et al.*, 2013). This finds use in practical applications as non-symmetric catalysts for a wide spectrum of applications, namely hydrogenation of alkenes, Diels-Alder processes and metathesis of alkenes (Castarlenas *et al.*, 2005). Bis-arene Ru(II) sandwich structure of the form shown in the **Figure 1** below, may be synthesized from the right chloride-bridged dimer, $[(\eta^6\text{-arene})\text{MCl}_2]_2$ (M= Ru), by reacting with silver salt in acetone (to eliminate bonded chloride molecules) providing a mono-arene acetone precursor (Mukherjee, 2015).

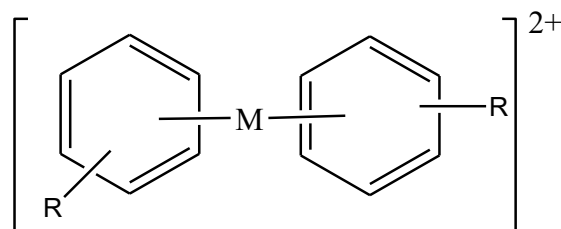


Figure 1 The general chemical structure of a metal bis-arene complex (M = Ru).

Mono-arene complexes of ruthenium featuring bioactive molecules are most commonly known for amino acids and peptides where metal interaction is through functional σ -bonded donor groups (Ramadevi *et al.*, 2017). Bis-arene complexes are less popular and notably, no pharmacologically active ligand complexes of Ru(III) bis-arenes are documented (Mukherjee, 2015). Nonetheless there have been a number of examples of ruthenium, notably compounds of both the essential amino acid phenylalanine and dopamine complexes (Wolff & Sheldrick, 1997), a neurochemical essential in controlling several internal pathways as indicated in the **Figure 2** below.

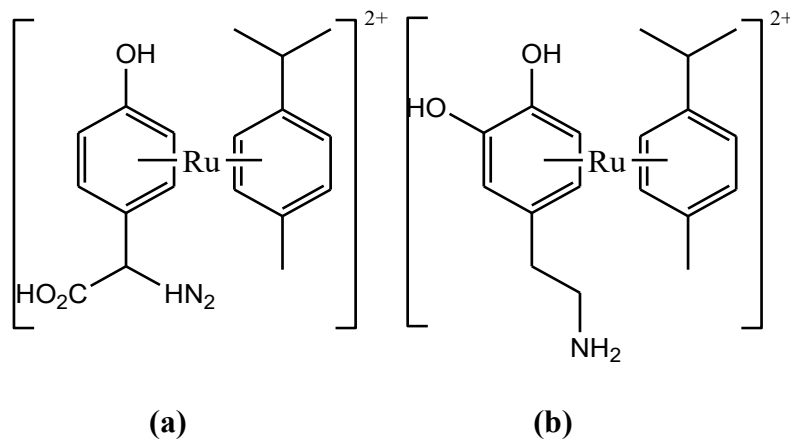


Figure 2 The chemical structures of $[(\eta^6\text{-p-cymene}) \text{Ru}(\eta^6\text{-phenylalanine})]^{2+}$ (a) and $[(\eta^6\text{-p-cymene}) \text{Ru}(\eta^6\text{-H-dopamine})]^{2+}$ (b).

1.1.2 Osmium

(Atomic symbol Os, Atomic number 76, Atomic weight 190.2 g mol⁻¹, Electronic configuration [Xe]4f¹⁴5d⁶6s²),

Transition elements in the third row are typically more inert compared to the second and first row, and in accordance with this, osmium is less reactive compared to ruthenium, with reported ligand exchange rates of about 105 times less (Mukherjee, 2015). Osmium appears in a broader range of oxidation conditions compared to ruthenium (-2 to +8 vs 0 to +8). Osmium is quite comparable in size to ruthenium owing to the lanthanide contraction, but because of its location in the third row, the outer 5d orbital shells are more de-shielded and therefore prone to the electronic influence of complexing ligands. the large percentage of Osmium complexes are octahedral and low spin in nature (Q.-Q. Su *et al.*, 2020).

Reported pharmaceutical uses for osmium compounds are rare because they are not usually considered clinically important and can be extremely toxic in some forms (Meier-Menches *et al.*, 2018). Nonetheless, there are few reports of osmium compounds which have been utilized in the treatment of rheumatoid arthritis in animals and some neutral complexes of Os (III) and Os (IV) have been documented as agents with anticancer activity (Novakova *et al.*, 2003). Furthermore, there are reports on osmium compounds showing trypanocidal activity against *Trypanosoma brucei* (Velásquez *et al.*, 2016).

1.1.3 Rhodium

(Atomic symbol Rh, Atomic number 45, Atomic weight g mol^{-1} 102.90550, Electronic configuration $[\text{Kr}] 4d^8 5s^1$).

Among the platinum metal group triad, rhodium finds the most varied applications owing to its various characteristics. For one, it is stable in air and moisture by up to 600°C and remains unchanged by a range of corrosives (Pu *et al.*, 2018). Rhodium is mainly used as an alloy component with platinum. A 10 per cent rhodium-platinum alloy is used among other things, in thermocouples and in the oxidation of ammonia (Lauster & Stegmaier, 2011). Motor vehicle exhaust catalytic converters utilize a rhodium-platinum alloy for the reduction of NO_x gases (Fernandez, 2017). Rhodium is also used in dental alloys where a small quantity is mixed with indium or ruthenium to create a fine-grained coating (Shirakawa *et al.*, 2017).

The most common oxidation states for rhodium are +1 and +3. The 1 and 0 oxidation states exist mostly in carbonyls including clusters and nitrosyls, the +2 states mostly in carboxylates, and the +4, +5 and +6 states principally as fluorides. Rhodium (I) is a d^8 structure and just like platinum, occurs mainly as square planar geometry, but some five-coordinate geometries are known to exist (Fuchigami *et al.*, 2017).

The square planar geometry is widely utilized in catalytic functions, because the metal center can coordinate with extra ligands along the dz^2 direction and increase its coordination number. In the +3-oxidation state with d_6 electron configuration, the configuration of rhodium is octahedral. The UV-Vis spectra of rhodium (III) compounds shows two absorption bands towards the blue end of the scale, though in many situations just the first spin enabled ligand-field absorption (${}^1T_{1g} \rightarrow {}^1A_{1g}$) is detected, as the second band is most often hidden by the CT transitions (Yang *et al.*, 2018).

Nitrogen donor from diimine ligands forming rhodium (III) octahedral compounds are of importance based on their ability to undergo two-electron redox processes which involves ligand detachment culminating in the formation of square planar structures of rhodium(I). This shift in coordination number from six to four frees coordination sites to bind substrates for catalysis. This has been used to perform the electrocatalytic production of methanol from carbon monoxide (Kang *et al.*, 2017).

Moreover, these complexes are of importance as they have been applied in the photochemical reduction of water to hydrogen (Kataoka *et al.*, 2010). Other useful complexes of rhodium (II) are

the tris-diimines and tris-dithiolates. The former displays a ligand-based π - π^* emissions at 77 K in frozen solution media but no emissions are exhibited at room temperature (Amarante *et al.*, 2005).

The coordination profiles of rhodium complexes with bio-ligands has attracted interest in recent years. An example is the binding profiles of Rhodium (II) acetate $[\text{Rh}_2(\text{O}_2\text{CCH}_3)_4]$ (**Figure 3** below), which is an anticancer complex, to plasmid DNA (Vekariya *et al.*, 2019).

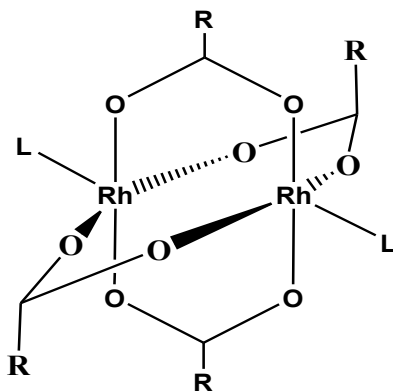


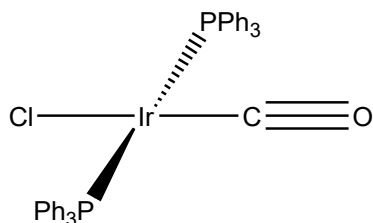
Figure 3 Structure of $[\text{Rh}_2(\text{O}_2\text{CCH}_3)_4]$. L= axial ligand; R= carbon chain of carboxylate groups.

1.1.4 Iridium

Atomic symbol Ir, Atomic number 77, Atomic weight g mol^{-1} 192.22, Electronic configuration $[\text{Xe}] 4f^{14} 5d^7 6s^2$.

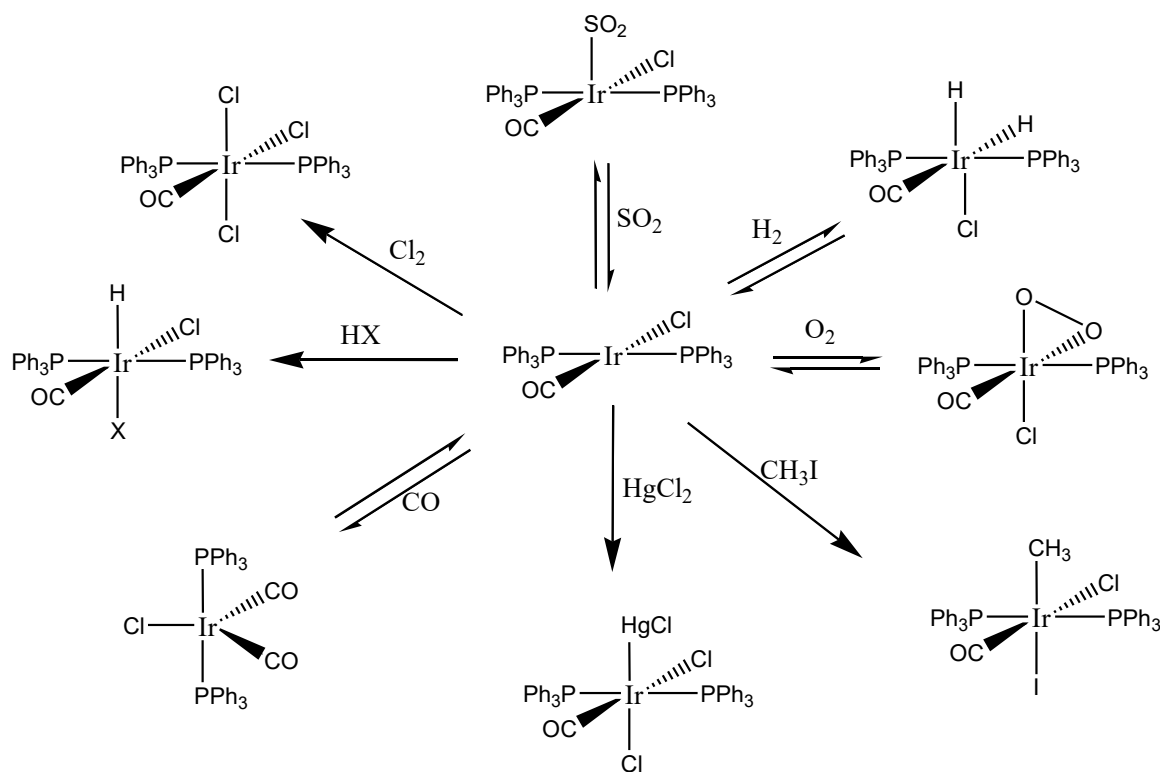
In organometallic and coordination complexes of iridium, the typical oxidation states are +1 and +3, while higher oxidation state complexes i.e. +4 and +5 are uncommon. The +3 oxidation state results in a $[\text{Xe}] 5d^6$ electronic arrangement. A d^6 electron arrangement for a 2nd or 3rd row metal ion is typically low-spin, indicating a pairing of electrons, resulting in diamagnetic compounds that are kinetically inactive (Nicholls, 2017). Ir(IV) and Ir(V) complexes are believed to be important intermediaries in the activation of the carbon-hydrogen bonds (Ryabov, 1990; Young *et al.*, 2007). The strong reactivity of the higher valency Iridium complexes and their reduced stability mostly hinder their isolation and characterization (Sharninghausen *et al.*, 2016; Shih & Ozerov, 2017).

Among the lower oxidation states organo-iridium complexes which harbours Ir–C bonds is the well-known Vaska's compound, $\text{IrCl}(\text{CO})[\text{P}(\text{C}_6\text{H}_5)_3]_2$, (**1** below) which is used in oxidation reactions.



1

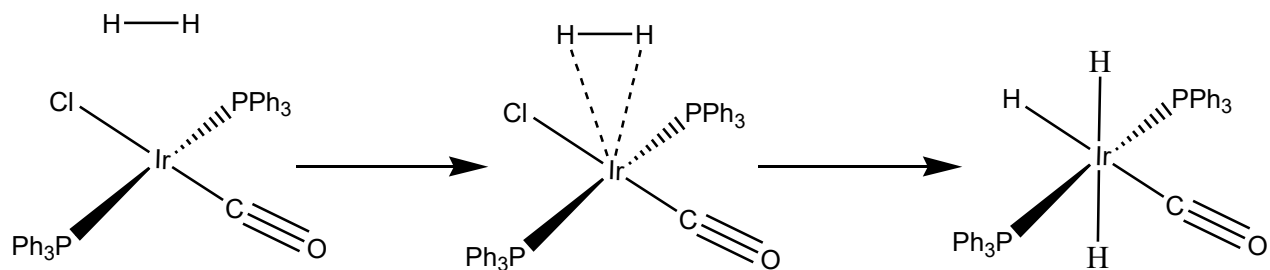
Vaska's compound is a 16-electron complex, and is "coordinatively unsaturated", therefore it can coordinate to one two-electron or two one-electron ligands through oxidative addition process to attain a stable 18-electron configuration (M.-D. Su & Chu, 2001). In these reactions, both the coordination number and oxidation state of the metal increase by two, as does the electron count. Typical reactions with the Vaska's compound are illustrated by **Scheme 1** below.



Scheme 1 Reactions with the Vaska's compound

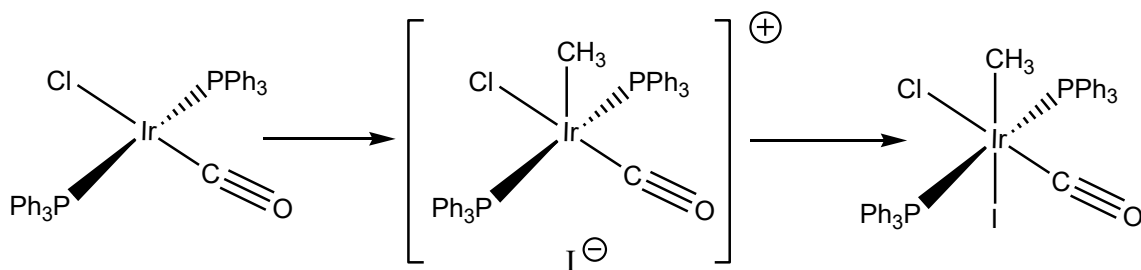
In some of the cases, the incoming molecule is attached without breaking up the integrity of the molecule concerned (*e.g.* O₂, SO₂).

In other cases, the concerted addition is followed by breaking up of the original molecule (*e.g.* H₂, Cl₂) (**Scheme 2**):



Scheme 2 Addition of Hydrogen to Vaska's Compound

The addition of methyl iodide proceeds by a S_N2 reaction with the slow step involving a five-coordinate cationic species (**Scheme 3**).



Scheme 3 addition of methyl iodide to Vaska's compound proceeds by a S_N2 type reaction

The changes are accompanied by a shift in the position of the CO stretching frequency in the IR spectrum. The shift occurs because bonding in carbonyl compounds involves both CO-to-metal σ -donation and metal-to-ligand π -backbonding, where electron density goes from filled metal d -orbitals into empty π antibonding ligand orbitals as shown in **Figure 4** below.

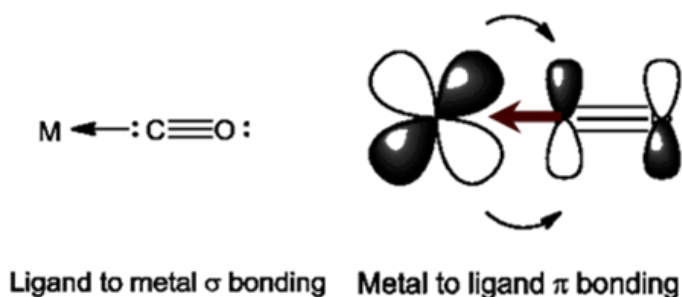


Figure 4 pi-backbonding in carbonyls

As the oxidation state of iridium increases, there are fewer d electrons available for backbonding, thus the CO bond becomes stronger and the value of ν_{CO} increases. So when one molecule of CO adds to form $[\text{IrCl}(\text{CO})_2(\text{PPh}_3)_2]$, the compound is still Ir(I) and the average CO stretching frequency

is hardly changed, but when one molecule of Cl₂ in the form of two chloro (Cl-) ligands is added forming the Ir(III) compound [IrCl₃(CO)(PPh₃)₂], there is a shift in ν_{CO} of over 100 cm⁻¹ (Durango-García *et al.*, 2016; Huber *et al.*, 2012; Rausch & Moser, 1974).

1.1.5 Palladium

Despite the fact that palladium can exist in various diverse oxidation states, important organic synthesis strategies are mainly achieved by the utilization of Pd (0) and Pd(II) oxidation states (P. B. White *et al.*, 2016), in spite of the fact that the utility of Pd (IV) has been relentlessly developing in its very own right (Canty *et al.*, 2015). There are generally scarcely any known complexes with palladium exclusively in the +3-oxidation state, however such complexes have been proposed as intermediates in numerous palladium-catalyzed cross-coupling reactions (Ghotbinejad *et al.*, 2014).

In 2002, palladium (VI) was first revealed (Aullón *et al.*, 2002). The observed stability of the even-numbered oxidation states (e.g., 0, +2, +4) can be justified by the low propensity of palladium to undergo one-electron transfer processes as opposed to a two-electron redox process (Camasso *et al.*, 2017). Processes like cross-coupling reactions and olefin hydrogenation are normally common to the Pd(0) state (L. Li *et al.*, 2015), while other reactions, for example, liquor oxidation and cycloisomerization can be accomplished utilizing Pd(II) (Hamasaki *et al.*, 2016).

Generally, Palladium prefers low oxidation states. The pioneering stable organopalladium complexes with this +4 stable oxidation state, Pd(IV)(C₈F₅)₂Cl₂(L-L) (L-L = bidentate ligands), were synthesized in 1975; at which time, alkylpalladium (IV) species were likewise synthesized (Murahashi & Kurosawa, 2002). Nonetheless, an organopalladium compound with a formal oxidation state surpassing +4 has never been isolated. It has been proposed that the highly electronegative fluorine ligands supposedly can produce +5 and +6 oxidation states in inorganic Pd complexes, but such species are not stable and have not been well characterized (Ibáñez *et al.*, 2014).

Reactions of elemental palladium with chlorine affords Palladium(II) chloride; it dissolves in nitric acid and precipitates Palladium(II) acetate upon addition of acetic acid. These two complexes and the palladium bromide are inexpensive, reacts easily and are readily available making them important precursors in palladium reactions. The chloride and bromide generally should be refluxed in acetonitrile to get the more reactive acetonitrile complex monomers.

Palladium(II) chloride is the chief precursor material for some other palladium catalysts. It is utilized to get ready heterogeneous palladium catalysts: palladium on barium sulfate, palladium on carbon,

and palladium chloride on carbon. It reacts with triphenylphosphine to give bis(triphenylphosphine) Palladium(II) dichloride, which is a useful catalyst. The other major palladium (0) compound, $(\text{Pd}_2(\text{dba})_3)$, is produced by the reduction of sodium tetrachloropalladate in presence of dibenzylidene acetone (Crabtree, 2009). $\text{Pd}(\text{cod})\text{Cl}_2$ is produced easily by the reaction of PdCl_2 with 1,5-cyclooctadiene under mild conditions.

The group of reactions wherein palladium complexes are used as catalysts are in general referred to as palladium-catalyzed coupling reactions. These includes the Heck coupling reaction (chemical reaction of an unsaturated halide with an alkene in the presence of a base and a palladium catalyst to form a substituted alkene) (Mpungose *et al.*, 2018), Suzuki coupling reaction (an organic reaction, classified as a cross-coupling reaction, where the coupling partners are a boronic acid and an organohalide catalyzed by a palladium complex) (Wolfson & Levy-Ontman, 2020) and Stille coupling reaction (palladium-catalyzed coupling reactions involving the coupling of two organic groups, one of which is carried as an organotin compound.

A variety of organic electrophiles provides the other coupling partner) (Lautens & Sanichar, 2020). Palladium(II) acetate, $(\text{Pd}(\text{PPh}_3)_4)$, $\text{Pd}_2(\text{dba})_3$, $\text{Pd}(\text{cod})\text{Cl}_2$ are valuable in this respect, either as catalysts or as starter precursors.

1.1.6 Platinum

Both +2 and +4 oxidation states in case of platinum are numerous and comprise of earlier as well as recent research in platinum chemistry. Platinum has a strong tendency to form square planar complexes. The kinetically inert Platinum(II) compounds have prompted their broad use in investigations of geometrical isomerism and reaction pathways. In the divalent state, platinum shows the class-b character for preference of CN^- and ligands with nitrogen donor atoms instead of oxygen or fluorine (Aguilera & Carolina, 2017; Henderson, 1986).

The organometallic chemistry of platinum metal is rich and diverse especially the ones that include unsaturated hydrocarbons which are the most common. Cis-diamminedichloroplatinum(II), or cisplatin, is an effective antitumor agent that has been utilized in cancer therapy from as early as 1978 (Kelland, 2007). The success with this simple coordination complex gave rise to the second-generation platinum drugs carboplatin and oxaliplatin. These three Platinum(II) drugs are known to work by a common reaction mechanism; that is, aquation of the leaving moieties (S. Ahmad, 2017); chloride for cisplatin and carboxylate and oxalate for carboplatin and oxaliplatin, produces reactive

cis diammineplatinum cations, which bind promptly with the purine nucleobases in DNA (Shtemenko *et al.*, 2015).

These interactions and structural modifications in DNA instigated by platinum complexes trigger different cell reactions that consequently lead to apoptosis (Todd & Lippard, 2010). Despite the clinical effectiveness of these products, the intravenous administration requirement and related long-term harmful side effects impair patient health. Platinum anticancer compounds in the 4+ state of oxidation have indicated great potential both for oral ingestion and for systemic toxicity reduction (M. D. Hall *et al.*, 2007).

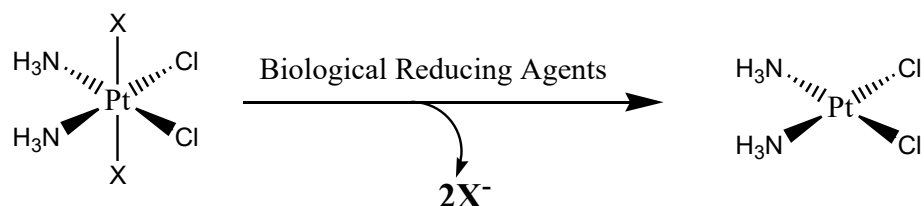
The most important feature in mitigating the adverse effects of cisplatin has been the advancement of analogs, i.e. the quest for cisplatin structural analogs that meet one or all of the following criteria:

- i. New selectivity advancement, including a broader activity range than cisplatin and, in general, show reactivity towards cisplatin-resistant tumours.
- ii. Enhancement of the curative index, i.e., a greater clinical efficacy to minimize toxic effects, with activity-range at least within the same spectrum as cisplatin.
- iii. Improvements in biochemical characteristics, like those of solubility, which might lead to improvements in administration.

Due to their low-spin d^6 electronic structure, the enhanced stability of these complexes results in their longevity in the gastrointestinal tract's acidic environment prior to assimilation into the bloodstream (Höfer *et al.*, 2017). They work by a process identical to that of first- and second-generation Platinum(II) analogs, but an activation stage involving the reduction from platinum (IV) to Platinum(II), must take place prior to aquation and DNA binding.

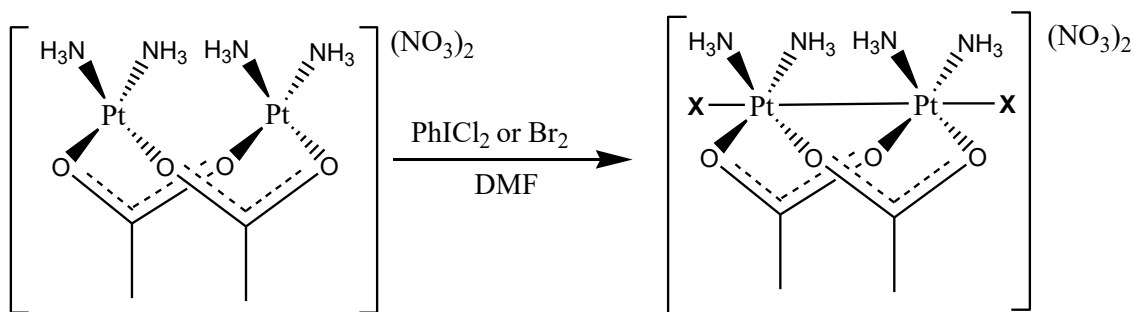
Together with their kinetically stable profiles, the presence of two extra binding locations that can be changed to modify their pharmacological characteristics is also a beneficial feature of the platinum (IV) compounds compared to their Platinum(II) equivalents (Bai *et al.*, 2017). By changing the two axial moieties (**Scheme 4**), one can change the platinum (IV) complex's electrochemical characteristics and hydrophobicity (Mukherjee, 2015), keeping the DNA-binding cisdiammineplatinum unit unaltered. In addition, the axial coordinating regions function as receptor locations for other bioactive molecules that may have synergetic effects with platinum treatment (Reithofer *et al.*, 2008).

A further benefit is the capability to attach platinum (IV) compounds to different nanodelivery systems through the axial groups for improved cellular absorption and selectivity (Almotairy *et al.*, 2017; Wilson & Lippard, 2011). Most recently examined platinum compounds (IV or II) carry either chloro, hydroxo, or axial carboxylate ligands (Johnstone & Lippard, 2013). Developing new synthesis techniques to reach the platinum ion manifold will extend the scope of structures with new properties.



Scheme 4 Activation step of cis-platin formation.

Due to their promising chemical properties, the focus in dinuclear platinum (III) compounds is growing steadily. These consists of a single metal-metal bond that is supported by two or four connecting groups (Vezzu *et al.*, 2014). Connecting ligands normally form five-member rings consisting of two platinum centers and a collection of three atoms creating an effective bite (**Scheme 5**), e.g. NCO (such as pyrimidine nucleotides), NCS, NCN, SCS, OXO (X= C, S, P) or PXP (X= O, C) (Cornacchia *et al.*, 2009; Wilson & Lippard, 2012).



Scheme 5 Nitrate salts of halide-capped platinum (IV) dimers.

Platinum's organometallic chemistry has been investigated in depth. It has significant historical importance and has offered a framework for understanding numerous catalytic pathways (Canovese *et al.*, 2016). Platinum(II) or platinum (IV) ligand displacement reactions are slower compared to their analogous palladium compounds (Rudakov & Shul'pin, 2015).

The ligand transfer properties of Pt complexes are generally determined by the nature of the leaving ligand but the properties of the non-leaving moieties also affect the reactivity of complexes. Steric bulk crowding and hydrogen-bonding potential of the ligands are essential determinants in their efficacy (F. Liu *et al.*, 2015). The amines can serve as hydrogen donor to the O-6 atom of a guanine and to a 5' phosphate group in DNA, thereby giving stable Pt-Guanine bonds. These relationships are essential for the thermodynamics (by stabilizing the Platinum- 2'-deoxy[5'-phosphate-guanyl- (3'-5')-phosphate-guanosine] (Pt-d(pGpG)) adduct) as well as for the kinetics of the reaction (by moving the Pt compound to the N7 of guanine).

1.2 Cancer

Cancer is the second leading cause of death globally, with an estimated 1 in 6 deaths, and is responsible for an estimated 9.6 million deaths in 2018 (Ferlay *et al.*, 2019). It is estimated that approximately 70% of all deaths are cancer-related and occur in low and middle-income countries (Ferlay *et al.*, 2019). The economic impact of cancer is significant and is increasing with a total annual economic cost of cancer in 2010 estimated at approximately US\$ 1.16 trillion. Only 1 in 5 low- and middle-income countries have the necessary data to drive cancer policy (Ferlay *et al.*, 2019).

Cancer is a classification of infections where a collection of cells suffers from unrestrained growth, with invasion and damage to neighbouring tissues, sometimes spreading to other sites in the body via lymph or blood (Bhunchu & Rojsitthisak, 2014). Most cancers form tumours but some, like leukaemia, do not. The disease is now recognized worldwide as one of the principal non-communicable diseases (Naanyu *et al.*, 2015).

Locally in Kenya, cancer positions at the third place as the cause of demise second to infectious and cardiovascular diseases. It causes 7 percent of entire nationwide mortality per year. More than 60 percent of the affected population are people under the age of seventy years. The risk of getting cancer in Kenya prior to age 75 years is estimated at 14% whereas the risk of one dying from the disease is estimated to be 12% (Topazian *et al.*, 2016).

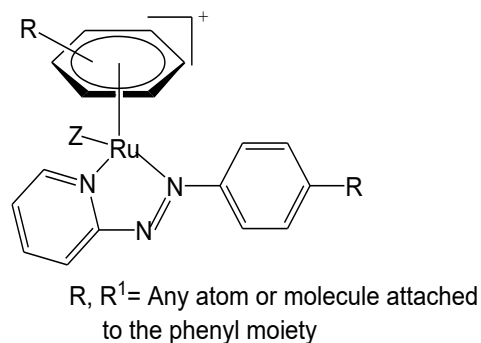
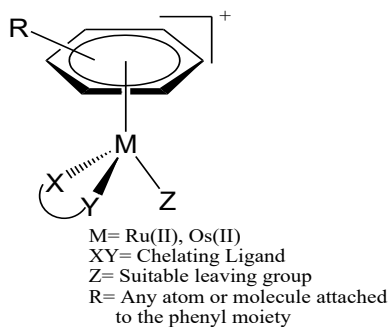
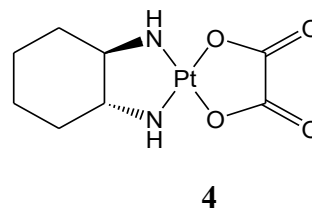
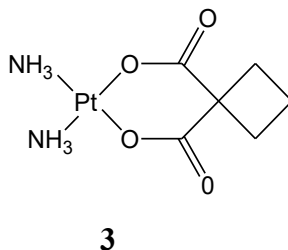
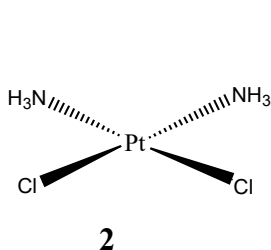
The most practiced efforts to combat cancer include surgery, chemotherapy using chemical drugs, and radiotherapy using electromagnetic radiation like x-rays to kill cancerous cells. New strategies like gene therapy are still being developed where genes from donors are inserted into the DNA of a patient to boost recognition of cancerous cells by the body's disease-fighting mechanisms. Some of

the most successful chemotherapeutic drugs include those derived from metals like platinum, ruthenium, titanium and palladium, among others.

1.3 Organometallic Complexes in Cancer Therapy: Targeting DNA

Organometallic pharmaceuticals are part of coordination complexes. Bio organometallics is an area that integrates the use of organometallic compounds in physiological useful roles that includes bio imaging, bio-sensors, bio probes, and catalysis in physiologically relevant processes, synthesis in biological processes, immunoassays, and as direct drug compounds or diagnostic mediators (Alderden *et al.*, 2006; Zaki *et al.*, 2019).

Examples of coordination complexes currently in use for cancer treatment include *cisplatin* (**2**), carboplatin (**3**), oxaliplatin (**4**), Ruthenium and Osmium ‘piano-stool’ arene complexes (**5**) and ruthenium azopyridine complexes (**6**).



Of these, *cisplatin* is the most effective and most widely used, and therefore, most research work into cancer therapy uses *cisplatin* as a reference. On the other hand, *trans* platin which is the geometrical isomer to *cisplatin* is not antitumor active (Goodsell, 2006; Najjar *et al.*, 2017). The reason behind this can be explained in terms of *trans* effect which is the labilizing influence a coordinated ligand has on a ligand(s) diagonally opposite to it in a metal complex. *Trans* platin

hydrolyses approximately 4 times faster compared to *cis*platin due to the greater *trans* influence of -Cl ligands compared to -NH₃ ligands. Its reaction with ammonia is reported to be about 30 times quicker, and after incubating it for 4h using red blood cells, it's found to complex with about 70% of glutathione, while for *cis* platin the complexation is only about 35% (Alderden *et al.*, 2006).

The other reason associated with the dissimilar profiles in the activity of the two coordination isomers is the mode of binding to DNA. *Trans* platin does not produce 1,2-intrastrand DNA adducts and, the 1,3-intrastrand and 1,2-interstrand adducts produced by *trans* platin are repaired more readily (Nafisi & Norouzi, 2009; Yuanyuan Wang *et al.*, 2017). Organometallic compounds play key roles as antitumor agents, by the induction of apoptosis, a physiological programmed cell death (Gao *et al.*, 2017). In apoptosis, the cellular processes recognize defective DNA in cells and these cells are targeted for elimination by the body. Inorganic metal compounds damage cancer cells by processes facilitated by the initiation of numerous signal transduction mechanisms.

These inhibit DNA replication and repair, thereby inducing apoptosis (Desoize & Madoulet, 2002). The drug, therefore, does not 'kill' the cells by necrosis (toxicity) but by simply damaging the cell's DNA, making that particular cell to be targeted for elimination. This is the preferred mechanism for antitumor drugs since DNA replication is vital to the progression of cancer.

They affect mitosis, and therefore they are quite effective on fast-dividing cells such as tumor cells. Moreover, other fast-dividing cells like the ones responsible for hair growth, in the replacement of the intestinal lining, or in the manufacture of white blood cells get affected too (Jordan, 2003).

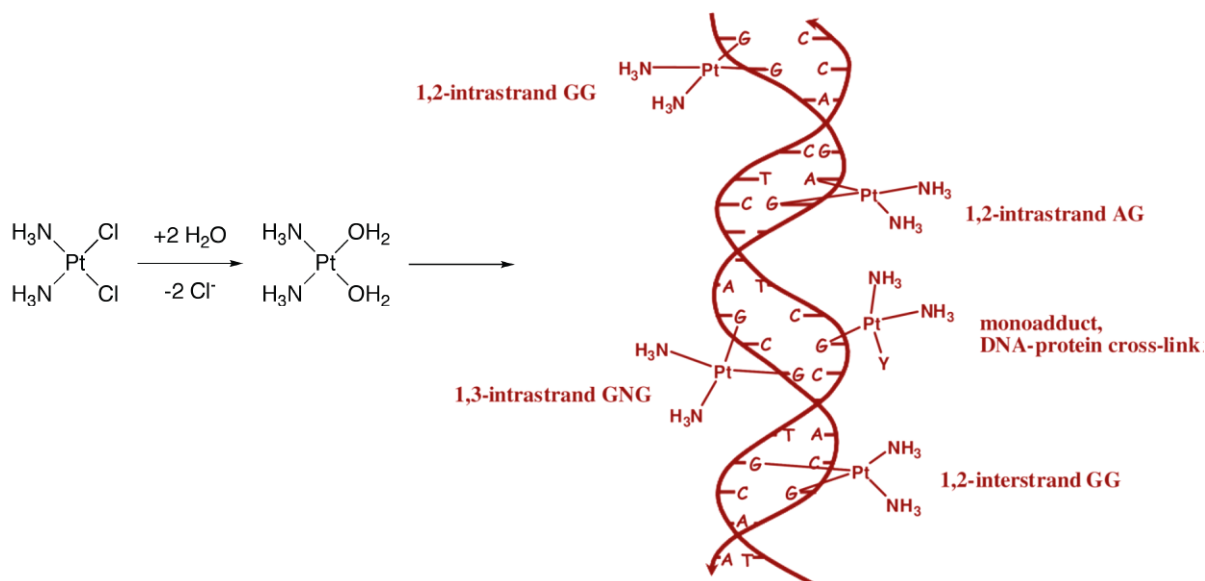
However, most promising antitumor complexes like *cis*platin still face the challenges of bio-availability due to low solubility (Karimian & Aghajani, 2019; Scalbert & Williamson, 2000). They also exhibit dose-dependent cytotoxicity since high amounts are used in a bid to reach target tumor cells. Their hydrophobicity is due to the absence of leaving groups or free electrons, and the presence of benzene rings which are highly hydrophobic. This makes their solubility in physiological media and distribution in the body challenging. One approach to address this problem is to derivatize these compounds with groups which conder solubility like -COOH or synthesize them as their metal salts. Another approach is to encapsulate the compounds into soluble matrices like cyclodextrins.

Metal-containing complexes offer exceptional flexibility in pharmaceutical chemistry due to diverse building units from which they can be fashioned, the variety of available interactions, ligand exchange kinetics during bonding with biomolecules, and due to their reduction-oxidation

characteristics (Burmakina *et al.*, 2017; Vessieres *et al.*, 2005). The discovery of the antitumor properties of the coordination metal complex cisplatin by Rosenberg and his co-workers stirred up awareness in medicinal metal complexes (Rosenberg *et al.*, 1965).

This discovery came along with clearer understanding of how to control new kinds of metal bonding, enabling the discovery of a wide variety of novel complexes (E. Wong & Giandomenico, 1999). In cisplatin, chloride ligands (ions) are displaced from the complex and they diffuse inside the cell permitting the complex to cross-link with 1,2-‘G-G’ and 1,2-‘A-G’ intra strand guanosine or adenosine groups of DNA strands.

As shown in **Scheme 6** below, the anti-cancer characteristics of cis-platin are accredited to the kinetics of its chloride ligand disarticulation reactions which lead to DNA cross-linking triggering DNA twisting and thereby disturbing DNA replication, transcription and other nuclear roles, and thereby checking cancer cell spread and tumor progress (Zhou *et al.*, 2018). Intra-strand cross-links to guanine-guanine (G-G) and to adenine-guanine (A-G) are the most common types in cisplatin-damaged DNA. Due to this reaction on the DNA, CDDP is strongly mutagenic and carcinogenic, both under in-vitro and in-vivo study experiments (Ballestreri *et al.*, 2018).



Scheme 6 Cisplatin aquation and DNA adduct formation on guanidine residues

The main disadvantages of organometallic compounds when considering their formulation are poor hydro solubility and hydrolytic instability, where the compounds are either insoluble or decomposes

in physiological media (Jurgens *et al.*, 2018). Solutions to these problems come from synthetically modifying the structure or finding new formulations with enhanced pharmacokinetic and pharmacodynamic properties.

This suggests the need to stabilize them through coordination to a strongly binding nitrogen donor and appropriate labile ligands (Conrad *et al.*, 2005). It has been found that when the leaving group consists of a relatively non-labile ligand, the compound can retain its structural integrity in physiological media for enough time to perform significant roles *in vivo* (Conrad *et al.*, 2005).

Most anticancer drugs have utilized either palladium or platinum in various oxidation states. Palladium and platinum metal centers were chosen for this work due to their prominence and wide literature reports on their use in similar anticancer studies. The similarities in the bonding profiles of the +2 oxidation states for these *d8* ions produces 16-electron low spin complexes with similar square planar geometry. However, the differences in their d-orbital energies, ligand substitution kinetics and effective nuclear charge affords interesting contrasts in the resulting compounds.

The +2 oxidation states for these square planar geometry produces complexes which are stable in solution and therefore suitable for physiological tests. The vacant orbital sites along the d_z^2 direction provides sites for binding to bioligands leading to the desired pharmacological response. The structures formed are also of the same square planar geometry to the common anticancer drug, cisplatin, making their biochemical characteristics to be compared and contrasted.

The nitrogen donor ligands were chosen since they are known to stabilize the +2 oxidation states for the *d8* Pd and Pt ions. The sulphur-donor ligands are also believed to confer selectivity to cancerous cells thereby reducing undesired side effects. The ligands chosen in this work had bulky groups which are known to shield the metal center from attack by bioligands, to an extent of controlling the ligand substitution and reactivity of these compounds. The bulky ligands also will mostly confer a *trans* geometry for the resulting complexes which would allow them to be compared with the *cis* counterparts.

The ligands were synthesized by refluxing a solution of pyrrole-2-carbaldehyde and the corresponding primary amine in 30mL dry methanol. The various ligands provided a wide variety of donor/ acceptor and steric properties which allowed for comparative studies on the effects of the ligands themselves and on the 10Dq splitting of the crystal field of the metal centers.

Although the Schiff base ligands are reported in literature for C-C coupling reactions (Layek *et al.*, 2017), their use in Pt or Pd complexes in anticancer studies has been limitedly studied particularly, the pyrrole based Schiff bases. In this regard, the ligands and their corresponding Pd (II) and Pt (II) complexes were synthesized and characterized followed by investigation of their DNA binding and anticancer activities.

The motivation behind this study was two-fold. Firstly, these complexes have square planar geometry analogous to the common anticancer drug, cisplatin, but bearing sterically bulky substituents around the metal center. This is a strategy reported in literature for prevention of axial approach to the metal atom from the z^2 -direction thus hindering the formation of a trigonal bipyramid intermediate, which leads to ligand substitution (Janssen-Müller *et al.*, 2017b).

In this way, the sterically bulky groups shield the labile ligands therefore reducing the rate of hydrolysis and substitution long enough for the complexes to bind to the desired target. Secondly, the trans-geometry complexes have not been widely explored as anticancer agents despite literature reports that they could exhibit cytotoxicity equivalent to or greater than that of cisplatin (Gaspari *et al.*, 2017; Popova *et al.*, 2017; B. Zhang *et al.*, 2017).

The complexes were synthesized under inert conditions at room temperature. Inert conditions were maintained during extraction and purification steps. The synthetic schemes were chosen since they appear in literature as standard methodology for this type of reactions.

1.4 Statement of the Problem

Activity problems in metal complexes emanating from challenges of stability, solubility and reactivity in terms of binding to DNA still remain a major challenge in anticancer drug development and therefore, seeking for new biologically active compounds for cancerous cells still remain an urgent requirement.

1.5 Aims and Objectives

1.5.1 Objectives of the Study

The Objectives of the Study was to synthesize Pd(II) and Pt(II) complexes with promising DNA binding profiles and study their anticancer activity.

1.5.2 Specific Objectives

The specific objectives were:

- i. Synthesize pyrrole and thiosemicarbazide Schiff base ligands.
- ii. Synthesize Pd(II) and Pt(II) complexes starting with the ligands synthesized in (i) above.
- iii. Determine the DNA binding modes for the complexes.
- iv. Evaluate the complexes *in vitro* anticancer activities.

1.6 Justification of the Study

Cancer is a major cause of deaths both locally and globally, contributing to disease and economic burden across the globe. Chemotherapy is a major approach used for fighting the disease due to the efficacy of the Pd(II) and Pt(II) complexes to various cancers. However, resistance and undesired side effects plague these therapeutic compounds and therefore coming up with effective compounds remains an active area for research. Studies on Palladium(II) compounds as non-platinum drugs have reported antitumor properties similar to *cisplatin*, while exhibiting less nephrotoxicity (Qin *et al.*, 2018). Derivatizing the pyrrole backbone using diverse pharmacophores has resulted in compounds with enhanced biological activities.

Effective cytotoxicity against breast cancer cell lines (MCF-7), normal breast cells (MCF-10A) and HT-29 colon cancer cell lines using a series of pyrrole-based complexes coupled with ferrocene has been reported (Pérez *et al.*, 2015). On the other hand, thiosemicarbazone ligands act as remarkably flexible multidentate ligands with ability to coordinate with many transition metals in various ways through covalent or dative type bonding (Selvamurugan *et al.*, 2017), where, as anticancer agents, the activity is shown to substantially increase for the complexed product as compared to the free ligand, and also, the undesirable cytotoxicity as side effects have been shown to be minimized in the complexes (Biswas *et al.*, 2017).

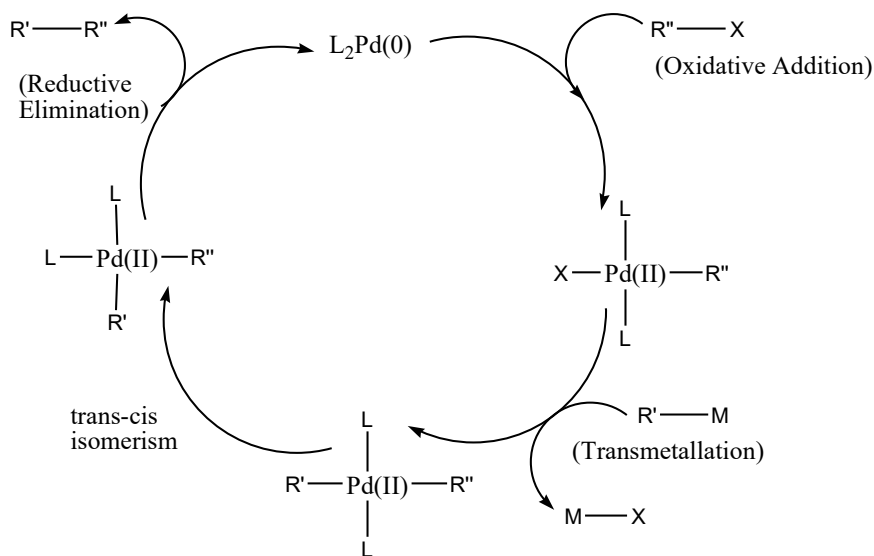
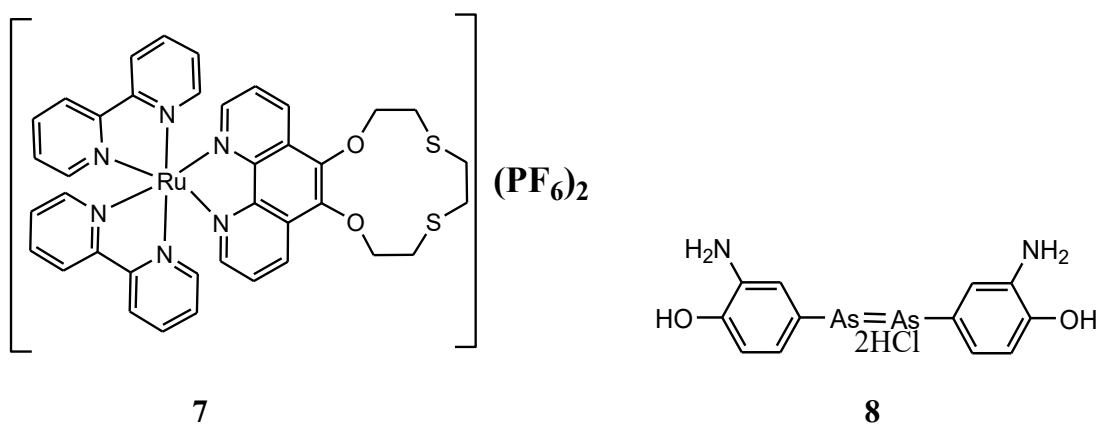
In line with the Millennium Development Goals (MDG's) and with Kenya's agenda four on affordable and better health care, this work aimed at contributing to research and development especially in the area of cancer drug development to address the gaps in effective compounds. Some of the Schiff base ligands in this study are reported in literature for C–C coupling reactions (Z. Chen *et al.*, 2012), but yet to be investigated in anticancer drug studies.

CHAPTER 2

LITERATURE REVIEW

2.1 Metal-Based Complexes

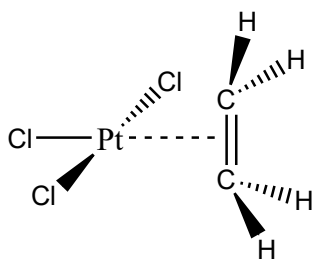
Metal-containing complexes (Werner and Organometallics) offer exceptional flexibility due to diverse building blocks from which they are fashioned. These include the variety of available interactions, ligand exchange kinetics arising from electronic and steric factors and trans effect/influence, and reduction-oxidation characteristics (Denny & Darensbourg, 2016). They offer economically relevant applications in various fields like chemosensors (**7**) (Odhiambo *et al.*, 2018), as therapeutic agents (**8**) (Rabiee, 2018) and, as C-C coupling catalysis (**Scheme 7**) (Hooshmand *et al.*, 2019).



Scheme 7 C-C Coupling using $Pd(0)$ catalyst

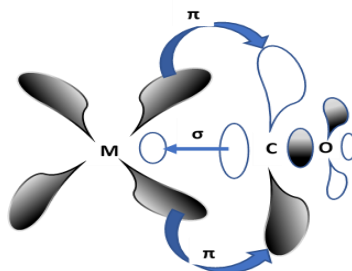
2.2 Bonding in Metal Complexes

Besides forming the usual sigma-bonded complexes with common ligands like H₂O, halides, nitrogen and sulphur donor ligands, transition metals are also capable of forming an extensive series of π -complexes (Walton & Wilkinson, 2018). This is a distinctive aspect of coordination chemistry where a wide variety of ligands containing π electron systems form bonds to metals. Common π ligands include both linear and cyclic hydrocarbons like ethylene or benzene respectively. One of the earliest organometallic compound is the platinum compound; Zeise's salt $[\text{Pt}(\eta^2\text{-C}_2\text{H}_4)\text{Cl}_3]^-$ (**9**), where ethylene acts as a side bound ligand with respect to the metal (L. Zhang, Tan, *et al.*, 2018).



9

This type of bonding is also observed in *cis*-Pd(cod)Cl₂ which is a common precursor in many synthetic procedures for palladium complexes. In this kind of bonding, the double bond donates electrons to a metal *d* orbital in a σ manner using its π bonding electron pair located in its highest occupied molecular orbital (HOMO). In a synergistic manner, the now electron rich metal can donate electron density back to the ligand's empty π^* orbitals of suitable orientation, specifically the d_{xy} symmetry orbitals which constitute the d_π orbitals in the crystal field. Similar bonding is observed in metal-carbonyl complexes where the carbon donates electrons to the metal center in a sigma manner and the now electron rich metal *d* orbitals donates back to π^* orbitals of CO as shown in **Scheme 8** below.



Scheme 8 Synergistic bonding in a pi complex

This is an example of synergistic effect of σ donation and π acceptance for these π -complexes. This type of bonding agrees with the measured C-C bond distances where the free ethylene has a C-C distance of 133.7pm while the corresponding C-C distance in Zeises's salt is 137.5pm (Hou *et al.*, 2012). This lengthening of bond distance is explained by a combination of the two factors involved in the synergistic σ donor- π acceptor nature of this bonds, i.e. donation to the metal in a σ manner which decreases the electron density in a filled π bonding orbital located in the ligand, thereby decreasing the C-C bond order. The other factor is the back-donation from the metal to the π^* orbital of the ligand which also weakens the C-C bond strength by populating this antibonding orbital. The net result is a weakened and hence lengthened of the C-C bond in the coordinated ligand (Love *et al.*, 1975).

Metal-based chemical complexes provide a wide flexibility and applicability in medicinal chemistry due to factors like rigidity around the metal center, diversity of the ligands which can be used, kinetics of ligand exchange and redox properties (Vessieres *et al.*, 2005). The first efficacious bio-active organometallic complex was the compound Salvarsan used against syphilis (Rabiee, 2018). The discovery of the antitumor properties of the coordination metal complex *cisplatin* by Rosenberg and co-workers which showed highly toxic effects on cancer cells was another major breakthrough in medicinal chemistry of metal complexes (Cassells *et al.*, 2018)

2.3 The Trans Influence/ Effect

In transition metal complexes of square planar geometry, some ligands are found to direct reactions in preference to *trans* substitution to themselves, an aspect called the *trans* effect (Rezabal *et al.*, 2017). The *trans* effect is explained as the influence of a bound ligand on the rate of substitution of a ligand(s) diagonally opposite to it in a metal complex.

Both thermodynamics and kinetics provide the basis for this tendency. When the reaction is controlled mainly by forces influencing the ground state energy of the complex, the *trans* effect is termed as the *trans* influence (Gregson *et al.*, 2017), whereas the kinetic *trans* effect is related to reactions in which forces influencing the transition state energy govern the final result outcome.

Ligands that coordinate strongly through σ bonds, e.g. hydrides and alkyls, or π acceptor ligands, e.g. cyanide (CN⁻), carbonyl (CO), and phosphines (PR₃), forming strong bonds with the metal, are found to weaken the metal-ligand bond *trans* to themselves. In an isolated complex, this is a thermodynamic factor termed as the *trans* influence. This has been shown by studies of platinum compounds of square planar geometry (Kirlikovali *et al.*, 2016). Using IR studies, these

investigations indicate that a substituent with a strong *trans* influence causes, in the IR region, a lowering of the M-L stretching frequency for the ligand *trans* to it (an indication of a weakened M-L bond) (Dimmer *et al.*, 2009).

Similar studies have been carried out using NMR investigations to measure the coupling constants, $J_{\text{Pt-P}}$, for square planar platinum(II) complexes (Greif *et al.*, 2015). Trialkyl phosphine ligands have been shown to have a higher *trans* influence compared to Cl, which is reflected in the greater coupling constant ($J_{\text{Pt-P}}$) when Cl is *trans* to the phosphine. The methyl group on the other hand, has higher *trans* influence than Cl, as reflected in the small $J_{\text{Pt-P}}$ of 1719 Hz when methyl is *trans* to the phosphine, and a $J_{\text{Pt-P}}$ equal to 4179 Hz when phosphine is *trans* to Cl (Hartley, 1973).

Since the methyl group is a strong σ bonding ligand, it causes the σ bonding character of the Pt—P bond to decrease, thus decreasing the coupling constant. Phosphines in general have a high *trans* influence because they exert both strong σ donation and π acceptance from the metal, thereby weakening the bond *trans* to the phosphine. Ligands that have a strong σ electron donating ability are listed in approximate descending order of their effect (Hartley, 1973).

$\text{H}^+ > \text{PR}_3 > \text{SCN}^- > \text{I}^-, \text{CH}_3^-, \text{CO}, \text{CN}^- > \text{Br}^- > \text{Cl}^- > \text{NH}_3 > \text{OH}^-$

2.4 Kinetic *trans* Effect

The tendency of certain ligands to direct incoming groups to the *trans* position also occurs with reactions under kinetic control. This case is known as the kinetic *trans* effect, whereby the influence of the ligand *trans* to the incoming one is felt due to the difference in energy between the ground state and the *transition* state in the rate-determining step. The σ donation effects are important, as well as the effect of π donation from the metal to the ligand. When a ligand forms strong π acceptor bonds with platinum, for instance, charge is removed from the metal.

The effect on the energy of the ground state is relatively small, but it is significant on the *transition*-state energy because, during ligand substitution of a square planar Pt complex, we usually expect an increase in coordination to trigonal bipyramidal geometry in the *transition* state. A π bonding ligand originally present in the substrate (the complex undergoing substitution) can contribute to stabilizing the *transition* state via the d_{xz} orbital from the metal. Overall, this effect increases the rate of reaction *trans* to the strong π acceptor ligand. The order of π bonding effects for various ligands is as follows (Hartley, 1973).

$\text{C}_2\text{H}_4, \text{CO} > \text{CN}^- > \text{NO}_2^- > \text{SCN}^- > \text{I}^- > \text{Br}^- > \text{Cl}^- > \text{NH}_3 > \text{OH}^-$

When σ donation and π acceptance effects are combined, the overall *trans* effect list is as follows (Hartley, 1973).

CO, CN⁻, NO₂⁻, C₂H₄, > PR₃, H⁻ > CH₃⁻, S=C(NH₂)₂ > Ph⁻ > NO₂⁻, SCN⁻, I⁻ > Br⁻ > Cl⁻ > Py, NH₃, OH⁻, H₂O

Ligands highest in the series are strong π acceptors, followed by strong σ donors. Ligands at the low end of the series are good σ donors but poor π acceptors since they do not possess π orbitals. Groups such as alkyl and hydride do not have π -acceptor orbitals and thus are unable to form π bonds to the metal that could effectively stabilize the trigonal bipyramidal transition state in an associative reaction involving a coordinatively unsaturated square planar complex (e.g a 16-electron complex with available sites for ligand binding). Ligands such as CO and the phosphines can stabilize the trigonal bipyramidal transition state through π bonding and can also decrease the energy of the M-X bond in the ground state through strong σ donation.

The *trans* effect is somewhat different in octahedral complexes due to the smaller s character of each bond and possibly due to steric effects caused by the relatively greater crowding found in octahedral versus square planar environments (Tognetti *et al.*, 2017). In general, however, it appears that *trans* effects are related to the capability of the ligand to stabilize the transition state during rate-limiting dissociation. Studies on octahedral Cr complexes (Atwood *et al.*, 1983) indicate that the order of the *trans* effect is rather similar and follows the general trend as shown above.

2.5 Stability and Spectra in Coordination Complexes

2.5.1 Stability of Square Planar Complexes

Square planar complexes are particularly important in the field of catalysis. This is because they contain vacant sites along the d_{z^2} direction which acts as binding sites for atoms/ molecules during a reaction. This way, the metal center moves from +2 to +4 oxidation state attaining an 18-electron configuration. Examples include the 16 electron d^8 species like the Vaska's compound of Iridium discussed above. Their stability is understood on considering the molecular orbital diagram in **Figure 5** below for a molecule of ML_4 where L is a ligand which is a purely σ -donor.

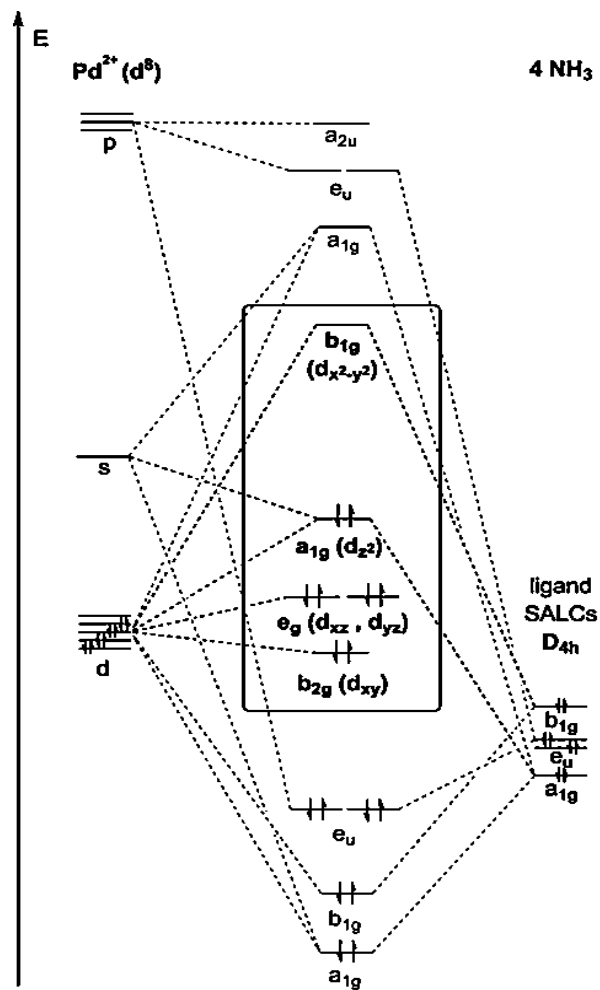


Figure 5 The σ -donor Orbitals of Square Planar Complexes

The four molecular orbitals are resultant from the σ -donor orbitals of the ligands. These orbitals are occupied by electrons which are bonding in nature. As is the case in any Lewis base/ Lewis acid reaction, the electrons from these orbitals are stabilized on interaction with the metal acting as a Lewis acid. Three additional orbitals are slightly bonding and are derived from d_{xy} (b_{2g}) and the doubly degenerate d_{xz} and d_{yz} (e_g) orbitals of the metal, and one is primarily nonbonding derived from d_z^2 (a_{1g}) orbitals of the metal.

These bonding and nonbonding orbitals can be filled by 16 electrons. If more electrons are added, that would occupy antibonding orbitals derived from antibonding interactions of a metal $d_{x^2-y^2}$ (b_{1g}) orbital with the σ -donor orbitals of the ligands, which would de-stabilize the complex. This means that a 16-electron configuration may be significantly more stable than an 18-electron configuration. A common reaction for these 16-electron square planar complexes is to accept one or two ligands at

the vacant coordination sites along the z-axis thereby achieving an 18-electron configuration (Mingos, 2004).

2.5.2 Stability of Octahedral Complexes ($\text{Cr}(\text{CO})_6$)

Strong σ -donor ability of CO raises the energy levels of e_g^* antibonding orbitals making them strongly antibonding. In a similar way, the strong π -acceptor ability of CO lowers the energy of t_{2g} orbitals making them strongly bonding (Crabtree, 2009).

Adding electrons would populate metal-ligand antibonding orbitals leading to a destabilization of the molecule. On the other hand, removing electrons would depopulate the filled t_{2g} orbitals which are bonding in nature on account of the strong π -acceptor capability of the CO ligands. A decrease in electron density in these orbitals would also tend to destabilize the complex. According to the crystal field (CF) model used to predict the relative energies of d -orbitals of transition metal complexes, d -orbitals pointing most directly toward the ligands are most destabilized as a result of raised energy from electron-electron repulsion; giving rise to antibonding orbitals as shown in **(Figure 6)**.

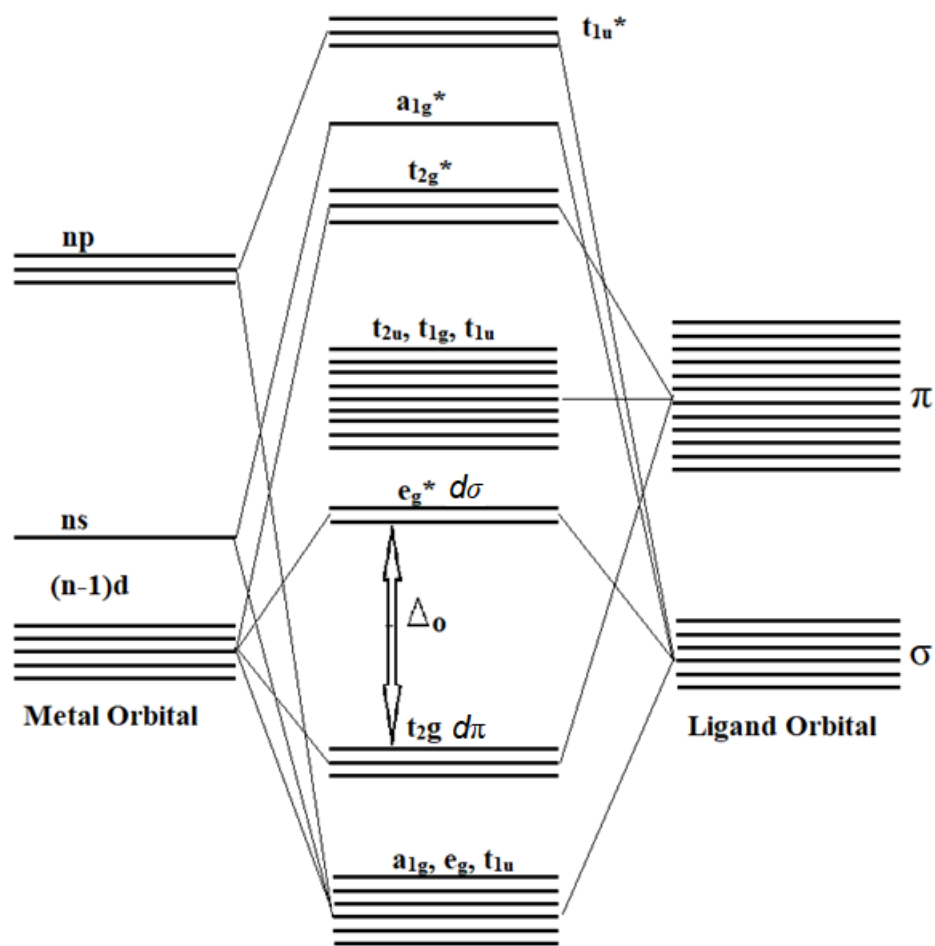


Figure 6 Molecular Orbital Energy Diagram for Octahedral Complex

In octahedral geometry, the two d -orbitals pointing directly toward the ligand are the d_z^2 and $d_{x^2-y^2}$. These give rise to the highest energy (antibonding) molecular orbitals, the e_g^* . The rest three d -orbitals form the bonding t_{2g} molecular orbitals (Deeth & Hitchman, 1986).

2.5.3 Spectra of Transition Metal Complexes

Spectra arise because electrons may be promoted from one energy level to another. Such electronic transitions are high energy charge transfer bands occurring in the UV region of the spectrum. These may be ligand-to-metal or metal-to-ligand charge transfers. In addition, much lower energy vibrational and rotational transitions take place which allow Laporte forbidden transition to occur. Since the vibrational and rotational levels are too close in energy to be resolved into separate absorption bands, they result in considerable broadening of the electronic absorption bands in $d-d$ spectra. These bands are low in energy and normally occur in the visible region of the spectrum

(above 400nm) and are responsible for the intense colors of most transition metal complexes. Band widths are commonly found to be of the order of $1000\text{-}3000\text{ cm}^{-1}$. Not all of the theoretically possible electronic transitions are actually observed. The position is formalized into a set of selection rules which distinguish between 'allowed' and 'Laporte forbidden' transitions. 'Allowed' transitions occur commonly. 'Forbidden' transitions do occur, but much less frequently, and they are consequently of much lower intensity (Eaton, 1968).

2.6 Ligands and Ligand Substitution Kinetics

2.6.1 Phosphines Ligands

Phosphines parallel the CO ligand in many ways. Like CO, phosphines are σ donors (via a hybrid orbital containing a lone pair on phosphorus) and π acceptors (Power, 1999). For many years it was thought that empty 3d orbitals of phosphorus functioned as the acceptor orbitals. By this view, as the R groups attached to phosphorus become more electronegative, they withdraw electrons from phosphorus, making the phosphorus more positive and better able to accept electrons from the metal via a d orbital.

The nature of the R groups, therefore, determines the relative donor/acceptor ability of the ligand. $\text{P}(\text{CH}_3)_3$ for example, is a strong σ donor by virtue of the electron-releasing methyl groups, at the same time, it is a relatively weak π acceptor. PF_3 on the other hand is a strong π acceptor and a weak σ donor. By changing the R-groups, it is possible to fine tune the phosphine to be a donor/ acceptor of a desired strength (W. Y. Wong & Harvey, 2010).

An additional factor important in phosphine chemistry is the amount of space occupied by the R group. This factor is important in a variety of contexts; for example, the rate at which phosphine dissociates from a metal is related to the amount of space occupied by the phosphine and the resultant crowding around the metal (Mathew *et al.*, 2000).

To describe the steric effects of phosphines and other ligands, Tolman defined the cone angle as the apex angle θ of a cone that encompasses the van der Waals radii of the outermost atoms of a ligand, as shown in Figure 7. If the R group has substituents, these are folded back away from the metal (Casey & Whiteker, 1990).

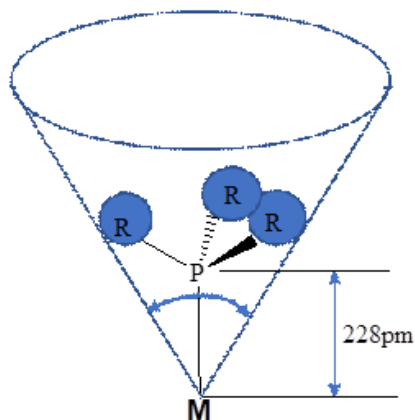
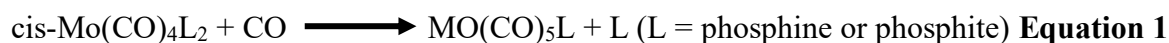


Figure 7 Tolman cone angle for phosphine ligands

As might be expected, the presence of bulky ligands can lead to more rapid ligand dissociation as a consequence of crowding around the metal. For example, in **Equation 1**, the rate of the reaction



which is first order in *cis*-Mo(CO)₄L₂, increases with increasing ligand bulk (Chu *et al.*, 2018; Xia Zhang, Ma, *et al.*, 2018).

2.6.2 Schiff base Ligands

The azomethine group's pi-acidity and its ability to stabilize low-valent redox states for metals have inspired research on this unit's chemistry and molecular structure design using this moiety (Al-Hassani & Abbas, 2018). Over the past 30 years, extensive research in both the chemistry and applications of Schiff base ligands in inorganic and coordination chemistry has been published (Yimer, 2015). As shown in **Figure 8**, azomethine region in a Schiff base consists of RHC=NR' π-system, where R and R' can be an alkyl, aryl, cycloalkyl or heterocyclic group which may consist various substitutions.

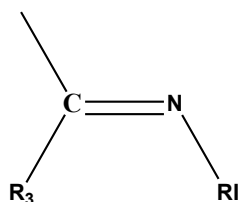


Figure 8 General structure of a Schiff base

These confers steric restrictions and thereby imposes certain stereochemistry, consequently affecting the physical, electronic and the bioactivity profiles of these ligands (Abu-Dief & Nassr, 2015). Playing around with various substitutions viz-a-viz electron-donor, electron-withdrawing, extended π -systems or simply sterically bulky groups enables the fine tuning of the various properties resulting in a wide range of chemical and biological response for these ligands (Taheri *et al.*, 2014; J. Zhang, Xu, *et al.*, 2018; K. Zhang *et al.*, 2017).

The ligands are versatile and readily synthesized by the condensation of primary amines with carbonyl moieties, either an aldehyde or a ketone. They find applications in the fields of medicinal and pharmaceutical chemistry where they exhibit biological profiles; as antibiotics, antifungal as well as antitumor agents (Prakash & Adhikari, 2011; Sahu *et al.*, 2012; Storr, 2014).

The other important feature is the lone pair of electrons residing in the sp^2 hybridized orbitals of the nitrogen atom of the azomethine group (Gudasi *et al.*, 2006). This makes the region even richer in electrons thereby conveying exceptional electron-donor ability in the chelation process (Yimer, 2015). The coordinating capability, the mild synthetic conditions, the high yields and flexibility in manipulating the electronic environment round the C=N moiety makes these ligands to play major roles in coordination chemistry. The mild synthetic conditions and high yields are also very attractive properties when economical industrial applications are required.

2.6.3 Ligand Substitution trends in the Periodic Table

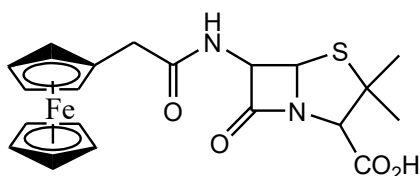
A clear characteristic of ligand substitution reactions is seen in the order of reactivity with respect to the metal in a triad such as Cr, Mo, W or Ni, Pd, Pt. The second-row transition metal complexes are usually reactive more than either of those containing first or third row elements. This maybe as a result of atomic covalent radius (for example, $Cr < Mo \sim W$; steric crowding among ligands decreases as one goes down the periodic table), nuclear charge ($Cr < Mo < W$; the incoming ligand is more attracted to the metal with higher nuclear charge), and M-L bond energy (bond dissociation energy for M—CO: $Cr < Mo < W$; the weaker the M-L bond, the more facile the substitution).

The first two factors favor heavier atoms and the last favors the lightest atom in the triad. Considering these, complexes containing the middle triad element are most reactive (Gichumbi & Friedrich, 2018).

2.7 Coordination Complexes in Cancer Therapy

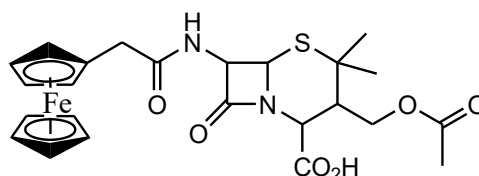
2.7.1 Ferrocene Compounds

Metallocenes are organometallic compounds which consist of a metal atom between two planar polyhapto rings. Metallocenes are small, rigid, and lipophilic molecules which can easily cross cellular membranes (Cerrato *et al.*, 2017). The relative stability of metallocenes in biological media has been exploited in applications such as tracers or vectorized bioactive compounds (Amatore *et al.*, 2017). This approach was used by Edwards and co-workers in the 1970s to produce ferrocenyl antibiotics (**10** and **11**) against penicillin resistant bacteria (E. I. Edwards *et al.*, 1976).



10

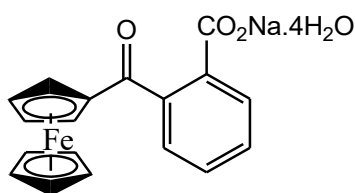
Ferrocenyl Penicillin



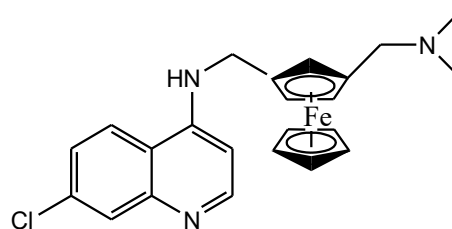
11

Ferrocenyl Cephalosporin

In ferrocene, all the carbon atoms of the cyclopentadienyl ligands (Cp) are firmly bound to the metal, and the Cp ring is described as penta hapto $\eta^5\text{-C}_5\text{H}_5^-$. Since all its bonding and non-bonding orbitals are exactly filled, ferrocene is the most stable compound in the metallocene series (A. Nguyen *et al.*, 2007). A sodium salt of o-carboxybenzoyl ferrocene (**12**) for the treatment of iron-deficiency anemia is well tolerated for oral administration and is also prescribed for gum diseases (Nesmeyanov & Kochetkova, 1974). The idea to modify the structure of organic bioactive compounds was taken up by Atteke to produce ferroquine (**13**) (Atteke, 2003). This compound is a ferrocenyl equivalent of the anti-malaria drug, chloroquine.



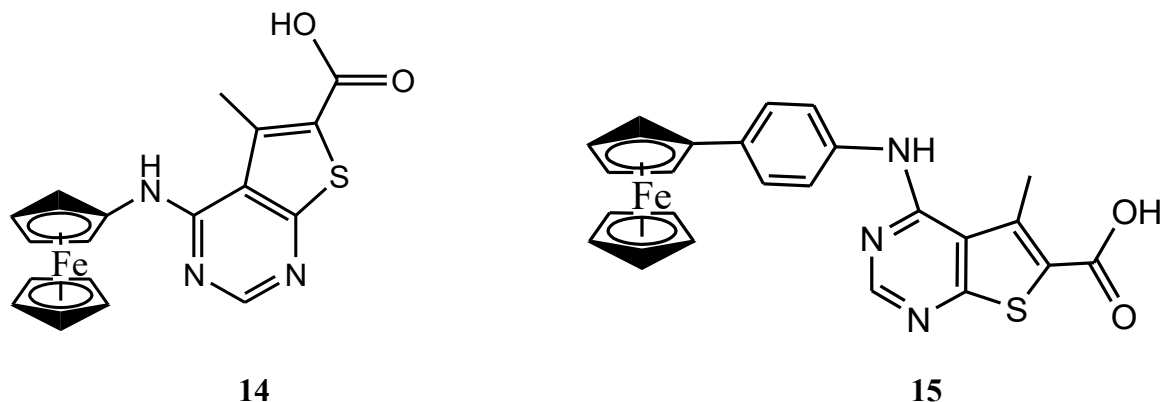
12



13

Recently, ferrocene complexes; 5-Methyl-4-(ferrocenylamino)thieno[2,3-d]pyrimidine-6-carboxylic acid (**14**) and 4-(Ferrocenyl-phenyl-4-ylamino)-5-methylthieno[2,3-d]pyrimidine-6-

carboxylic acid (**15**) have been synthesized and Screened for anticancer potency where they showed potent anticancer profiles in a number of breast cancer and acute myeloid leukemia (AML) cell lines. The complexes are as shown below (Sansook *et al.*, 2018).

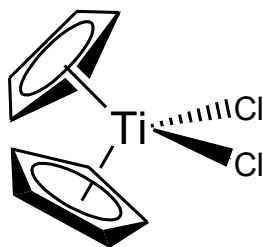


2.7.2 Titanocene Complexes

Titanocene dichloride (**16**) is a pioneer organometallic anti-cancer compound to go up to phase II clinical trials (Pizarro *et al.*, 2010). It was withdrawn from the trials due to aqueous stability challenges common with organometallic complexes, especially due to rapid hydrolysis of the Ti-Cl bonds. It is characterized by complicated aquation reaction at physiological pH making it difficult to characterize the active aqua species which are responsible for its antitumor action in which the Cp ligands breaks off at pH values above 4 leading to insoluble Titanium-oxo species (Fish & Jaouen, 2003).

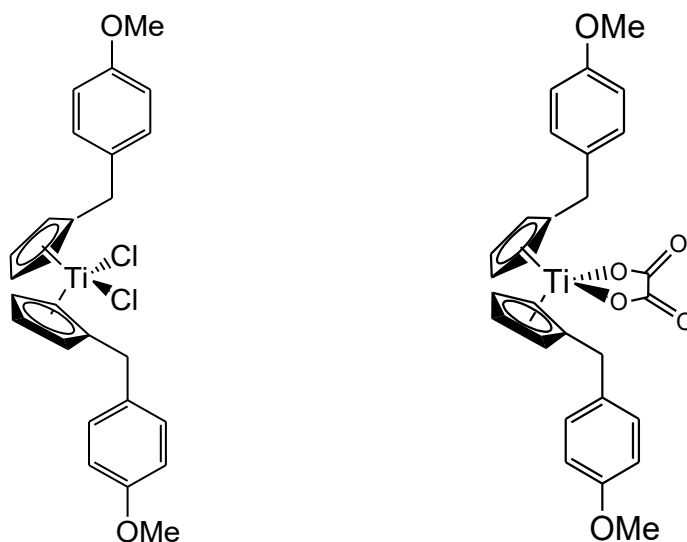
It is proposed through biological experiments that nuclear DNA is a possible intra-cellular target of titanocene dichloride where the hydrolysed adducts of the complex interact with the DNA (McLaughlin *et al.*, 1990). The other theory is that since Ti(IV) binds firmly to the human serum transferrin protein, this protein is likely to be involved in the process of delivering titanium (IV) into cancerous cells in the body (Nestle *et al.*, 1998).

In this case, the mechanism of drug delivery through transferrin-mediated process could involve the dissociation of the Ti-Cp bonds together with the hydrolysis of the Ti-Cl bonds, followed by attaching of the Ti(IV) to the iron sites of human transferrin (hTF), producing the adduct Ti₂-hTF. Titanium (IV) attaches firmly to hTF, but ATP mediates the detachment of Ti(IV) from Ti₂-hTF adducts (Guo, 2000)



16

To tackle the above challenges of aqueous stability, other organometallic titanocenes complexes with bridged-Cp rings (**17** and **18**), the ansa-titanocenes have been reported. They have optimized labile ligands, substituting the chloride ligands with more appropriate anions. In vivo studies in renal cancer (CAKI-1) tumour-bearing mice have indicated a statistically-significant tumour growth decrease (Fichtner *et al.*, 2008).

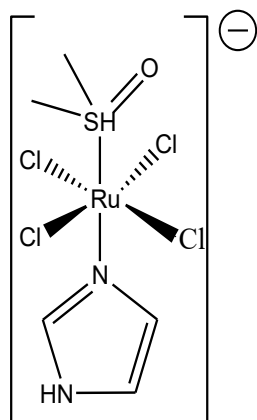


17

18

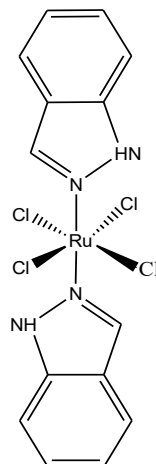
2.7.3 Ruthenium and Osmium Arene Complexes

Ruthenium (III) complexes especially of octahedral geometry (**19** and **20**) are fairly inactive towards ligand exchange. The reduction from ruthenium (III) to ruthenium (II) has been suggested to be a prior activation route to DNA binding (Clarke *et al.*, 1980). Two Ru-based anticancer drugs which has reached clinical trials stage are code NAMI-A (New Anti-tumor Metastasis Inhibitor A) (**21**) which was produced by Alessio and co-workers (Alessio, 2004), and code KP1019 (**22**), produced by Hartinger and co-workers (Hartinger *et al.*, 2006).



NAMI-A

19

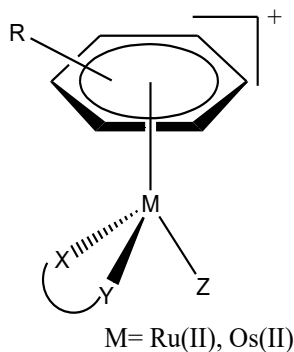


KP1019

20

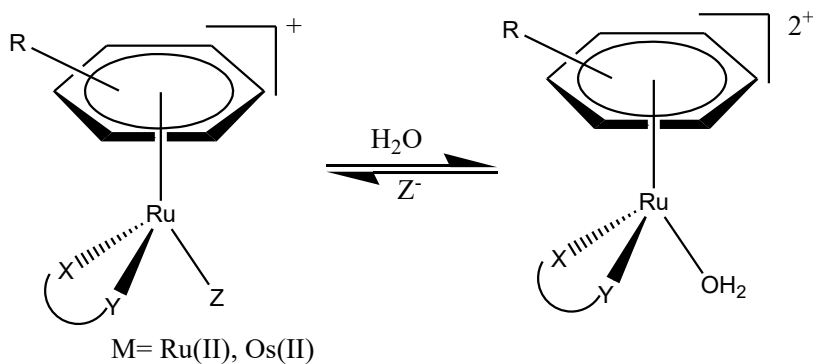
Morris and co-workers investigated the antitumour viability of RuII and OsII η^6 -bound arene structures of the type [RuII (η^6 -arene) (X)(Y)(Z)] (R. E. Morris, Aird, Murdoch, *et al.*, 2001). These compounds have a distinctive ‘piano-stool’ assembly whereby XY is a neutral chelating ligand group, and Z is a mono-anionic ligand (**21**). The arene group, coordinating as a η^6 -electron donor and a π -acceptor (back bonding form the metal), contributes to the stability of the +2-oxidation states. The XY chelating ligand confers further stability to the whole complex and the possibility of adjusting the electronic characteristics of the metal center.

The monodentate ligand Z permits activation of the molecule, that is, if labile enough e.g. halide, it can leave behind a vacancy coordination center for biomolecules. These means that varying both the arene and the X-Y-Z ‘legs of the stool’ can confer flexibility to the complex and the ability to fine-tune their pharmacological characteristics (Peacock *et al.*, 2006).



Generally, RuII and OsII arene complexes display favourable cytotoxic properties against human ovarian cancer cell lines where structure–activity correlations have been proven (Peacock & Sadler, 2008). A notable example is when the chelating ligand group is ethylene diamine and the leaving group is a chloride, in which case the cytotoxicity against A2780 human ovarian cancer cells rises with increasing size of the coordinated arene (Habtemariam *et al.*, 2006). When the chloride is however substituted by a -Br or an iodide as leaving group, the observed effect on the cytotoxicity of ethylenediamine complexes is only minimal (F. Wang *et al.*, 2005). Moreover, substituting the chelating ligand by comparatively labile monodentate ligands results in reduction of cytotoxicity for the complexes (R. E. Morris, Aird, Murdoch, *et al.*, 2001). The Ruthenium arene compounds with monodentate ligands exhibit reduced or no activity (IC₅₀ values > 150 mM) whereas the chelated ligand-containing complexes show enhanced reactivity- 9 mM, compared to 0.5 mM for *cisplatin* in similar experiments.

A likely reason for this observed low activity could be due to their elevated reactivity *in vivo* where they get inactivated prior to reaching their biological targets. Activation via hydrolysis of the Ru–Z bond (**Scheme 9**) might be an important part of the mechanism of action for this class of complexes and their biochemical actions in aqueous environment has been widely studied (Dougan, 2006). The rate plus the degree of hydrolysis of the Ru–Z link are to a great extent reliant on the nature of ligand-Z, where the more labile leaving groups result to faster hydrolysis (Dong Wang & Lippard, 2005).



Scheme 9 Hydrolysis of Ru-Z bond in RuII arene complexes.

After activation of ruthenium or osmium arene complexes and the creation of the aqua adducts [Ru/Os(η^6 -arene)(OH₂)(X)(Y)], as shown in **Scheme 9** above, the metal center becomes susceptible

to nucleophilic attacks by biomolecules, where interactions with DNA nucleobases are thought to be the final targets for these group of complexes. Several experiments have been carried out to explore this hypothesis in detail (Novakova *et al.*, 2005); (Pizarro & Sadler, 2009). As shown in **Figure 9** below, Ruthenium arene complexes preferentially coordinate to guanine nucleobases in the DNA double helix.

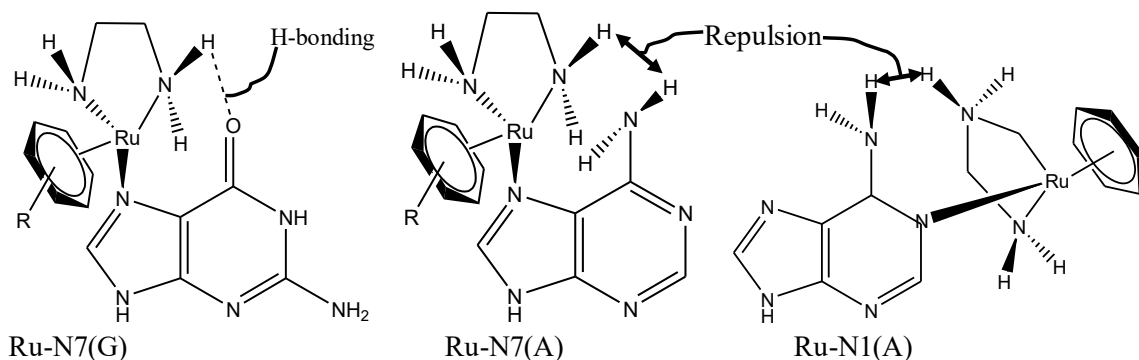
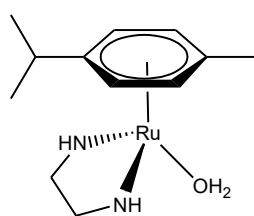


Figure 9 Guanine (G) and Adenine (A) adducts formed by DNA interactions of arene Ru-en anticancer Complexes

The derivatives of these complexes in aqueous media have also been studied after interaction with guanine, thymine, cytosine and adenine nucleobases (Brabec & Nováková, 2006). It is observed that the reactivity of Ru(II) complexes with the various binding sites of DNA nucleobases at neutral pH progresses in a decreasing manner (Nitrogen N7)-Guanine > (Nitrogen N3)-Thymine > (Nitrogen N3)-Cytosine > (Nitrogen N7)-Adenine, (Nitrogen N1)-Adenine, weakly binding to cytosine-N and almost no binding to adenine nucleobases.

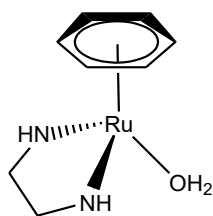
The observed selectivity to particular nucleobase seems to be favoured by the ethylenediamine (en) -NH₂ groups, which form hydrogen-bonding with the exocyclic oxygens e.g. Carbon C8-Oxygen of Guanine, but do not bond and repel towards the exocyclic amino groups of the nucleobases e.g. C8-NH₂ of Adenine as shown in **Figure 9** above (K. G. Chen *et al.*, 2009). As shown in (22-24), the arene moiety can also exert substantial influence on the rate and level of hydrolysis reactions for these complexes. Wang and co-workers observed a 2-fold variance in the rate of hydrolysis between the [Ru(η^6 -biphenyl)Cl(en)]PF₆ biphenyl compound and the tetra hydro-anthracene complex [Ru(η^6 -5,8,9,10-tetrahydroanthracene)Cl(en)]PF₆ or the dihydroanthracene complex [Ru(η^6 -9,10-dihydroanthracene)Cl(en)]PF₆.

This demonstrated that disparities in the steric and electronic effects of different arene ligands can moderate the rates of aquation (F. Wang *et al.*, 2005). Other effects on the rate of hydrolysis and equilibrium constant is observed from varying the chelating ligand group. This is attributed to not only the electronic- vis-à-vis strength of π interactions, but also to steric effects vis-à-vis competitive interactions of the Z-ligand and H_2O . Another significant factor compared to the rate of hydrolysis for drug activation is the pK_a of the bonded H_2O of the activated aqua adduct. The pK_a value is a determinant of whether the active species coordinated to the more labile $\text{Ru}-\text{OH}_2$ bond or the less reactive deprotonated form $\text{Ru}-\text{OH}$ prevails in solution at a given pH (K. G. Chen *et al.*, 2009). Since the pK_a values for the bonded H_2O ligand in most of Ruthenium- arene compounds are around 8, this implies that at pH 7, aqua adducts should dominate. With a $\text{pK}_a > 7$ an active complex is formed, while a $\text{pK}_a < 7$, the physiological pH, results in an inactive species due to the formation of the hydroxo form which renders the complexes non-cytotoxic (F. Wang *et al.*, 2005)



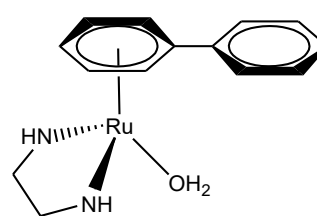
(p-cym= para cymene)

22



(bz= benzene)

23



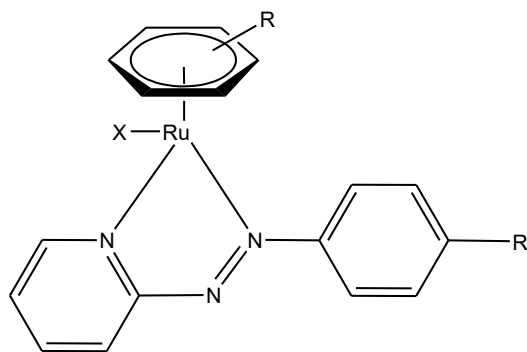
(biph= biphenyl)

24

The other variable in altering the pK_a of these complexes is the chelating ligand. Better electron withdrawing groups, i.e. better π -acceptors, tend to avert the electron cloud farther from the metal center, making it more deficient of negative charges, and causing the attached water molecule to be more acidic i.e. of lower pK_a (Pizarro *et al.*, 2010).

2.7.4 Ruthenium Azopyridine Complexes

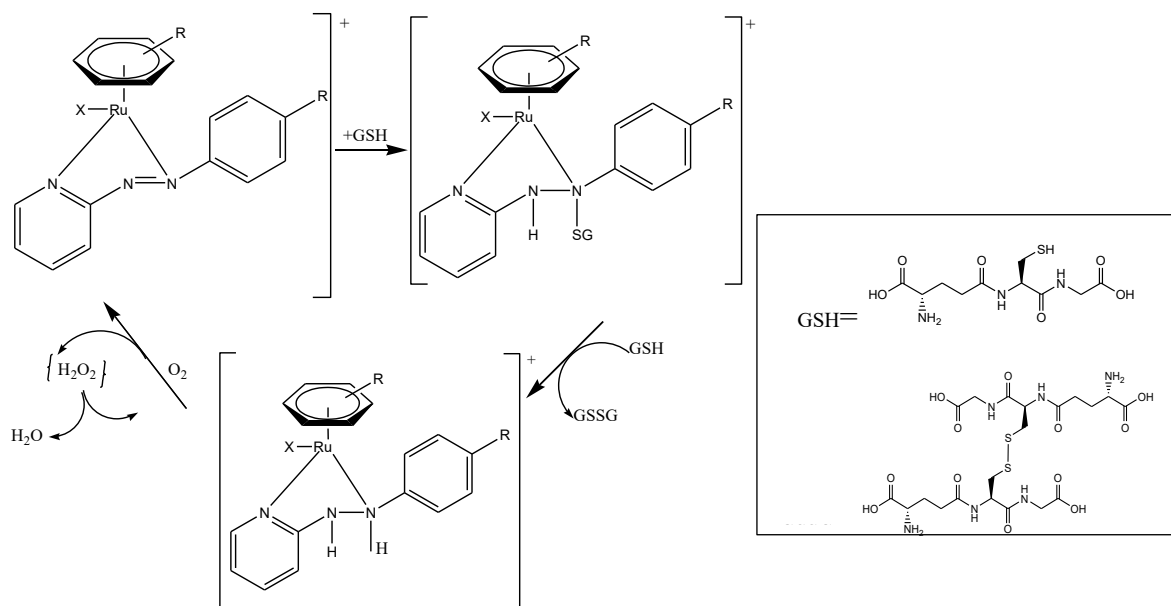
Another group of interesting metal complexes comes from coordinating a π bonded arene group with an σ donor/ π acceptor strongly chelating azopyridine ligand (where arene = p-cymene or biphenyl, and azpy= N,N-dimethylphenyl- or hydroxyphenyl-azopyridine) together with an iodide as a strong monodentate ligand- $[\text{Ru}(\eta^6\text{-arene})(\text{azpy})\text{I}]^+$ (**25**) (Pizarro *et al.*, 2010).



25

These complexes produce Ru(II) arene complexes that are fairly inactive to activation via hydrolysis in aqueous media. Nevertheless, notwithstanding these compounds being inert, they show a high cytotoxicity towards human ovarian cancer cell line (A2780) and human lung cancer cell line (A549). The cytotoxicity of these complexes arises from an increased generation of reactive oxygen species (ROS) (Vidimar, 2012). The mechanism of activation is through the reduction of the ligand. Despite the fact that it is challenging to reduce the azopyridine ligand on its own, the reduction potential of the azopyridine is physiologically attainable by glutathione when the azopyridine moiety is coordinated to Ru(II) (Vidimar, 2012).

The ruthenium coordinated complex works as a promoter/ catalyst in reactions with glutathione (GSH) where GSH is oxidized to GSSG in a reaction which seems to go through a ligand-centered reduction of the N=N (azo) double bond by glutathione producing a hydrazo-intermediate. The release of GSSG follows and the re-generation of the azo bond as displayed in **Scheme 11** below.



Scheme 10 Scheme Possible scheme for catalytic activity of ruthenium azopyridine complexes

These ligand-based redox mechanisms may provide new approaches and concepts for designing catalytic medicines (Vidimar, 2012)

2.7.5 Platinum Complexes

The ligand substitution kinetics of Pt complexes is mainly controlled by the existence of the exiting ligands (i.e., the entity that exits the Pt first under the conditions of reaction used) (Omondi *et al.*, 2018). Structures with firmly coordinated departing units do not have anticancer efficacy, similar to very weakly coordinated ligands which also do not result in high activity. Such inactivity in response can be influenced by either the low reactivity (from strongly bonded ligands) or those compounds with very high reactivity (leading to early inactivation before reaching target sites). Furthermore, the firmly coordinated group's trans effect will allow the amine ligand to be released.

Pt compounds with poorly coupled ligands are not effective since they have too high reactivity, leading to fast intracellular displacement with other molecules (S. Ahmad, 2017). The character of the non-leaving ligands also affects platinum complexes' reactivity. Antitumor activity has been shown to exist for complexes with the general formula; $cis\text{-}[\text{PtCl}_2(\text{amine})_2]$ with several ligands as non-leaving groups (S. Ahmad, 2017).

Platinum complexes destroy tumors by inducing apoptosis, facilitated by the instigation of several signal transduction routes. *Cisplatin* ($[cis\text{-}(\text{NH}_3)_2\text{PtCl}_2]$), (**2**) is one of the most successful anti-tumor

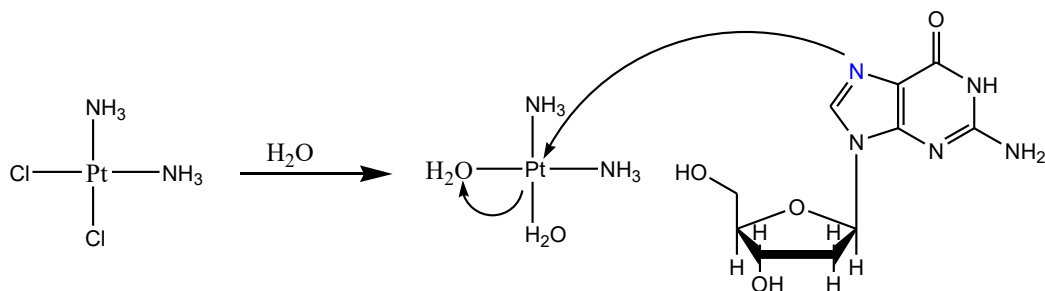
complexes (Xiao *et al.*, 2020). Chloride ions detach from the complex following its diffusion into a cell permitting the complex to cross-link with the DNA, notably to guanine sequence groups.

This results in intra-strand and inter-strand DNA cross-linking, causing an inhibition of DNA, RNA and protein synthesis (Xiao *et al.*, 2020). Carboplatin (**3**) has similar platinum moiety as *cisplatin*, but is coordinated to an organic carboxylate group. The result is an increase in hydro-solubility and lower hydrolysis. Oxaliplatin (**4**) contains a platinum atom coordinated with oxalate and a bulky diaminocyclohexane (DACH) group.

Clinical use of CDDP has resulted in many patients with diverse kinds of cancers being successfully treated, including: sarcoma, soft tissue cancers, cancer of the bones, muscles, and myeloma. Such cancers have over the years received improved prognosis and consequently they have become less life threatening (Abou-Alfa *et al.*, 2020; Wan *et al.*, 2019). Hydrolysis of the Platinum–Chloride bonds in *cisplatin* inside the cells is assumed to produce active aqua species (Lajous *et al.*, 2018). In serum, there is a high chloride ion concentration (150 milli Mole).

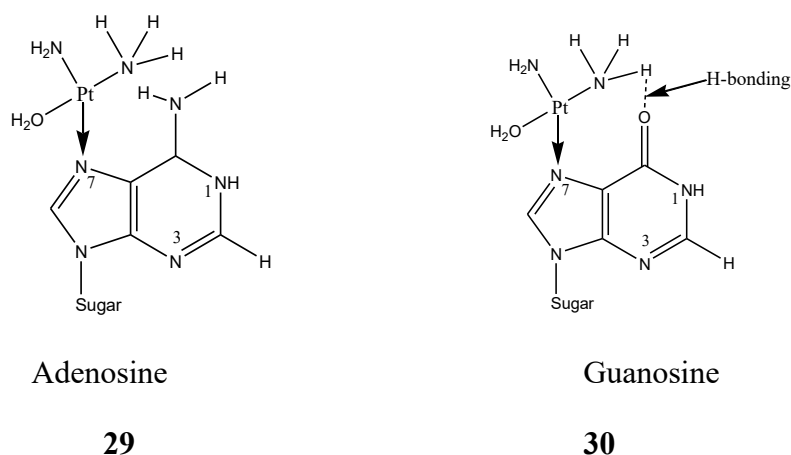
This prevents the exchange of chloride groups by water molecules implying that the aquation reaction of *cisplatin* in the blood happens to a very low extent. After dispersing inside the cells with an environment of low chloride concentration, (4 milli Mole), the neutral state of the drug is hydrolyzed to produce various aqua species; mono-aqua and di-aqua species (Lajous *et al.*, 2018). These aqua products react readily towards nucleophilic sites of biomolecules like DNA, RNA, and proteins (Fuertes *et al.*, 2003). This increased reactivity of the resultant aqua species is because the OH₂ group is a better leaving ligand compared to the chloride (Cl⁻) (Papo *et al.*, 2020). As shown in **Scheme 11** below, the drug exerts its cytotoxic effects by the interaction of this aqua adduct with the biological target, DNA (Pizarro *et al.*, 2010).

In the hydrolysis reaction of *cisplatin*, the first step is the rate-determining step, whereby the rate of hydrolysis is way slower compared to the subsequent reaction of the mono-aqua adduct with cellular platinophiles including DNA. As shown in **Scheme 11**, the lability of the coordinated water groups is the main determinant of the high reactivity and the observed toxicity of these species (Papo *et al.*, 2020). The monohydrate complex is also associated with nephrotoxicity of *cisplatin* derivatives, whereby it is three times more nephrotoxic than the parent *cisplatin* complex (Andersson *et al.*, 1996).



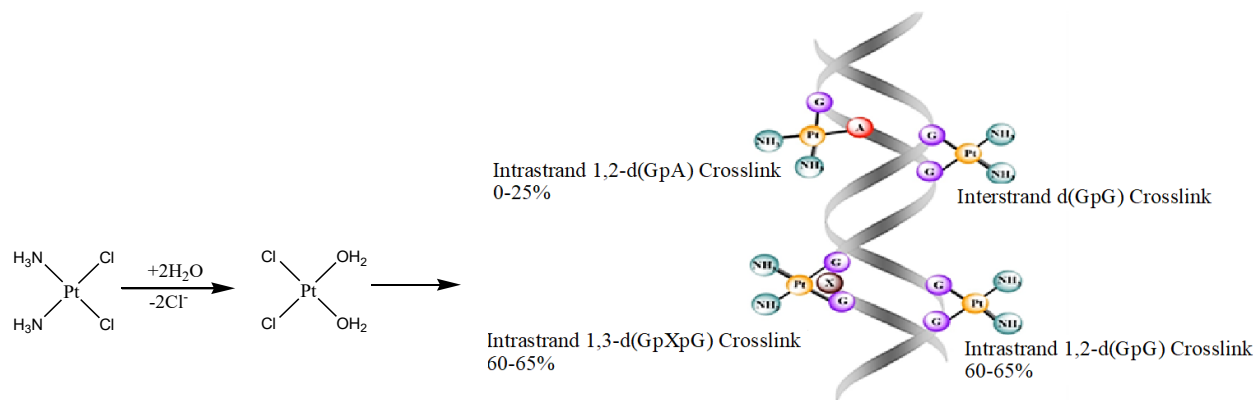
Scheme 11 Aquation reaction of cisplatin by DNA base

Chloride ligands dissociate from the platinum center and are replaced with water which is more easily displaced by N7 of purines. The binding of platinum to the N-7 site of guanosine is kinetically favored compared to that of adenosine. This can be explained in terms of hydrogen bonding with the O-6 of guanosine moiety which is absent in adenosine as shown below (**29** and **30**).



As shown in **Scheme 12** below, the anti-cancer characteristics of *cisplatin* are accredited to the kinetics of its chloride ligand disarticulation reactions which lead to DNA cross-linking triggering DNA twisting and thereby disrupting DNA replication, *transcription* and other nuclear roles, and thereby arresting cancer cell spread and tumor progress (Venter, 2011). Intra-strand cross-links to guanine-guanine (G-G) and to adenine-guanine (A-G) are the most common types in *cisplatin*-damaged DNA. 1,2-G-G DNA intra-strand cross-links stall RNA polymerase II (Pol II) and initiate *transcription-coupled* DNA repair; Pol II stalling is as a result of translocation barrier which inhibits the transport of the lesion to the desired location (Damsma *et al.*, 2007).

Due to this reaction on the DNA, *cisplatin* is strongly mutagenic and carcinogenic, both under *in vitro* and *in vivo* study experiments (Sanderson *et al.*, 1996).



Scheme 12 Aquation and DNA adduct formation with *cisplatin*

Although clinical trials of CDDP and its derivatives were a success that prompted extensive efforts to develop other metal-based anti-cancer complexes (K. G. Chen *et al.*, 2009); (Frezza *et al.*, 2010), its application is hindered by the unpleasant side effects experienced in normal tissues. *Cisplatin* is known to have major drawbacks such as a narrow therapeutic window and drug resistance complications (Lippert, 1999). Although it is not used to treat breast cancer, it is widely used for other kinds of cancers for instance testes carcinoma. Currently, two most widely used *cisplatin* analogues are carboplatin and oxaliplatin (Jakupec *et al.*, 2003). Oxaliplatin produces similar inter-strand and 1,2-G-G intra-strand cross-links as *cisplatin* but with a different range of activities and schemes of action from those of *cisplatin* and carboplatin as shown in (**Figure 10**) below.

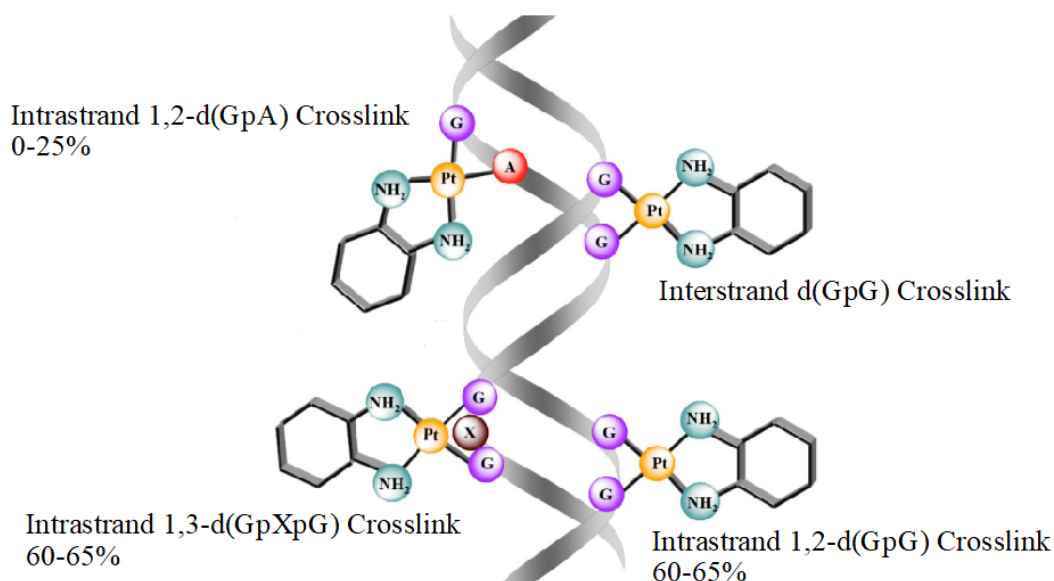


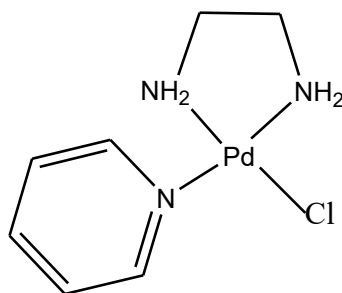
Figure 10 DNA Adducts Formed by Oxaliplatin

Adducts formed are from 1,2-intra-strand cross-links among two neighboring guanosine moieties bending the DNA double helix by about 30 degrees towards the major groove (Spingler *et al.*, 2001). The adduct lesions are fixed *in vivo* by the nucleotide excision repair mechanism and the drugs are detoxified from the body by glutathione (GSH)-related enzymes (Venter, 2011). Consequently, a variety of complexes have been proposed whereby steroidal or non-steroidal targeting ligands are bound to platinum to selectively transport the platinum active site to the desired biological target. Use of antiestrogen bioligands combines the antiestrogenic and cytotoxic properties in a single drug molecule, bringing forth an all new therapeutic diversity (A. Nguyen *et al.*, 2007).

2.7.6 Palladium Complexes

Another notable example of organometallics extreme reactivity and rapid hydrolysis comes from palladium complexes. Ligand exchange kinetics, the main key feature of these compounds that makes them interesting anticancer drug candidates is simultaneously a considerable problem when considering their stability and hydro solubility issues (Abu-Surrah & Abdalla, 2008). Strong coordinated nitrogen ligand and suitable leaving group has been suggested as a possible way to stabilize and activate antitumor palladium anticancer drug candidates. The other method used to control ligand dissociation for these square planar complexes is to use bulky ligands to block off the vacant sites along z-direction of the incoming ligand.

Palladium(II) complexes with ethylene diamine as coordinating ligand and pyridine (**31**) derivatives has been reported (Zhao *et al.*, 1999). It is observed that an increase in donor properties of the coordinated pyridines directly leads to increased cytotoxicity for these palladium drugs (Abu-Surrah & Abdalla, 2008).



31

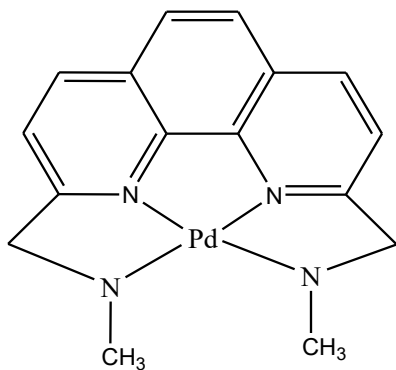
The resemblance that exists in the coordination chemistry of Pd(II) and Pt(II) complexes has encouraged research of Palladium(II) compounds as anticancer agents (Rau, 1996). The hydrolysis

reaction in Pd(II) is about 10^5 times higher compared to the equivalent platinum complexes. Disassociation in solution results in highly reactive products which fail to get to their desired biological targets (Abu-Surrah & Abdalla, 2008). This significantly greater reactivity of Pd(II) compounds suggests that if an antitumoral palladium complex is to be synthesized, it will have to be stabilized by a strong coordinated nitrogen group and an appropriate labile group.

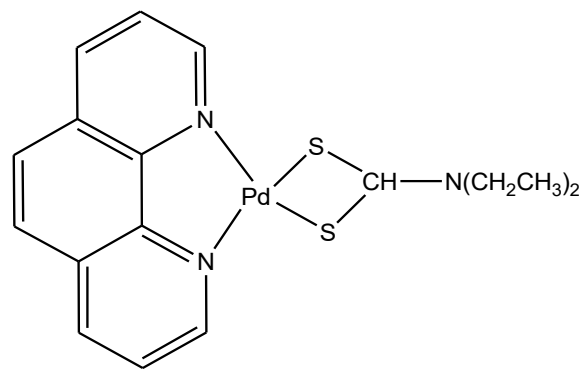
It has been found that when the leaving group is relatively non-labile, the compound can retain its structural integrity in physiological media for sufficient time to perform significant roles in vivo.

Fairly bulky coordinating groups have been employed to yield complexes where, owing to the steric effects of the bulky ligands, they reduce any potential *cis-trans* isomerism and guaranteeing isolation of the preferred *trans*- Palladium isomers (Abu-Surrah & Abdalla, 2008).

Aromatic ligands like 1,10-phenanthroline, a commonly used ligand in coordination chemistry, has also been exploited in synthesizing organometallic complexes. The planar structure permits its involvement as a DNA intercalating agent (Zhao *et al.*, 1999). Complexes of Pd(II) containing S-donors together with the N-N coordinating ligands of either DACH, phenanthroline or bipyridine (**32** and **33** respectively) have also been explored with bipyridine and phenanthroline-based complexes proving the most active (Mital *et al.*, 1989).



32



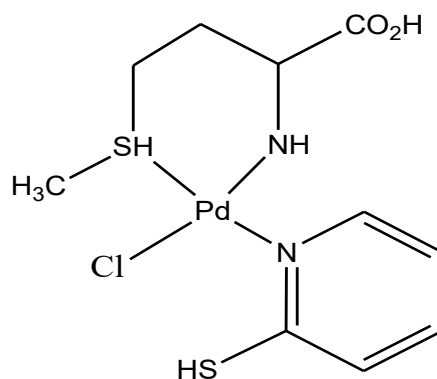
33

2.7.7 Palladium(II) Complexes with Mixed Donor Ligand: N, S and O donor ligands

Given the flexibility and relevance of platinum compounds with organic moieties bearing N, S, and O donors in various fields such as biology, manufacturing and catalysis; numerous organic complexes comprising N, S, and O donor groups have been utilized for many years to develop new coordination compounds for these fields. The hard (amidato-N), marginal (pyridine-N) and mild

(amine-N, azo-N, pyrrol-N, and dithiocarbamate-S) existence of ligand donor locations and their ability to fill the various functional coordination locations around the metal ions essentially determine the distinctive characteristics of synthetic metal compounds as well as the bio-active site(s) in bio-molecules.

Khan and co-workers have reported Pd(II) compounds bearing nitrogen and sulphur ligands like methionine and substituted pyrimidines (**34**) (B. T. Khan *et al.*, 1991). Methionine bonds to Palladium via amino group nitrogen and sulphur, thus leaving a free carboxylic group and forming a complex with $IC_{50} < 10 \mu\text{g/ml}$ in *in vitro* experiments proving that it can perform as a potential antitumor agent (Abu-Surrah & Abdalla, 2008).



34

Generally, research results from literature indicates that the greater number of the *trans*-palladium compounds show an improved and better activity compared to *cis*platin and *cis*-palladium isomers. Even better, they show activities comparable to (or higher than) those for *cis*platin, carboplatin, and oxaliplatin *in vitro* (Abu-Surrah & Abdalla, 2008). Zhao and co-workers, (1999) reported Ethylenediamine-based Pd(II) complexes utilizing pyridine or its derivatives. Increasing the electron-donation characteristics of the substituents leads to the coordinated pyridines having an increased donor-strength. this leads to a corresponding increase in the cytotoxicity of these palladium complexes (Zhao *et al.*, 1999).

2.7.8 Complexes from Five Membered Heterocycles: Pyrrole Scaffolds

Pyrrole scaffolds are very interesting bioactive core exhibiting several biological activities including anticancer, anti-inflammatory, antimicrobial, antifungal, antiviral and antioxidant properties (Almerico *et al.*, 2000). Natural as well as synthetic five-member heterocyclic compounds are

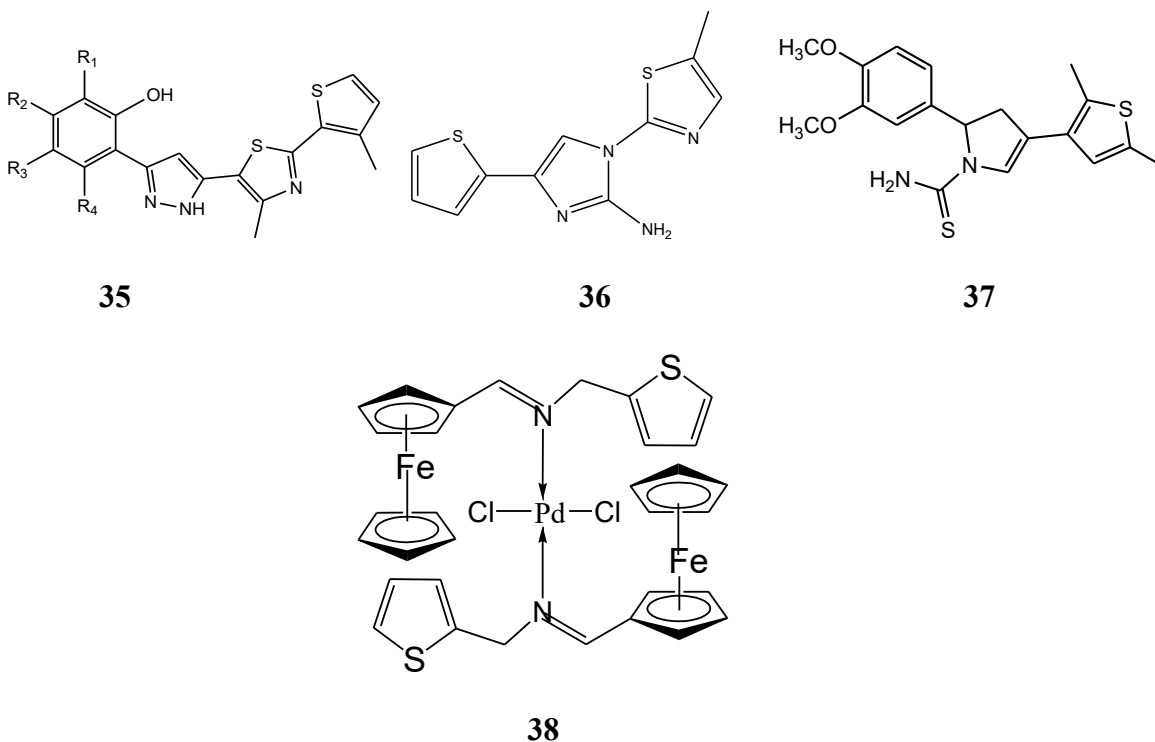
biologically important in particular Pyrrole derivatives, in pharmacological activity such as cytotoxicity against solid tumor models (Evans *et al.*, 2003), antibiotic (S. White *et al.*, 1997), anticancer (Sugiyama *et al.*, 1996) and antimicrobial activity (Mohamed *et al.*, 2011).

Substituted pyrroles have been used as intermediates in the synthesis of mitomycin anti-tumor antibiotics possessing antibacterial activity (de Leon & Ganem, 1997). Pyrazoles and their derivatives are of much importance on account of their use in therapy in different diseases (Salgın-Gökşen *et al.*, 2007). Pyrrole containing analogues are considered as a potential source of biologically active compounds that contains a significant set of advantageous properties (Artico *et al.*, 1995).

The complexes bound to pyrrole moieties exist in numerous naturally occurring and artificial products with the broad-spectrum pharmacological effects including antifungal (Artico *et al.*, 1995) antimicrobial (Padmavathi *et al.*, 2011), antiviral (T. G. Edwards *et al.*, 2011), and anticancer properties (Jouanneau *et al.*, 2016). A new range of possible drug compounds using pyrrolo[3,2-d]pyrimidines have been studied and they have shown promising anti-proliferative activity against cancer cells (Temburnikar *et al.*, 2015). The combination of different pharmacophores in a pyrrole ring system has led to the formation of more active compounds. Work by Pérez and co-workers reported a series of ferrocenyl pyrrole compounds and tested their cytotoxicity against MCF-7 breast cancer, MCF-10A normal breast and HT-29 colon cancer cell lines (Pérez *et al.*, 2015).

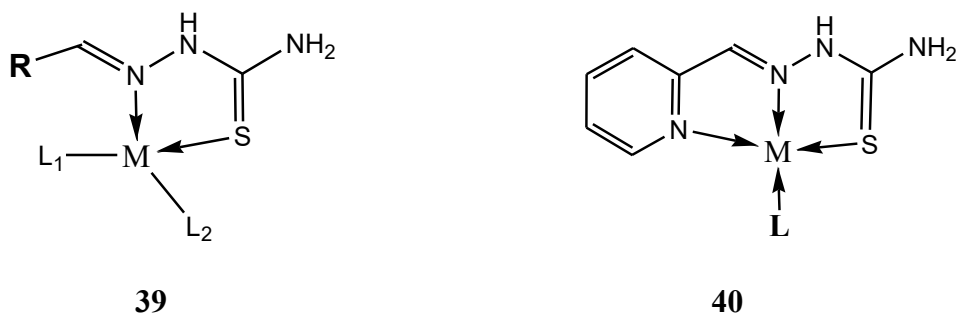
Work on a series of pyrrole derivatives specifically pyrrolopyrimidines, pyrazolopyrrolopyrimidine, triazolopyrrolopyrimidines, tetrazolopyrrolopyrimidine, triazinopyrrolopyrimidines and pyrrolopyrimidotriazepines, and their cytotoxicity profiles against MCF-7 cell lines has been published (Ghorab *et al.*, 2014). Another useful and important heterocycle is the thiophene moiety. Compounds with a thiophene nucleus show numerous pharmacological profiles and various other uses, for example; the substituted compound (**35**) showed anti-bacterial and anti-fungal properties (Karale *et al.*, 2015), 1-(5-methylthiazol-2-yl)-4-(thiophen-2-yl)-1H-imidazol-2-amine (**36**) is an anticancer agent (W.-T. Li *et al.*, 2012), and 2,3-dihydro-2-(3,4-dimethoxyphenyl)-4-(2,5-dimethylthiophen-3-yl)pyrrole-1-carbothioamide (**37**) is antibacterial (S. A. Khan *et al.*, 2014).

Ferrocenyl complexes (**38**) from ligands containing thiophene moieties have been synthesized by Motswainyana *et al.* (2012), but tests on breast cancer cell lines showed low cytotoxicity compared to cisplatin (Motswainyana *et al.*, 2012).



2.7.9 Complexes from Thiosemicarbazone Derivatives

Thiosemicarbazones are part of thiourea class of compounds. They commonly coordinate as ligating agents with *transition* group metals through bonding via the azomethine nitrogen and sulphur atoms (39) (Padhye & Kauffman, 1985), but they also act as three-donor tridentate ligands by bonding through two nitrogen centers and sulphur atoms (40) (West *et al.*, 1993).



Analogous to ketol-enol tautomerism, thiosemicarbazones can exist at an equilibrium for the thione (C=S) and thiol C-SH) tautomers, where the thione tautomer behaves as neutral bidentate ligand. Upon losing the thiol proton, the ligand becomes a negatively charged bidentate ligand. These tautomers depend on the pH of the experimental conditions during complexation reactions to

produce cationic, neutral or anionic complexes. Most work focus on the neutral thiosemicarbazones from reactions carried out at neutral pH.

Thiosemicarbazones act as remarkably flexible multidentate ligands able to form coordination complexes with transition metals in various ways through covalent or dative type bonding. The earliest reported medical applications of thiosemicarbazones appeared in the 1950's when they were used as compounds against TB and leprosy (Bavin *et al.*, 1951). The following decade saw these compounds tested for antiviral properties which were confirmed leading to intense research which eventually culminated to the commercialization of some thiosemicarbazone products under trade names methisazone and Marboran®, in the treatment of smallpox (GA, 1964).

Another major step in utilization of these compounds was the publication of the first antitumor tests (Sartorelli & Booth, 1967). Finch and co-workers explored the broad areas of application where thiosemicarbazones have received most attention, classifying them in relation to their activities against cancerous cells, protozoa, bacteria or viruses. Their activity is found to correlate to the type of metal center (Finch *et al.*, 1999). As anticancer agents, the activity is shown to substantially increase for the complexed product as compared to the free ligand, and also, the undesirable cytotoxicity as side effects were shown to be minimized in the complexes (Finch *et al.*, 1999).

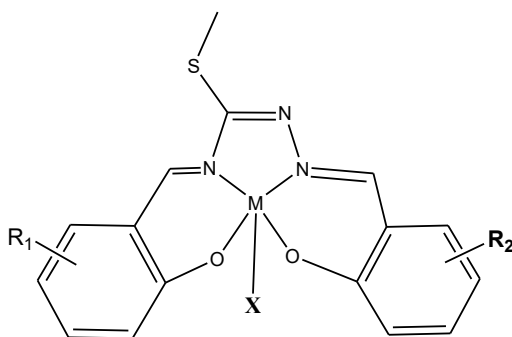
Brockman and co-workers first published the anti-leukemic properties of 2-formylpyridine thiosemicarbazone (R. W. Brockman *et al.*, 1956). Following this, various authors delved deeper to try and understand their mode of action as anticancer agents. The compounds were explored for activity as ribonucleotide reductase (RR) inhibitors (R. Brockman *et al.*, 1970), as topoisomerase II (Topo-II) inhibitors (I. Hall *et al.*, 2000), for properties as multidrug resistance protein (MDR1) inhibitors (I. Hall *et al.*, 2000), and, for their ability to produce oxygen radicals (Reactive Oxygen Species) (Shao *et al.*, 2006).

Since ribonucleotide reductase enzyme is iron-dependent and favors reduction of ribose to deoxyribose via a free radical process through a tyrosyl radical, inhibiting this enzyme effects an obstruction at the synthesis phase of cell cycle, culminating in the instigation of apoptotic process (Elford *et al.*, 1970). Topoisomerase II is an enzyme in eukaryotic cells that acts by decatenation of DNA coils of daughter chromosomes to avert supercoiling in the process of DNA replication and is necessary for synthesis of DNA and for cellular division (Larsen & Skladanowski, 1998).

Since rapidly dividing cells contain high levels of this enzyme, targeting the inhibition of this enzyme has a direct effect on proliferation of fast dividing cells like those found in tumours. Coordination of thiosemicarbazones to metal ions always orients the complex in such a way that the lipophilic regions of the ligands point the opposite direction to the metal center towards the bulk of the solvent, which partly explains the hydrophobic nature for most of the resulting complexes leading to poor solubility in physiological media.

However, the exposure of the hydrophobic part of the molecule makes it possible for these compounds to pass through cell membranes into the cell. Complexation with metal centers also increases the acidity of the ligands as electron density is shifted towards the metal either through sigma or dative donor mechanism leading to stabilization of the ligand partial negative charge of the thiolate region by the metal ion. Preparation is usually through a Schiff-base type condensation between an appropriate aldehyde or ketones with an appropriate thiosemicarbazide (Bjelogrić *et al.*, 2010).

Work on thiosemicarbazones bearing aromatic rings have shown the cytotoxicity of these compounds correlates with both the complexing metal ion and the position of attachment of substituents attached to the aromatic framework. 3-(4,5-Dimethylthiazol-2-yl)-2,5-diphenyltetrazolium bromide (MTT) assays by Atasever *et al.*, against chronic myeloid leukaemia (K562) and endothelial (ECV304) cells using iron (III) and nickel (II) compounds with 2-hydroxy-R-benzaldehyde-S-methyl-thiosemicarbazones (**41**), showed the highest cytotoxicity activity when a methoxy (-OCH₃) substituent was on the side chain of the aromatic ring (Atasever *et al.*, 2010).



The iron chelates displayed better activity against K562 when the methoxy substituent was at the 4-position while the nickel complexes tested against ECV304 and K562 cell lines showed better activity with the methoxy substituent appearing at the 3-position (Atasever *et al.*, 2010).

2.7.10 Complexes from Quinolone Derivatives

The quinoline backbone appears in various natural products, particularly in alkaloids. They exhibit useful biological profiles in pharmaceutical (e.g., antimalarials, such as quinine or chloroquine) and agrochemicals, together with being important building blocks in organic synthesis (Xiaoxia Zhang *et al.*, 2010). Quinolone containing compounds have been shown to have resourceful pharmacological profiles. Work by Chen and co-workers on compounds containing quinolone proved that these compounds have anti-inflammatory properties (Y.-L. Chen *et al.*, 2004).

Diacon and co-workers., showed that quinoline compounds are good candidates against multi-drug resistant tuberculosis (Diacon *et al.*, 2009). Khan and co-workers carried out synthesis and tests on these compounds and showed that they have cytotoxic, antimicrobial, antifungal and as cardiovascular agents (K. M. Khan *et al.*, 2000). Quinolone is a well-known backbone of antimalarial drugs and these activities have been studied by Kaur *et al.* (Kirandeep Kaur *et al.*, 2010). Anticancer properties of quinolone containing compounds were carried out separately by (A. Vaidya *et al.*, 2011) and Kouznetsov (V Kouznetsov *et al.*, 2012). Studies on free radical scavenging activities have proved the anti-oxidant properties of these compounds (Orhan Puskullu *et al.*, 2013).

2.8 DNA Binding to Metal Complexes

Binding to DNA by metal complexes can either occur through covalent bonds; where fairly labile ligands in the complex are replaced by the nitrogenous bases in DNA; specifically, N7 in guanine; or through noncovalent interaction. In non-covalent bonding, the forces involved include either electrostatic, intercalation or groove binding in the major or minor grooves on the outer surface of the DNA helix.

This happens in either of the two ways, intercalative and/ or groove binding. Intercalative process comprises the addition by insertion of a planar molecule between DNA base pairs which causes uncoiling in the DNA helical coils and a resultant elongation of the DNA (O'Reilly *et al.*, 2012). This is caused by planar heterocyclic moieties which stack in between neighbouring DNA base pairs. The resulting DNA-complex is stabilized by π - π overlaps between the DNA bases and the intercalating complex causing strong structural perturbations in DNA (San Tan *et al.*, 2014).

Intercalators are normally more toxic to cancerous cells compared to normal cells because the complex formed with DNA and topoisomerase is more lethal to proliferating cells. This hinders the replication and transcription of DNA (KR *et al.*, 2014). This is explored by observing the alterations

that appear in the λ_{\max} absorption values of π - π^* intra ligand transitions, ligand \rightarrow metal charge transfers or on the d - d transitions as the DNA concentration is serially increased to a metal complex. Various modes of binding are then deduced from the spectral response whereby, an intercalative manner of interaction is specified by a hypochromic shift, and bathochromic shift or hypsochromism. Intercalation of a complex with the base pairs of DNAs is as a result of overlaps of π^* antibonding orbitals of the ligands bound to the complex with π bonding orbitals of the DNA base pairs. This decreases the probable transitions and the effect is observed as hypochromic shift (Raman & Sobha, 2012)

On the other hand, a hyperchromic shift suggests electrostatic mode of binding. The spectral shift in the metal complex absorption is correlated to the binding strength from which the kinetics can then be determined (Ashfaq *et al.*, 2014). Observation on the spectral changes of metal complexes in the UV-Vis range after the addition of serial concentrations of DNA is a generally accepted technique in assessing the binding modes and the kinetics of DNA-metal complex interactions (Olsztyńska & Komorowska, 2011).

2.9 Beyond DNA-Targeting in Cancer Chemotherapy. Emerging Frontiers

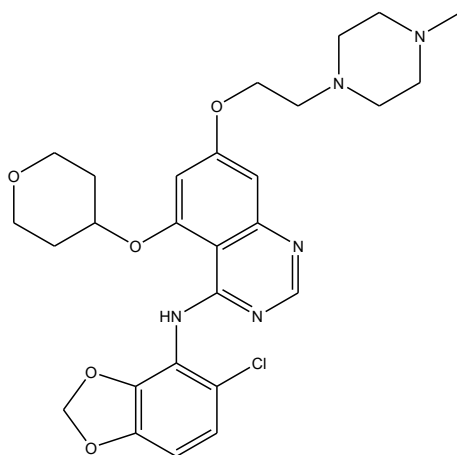
Although major steps have been made in medicine, many difficulties still need to be resolved in order to boost cancer therapy. In line with this, research is putting a great deal of effort into discovering new and effective therapies that can mitigate the pertinent adverse effects from therapies. Many research reports have focused on creating alternative treatments to minimize the side effects of traditional medicines over the past decade (R. S. Riley *et al.*, 2019a).

Various technologies are now being tested in clinical studies, with some already been implemented in clinical practice (Galon & Bruni, 2019). These includes targeting overexpressed proteins and antigens on tumour cell surfaces, targeted drug delivery, nanoparticle delivery among others. In the last 70 years or so, cancer treatment has progressed exponentially, from cytotoxic drugs that reduce tumors but with severe systemic side effects to specific treatments that can cause cancer-cell death but leaving healthy tissues unchanged (Ntziachristos *et al.*, 2014).

The origins of many tumors are not fully understood. This makes it difficult to come up with effective therapies and this is as evident from the high cancer drug rate failure during clinical trials (Boyer *et al.*, 2016; LeBleu & Kalluri, 2018). Directed or not, resistance to chemotherapy drugs is an endemic problem, and scientists are trying to find ways to bypass the resistance. The easiest

solution is to switch the treatment of an individual from one treatment to another via a different target or mechanism, or to introduce another medication to the protocol (Sanmamed & Chen, 2018)..

Scientists are studying cellular mechanisms and genes that might cause resistance and using these as targets (Gurunathan *et al.*, 2018). Through inserting an agent that prevents or creates another route, this resistance can be partly solved, rising the response rate from 40 to 60% (Ribas & Wolchok, 2018). In preclinical study, the application of saracatinib (7-(2-(4-methylpiperazin-1-yl)ethoxy)-N-(5-chlorobenzo[d][1,3]dioxol-4-yl)-5-(tetrahydro-2H-pyran-4-yloxy)quinazolin-4-amine) (42) to trastuzumab, a monoclonal antibody used to treat breast cancer and stomach cancer, demonstrated a decrease of 90 percent in tumor volume in previously trastuzumab-resistant mice (McGivern *et al.*, 2018).



42

Trastuzumab is normally overexpressed in chronic myeloid leukemia cells (W. Xie *et al.*, 2020). It is a dual-specific protein tyrosine kinase inhibitor that binds and inhibits these tyrosine kinases thus affecting cell motility, cell migration, adhesion, invasion, proliferation, differentiation and survival (Feng *et al.*, 2020; Sand *et al.*, 2020).

Patients vaccinated against cancer may still develop resistance from chemicals released by tumors which inhibit an immune response to the tumor or from genetic changes in the tumor itself (Sanmamed & Chen, 2018). Scientists look at ways of reducing this tolerance through the use of vaccines that combine various antigens in one vaccination or through targeting of T-cells that can diminish the immune system response (Sahin & Türeci, 2018; Tanyi *et al.*, 2018).

Modern anticancer drugs target DNA specifically on rapid division of malignant cells. One downside of this approach is that they also target other rapidly dividing healthy cells such as those involved in hair growth leading to serious toxic side effects and hair loss. Therefore, it would be better to develop novel agents that address cellular signalling mechanisms unique to cancerous cells, and new research is now focussing on such approaches.

Although the classical chemotherapy area involving DNA as the set target continues to produce important findings, nevertheless, a distinctly discernible, emerging trend is the divergence from the cisplatin operation model that uses the metal as the primary active center of the drug. Many successful anti-cancer drugs present are associated with elevated toxicity levels. Cancers also develop immunity against most therapies and the area of cancer research can therefore be seen as an area with a high unaddressed need.

Hence, ongoing work into cancer pathogenesis is important to create accurate preclinical tests which can contribute to the development of innovative drugs to manage and treat cancer.

Some of the emergent frontiers utilizing different approaches include immunotherapy, natural antioxidants, gene therapy, tumor ablation, magnetic hypothermia and hyperthermia by use of SuperParamagnetic Iron oxide Nanostructures (SPIONs), laser surgery, pathomics and radiomics, exosomes, and organometallic pharmaceuticals.

2.9.1 Immunotherapies

The aim of immunotherapy treatments is to boost a patient's immune system for it to be able to fight tumor invasion, rather than targeting the tumor itself. Immunotherapies, which are also regarded as cancer vaccines, induce the immune function of a patient to kill cancerous cells (Kruger *et al.*, 2019). By either enhancing the host's immune responses to cancers or countering the signals generated by cancer cells that inhibit immune response, immunotherapy has become a successful procedure alone, or paired with other therapies such as surgery, chemotherapy and radiation therapy (Souza-Fonseca-Guimaraes *et al.*, 2019).

Additionally, interventions can be categorized into two broad categories: active and passive immunotherapy (Kawalpreet Kaur & Khatik, 2020; Vander Zanden & Chi, 2020). The active approach entails channeling the host immune response toward tumor-associated antigens (TAAs) on

the tumor surface (Ondrej *et al.*, 2020; Manpreet Sambi *et al.*, 2019b). These antibodies can be particular proteins or carbohydrates which are expressed exclusively or expressed excessively in tumor cells (Rashidijahanabad & Huang, 2020; Rodrigues *et al.*, 2018). Passive immunotherapy, by contrast, entails strengthening the immune system's generic anticancer approach using monoclonal antibodies, lymphocytes, and cytokines (Kawalpreet Kaur & Khatik, 2020).

A drug combination therapy would by extension constitute one or several elements of these two kinds of immunotherapy (Sicklick *et al.*, 2019). It is notable that immunotherapy distribution and efficacy are heavily reliant on the version, grade, predictive response rate, and relevant biomarker expression of the cancer although response rates from patients may still vary (Camidge *et al.*, 2019; Havel *et al.*, 2019; Marra *et al.*, 2019; Otsoshi *et al.*, 2019).

The opposite effect is to decrease the immunosuppressive effects that promote the growth of cancer cells. Food and Drug Administration (FDA) approved the first vaccine of its kind in 2010 in the treatment of advanced hormone refractory prostate cancer (Golchin & Farahany, 2019; Saito *et al.*, 2017; Zaidi & Jaffee, 2019). The main advantage associated with immunotherapy is that since vaccines induce an immune system response, patients can be protected from metastasis and relapsing. Their side-effects profiles are relatively mild, restricted mainly to inflammatory irritation at the injection site (Kruger *et al.*, 2019; Souza-Fonseca-Guimaraes *et al.*, 2019; Wallis *et al.*, 2019).

Some of the challenges are that although it has been shown that immunotherapy is effective, patient success rates differ and, most often, only a small percentage of patients within a broad subset respond positively to the therapy (Hellmann *et al.*, 2018). This problem is a hurdle to immunotherapy efficacy and rates of response from patients. A major factor contributing to discrepancies in the rates of response to cancer vaccinations is the specific nature of the vaccination as well as whether off-the-shelf forms of the vaccination is manufactured with similar antigen existing in the client's tumor in order for their immune system to recognize its presence in the system (Martin *et al.*, 2020).

Genetic mutations may also contribute to the activation of neoantigens (Malekzadeh *et al.*, 2020) which are recognized by the immune system during tumor growth (Damo *et al.*, 2020). Nevertheless, once cancerous cells are formed, they are able to evade this immunity protection by shutting these antibodies off through a procedure known as of immune tolerance induction (Schep *et al.*, 2018).

Another immune avoidance method may arise when a tumor associates with its microenvironment to prevent antitumor response (Binnewies *et al.*, 2018).

Several methods exist to improve response levels such as the identification of more specialized genetic markers and agonists of immune control points (Ren *et al.*, 2020). Better predictive tools and assays are also capable of identifying patients who will react well to immunotherapy (P. Jiang *et al.*, 2018). Cancerous cells have evolved specific cellular processes to aid tumor microenvironment development (Roma-Rodrigues *et al.*, 2019). One technique employed by cancer cells to ensure survival and advancement is to avoid checkpoints on the immune system (Havel *et al.*, 2019).

Immune system check points operate to track autoimmunity and alleviate damage to tissue caused by immune responses through modulation of costimulatory and inhibitory signals (Sanchez-Correa *et al.*, 2019). During carcinogenesis, however, the dysregulation of protein expression at the checkpoint may lead to aberrant activation of inhibitory checkpoint receptors thus hindering T cells from identifying and eradicating tumorigenic cells (Taylor *et al.*, 2020; Yongbo Wang, Bao, *et al.*, 2020).

The development of the tumor microenvironment (TME) not only enables the tumor to evolve but also causes it to recruit host immune system components (Corrales *et al.*, 2017). In addition to fostering tumor growth, these TME components principally act as cellular obstacles to avoid any intrusion by antitumor immune cells (Gulzar *et al.*, 2019). The growth of a thick epithelial layer enveloping the malignant mass produces a protective barrier marked by several traits known to enhance tumor growth, such as hypoxic conditions and anomalous neovascularization of tumors (Jain *et al.*, 2020; Katayama *et al.*, 2019).

Not only does this deter prospective immune system cells from entering the tumor but also establishes blood vessels to enable cells to metastasize into remote tissues (Samanta & Semenza, 2018). Until such time as these processes are eliminated, tumors will continue to evade the body's immune defences (Fleming *et al.*, 2018). Currently immunotherapy treatments are obtainable as cancer vaccinations. Immunotherapy works similar to standard methods of vaccination where the goal is to stimulate an immune response. In short, cancer vaccinations containing whole or fragments of antibodies are intended to induce an immune reaction (Manpreet Sambi *et al.*, 2019b) as shown in **Figure 11**.

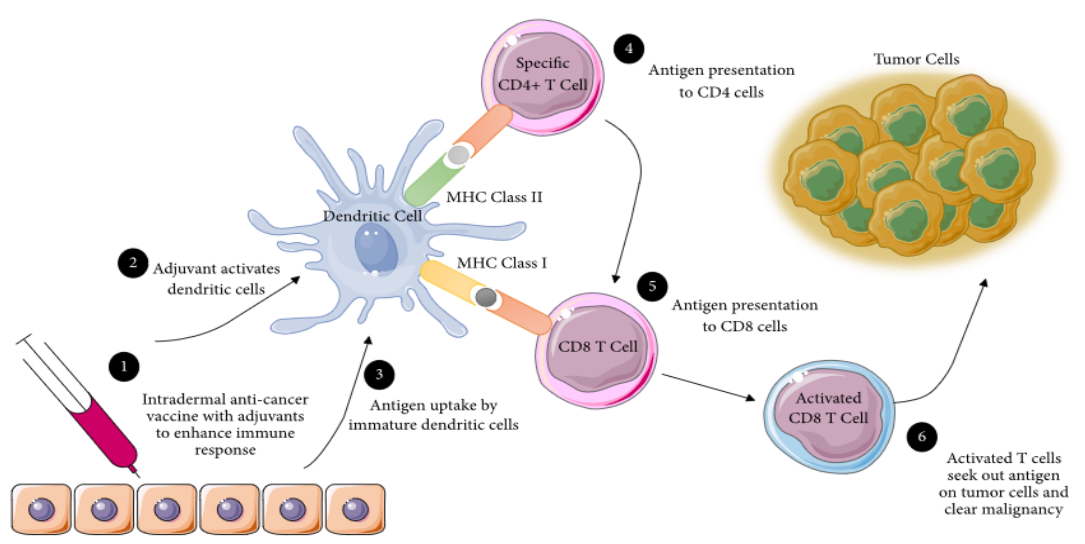


Figure 11 Mechanism of Action of Cancer Vaccines. Administered through injection with adjuvants that activate dendritic cells.

[Adapted from (M. Sambi *et al.*, 2019a)]

Since many antigens reflected on cancer cells are also present on normal cells, treatment with a non-tumor-specific antigen will also be cytotoxic to healthy cells. This means that although immunotherapy have transformed the therapy of multiple advanced-stage malignancies, it has not been beneficial to many patients for whom immune functions have been jeopardized by traditional treatments (Martin *et al.*, 2020). In order for immunotherapies to be administered to a wider patient demography, more diverse biomarkers which are expressed on the tumor cell surface need to be discovered.

This will establish particular patterns which are displayed solely on cancer cells, the so called neoantigens or tumor-specific antigens (TSA), allowing for better immunotherapy targets (Durgeau *et al.*, 2018). Determining the proper target for TSA will certainly lead to higher efficacy of immunotherapy treatment results in terms of reduced adverse effects to normal cells (Conte *et al.*, 2018; Wagner *et al.*, 2018). One of the proposed approaches in overcoming immunotherapy resistance from cancer cells is to use combined immunotherapy or multi-modal strategies (Sang *et al.*, 2019).

This method could efficiently raise the likelihood of antigens being targeted by immunotherapies, and therefore overcome the cancer cells' compensatory nature (Bolm *et al.*, 2018; Schaaf *et al.*, 2018).

2.9.2 Natural antioxidants

The human body faces various exogenous assaults on a daily basis, such as ultraviolet (UV) radiation, air pollution and tobacco smoke, culminating in the development of reactive species, particularly oxidants and free radicals, blamed for the emergence of many diseases like cancer (Ighodaro & Akinloye, 2018). Such molecules could also be formed as a result of medicinal drug treatment, but they are also spontaneously generated by mitochondria and peroxisomes within the cells and tissues, and by metabolism from macrophages, during regular aerobic physiological activities.

Oxidative stress from reactive oxygen species is capable of destroying DNA (genetic changes, DNA double strand splits and chromosomal aberrations) (Ford & Kastan, 2020), and other biomacromolecules such as lipids and proteins (Shastri *et al.*, 2018), significantly altering the function of transcription factors and, ultimately, of important metabolic pathways (Bhatti *et al.*, 2017; Islam, 2017). Our body's defences against these molecules are often inadequate to overcome the tremendous losses that have been created.

Together with studies into the functions of the superoxide dismutase (SOD), catalase (CAT) and glutathione peroxidase (GP) biological enzymes, natural antioxidants such as vitamins, polyphenols and bioactive compounds derived from plants are being researched to be incorporated as protective agents and possible medicinal drugs (Altemimi *et al.*, 2017; Reis *et al.*, 2017). The anti-inflammatory and anti-oxidant effects of these molecules are present in many foods and spices (Baenas *et al.*, 2019).

Vitamins, alkaloids, flavonoids, carotenoids, curcumin, berberin, quercetin plus many other substances have been tested *in vitro* and checked *in vivo*, exhibiting strong antiproliferative and pro-apoptotic effects, and have been fronted to complement existing cancer treatments (Goyal *et al.*, 2020; Iqbal *et al.*, 2017; Mohiuddin, 2019). The advantages associated with this approach include the fact that they are available easily and in large quantities. However, due to their limited bioavailability, their integration through clinical practice remains difficult (Pan *et al.*, 2017; Rezaeihamiri *et al.*, 2020).

2.9.3 Tumor ablation and magnetic hyperthermia

Use of heat for tumor ablation and magnetic hyperthermia opened up new possibilities for precision therapy, rendering the medication to be focussed in very tight and precise regions (S. Kumar *et al.*,

2020). These techniques could also be a suitable replacement for the more intrusive methods like surgery. Tumor thermal ablation requires a set of procedures utilizing heat (hyperthermia) or cold (hypothermia) to kill metastatic cells (Prasad *et al.*, 2018) (**Figure 12**). Cell necrosis is known to occur at temperatures below -40°C , or above 60°C (Kaija *et al.*, 2020; Mitxelena-Iribarren *et al.*, 2020).

Long temperature periods between 41°C and 55°C are also successful in damaging tumour cells (Mitxelena-Iribarren *et al.*, 2020).

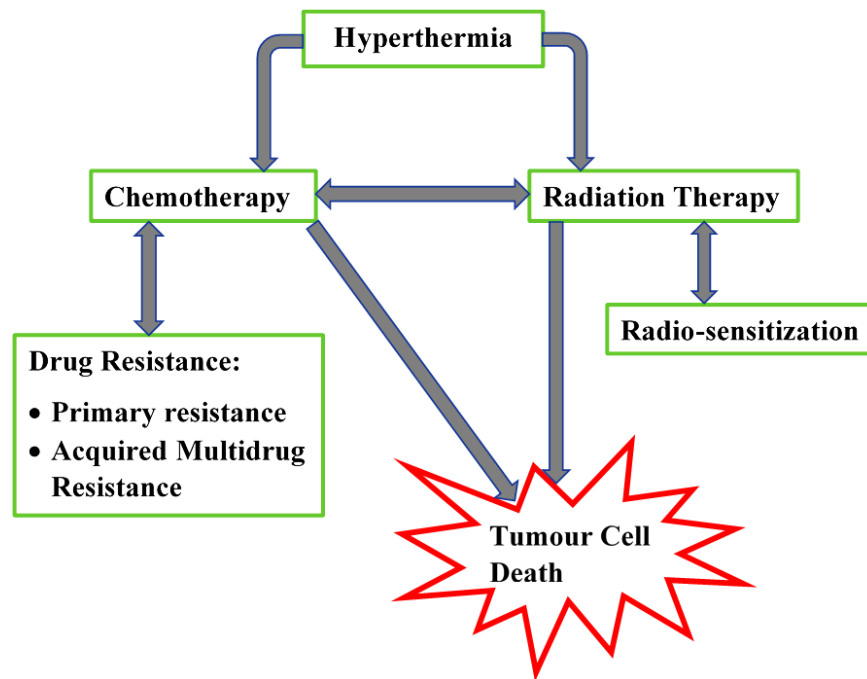


Figure 12 Hyperthermia Process complementing traditional cancer therapy. (Prasad *et al.*, 2018) Furthermore, cancer cells are known to be more temperature sensitive at high temperatures than normal cells (J. Chen *et al.*, 2019). Upon cooling, hypothermic ablation is due to the forming of ice crystals which break cell membranes and eventually kill cells (Baumann, 2019; Camacho & Covey, 2020). Argon gas is the ideal coolant in these studies because it can disinfect the surrounding tissues to -160°C (Camacho & Covey, 2020; Ward *et al.*, 2020).

Gasses, such as ammonia, can also be used at their critical point because they have a higher heat capacity compared to argon (Camacho & Covey, 2020). Yet the technologies for manipulating and controlling them is still not well developed. Ablation through Hyperthermia currently utilizes microwave radiofrequencies (RF) and laser (Izzo *et al.*, 2019; Xu *et al.*, 2019). Microwave ablation

is based on the electromagnetic interaction between microwaves and polar molecules in fluids, such as liquids, which induces oscillation and therefore temperature changes.

The more conductive the medium, the more effective the process. For this reason, Radio frequency ablation works very well in the liver and in other areas with a high content of water and ions, whereas it has a poor effect in lungs (Hsieh *et al.*, 2019). Radio frequency ablation has been the most widely used in hospitals, since it is efficient and safe (Sun *et al.*, 2019). An alternated current of Radio frequency waves is applied to a target zone by an insulated electrode tip, while a second electrode, needed to close the circuit, is placed on the skin surface (Pacella & Mauri, 2020). The interaction with the current causes the oscillation of ions in the extracellular fluid, which, in turn, produces heat (Prasad *et al.*, 2018).

In contrast to the electrical current in Radio frequency ablation, microwaves will spread through any type of tissue allowing high temperatures to be achieved in a short time, greater infiltration and treatment of wider tumor areas (Meijerink *et al.*, 2018; Tan *et al.*, 2019).

Advantages associated with these strategies include precise treatment of the interested area and the possibility of performing the treatment along with MRI imaging (magnetic hyperthermia). Challenges include low penetration power and the need for a skilled operator to perform the treatment (Guttman *et al.*, 2018).

2.9.4 Laser therapy

Laser therapy uses the characteristics of laser beams that are very small at a specific wavelength and are extremely focused (Drain, 2019). This makes the procedure very effective and precise, making it a viable alternative to traditional surgery (Seago *et al.*, 2019). The laser-emitted absorption of the light results in heating and eventual damages to the affected area (Hong *et al.*, 2020). Different types of lasers may be used according to the specific application. Neodymium: yttrium-aluminum-garnet (Nd: YAG) lasers (1064 nm wavelength) and diode lasers (800–900 nm wavelength), with a penetration range of up to 10 cm, are used for the treatment of internal organs (Lisiecki, 2015).

Conversely, for superficial therapies, CO₂ lasers (10,600 nm) with a penetration depth of 10 μm up to 1 mm are used (Strieth *et al.*, 2020). Laser therapy is receiving a lot of interest in science over other ablation methods because of its benefits such as higher effectiveness, safety and accuracy, and

a shorter treatment session required to achieve similar results (C. Chen *et al.*, 2020). In fact, the fibers to relay laser light are compliant with magnetic resonance imaging so that the temperature and thermal dosage can be calculated accurately (Olshansky *et al.*, 2019).

However, certain drawbacks still need to be addressed, such as the need for a highly skilled operator to bring the fiber in the right position (Suter *et al.*, 2020). Ultimately, despite new methods of heating tumor tissues via electromagnetic hyperthermia (as discussed above) showing better advantages by using superparamagnetic or ferromagnetic nanoparticles to generate heat through alternating magnetic fields, laser surgery still remains one of the most precise in tumor ablation.

2.9.5 Radiomics and pathomics

Although surgery still remains one of the main procedures for cancer treatment, however, about 50 percent of patients undergo radiation therapy. Radiation therapy is administered by use of an external source of light beam or by adding a radioactive source locally (brachytherapy), to achieve intense irradiation (Zeman *et al.*, 2020). Localization of the pulse is now enabled by image-guided radiation therapy (IGRT), in which the patient's images are obtained during treatment enabling the correct amount of radiation to be determined (Kontaxis *et al.*, 2020).

Through the emergence of intensity-modulated radiotherapy (IMRT), varying strengths of radiation fields can be generated, significantly reducing the doses reaching healthy tissues and therefore limiting negative side effects (Au *et al.*, 2018). Finally, it is possible, by stereotactic ablative radiation therapy (SABR), to deliver an ablative radiation dose only to a specific target range, greatly reducing unwanted side effects (Albuquerque *et al.*, 2020; T. K. Nguyen *et al.*, 2018).

Cancer is a complex ailment and its successful treatment requires enormous efforts to combine the amount of information gained through testing and therapy procedures. The ability to connect data gathered from diagnostic images and molecular analyses has enabled un-invasive imaging techniques to achieve an analysis of the entire three-dimensional structure of the tumor. This is in accordance with the main objective of precision therapy, which is to reduce adverse effects linked to treatment while maximizing its success in order to obtain the best individualized therapy (Mi *et al.*, 2019).

Radiomics has the advantage that a whole tridimensional image of the tumour can be created by non-invasive imaging techniques. However, standardisation of procedures to facilitate clinical translation still remains a challenge (Prior *et al.*, 2020).

2.9.6 Exosomes

Exosomes serve as an essential regulatory factor during metastasis (Fang *et al.*, 2018). These includes the initiation, development and colonizing of metastases in surrounding regions by transmitting functional molecules thereby directly affecting targeted cells (Zang *et al.*, 2020). Organs prone to metastasis may be modified to be optimal for tumor colonization prior to the arrival of cancer cells, i.e. premetastatic niche formation (Zeng *et al.*, 2018). In physiological system, GFP-exosomes are secreted into the neighbouring tumor tissues and are distributed from primary to metastatic niche tumors cells (T. Huang & Deng, 2019b).

Studies show that exosomes play a critical part in cancer metastasis (Whiteside, 2018). This include taking part in the formation of the premetastatic niche, microenvironment of tumor cells, and in the determination of specific organotropic metastasis (Chicón-Bosch & Tirado, 2020; Groza *et al.*, 2020). Upon drug treatment, exosomes originating from drug resistance cells, may also transfer the resistant characteristics to the recipient cells for induction of resistance (H. Y. Huang, Lin, Li, Huang, Shrestha, Hong, Tang, Chen, Jin, Yu, *et al.*, 2020). In fact, exosomes will usually activate the immune response to suppress the activity of the immune cells, thus growing immunogenicity to enhance the anti-tumor activity under certain particular stress conditions (Tao Huang & Deng, 2019a).

Attacking metastasis-related exosomes offers a new strategy to designing innovative, effective anti-tumor treatment agents (S. Jiang *et al.*, 2019; Spugnini *et al.*, 2018). Increasing evidence indicates that exosomes and their contents lead to pre-metastatic microenvironment development and trends of non-random metastasis (Do *et al.*, 2020; Pitarresi & Rustgi, 2019; Ruysen, 2019). Exosomes are secreted by practically all types of cells and can deliver proteins, lipids, DNA, and RNA into the receiver cells (Pitarresi & Rustgi, 2019).

This happens in three pathways namely; attachment of the surface receptor, binding to the target cells or internalization of the vesicle, thereby controlling the functional state of the cells (Tao Huang & Deng, 2019a). The structure and contents of an exosome is as shown in **Figure 13**.

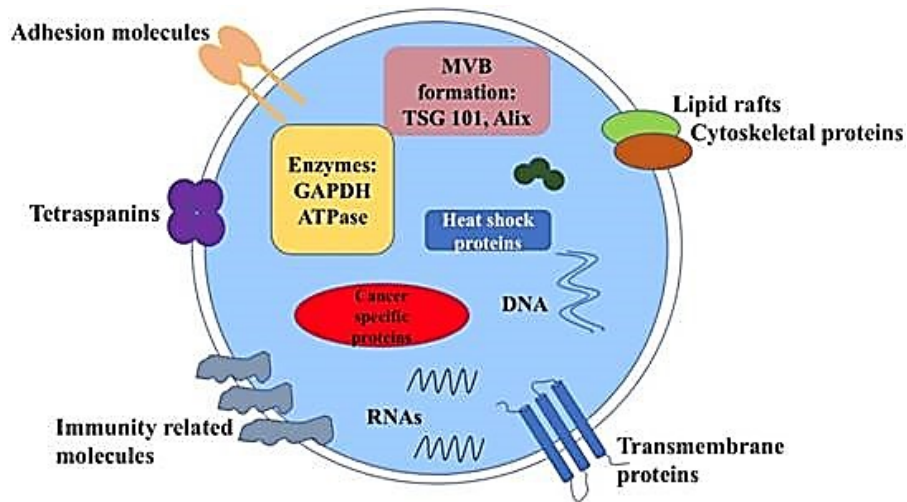


Figure 13 Structure and Composition of exosomes derived from cancerous Cells.

[Adapted from Cells (T. Huang & Deng, 2019b)]

The proteins include many of the major raft lipids present in cell membranes, such as ceramides, sphingolipids, cholesterol and glycerophospholipids (Scavo *et al.*, 2020). Exosomes' primary RNA is miRNA, but they also contain long non-coding RNAs (LncRNAs), which in many respects control gene expression (Y. Xie *et al.*, 2019). There is, however, still a shortage of preclinical data and further clinical treatment trials of antimetastatic-active agents (Lu *et al.*, 2018). Hence, explicitly designing antimetastatic medication for clinical use will be very necessary to allow researchers to concentrate on the dynamics of cancer metastasis.

Today, the most common reports on chemotherapy treatments in the clinical research database (www.clinicaltrials.gov) refer to the words precision therapy, immunotherapy and gene therapy, demonstrating that these are the most prevalent techniques (**Figure 14**) under study, especially when they have displayed success and effectiveness as already stated. The rising in number of these new technologies demonstrate how the potential and applicability is increasing rapidly to substitute and/or strengthen traditional therapeutics. Radiomics, immunotherapy, and exosomes can be seen as the categories whose numbers has risen most in the last decade.

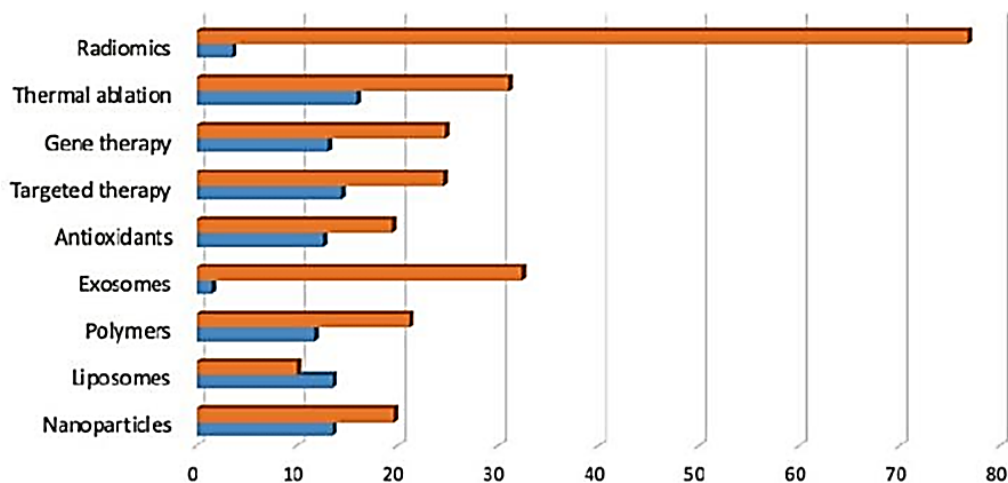


Figure 14 Summary of the number of clinical trials started during the years 2008–2010 (blue) and from 2017 until today (orange) www.clinicaltrials.gov

The current situation for cancer research is broad providing several opportunities for innovation taking into account not just the rehabilitation of patients but rather their well-being during treatment (Tang *et al.*, 2018). Such new techniques offer several benefits in comparison to conventional treatments. Nonetheless, to boost their performance, several drawbacks have yet to be resolved (Cecchini *et al.*, 2019; J. Liu *et al.*, 2018; McClure *et al.*, 2018; Philip *et al.*, 2018; Singh *et al.*, 2018). Great advances have been made, but even more are likely to emerge in the coming years, creating more *ad hoc* customized treatment.

Even though there are quite a variety of plausible hypotheses on how to manage cancer, there are still some inherent issues which cannot be overlooked in finding a cure, especially for solid tumors. First, tumors are not just a single disease but a number of diseases that have selective response to different anticancer agents. In order to detect disease genotypes, robust repositories are needed to manage vast volumes of data from expression of genes, histology, 3D tissue modeling (MRI) and metabolism characteristics (positron emission tomography, PET) (H.-Y. Huang, Lin, Li, Huang, Shrestha, Hong, Tang, Chen, Jin, & Yu, 2020; G. Lee *et al.*, 2020; Nadeem *et al.*, 2020).

Progress into cancer therapy has taken significant strides in recent years toward a more reliable, accurate and less intrusive therapies (**Figure 14**). While nanomedicine, along with targeted therapy, has continued to enhance the biodistribution of emerging or already approved therapeutic drugs around the particular tissue to be handled, other methods, such as gene therapy, nanoparticle delivery, immunotherapy, and antioxidant molecules, offer new opportunities to cancer victims (He

et al., 2020; Nagaraju *et al.*, 2020; Zins & Abraham, 2020). Thermal ablation and electrical hyperthermia, on the other side, offer solutions to resection of tumours (Amini *et al.*, 2018; Anghileri & Robert, 2019). Not only can tumors from the same population be distinct but not all cells are identical even from the same tumor in that same individual. Genotyping have shown that, when analysed using the standard histological staining method, what appears like a single disease could possibly be multiple cancers, with separate prognoses, that could require different treatments (Nicolás *et al.*, 2020).

Ultimately, approaches to radiomics and pathomics help enhance diagnosis and result in the handling of large data collections from cancer victims (Madabhushi *et al.*, 2019; Prior *et al.*, 2020; Tran *et al.*, 2019; P. Vaidya *et al.*, 2018). Taken collectively, these approaches would be able to provide people with cancer with the most tailored treatments, emphasizing the importance of combining different fields to achieve the best result (Phua *et al.*, 2019; Roma-Rodrigues *et al.*, 2019).

Cells can develop inhibitors in the form of enzymes to render drugs inactive (Bandari *et al.*, 2018; Luthra *et al.*, 2018). They may also develop various pathways to eject cell-based anticancer agents through specific proteins such as P-glycoprotein 1 also known as multidrug resistance protein 1 (PgP) (Macks *et al.*, 2018; J. K. Park *et al.*, 2020). While cancerous cells vary from healthy cells in many ways, the distinction has so far been difficult to analyze and exploit (D. S. Chen & Mellman, 2017).

Chemotherapeutic medications are thus expected to also impose adverse effects on healthy cells, despite their innermost modes of action (Petrylak *et al.*, 2020). This is demonstrated by the cardiotoxicity of trastuzumab, a medication that directly binds to HER-2 receptors (Han *et al.*, 2020; McCauley *et al.*, 2020). The use of different drug combinations is undoubtedly quite relevant, though it has not proven to be the final solution so far. Since cancer contributes to the breakdown of many complicated cellular functions, the most effective path may be to combine multiple strategies (Rachel S Riley *et al.*, 2019b; Yifan Wang, Deng, *et al.*, 2018).

This may include, focusing on specific targets in cancer cells and several other rapidly-growing cells and triggering immune response by increasing the normal immune response of the specific cancer cells (Galon & Bruni, 2019)

CHAPTER 3

METHODOLOGY

3.1 Synthesis

The ligands were synthesized by Schiff base condensation process and characterized by FTIR, ^1H and ^{13}C NMR, UV-Vis, elemental analysis and single crystal x-ray crystallography. All the ligands were characterized by ^1H NMR against a TMS reference standard. The splitting designated as s (singlet), d (doublet), dd (doublet of a doublet), t (triplet) m (multiplet) or br (broad). Frequency shifts were observed for the various chemical environments as a result of electronic and steric effects of different substituents.

The metal pyrrole complexes (**C1- C5**) were obtained through the reaction of Pd(cod)Cl₂, Pd(cod)ClMe or Pt(DMSO)₂Cl₂ precursors with a solution of the respective ligand in DCM at room temperature. The complexes (**C1- C3**) were formed through a reaction of 1:2 (metal:ligand) molar ratios using ligands **L1- L3**; **C4** was formed from a 1:1 molar ratio using ligand **L4**, while **C6** was formed from a 1:1 molar ratio using ligand **L1**.

The thiosemicarbazide complexes (**C7-C11**) were synthesized through a reaction of the metal precursors Pd(cod)Cl₂, Pd(cod)ClMe, K₂PtCl₄ or PdCl₂(PPh₃)₂ with a solution of the respective ligand in THF at room temperature. These ratios were confirmed by elemental analysis.

Recrystallizations were carried out by dissolving the particular compound in minimum solvent and dropwise adding a second solvent in which the compound has less solubility. The solubility gradient forces the compound to come out of solution and form a precipitate. All the yields were calculated against the limiting reagent.

3.2 Instrumentation

The results from the elemental (C, H, N) percentages were compared with the theoretical formulation and acceptable values fell within $\pm 0.4\%$ of the expected value.

Single crystals suitable for x-ray crystallography were grown by slow diffusion of hexane into DCM which gave crystal for **L1**, or by slow evaporation of a DCM solution for **L2, L3, L5** and complex **C6**. Crystallography was performed on a Bruker SMART CCD APEXII area-detector diffractometer and were kept at 100.03 K during data collection. Using Olex2 software the structures were solved with the ShelXS-1997 (Sheldrick, 2015) structure solution program using Direct Methods and refined with the Olex2 refinement package (Bourhis *et al.*, 2015).

Melting point determinations were performed on glass capillaries on a SMP-10 melting point apparatus. FTIR spectra were recorded using Perkin-Elmer Spectrum 100 Series FT-IR instrument on KBr pellets on the range 4000-400 cm^{-1} and ^1H nuclear magnetic resonance (NMR) spectra were run on a Bruker 400 MHz spectrometer available at the University of Western Cape (UWC), South Africa. The chemical shifts were measured in ppm relative to TMS standard.

Elemental analysis was carried out on Server 1112 series Elemental Analyzer at Stellenbosch University. GC-MS Mass spectroscopy for the ligands was performed at UWC using Mass Hunter GC-MS analyser from Agilent Technologies. LC-MS for the complexes was performed at Stellenbosch University using a Waters Synapt G2 instrument, ESI probe, at a cone Voltage of 15V. UV-Vis spectra were run in DMSO at a range of 200-800nm using Nicolet evolution 100 spectrophotometer from Thermo Electron Corporation, and the data analysed using VisionPro software.

Cyclic voltammetry studies were performed using PalmerScan3 instrument equipped with glassy carbon electrodes as working electrodes, Ag/AgCl as reference electrode and platinum wire as counter electrode, scan range of -1.8 to +1.8, and a scan rate of 200mV/s. The supporting electrolyte was 5ml 10mMol PBS buffer at pH7. Single crystal x-ray crystallography was run on Bruker SMART CCD APEXII area-detector diffractometer available at Rutgers University, USA and structures were solved and refined using ShelXS-1997 software and presented as ORTEP plots.

3.3 Synthesis of Pyrole-based Ligands

3.3.1 Synthesis of (E)-N-((1H-pyrrol-2-yl) methylene) (phenyl)methanamine (L1)

The ligand was synthesized using 0.3882g (4mmol) Pyrrole-2-carbaldehyde and 440ul (4mmol) benzylamine in dry methanol and refluxed for 12h. The mixture was vacuumed via rotary evaporator to dryness and the product obtained as an orange powder. It was recrystallized in DCM/Et₂O and kept in fridge for 12 h to complete precipitation.

3.3.2 Synthesis of (E)-N-((1H-pyrrol-2-yl) methylene) (thiophen-2-yl) methanamine (L2)

The ligand was synthesized with a similar procedure to **L1** using 0.4853g (5mmol) Pyrrole-2-carbaldehyde and 5mmol (515ul) 2-thiophenmethylamine and refluxed for 18h. The mixture was vacuumed to dryness by a rotary evaporator and the product obtained as an orange powder. It was re-dissolved in minimum diethyl ether, activated charcoal added, shaken and filtered. The solution

was kept for 12h in the fridge whereby it formed a crystalline product. Some of the crystalline product was used to grow crystals suitable for XRD by slow evaporation of the diethyl ether solution at 4°C in the fridge for 3days.

3.3.3 Synthesis of (E)-N-((1H-pyrrol-2-yl) methylene) (furan-2-yl)methanamine (L3)

The ligand was synthesized with a similar procedure to **L1** using 0.4853g (5mmol) Pyrrole-2-carbaldehyde and 450ul (5mmol) furfurylamine but stirred in room temperature for 18h in the presence of MgSO₄. The product was isolated as an orange powder which turned to brown. It was recrystallized from DCM with ether.

3.3.4 Synthesis of (E)-N-((1H-pyrrol-2-yl) methylene) (pyridin-2-yl)methanamine (L4)

The ligand was synthesized with a similar procedure to **L1** using 0.3882g (4mmol) Pyrrole-2-carbaldehyde and 420ul (4mmol) 2-methylamino pyridine. The reaction mixture turned to yellow during reflux. The solvent was evaporated to dryness via rotary evaporator and the product isolated as a dark brown paste.

3.4 Synthesis of Thiosemicarbazide-based Ligands

3.4.1 Synthesis of (E)-1-((thiophen-2-yl) methylene) thiosemicarbazide (L5)

The ligand was synthesized using 475ul (5mmol) thiophene-2-carbaldehyde and 0.4558g (5mmol) thiosemicarbazide and refluxed in dry methanol for 12h. after cooling down, a light brown precipitate was formed which was filtered and re-dissolved in Et₂O, filtered on activated carbon and kept in fridge for slow evaporation and the ligand was isolated as shiny brown crystalline product.

3.4.2 Synthesis of (E)-1-((5-bromothiophen-2-yl)methylene)thiosemicarbazide (L6)

The ligand was synthesized with a similar procedure to **L5** using 625ul (5mmol) 4-Bromothiophene-2-carbaldehyde and 0.4558g (5mmol) thiosemicarbazide. The ligand was obtained as a light brown precipitate.

3.4.3 Synthesis of (E)-1-((4-bromothiophen-2-yl)methylene)thiosemicarbazide (L7)

The ligand was synthesized with a similar procedure to **L5** using 1.061g (5mmol) 4-Bromothiophene-2-carbaldehyde and 0.4558g (5mmol) thiosemicarbazide. The ligand was obtained as a light brown precipitate.

3.4.4 Synthesis of (E)-1-((quinolin-2-yl)methylene)thiosemicarbazide (L8)

The ligand was synthesised with a similar procedure to **L5** using 3.7mmol (0.6022g) quinolone-2-carbaldehyde and 3.7mmol (0.3394g) thiosemicarbazide. The ligand was isolated as a red precipitate.

3.5 Characterization of the Ligands

3.5.1 Gas Chromatography-Mass Spectroscopy

Mass spectra (EI) were recorded as methanol solutions using a Mass Hunter GC-MS instrument available at UWC. An equilibration time of 0.5 min was used and a maximum temperature of 325⁰C. The fragmentation patterns were studied and the molecular ion peak observed for all the compounds studied.

3.5.2 Elemental Analysis

Elemental analysis was carried out on Server 1112 series Elemental Analyzer at Stellenbosch University. The results for C, H and N were calculated from the expected formulation and compared with the values obtained from the synthesized compounds. The experimental micro-analysis data fell within the expected values by $\pm 0.4\%$ confirming the formulations and purity.

3.5.3 UV-Visible Spectroscopy

UV/Visible data was recorded on within a spectral range of 200-800 nm. The instrument was first calibrated with a blank reference sample and taken in 1 cm quartz cells at molar concentration of 1.0×10^{-3} M.

3.5.4 Fourier Transform InfraRed Spectroscopy

FTIR spectroscopy was recorded using Perkin-Elmer Spectrum 100 Series FT-IR instrument on KBr pellets or ATR on a spectral range of 4000-400 cm^{-1} .

3.5.5 Proton Nuclear Magnetic Resonance Spectroscopy

¹H nuclear magnetic resonance (¹HNMR) spectra were performed on a Bruker 400 MHz spectrometer and analysed using Mestre Nova software. Samples were dissolved in an appropriate deuterated solvent (CDCl₃ or DMSO-d₆) and chemical shifts recorded against tetramethyl silane (TMS) internal standard peak and the shifts reported as parts per million (ppm) with respect to CDCl₃ at $\delta_{\text{H}} = 7.26\text{ppm}$ or DMSO-d₆ at $\delta_{\text{H}} = 2.50\text{ppm}$.

3.5.6 Carbon-13 Nuclear Magnetic Resonance Spectroscopy

¹³C nuclear magnetic resonance spectra data was performed on a Bruker 400 MHz spectrometer and analysed using Mestre Nova software. Samples were dissolved in an appropriate deuterated solvent (CDCl₃ or DMSO-d₆) and chemical shifts recorded against tetramethyl silane (TMS) internal standard peak and the shifts reported as parts per million (ppm) with respect to CDCl₃ at $\delta_C = 77.00\text{ppm}$ or DMSO-d₆ at $\delta_C = 39.52\text{ppm}$.

3.5.7 Single Crystal x-ray Crystallography

Single crystal x-ray crystallography was performed on Bruker SMART CCD APEXII area-detector diffractometer available at Rutgers University, USA. This was performed for five of the ligands that gave suitable crystals. The results obtained for the structures were compared with elemental analysis results and for any unexpected or unusual bonding.

3.6 Preparation for Precursor Complexes

3.6.1 Preparation of cis-Cyclooctadienepalladium(II) Chloride Precursor

Synthesis was performed at room temperature. A suspension of PdCl₂ (2.50 g, 14.1 mmol) in dry methanol (75 ml) was treated with 1,5-cyclooctadiene (cod) (5.2 ml, 42.3 mmol) and stirred for 48 h at room temperature. The product was obtained as a bright yellow air stable precipitate. It was filtered and washed severally with methanol, and dried under reduced pressure. Yield: 3.72 g 91%.

3.6.2 Synthesis of cis-dichloro bis-(dimethylsulfoxide) Platinum(II) Precursor

This was synthesized by dissolving 300mg (1.13 mmol) of PtCl₂ powder in 10ml DMSO and leaving the mixture to stand for four weeks. Light yellow crystals were isolated and filtered, washed with acetone and dried. Yield 248mg 52%.

3.6.3 Synthesis of cis-dichloro bis-(triphenylphosphine) Platinum(II) Precursor

The precursor was synthesized according to a reported literature procedure (Kukushkin *et al.*, 2002). A beaker containing solution of 313mg (1.19mmol) PPh₃ in ethanol was heated in an oil bath and brought gently to boil. Into this boiling solution, a 250mg (0.6mmol) K₂PtCl₄ dissolved in 5ml water was added dropwise. The temperature was then maintained at 60°C and stirred for 2h. A pale white crystalline precipitate was formed which was filtered and washed with hot water, hot ethanol and finally with diethyl ether and dried. Yield 205mg, 42%

3.7 Synthesis of the Pyrrole-based complexes

3.7.1 Synthesis of trans-Chloridobis[(pyrrolylmethylidene)(benz-2-ylmethyl) amine- κ N] methylPalladium(II) (C1)

To a stirring solution of 92mg (0.5mmol) ligand **L1** in dry DCM, a solution of 66mg (0.25mmol) Pd(cod)ClMe also in DCM was added dropwise. The solution turned green and stirring was continued at room temperature for 12h. The solution was concentrated under vacuum under liquid nitrogen to about 1ml and hexane added in excess to precipitate out the product. The mixture was kept in fridge for 12h to allow complete precipitation, liquor filtered off and isolated as a green precipitate which was washed with more hexane, filtered and dried in inert conditions under vacuum.

3.7.2 Synthesis of trans-Chloridobis[(pyrrolylmethylidene)(thiophen-2-ylmethyl) amine- κ N] methylPalladium(II) (C2)

The complex was synthesized similar to **C1** using 95mg (0.5mmol) **L2**. The product was isolated as a green powder.

3.7.3 Synthesis of trans-dichloridobis[(pyrrolylmethylidene)(furan-2-ylmethyl) amine- κ N] methylPalladium(II)- (C3)

The complex was synthesized as for the previous one using 174mg (1mmol) of **L3** and 144mg (0.5mmol) Pd(cod)Cl₂. The mixture formed an orange solution which was reduced to about 1ml by vacuum and the product recrystallized with diethyl ether. It was filtered and washed with 5ml Et₂O and further 2x5ml hexane, dried under vacuum to afford an orange powder product.

3.7.4 Synthesis of cis-dichlorido[(pyrrolylmethylidene)(pyridyl-2-ylmethyl) amine N,N] Palladium(II)- (C4)

The complex was synthesized using 93mg (0.5mmol) **L4** and 144mg (0.5mmol) Pd(cod)Cl₂. The product precipitated immediately and the mixture was stirred for 12h. It was filtered, washed with 5ml Et₂O and further 2x5ml hexane and dried under reduced pressure to obtain a grey powder product.

3.7.5 Synthesis of Pt₂Cl₂(dmsO)₂-L1 (C5)

Into a stirring solution of 42mg (0.125mmol) Pt(dmsO)₂Cl₂ in 15ml DCM, 0.125mmol (23mg) **L1** dissolved in 5ml DCM was added dropwise using a nitrogen filled syringe. Stirring was continued

for 12h after which the solvent was removed under reduced pressure to yield a yellow precipitate of **C5** which was washed with 3x2ml hexane, filtered and dried under vacuum to yield a yellow powder.

3.7.6 Synthesis of PtCl₂(dmsO)-L1 (C6)

The complex was prepared by growing crystals of **C5** by slowly evaporating a DCM solution of **C5** at 4°C after 1 week. It was obtained as light-yellow crystals.

3.8 Synthesis of the Thiosemicarbazone-based complexes (C7-C11)

3.8.1 Synthesis of L5-PdCl₂ (C7)

The complex was synthesized by dropwise addition of 92mg (0.25mmol) of **L5** dissolved in 2ml THF, into a stirring solution of 72mg (0.25mmol) Pd(cod)Cl₂ in 15ml DCM under argon. The solution turned red with precipitation immediately and stirring was carried on at ambient conditions for 24h. The solvent was reduced to about 1ml, excess hexane added followed by filtration and washing of the red powder product with 3x5ml hexane, filtration and drying under vacuum.

3.8.2 Synthesis of L6-PdCl₂ (C8)

Synthesized with a similar procedure to **C7** using 66mg(0.25mmol) **L6**. It was isolated as a brown precipitate.

3.8.3 Synthesis of L8-PdClMe (C9)

The complex was synthesized by the slow addition of 58mg (0.25mmol) of **L8** in 10ml THF to a stirring solution of 66mg (0.25mmol) Pd(cod)MeCl in 10ml DCM in a schlenk tube. After stirring for 24h at room temperature at which time it precipitated a red powder product. The mother liquor was filtered off and the precipitate washed twice with 15ml Et₂O and dried under vacuum.

3.8.4 Synthesis of L5-PtCl₂ (C10)

A solution of 104mg (0.25mmol) K₂PtCl₄ dissolved in 3ml MeOH/H₂O (2:1) was added dropwise into a stirring solution of 46mg (0.25mmol) **L5** in 2ml THF. A yellow precipitate was formed immediately and stirring was continued for one and half hours at room temperature. The precipitate was filtered and washed with 3x5ml diethyl ether and dried under vacuum.

3.8.5 Synthesis of L7-PtPPh₃ (C11)

The complex was synthesized following the procedure for **C10** by adding 198mg(0.25mmol) of PtCl₂[(PPh₃)₂]₂ dissolved in 5ml DCM, into a stirring solution of 66mg (0.25mmol) of **L7** in 20ml

benzene at room temperature. Stirring was continued for 24h and the product was isolated as a yellow precipitate.

3.9 Characterization of the Complexes

3.9.1 Liquid Chromatography-Mass Spectroscopy Analysis

This was conducted on a Waters Synapt G2, ESI probe, ESI Pos, Cone Voltage 15 V instrument, on the pyrrole complexes to ascertain their molecular masses.

3.9.2 Elemental Analysis

Elemental analysis was performed on Server 1112 series Elemental Analyzer at Stellenbosch University. The results for C, H and N were calculated from the expected formulation and compared with the values obtained from the synthesized compounds.

3.9.3 Electrochemical Properties of the Complexes by Cyclic Voltammetry

Electrochemical studies to understand the redox properties of these type of compounds in solution were performed on the complexes using PalmerScan3 instrument equipped with glassy carbon electrodes as working electrodes, Ag/AgCl as reference electrode and platinum wire as counter electrode. A scan range of -1.8 to +1.8 was used at different scan rates, with 5ml 10mMol Phosphate Buffered Saline buffer used as supporting electrolyte at pH 7.0.

3.9.4 UV-Visible Spectroscopy

UV/Visible data was scanned within a spectral range of 200-800 nm using Nicolet evolution 100 spectrophotometer from Thermo Electron Corporation. The instrument was first calibrated with a blank reference sample and taken in 1 cm quartz cells at molar concentration of 1.0×10^{-3} M.

3.9.5 Fourier Transform Infrared Spectroscopy

FTIR spectra were run on a Perkin-Elmer Spectrum 100 Series FT-IR instrument on KBr pellets or ATR on a spectral range of $4000-400\text{cm}^{-1}$.

3.9.6 Proton Nuclear Magnetic Resonance Spectroscopy

^1H nuclear magnetic resonance (^1H NMR) spectra were run on a Bruker 400 MHz spectrometer and analysed using Mestre Nova software. Samples were dissolved in an appropriate deuterated solvent (CDCl_3 or DMSO-d_6) and chemical shifts recorded against tetramethyl silane (TMS) internal

standard peak and the shifts reported as parts per million (ppm) with respect to CDCl_3 at $\delta_{\text{H}} = 7.26\text{ppm}$ or DMSO-d_6 at $\delta_{\text{H}} = 2.50\text{ppm}$.

3.9.7 Carbon-13 Nuclear Magnetic Resonance Spectroscopy

^{13}C nuclear magnetic resonance spectra data was recorded on a Bruker 400 MHz spectrometer and analysed using Mestre Nova software. Samples were dissolved in an appropriate deuterated solvent (CDCl_3 or DMSO-d_6) and chemical shifts recorded against tetramethyl silane (TMS) internal standard peak and the shifts reported as parts per million (ppm) with respect to CDCl_3 at $\delta_{\text{C}} = 77.00\text{ppm}$ or DMSO-d_6 at $\delta_{\text{C}} = 39.52\text{ppm}$.

3.9.8 Single Crystal x-ray Crystallography

Single crystal x-ray crystallography was performed on Bruker SMART CCD APEXII area-detector diffractometer available at Rutgers University, USA. This was performed for **C6** that gave suitable crystals. The results obtained for the structure was compared with elemental analysis results and for any unexpected or unusual bonding.

3.9.9 Partition Coefficient: Lipophilicity studies

Lipophilicity was determined as log P values by the shake-flask method as reported in literature (Sangster, 1997). The complexes were partitioned between 10ml of deionized water (the medium inside and outside the cells) and 10ml of 99% n-octanol (a model of the lipid bilayer of cell membrane), and stirring for 48h. This was done after the two layers were first pre-saturated with each other to avoid solubility-induced volume changes during the extraction step.

The mixture was then left to settle for 24h after which 3ml aliquots were micro-pipetted from each layer and centrifuged for 2h at 7000 rpm using Minispin Eppendorf centrifuge. The UV-Vis absorbance for the two layers was taken after appropriately diluting the layers as per a method described in literature (Minick *et al.*, 1988). Absorbance was read using a 96-well micro plate on a POLARstar Omega microplate reader instrument from BMG Labtech.

The partition coefficients were determined by UV-Vis and was calculated as $\log(C_{\text{O}}/C_{\text{W}})$ where C_{O} is the concentration in oil layer and C_{W} is the concentration in water layer. Triplicate tests were performed under different volumes and the data reported as mean log partitioning coefficient ($\log P_{\text{ow}}$) \pm standard deviation.

3.9.10 Stability studies

The tests were performed in DMSO-d₆ after addition of 200ul of D₂O and running ¹H NMR scans at 6h intervals over a 72h period. The spectra were studied for any changes in proton environments with time.

3.9.11 DNA binding Studies

To study the binding modes of the complexes with DNA, the samples were prepared in 10mM Tris(hydroxymethyl)aminomethane hydrochloride (tris-HCl; linear formula NH₂C(CH₂OH)₃.HCl) buffer at pH 7.21. The UV-Vis scans were performed by serial titrations of incremental amounts of calf thymus DNA (CT-DNA) to a fixed concentration of all the complexes. Complex **C2** was not studied due to solubility problems. The complex-DNA mixture was allowed to equilibrate 10minutes prior to taking of measurements.

The binding kinetics for the complex-DNA interaction was determined from the variations in the absorbance of a complex on serial titrations with DNA. This was done by determining the binding constant, K_b from the plots of the Benesi-Hildebrand host-guest equation (**Equation 2**) (Kuntz Jr *et al.*, 1968).

$$\frac{A_o}{A - A_o} = \frac{\epsilon_G}{\epsilon_{H-G} - \epsilon_G} + \frac{\epsilon_G}{\epsilon_{H-G} - \epsilon_G} \frac{1}{K_b[\text{DNA}]}$$

Equation 2

where A_o and A are the absorbances of the blank sample without DNA, and absorbance of complex-DNA after addition of serial concentrations of DNA respectively; while ε_G and ε_{H-G} are the molar extinction coefficients of complex only and complex-DNA respectively. The binding constant is determined by plotting A_o/(A - A_o) vs 1/[DNA] to give a straight line graph. The equation of the straight line gives the slope and intercept where the K_b value is calculated from the ratio of the intercept to the slope.

3.9.12 Cytotoxicity Assay

These assays were performed using commercially available cancer cell lines and standard procedures for tetrazolium assays. Select cells were seeded at a density of 2–4 × 10⁴ cells/well in a 96-well-plate (rows A-H) in 100 μL of culture medium containing 10% Foetal Bovine Serum (FBS) and incubated at 37 °C in humidified CO₂ atmosphere in an incubator. After 12-hour duration, test compounds were added to the cultured cells at various concentrations and incubated again for 48h. 0.5 mg/ml solution of 3-(4,5-dimethylthiazol-2-yl)-2,5-diphenyltetrazolium -Bromide dye (MTT)

dissolved in Phosphate Buffered Saline (PBS) was added to each well 5h before the end of incubation time and incubation continued for the 5h.

100 μ L DMSO was then added to the well after which the absorbance of the dye was measured at a wavelength of 570 nm according to literature reports (da Silva Frozza, 2017). Dilutions were spread across the 96 well micro titre plates to provide different concentrations which were used to calculate the IC₅₀ values. Triplicate tests were performed for each preparation and the data analysed as mean \pm standard deviation. The degree of reduction of the colourless dye by NADH or NADPH from viable cells to form a red formazan product was then determined by comparison of the UV-absorbance of the drug-spiked test cells to the one of untreated controls since the extent of colour formation is proportional to the number of live cells (da Silva Frozza, 2017)

CHAPTER 4

RESULTS AND DISCUSSION

4.1 Background

The ligands were synthesized by Schiff base condensation process and characterized by FTIR, ^1H and ^{13}C NMR, UV-Vis, elemental analysis and single crystal x-ray crystallography. All the ligands were characterized by ^1H NMR against a TMS reference standard. The splitting designated as s (singlet), d (doublet), dd (doublet of a doublet), t (triplet) m (multiplet) or br (broad). Frequency shifts were observed for the various chemical environments as a result of electronic and steric effects of different substituents.

UV-visible spectra for the compounds were recorded in DMSO at range 200- 800 nm using quartz cells at a concentration of $1.0 \times 10^{-3}\text{M}$ from which the molar absorptivity was calculated. Ligand spectra showed peaks falling in the range 233-292nm and 340-390nm, corresponding to intra-ligand, spin-allowed $\pi \rightarrow \pi^*$ in addition to $n \rightarrow \pi^*$ centered on the aromatic units. These transitions had molar extinction coefficients ranging from 10^3 - 10^4 $\text{LMol}^{-1}\text{cm}^{-1}$. The elemental analysis for carbon, hydrogen and nitrogen (C, H, N) was carried out to confirm the proposed structures and therefore the successful synthesis and purity of the compounds.

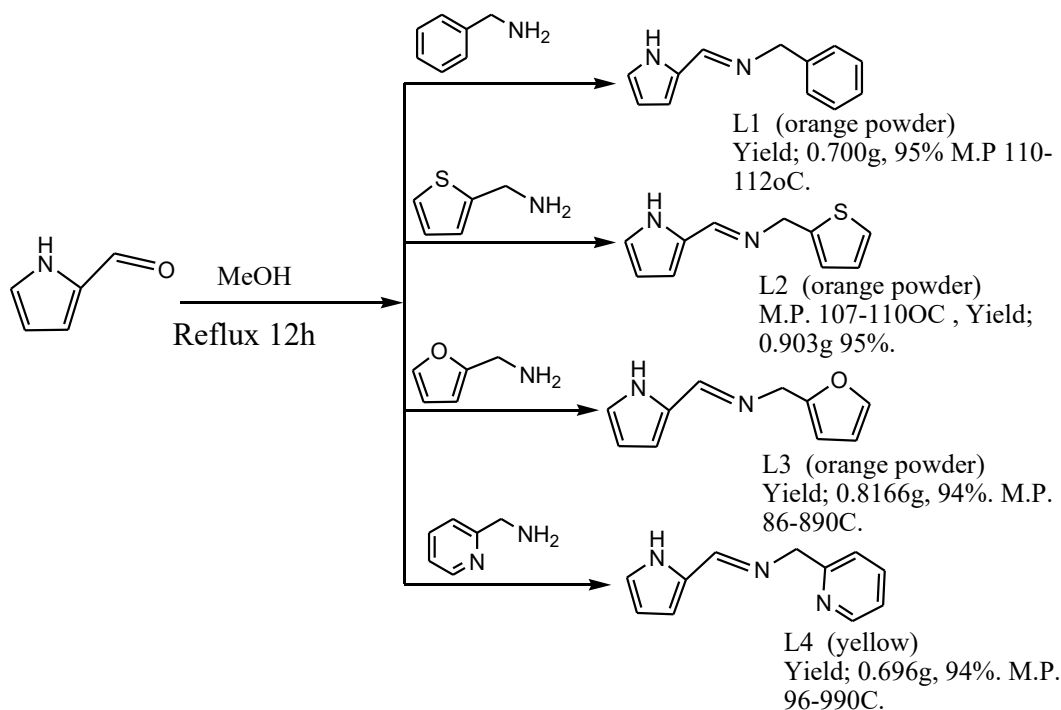
The results from the elemental (C, H, N) percentages were compared with the theoretical formulation and acceptable values fell within $\pm 0.4\%$ of the expected value. The metal pyrrole complexes (**C1-C5**) were obtained through the reaction of $\text{Pd}(\text{cod})\text{Cl}_2$, $\text{Pd}(\text{cod})\text{ClMe}$ or $\text{Pt}(\text{DMSO})_2\text{Cl}_2$ precursors with a solution of the respective ligand in DCM at room temperature. The complexes (**C1-C3**) were formed through a reaction of 1:2 (metal:ligand) molar ratios using ligands **L1-L3**; **C4** was formed from a 1:1 molar ratio using ligand **L4**, while **C6** was formed from a 1:1 molar ratio using ligand **L1**.

Due to steric factors, the complexes binding at 1:2 ratio (metal:ligand) are believed to be of *trans* geometry. Similar work was reported on bis-ferrocenyl Schiff base complexed with Pd which confirmed a monodentate binding of the Schiff bases to the metal center through the imine-N without involving the heteroatoms on the rings (Motswainyana *et al.*, 2012). The thiosemicarbazide complexes (**C7-C11**) were synthesized through a reaction of the metal precursors $\text{Pd}(\text{cod})\text{Cl}_2$, $\text{Pd}(\text{cod})\text{ClMe}$, K_2PtCl_4 or $\text{PdCl}_2(\text{PPh}_3)_2$ with a solution of the respective ligand in THF at room temperature. These ratios were confirmed by elemental analysis.

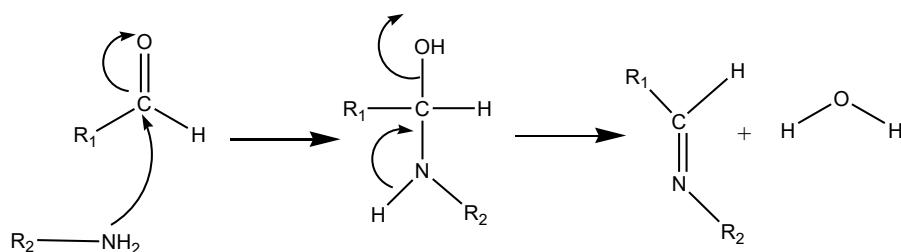
Single crystals suitable for x-ray crystallography were grown by slow diffusion of hexane into DCM which gave crystal for **L1**, or by slow evaporation of a DCM solution for **L2**, **L3**, **L5** and complex **C6**. Crystallography was performed on a Bruker SMART CCD APEXII area-detector diffractometer and were kept at 100.03 K during data collection. Using Olex2 software the structures were solved with the ShelXS-1997 (Sheldrick, 2015) structure solution program using Direct Methods and refined with the Olex2 refinement package (Bourhis *et al.*, 2015).

4.2 Synthesis of the Pyrrole-based Ligands (L1-L4)

The synthetic procedure for ligands **L1-L4** is as outlined in **Scheme 13** below while the reaction mechanism between the primary amines and the aldehydes used is outlined in **Scheme 14**.



Scheme 13 Synthesis of the Pyrrole-based ligands **L1-L4**



Scheme 14 Reaction Mechanism for the Schiff base formation between the primary amines and the aldehydes

The ligands (**L1-L4**) were synthesized according to methods given in the methodology section. They were then characterized by FTIR, ^1H and ^{13}C NMR spectral analyses, UV-vis, and elemental analysis, in addition to x-ray crystallography for **L1-L3**. This confirmed the structures of the ligands as explained below:

4.3 Structure Confirmation for Ligand L1

FTIR was used to assess the formation of an azomethine bond which is the main characteristic of Schiff bases. The disappearance of a vibrational band at 1700 cm^{-1} indicated the absence of the starter aldehyde, while the appearance of a strong vibration band at 1636 cm^{-1} indicated the formation of an imine ($\text{C}=\text{N}$) bond; confirming a successful reaction. This agrees with literature reports where the imine stretch is reported to occur between $1630\text{-}1650\text{ cm}^{-1}$ (Hussain *et al.*, 2014).

The absence of an aldehyde proton peak at around $\delta 9\text{ ppm}$ and the appearance of a peak at $\delta 8.15\text{ ppm}$ (iminic proton) in the ^1H NMR also agreed with literature reports confirming a successful reaction (J. Wang, Liu, Jiang, *et al.*, 2018) (García-Valle *et al.*, 2018). The shift to higher frequency is as a result of a less electronegative atom (N vs O), causing less deshielding of the neighbouring proton. Carbon-13 NMR showed no aldehyde peak at around $\delta 190\text{ ppm}$, with a $\text{C}=\text{N}$ carbon peak appearing at 153.35 ppm which is within the range reported in literature (Xavier *et al.*, 2018), further confirming an imine formation. (Similar trend was observed for the other ligands **L2-L4**).

4.3.1 Gass Chromatography-Mass Spectroscopy Analysis for L1

GC-MS was performed on the ligand which indicated a clear molecular ion peak, M^+ at M/z 184.1 which agreed with the molecular mass of the molecule of 184.1 as shown by **Figure 15** and by the fragmentation pattern in Scheme 15 below.

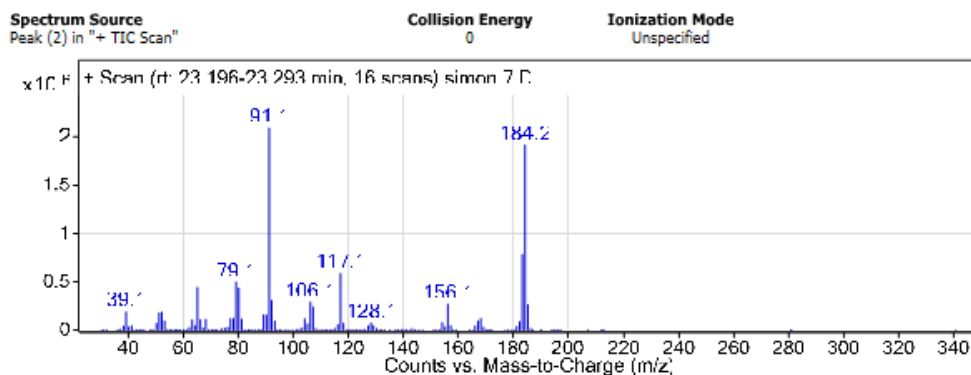
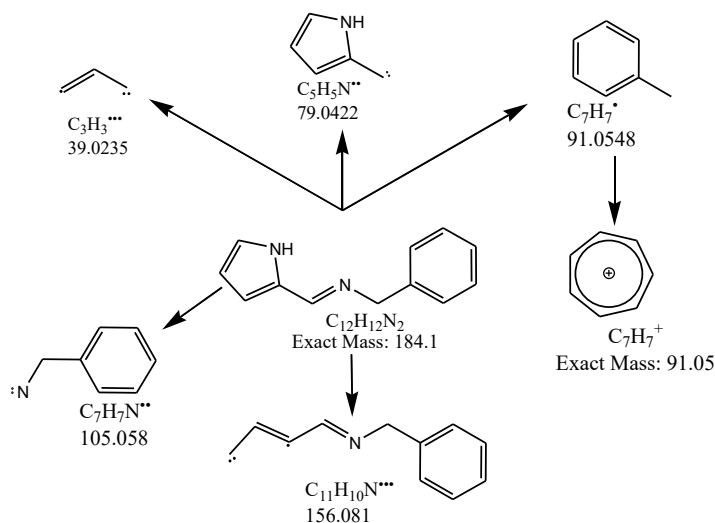


Figure 15 GC-MS peaks for L1



Scheme 15 Proposed fragmentation for **L1**

Further confirmation of the structure was achieved by single crystal x-ray structure crystallography and elemental analysis; where the obtained data was in agreement with the calculated values; obtained (calculated) C 74.2 (74.46), N 15.21 (15.63), H 6.8 (7.0).

4.3.2 Single Crystal X-ray Structure for **L1**

The molecular packing in the unit cell shows a stack of 8 molecules per unit when viewed down the crystallographic 'a' axis and rotated along the y-axis as shown in **Figure 16** (a) below. **Figure 16**(b) shows the intermolecular hydrogen bonding between the molecular pairs.

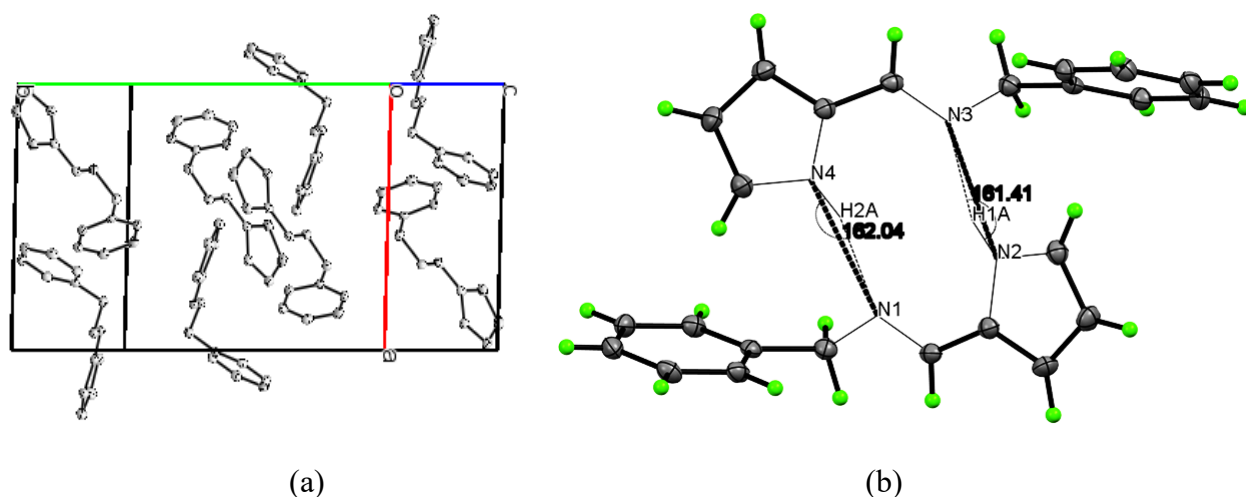


Figure 16. The unit Cell for ligand **L1** showing the crystal packing

The ligand crystallizes in the $P 2_1/n$ space group. Stabilization within the molecule is through intermolecular hydrogen bonding between the imine nitrogen of one molecule and the hydrogen attached to the pyrrole nitrogen of the second molecule. The intermolecular bond distances for this ligand were found to be different, being 2.136 Å and 2.193 Å. The intermolecular bond angles subtended by the H-bonded hydrogen are also different, being 161.41° for N2-H1-N3, and 162.04° for N1-H2-N4 as shown in (b). The pyrrole and the benzyl rings lie at a torsion angle of 123.57° for one molecule and 118.97° for the second molecule.

4.4 Structure Confirmation for Ligand L2

Similar to the FTIR spectra of **L1**, the disappearance of a vibrational band at 1700 cm^{-1} indicated the absence of the starter aldehyde, while the appearance of a strong vibration band at 1640 cm^{-1} indicated the formation of an imine (C=N) bond; confirming a successful reaction. This observation agrees with literature reports for the imine bond formation (Hussain *et al.*, 2014). ^1H NMR also confirmed a successful reaction by the absence of a peak at around δ 9ppm (aldehyde proton), and the appearance of an iminic proton peak at δ 8.13ppm.

Literature reports support this observation for an iminic proton (García-Valle *et al.*, 2018). Carbon-13 NMR showed no aldehyde peak at around δ 190ppm, with a C=N carbon peak appearing at 153.78, further confirming an imine bond.

4.4.1 Gas Chromatography-Mass Spectroscopy for Ligand 2

GC-MS was performed on the ligand which indicated a clear molecular ion peak, M^+ at M/z 190.1 which agreed with the molecular mass of the molecule of 190.06 as shown by **Figure 17** and by the fragmentation pattern in **Scheme 16** below.

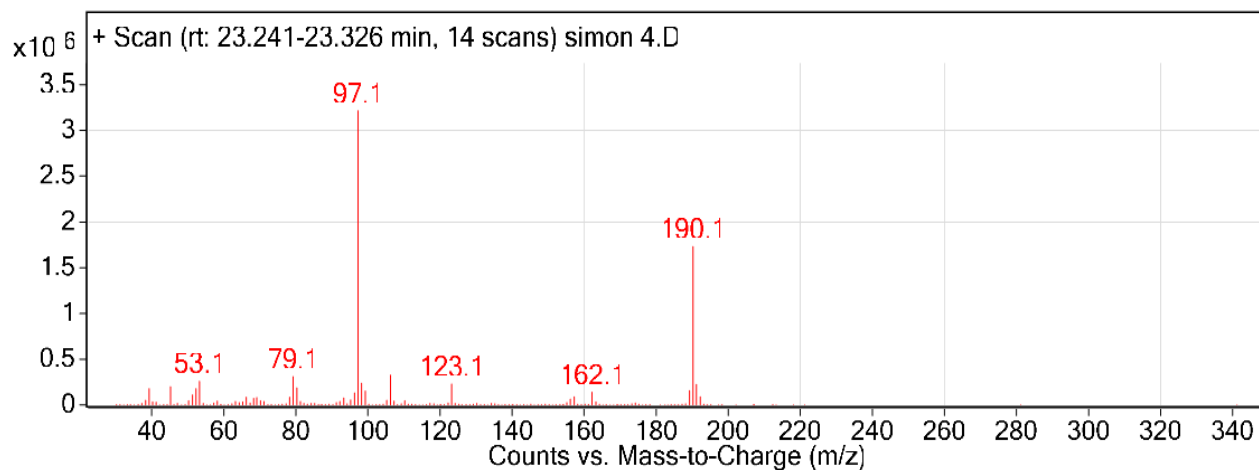
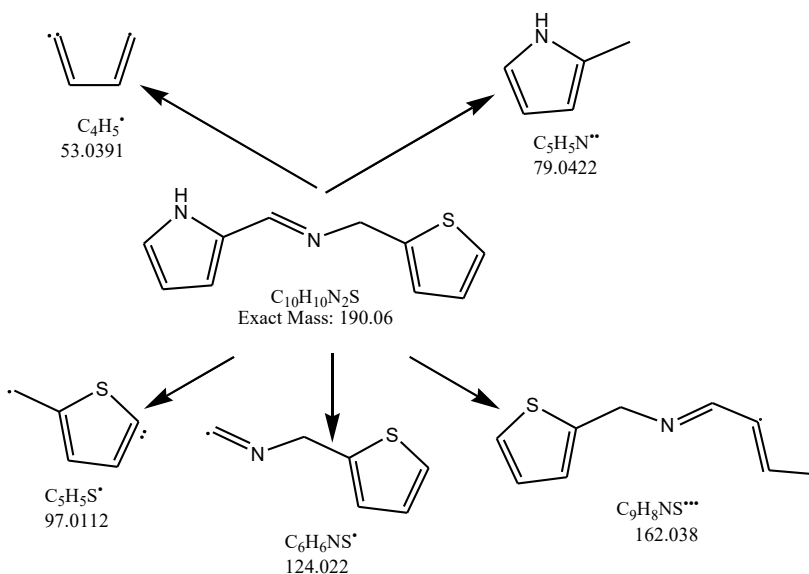


Figure 17 GC-MS for L2



Scheme 16 Proposed Fragmentation Pattern for L2

Further confirmation of the structure was achieved by elemental analysis where the obtained data agreed well with the calculated values; obtained (calculated) C 63.12 (63.13), N 14.7 (15.41), H 5.3 (5.8), S 16.9 (16.9) and single crystal x-ray structure determination.

4.4.2 Single Crystal X-ray Structure for L2

The structure and ORTEP ellipsoid diagram for L2 are shown in **Figure 18** at 50% probability showing numbering and the intermolecular stabilization through H-bonding (dashed lines) (N- blue Colour, H- green, C- Grey, S- Yellow).

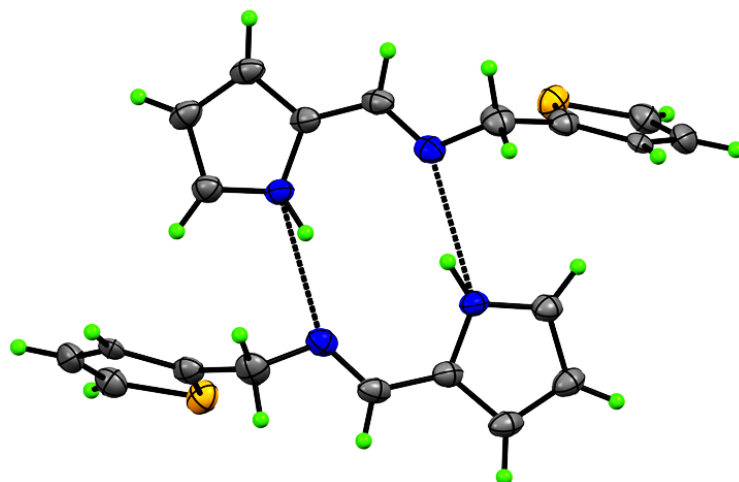


Figure 18 ORTEP Ellipsoids for **L2**

The ligand crystallizes in the $C 2/c$ space group. Stabilization within the molecule occurs through intermolecular hydrogen bonding between the imine nitrogen of one molecule and the hydrogen attached to the pyrrole nitrogen of the second molecule. The bond distances for both bonds is 2.165 Å and bond angles for N1-H-N2 of 152.44°. The pyrrole and the thiophenyl rings lie in nearly perpendicular planes to each other with a torsion angle of 82.96°. The molecular packing in the unit cell shows regular layered stacks of 8 molecules per unit when viewed down the crystallographic ‘b’ axis and rotated along the x-axis as shown in (**Figure 19**).

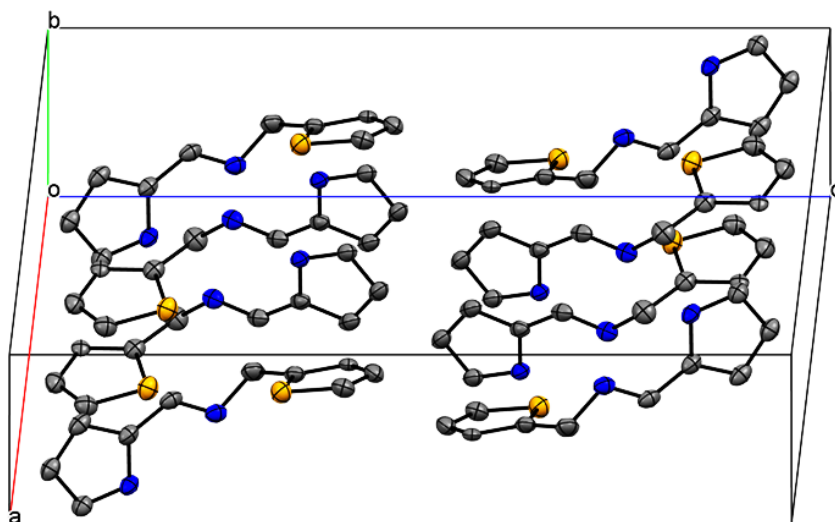


Figure 19 The unit Cell for **L2** showing the crystal packing

4.5 Structure Confirmation for Ligand L3

The appearance of a strong vibration band at 1644 cm^{-1} indicated the formation of an imine ($\text{C}=\text{N}$) bond; confirming a successful reaction. ^1H NMR also confirmed a successful reaction by the absence of a peak at around δ 9ppm (aldehyde proton), and the appearance of an iminic proton peak at δ 8.12ppm. Carbon-13 NMR showed no aldehyde peak at around δ 190ppm, with a $\text{C}=\text{N}$ carbon peak appearing at 153.19, further confirming an imine.

4.5.1 Gas Chromatography-Mass Spectroscopy for Ligand 3

GC-MS was performed on the ligand which indicated a clear molecular ion peak, M^+ at M/z 174.1 which agreed with the molecular mass of the molecule of 174.08 as shown by **Figure 20** and by the fragmentation pattern in **Scheme 17** below.

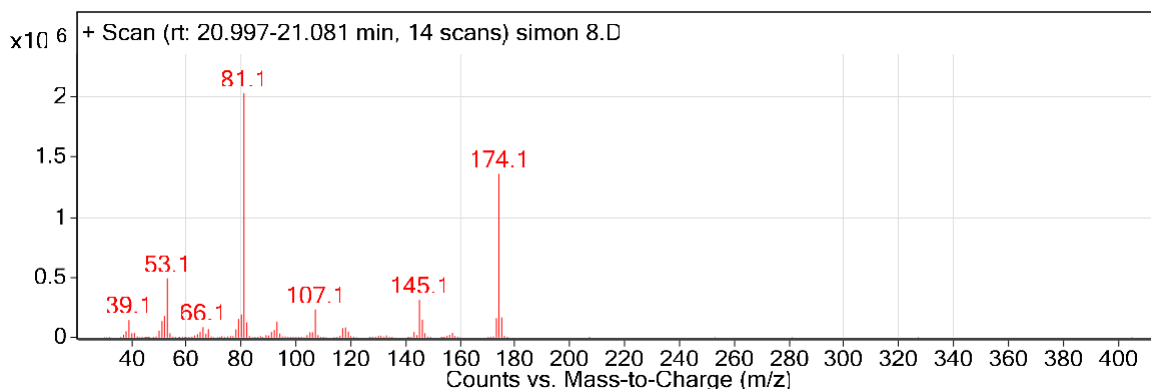
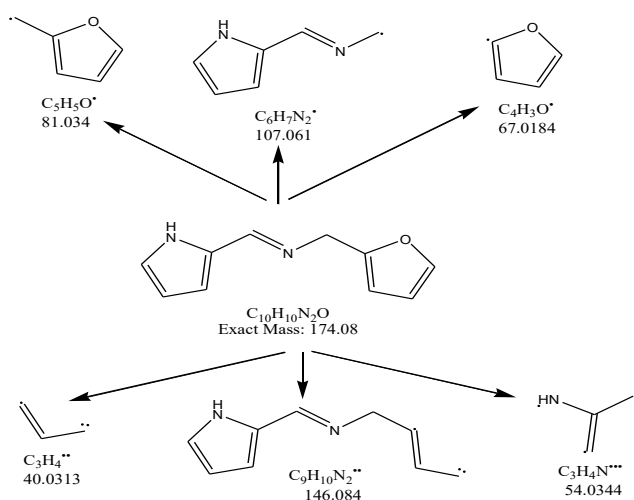


Figure 20 GC-MS peaks for L3



Scheme 17 Proposed Fragmentation Pattern for L3

Further confirmation of the structure was achieved by elemental analysis where the obtained data agreed well with the calculated values; obtained (calculated) C 68.95(68.61), H 5.79(6.2), N 16.08(16.47) and single crystal x-ray structure determination.

4.5.2 Single Crystal X-ray Structure for L3

The ligand crystallizes into the centrosymmetric P-1 triclinic space system, implying a complete absence of any symmetry constraint on the unit cell parameters. The crystal packing shows two molecules per unit as shown in (**Figure 21**). The atoms are colour coded as; C- grey; H- green; N- blue; O- red.

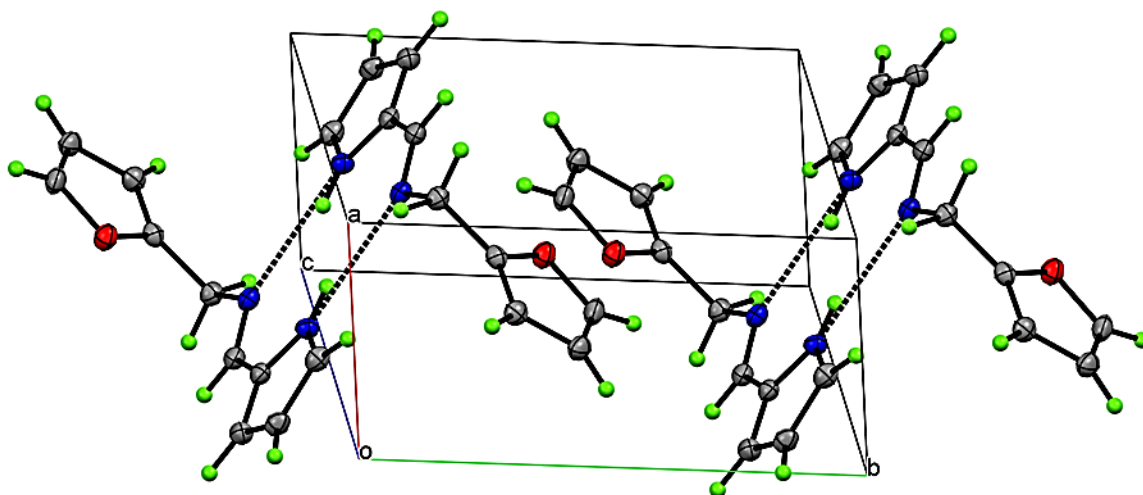


Figure 21 ORTEP Ellipsoids for L3 at 50% probability

As shown, the crystal is stabilized by intermolecular hydrogen bonding (dashed lines) of the hydrogens attached to imine and pyrrole nitrogen of adjacent molecules, but facing away from the center of the crystal.

4.6 Structure Confirmation for Ligand L4

4.6.1 Gas Chromatography-Mass Spectroscopy for Ligand 4

GC-MS was performed on the ligand which indicated a clear molecular ion peak, M^+ at M/Z 185.2 which agreed with the molecular mass of the molecule of 185.23 as shown by **Figure 22** and by the fragmentation pattern in **Scheme 18** below

Spectrum Source
Peak (5) in "+ TIC Scan"

Collision Energy
0

Ionization Mode
Unspecified

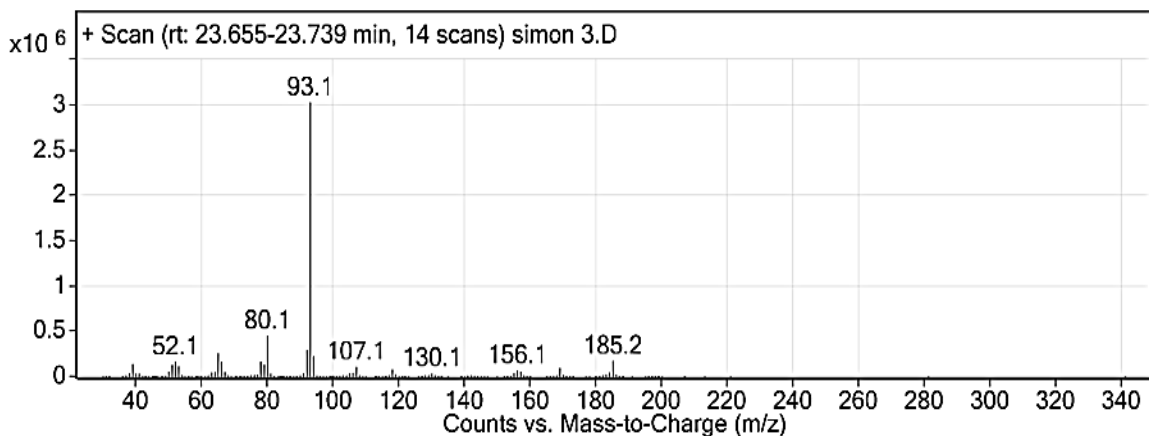
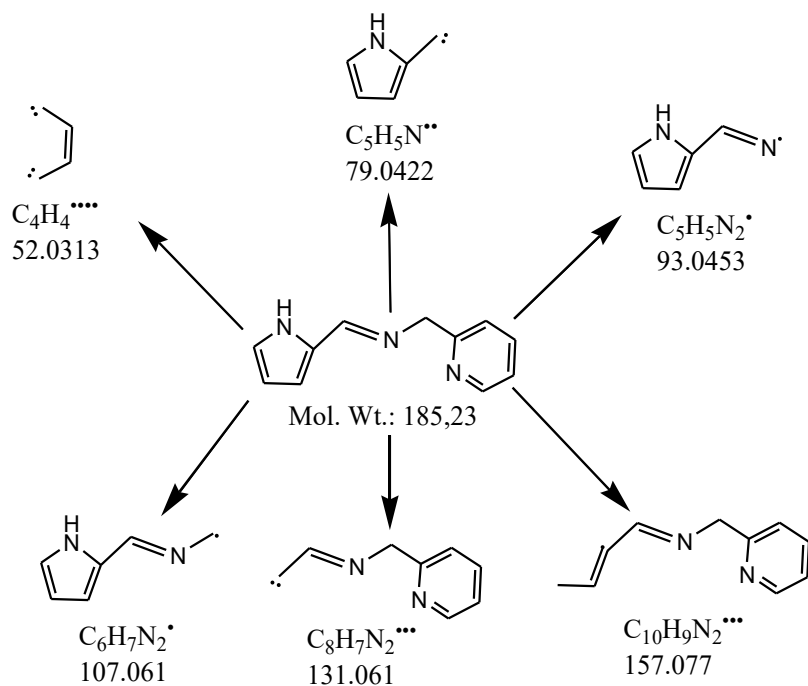


Figure 22 GC-MS peaks for L4



Scheme 18 Proposed Fragmentation Pattern for L4

4.6.2 UV-Visible Spectra for Ligands 1- 4

The UV-Vis absorption bands for the ligands were observed at 234–284 nm. The band at higher energy (234nm) is attributed to π - π^* transitions of the aromatic units while the lower energy band at 284nm is assigned to π - π^* transition of the azomethine (-CH=N-) chromophore. This agrees with literature reports on azomethine UV-vis bands for the imine bonds (Khanmohammadi *et al.*, 2009).

This bands probably relates to the electronic transitions corresponding to HOMO (highest occupied molecular orbital) located in the imine region and LUMO (lowest unoccupied molecular orbital) frontier orbitals located in the pyrrole as suggested in literature (N. Ahmad *et al.*, 2020). These transitions had molar extinction coefficients ranging from 10^3 - 10^4 LMol⁻¹cm⁻¹. A representative spectrum for **L2** is shown in **Figure 23**.

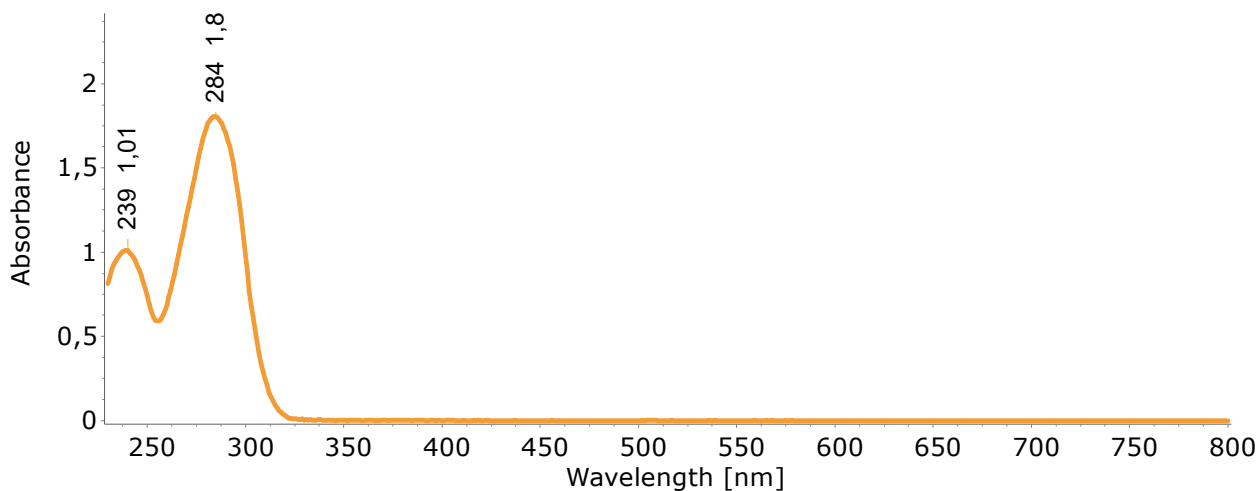


Figure 23 UV-Vis Spectrum for **L2**

The summarized UV-vis data for **L1- L4** is as shown in the **Table 1** below.

Table 1 UV-Vis data for **L1-L4**

Ligand	UV-vis (λ_{max} nm)
L1	286
L2	239, 284
L3	282
L4	283, 340

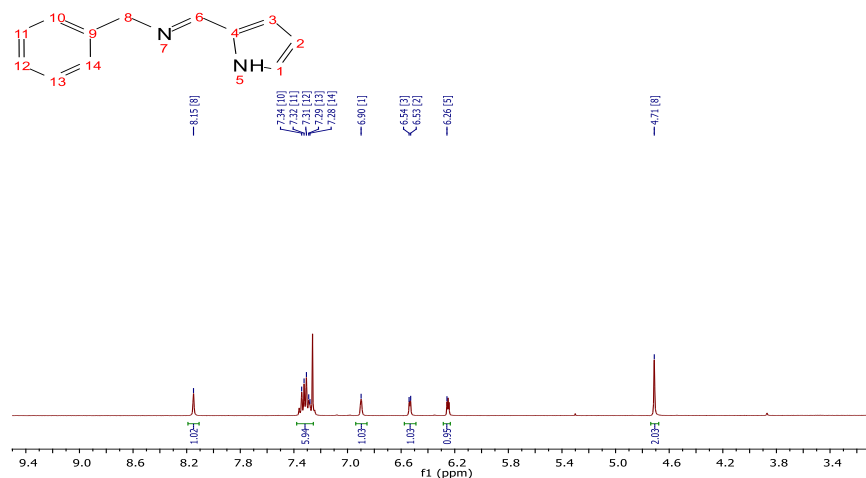
4.6.3 Fourier Transform Infrared for **L4**

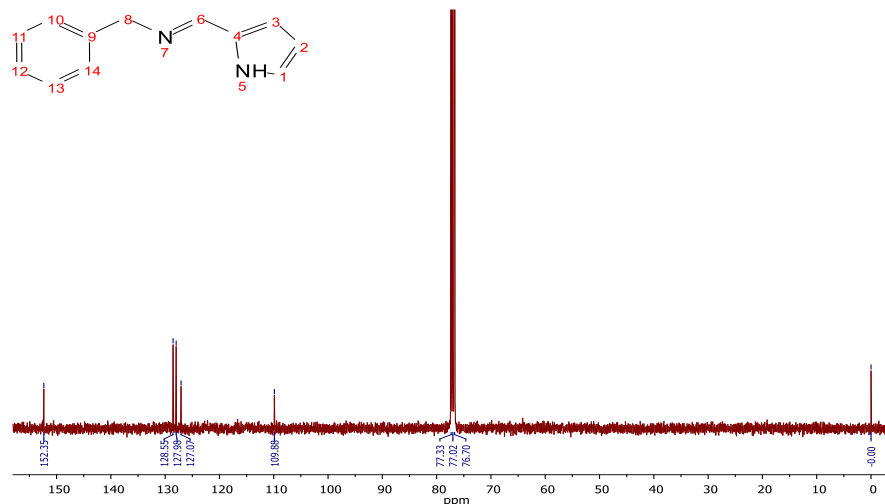
The appearance of a strong vibration band at 1638 cm^{-1} indicated the formation of an imine (C=N) bond; confirming a successful reaction.

4.6.4 Proton and Carbon-13 Nuclear Magnetic Resonance for Ligand 4

^1H NMR also confirmed a successful reaction by the absence of a peak at around δ 9ppm (aldehyde proton), and the appearance of an iminic proton peak at δ 8.56ppm. ^{13}C NMR showed no aldehyde peak at around δ 190ppm, with a C=N carbon peak appearing at 153.67, further confirming an iminic carbon forming an imine bond. These values were within the ranges reported in literature for Schiff base formation (Lakouraj *et al.*, 2018; Xavier *et al.*, 2018). Conclusive confirmation of the structure was achieved by elemental analysis where the obtained data agreed well with the calculated values; obtained (calculated) C 70.33(69.38), N 22.69(22.45), and H 5.99 (5.6).

A representative ^1H NMR and ^{13}C NMR scans for **L1** are shown in **Figure 24**. Scans for the other ligands appear in the Appendices section. A summary of the data obtained from the electronic spectra for the four ligands is summarized in **Table 2**.





(b)

Figure 24 ^1H NMR (a) and ^{13}C NMR (b) spectra for L1

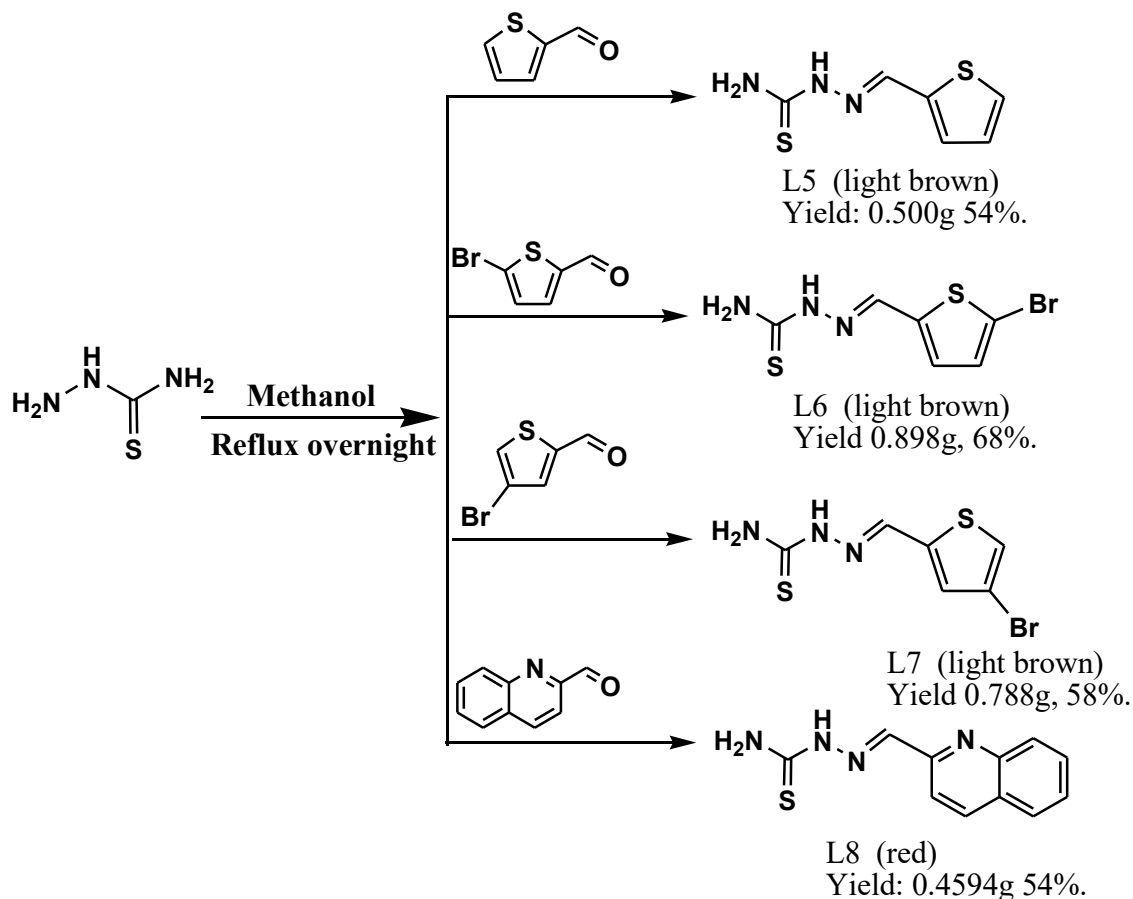
Table 2 Electronic spectra for the Ligands L1-L4

Ligand	FTIR (KBr cm^{-1})	^1H -NMR (400 MHz, CDCl_3 δ ppm)	^{13}C -NMR (400 MHz, CDCl_3 δ ppm)
L1	1636 , (C=N); 2829 (sp^3 -C-H); 2888 (-C-H benzene), 3369, (-N-H)	δ 8.15 (s, 1H), 7.24 - 7.37 (m, 5H), 6.90 (s, 1H), 6.53 (dd, $J = 1.22, 3.55$ Hz, 1H), 6.22 - 6.27 (m, 1H), 4.71 (s, 2H)	δ 152.35 (imine C=N), 137.04(C2C-N pyrrole), 128.55, 128.19, 127.98, 127.56, 127.07, 120.23(CC-N pyrrole), 109.88, 88.93, 55.29(CH ₂)
L2	1312 -C-S stretch (thiophene); 1640 , (-C=N); 2864 (sp^3 -C-H); 2967 (-C-H aromatic), 3062; (-N-H)	δ 8.13 (s, 1H), 7.17 - 7.23 (m, 1H), 6.89 - 6.99 (m, 2H), 6.80 (s, 1H), 6.52 (dd, $J = 1.22, 3.55$ Hz, 1H), 6.22 (dd, $J = 2.81, 3.42$ Hz, 1H), 4.87 (s, 2H)	152.78 (C=N imine), 142.52(C2C-S), 129.88(C2C-N pyrrole), 126.87, 124.67(C=C-S), 122.19(C=C-N pyrrole), 114.94, 109.76, 58.59(CH ₂)
L3	1644 , C=N (stretch); 2868 sp^3 -C-H stretch; 2975 -C-H (aromatic)	δ 8.12 (s, 1H), 7.38 (s, 1H), 6.89 (s, 1H), 6.53 (br. s., 1H), 6.34 (d, $J = 3.06$ Hz, 1H)	153.19 (C=N imine), 153.09(C2C-O furan), 152.68(C-O furan), 149.24(C2C=N pyrrole), 142.21(CC-N pyrrole),

Ligand	FTIR (KBr cm ⁻¹)	¹ H-NMR (400 MHz, CDCl ₃ δ ppm)	¹³ C-NMR (400 MHz, CDCl ₃ δ ppm)
	stretch, 3177; N-H stretch.	1H), 6.24 (s, 2H), 4.67 (s, 2H)	124.79, 122.09, 120.07, 114.97, 56.47(CH ₂)
L4	3117, (aromatic C-H); 3015, (aliphatic C-H); 1638 , (C=N).	δ 8.56 (d, J = 4.16 Hz, 1H), 8.24 (s, 1H), 7.61 (dt, J = 1.71, 7.64 Hz, 1H), 7.31 (d, J = 7.82 Hz, 1H), 7.15 (dd, J = 5.32, 6.91 Hz, 1H), 6.83 (s, 1H), 6.54 (dd, J = 3.55 Hz, 2H), 6.23 (dd, J = 2.81, 3.42 Hz, 1H), 4.86 (s, 2H)	160.03 (C2C=N pyridine), 153.67 (C=N imine), 150.50, 149.30, 142.99, 136.62(C2C-N pyrrole), 131.59, 130.08, 119.80(CC-N pyrrole), 114.87, 111.11, 66.18(CH ₂)

4.7 Synthesis of the Thiosemicarbazide-based Ligands (L5-L8)

The procedure for the synthesis of the ligands **L5-L8** is as outlined in **Scheme 19** below.



Scheme 19 Synthesis of the Thiosemicarbazide-based ligands **L5-L8**

The ligands were isolated as light powdery products. Attempt to grow crystal structures by slow diffusion of hexane into a THF solution of the ligand was successful only for **L5**.

The ligands were then characterized by FTIR, ^1H NMR, ^{13}C NMR spectral analyses and elemental analysis UV-vis. In addition, x-ray crystallography was performed for ligand **L5**. The elemental analysis results for all the ligands agreed well with the calculated results confirming the molecular formulae of the structures.

4.8 Structure Confirmation for the Ligand **L5-L8**

4.8.1 UV-Visible Spectra for **L5- L8**

The UV-Vis spectra bands for the ligands were observed at 340nm (**L5**), 347nm (**L6**), 343nm (**L7**) and 360 and 84nm (**L8**). According to similar literature reports (West *et al.*, 1999), these transitions are attributed to to $n-\pi^*$ transitions centered on the imine and thioamide moieties.

Another observation was a bathochromic shift for ligands with a -Br attached compared to **L5** without a -Br substituent. A higher bathochromic shift (7nm) was observed in **L6** with a -Br at position 5 of the thiophene ring, than in **L7** (3nm) with the -Br at position 4. An auxochrome at position 5, as opposed to position 4, has better conjugation with the rest of the π system from the possible resonance donation of the lone pair on -Br. This increased conjugation and led to the observed bathochromic effect in **L6**. Elemental analysis results on the experimental values tallied well with the calculated values which was a conclusive proof for successful synthesis.

The elemental analysis and UV-vis spectra for ligands **L5-L8** are summarized in **Table 3**.

Table 3 UV-vis Spectral Data for **L5-L8**.

Ligand	Molecular Formula	% C, H, N Calculated (Obtained)	UV-vis (λ_{\max}nm)
L5	$C_8H_7N_3S_2$	C 38.90(38.63), H 3.81(3.77), N 22.68(22.33), S 34.61(34.43)	340
L6	$C_8H_6BrN_3S_2$	C 27.28(27.16), H 2.29(2.37), N 15.91(15.66), S 24.28(25.47)	347
L7	$C_8H_6BrN_3S_2$	C 27.28(27.22), H 2.29(2.34), N 15.91(15.77), S 24.28(24.47)	343
L8	$C_{10}H_{10}N_4S$	C 57.37(58.88), H 4.38(4.9), N 24.33(25.49), S 13.92(14.56)	360, 384

4.8.2 Single Crystal X-ray Structure for **L5**

The ligand belongs to Monoclinic P21/n space group. The molecular pair adopts a different conformation for each unit molecule in the molecular pair with one molecule lying on a flat plane but the other having a torsion angle of about 17° showing the torsion in one molecule (a), H-bonding (b) and the packing in the crystal unit viewed along 'b' plane and rotated along y-axis. The molecule is stabilized through intermolecular hydrogen bonding between the hydrogen attached to N-5 of one molecule and thiosemicarbazide sulphur of the other molecule. Further hydrogen bonding extends towards the adjacent molecular pair as shown in **Figure 25**. Further confirmation of the thioamide form of the ligands was confirmed by the crystal structure of **L5**.

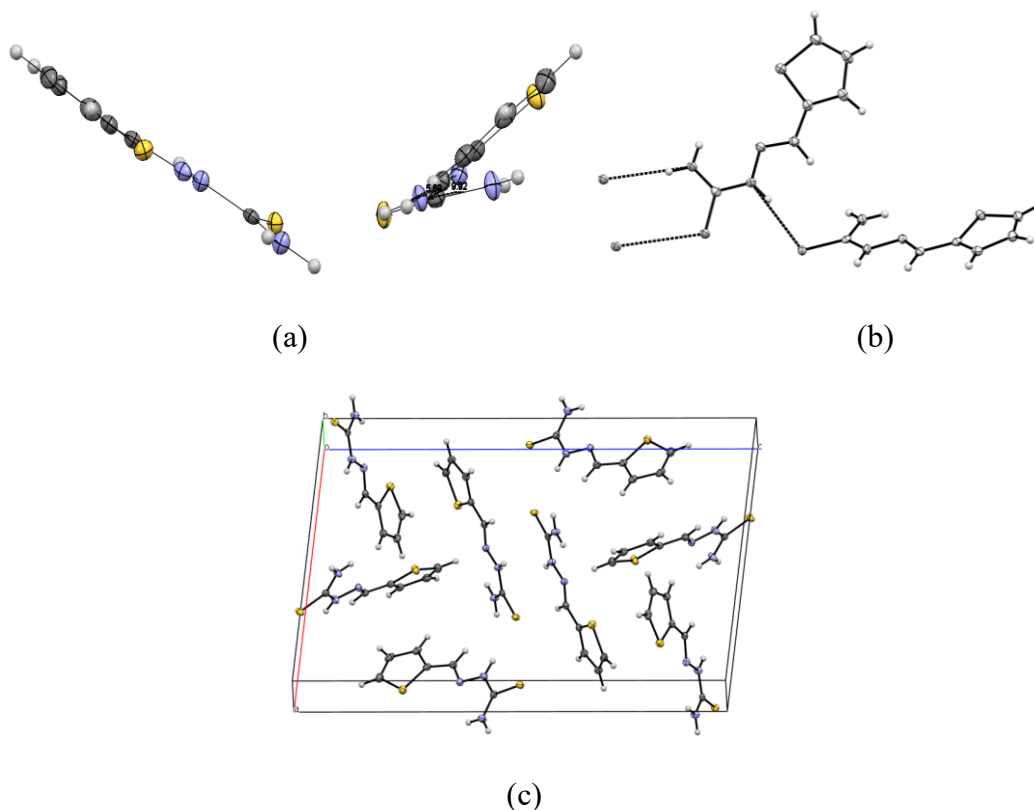


Figure 25 ORTEP view for the molecular pair for **L5**

4.8.3 Fourier Transform InfraRed Spectroscopy for Ligands 5- 8

In the FTIR spectra of these ligands, the vibrational band at around $3369\text{-}3430\text{ cm}^{-1}$ was assigned to the asymmetric $\nu(\text{N-H})$ vibration of the terminal NH_2 group. The peaks around $3246\text{-}3279\text{ cm}^{-1}$ and $3149\text{-}3179\text{ cm}^{-1}$ were attributed to the symmetric $\nu(\text{N-H})$ vibrations of the imino and amino groups respectively. These agreed with similar observations appearing in literature on thiosemicarbazone ligands which reports these vibrations between 3232 cm^{-1} and 3167 cm^{-1} (Netalkar *et al.*, 2015).

Another observation made in all the ligands was the absence of a vibrational band at $2500\text{-}2600\text{ cm}^{-1}$ which is characteristic of the thioimidol group (Netalkar *et al.*, 2015). This ruled out the possibility of thioamide - thioimidol tautomerism (H-N-C=S to N=C-SH). The disappearance of an absorption band at around 1700 cm^{-1} indicated the absence of the starter aldehyde, while the appearance of a strong vibration band between $1605\text{-}1611\text{ cm}^{-1}$ indicated the formation of an imine (C=N) bond; confirming a successful reaction.

This agrees with literature reports for these type of ligands where the imine stretch is reported to occur slightly above 1605 cm^{-1} (Netalkar *et al.*, 2015). Thioamide absorption bands appeared around

1326 cm^{-1} and 940 cm^{-1} . Literature reports the vibration for these band appearing at 1200 and 830 cm^{-1} (Sinniah *et al.*, 2017). A representative spectrum for **L6** is shown in **Figure 26**.

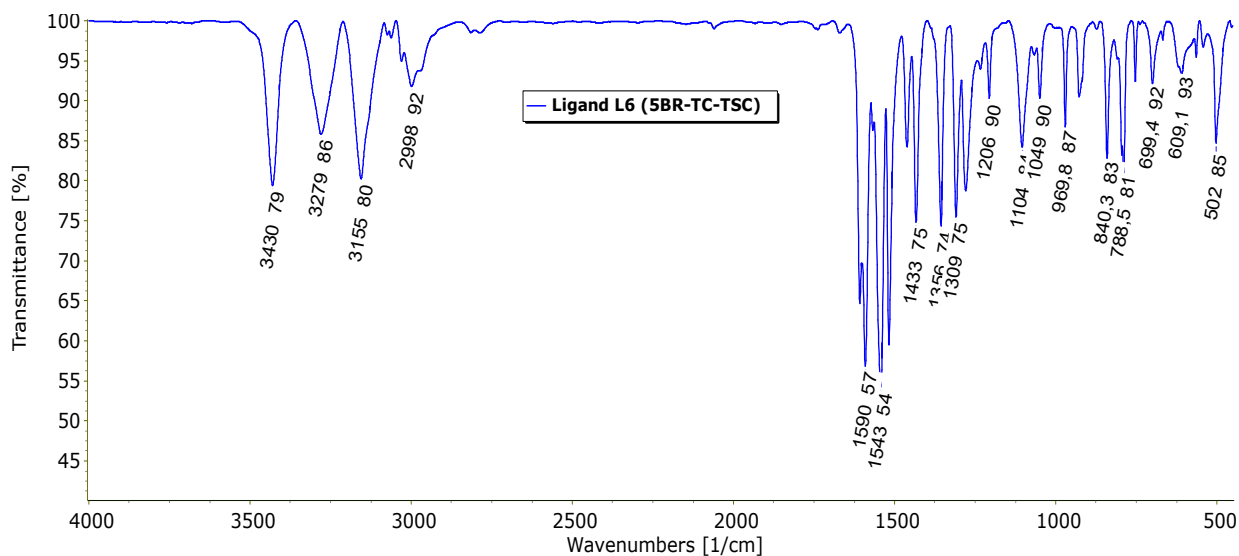


Figure 26 FTIR Spectra for Ligand **L6**

The difference in energy for the iminic bands can be explained by considering the different groups and substituents attached to the imine bond. Ligand **L5** has an unsubstituted thiophene and shows the highest energy for the imine bond at 1611 cm^{-1} . Ligand **L6** with a -Br introduced to position 5 on the thiophene ring showed a shift in energy (3 cm^{-1}) from 1611 cm^{-1} to 1608 cm^{-1} . The -Br at position 5 has a possible resonance donation from its lone pair of non-bonding electrons which contributes to an increased electron density to the thiophene ring and consequently to the imine region.

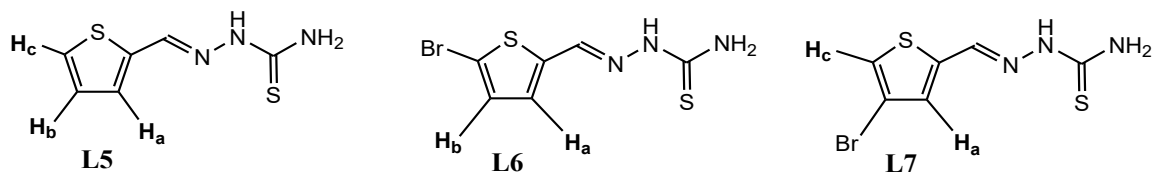
On introducing a -Br at position 4 on the thiophene ring (**L7**), there is a shift of 6 cm^{-1} to 1605 cm^{-1} . This is probably due to the electronegative dipole of -Br which draws electron density away from the thiophene ring (with minimal resonance donation of the lone pair with Br at position 4) and consequently from the imine region and thereby raising the σ character of the imine bond resulting to the observed shift in energy to a lower value.

4.8.4 Proton and Carbon-13 Nuclear Magnetic Resonance for Ligand 5- 8

^1H NMR also agreed with literature reports confirming a successful reaction by the absence of an aldehyde proton peak at around δ 9 ppm (J. Wang, Liu, Jiang, *et al.*, 2018). A singlet peak was observed between 11.45-11.80 ppm in the free ligands and was assigned to the hydrazine NH proton. These values were within the ranges reported in literature where the hydrazine proton is reported to

occur around 10.01ppm (Netalkar *et al.*, 2015). The primary amine peaks (-NH₂) of the free ligands occurred as singlet between 3.34- 3.35ppm. The two protons attached to the thiophene occurred as duplets between 7.13-8.14ppm. The azomethine peaks appeared between 8.09- 8.24ppm which agreed well with literature reports of 7.75–7.85ppm (Nyawade *et al.*, 2020).

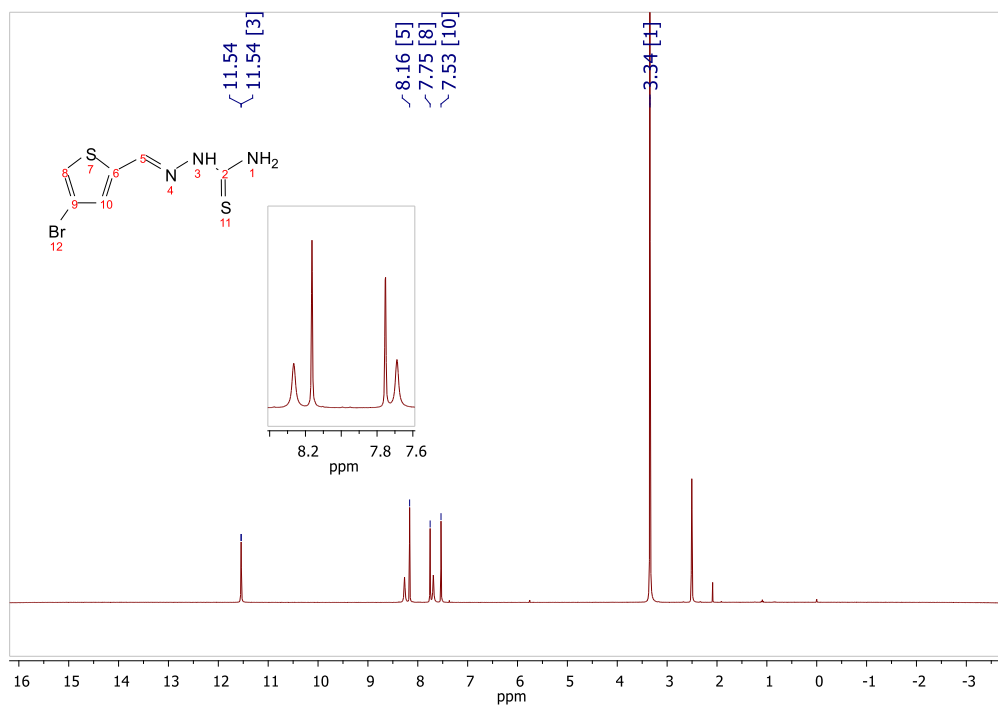
Comparing the ¹H NMR spectra of the ligands after introduction of the -Br substituent to the thiophene ring;



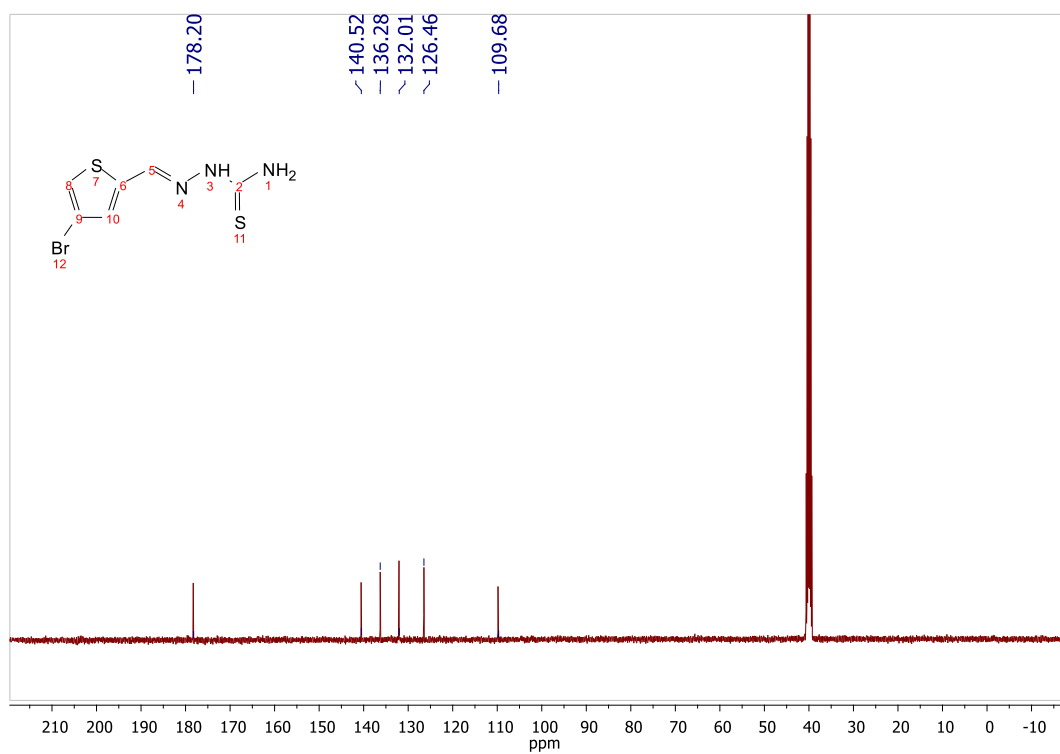
For **L5**, the resonance for H_a, H_b and H_c protons occurred at δ 7.13, 7.45 and 7.65ppm respectively, while the azomethine proton resonated at 8.25ppm. Upon introduction of -Br at position 4 (**L7**), the remaining protons; H_a and H_c appeared more downfield (7.53 and 7.75ppm respectively), as a result of de-shielding by the electronegative Br substituent. Similar trend is observed when the Br is introduced at position 5 (**L6**). The peaks for H_a and H_b now appear further downfield at 7.27 and 8.14ppm respectively.

Together with the inductive electron withdrawal effect by Br, the protons at ortho-position to Br experience steric de-shielding as the hydrogen *s*-orbitals are disrupted from the normal spherical symmetry. The azomethine proton for **L5** appeared at 8.25ppm. On introduction of a Br at position 4 (**L7**) and position 5 (**L6**) of the thiophene ring, an up-field shift of about 0.10ppm (to 8.16ppm-**L7**) and 0.11ppm (to 8.14ppm-**L6**) was observed. This trend is expected due to resonance donation of Br lone pair at position 5, and therefore the azomethine proton for **L6** experiences higher shielding effect thus resonates more up field compared to **L7**.

¹³C NMR showed no aldehyde peak at around δ 190ppm, instead a C=N carbon peak appearing at 177-178ppm, further confirming an imine formation. Similar shifts occurring around 170ppm are reported in literature (Xavier *et al.*, 2018). Representative ¹H NMR and ¹³C NMR spectra for **L7** are shown in **Figure 27** (a) and (b). A summary of the data obtained from the electronic spectra for the four ligands is summarized in **Table 4**.



(a)



(b)

Figure 27 ^1H NMR spectra (a) and ^{13}C NMR spectra for **L7**

Table 4 Electronic spectral data for **L5-L8**

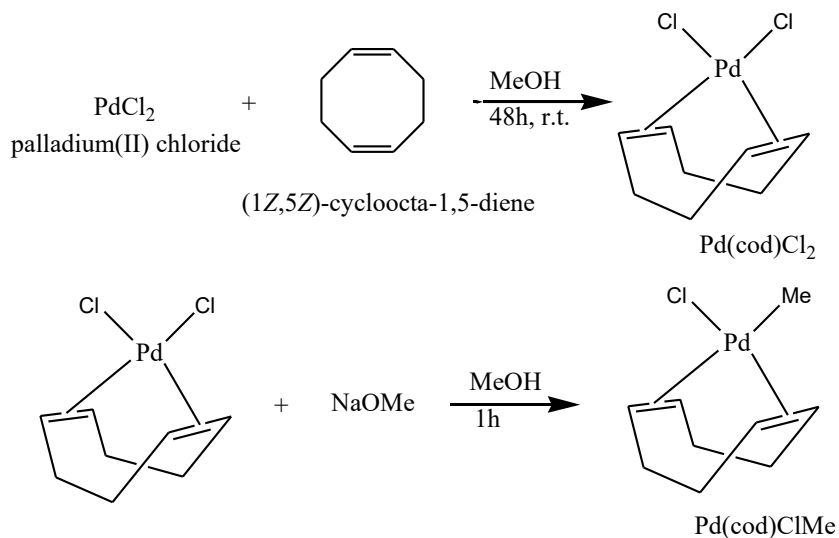
Ligand	FTIR (KBr cm⁻¹)	¹H-NMR (400 MHz, DMSO-d₆ δppm)	¹³C-NMR (400 MHz, DMSO-d₆ δppm)
L5	(3414-3149 N-H stretch) 3000 (sp ² C-H bend), 2500-2600 C=N-SH, 1611 CH=N stretch, 1538 C=S stretch, 1326 and 940 H-N-C=S.	δ 11.45 (s, 1H), 8.09 - 8.33 (m, 1H), 7.65 (d, J = 5.01 Hz, 1H), 7.45 (dd, J = 0.73, 3.55 Hz, 1H), 7.12 (dd, J = 3.67, 5.01 Hz, 1H), 3.35 (s, 2H)	178.27 (C=N imine), 139.24, 138.22, 130.92, 129.33. 128.41.
L6	(3429-3276 N-H stretch), 3155-2999 (sp ² C-H bend), 1608 CH=N stretch, 1543 C=S stretch	δ 11.50 (s, 1H), 8.14 (s, 1H), 7.64 (br. s., 1H), 7.24 (s, 1H), 3.35 (s, 2H)	184.27(C=N imine), 178.25 141.07, 137.29, 131.58, 115.03.
L7	(3378-3246 N-H stretch), 3155-3008 (sp ² C-H bend), 1605 CH=N stretch, 1545 C=S stretch.	δ 11.54 (s, 1H), 8.16 (d, 1H), 7.75 (d, 1H), 7.53 (s, 1H), 3.34 (s, 2H), 2.51 (s, 2H)	178.27 (C=N imine), 140.80, 136.35, 132.21, 126.46. 109.97.
L8	3396; N-H stretch, 1608; CH=N stretch, 1529, C=S stretch	δ 11.81 (s, 1H), 8.45 (d, 1H), 8.38 (d, 1H), 8.24 (d, 1H), 8.00 (br. d., 2H), 7.78 (m, 1H), 7.62 (m, 1H), 2.51 (m, 2H)	178.93(C=S), 154.39(C=N quinolone), 147.79, 142.99(C=N imine), 136.76, 130.40, 129.25, 128.40, 128.30, 127.62, 118.59.

4.8.5 Solubility

The ligands were soluble in common organic solvents like DCM, THF, acetone, DMSO and chloroform.

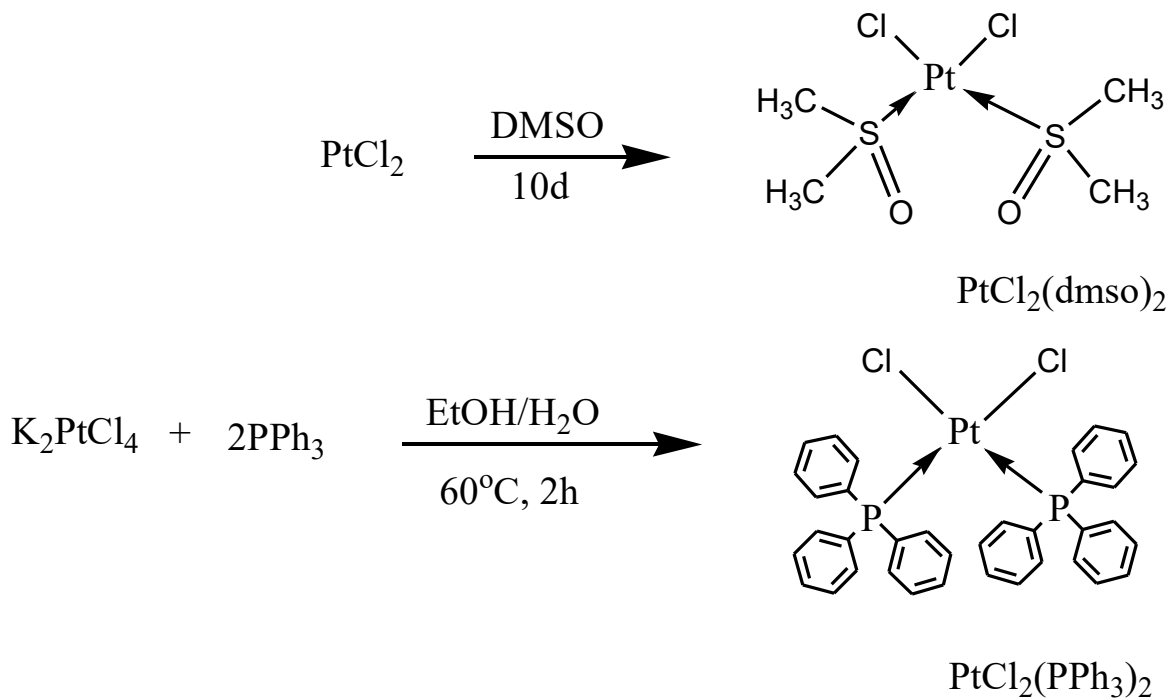
4.9 Synthesis of the precursor complexes

The well-known precursors were prepared according to literature procedures (Kukushkin *et al.*, 2002; Mohanty *et al.*, 2006). The synthesis of the palladium precursors is as outlined in Scheme 20 below.



Scheme 20 Synthetic Routes for the precursor complexes

Similarly, the synthesis of the platinum precursors is as outlined in **Scheme 21** below.

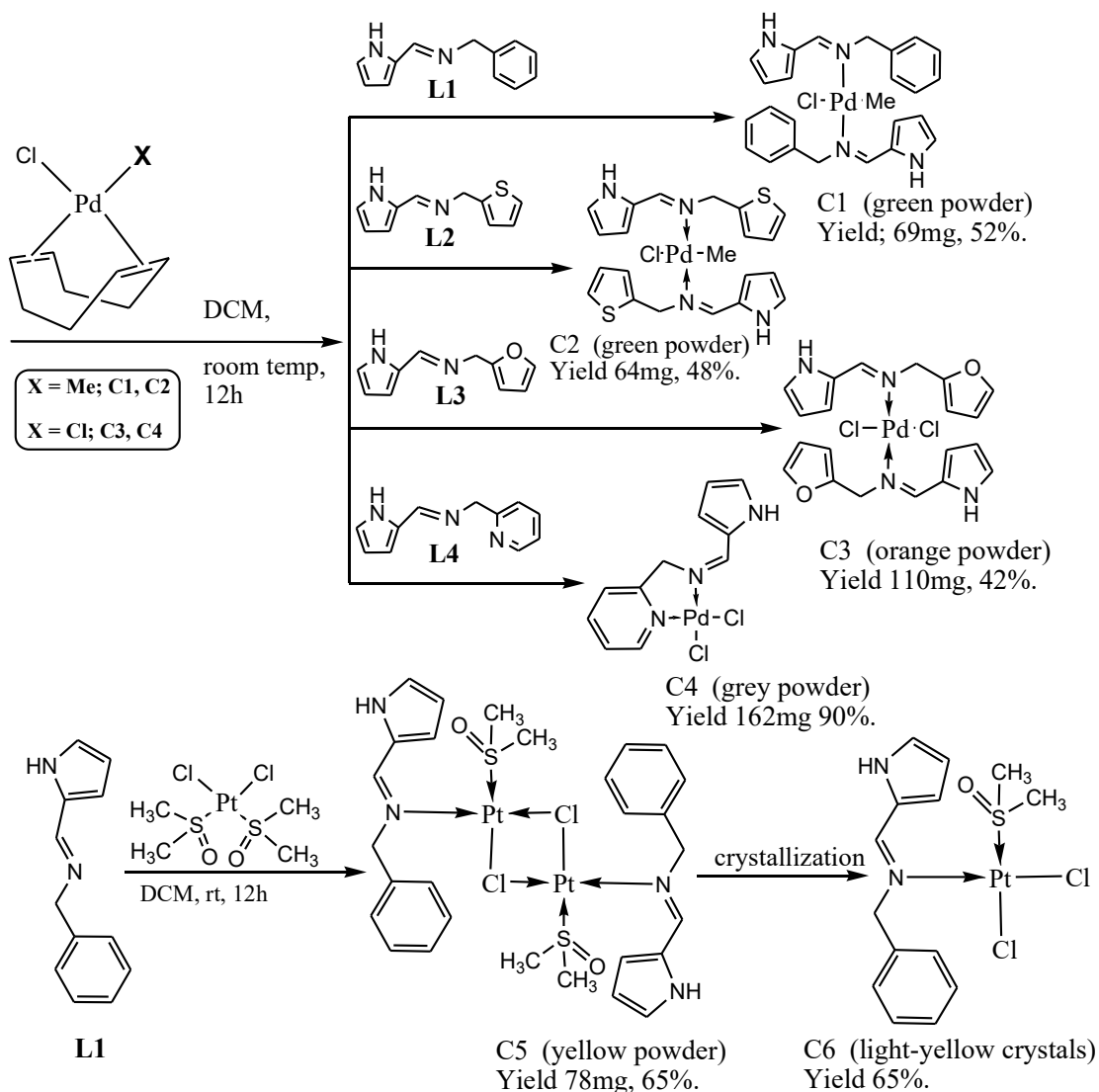


Scheme 21 Synthetic Routes for the precursor complexes

4.10 Synthesis of the Complexes

4.10.1 Synthesis of the Pyrrole-based Complexes (C1-C6)

The synthetic routes and the corresponding structures are as shown in **Scheme 22** below.

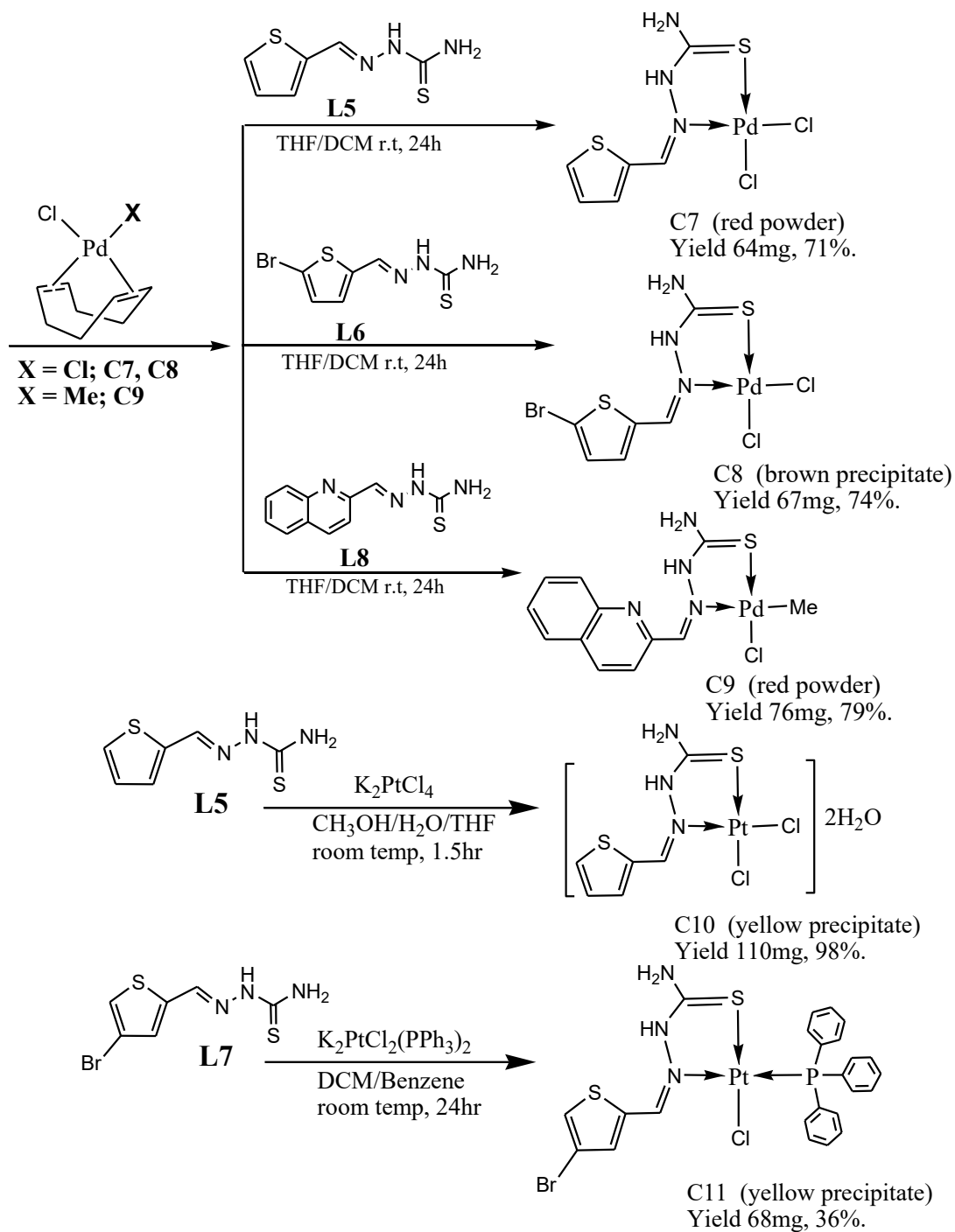


Scheme 22 Synthetic Routes for the Pyrrole-based Pd(II) and Pt(II) complexes **C1-C6**

The complexes were then characterized by FTIR, UV-Vis, ¹HNMR and elemental analysis. Due to steric factors, the palladium complexes binding in 1:2 (metal: ligand) ratio are believed to be of *trans* geometry, while the 1:1 ratio complexes formed from bidentate coordinating ligand are believed to be of *cis*-conformation. These ratios were confirmed by elemental analysis.

4.10.2 Synthesis of Thiosemicarbazide-based Complexes (C7-C11)

The synthetic route and the corresponding structures are shown in **Scheme 23** below.



Scheme 23 Synthetic Routes for the Palladium complexes **C7-C11**

The complexes were characterized by FTIR, ^1H NMR, ^{13}C NMR, Elemental analysis, x-ray single crystal crystallography, UV-Vis, cyclic voltammetry (CV), molar conductance, partition coefficient, stability tests and bioassays for anticancer properties as discussed below.

4.11 Characterization and Structure Confirmation for the Pyrrole-based Complexes

4.11.1 Liquid Chromatography-Mass Spectroscopy Analysis for the Complexes

The LC-MS results were as shown in **Table 5** below. These were conducted to give the molecular ion peaks which confirmed the molecular masses for the complexes.

Table 5 LC-MS Data for the pyrrole complexes

Complex	Molecular formula	$[\text{M}+\text{H}]^+$ (m/z) Calculated	LC-MS $[\text{M}+\text{H}]^+$ (m/z) found
C1	$\text{C}_{25}\text{H}_{27}\text{ClN}_4\text{Pd}$,	525.38	525.30
C3	$\text{C}_{20}\text{H}_{20}\text{Cl}_2\text{N}_4\text{O}_2\text{Pd}$	525.72	525.29
C4	$\text{C}_{11}\text{H}_{11}\text{Cl}_2\text{N}_3\text{Pd}$	362.55	362.04
C6	$\text{C}_{14}\text{H}_{18}\text{Cl}_2\text{N}_2\text{OPtS}$	528.3	530.07

A representative LC-MS spectrum for C1 is shown in **Figure 28** below

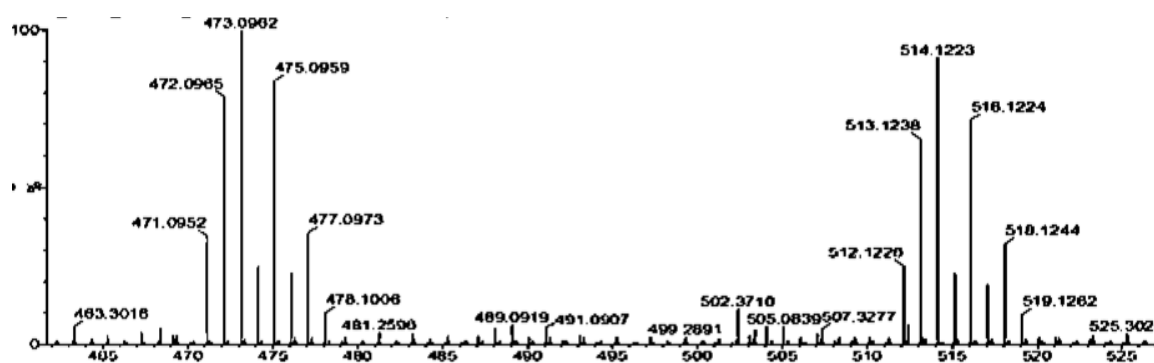


Figure 28 LC-MS for Complex C1.

4.11.2 Elemental Analysis for Pyrrole-based Complexes C1- C6

The elemental analysis for C, H, N, S content for these complexes was carried out to make a conclusive confirmation of the proposed structures and therefore verify the successful synthesis and purity of the complexes. The results from the elemental (C, H, N, S) percentages were compared with the theoretical calculations, and acceptable values fell within the acceptable ranges of $\pm 4\%$ of the expected values. The values are as shown in **Table 6**.

Table 6 Elemental Analysis Data for C1- C6

Compound	Molecular Formula	% C, H, N Calculated (Obtained)
C1	C ₂₅ H ₂₇ ClN ₄ Pd	N 11.70 (11.39), C 55.20 (55.79), H 5.20 (5.19)
C2	C ₂₁ H ₂₃ ClN ₄ PdS ₂	N 8.97 (9.25), C 84.58 (83.89), H 6.50 (6.90).
C3	C ₂₀ H ₂₀ Cl ₂ N ₄ O ₂ Pd	C 45.69(45.84); H 2.84(2.79); N 5.30(5.65).
C4	C ₁₀ H ₁₁ Cl ₂ N ₃ Pd	C 36.40 (36.50); H 3.10 (3.50); N 11.60 (11.28)
C5	C ₂₈ H ₃₈ Cl ₂ N ₄ O ₂ Pt ₂ S ₂	C 31.83 (31.15); H 3.70 (3.43); N 5.69 (5.30); S, 6.50 (6.07).
C6	C ₂₈ H ₃₆ Cl ₂ N ₄ O ₂ Pt ₂ S ₂	C 34.11 (34.15); H 3.68 (3.70); N 5.68 (5.69); S, 6.51 (6.50)

4.11.3 UV-Visible Spectroscopy for the Pyrrole-based Complexes 1- 6

The UV-visible spectra for the compounds were recorded in DMSO at range 200- 800 nm using quartz cells at a concentration of 1.0×10^{-3} M. The calculated molar absorptivity for the compounds is summarized in **Table 7** below.

Table 7 UV-Vis Spectra for the Pyrrole-based Complexes

Compound	λ_{\max} (nm)	Calculated ϵ ($\times 10^4$ LMol ⁻¹ cm ⁻¹)
C1	289, 324, 378	1.60, 1.41, 1.06
C2	324, 380	0.0865, 0.0736
C3	280, 334	3.35, 4.84
C4	265, 322, 396	0.98, 1.99, 6.88
C5	253	3.38
C6	256	2.018

The absorption bands of complexes occurred below 600 nm. This agrees with literature reports that a lack of any electronic transition at longer wavelengths indicates large crystal-field splitting and is consistent with square-planar geometry since there is a large energy gap between the HOMO and

LUMO d-orbitals (Das *et al.*, 2011). The bands occurring between 280- 380nm were assigned to $d\pi-\pi^*$ metal to ligand charge transfer (MLCT) from metal d -orbitals to the anti-bonding π^* orbitals of the ligand. Work appearing in literature on similar palladium complexes report a wavelength range of 300-400nm (Krogul *et al.*, 2012) . The UV–Vis absorption bands in the complexes for the azomethine C=N bonds observed at 320-340 nm were assigned to the $\pi-\pi^*$ transitions, and 378–389 nm assigned to the $n-\pi^*$ transitions. Similar reports on these types of transitions have been reported in literature (Ali *et al.* 2006; Biyala *et al.* 2008).

The UV-Vis spectra for all the complexes showed two peaks corresponding to a combination of the spin allowed $^1A_{1g} \rightarrow ^1B_{1g}$ transitions with molar extinction coefficients ranging from 10^3 - 10^4 LMol $^{-1}$ cm $^{-1}$. These transitions are characteristic of square planar geometry.

A representative spectrum for **C1** is shown **Figure 29**.

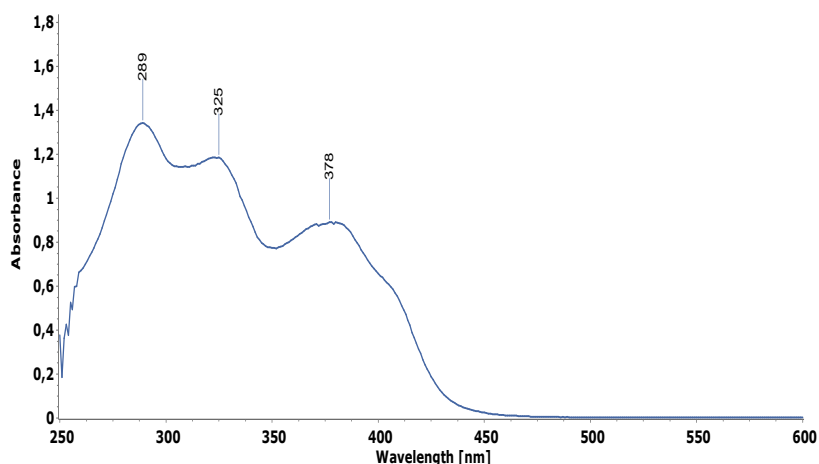


Figure 29 UV-vis Spectra for **C1**

4.11.4 Fourier Transform InfraRed Spectroscopy for Pyrrole Complexes 1-6

The FTIR analysis for the complexes was performed in the solid state using KBr pellets or ATR. Spectra for the pyrrole-based palladium complexes **C1-C4** and platinum complexes **C5** and **C6** showed clear bands at 1602 cm $^{-1}$, 1599cm $^{-1}$, 1610 cm $^{-1}$, 1662 cm $^{-1}$, 1628 cm $^{-1}$ and 1592 cm $^{-1}$ respectively, which were assigned to $\nu(C=N)$ stretch. The IR spectrum for the parent ligands **L1**, **L2**, **L3** and **L4** showed a clear vibrational imine C=N (stretch) bands at 1636 cm $^{-1}$, 1640 cm $^{-1}$, 1638 cm $^{-1}$ and 1644 cm $^{-1}$ respectively.

These were shifts of 34 cm⁻¹, 41cm⁻¹, 28 cm⁻¹, 18 cm⁻¹ 8cm⁻¹ and 44cm⁻¹ for **C1-C6** respectively. These types of shifts are reported in literature as a likely result of coordination to the metal via the electron rich azomethine nitrogen (Abdel-Rahman *et al.*, 2019). The electron density on the azomethine bond decreases; hence, π character decreases, the bond order decreases and the C=N bond strength decreases (Jayabharathi *et al.*, 2015). New bands assigned to $\nu(\text{M-N})$ stretching vibrations appeared at 531cm⁻¹- 534cm⁻¹.

Complex **C5** which is a chloro-bridged dimer has effectively less π - donation from the chlorides compared to **C6** which is a monomer. This is due to the fact that an extra pair of electrons is used to form a dative bond with the second platinum center in the dimer. This explains the differences in the observed shifts (8cm⁻¹ and 44cm⁻¹ respectively) to 1628cm⁻¹ and 1592cm⁻¹ respectively, compared to the parent ligand **L1** (1636cm⁻¹).

The different FTIR vibrations for the complexes could be attributed to the electronic effects of the different ligands attached to the metal center and to the groups attached to the azomethine bond. The peaks due to methylene CH=N- were compared for the complexes and the parent ligands, and between the complexes themselves according to the various substituents on ligands coordinated to the metal centers.

This was most notable for complex **C1** with a methyl ligand, which is a strong σ -donor, and a π -donor Cl attached to the metal center. This enriched the metal center with electron density resulting in a more effective back donation to the π -antibonding orbital of the azomethine bond, thereby weakening the C=N bond as indicated in the shift of 34 cm⁻¹ (from 1636 cm⁻¹ in **L1**) to 1602 cm⁻¹ in **C1**. Similar observation was made in **C2**, also with a methyl and Cl ligands attached to the metal center which shifted by 41 cm⁻¹ (from 1599 cm⁻¹ in **L2**) to 1640 cm⁻¹ in **C2**.

The other likely reason is that on coordination to the metal via the azomethine nitrogen, the electron density on the azomethine bond decreases and hence the π character decreases. This in turn decreases the bond order leading to a decrease in the C=N bond strength (Abu-Dief & Mohamed, 2015). A similar trend in shift of 28 cm⁻¹ was observed in **C4** (1610 cm⁻¹) compared to **L4** (1638 cm⁻¹). In complex **C4** with the more electronegative pyridine directly attached to the metal center, a slightly less shift (28 cm⁻¹) was observed compared to **C1** (34 cm⁻¹).

This is explained by the fact that the electronegative ligands draw electrons away from the metal reducing the metal's back-donation properties in **C4** resulting in less weakening of the C=N bond.

A representative spectrum is shown in **Figure 30** for the palladium complex, **C1**.

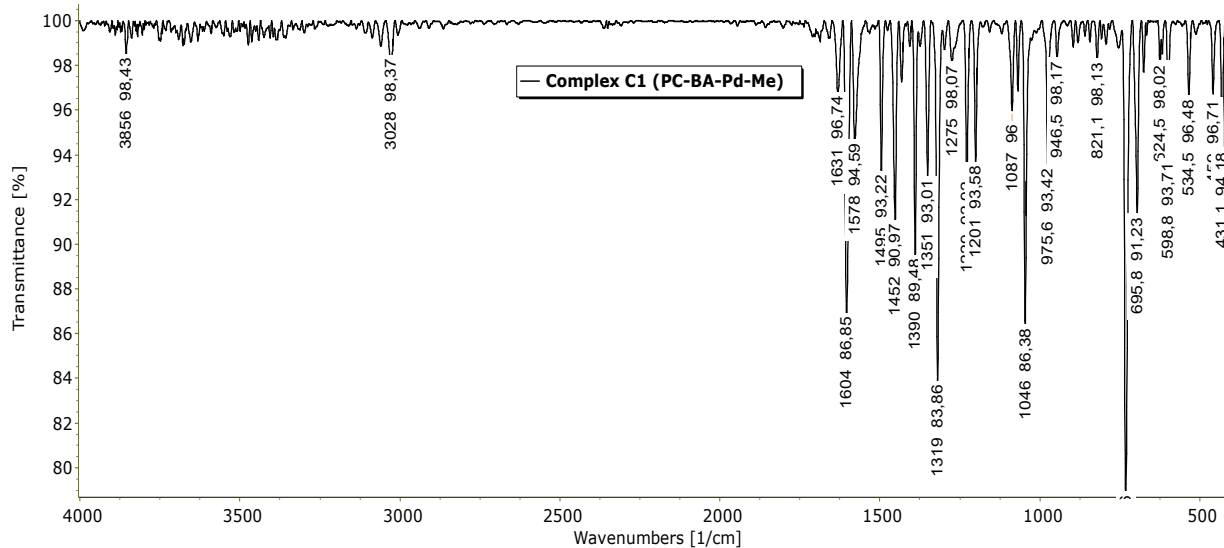


Figure 30 FTIR Spectrum for **C1**

4.11.5 Proton and Carbon-13 Nuclear Magnetic Resonance spectra for the Pyrrole-based Complexes 1- 6

^1H NMR and ^{13}C NMR data were further used to confirm the coordination manner of the ligands to the metal centers. In complexes **C1** and **C5**, the ^1H NMR iminic peaks occurred at 7.41ppm and 7.81ppm respectively compared to 8.15ppm in the spectrum of the free ligand **L1**. In the complex **C4**, the methylene peak appeared at 7.53ppm compared to 8.57ppm in the parent ligand, **L4**.

This up-field shift of 0.74ppm, 0.34ppm and 1.04ppm respectively to lower frequency is an indication of bonding of the lone pair in azomethine nitrogen to the palladium and platinum metal centers; due to π -electrons of azomethine group shifting towards the d -orbitals of metal leading to de-shielding of the azomethine proton (Al-Fregi, 2015). Similarly, ^{13}C NMR spectra showed shifts to higher frequencies. Upon complexation with palladium, the azomethine peak for **C1** appeared more down field at 162.8ppm compared to the parent ligand **L1** which had the peak appearing at 137.04ppm.

This was an indication of the involvement of the azomethine bond in coordination to the metal resulting in the observed de-shielding of the azomethine carbon. Comparing the ^1H NMR, complexes **C1** and **C5** the shift occurred at 7.41ppm and 7.81ppm respectively compared to 8.15ppm in the spectrum of the free ligand **L1**. In the complex **C4**, the methylene peak appeared at 7.53ppm

compared to 8.57ppm in the parent ligand, **L4**. This up-field shift of 0.74ppm, 0.34ppm and 1.04ppm respectively to lower frequency is an indication of bonding of the lone pair in azomethine nitrogen to the palladium and platinum metal centers. Literature reports indicate this as due to π -electrons of azomethine group shifting towards the d -orbitals of metal leading to de-shielding of the azomethine proton (A. A. Al-Fregi, 2015)

A representative spectrum showing the proton shifts is shown in **Figure 31** for complex **C1** in CDCl_3 .

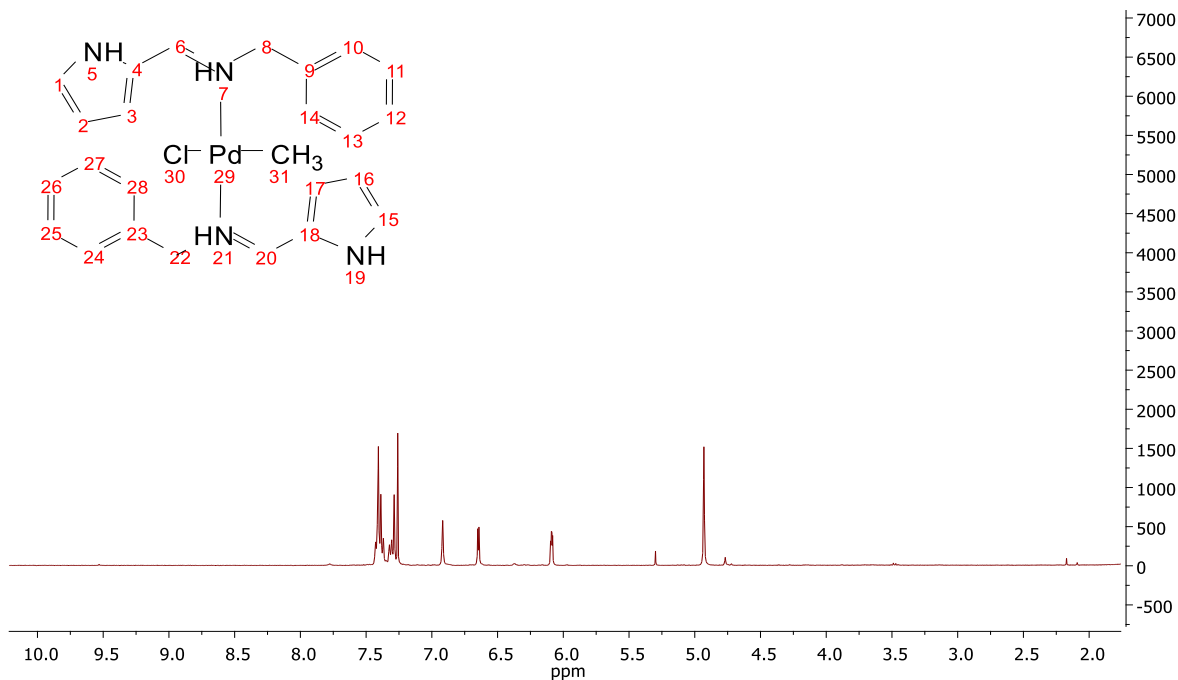


Figure 31 ^1H NMR spectrum for **C1**

The ^1H NMR and ^{13}C NMR spectral data for C1- C6 is as summarized in **Table 8** below. Due to low solubility problems, some of the complexes did not give good carbon-13 spectra.

Table 8 ^1H NMR Spectral Data for the Complexes

Complex	^1H NMR 400MHz, CDCl_3 (δ ppm)	^{13}C NMR 400MHz, CDCl_3 (δ ppm)
C1	δ 7.41 (6H, s, M07), 7.26 (4H, s, M06), 6.92 (1H, s, M05), 6.64 (1H, s, M04), 6.09 (1H, br. s., M03), 4.93 (3H, s, M02), 1.58 (7H, br. s., M01).	δ 162.8, 139.5, 137.5, 136.7, 129.0, 127.8, 117.7, 111.0, 61.3

C3	δ 7.69 (s, 1H), 7.54 (br. s., 2H), 7.13 (br. s., 1H), 6.46 (br. s., 3H), 4.81 (br. s., 2H), 3.49 (s, 2H), 1.59 (s, 3H), 1.21 (s, 3H)
C4	δ 7.44 (d, 1H), 7.26 (s, 1H), 6.44 (m., 1H), 6.31 (m., 2H), 5.30 (m, 1H), 4.81 (m., 1H), 3.49 (m, 1H), 1.57 (d., 1H), 1.21 (s, 2H)
C5	δ 7.78 - 7.85 (m, 2H), 7.26 (s, 10H), 6.90 - 7.01 (m, 4H), 6.55 - 6.61 (m, 2H), 3.43 - 3.52 (m, 2H), 2.17 (s, 4H), 1.56 (s, 12H)
C6	δ 8.72 (br. s., 1H), 8.44 (s, 1H), 7.45 (s, 5H), 6.45 (br. s., 1H), 5.11 (s, 1H), 4.92 (s, 1H), 3.35 (s, 2H), 2.54 (s, 6H)

4.11.6 Single Crystal X-ray Analysis for Complex 6

Crystals suitable for x-ray crystallography were grown by slow evaporation of a DCM solution of the platinum complex **C5** which yielded crystals for **C6**. X-ray crystallography was performed on a Bruker SMART CCD APEXII area-detector diffractometer and were kept at 100.03 K during data collection. Using Olex2 software (Dolomanov *et al.*, 2009), the structure was solved with the ShelXS-1997 (Sheldrick, 2015) structure solution program using Direct Methods and refined with the Olex2 refinement package (Bourhis *et al.*, 2015).

The complex crystallizes in monoclinic P 21/c space system. The crystal data for the complex is as shown in **Table 9** below.

Table 9 Single Crystal data and Structure Refinement Parameters for **C6**.

Formula	Space Group	Cell Lengths	Cell Angles	Cell Volume	Z	Temperature
C₁₁H₁₈Cl₂N₂OPtS	P21/c	a =8.0734(1) b =18.0661(3) c =11.5367(2)	α =90 β =94.229(1) γ =90	1678.10(5)	4	100K

The ORTEP plot for platinum complex **C6** is as shown in **Figure 32**(a, b) with the unit cell consisting of 4 molecules. The angles subtended around the platinum center are approximately right angles confirming the square planar geometry of a Pt(II) metal oxidation state. Hydrogen atoms are omitted for clarity.

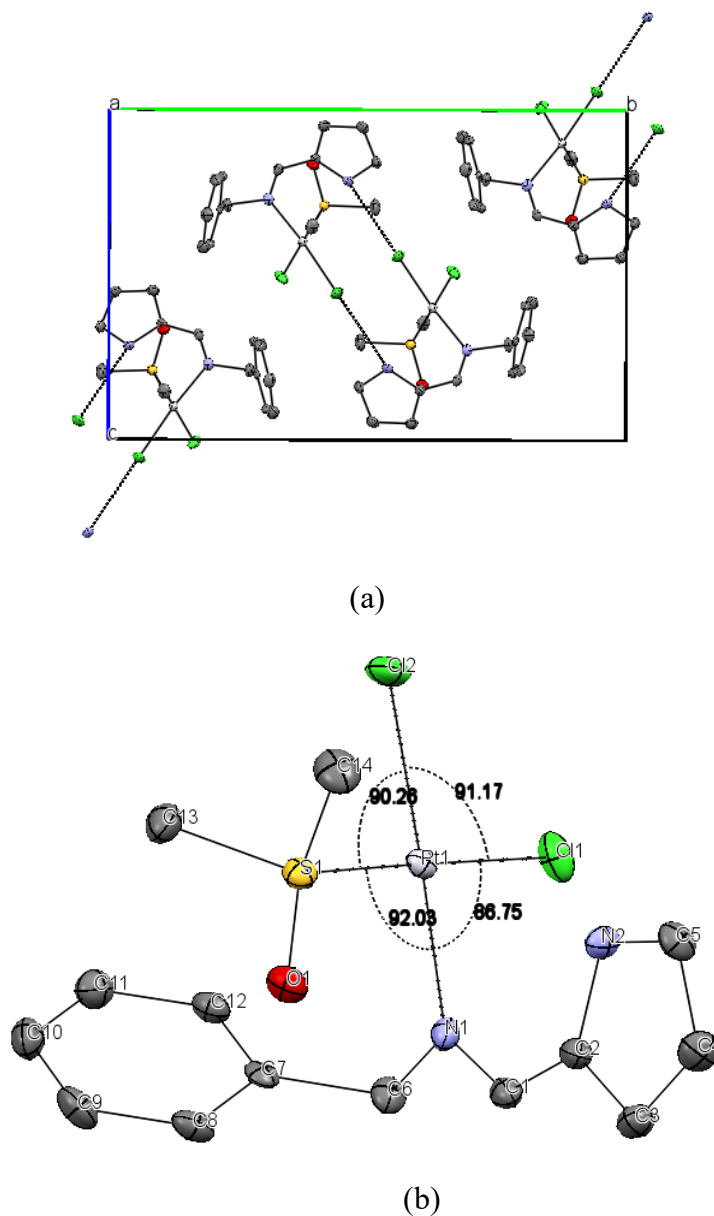


Figure 32 Unit cell packing (a) and bond angles (b) for **C6**

The crystal is stabilized through intermolecular hydrogen bonding (3.198Å) between the pyrrole hydrogen and chloride atom para to the imine nitrogen of adjacent molecules. A notable property of this complex is the unequal bond distances between the platinum metal center and the two chloride atoms attached to it. The bond length between the platinum and chloride para to the imine nitrogen

is 2.302 Å while the distance between platinum center and chloride atom para to sulphur atom of DMSO is 2.317 Å. This is credited to the stronger ground state *trans*-influence of sulphur compared to nitrogen, leading to a lengthening (and weakening) of interatomic bonds.

These agrees with similar literature observations by Murray and co-workers working on N and S-bonded PdCl₂ on amino acid backbones. In their work, they observed a bond length of 2.305Å for Pd-Cl *trans*- to N-atom and 2.324Å for Pd-Cl *trans* to S (Murray & Hartley, 1981). It is observed that coordination occurs preferentially between platinum and sulphur of DMSO rather than with oxygen atom despite the latter being less sterically hindered.

This is expected since platinum being a soft acid prefers coordinating with soft donors like Sulphur as opposed to Oxygen. The other reason could be due to the fact that sulphur has empty *d*-orbitals which will form a more preferred overlap with the *d*-orbitals of Platinum forming more stable bonding compared to Oxygen with no vacant *d*-orbitals.

4.12 Characterization and Structure Confirmation for the Thiosemicarbazide-based Complexes (C7- C11)

4.12.1 UV-Vis Spectroscopy for Thiosemicarbazide Complexes C7-C11

The UV-visible spectra for the compounds were recorded in DMSO at range 200- 800 nm using quartz cells at a concentration of 1.0 x 10⁻³M. The calculated molar absorptivity for the compounds is summarized in **Table 10** below.

Table 10 UV-Vis Spectra for the Thiosemicarbazone-based Complexes

Compound	$\lambda_{\max}(\text{nm})$	Calculated ϵ (x10 ⁴ LMol ⁻¹ cm ⁻¹)
C7	364, 382	1.51, 1.34
C8	371, 390	1.41, 1,31
C9	316, 385, 403, 461, 502	1.84, 1.46, 1.62, 0.395
C10	348, 363, 571	1.16, 1.09, 0.0557
C11	348, 401, 555	1.30, 0.86, 0.0087

Here again, the absorption bands of complexes occurred below 600 nm indicating large crystal-field splitting suggestive of square-planar geometry (Ünver & Hayvali, 2010). Literature reports indicate that Palladium(II) with $4d^8$ electronic configuration is expected to exhibit a square planar geometry associated with the three $d-d$ transitions; $^1A_{1g} \rightarrow ^1A_{2g}$ (463–522 nm), $^1A_{1g} \rightarrow ^1B_{1g}$ (405–418 nm) and $^1A_{1g} \rightarrow ^1E_g$ (344–386 nm) (Biyala *et al.*, 2008; Lever, 1984). In this work, bands observed in the regions 502-571 nm, 401-403 nm and 348-385 nm could be assigned to $^1A_{1g} \rightarrow ^1A_{2g}$, $^1A_{1g} \rightarrow ^1B_{1g}$, and $^1A_{1g} \rightarrow ^1E_g$ respectively, suggesting a square planar geometry for these complexes.

A representative UV-Vis spectrum for **C9** in DMSO is represented in **Figure 33**.

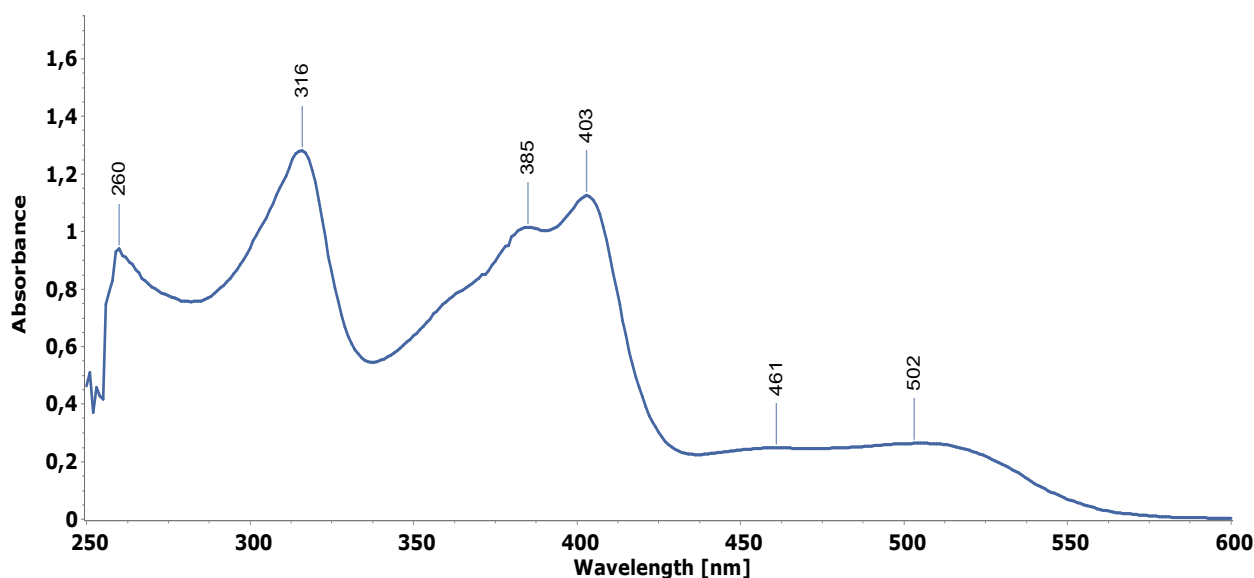


Figure 33 UV-Vis Spectrum of **C9**

The different complexes with different metal centers and ligands coordinated to the metal showed different trends in their UV-Vis spectra. **C7** and **C10** differed only by the metal center. The absorbance for **C10** with a platinum metal center occurred at a lower wavelength (348nm) compared to **C7** (364nm) with a palladium metal center. A possible reason for this is the higher nuclear charge of platinum and the larger d -orbital size, which draws electron density away from the π system effectively lowering the energy of π orbitals thereby increasing the ΔE between π - π^* levels of **C10**. **C7** and **C8** differed only by the presence of a -Br in position 5 of **C8**.

The presence of the auxochrome increased the electron density of the π bonding orbitals (HOMO) resulting in raised energy level through electron- electron repulsion, leading to the observed longer wavelength in **C8**.

C10 and **C11** differed in that there was a Br substituent in position 4 of the thiophene ring and PPh₃ coordinated to the metal center of **C11**. PPh₃ is a better σ donor- π acceptor compared to the Cl ligand. This makes it a stronger field splitter widening the 10Dq crystal field causing the blue shift observed in the *d-d* transition in **C11** (555nm in **C10** vs 571nm in **C11**).

In general, spectra for all the complexes displayed two or more peaks corresponding to a combination of the π - π^* and $d_{\pi-\pi^*}$ transitions (Greenwood, 2002), together with broad and weak *d-d* transition (in **C9**, **C10** and **C11**) with molar extinction coefficients of 10¹- 10² LMol⁻¹cm⁻¹.

4.12.2 Elemental Analysis for Thiosemicarbazide Complexes

The elemental analysis for C, H, N, S content for these complexes was carried out to make a conclusive confirmation of the proposed structures and therefore verify the successful synthesis and purity of the complexes. The results from the elemental (C, H, N, S) percentages were compared with the theoretical calculations, and acceptable values fell within the acceptable ranges of $\pm 4\%$ of the expected values. The values are as shown in **Table 11**.

Table 11 Elemental Analysis Data for **C7- C11**

Compound	Molecular Formula	% C, H, N Calculated (Obtained)
C7	C ₈ H ₇ Cl ₂ N ₃ PdS ₂	C, 19.87(19.67); H, 1.95(1.36); N, 11.59(10.82); S, 17.69(15.90)
C8	C ₁₁ H ₁₃ ClN ₄ PdS ₂	C, 37.22(34.47); H, 3.38(2.73); N, 14.47(14.32); S, 8.28(8.17)
C9	C ₁₁ H ₁₃ ClN ₄ PdS	C, 37.22(34.47); H, 3.38(2.73); N, 14.47(14.32); S, 8.28(8.17)
C10	C ₈ H ₇ Cl ₂ N ₃ PtS ₂	C, 14.79(14.71); H, 2.28(2.21); N, 8.62(8.58); S, 13.16(12.36)
C11	C ₂₄ H ₂₁ BrClN ₃ PPtS ₂	C, 38.08(38.30); H, 2.80(2.99); N, 5.55(5.93); S, 8.90(8.87)

4.12.3 Fourier Transform InfraRed Spectroscopy for the Thiosemicarbazide Complexes

For the thiosemicarbazide-based complexes **C7-C11**, the FTIR vibrations due to symmetric and asymmetric $\nu(\text{N-H})$ stretch ($3150\text{-}3430\text{cm}^{-1}$) arising from the primary amine were observed in complexes **C7**, and **C9**. This is a clear indication that the $-\text{NH}_2$ group was not involved in coordination to the metal centers. In **C10**, these vibrations are masked by a broad band occurring at around $3600\text{-}3700\text{ cm}^{-1}$. This was attributed to the possibility of water molecules in the coordination spheres of the complex. Further observations of the disappearance of the thioamide $\nu(\text{C=S})$ region peaks (around 840 and 1350cm^{-1}) indicated the participation of thione sulphur in the coordination to the metal centers. These results indicate an $\text{N}^{\wedge}\text{S}$ bidentate manner of coordination for these ligands.

Comparing the FTIR spectra of the complexes **C7** and **C10** to the parent ligand **L5**, it was observed that complexation with Palladium(II) caused a shift to higher energy by 8cm^{-1} (1611cm^{-1} to 1619cm^{-1}) for **C7**, while complexation with Platinum(II) shifted the energy to a lower energy by 18cm^{-1} (1593cm^{-1} from 1611cm^{-1}) for **C10**. This is understood in terms of nuclear charge for the two metals. Platinum(II) has a higher nuclear charge inferring that the incoming ligand will be attracted more to Platinum than to Palladium.

This leaves the azomethine region with less electron density and more single bond character for the Platinum(II) complex compared to the Palladium(II) complex. Another factor is the larger spatial size of the d -orbitals of platinum ($5d$) compared to palladium ($4d$). This results in less repulsion for electrons occupying the larger orbitals in platinum complexes and better back donation to π^* of azomethine.

Compared to **C7**, **C8** had a Br at position 5 on the thiophene ring. At position 5, there is a possible resonance donation from the halide lone pair implying that the imine bond retains more π character in **C8** compared to **C7**, reflected in the hypsochromic shift observed in **C8** (1621cm^{-1} compared to 1608cm^{-1} for parent ligand, **L6**). Complex **C11** compared to **C10** had one $-\text{Cl}$ substituted for $-\text{PPh}_3$. The $-\text{PPh}_3$ group is a much better σ donor and π acceptor which effectively weakens the Pt-N bond *trans* to itself in **C11** through ground state *trans* influence. The better π acceptor properties of the PPh_3 moiety means less electron density is available to the platinum metal center for back donation to the imine region. This leaves the imine bond in **C11** with a higher bond order due to less

antibonding interactions via $M \rightarrow L$ back-bonding. These factors resulted in the observed difference in energy for the imine bonds; 1608cm^{-1} versus 1593cm^{-1} for **C11** and **C10** respectively.

In general, the shifting to lower frequencies is ascribed to the π -back donation from metal d -orbitals to empty π -antibonding orbitals of $\text{CH}=\text{N}$ (Adil Ali Al-Fregi *et al.*, 2017). A characteristic peak at 696cm^{-1} for platinum complexes and 534cm^{-1} for palladium complexes appeared and was ascribed to the $\nu[\text{M}-\text{N}]$ vibration. A representative FTIR spectrum for **C9** is shown in **Figure 34**.

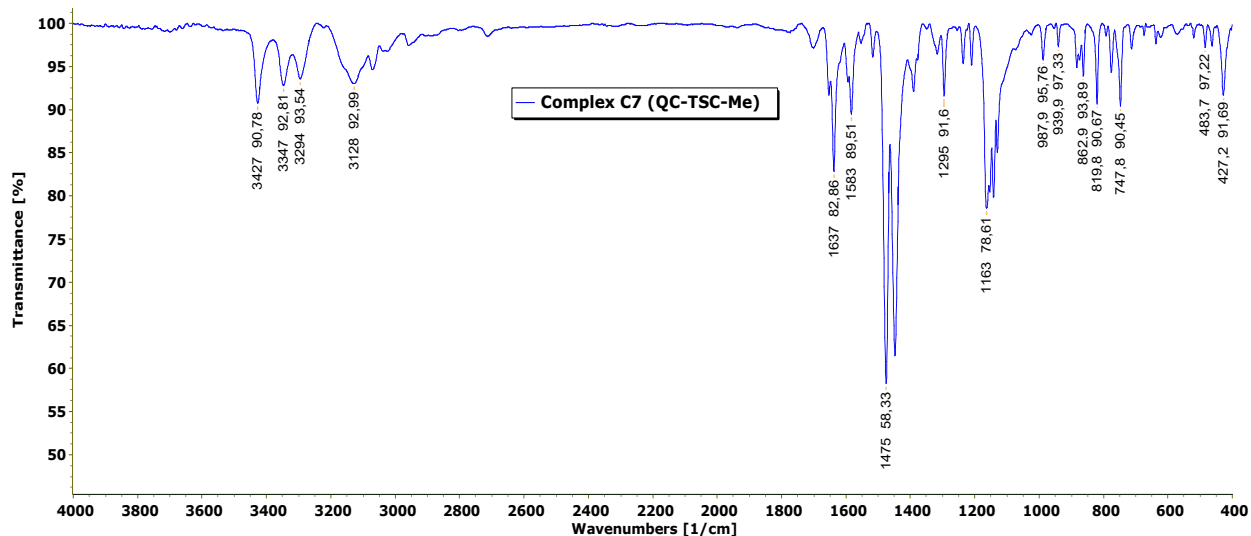


Figure 34 FTIR Spectra for **C9**

4.12.4 Proton and Carbon-13 Nuclear Magnetic Resonance for the Thiosemicarbazide Complexes

For the ^1H NMR for these complexes, the singlet peak observed at around 11.45-11.80ppm in the free ligands due to the hydrazine NH proton disappeared in the spectra of the complex **C7-C9** and **C11**. This observation indicated the participation of $\text{C}=\text{S}$ group in the coordination to the metal ion through thioenolization in these four complexes. A broad sharp peak at 3.46ppm (**C10**) indicated the presence of water in the coordination sphere of the complex. Similar observations appear in literature for thiosemicarbazone-based complexes (Netalkar *et al.*, 2015).

The ^{13}C NMR spectra for the complexes were determined in either CDCl_3 or $\text{DMSO}-d_6$. After complexation, the ^{13}C NMR shifts for the imine carbon of complexes **C7** and **C10** occurred up-field (146.04ppm and 145.86ppm respectively) in relation to the parent ligand **L5** (178.27 ($\text{C}=\text{N}$ imine)). This increase in shift by 6.95ppm and 5.28ppm is as a result of coordination to the metal as electron

density is pulled away from the azomethine bond de-shielding the carbon nucleus. This means that only a smaller external magnetic field is necessary to bring the nucleus into resonance, resulting in the observed higher chemical shifts in ^{13}C -NMR. Similar trend is observed for complexes **C8** (145.86ppm) compared to the parent ligand **L6** (141.16ppm).

Comparing the ^1H NMR spectra, the palladium complex **C7** and the platinum complex **C10** were compared to the parent ligand, **L5** where a downfield shift was observed in both complexes. The palladium complex showed a lesser shift of 0.16ppm compared to 0.30ppm observed in the platinum complex. This can be attributed to the higher nuclear charge of platinum compared to palladium, which causes a higher de-shielding of the azomethine region in the platinum complex leading to a more downfield shift for the azomethine proton.

Complex **C7** and **C8** differed only on the Br-substituent at position 5 of the thiophene ring of **C8**. At position 5, the Br-substituent has possible resonance donation to the adjacent π system. This increases the shielding of the azomethine proton making it to resonate at higher field compared to that of **C7**. Comparing **C10** and **C11**, they differed with a Br-substituent attached to the thiophene ring, and PPh_3 group coordinated to the metal center in **C11**, while no substituent was present in **C10** and coordination to the metal was by Cl^- ligands.

Considering **C11** with a PPh_3 directly coordinated to the metal center, the PPh_3 is both a good σ donor and a π acceptor. The σ donation is through a hybrid orbital containing a lone pair located on phosphorus (Konishi *et al.*, 2018; Nhung, 2018). The steric bulk of a PR_3 group and the resultant crowding around the metal center is a determinant in the rate at which the group dissociates from a metal, where, the bulkier the R group, the faster the rate of dissociation (Tolman, 1970). These factors together with the higher *trans* influence of PPh_3 compared to Cl^- make **C11** to be more shielded at the azomethine region compared to **C10**.

This resulted in the observed difference of 0.59ppm between the azomethine protons of the two complexes.

A representative ^1H NMR spectra for **C7** is shown in **Figure 35**.

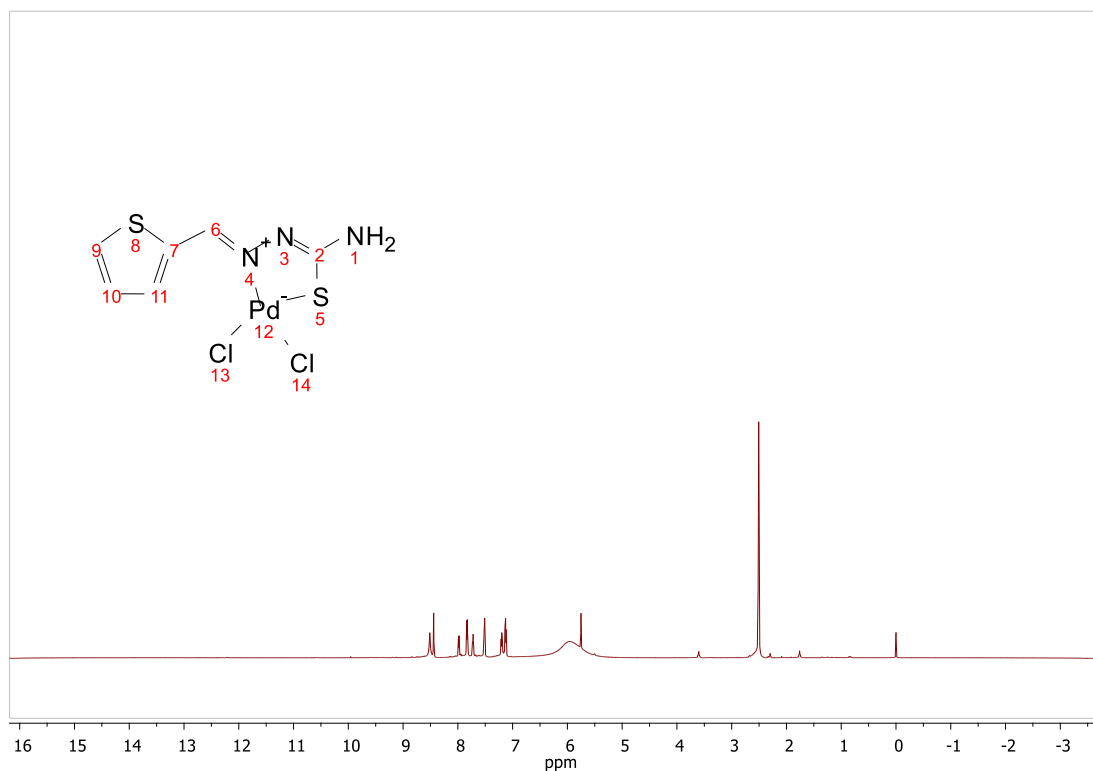


Figure 35 ^1H NMR Spectra for **C7**

The ^1H NMR and ^{13}C NMR spectral data for **C7- C11** is as summarized in **Table 12** below. Due to low solubility problems, some of the complexes did not give good carbon-13 spectra.

Table 12 ^1H NMR Spectral Data for **C7- C11**

Complex	^1H NMR (400 MHz, DMSO- d_6) (δ ppm)	^{13}C NMR (400 MHz, DMSO- d_6) (δ ppm)
C7	δ 8.35 - 8.60 (m, 1H), 7.98 (s, 1H), 7.84 (s, 1H), 7.51 (br. s., 1H), 7.13 (d, J = 4.89 Hz, 1H), 3.60 (s, 2H)	δ 177.24 (C=N imine), 172.16, 146.15, 135.36, 133.53. 127.13
C8	δ 8.34 (s, 1H), 7.59 (s, 1H), 7.32 (s, 1H), 6.97 (s, 1H), 5.76 (s, 1H), 3.60 (br. s., 2H)	δ 172.83 (C=N imine), 144.86, 136.01, 134.09, 130.64. 124.92

Complex	¹ H NMR (400 MHz, DMSO-d ₆) (δppm)	¹³ C NMR (400 MHz, DMSO-d ₆) (δppm)
C9	δ 12.07 (s, 1H), 8.72 (s, 1H), 8.44 (s, 1H), 7.48 (m, 3H), 6.45 (s, 1H), 4.92 (s, 2H), 3.35 (s, 3H)	δ 183.24 (C2C=N quinoline), 159.68 (C=N imine), 141.78(C2C-N quinolone), 127.38, 147.97, 122.08, 132.77, 128.92
C10	δ 12.34 (br. s., 1H), 8.55 (s, 1H), 7.60 (br. s., 1H), 7.16 (br. s., 1H), 6.95 (s, 1H), 3.46 (br. s., 2H)	δ 173.45 (C=N imine), 145.86, 143.94, 136.93, 133.14. 127.79
C11	δ 8.72 (s, 1H), 7.96 (s, 1H), 7.43 (m, 15H), 3.43 (s, 1H), 2.89 (s, 1H), 2.74 (s, 2H).	

4.13 Cyclic Voltammetry

Electrochemical studies to understand the redox properties of the palladium complexes was performed in solution using PalmerScan3 CV instrument equipped with glassy carbon electrodes as working electrodes, Ag/AgCl as reference electrode and platinum wire as counter electrode. The scan range of -1.8 to +1.8, and a scan rate of 200mV/s were used. The supporting electrolyte was 5ml 10mMol PBS buffer at pH 7.0.

Typical cyclic voltammograms showing the electron processes are shown in **Figure 36** for **C3** and **C4**. The complexes exhibit two reduction peaks; at -0.57V and a completely irreversible reduction at $E_{p,c} = -1.47$ V and -1.7V respectively, with no anodic peak present.

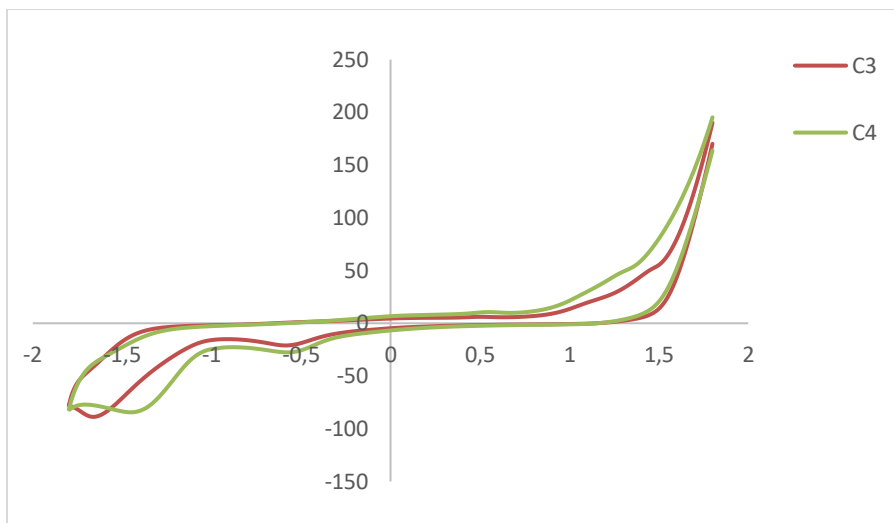


Figure 36 Cyclic Voltammetry for **C3** and **C4**

Experimental conditions: pH 7.0 vs Ag/AgCl, WE= glassy carbon, and CE= platinum wire, scan rate= 200mV/s.

Since the splitting of the *d*-orbital energy levels reflects the antibonding interaction between the metal orbitals and the ligands, we expect ligand field splitting strength to correlate with metal-ligand orbital overlap according to the spectrochemical series. **C3** with 2-Cl ligands *trans* to each other has a better orbital overlap compared to **C4** with *cis* Cl ligands. With this background, the larger shift in the peak potential of **C3** (coordinating through two N and two Cl ligands *trans* to each other) (-1.60), is expected since the *trans* conformation affords better pi-orbital overlap. The *cis* conformation of the Cl's in **C4** has less orbital overlap due to steric crowding.

The observed process most likely corresponds to a metal-centered one-electron reduction process for the two peaks as shown in **Equations 3** and **4**.



The cyclic voltammetry for platinum complexes was done at different scan rates between 20mV/s to 100mV/s. As shown in the typical CV scan for **C6** in **Figure 37**, these complexes showed peaks at around -0.02V corresponding to oxygen reduction, and another one at around -0.5 V vs Ag/AgCl. This peak was credited to the diffusion-controlled H⁺ reduction to H₂ which occurs around -0.41V at pH 7 (Alpuche-Aviles *et al.*, 2018).

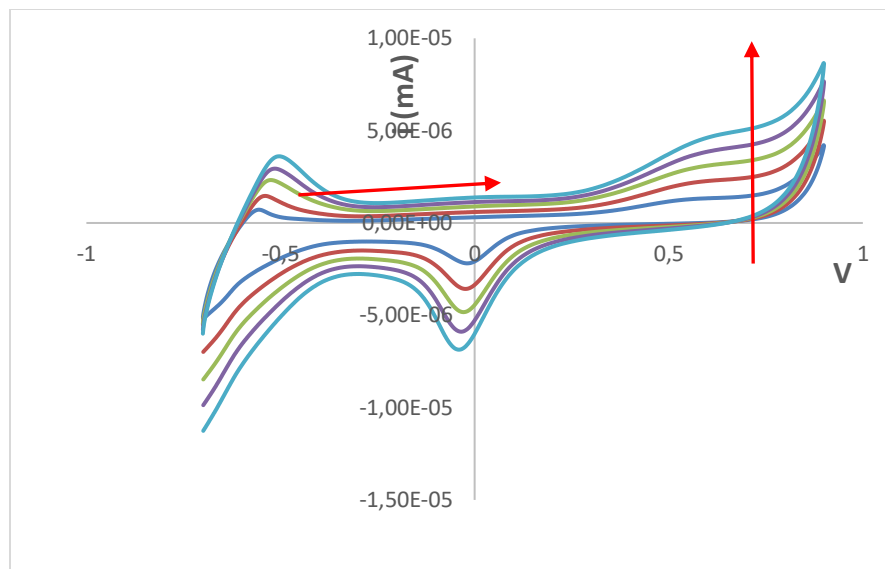


Figure 37 CV Scans for **C6** at different scan Rates

In biological physiological environments, the redox stability is closely controlled (P. Zhang & Sadler, 2017) with an accessible window of potential ranging between - 0.4V to + 0.8V versus normal hydrogen electrode (NHE) (Kirlin *et al.*, 1999). These values correspond to the potentials for the main redox agents in biological systems; NADPH with approximately - 0.38V and oxygen at around+ 0.815V, at pH 7.0 versus NHE (Schafer & Buettner, 2001).

Typically, all redox processes with a bigger or lesser value of potential compared to this physiological range cannot happen in the biological setting. However, there are other routes by which metal complexes interfere with cellular redox reactions through interaction via their redox centers either on the metal or ligand, or through coordinating to biomolecules which facilitate cellular redox mechanisms (P. Zhang & Sadler, 2017).

4.14 Lipophilicity Studies

4.14.1 Partition Coefficient

The values for the partition coefficient were determined as $\log P$ ($\log C_o/C_w$) for the palladium complexes **C1**, **C3**, **C4**, **C7-C9** and the platinum complexes **C6**, **C10** and **11** by the method described in the methodology section. This gave values of 1.3979 ± 0.00015 for **C1**, 1.3803 ± 0.00015 for **C3**, 1.2652 ± 0.00025 for **C4**, 0.5 for **C7**, 1.3762 for **C8**, 0.6 for **C9**, 1.3085 ± 0.00050 for **C6**, 0.3202 for **C10** and 1.9927 for **C11**. These values indicated a more than 20times partitioning of most of the

compounds in oil layer compared to the water layer. The partitioning was evident from the colours in both layers as indicated in (**Figure 38**).

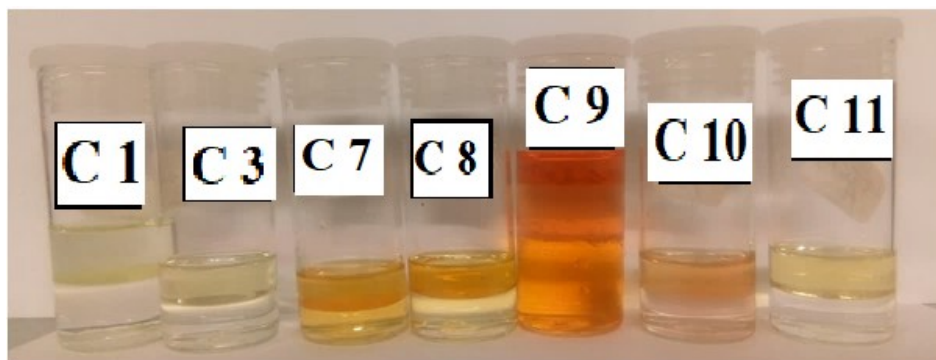
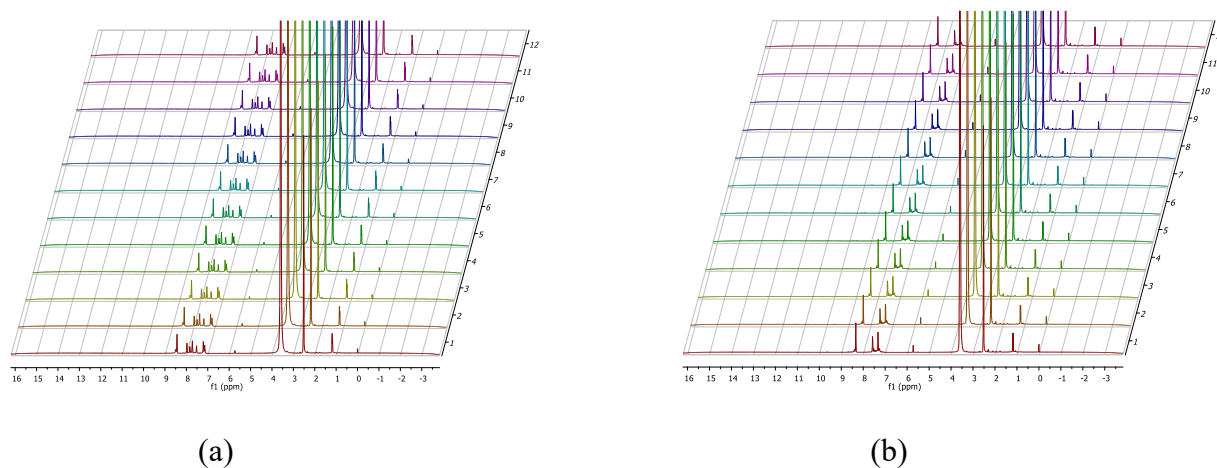


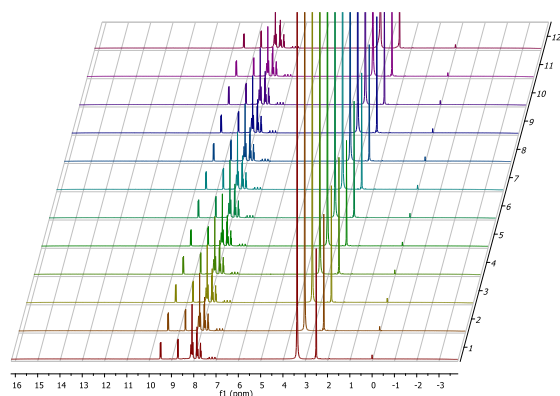
Figure 38 Partitioning of complexes **C1**, **C3**, **C7-C11** between water (bottom layer) and n-octanol (top layer)

The high log P for complex **C11** was as a result of the presence of benzene rings which are highly hydrophobic. **C10** with water incorporated in the coordination sphere was the most hydrophilic as indicated by the low Log P value of 0.3. The high log P values for these complexes implies that they can be suitable for oral administration (Bhal, 2011).

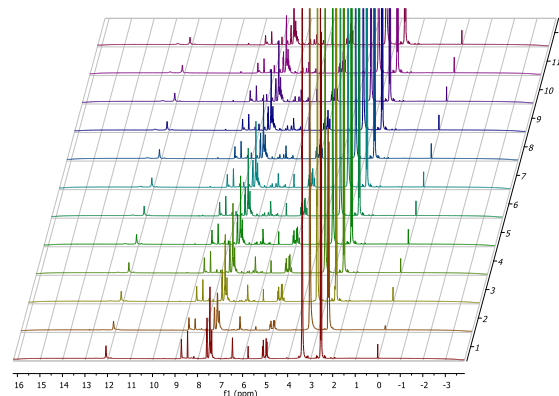
4.15 Stability studies

Stability studies were performed for five of the complexes; three palladium complexes **C7**, **C8**, and **C9**; and two platinum complexes; **C6** and **C11** in DMSO- d_6 containing 200 μ L of D_2O . The spectra were monitored over 72h period for any changes in proton environments to establish any hydrolysis or decomposition with time. As shown in **Figure 39**, there were no changes observed in the spectra of these compounds which meant that they maintained their structural integrity in solution as shown in the 1H -NMR plots, and therefore could be analysed for bioassay (Motswainyana *et al.*, 2012).

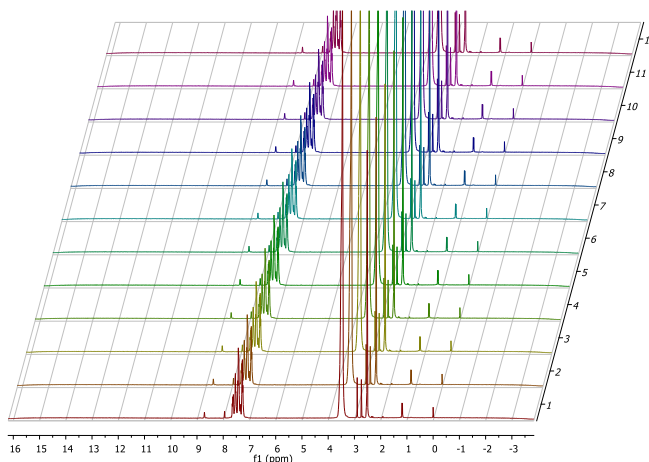




(c)



(d)



(e)

Figure 39 $^1\text{H-NMR}$ Stability Scans for (a) C7, (b) C8, (c) C9, (d) C6, (e) C11

4.16 DNA binding Kinetics

Observation on the spectral changes of metal complexes in the UV-Vis range after the addition of serial concentrations of DNA is a generally accepted technique in evaluating the binding modes and the kinetics of DNA-metal complex interactions (Olsztynska & Komorowska, 2011).

In this study, we used calf thymus-DNA prepared in 10mM tris-HCl buffer at pH 7.21 and the DNA concentration was determined by scanning serial dilutions at λ_{max} of 260nm, and was calculated using the molar absorptivity of the ct-DNA, $\epsilon = 6600\text{M}^{-1}$ as shown in **Figure 40**.

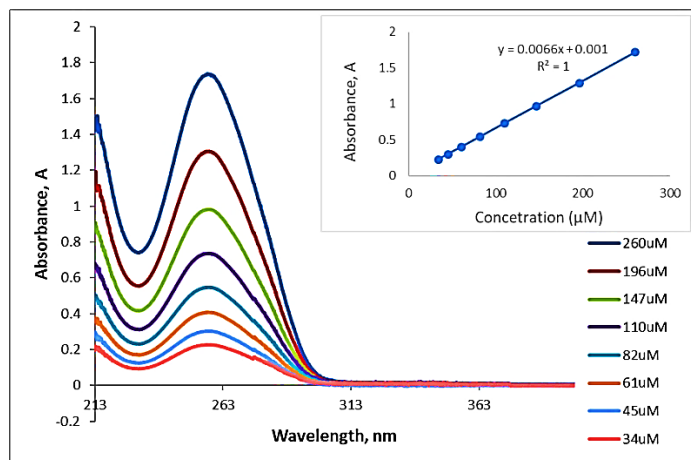
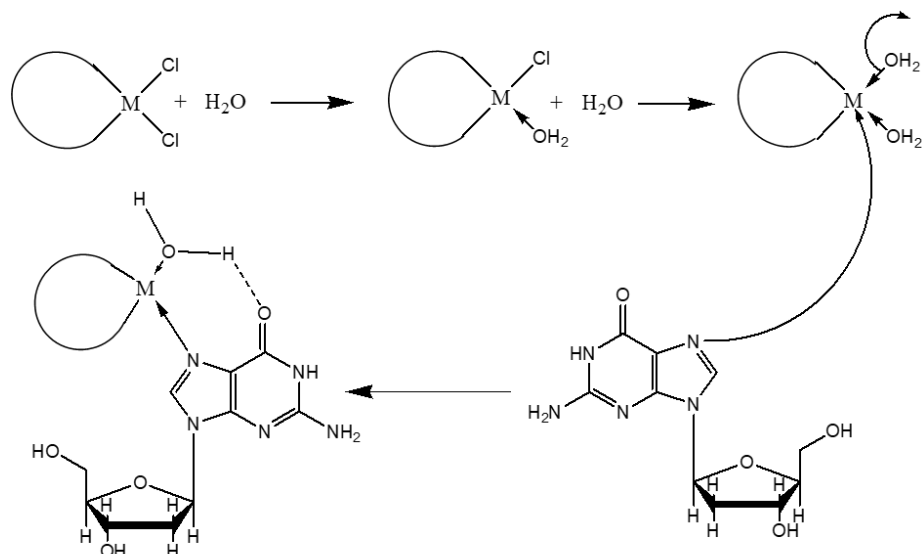


Figure 40 Dilutions for determination of DNA concentration used. Inset is Absorbance vs Concentration at 260nm

The DNA sample was stored at 4°C and used within four days. The UV-Vis scans from 200-800nm were performed by serial titrations of incremental amounts of calf thymus DNA (CT-DNA) to a fixed concentration of the complexes. The complex-DNA mixture was allowed to equilibrate 10minutes prior to taking UV-Vis measurements. With continued addition of DNA, the peaks of interest eventually decreased up to a point where they disappeared and at the same time there appeared a peak at 260nm.

This clearly showed that all the complex had been bound to DNA and further additions resulted in free DNA in the mixture which was indicated by the characteristic DNA peak at 260nm. The proposed binding mechanism is as outline in **Scheme 24** below



Scheme 24 Proposed mechanism for the binding of complexes to DNA

The binding kinetics for the complex-DNA interaction was then determined from the intrinsic binding constant, K_b by plots of the Benesi-Hildebrand host-guest equation results (Kuntz Jr *et al.*, 1968), **Equation 5**, where the strength of the interaction is reflected by the value of the binding constant.

$$\frac{A_o}{A - A_o} = \frac{\varepsilon_G}{\varepsilon_{H-G} - \varepsilon_G} + \frac{\varepsilon_G}{\varepsilon_{H-G} - \varepsilon_G} \frac{1}{K_b[\text{DNA}]}$$

Equation 5

where A_o and A are the absorbances of the blank sample without DNA, and absorbance of complex-DNA after addition of serial concentrations of DNA respectively; while ε_G and ε_{H-G} are the molar extinction coefficients of complex only and complex-DNA respectively. The binding constant is determined by plotting $A_o/(A - A_o)$ vs $1/[\text{DNA}]$ to give a straight line graph. The equation of the straight line gives the slope and intercept where the K_b value was calculated from the ratio of the intercept to the slope. From the K_b values, Gibbs free energy changes ΔG for the complex-DNA interactions were calculated using **Equation 6**.

$$\Delta G = -RT \ln K_b \text{ kJ mol}^{-1}$$

Equation 6

where R is the gas constant and T is the absolute temperature.

4.17 DNA binding Studies for Pyrrole-based Complexes (C1, C3, C4, C6)

The absorption spectra of the interaction of CT DNA with the pyrrole-based complexes C1, C3, C4 and C6 together with the Benesi-Hildebrand plots are shown in **Figure 41-Figure 44**. All the studies were carried out at a concentration of 18 μ M for the complexes, with serial addition of DNA in tris-HCl buffer. The buffer was maintained at a concentration of 10mM and pH of 7.21. The arrows in the graphs show the spectral changes upon increasing concentration of CT DNA. Inset is the Benesi-Hildebrand plots for the Determination of binding constant.

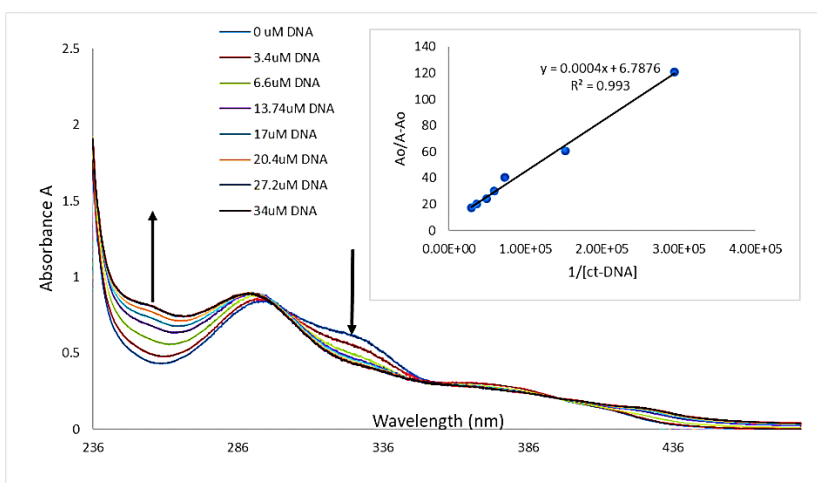


Figure 41 DNA-Binding UV-visible absorption spectra for complex C1.

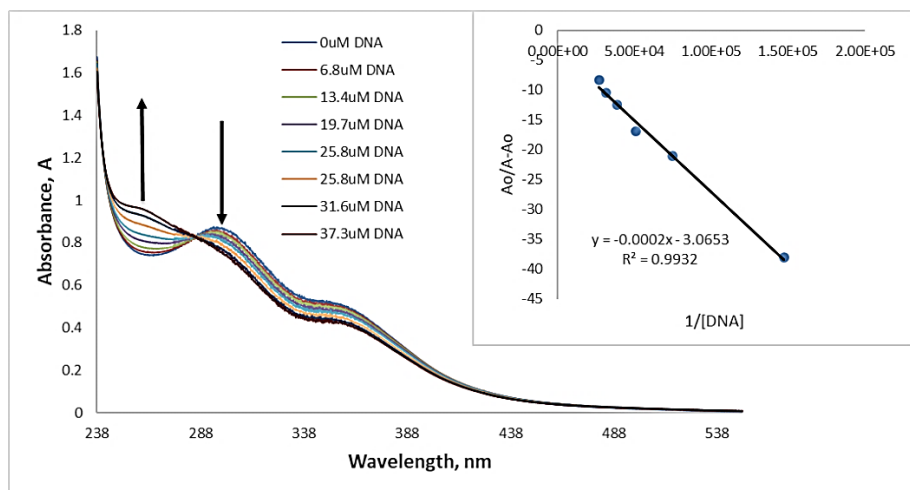


Figure 42 DNA-Binding UV-visible absorption spectra for complex C3.

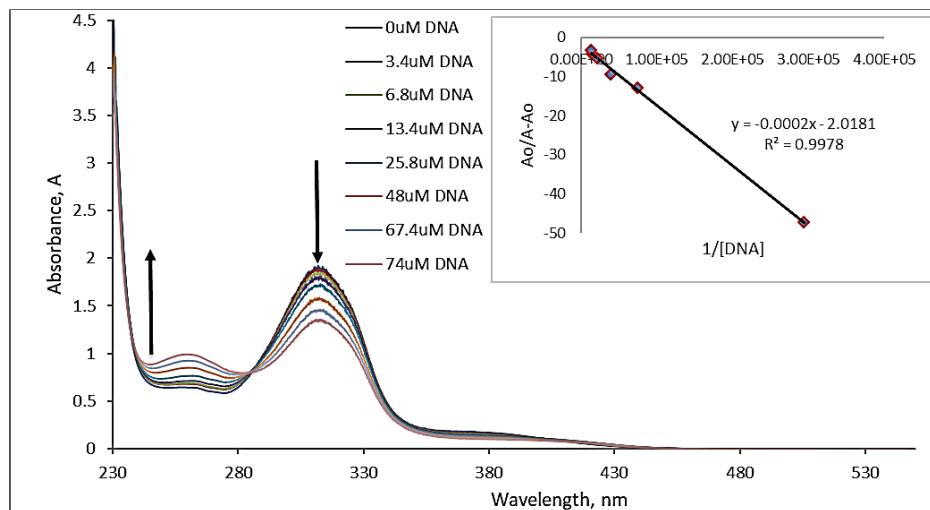


Figure 43 DNA-Binding UV-visible absorption spectra for complex **C4**.

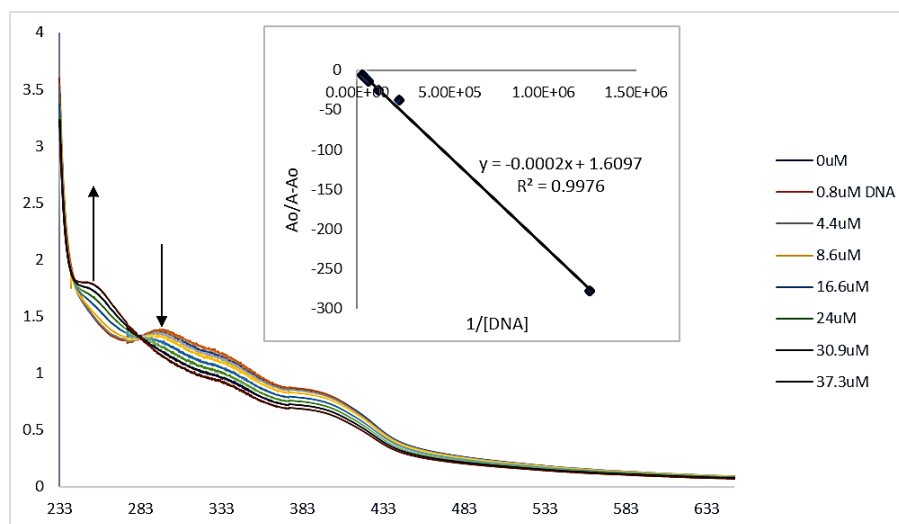


Figure 44 DNA-Binding UV-visible absorption spectra for complex **C6**.

The absorption spectra for **C1** with increasing amounts of CT DNA showed a 5% hyperchromism at 294nm. The observed hyperchromism is attributed to external associations by electrostatic interactions of the complex with the groove bases in the DNA possibly through the planar aromatic phenyl and pyrrole moieties and from hydrogen bonding with the negatively charged phosphate DNA backbone (Suntharalingam *et al.*, 2013).

This is further supported by the hypsochromic shift of 6 nm since a decrease in electron density in π -orbitals stabilizes the orbitals, which causes an increase in the energy gap between π and π^* orbitals, shifting the absorption to a lower wavelength. On the other hand, the spectra for **C3**, **C4** and **C6** showed hypochromic shifts with no shift in wavelength. Literature reports explains this type

of hypochromism as the probability of intercalative interactions of the chromophores in the complexes with the DNA base pairs (Pyle *et al.*, 1989).

Furthermore, distinct isosbestic points appeared at 300nm in the spectrum of **C1**, and 285nm in the spectra of **C3**, **C4** and **C6**. This is a clear indication of equilibrium between bound DNA and the free form of the compounds confirming literature reports that no other species apart from the free and the intercalated forms are present in the mixture (Arshad *et al.*, 2016). The K_b values and Gibbs free energy were then calculated for these complexes and compared to those of known DNA intercalators as shown in **Table 13**.

Table 13 Comparison of Binding constants (K_b) and Gibbs free energy ($-\Delta G$) values for the Pyrrole-based complexes–DNA interactions derived from UV-vis spectrophotometric data with other reported intercalators.

Complex	Mode of binding	Binding constant K_b (M^{-1})	Gibbs free Energy ($-\Delta G$) ($kJ\ mol^{-1}$)	References
C1	Electrostatic	1.6969×10^4	24.13	CW
C3	Intercalative	1.5327×10^4	23.88	CW
C4	Intercalative	1.0091×10^4	22.84	CW
C6	Intercalative	8.049×10^4	27.99	CW
Ethidium bromide	Intercalative	1.4×10^6	35.06	(LePecq & Paoletti, 1967)
Lumazine	Intercalative	1.74×10^4	24.19	(Ibrahim <i>et al.</i> , 2002)
Epirubicin	Intercalative	3.4×10^4	25.85	(Aslanoglu, 2006)
Proflavine	Intercalative	2.32×10^4	24.90	(Aslanoglu, 2006)

*Note: CW= Current Work

These values indicate a comparatively strong interactions between these complexes and CT-DNA. Complexes **C1**, **C3** and **C4** have lower binding constants but still comparable to the values of the known DNA intercalators; Lumazine, Epirubicin and Proflavine. The platinum complex; **C6** showed higher K_b values than those of Lumazine, Epirubicin and Proflavine, but lower than that of the well-known intercalator- ethidium bromide. This signifies its stronger affinity to bind to the DNA, indicating its significance as possible candidate in the line of potential anticancer drug candidates.

Similar results of the efficacy of **C6** as a potential candidate for further anticancer tests was shown by its selectivity and cytotoxicity against various cancer cell lines as discussed in the section for invitro cytotoxicity. The binding constant for complex **C6** suggests that it can also be a viable candidate for new intercalator compounds. All the obtained values of ΔG were negative indicating the spontaneity of the complex-DNA interactions.

4.18 DNA binding Studies for Thiosemicarbazide Complexes (C7-C11)

The absorption spectra of the interaction of CT DNA with the thiosemicarbazide complexes together with the Benesi-Hildebrand plots are shown in **Figure 45- Figure 49**. All the studies were carried out at a concentration of $18\mu\text{M}$ for the complexes, with serial addition of DNA in tris-HCl buffer. The buffer was maintained at a concentration of 10mM and pH of 7.21. The arrows in the graphs show the spectral changes upon increasing concentration of CT DNA. Inset is the Benesi-Hildebrand plots for the Determination of binding constant.

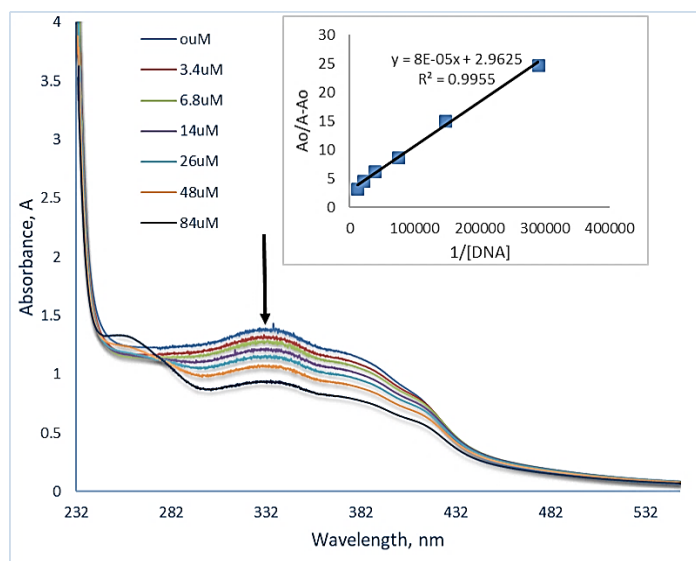


Figure 45 DNA-Binding UV-visible absorption spectra for complex **C7**.

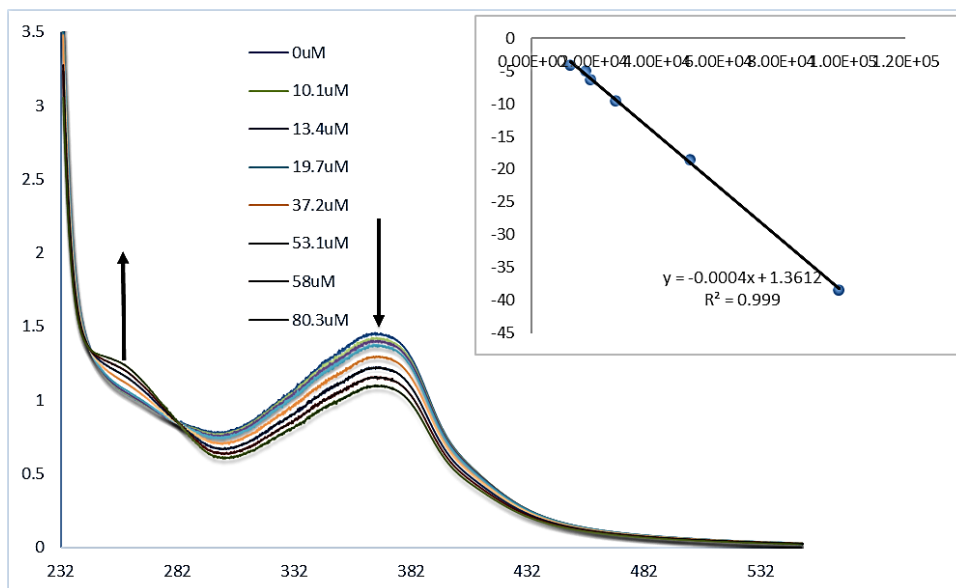


Figure 46 DNA-Binding UV-visible absorption spectra for complex C8.

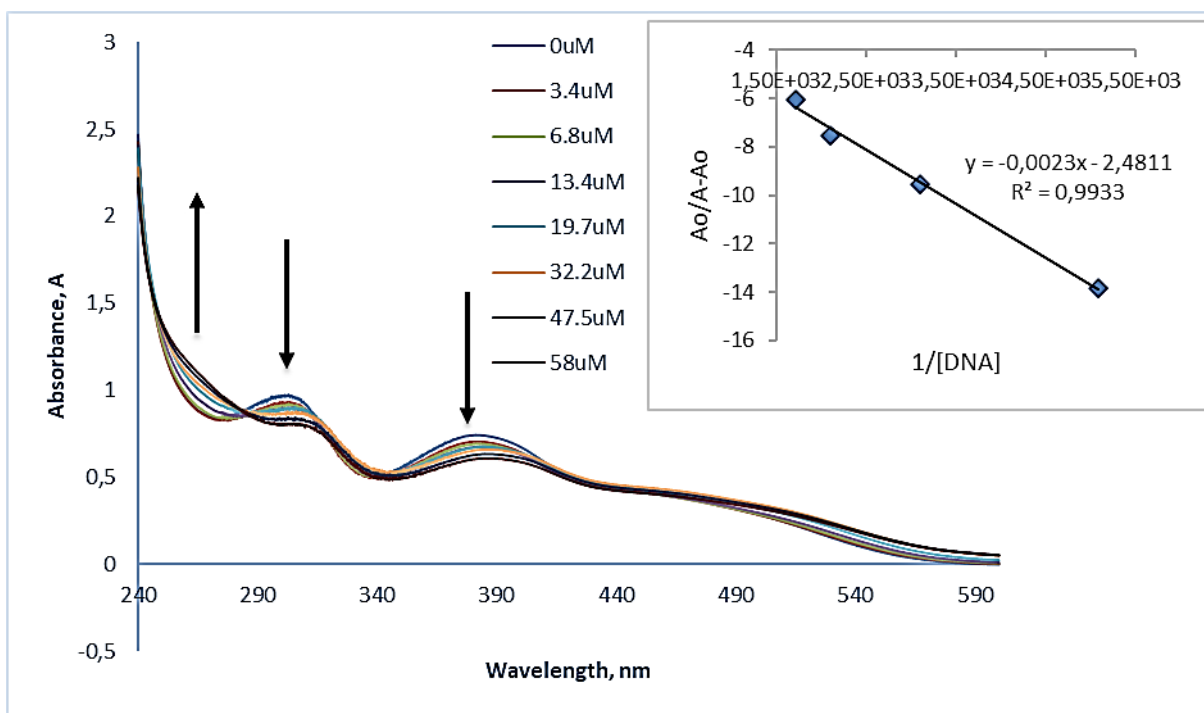


Figure 47 DNA-Binding UV-visible absorption spectra for complex C9.

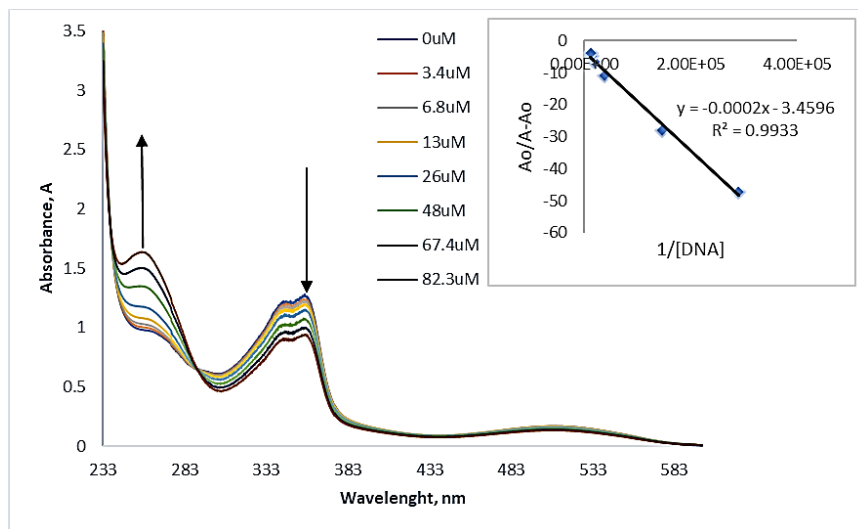


Figure 48 U DNA-Binding UV-visible absorption spectra for complex **C10**.

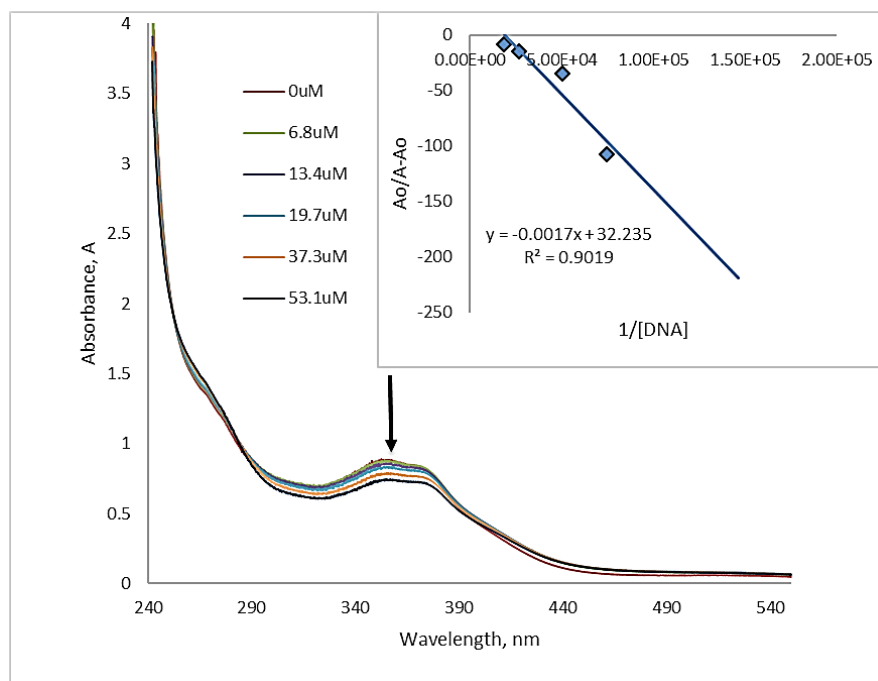


Figure 49 DNA-Binding UV-visible absorption spectra for complex **C11**.

All the complexes exhibited hypochromic shifts at λ_{max} . The hypochromism is probably the result of intercalative mode of binding as a result of the overlap of π^* antibonding orbitals of the ligands bound to the complex, with π bonding orbitals of the DNA base pairs (Pyle *et al.*, 1989). This decreases the probable transitions and the effect is observed as a hypochromic shift (Raman & Sobha, 2012)

Furthermore, distinct isosbestic points appeared at 283nm in the spectra of **C8** and **C11**, 286nm for **C9** and 292nm for **C10**. This is as a result of equilibrium between bound and free form of DNA and indicates that there are no other species in the mixture (Arshad *et al.*, 2016). Binding constant and Gibbs free energy values were then evaluated and compared to those of common DNA intercalators as shown in **Table 14**.

Table 14 Comparison of K_b and $-\Delta G$ values for the thiosemicarbazide complexes–DNA interactions with other reported intercalators.

Complex	Mode of binding	K_b (M^{-1})	$-\Delta G$ ($kJ\ mol^{-1}$)	References
C7	Intercalative	3.7031×10^4	26.03	CW
C8	Intercalative	3.403×10^3	20.15	CW
C9	Intercalative	1.211×10^3	17.59	CW
C10	Intercalative	1.7298×10^4	24.18	CW
C11	Intercalative	1.8962×10^4	24.04	CW
Ethidium bromide	Intercalative	1.4×10^6	35.06	(LePecq & Paoletti, 1967)
Lumazine	Intercalative	1.74×10^4	24.19	(Ibrahim <i>et al.</i> , 2002)
Epirubicin	Intercalative	3.4×10^4	25.85	(Aslanoglu, 2006)
Proflavine	Intercalative	2.32×10^4	24.90	(Aslanoglu, 2006)

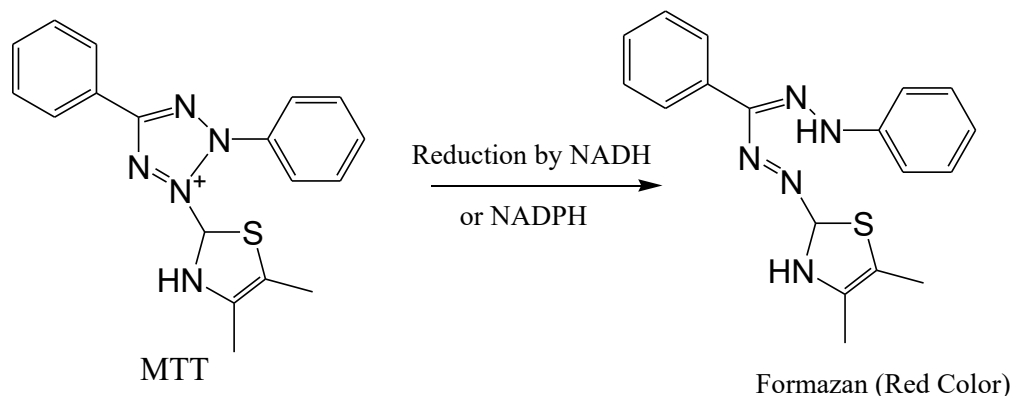
*Note: CW= Current Work

The palladium complex **C7** showed higher values compared to those of Lumazine, Epirubicin and Proflavine indicating a strong binding between this complexes and DNA. Complex **C8** showed a lower binding constant probably due to the presence of the Br-substituent. The bulky Br- substituent may have sterically hindered the binding of the molecule to the DNA grooves leading to the observed low binding constant, which may have contributed to the low binding profile of **C8**. These complexes also gave negative ΔG values. Literature reports this as an indication of spontaneity of interaction during the complex-DNA formation process (Ibrahim *et al.*, 2002).

4.19 Bioassays- Apoptotic Activity for the Complexes

Assays using 3-(4,5-Dimethylthiazol-2-yl)-2,5-diphenyltetrazolium bromide (MTT) assays were used to determine cytotoxicity of compounds in selected cells after 24h, while the IC_{50} values were

determined by Graphpad Prism software. The degree of reduction of the yellow dye by NADH or NADPH from viable cells to form a reddish-purple formazan product was then quantified by measuring the UV-vis absorbance. The extent of colour formation is proportional to the amount of living cells (Denizot, 1986) The mechanism of the colour transformation is as shown in **Scheme 25** below.



Scheme 25 The reduction of the MTT by NADH or NADPH in viable cells

The percentage cell viability was calculated using **Equation 7**:

$$\% \text{ Cell Viability} = \left(\frac{\text{Average absorbances of treated cells}}{\text{Average absorbances of control}} \right) \times 100 \% \quad \text{Equation 7}$$

Two groups of the complexes were studied; the pyrrole-based complexes (**C1**, **C3**, **C4**, **C6**) and the thiosemicarbazide-based complexes (**C7-C11**). Their anticancer activity was evaluated against various human cancer cells; Caco-2 (human colon), HeLa (Human cervical), HepG2 (human hepatocellular), MCF-7 (breast cancer), PC-3 (human prostate) and MCF-12A (non-cancer human breast) cells. For the pyrrole complexes, it was observed that **C2** crystallized out of solution and therefore it was not possible to carry out bioassays on it. Of the other three complexes, **C1** proved more toxic to normal cells than the cancerous ones.

C4 was cytotoxic but had no selectivity against the normal human breast cell lines (MCF-12A) while **C3** had little activity on the cancer cells tested. The platinum complex **C6**, however, showed very promising characteristics as a viable compound against the cancer cells tested. As shown in **Figure 50**, it showed good selectivity and cytotoxicity, selectively killing the targeted cancerous cells without affecting the normal MCF-12A.

A possible reason for this complex's good selectivity could be its binding to sulphur. Toxicity and tumour resistance of platinum-based drugs has been partly shown to be due to the affinity of platinum for bioligands containing sulphur donors (Qi *et al.*, 2019). It is supposed that platinum coordinates with sulphur-containing bioligands such as amino acids (cysteines and methionines), peptides (glutathione), proteins (metallothionein), and others, disturbing their functions. Once inside the cells and after being activated by binding to water molecules, cisplatin preferentially binds to bioligands that contain sulphur groups e.g., cysteine or methionine (Qi *et al.*, 2019). Some cancer cells contain high levels of glutathione and metallothionein which mop up the activated platinum complexes before reaching the DNA targets. This is believed to result in the observed resistance. This has caused research into these complexes to emphasize towards the study of Platinum(II) and Palladium(II) complexes containing N- and S-donor ligands.

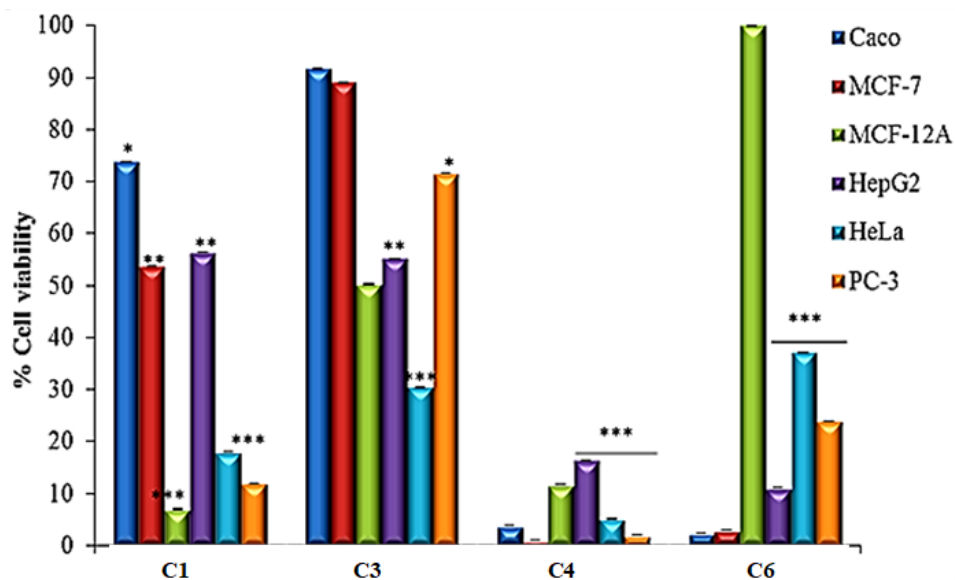


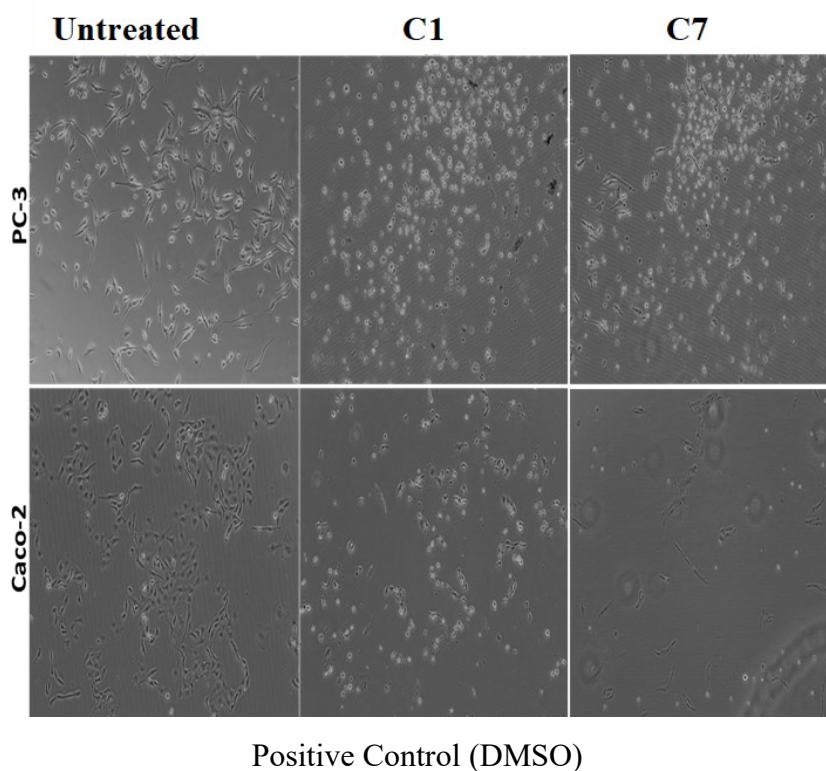
Figure 50 Screening of anti-cancer activity of Pyrrole complexes (C1, C3, C4 and C6) against selected human cell lines. The cells were exposed to 100 µg/ml of compounds for 24 h, cell viability was assessed by MTT assay. *indicates statistical significance at $p < 0.05$, ** $p < 0.01$, *** $p < 0.001$

The complexes with *cis* geometry, C4 and C6 showed enhanced cytotoxicity compared to the *trans* geometry complexes C1 and C3. The IC_{50} values for the complexes (C1, C3, C4 and C6) are as shown in Table 15 the ligands (L1-4) were not cytotoxic at the highest concentration (100 µg/ml) tested.

Table 15 IC₅₀ values for the ligands and their respective pyrrole complexes

	[Complex] (µg/mL)				
	L1-3	C1	C3	C4	C6
Caco-2	>100	>100	>100	15.81± 0.039	16.63± 0.006
MCF-7	>100	>100	>100	64.5 ± 0.0171	23.3 ± 0.0031
MCF-12A	>100	22.95 ± 0.014	53.5 ± 0.0753	24.9 ± 0.0199	>100
HeLa	>100	66.62 ± 0.051	86.4 ± 0.0286	45.5± 0.1665	84.86± 0.087
Hep-G2	>100	>100	>100	13.0 ± 0.0294	0.3 ± 0.0054
PC-3	>100	25.1 ± 0.0161	>100	20.9 ± 0.0179	29.5 ± 0.0961

As shown in **Figure 51** below, representative tests on PC-3 and Caco-2 cells showed that the complexes demonstrated some of the morphological changes associated with apoptosis such as cell shrinking, loss of cell contact (detachment), membrane blebbing, and formation of apoptotic bodies (Meyer *et al.*, 2008; Yingying Zhang, Chen, *et al.*, 2018). Similar effects were observed in other cells. The tests were done in a 24hour period using 100µg/ml concentration of the complexes.



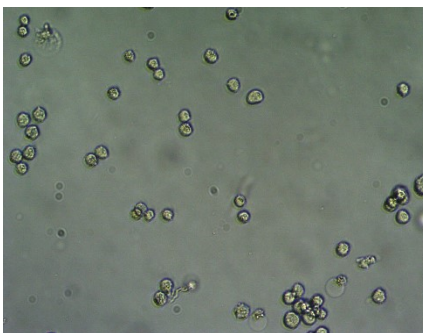


Figure 51 Effect of **C1** and **C7** on cellular morphology. PC-3 and Caco-2 cells were exposed to IC_{50} of the organometallic complexes, were observed under inverted contrast microscope at $10\times$ magnification. DMSO was used a positive control.

To further confirm if the cytotoxic effects of the complexes were exerted through apoptotic cell death, phosphatidyl serine (PS) externalization as one of molecular markers of apoptosis was investigated using Apopercantage dye. PS is localized in the inner membrane of viable intact cells. Transmembrane lipid translocation during apoptosis result in the translocation of PS to the outside of the membrane. At this stage of apoptosis, apoptotic cells can be detected with the APOPercentage dye, which become entrapped within apoptotic cells. PS is used by cells undergoing apoptosis as signal that will lead to engulfment and removal of the dying cells by macrophages and phagocytes. PS is localized in the inner membrane of normal and intact cells and inaccessible by the APOPercentage dye which is only recognized by apoptotic cells that have exposed PS in response to treatment (S.-Y. Park & Kim, 2017). Translocation of PS was investigated in selected cells (Hep-G2, PC-3 and Caco-2) treated with the complexes as a function of apoptosis after 24-hour treatment. The numbers of apoptotic cells were quantified by a flow cytometer.

As shown in **Figure 52**, representative histograms (A) depict untreated (in black) and **C3** -treated (in red) Caco-2 cells. Cell population in –Apo Dye represented cells with intact membrane while the ones in +Apo Dye were the apoptotic cells with a compromised cell membrane. The percentage of population in +Apo Dye gate suggests that the complexes induced cell death following the apoptosis pathway. The bar graph in (B) show the percentage apoptotic cells when Hep-G2, PC3 and Caco-2 cells are treated with the complexes.

Compared to the other cell lines, significantly higher levels of apoptosis were observed for the Caco-2 cell line when the cells were treated with **C3**, **C4** and **C6**. Interestingly, **C1** did not induce significant levels of apoptosis in Caco-2 cells. The Caco-2 cell line was the only cell line that showed

a significant increase in the percentage of apoptotic cells when treated with C6. Only C1 and C4 were able to induce significant levels of apoptosis in Hep-G2 cells, while C1, C3 and C4 induced significant levels of apoptosis in Hep-G2 cells and PC3 cells. Cisplatin, which was used as a positive control induced significant levels of apoptosis in PC3 cells, but not Hep-G2 cells. Cisplatin is an apoptosis inducer and was used as a positive control (Yibo Zhang *et al.*, 2014).

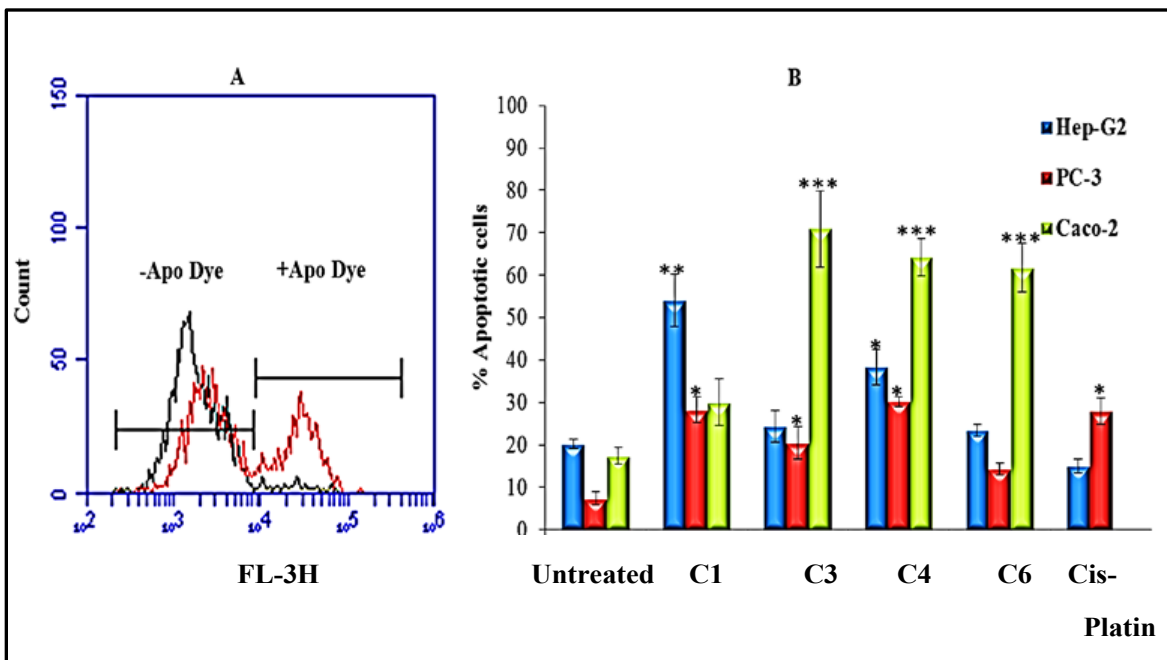


Figure 52 Apoptotic effects of the complexes on human cancer cells after exposure for 24 h. Apoptosis was assessed by Apopercantage assay. *indicates statistical significance at $p < 0.05$, ** $p < 0.01$, *** $p < 0.001$.

Cytotoxicity of the thiosemicarbazide complexes (C7-C8, C10, and C11) was performed in a similar procedure at 100ug/ml for 24h. The results are as shown in the **Figure 53**.

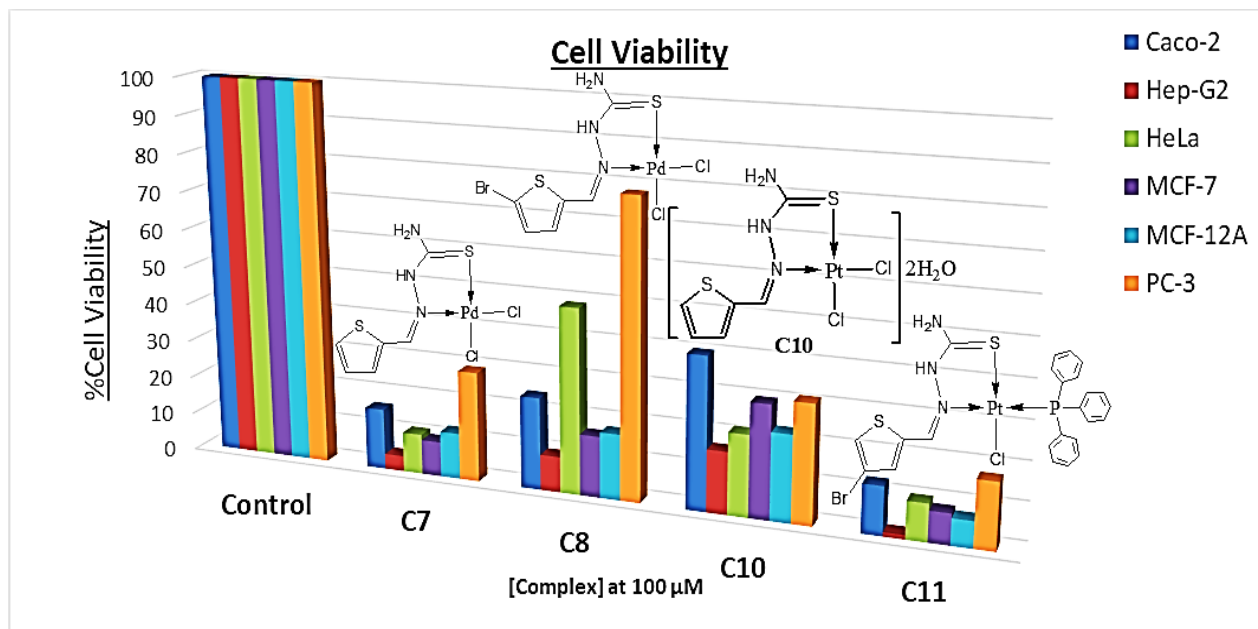


Figure 53 Percent cell viability for the Thiosemicarbazide-based complexes

Structure activity correlations were drawn on the different trends in cytotoxicity of these complexes. **C7** was similar to **C8** differing only by a -Br substituent on position 5 of the thiophene moiety of **C8**. Comparing the results for these two complexes, the introduction of the -Br (**C8**) resulted in significant difference in activity where cell viability in all cell lines increased remarkably; Caco-2 (8%), Hep-G2 (5%), HeLa (38%), MCF-7 (6%), MCF-12A (5%) and PC3 (49%).

This difference could be attributed to the electronegativity of -Br in **C8** which decreased the electron density around the metal center. This caused the -Cl ligands to be held more firmly, which in turn decreased the rate of -Cl substitution reducing the cytotoxicity of **C8**. Similar observation was made in **C9** with a more electronegative heteroatom attached to the adjacent π system in pyridine. **C7** and **C10** had similar structures differing only by the metal center, Pd(II) for **C7** and Pt(II) for **C10**. Complex **C7** was found to be more cytotoxic than **C10** in all the tested cells.

Since Palladium(II) has a lower nuclear charge compared to Platinum(II), the ligands are less strongly held in **C7**. Together with the steric crowding in Palladium(II) compared to Platinum(II) center, this probably resulted in faster rates of ligand substitution in **C7** raising the cytotoxicity. The observed higher cytotoxicity in **C11** in comparison to **C10** could be attributed to the steric crowding effects of the bulky PPh_3 group in **C11**, since the steric bulk of a PR_3 group and the resultant

crowding around the metal center is a determinant in the rate at which the group dissociates from the metal.

Tolman (1970) working on Nickel complexes made similar observations where steric hindrance played a bigger role than electronic effects in influencing the rate of attaining equilibrium in a number of phosphorus ligands on Nickel(0) (Tolman, 1970). The expected faster ligand dissociation rates might have determined the observed higher cytotoxicity for **C11** compared to **C10** with -Cl groups.

4.20 IC₅₀ values for Thiosemicarbazide Complexes

The IC₅₀ values for thiosemicarbazide complexes **C7**, **C8**, **C9** and **C11** are as shown in **Table 16**.below.

Table 16 IC₅₀ values for thiosemicarbazide complexes.

	[Complex] (µg/mL)				
	C7	C8	C9	C11	Ligands
Caco-2	14.71±0.016	43.08±0.001	17.52±0.005	31.14±0.002	>100(L1-L4)
MCF-7	1.973±0.048	59.56±0.010	12.52±0.011	70.09±0.006	>100(L1-L4)
HeLa	16.65±0.051	72.25±0.003	19.2±0.003	46.25±0.011	>100(L1-L4)
Hep-G2	14.64±0.037	94.34±0.003	29±0.003	48.03±0.006	>100(L1-L4)
PC-3	14.05±0.042	>100	6.98±0.008	12.63±0.036	>100(L1-L4)

CHAPTER 5

CONCLUSION AND RECOMMENDATIONS

5.1 Conclusion

The objectives of this research were achieved whereby, moderately bulky ligands were successfully synthesized as proved by the various characterization procedures and GC-MS, which gave clear molecular ion peaks. A total of eight ligands were synthesized which were complexed with various Pd(II) and Pt(II) precursors to produce a total of eleven complexes. Characterization provided insights on tuning their physical-chemical properties and structure-activity relationships established. Synthesis, isolation and purification were all performed under mild conditions.

The expected square planar geometry was confirmed by UV-vis and x-ray crystallography. Elemental analysis confirmed the proposed chemical formulae, in addition to the molecular structure and geometry for 4 ligands and one platinum complex which were confirmed by single crystal x-ray crystallography. The DNA binding studies showed strong intercalative mode for these complexes to the DNA base pairs. Complexes **C1**, **C3** and **C4** showed lower binding constants ranging from $1.0091 \times 10^4 - 1.6969 \times 10^4 \text{ M}^{-1}$, but still comparable to the values of the known DNA intercalators; Lumazine, Epirubicin and Proflavine which ranged from $1.74 \times 10^4 - 3.4 \times 10^4 \text{ M}^{-1}$.

The platinum complex **C6** and the palladium complex **C7** showed K_b values of $8.049 \times 10^4 \text{ M}^{-1}$ and $3.7031 \times 10^4 \text{ M}^{-1}$ respectively indicating a strong binding between these complexes and DNA. This signifies their significance as possible candidates in the line of potential intercalators and possible anticancer agents for further studies. Preliminary anticancer screening tests against selected cancer cells *in vitro* showed that the ligands were not active ($>100 \mu\text{M}$). This indicated that the activity observed in the complexes was as a result of complexing to the metal centers. For the complexes, despite literature reports that using bulky ligands in *trans* palladium complexes may confer better cytotoxic effects, this was not observed in this work.

This shows that bulky ligands which shield the metal center to a point where it is not accessible for ligand substitution, may in fact reduce the efficacy of these compounds. The challenge is to balance the extent of shielding and the extent of accessibility of the metal center to the biological target sites. This conclusion was informed considering **C3** (*trans*-geometry with bulky ligands) and **C4** (*cis* geometry with a less shielded metal center). **C3** was neither selective nor cytotoxic while **C4** was

outright cytotoxic killing both normal and cancerous cells non selectively. In general, the platinum complexes proved of better activity than the palladium complexes.

The tests showed that their anticancer activities correlated with their corresponding structures, where the different ligands around the metal center effected different rates of ligand substitution, which reflected on the observed cytotoxicity profiles. This was most notable on **C7** which differed from **C8** by the presence of -Br at position 5 of thiophene ring of **C8**. This caused a remarkable increase in cell viability, from 11% to 48% in HeLa cells, and 28% to 78% in PC-3 cells, a difference of 37% and 50% respectively.

The platinum complex, **C6**, was selective against normal cell lines but reduced the viability of the 5 cancerous cell lines, which included one breast cancer cell line, by more than 60%. This suggests that it can be a viable anticancer candidate for further *in vivo* tests. The structural advantages associated with this platinum complex's observed selectivity could be its binding to sulphur. This is because it is postulated that toxicity and tumour resistance of platinum-based complexes are due to the favoured affinity of platinum for bioligands containing sulphur donors such as cysteines, methionines glutathione and metallothionein, from the soft-soft bonding and the presence of empty d-orbitals in sulphur which favours synergistic back bonding. Complexes already having a sulphur-donor ligated to its structure means that the compound has a lower chance of being mopped up by sulphur-containing bioligands.

5.2 Recommendations

1. The positive and promising results obtained from this work calls for further funding to not only sustain the research and optimize the synthesis of these complexes, but also to focus on the properties that made one of the complexes so selective against the breast cancer cell line. This was significant because breast cancer accounts for 25% of all cancers in women globally and 21% in Kenya. It is recommended that the activity of these complexes be studied *in vivo* to further understand their activity in actual physiological environment. This way, conclusive data will be obtained on their mode of action and open ways for further biological tests.
2. The thiosemicarbazone complexes have ligand backbones known to have antibacterial and antifungal properties. It is recommended that other tests like antibacterial, antiviral and antifungal properties for these compounds also be attempted to explore bioactivity of these complexes.

3. On the chemistry part, the bulky ligands used in the experiments did not correlate with better activity for the complexes. It is recommended that more studies be carried out on the relationships on size of ligands to the observed cytotoxicity especially on the palladium complexes. This way, optimum ligand bulk can be designed for optimum activity profiles

REFERENCES

- Abdel-Rahman, L. H., Abu-Dief, A. M., Shehata, M. R., Atlam, F. M., & Abdel-Mawgoud, A. A. H. (2019). Some new Ag (I), VO (II) and Pd(II) chelates incorporating tridentate imine ligand: Design, synthesis, structure elucidation, density functional theory calculations for DNA interaction, antimicrobial and anticancer activities and molecular docking studies. *Applied Organometallic Chemistry*, 33(4), e4699.
- Abou-Alfa, G. K., Jarnagin, W., El Dika, I., D'Angelica, M., Lowery, M., Brown, K., . . . Crane, C. H. (2020). Liver and bile duct cancer *Abeloff's clinical oncology* (pp. 1314-1341. e1311): Elsevier.
- Abu-Dief, A. M., & Mohamed, I. M. (2015). A review on versatile applications of transition metal complexes incorporating Schiff bases. *Beni-suef university journal of basic and applied sciences*, 4(2), 119-133.
- Abu-Dief, A. M., & Nassr, L. A. (2015). Tailoring, physicochemical characterization, antibacterial and DNA binding mode studies of Cu (II) Schiff bases amino acid bioactive agents incorporating 5-bromo-2-hydroxybenzaldehyde. *Journal of the Iranian Chemical Society*, 12(6), 943-955.
- Abu-Surrah, A. S., & Abdalla, M. Y. (2008). Al-Sa'doni, H. H., & Palladium-based chemotherapeutic agents: routes toward complexes with good antitumor activity. *Cancer therapy*, 6 SRC - BaiduScholar, 1-10.
- Aguilera, C., & Carolina, A. (2017). Computational study of nuclear magnetic shielding constants. (Doctoral dissertation, Universitat de Girona)
- Ahmad, N., Anouar, E. H., Tajuddin, A. M., Ramasamy, K., Yamin, B. M., & Bahron, H. (2020). Synthesis, characterization, quantum chemical calculations and anticancer activity of a Schiff base NNOO chelate ligand and Pd(II) complex. *PloS one*, 15(4), e0231147.
- Ahmad, S. (2017). Kinetic aspects of platinum anticancer agents. *Polyhedron*, 138, 109-124.
- Al-Fregi, A. A. (2015). Synthesis, Characterization and Molar Conductivity Study of Some New Palladium(II) and Platinum(II) Complexes Containing Heterocyclic Tellurium-Dicarboxylato Ligands. *International Journal*, 3(3)(637-647).
- Al-Fregi, A. A., Al-Fadhly, A. L., & Al-Salami, B. K. (2017). Synthesis, characterization and biological activity study of some new Palladium(II) complexes containing amine or azomethine groups. *European Journal of Chemistry*, 8(2), 155-161.
- Al-Hassani, R., & Abbas, H. (2018). Synthesis, Characterization and Biological Activities of New Azo Dyes–Azomethine Compound and Their Metal Complexes. *J. Glob. Pharma Technol*, 289-301.
- Albuquerque, K., Tumati, V., Lea, J., Ahn, C., Richardson, D., Miller, D., & Timmerman, R. (2020). A phase II Trial of stereotactic ablative radiation therapy as a boost for locally advanced cervical cancer. *International Journal of Radiation Oncology* Biology* Physics*, 106(3), 464-471.
- Alderden, R. A., Hall, M. D., & Hambley, T. W. (2006). The discovery and development of cisplatin. *Journal of chemical education*, 83(5), 728.

- Alessio, E. (2004). Synthesis and reactivity of Ru-, Os-, Rh-, and Ir-halide– sulfoxide complexes. *Chemical reviews*, 104(9), 4203-4242.
- Almerico, A. M., Lauria, A., Diana, P., Barraja, P., Cirrincione, G., & Dattolo, G. (2000). Glycosidopyrroles. part 4. 1- β -D-ribofuranosyl-pyrroles and indoles as potential antiviral agents. *Arkivoc*, 4, 486-496.
- Almotairy, A. R. Z., Gandin, V., Morrison, L., Marzano, C., Montagner, D., & Erxleben, A. (2017). Antitumor platinum (IV) derivatives of carboplatin and the histone deacetylase inhibitor 4-phenylbutyric acid. *Journal of inorganic biochemistry*, 177, 1-7.
- Alpuche-Aviles, M., Farina, F., Ercolano, G., Subedi, P., Cavaliere, S., Jones, D., & Rozière, J. (2018). Electrodeposition of two-dimensional Pt nanostructures on highly oriented pyrolytic graphite (HOPG): the effect of evolved hydrogen and chloride ions. *Nanomaterials*, 8(9), 668.
- Altemimi, A., Lakhssassi, N., Baharlouei, A., Watson, D. G., & Lightfoot, D. A. (2017). Phytochemicals: Extraction, isolation, and identification of bioactive compounds from plant extracts. *Plants*, 6(4), 42.
- Amarante, D., Cherian, C., Catapano, A., Adams, R., Wang, M. H., & Megehee, E. G. (2005). Synthesis and electronic characterization of bipyridine dithiolate rhodium (III) complexes. *Inorganic Chemistry*, 44(24), 8804-8809.
- Amatore, C., Labbé, E., & Buriez, O. (2017). Molecular electrochemistry: A central method to understand the metabolic activation of therapeutic agents. The example of metalocifen anti-cancer drug candidates. *Current Opinion in Electrochemistry*, 2(1), 7-12.
- Amini, S. M., Kharrazi, S., Rezayat, S. M., & Gilani, K. (2018). Radiofrequency electric field hyperthermia with gold nanostructures: role of particle shape and surface chemistry. *Artificial cells, nanomedicine, and biotechnology*, 46(7), 1452-1462.
- Andersson, A., Fagerberg, J., Lewensohn, R., & Ehrsson, H. (1996). Pharmacokinetics of cisplatin and its monohydrated complex in humans. *Journal of pharmaceutical sciences*, 85(8), 824-827.
- Anghileri, L. J., & Robert, J. (2019). *Hyperthermia in cancer treatment* (Vol. 2): CRC Press.
- Arshad, N., Bhatti, M. H., Farooqi, S. I., Saleem, S., & Mirza, B. (2016). Synthesis, photochemical and electrochemical studies on triphenyltin (IV) derivative of (Z)-4-(4-cyanophenylamino)-4-oxobut-2-enoic acid for its binding with DNA: Biological interpretation. *Arabian Journal of Chemistry*, 9(3), 451-462.
- Artico, M., Di Santo, R., Costi, R., Massa, S., Retico, A., Artico, M., . . . Strippoli, V. (1995). Antifungal agents. 9. 3-Aryl-4-[. alpha.-(1H-imidazol-1-yl) arylmethyl] pyrroles: A new class of potent anti-candida agents. *Journal of medicinal chemistry*, 38(21), 4223-4233.
- Ashfaq, M., Najam, T., Shah, S., Ahmad, M., Shaheen, S., Tabassum, R., & Rivera, G. (2014). DNA binding mode of transition metal complexes, a relationship to tumor cell toxicity. *Current medicinal chemistry*, 21(26), 3081-3094.
- Aslanoglu, M. (2006). Electrochemical and spectroscopic studies of the interaction of proflavine with DNA. *Analytical sciences*, 22(3), 439-443.

- Atasever, B., Ülküseven, B., Bal-Demirci, T., Erdem-Kuruca, S., & Solakoğlu, Z. (2010). Cytotoxic activities of new iron (III) and nickel (II) chelates of some S-methyl-thiosemicarbazones on K562 and ECV304 cells. *Investigational new drugs*, 28(4), 421-432.
- Atteke, C., Ndong, J. M. M., Aubouy, A., Maciejewski, L., Brocard, J., Lébibi, J., & Deloron, P. . (2003). In vitro susceptibility to a new antimalarial organometallic analogue, ferroquine, of Plasmodium falciparum isolates from the Haut-Ogooue region of Gabon. . *Journal of Antimicrobial Chemotherapy*, 51(4), 1021-1024.
- Atwood, J. D., Wovkulich, M. J., & Sonnenberger, D. C. (1983). Ligand effects on organometallic substitution reactions. *Accounts of Chemical Research*, 16(9), 350-355.
- Au, K., Ngan, R. K., Ng, A. W., Poon, D. M., Ng, W., Yuen, K., . . . Sze, H. C. (2018). Treatment outcomes of nasopharyngeal carcinoma in modern era after intensity modulated radiotherapy (IMRT) in Hong Kong: A report of 3328 patients (HKNPCSG 1301 study). *Oral oncology*, 77, 16-21.
- Aullón, G., Lledós, A., & Alvarez, S. (2002). Hexakis (silyl) palladium (VI) or Palladium(II) with η^2 -Disilane Ligands? *Angewandte Chemie International Edition*, 41(11), 1956-1959.
- Baenas, N., Belović, M., Ilic, N., Moreno, D., & García-Viguera, C. (2019). Industrial use of pepper (*Capsicum annum* L.) derived products: Technological benefits and biological advantages. *Food chemistry*, 274, 872-885.
- Bai, L., Gao, C., Liu, Q., Yu, C., Zhang, Z., Cai, L., . . . Liao, X. (2017). Research progress in modern structure of platinum complexes. *European journal of medicinal chemistry*, 140, 349-382.
- Ballestreri, É., Simon, D., de Souza, A. P., Grott, C. S., Nabinger, D. D., Dihl, R. R., & Grivicich, I. (2018). Resistance mechanism to cisplatin in NCI-H460 non-small cell lung cancer cell line: investigating apoptosis, autophagy, and cytogenetic damage. *Cancer Drug Resist*, 1, 72-81.
- Bandari, S. K., Purushothaman, A., Ramani, V. C., Brinkley, G. J., Chandrashekar, D. S., Varambally, S., . . . Vlodaysky, I. (2018). Chemotherapy induces secretion of exosomes loaded with heparanase that degrades extracellular matrix and impacts tumor and host cell behavior. *Matrix Biology*, 65, 104-118.
- Baumann, K. W. (2019). *Impact of Thermal Ablation Modalities and Investigation into Molecular Stress Pathways for the Treatment of Pancreatic Cancer*. State University of New York at Binghamton.
- Bavin, E., Rees, R., Robson, J., Seiler, M., Seymour, D., & Suddaby, D. (1951). The tuberculostatic activity of some thiosemicarbazones. *Journal of Pharmacy and Pharmacology*, 3(1), 46-46.
- Bhal, S. K. (2011). LogP—Making Sense of the Value: Advanced Chemistry Development Inc.(ACD/Labs). From <http://www.acdlabs.com> . . .
- Bhatti, J. S., Bhatti, G. K., & Reddy, P. H. (2017). Mitochondrial dysfunction and oxidative stress in metabolic disorders—A step towards mitochondria based therapeutic strategies. *Biochimica et Biophysica Acta (BBA)-Molecular Basis of Disease*, 1863(5), 1066-1077.
- Bhunchu, S., & Rojsitthisak, P. (2014). Biopolymeric alginate-chitosan nanoparticles as drug delivery carriers for cancer therapy. *Die Pharmazie-An International Journal of Pharmaceutical Sciences*, 69(8), 563-570.

- Binnewies, M., Roberts, E. W., Kersten, K., Chan, V., Fearon, D. F., Merad, M., . . . Hedrick, C. C. (2018). Understanding the tumor immune microenvironment (TIME) for effective therapy. *Nature medicine*, 24(5), 541-550.
- Biswas, N., Khanra, S., Sarkar, A., Bhattacharjee, S., Mandal, D. P., Chaudhuri, A., . . . Choudhury, C. R. (2017). One new azido bridged dinuclear copper (II) thiosemicarbazide complex: synthesis, DNA/protein binding, molecular docking study and cytotoxicity activity. *New Journal of Chemistry*, 41(21), 12996-13011.
- Biyala, M. K., Sharma, K., Swami, M., Fahmi, N., & Singh, R. V. (2008). Spectral and biocidal studies of Palladium(II) and Platinum(II) complexes with monobasic bidentate Schiff bases. *Transition Metal Chemistry*, 33(3), 377-381.
- Bjelogrlić, S., Todorović, T., Bacchi, A., Zec, M., Sladić, D., Srdić-Rajić, T., . . . Anđelković, K. (2010). Synthesis, structure and characterization of novel Cd (II) and Zn (II) complexes with the condensation product of 2-formylpyridine and selenosemicarbazide: antiproliferative activity of the synthesized complexes and related selenosemicarbazone complexes. *J Inorg Biochem*, 104(6), 673-682.
- Bolm, L., Kaesmann, L., Paysen, A., Karapetis, C., Rades, D., Wellner, U. F., . . . Hussey, D. J. (2018). Multimodal anti-tumor approaches combined with immunotherapy to overcome tumor resistance in esophageal and gastric cancer. *Anticancer research*, 38(6), 3231-3242.
- Bourhis, L. J., Dolomanov, O. V., Gildea, R. J., Howard, J. A., & Puschmann, H. (2015). The anatomy of a comprehensive constrained, restrained refinement program for the modern computing environment—Olex2 dissected. *Acta Crystallographica Section A: Foundations and Advances*, 71(1), 59-75.
- Boyer, A.-S., Walter, D., & Sørensen, C. S. (2016). *DNA replication and cancer: From dysfunctional replication origin activities to therapeutic opportunities*. Paper presented at the Seminars in cancer biology.. "In *Seminars in cancer biology*, vol. 37, pp. 16-25. Academic Press, 2016
- Brabec, V., & Nováková, O. (2006). DNA binding mode of ruthenium complexes and relationship to tumor cell toxicity. *Drug Resistance Updates*, 9(3), 111-122.
- Brockman, R., Sidwell, R. W., Arnett, G., & Shaddix, S. (1970). Heterocyclic thiosemicarbazones: correlation between structure, inhibition of ribonucleotide reductase, and inhibition of DNA viruses. *Proceedings of the Society for Experimental Biology and Medicine*, 133(2), 609-614.
- Brockman, R. W., Thomson, J. R., Bell, M. J., & Skipper, H. E. (1956). Observations on the antileukemic activity of pyridine-2-carboxaldehyde thiosemicarbazone and thiocarbohydrazone. *Cancer research*, 16(2), 167-170.
- Burmakina, G. V., Verpekin, V. V., Maksimov, N. G., Zimonin, D. V., Piryazev, D. A., Chudin, O. S., & Rubaylo, A. I. (2017). Electrochemically induced transformations of bi- and trinuclear heterometallic vinylidene complexes containing Re, Pd and Fe. *Inorganica chimica acta*, 463, 70-79.
- Camacho, J. C., & Covey, A. M. (2020). Principles of Percutaneous Ablation in the Liver *Cancer Regional Therapy* (pp. 43-53): Springer.

- Camasso, N. M., Canty, A. J., Ariafard, A., & Sanford, M. S. (2017). Experimental and computational studies of high-valent nickel and palladium complexes. *Organometallics*, 36(22), 4382-4393.
- Camidge, D. R., Doebele, R. C., & Kerr, K. M. (2019). Comparing and contrasting predictive biomarkers for immunotherapy and targeted therapy of NSCLC. *Nature Reviews Clinical Oncology*, 16(6), 341-355.
- Canovese, L., Visentin, F., Scattolin, T., Santo, C., & Bertolasi, V. (2016). Addition of halogens and interhalogens on palladacyclopentadienyl complexes stabilized by pyridyl– thioether N– S spectator ligands. *Journal of organometallic chemistry*, 808, 48-56.
- Canty, A. J., Ariafard, A., Yates, B. F., & Sanford, M. S. (2015). Computational study of intramolecular arene palladation at a palladium (IV) center. *Organometallics*, 34(6), 1085-1090.
- Casey, C. P., & Whiteker, G. T. (1990). The natural bite angle of chelating diphosphines. *Israel journal of chemistry*, 30(4), 299-304.
- Cassells, I., Stringer, T., Hutton, A. T., Prince, S., & Smith, G. S. (2018). Impact of various lipophilic substituents on ruthenium (II), rhodium (III) and iridium (III) salicylaldimine-based complexes: synthesis, in vitro cytotoxicity studies and DNA interactions. *JBIC Journal of Biological Inorganic Chemistry*, 23(5), 763-774.
- Castarlenas, R., Esteruelas, M. A., & Oñate, E. (2005). N-Heterocyclic Carbene– Osmium Complexes for Olefin Metathesis Reactions. *Organometallics*, 24(18), 4343-4346.
- Cecchini, M., Rubin, E. H., Blumenthal, G. M., Ayalew, K., Burris, H. A., Russell-Einhorn, M., . . . Boerner, S. (2019). Challenges with novel clinical trial designs: master protocols. *Clinical Cancer Research*, 25(7), 2049-2057.
- Cerrato, C. P., Künnapuu, K., & Langel, Ü. (2017). Cell-penetrating peptides with intracellular organelle targeting. *Expert opinion on drug delivery*, 14(2), 245-255.
- Chen, C., Ou, H., Liu, R., & Ding, D. (2020). Regulating the photophysical property of organic/polymer optical agents for promoted cancer phototheranostics. *Advanced Materials*, 32(3), 1806331.
- Chen, D. S., & Mellman, I. (2017). Elements of cancer immunity and the cancer–immune set point. *Nature*, 541(7637), 321-330.
- Chen, J., Ning, C., Zhou, Z., Yu, P., Zhu, Y., Tan, G., & Mao, C. (2019). Nanomaterials as photothermal therapeutic agents. *Progress in materials science*, 99, 1-26.
- Chen, K. G., Valencia, J. C., Gillet, J.-P., Hearing, V. J., & Gottesman, M. M. (2009). Involvement of ABC transporters in melanogenesis and the development of multidrug resistance of melanoma. *Pigment cell & melanoma research*, 22(6), 740-749.
- Chen, Y.-L., Hung, H.-M., Lu, C.-M., Li, K.-C., & Tzeng, C.-C. (2004). Synthesis and anticancer evaluation of certain indolo [2, 3-b] quinoline derivatives. *Bioorganic & medicinal chemistry*, 12(24), 6539-6546.
- Chen, Z., Wu, J., Chen, Y., Li, L., Xia, Y., Li, Y., . . . Gao, D. (2012). Rapid Access to Substituted Piperazines via Ti (NMe₂)₄-Mediated C–C Bond-Making Reactions. *Organometallics*, 31(17), 6005-6013.

- Chicón-Bosch, M., & Tirado, O. M. (2020). Exosomes in Bone Sarcomas: Key Players in Metastasis. *Cells*, 9(1), 241.
- Chu, C. K., Lin, T.-P., Shao, H., Liberman-Martin, A. L., Liu, P., & Grubbs, R. H. (2018). Disentangling Ligand Effects on Metathesis Catalyst Activity: Experimental and Computational Studies of Ruthenium–Aminophosphine Complexes. *Journal of the American Chemical Society*, 140(16), 5634-5643.
- Conrad, M. L., Enman, J. E., Scales, S. J., Zhang, H., Vogels, C. M., Saleh, M. T., . . . Westcott, S. A. (2005). Synthesis, characterization, and cytotoxicities of Platinum(II) complexes bearing pyridinecarboxaldehydes containing bulky aromatic groups. *Inorganica Chimica Acta*, 358(1), 63-69.
- Conte, M., De Palma, R., & Altucci, L. (2018). HDAC inhibitors as epigenetic regulators for cancer immunotherapy. *The international journal of biochemistry & cell biology*, 98, 65-74.
- Cornacchia, D., Pellicani, R. Z., Intini, F. P., Pacifico, C., & Natile, G. (2009). Solution behavior of amidine complexes: an unexpected cis/trans isomerization and formation of di- and trinuclear platinum (III) and Platinum(II) species. *Inorganic Chemistry*, 48(22), 10800-10810.
- Corrales, L., Matson, V., Flood, B., Spranger, S., & Gajewski, T. F. (2017). Innate immune signaling and regulation in cancer immunotherapy. *Cell research*, 27(1), 96-108.
- Crabtree, R. H. (2009). *The organometallic chemistry of the transition metals*: John Wiley & Sons.
- da Silva Frozza, C. O., Santos, D. A., Rufatto, L. C., Minetto, L., Scariot, F. J., Echeverrigaray, S., ... & Savegnago, L. (2017). Antitumor activity of Brazilian red propolis fractions against Hep-2 cancer cell line. *Biomedicine & Pharmacotherapy*, 91(951-963).
- Damo, M., Fitzgerald, B., Lu, Y., Nader, M., William, I., Cheung, J., . . . Lee, D.-Y. (2020). NINJA: an inducible genetic model for creating neoantigens in vivo. *bioRxiv*.
- Damsma, G. E., Alt, A., Brueckner, F., Carell, T., & Cramer, P. (2007). Mechanism of transcriptional stalling at cisplatin-damaged DNA. *Nature structural & molecular biology*, 14(12), 1127-1133.
- Das, M., Chatterjee, S., & Chattopadhyay, S. (2011). Unique example of a trigonal dodecahedral Na⁺ in a compartmental Schiff base N, N'-(1, 2-Phenylene)-bis (3-methoxysalicylideneimine). *Inorganic Chemistry Communications*, 14(9), 1337-1340.
- de Leon, C. Y., & Ganem, B. (1997). A new approach to porphobilinogen and its analogs. *Tetrahedron*, 53(23), 7731-7752.
- Deeth, R. J., & Hitchman, M. A. (1986). Factors influencing Jahn-Teller distortions in six-coordinate copper (II) and low-spin nickel (II) complexes. *Inorganic Chemistry*, 25(8), 1225-1233.
- Denizot, F., & Lang, R. (1986). Rapid colorimetric assay for cell growth and survival: modifications to the tetrazolium dye procedure giving improved sensitivity and reliability. *Journal of immunological methods*, 89(2), 271-277.
- Denny, J. A., & Darensbourg, M. Y. (2016). Approaches to quantifying the electronic and steric properties of metallodithiolates as ligands in coordination chemistry. *Coordination Chemistry Reviews*, 324, 82-89.
- Desoize, B., & Madoulet, C. (2002). Particular aspects of platinum compounds used at present in cancer treatment. *Critical reviews in oncology/hematology*, 42(3), 317-325.

- Diacon, A. H., Pym, A., Grobusch, M., Patientia, R., Rustomjee, R., Page-Shipp, L., . . . Churchyard, G. (2009). The diarylquinoline TMC207 for multidrug-resistant tuberculosis. *New England Journal of Medicine*, 360(23), 2397-2405.
- Dimmer, J. A., Schubert, H., & Wesemann, L. (2009). Germa-closo-dodecaborate: A New Ligand in Transition-Metal Chemistry with a Strong trans Influence. *Chemistry—A European Journal*, 15(40), 10613-10619.
- Do, H. T. T., Lee, C. H., & Cho, J. (2020). Chemokines and their Receptors: Multifaceted Roles in Cancer Progression and Potential Value as Cancer Prognostic Markers. *Cancers*, 12(2), 287.
- Dolomanov, O. V., Bourhis, L. J., Gildea, R. J., Howard, J. A., & Puschmann, H. (2009). OLEX2: a complete structure solution, refinement and analysis program. *Journal of Applied Crystallography*, 42(2), 339-341.
- Dougan, S. J., Melchart, M., Habtemariam, A., Parsons, S., & Sadler, P. J. . (2006). Phenylazo-pyridine and phenylazo-pyrazole chlorido ruthenium (II) arene complexes: arene loss, aquation, and cancer cell cytotoxicity. *Inorganic chemistry*, 45(26), 10882-10894.
- Drain, L. (2019). *Laser ultrasonics techniques and applications*: Routledge.
- Durango-García, C. J., Jalife, S., Cabellos, J. L., Martínez, S. H., Jimenez-Halla, J. O. C., Pan, S., . . . Montiel-Palma, V. (2016). Back to basics: identification of reaction intermediates in the mechanism of a classic ligand substitution reaction on Vaska's complex. *RSC Advances*, 6(4), 3386-3392.
- Durgeau, A., Virk, Y., Corgnac, S., & Mami-Chouaib, F. (2018). Recent advances in targeting CD8 T-cell immunity for more effective cancer immunotherapy. *Frontiers in immunology*, 9, 14.
- Eaton, D. (1968). Selection rules for the isomerization and substitution reactions of transition metal complexes. *Journal of the American Chemical Society*, 90(16), 4272-4275.
- Edwards, E. I., Epton, R., & Marr, G. (1976). 1, 1'-Ferrocenyldiacetic Acid Anhydride and its Use in the preparation of heteroannularly substituted ferrocenyl-penicillins and-cephalosporins. *Journal of Organometallic Chemistry*, 122(3 SRC - BaiduScholar), C49-C53.
- Edwards, T. G., Koeller, K. J., Slomczynska, U., Fok, K., Helmus, M., Bashkin, J. K., & Fisher, C. (2011). HPV episome levels are potently decreased by pyrrole-imidazole polyamides. *Antiviral research*, 91(2), 177-186.
- Elford, H. L., Freese, M., Passamani, E., & Morris, H. P. (1970). Ribonucleotide reductase and cell proliferation I. Variations of ribonucleotide reductase activity with tumor growth rate in a series of rat hepatomas. *Journal of Biological Chemistry*, 245(20), 5228-5233.
- Evans, M. A., Smith, D. C., Holub, J. M., Argenti, A., Hoff, M., Dalglish, G. A., . . . Burnham, B. S. (2003). Synthesis and Cytotoxicity of Substituted Ethyl 2-Phenacyl-3-phenylpyrrole-4-carboxylates. *Archiv der Pharmazie*, 336(3), 181-190.
- Fang, T., Lv, H., Lv, G., Li, T., Wang, C., Han, Q., . . . Huang, S. (2018). Tumor-derived exosomal miR-1247-3p induces cancer-associated fibroblast activation to foster lung metastasis of liver cancer. *Nature communications*, 9(1), 1-13.
- Feng, W. W., Bang, S., & Kurokawa, M. (2020). CD36: a key mediator of resistance to HER2 inhibitors in breast cancer. *Molecular & Cellular Oncology*, 1715766.

- Ferlay, J., Colombet, M., Soerjomataram, I., Mathers, C., Parkin, D., Piñeros, M., . . . Bray, F. (2019). Estimating the global cancer incidence and mortality in 2018: GLOBOCAN sources and methods. *International journal of cancer*, *144*(8), 1941-1953.
- Fernandez, V. (2017). Some facts on the platinum-group elements. *International Review of Financial Analysis*, *52*, 333-347.
- Fichtner, I., Rolff, J., Soong, R., Hoffmann, J., Hammer, S., Sommer, A., . . . Merk, J. (2008). Establishment of patient-derived non-small cell lung cancer xenografts as models for the identification of predictive biomarkers. *Clinical cancer research : an official journal of the American Association for Cancer Research*, *14*(20), 6456-6468.
- Finch, R. A., Liu, M.-C., Cory, A. H., Cory, J. G., & Sartorelli, A. C. (1999). Triapine (3-aminopyridine-2-carboxaldehyde thiosemicarbazone; 3-AP): an inhibitor of ribonucleotide reductase with antineoplastic activity. *Advances in enzyme regulation*, *39*, 3-12.
- Fish, R. H., & Jaouen, G. (2003). Bioorganometallic chemistry: structural diversity of organometallic complexes with bioligands and molecular recognition studies of several supramolecular hosts with biomolecules, alkali-metal ions, and organometallic pharmaceuticals. *Organometallics*, *22*(11 SRC - BaiduScholar), 2166-2177.
- Fleming, V., Hu, X., Weber, R., Nagibin, V., Groth, C., Altevogt, P., . . . Umansky, V. (2018). Targeting myeloid-derived suppressor cells to bypass tumor-induced immunosuppression. *Frontiers in immunology*, *9*, 398-409.
- Ford, J. M., & Kastan, M. B. (2020). DNA damage response pathways and cancer *Abeloff's Clinical Oncology* (pp. 154-164. e154): Elsevier.
- Frezza, M., Hindo, S., Chen, D., Davenport, A., Schmitt, S., Tomco, D., & Dou, Q. P. (2010). Novel metals and metal complexes as platforms for cancer therapy. *Current pharmaceutical design*, *16*(16), 1813-1825.
- Fuchigami, K., Rath, N. P., & Mirica, L. M. (2017). Mononuclear Rhodium (II) and Iridium (II) Complexes Supported by Tetradentate Pyridinophane Ligands. *Inorganic Chemistry*, *56*(16), 9404-9408.
- Fuertes, M., Castilla, J., Alonso, C., & Prez, J. (2003). Cisplatin biochemical mechanism of action: from cytotoxicity to induction of cell death through interconnections between apoptotic and necrotic pathways. *Current medicinal chemistry*, *10*(3), 257-266.
- GA, K. (1964). TO-DAY'S DRUGS: METHISAZONE. *British Medical Journal*, *2*(5409), 621-621.
- Galon, J., & Bruni, D. (2019). Approaches to treat immune hot, altered and cold tumours with combination immunotherapies. *Nature reviews Drug discovery*, *18*(3), 197-218.
- Gao, E., Ding, Y., Sun, N., Zhang, S., Qiu, X., Zhan, Y., & Zhu, M. (2017). Synthesis, characterization, DNA interaction, apoptosis and molecular docking of Cu (II) and Mn (II) complexes with endo-norbornene-cis-5, 6-dicarboxylic acid. *Applied Organometallic Chemistry*, *31*(3), e3575.
- García-Valle, F. M., Tabernero, V., Cuenca, T., Cano, J., & Mosquera, M. E. (2018). Schiff-base-ate derivatives with main group metals: generation of a tripodal aluminate metalloligand. *Dalton Transactions*, *47*(18), 6499-6506.

- Ghorab, M. M., Alsaid, M. S., Ceruso, M., Nissan, Y. M., & Supuran, C. T. (2014). Carbonic anhydrase inhibitors: synthesis, molecular docking, cytotoxic and inhibition of the human carbonic anhydrase isoforms I, II, IX, XII with novel benzenesulfonamides incorporating pyrrole, pyrrolopyrimidine and fused pyrrolopyrimidine moieties. *Bioorganic & medicinal chemistry*, 22(14), 3684-3695.
- Ghotbinejad, M., Khosropour, A. R., Mohammadpoor-Baltork, I., Moghadam, M., Tangestaninejad, S., & Mirkhani, V. (2014). SPIONs-bis (NHC)-Palladium(II): A novel, powerful and efficient catalyst for Mizoroki–Heck and Suzuki–Miyaura C–C coupling reactions. *Journal of Molecular Catalysis A: Chemical*, 385, 78-84.
- Gichumbi, J. M., & Friedrich, H. B. (2018). Half-sandwich complexes of platinum group metals (Ir, Rh, Ru and Os) and some recent biological and catalytic applications. *Journal of organometallic chemistry*, 866, 123-143.
- Golchin, A., & Farahany, T. Z. (2019). Biological Products: Cellular Therapy and FDA Approved Products. *Stem Cell Rev Rep*, 15(2), 166-175. doi: 10.1007/s12015-018-9866-1
- Goodsell, D. S. (2006). The molecular perspective: cisplatin. *The oncologist*, 11(3), 316-317.
- Goyal, M. R., Suleria, H. A. R., & Harikrishnan, R. (2020). *The Role of Phytoconstituents in Health Care: Biocompounds in Medicinal Plants*: CRC Press.
- Greenwood, Norman Neill, and Alan Earnshaw. *Chemistry of the Elements*. Elsevier, 2012.
- Gregson, M., Lu, E., Mills, D. P., Tuna, F., McInnes, E. J., Hennig, C., . . . Blake, A. J. (2017). The inverse-trans-influence in tetravalent lanthanide and actinide bis (carbene) complexes. *Nature communications*, 8, 14137.
- Greif, A. H., Hrobárik, P., Hrobáriková, V., Arbuznikov, A. V., Autschbach, J., & Kaupp, M. (2015). A relativistic quantum-chemical analysis of the trans influence on ¹H NMR hydride shifts in square-planar Platinum(II) complexes. *Inorganic Chemistry*, 54(15), 7199-7208.
- Groza, M., Zimta, A. A., Irimie, A., Achimas-Cadariu, P., Cenariu, D., Stanta, G., & Berindan-Neagoe, I. (2020). Recent advancements in the study of breast cancer exosomes as mediators of intratumoral communication. *Journal of cellular physiology*, 235(2), 691-705.
- Gudasi, K. B., Patil, M. S., Vadavi, R. S., Shenoy, R. V., Patil, S. A., & Nethaji, M. (2006). X-ray crystal structure of the N-(2-hydroxy-1-naphthalidene) phenylglycine Schiff base. Synthesis and characterization of its transition metal complexes. *Transition Metal Chemistry*, 31(5), 580-585.
- Gulzar, A., Xu, J., Wang, C., He, F., Yang, D., Gai, S., . . . Xing, B. (2019). Tumour microenvironment responsive nanoconstructs for cancer theranostic. *Nano Today*. Nano Today 26 (2019): 16-56
- Guo, M., Sun, H., McArdle, H. J., Gambling, L., & Sadler, P. J. . . (2000). TiIV uptake and release by human serum transferrin and recognition of TiIV-transferrin by cancer cells: understanding the mechanism of action of the anticancer drug titanocene dichloride. . *Biochemistry*, 39 (33), 10023-10033.
- Gurunathan, S., Kang, M.-H., Qasim, M., & Kim, J.-H. (2018). Nanoparticle-mediated combination therapy: Two-in-one approach for cancer. *International journal of molecular sciences*, 19(10), 3264.

- Guttman, M. A., Tao, S., Fink, S., Kolandaivelu, A., Halperin, H. R., & Herzka, D. A. (2018). Non-contrast-enhanced T1-weighted MRI of myocardial radiofrequency ablation lesions. *Magnetic resonance in medicine*, 79(2), 879-889.
- Habtemariam, A., Melchart, M., Fernandez, R., Parsons, S., Oswald, I. D. H., Parkin, A., . . . Sadler, P. J. (2006). Structure-activity relationships for cytotoxic ruthenium(II) arene complexes containing N,N-, N,O-, and O,O-chelating ligands. *Journal of medicinal chemistry*, 49(23), 6858-6868.
- Hall, I., Lackey, C., Kistler, T., Durham, J. R., Jouad, E. M., Khan, M., . . . Bouet, G. (2000). Cytotoxicity of copper and cobalt complexes of furfural semicarbazone and thiosemicarbazone derivatives in murine and human tumor cell lines. *Die Pharmazie*, 55(12), 937-941.
- Hall, M. D., Mellor, H. R., Callaghan, R., & Hambley, T. W. (2007). Basis for design and development of platinum (IV) anticancer complexes. *Journal of medicinal chemistry*, 50(15), 3403-3411.
- Hamasaki, T., Kakiuchi, F., & Kochi, T. (2016). Chain-walking Cycloisomerization of 1, n-Dienes Catalyzed by Pyridine–Oxazoline Palladium Catalysts and Its Application to Asymmetric Synthesis. *Chemistry Letters*, 45(3), 297-299.
- Han, M., Hu, J., Lu, P., Cao, H., Yu, C., Li, X., . . . Han, N. (2020). Exosome-transmitted miR-567 reverses trastuzumab resistance by inhibiting ATG5 in breast cancer. *Cell Death & Disease*, 11(1), 1-15.
- Hartinger, C. G., Zorbas-Seifried, S., Jakupec, M. A., Kynast, B., Zorbas, H., & Keppler, B. K. (2006). From bench to bedside--preclinical and early clinical development of the anticancer agent indazolium trans-[tetrachlorobis(1H-indazole)ruthenate(III)] (KP1019 or FFC14A). *J Inorg Biochem*, 100(5-6), 891-904.
- Hartley, F. (1973). The cis-and trans-effects of ligands. *Chemical Society Reviews*, 2(2), 163-179.
- Havel, J. J., Chowell, D., & Chan, T. A. (2019). The evolving landscape of biomarkers for checkpoint inhibitor immunotherapy. *Nature Reviews Cancer*, 19(3), 133-150.
- Hayashi, H., Ueno, T., Kim, C., & Uchida, T. (2020). Ruthenium-Catalyzed Cross-Selective Asymmetric Oxidative Coupling of Arenols. *Organic Letters* 22, no. 4 (2020): 1469-1474.
- He, M., Wang, Y., Chen, X., Zhao, Y., Lou, K., Wang, Y., . . . Cai, X. (2020). Spatiotemporally controllable diphtheria toxin expression using a light-switchable transgene system combining multifunctional nanoparticle delivery system for targeted melanoma therapy. *Journal of Controlled Release*, 319, 1-14.
- Hellmann, M. D., Nathanson, T., Rizvi, H., Creelan, B. C., Sanchez-Vega, F., Ahuja, A., . . . Abu-Akeel, M. (2018). Genomic features of response to combination immunotherapy in patients with advanced non-small-cell lung cancer. *Cancer cell*, 33(5), 843-852. e844.
- Henderson, S. G., Ebsworth, E. A. V., Fraser, T. E., Leitch, D. M., & Rankin, D. W. (1981). Reactions of silanes and germanes with iridium complexes. Part 4. Reactions with carbonylhydridotris (triphenylphosphine) iridium (I). *Journal of the Chemical Society, Dalton Transactions*, (4), 1010-1018.
- Höfer, D., Varbanov, H. P., Hejl, M., Jakupec, M. A., Roller, A., Galanski, M., & Keppler, B. K. (2017). Impact of the equatorial coordination sphere on the rate of reduction, lipophilicity

- and cytotoxic activity of platinum (IV) complexes. *Journal of inorganic biochemistry*, 174, 119-129.
- Hong, C. S., Beckta, J. M., Kundishora, A. J., Elsamadicy, A. A., & Chiang, V. L. (2020). Laser interstitial thermal therapy for treatment of cerebral radiation necrosis. *International Journal of Hyperthermia*, 37(2), 68-76
- Hooshmand, S. E., Heidari, B., Sedghi, R., & Varma, R. S. (2019). Recent advances in the Suzuki–Miyaura cross-coupling reaction using efficient catalysts in eco-friendly media. *Green chemistry*, 21(3), 381-405.
- Hou, G. L., Wen, H., Lopata, K., Zheng, W. J., Kowalski, K., Govind, N., . . . Xantheas, S. S. (2012). A Combined Gas-Phase Photoelectron Spectroscopic and Theoretical Study of Zeise’s Anion and Its Bromine and Iodine Analogues. *Angewandte Chemie International Edition*, 51(26), 6356-6360.
- Hsieh, Y.-C., Limquiacco, J. L., Lin, C.-C., Chen, W.-T., & Lin, S.-M. (2019). Radiofrequency ablation following artificial ascites and pleural effusion creation may improve outcomes for hepatocellular carcinoma in high-risk locations. *Abdominal Radiology*, 44(3), 1141-1151.
- Huang, H.-Y., Lin, Y.-C.-D., Li, J., Huang, K.-Y., Shrestha, S., Hong, H.-C., . . . Yu, Y. (2020). miRTarBase 2020: updates to the experimentally validated microRNA–target interaction database. *Nucleic acids research*, 48(D1), D148-D154.
- Huang, H. Y., Lin, Y. C., Li, J., Huang, K. Y., Shrestha, S., Hong, H. C., . . . Huang, H. D. (2020). miRTarBase 2020: updates to the experimentally validated microRNA-target interaction database. *Nucleic Acids Res*, 48(D1), D148-D154. doi: 10.1093/nar/gkz896
- Huang, T., & Deng, C.-X. (2019a). Current progresses of exosomes as cancer diagnostic and prognostic biomarkers. *International journal of biological sciences*, 15(1), 1.
- Huang, T., & Deng, C. X. (2019b). Current Progresses of Exosomes as Cancer Diagnostic and Prognostic Biomarkers. *Int J Biol Sci*, 15(1), 1-11. doi: 10.7150/ijbs.27796
- Huber, C. J., Anglin, T. C., Jones, B. H., Muthu, N., Cramer, C. J., & Massari, A. M. (2012). Vibrational Solvatochromism in Vaska’s Complex Adducts. *The Journal of Physical Chemistry A*, 116(37), 9279-9286.
- Hussain, Z., Yousif, E., Ahmed, A., & Altaie, A. (2014). Synthesis and characterization of Schiff’s bases of sulfamethoxazole. *Organic and medicinal chemistry letters*, 4(1), 1.
- Ibáñez, S., Vrečko, D. N., Estevan, F., Hirva, P., Sanaú, M., & Úbeda, M. (2014). Further orthometalated dinuclear palladium (III) compounds with bridging N, S-donor ligands. *Dalton Transactions*, 43(7), 2961-2970.
- Ibrahim, M., Shehatta, I., & Al-Nayeli, A. (2002). Voltammetric studies of the interaction of lumazine with cyclodextrins and DNA. *Journal of pharmaceutical and biomedical analysis*, 28(2), 217-225.
- Ighodaro, O., & Akinloye, O. (2018). First line defence antioxidants-superoxide dismutase (SOD), catalase (CAT) and glutathione peroxidase (GPX): Their fundamental role in the entire antioxidant defence grid. *Alexandria Journal of Medicine*, 54(4), 287-293.

- Iqbal, J., Abbasi, B. A., Mahmood, T., Kanwal, S., Ali, B., Shah, S. A., & Khalil, A. T. (2017). Plant-derived anticancer agents: A green anticancer approach. *Asian Pacific Journal of Tropical Biomedicine*, 7(12), 1129-1150.
- Islam, M. T. (2017). Oxidative stress and mitochondrial dysfunction-linked neurodegenerative disorders. *Neurological research*, 39(1), 73-82.
- Izzo, F., Granata, V., Grassi, R., Fusco, R., Palaia, R., Delrio, P., . . . Curley, S. A. (2019). Radiofrequency Ablation and Microwave Ablation in Liver Tumors: An Update. *Oncologist*, 24(10).
- Jain, R. K., Martin, J. D., Chauhan, V. P., & Duda, D. G. (2020). Tumor microenvironment: vascular and extravascular compartment *Abeloff's Clinical Oncology* (pp. 108-126. e107): Elsevier.
- Jakupec, M. A., Galanski, M., & Keppler, B. K. (2003). Tumour-inhibiting platinum complexes--state of the art and future perspectives. *Reviews of physiology, biochemistry and pharmacology*, 146, 1-54.
- Jayabharathi, J., Ramanathan, P., Thanikachalam, V., & Karunakaran, C. (2015). Optical and theoretical studies on Fe₃O₄-imidazole nanocomposite and clusters. *New Journal of Chemistry*, 39(5), 3801-3812.
- Jiang, P., Gu, S., Pan, D., Fu, J., Sahu, A., Hu, X., . . . Li, B. (2018). Signatures of T cell dysfunction and exclusion predict cancer immunotherapy response. *Nature medicine*, 24(10), 1550-1558.
- Jiang, S., Hu, C., Liu, P., & Lu, M. (2019). Tumor-derived exosomes in cancer metastasis risk diagnosis and metastasis therapy. *Clinical and Translational Oncology*, 21(2), 152-159.
- Johnstone, T. C., & Lippard, S. J. (2013). The effect of ligand lipophilicity on the nanoparticle encapsulation of Pt (IV) prodrugs. *Inorganic Chemistry*, 52(17), 9915-9920.
- Jordan, V. C. (2003). Tamoxifen: a most unlikely pioneering medicine. *Nature reviews Drug discovery*, 2(3), 205.
- Jouanneau, M., McClary, B., Reyes, J. C. P., Chen, R., Chen, Y., Plunkett, W., . . . Liu, J. O. (2016). Derivatization of agelastatin A leading to bioactive analogs and a trifunctional probe. *Bioorganic & medicinal chemistry letters*, 26(8), 2092-2097.
- Jurgens, S., Kuhn, F. E., & Casini, A. (2018). Cyclometalated complexes of platinum and gold with biological properties: state-of-the-art and future perspectives. *Current medicinal chemistry*, 25(4), 437-461.
- Kaija, H., Pakanen, L., & Porvari, K. (2020). RNU6B, a frequent reference in miRNA expression studies, differentiates between deaths caused by hypothermia and chronic cardiac ischemia. *International journal of legal medicine*, 134(1), 159-162.
- Kanaoujiya, R., Singh, M., Singh, J., & Srivastava, S. (2020). Ruthenium Based Anticancer Compounds and Their Importance. *Journal of Scientific Research*, 64(1).
- Kang, Y., Xue, Q., Jin, P., Jiang, J., Zeng, J., & Chen, Y. (2017). Rhodium nanosheets-reduced graphene oxide hybrids: a highly active platinum-alternative electrocatalyst for the methanol oxidation reaction in alkaline media. *ACS Sustainable Chemistry & Engineering*, 5(11), 10156-10162.

- Karale, B., Takate, S., Salve, S., Zaware, B., & Jadhav, S. (2015). Synthesis and biological screening of some novel thiazolyl chromones and pyrazoles. *Indian Journal of Chemistry* Vol 54B pp 798-804.
- Karimian, R., & Aghajani, M. (2019). Cyclodextrins and their Derivatives as Carrier Molecules in Drug and Gene Delivery Systems. *Current Organic Chemistry*, 23(11), 1256-1269.
- Kataoka, Y., Sato, K., Miyazaki, Y., Suzuki, Y., Tanaka, H., Kitagawa, Y., . . . Mori, W. (2010). Photocatalytic hydrogen production from water using heterogeneous two-dimensional rhodium coordination polymer [Rh₂ (p-BDC) 2] n. *Chemistry Letters*, 39(4), 358-359.
- Katayama, Y., Uchino, J., Chihara, Y., Tamiya, N., Kaneko, Y., Yamada, T., & Takayama, K. (2019). Tumor neovascularization and developments in therapeutics. *Cancers*, 11(3), 316.
- Kaur, K., Jain, M., Reddy, R. P., & Jain, R. (2010). Quinolines and structurally related heterocycles as antimalarials. *Eur J Med Chem*, 45(8), 3245-3264.
- Kaur, K., & Khatik, G. L. (2020). Cancer Immunotherapy: An Effective Tool in Cancer Control and Treatment. *Current Cancer Therapy Reviews*, 16(1), 62-69.
- Kelland, L. (2007). The resurgence of platinum-based cancer chemotherapy. *Nature Reviews Cancer*, 7(8), 573-584.
- Khan, B. T., Bhatt, J., Najmuddin, K., Shamsuddin, S., & Annapoorna, K. (1991). Synthesis, antimicrobial, and antitumor activity of a series of palladium(II) mixed ligand complexes. *J Inorg Biochem*, 44(1), 55-63.
- Khan, K. M., Saify, Z. S., Khan, Z. A., Ahmed, M., Saeed, M., Schick, M., . . . Voelter, W. (2000). Syntheses and cytotoxic, antimicrobial, antifungal and cardiovascular activity of new quinoline derivatives. *Arzneimittelforschung*, 50(10), 915-924.
- Khan, S. A., Asiri, A. M., Kumar, S., & Sharma, K. (2014). Green synthesis, antibacterial activity and computational study of pyrazoline and pyrimidine derivatives from 3-(3, 4-dimethoxyphenyl)-1-(2, 5-dimethyl-thiophen-3-yl)-propenone. *European Journal of Chemistry*, 5(1), 85-90.
- Khanmohammadi, H., Salehifard, M., & Abnosi, M. (2009). Synthesis, characterization, biological and thermal studies of Cu (II) complexes of salen and tetrahydro-salen ligands. *Journal of the Iranian Chemical Society*, 6(2), 300-309.
- Kirlikovali, K. O., Axtell, J. C., Gonzalez, A., Phung, A. C., Khan, S. I., & Spokoyny, A. M. (2016). Luminescent metal complexes featuring photophysically innocent boron cluster ligands. *Chemical Science*, 7(8), 5132-5138.
- Kirlin, W. G., Cai, J., Thompson, S. A., Diaz, D., Kavanagh, T. J., & Jones, D. P. (1999). Glutathione redox potential in response to differentiation and enzyme inducers. *Free Radical Biology and Medicine*, 27(11-12), 1208-1218.
- Konishi, S., Iwai, T., & Sawamura, M. (2018). Synthesis, Properties, and Catalytic Application of a Triptycene-Type Borate-Phosphine Ligand. *Organometallics*, 37(12), 1876-1883.
- Kontaxis, C., Bol, G. H., & Raaymakers, B. W. (2020). Image-guided radiation therapy: Google Patents.
- KR, S. G., Mathew, B. B., Sudhamani, C., & Naik, H. B. (2014). Mechanism of DNA binding and cleavage. *Biomedicine*, 2(1), 1-9.

- Krogul, A., Cedrowski, J., Wiktorska, K., Ozimiński, W. P., Skupińska, J., & Litwinienko, G. (2012). Crystal structure, electronic properties and cytotoxic activity of palladium chloride complexes with monosubstituted pyridines. *Dalton Transactions*, 41(2), 658-666.
- Kruger, S., Ilmer, M., Kobold, S., Cadilha, B. L., Endres, S., Ormanns, S., . . . Schloesser, H. (2019). Advances in cancer immunotherapy 2019–latest trends. *Journal of Experimental & Clinical Cancer Research*, 38(1), 268.
- Kukushkin, V. Y., Pombeiro, A. J., Ferreira, C. M., & Elding, L. I. (2002). Dimethylsulfoxide complexes of Platinum(II): K [PtCl₃ (Me₂SO)], cis-[PtCl₂L (Me₂SO)](L= Me₂SO, MeCN), [PtCl (μ-Cl)(Me₂SO)](2), and [Pt (Me₂SO)(4)](CF₃SO₃)(2). *Inorganic Syntheses*, 33, 189-196.
- Kumar, P., Gupta, R. K., & Pandey, D. S. (2014). Half-sandwich arene ruthenium complexes: synthetic strategies and relevance in catalysis. *Chemical Society Reviews*, 43(2), 707-733.
- Kumar, S., Kumari, P., & Singh, R. (2020). Emerging Nanomaterials for Cancer Therapy *Nanoparticles in Medicine* (pp. 25-54): Springer.
- Kuntz Jr, I., Gasparro, F., Johnston Jr, M., & Taylor, R. (1968). Molecular interactions and the Benesi-Hildebrand equation. *Journal of the American Chemical Society*, 90(18), 4778-4781.
- Lajous, H., Riva, R., Lelièvre, B., Tétaud, C., Avril, S., Hindré, F., . . . Garcion, E. (2018). Hybrid Gd 3+/cisplatin cross-linked polymer nanoparticles enhance platinum accumulation and formation of DNA adducts in glioblastoma cell lines. *Biomaterials science*, 6(9), 2386-2409.
- Lakouraj, M. M., Hasantabar, V., Tashakkorian, H., & Golpour, M. (2018). Novel anticancer and antibacterial organometallic polymer based on ferrocene as a building block and xanthone bioactive scaffolds: Synthesis, characterization, and biological study. *Polymers for Advanced Technologies*, 29(11), 2784-2796.
- Larsen, A. K., & Skladanowski, A. (1998). Cellular resistance to topoisomerase-targeted drugs: from drug uptake to cell death. *Biochimica et Biophysica Acta (BBA)-Gene Structure and Expression*, 1400(1-3), 257-274.
- Lauster, M., & Stegmaier, M. (2011). Process for the deposition of platinum-rhodium layers having improved whiteness: Google Patents.
- Lautens, M., & Sanichar, R. (2020). The Stille Carbonylative Cross-Coupling Reaction. *Synfacts*, 16(03), 0314.
- Lazarević, T., Rilak, A., & Bugarčić, Ž. D. (2017). Platinum, palladium, gold and ruthenium complexes as anticancer agents: Current clinical uses, cytotoxicity studies and future perspectives. *European journal of medicinal chemistry*, 142, 8-31.
- LeBleu, V. S., & Kalluri, R. (2018). A peek into cancer-associated fibroblasts: origins, functions and translational impact. *Disease models & mechanisms*, 11(4), dmm029447.
- Lee, G., Park, H., Bak, S. H., & Lee, H. Y. (2020). Radiomics in Lung Cancer from Basic to Advanced: Current Status and Future Directions. *Korean Journal of Radiology*, 21(2), 159-171.
- Lee, R. F., Chernobrovkin, A., Rutishauser, D., Allardyce, C. S., Hacker, D., Johnsson, K., . . . Dyson, P. J. (2017). Expression proteomics study to determine metallodrug targets and optimal drug combinations. *Scientific reports*, 7(1), 1-11.

- LePecq, J.-B., & Paoletti, C. (1967). A fluorescent complex between ethidium bromide and nucleic acids: physical—chemical characterization. *Journal of molecular biology*, 27(1), 87-106.
- Lever, A. P. (1984). Inorganic electronic spectroscopy. *Studies in physical and theoretical chemistry*, 33.
- Li, L., Zhou, C., Zhao, H., & Wang, R. (2015). Spatial control of palladium nanoparticles in flexible click-based porous organic polymers for hydrogenation of olefins and nitrobenzene. *Nano Research*, 8(3), 709-721.
- Li, W.-T., Hwang, D.-R., Song, J.-S., Chen, C.-P., Chen, T.-W., Lin, C.-H., . . . Huang, C.-L. (2012). Synthesis and biological evaluation of 2-amino-1-thiazolyl imidazoles as orally active anticancer agents. *Investigational new drugs*, 30(1), 164-175.
- Liberka, M., Kobylarczyk, J., & Podgajny, R. (2020). Structural Disorder in High-Spin {CoII9WV6}(Core)-[Pyridine N-Oxides](Shell) Architectures. *Molecules*, 25(2), 251.
- Lippert, B. (1999). *Ed.). . Cisplatin: chemistry and biochemistry of a leading anticancer drug*.
- Lisiecki, A. (2015). Titanium matrix composite Ti/TiN produced by diode laser gas nitriding. *metals*, 5(1), 54-69.
- Liu, F., Gou, S., Chen, F., Fang, L., & Zhao, J. (2015). Study on antitumor Platinum(II) complexes of chiral diamines with dicyclic species as steric hindrance. *Journal of medicinal chemistry*, 58(16), 6368-6377.
- Liu, J., Lichtenberg, T., Hoadley, K. A., Poisson, L. M., Lazar, A. J., Cherniack, A. D., . . . Lee, A. V. (2018). An integrated TCGA pan-cancer clinical data resource to drive high-quality survival outcome analytics. *Cell*, 173(2), 400-416. e411.
- Love, R. A., Koetzle, T. F., Williams, G. J., Andrews, L. C., & Bau, R. (1975). Neutron diffraction study of the structure of Zeise's salt, KPtCl₃ (C₂H₄). H₂O. *Inorganic Chemistry*, 14(11), 2653-2657.
- Lu, D., Lu, T., Xu, B., Che, J., Wu, S., Wu, H., & Yarla, N. (2018). Anti-Metastatic Drug Developments: Work Out towards New Direction. *Med. Chem*, 8(7), 192-196.
- Luthra, S., Rominski, A., & Sander, P. (2018). The role of antibiotic-target-modifying and antibiotic-modifying enzymes in Mycobacterium abscessus drug resistance. *Frontiers in microbiology*, 9, 2179.
- Macks, C., Gwak, S.-J., Lynn, M., & Lee, J. S. (2018). Rolipram-loaded polymeric micelle nanoparticle reduces secondary injury after rat compression spinal cord injury. *Journal of neurotrauma*, 35(3), 582-592.
- Madabhushi, A., Wang, X., Vaidya, P., & Velcheti, V. (2019). Predicting recurrence in early stage non-small cell lung cancer (nslc) with integrated radiomic and pathomic features: Google Patents.
- Malekzadeh, P., Yossef, R., Cafri, G., Paria, B. C., Lowery, F. J., Jafferji, M., . . . Kim, S. P. (2020). Antigen Experienced T Cells from Peripheral Blood Recognize p53 Neoantigens. *Clinical Cancer Research*.
- Marra, A., Viale, G., & Curigliano, G. (2019). Recent advances in triple negative breast cancer: the immunotherapy era. *BMC medicine*, 17(1), 90.

- Martin, J. D., Cabral, H., Stylianopoulos, T., & Jain, R. K. (2020). Improving cancer immunotherapy using nanomedicines: Progress, opportunities and challenges. *Nature Reviews Clinical Oncology*, 1-16.
- Mathew, N., Jagirdar, B. R., Gopalan, R. S., & Kulkarni, G. (2000). Influence of the cone angles and the π -acceptor properties of phosphorus-containing ligands in the chemistry of dihydrogen complexes of ruthenium. *Organometallics*, 19(22), 4506-4517.
- McCauley, S., Carter, G., Bennett, M., McNally, O., & Rogers, K. M. (2020). Pharmacotherapeutics of capecitabine and trastuzumab in the treatment of metastatic breast cancer. *British Journal of Nursing*, 29(3), S4-S9.
- McClure, J. J., Li, X., & Chou, C. J. (2018). Advances and challenges of HDAC inhibitors in cancer therapeutics *Advances in cancer research* (Vol. 138, pp. 183-211): Elsevier.
- McGivern, N., El-Helali, A., Mullan, P., McNeish, I. A., Harkin, D. P., Kennedy, R. D., & McCabe, N. (2018). Activation of MAPK signalling results in resistance to saracatinib (AZD0530) in ovarian cancer. *Oncotarget*, 9(4), 4722.
- McLaughlin, M. L., Jr, J. M., Schaller, T. R., & Snelling, R. D. (1990). Cronan & DNA-metal binding by antitumor-active metallocene dichlorides from inductively coupled plasma spectroscopy analysis: titanocene dichloride forms DNA-Cp2Ti or DNA-CpTi adducts depending on pH. *Journal of the American Chemical Society*, 112(24 SRC - BaiduScholar), 8949-8952.
- Medina, E., & Pinter, B. (2020). A DFT Study on the Redox Active Behavior of Carbene and Pyridine Ligands in the Oxidative and Reductive Quenching Cycles of Ruthenium Photoredox Catalysts. *Catalysts*, 10(1), 80.
- Meier-Menches, S. M., Gerner, C., Berger, W., Hartinger, C. G., & Keppler, B. K. (2018). Structure–activity relationships for ruthenium and osmium anticancer agents—towards clinical development. *Chemical Society Reviews*, 47(3), 909-928.
- Meijerink, M. R., Puijk, R. S., van Tilborg, A. A., Henningsen, K. H., Fernandez, L. G., Neyt, M., . . . Richel, D. J. (2018). Radiofrequency and microwave ablation compared to systemic chemotherapy and to partial hepatectomy in the treatment of colorectal liver metastases: a systematic review and meta-analysis. *Cardiovascular and interventional radiology*, 41(8), 1189-1204.
- Meyer, M., Essack, M., Kanyanda, S., & Rees, J. G. (2008). A low-cost flow cytometric assay for the detection and quantification of apoptosis using an anionic halogenated fluorescein dye. *Biotechniques*, 45(3), 317-320.
- Mi, P., Cabral, H., & Kataoka, K. (2019). Ligand-Installed Nanocarriers toward Precision Therapy. *Advanced Materials*, 1902604.
- Mingos, D. M. P. (2004). Complementary spherical electron density model and its implications for the 18 electron rule. *Journal of organometallic chemistry*, 689(24), 4420-4436.
- Minick, D. J., Frenz, J. H., Patrick, M. A., & Brent, D. A. (1988). A comprehensive method for determining hydrophobicity constants by reversed-phase high-performance liquid chromatography. *Journal of medicinal chemistry*, 31(10), 1923-1933.
- Mital, R., Jain, N., & Srivastava, T. (1989). Synthesis, characterization and cytotoxic studies of diamine and diimine Palladium(II) complexes of diethyldithiocarbamate and binding of these

- and analogous Platinum(II) complexes with DNA. *Inorganica Chimica Acta*, 166(1), 135-140.
- Mitxelena-Iribarren, O., Campisi, J., de Apellániz, I. M., Lizarbe-Sancha, S., Arana, S., Zhukova, V., . . . Zhukov, A. (2020). Glass-coated ferromagnetic microwire-induced magnetic hyperthermia for in vitro cancer cell treatment. *Materials Science and Engineering: C*, 106, 110261.
- Mohamed, M. S., Kamel, R., & Fatahala, S. S. (2011). New condensed pyrroles of potential biological interest: Syntheses and structure–activity relationship studies. *Eur J Med Chem*, 46(7), 3022-3029.
- Mohanty, S., Punji, B., & Balakrishna, M. S. (2006). Synthesis and reaction kinetics of Pd (1, 5-cyclooctadiene) Cl₂ with N, N'-methylene-bis (2-aminopyridyl): An efficient catalyst for Suzuki-cross-coupling reactions. *Polyhedron*, 25(3), 815-820.
- Mohite, B. V., Koli, S. H., Narkhede, C. P., Patil, S. N., & Patil, S. V. (2017). Prospective of microbial exopolysaccharide for heavy metal exclusion. *Applied biochemistry and biotechnology*, 183(2), 582-600.
- Mohiuddin, A. K. (2019). Complementary and Alternative Treatments For Cancer Prevention and Cure (part 1). *Journal of Experimental and Clinical Toxicology*, 1(2), 17.
- Morris, R. E., Aird, R. E., del Socorro Murdoch, P., Chen, H., Cummings, J., Hughes, N. D., . . . Jodrell, D. I. (2001). Inhibition of cancer cell growth by ruthenium (II) arene complexes. *Journal of medicinal chemistry*, 44(22), 3616-3621.
- Morris, R. E., Aird, R. E., Murdoch, P. d. S., Chen, H., Cummings, J., Hughes, N. D., . . . Sadler, P. J. (2001). Inhibition of cancer cell growth by ruthenium(II) arene complexes. *Journal of medicinal chemistry*, 44(22), 3616-3621.
- Motswainyana, W. M., Onani, M. O., & Madiehe, A. M. (2012). Bis (ferrocenylimine) Palladium(II) and Platinum(II) complexes: Synthesis, molecular structures and evaluation as antitumor agents. *Polyhedron*, 41(1), 44-51.
- Mpungose, P. P., Vundla, Z. P., Maguire, G. E., & Friedrich, H. B. (2018). The current status of heterogeneous palladium catalysed Heck and Suzuki cross-coupling reactions. *Molecules*, 23(7), 1676.
- Mukherjee, T. (2015). Coordination Chemistry of some platinum metals with NS and O donor ligands.
- Murahashi, T., & Kurosawa, H. (2002). Organopalladium complexes containing palladium–palladium bonds. *Coordination Chemistry Reviews*, 231(1-2), 207-228.
- Murray, S. G., & Hartley, F. R. (1981). Coordination chemistry of thioethers, selenoethers, and telluroethers in transition-metal complexes. *Chemical reviews*, 81(4), 365-414.
- Naanyu, V., Asirwa, C. F., Wachira, J., Busakhala, N., Kisuya, J., Otieno, G., . . . Inui, T. (2015). Lay perceptions of breast cancer in Western Kenya. *World journal of clinical oncology*, 6(5), 147.
- Nadeem, M. W., Ghamdi, M. A. A., Hussain, M., Khan, M. A., Khan, K. M., Almotiri, S. H., & Butt, S. A. (2020). Brain Tumor Analysis Empowered with Deep Learning: A Review, Taxonomy, and Future Challenges. *Brain Sciences*, 10(2), 118.

- Nafisi, S., & Norouzi, Z. (2009). A comparative study on the interaction of cis- and trans-platin with DNA and RNA. *DNA and cell biology*, 28(9), 469-477.
- Nagaraju, G. P., Srivani, G., Dariya, B., Chalikonda, G., Farran, B., Behera, S. K., . . . Kamal, M. A. (2020). *Nanoparticles guided drug delivery and imaging in gastric cancer*. Paper presented at the Seminars in Cancer Biology.
- Najjar, A., Rajabi, N., & Karaman, R. (2017). Recent approaches to platinum (IV) prodrugs: a variety of strategies for enhanced delivery and efficacy. *Current pharmaceutical design*, 23(16), 2366-2376.
- Nesmeyanov, A. N., & Kochetkova, N. S. (1974). Principal Practical Applications of Ferrocene and Its Derivatives. *Russian Chemical Reviews* 710, 43(9 SRC - BaiduScholar).
- Nestle, F. O., Alijagic, S., Gilliet, M., Sun, Y., Grabbe, S., Dummer, R., . . . Schadendorf, D. (1998). Vaccination of melanoma patients with peptide- or tumor lysate-pulsed dendritic cells. *Nature medicine*, 4(3), 328-332.
- Netalkar, P. P., Netalkar, S. P., & Revankar, V. K. (2015). Transition metal complexes of thiosemicarbazone: Synthesis, structures and invitro antimicrobial studies. *Polyhedron*, 100, 215-222.
- Nguyen, A., Hillard, E. A., Top, S., Pigeon, P., Jaouen, G., & Chimia. (2007). Vessières, A., & Ferrocifens and ferrocifenols as new potential weapons against breast cancer. *Journal for Chemistry*, 61(11 SRC - BaiduScholar), 716-724.
- Nguyen, T. K., Senan, S., Bradley, J. D., Franks, K., Giuliani, M., Guckenberger, M., . . . Onishi, H. (2018). Optimal imaging surveillance after stereotactic ablative radiation therapy for early-stage non-small cell lung cancer: Findings of an International Delphi Consensus Study. *Practical Radiation Oncology*, 8(2), e71-e78.
- Nhung, N. T. A. (2018). Quantum chemical assessment of magnesium hydride complexes with bistrisphenylphosphine of group 14 elements [H₂Mg- $\{E(PPH_3)_2\}$](E= C to Pb). *VIETNAM JOURNAL OF CHEMISTRY*, 56(3E12), 445-451.
- Nicholls, D. (2017). *Complexes and first-row transition elements*: Macmillan International Higher Education.
- Nicolás, I., Saco, A., Barnadas, E., Marimon, L., Rakislova, N., Fusté, P., . . . Gil-Ibañez, B. (2020). Prognostic implications of genotyping and p16 immunostaining in HPV-positive tumors of the uterine cervix. *Modern Pathology*, 33(1), 128-137.
- Novakova, O., Chen, H., Vrana, O., Rodger, A., Sadler, P. J., & Brabec, V. (2003). DNA interactions of monofunctional organometallic ruthenium (II) antitumor complexes in cell-free media. *Biochemistry*, 42(39), 11544-11554.
- Novakova, O., Kasparkova, J., Bursova, V., Hofr, C., Vojtiskova, M., Chen, H., . . . Brabec, V. (2005). Conformation of DNA modified by monofunctional Ru(II) arene complexes: recognition by DNA binding proteins and repair. Relationship to cytotoxicity. *Chem Biol*, 12(1), 121-129.
- Ntziachristos, P., Lim, J. S., Sage, J., & Aifantis, I. (2014). From fly wings to targeted cancer therapies: a centennial for notch signaling. *Cancer cell*, 25(3), 318-334.

- O'Reilly, B., Plutín, A. M., Pérez, H., Calderón, O., Ramos, R., Martínez, R., . . . Martínez-Alvarez, R. (2012). Synthesis and structural characterization of cobalt (II) and copper (II) complexes with N, N-disubstituted-N'-acylthioureas. *Polyhedron*, *36*(1), 133-140.
- Odhiambo, R. A., Aluoch, A. O., Njenga, L. W., Kagwanja, S. M., Wandiga, S. O., & Wendt, O. F. (2018). Synthesis, characterisation and ion-binding properties of oxathiacrown ethers appended to [Ru (bpy) 2] 2+. Selectivity towards Hg 2+, Cd 2+ and Pb 2+. *RSC Advances*, *8*(7), 3663-3672.
- Olshansky, O., Hubeny, E., & Kolosov, A. (2019). The method of generating thermal energy, devices of its implementation and heat generation systems: Google Patents.
- Olsztyńska, S., & Komorowska, M. (2011). *Biomedical Engineering: Trends, Research and Technologies*: BoD–Books on Demand.
- Omondi, R. O., Ojwach, S. O., Jaganyi, D., & Fatokun, A. A. (2018). (Pyrazolyl) pyridine ruthenium (III) complexes: Synthesis, kinetics of substitution reactions with thiourea and biological studies. *Inorganic Chemistry Communications*, *94*, 98-103.
- Ondrej, P., Nada, P. H., Mysiková, D., Kutna, B., Mrazkova, H., Lischke, R., . . . Adkins, I. (2020). Detection of tumor antigens and tumor-antigen specific T cells in NSCLC patients: correlation of the quality of T cell responses with NSCLC subtype. *Immunology Letters*.
- Orhan Puskullu, M., Tekiner, B., & Suzen, S. (2013). Recent studies of antioxidant quinoline derivatives. *Mini reviews in medicinal chemistry*, *13*(3), 365-372.
- Otoshi, T., Nagano, T., Tachihara, M., & Nishimura, Y. (2019). Possible biomarkers for cancer immunotherapy. *Cancers*, *11*(7), 935.
- Pacella, C. M., & Mauri, G. (2020). History of Laser Ablation *Image-guided Laser Ablation* (pp. 1-5): Springer.
- Padhye, S., & Kauffman, G. B. (1985). Transition metal complexes of semicarbazones and thiosemicarbazones. *Coordination Chemistry Reviews*, *63*, 127-160.
- Padmavathi, V., Venkatesh, B., & Padmaja, A. (2011). Synthesis and antimicrobial activity of amido linked pyrrolyl and pyrazolyl-oxazoles, thiazoles and imidazoles. *Eur J Med Chem*, *46*(11), 5317-5326.
- Pan, P., Skaer, C., Yu, J., Zhao, H., Ren, H., Oshima, K., & Wang, L.-S. (2017). Berries and other natural products in pancreatic cancer chemoprevention in human clinical trials. *Journal of berry research*, *7*(3), 147-161.
- Papo, T., Jaganyi, D., & Mambanda, A. (2020). The effect of the chelate ligand on the rate of chloride substitution from Pt(II) complexes with picolyl and isoquinolinylcarboxamide moieties on the non-leaving ligand. *Inorganica chimica acta*, *499*, 119180.
- Park, J. K., Coffey, N. J., Bodine, S. P., Zawatsky, C. N., Jay, L., Gahl, W. A., . . . Cinar, R. (2020). Bleomycin Induces Drug Efflux in Lungs. A Pitfall for Pharmacological Studies of Pulmonary Fibrosis. *American Journal of Respiratory Cell and Molecular Biology*, *62*(2), 178-190.
- Park, S.-Y., & Kim, I.-S. (2017). Engulfment signals and the phagocytic machinery for apoptotic cell clearance. *Experimental & molecular medicine*, *49*(5), e331.

- Peacock, A. F. A., Habtemariam, A., Fernández, R., Walland, V., Fabbiani, F. P. A., Parsons, S., . . . Sadler, P. J. (2006). Tuning the reactivity of osmium(II) and ruthenium(II) arene complexes under physiological conditions. *Journal of the American Chemical Society*, *128*(5), 1739-1748.
- Peacock, A. F. A., & Sadler, P. J. (2008). Medicinal organometallic chemistry: designing metal arene complexes as anticancer agents. *Chemistry, an Asian journal*, *3*(11), 1890-1899.
- Peng, Z., Li, Z., Lin, X., Tang, H., Ye, L., Ma, Y., . . . Jiang, T. (2017). Pyrometallurgical recovery of platinum group metals from spent catalysts. *Jom*, *69*(9), 1553-1562.
- Pérez, W. I., Soto, Y., Ortíz, C., Matta, J., & Meléndez, E. (2015). Ferrocenes as potential chemotherapeutic drugs: Synthesis, cytotoxic activity, reactive oxygen species production and micronucleus assay. *Bioorganic & medicinal chemistry*, *23*(3), 471-479.
- Petrylak, D. P., De Wit, R., Chi, K. N., Drakaki, A., Sternberg, C. N., Nishiyama, H., . . . Bamias, A. (2020). Ramucirumab plus docetaxel versus placebo plus docetaxel in patients with locally advanced or metastatic urothelial carcinoma after platinum-based therapy (RANGE): overall survival and updated results of a randomised, double-blind, phase 3 trial. *The Lancet Oncology*, *21*(1), 105-120.
- Philip, C. C., Mathew, A., & John, M. J. (2018). Cancer care: Challenges in the developing world. *Cancer Research, Statistics, and Treatment*, *1*(1), 58.
- Phua, S. Z. F., Xue, C., Lim, W. Q., Yang, G., Chen, H., Zhang, Y., . . . Zhao, Y. (2019). Light-responsive prodrug-based supramolecular nanosystems for site-specific combination therapy of cancer. *Chemistry of Materials*, *31*(9), 3349-3358.
- Pitarresi, J. R., & Rustgi, A. K. (2019). Mechanisms Underlying Metastatic Pancreatic Cancer *Human Cell Transformation* (pp. 3-10): Springer.
- Pizarro, A. M., Melchart, M., Habtemariam, A., Salassa, L., Fabbiani, F. P. A., Parsons, S., & Sadler, P. J. (2010). Controlling the reactivity of ruthenium(II) arene complexes by tether ring-opening. *Inorganic Chemistry*, *49*(7), 3310-3319.
- Pizarro, A. M., & Sadler, P. J. (2009). Unusual DNA binding modes for metal anticancer complexes. *Biochimie*, *91*(10), 1198-1211. doi: <https://doi.org/10.1016/j.biochi.2009.03.017>
- Power, P. P. (1999). π -Bonding and the lone pair effect in multiple bonds between heavier main group elements. *Chemical reviews*, *99*(12), 3463-3504.
- Prakash, A., & Adhikari, D. (2011). Application of Schiff bases and their metal complexes-A Review. *Int. J. Chem. Tech. Res*, *3*(4), 1891-1896.
- Prasad, B., Kim, S., Cho, W., Kim, S., & Kim, J. K. (2018). Effect of tumor properties on energy absorption, temperature mapping, and thermal dose in 13.56-MHz radiofrequency hyperthermia. *Journal of thermal biology*, *74*, 281-289.
- Prior, F., Almeida, J., Kathiravelu, P., Kurc, T., Smith, K., Fitzgerald, T., & Saltz, J. (2020). Open access image repositories: high-quality data to enable machine learning research. *Clinical radiology*, *75*(1), 7-12.
- Pu, Z., Amiin, I. S., He, D., Wang, M., Li, G., & Mu, S. (2018). Activating rhodium phosphide-based catalysts for the pH-universal hydrogen evolution reaction. *Nanoscale*, *10*(26), 12407-12412.

- Pyle, A., Rehmann, J., Meshoyrer, R., Kumar, C., Turro, N., & Barton, J. K. (1989). Mixed-ligand complexes of ruthenium (II): factors governing binding to DNA. *Journal of the American Chemical Society*, 111(8), 3051-3058.
- Qi, L., Luo, Q., Zhang, Y., Jia, F., Zhao, Y., & Wang, F. (2019). Advances in toxicological research of the anticancer drug cisplatin. *Chemical research in toxicology*, 32(8), 1469-1486.
- Qin, Q.-P., Zou, B.-Q., Tan, M.-X., Luo, D.-M., Wang, Z.-F., Wang, S.-L., & Liu, Y.-C. (2018). High in vitro anticancer activity of a dinuclear Palladium(II) complex with a 2-phenylpyridine ligand. *Inorganic Chemistry Communications*, 96, 106-110.
- Rabiee, N. (2018). Metallodrugs: Medicinal chemistry investigation: OAT.
- Ramadevi, P., Singh, R., Jana, S. S., Devkar, R., & Chakraborty, D. (2017). Mixed ligand ruthenium arene complexes containing N-ferrocenyl amino acids: biomolecular interactions and cytotoxicity against MCF7 cell line. *Journal of organometallic chemistry*, 833, 80-87.
- Raman, N., & Sobha, S. (2012). Exploring the DNA binding mode of transition metal based biologically active compounds. *Spectrochimica Acta Part A: Molecular and Biomolecular Spectroscopy*, 85(1), 223-234.
- Rao, K. M., Nongbri, S. L., & Therrien, B. (2013). Reactivity study of arene (azido) ruthenium N\O-base complexes with activated alkynes.
- Rashidjahanabad, Z., & Huang, X. (2020). *Recent advances in tumor associated carbohydrate antigen based chimeric antigen receptor T cells and bispecific antibodies for anti-cancer immunotherapy*. Paper presented at the Seminars in Immunology.
- Rau, T. (1996). Mechanistic insight from kinetic studies on the interaction of model Palladium(II) complexes with nucleic acid components. *Metal ions in biological systems*, 32, 339-378.
- Rausch, M., & Moser, G. (1974). Formation and properties of some new. sigma.-aryl derivatives of iridium (I) and iridium (III). *Inorganic Chemistry*, 13(1), 11-13.
- Reis, F. S., Martins, A., Vasconcelos, M. H., Morales, P., & Ferreira, I. C. (2017). Functional foods based on extracts or compounds derived from mushrooms. *Trends in Food Science & Technology*, 66, 48-62.
- Reithofer, M. R., Valiahdi, S. M., Galanski, M., Jakupec, M. A., Arion, V. B., & Keppler, B. K. (2008). Novel Endothall-Containing Platinum (IV) Complexes: Synthesis, Characterization, and Cytotoxic Activity. *Chemistry & biodiversity*, 5(10), 2160-2170.
- Ren, D., Hua, Y., Yu, B., Ye, X., He, Z., Li, C., . . . Chen, Y. (2020). Predictive biomarkers and mechanisms underlying resistance to PD1/PD-L1 blockade cancer immunotherapy. *Molecular cancer*, 19(1), 1-19.
- Rezabal, E., Ugalde, J., & Frenking, G. (2017). The trans Effect in Palladium Phosphine Sulfonate Complexes. *The Journal of Physical Chemistry A*, 121(40), 7709-7716.
- Rezaeihamiri, E., Bahramsoltani, R., & Rahimi, R. (2020). Plant-derived natural agents as dietary supplements for the regulation of glycosylated hemoglobin: A review of clinical trials. *Clinical Nutrition*, 39(2), 331-342.
- Ribas, A., & Wolchok, J. D. (2018). Cancer immunotherapy using checkpoint blockade. *Science*, 359(6382), 1350-1355. doi: 10.1126/science.aar4060

- Riley, R. S., June, C. H., Langer, R., & Mitchell, M. J. (2019a). Delivery technologies for cancer immunotherapy. *Nat Rev Drug Discov*, *18*(3), 175-196. doi: 10.1038/s41573-018-0006-z
- Riley, R. S., June, C. H., Langer, R., & Mitchell, M. J. (2019b). Delivery technologies for cancer immunotherapy. *Nature reviews Drug discovery*, *18*(3), 175-196.
- Rodrigues, J. G., Balmaña, M., Macedo, J. A., Poças, J., Fernandes, Â., de-Freitas-Junior, J. C. M., . . . Gomes, C. (2018). Glycosylation in cancer: Selected roles in tumour progression, immune modulation and metastasis. *Cellular Immunology*, *333*, 46-57.
- Roma-Rodrigues, C., Mendes, R., Baptista, P. V., & Fernandes, A. R. (2019). Targeting tumor microenvironment for cancer therapy. *International journal of molecular sciences*, *20*(4), 840.
- Rosenberg, B., Vancamp, L., & Krigas, T. (1965). INHIBITION OF CELL DIVISION IN ESCHERICHIA COLI BY ELECTROLYSIS PRODUCTS FROM A PLATINUM ELECTRODE. *Nature*, *205*, 698-699.
- Rudakov, E. S., & Shul'pin, G. B. (2015). Stable organoplatinum complexes as intermediates and models in hydrocarbon functionalization. *Journal of organometallic chemistry*, *793*, 4-16.
- Ruyssen, N. (2019). *THERAPY-INDUCED METASTASIS*. Ghent University.
- Ryabov, A. D. (1990). Mechanisms of intramolecular activation of carbon-hydrogen bonds in transition-metal complexes. *Chemical reviews*, *90*(2), 403-424.
- Safarzadeh, M. S., Horton, M., & Van Rythoven, A. D. (2018). Review of recovery of platinum group metals from copper leach residues and other resources. *Mineral Processing and Extractive Metallurgy Review*, *39*(1), 1-17.
- Sahin, U., & Türeci, Ö. (2018). Personalized vaccines for cancer immunotherapy. *Science*, *359*(6382), 1355-1360.
- Sahu, R., Thakur, D., & Kashyap, P. (2012). Schiff base: An overview of its medicinal chemistry potential for new drug molecules. *International Journal of Pharmaceutical Sciences and Nanotechnology*, *5*(30), 1757-1764.
- Saito, H., Kitagawa, K., Yoneda, T., Fukui, Y., Fujisawa, M., Bautista, D., & Shirakawa, T. (2017). Combination of p53-DC vaccine and rAd-p53 gene therapy induced CTLs cytotoxic against p53-deleted human prostate cancer cells in vitro. *Cancer Gene Ther*, *24*(7), 289-296. doi: 10.1038/cgt.2017.21
- Salgın-Gökşen, U., Gökhan-Kelekçi, N., Göktaş, Ö., Köysal, Y., Kılıç, E., Işık, Ş., . . . Özalp, M. (2007). 1-Acylthiosemicarbazides, 1, 2, 4-triazole-5 (4H)-thiones, 1, 3, 4-thiadiazoles and hydrazones containing 5-methyl-2-benzoxazolinones: synthesis, analgesic-anti-inflammatory and antimicrobial activities. *Bioorganic & medicinal chemistry*, *15*(17), 5738-5751.
- Samanta, D., & Semenza, G. L. (2018). Metabolic adaptation of cancer and immune cells mediated by hypoxia-inducible factors. *Biochimica et Biophysica Acta (BBA)-Reviews on Cancer*, *1870*(1), 15-22.
- Sambi, M., Bagheri, L., & Szewczuk, M. R. (2019a). Current Challenges in Cancer Immunotherapy: Multimodal Approaches to Improve Efficacy and Patient Response Rates. *J Oncol*, *2019*, 4508794. doi: 10.1155/2019/4508794

- Sambi, M., Bagheri, L., & Szewczuk, M. R. (2019b). Current challenges in cancer immunotherapy: multimodal approaches to improve efficacy and patient response rates. *Journal of oncology*, 2019.
- San Tan, S., Al-Abbasi, A. A., Tahir, M. I. M., & Kassim, M. B. (2014). Synthesis, structure and spectroscopic properties of cobalt (III) complexes with 1-benzoyl-(3, 3-disubstituted) thiourea. *Polyhedron*, 68, 287-294.
- Sanchez-Correa, B., Lopez-Sejas, N., Duran, E., Labella, F., Alonso, C., Solana, R., & Tarazona, R. (2019). Modulation of NK cells with checkpoint inhibitors in the context of cancer immunotherapy. *Cancer Immunology, Immunotherapy*, 68(5), 861-870.
- Sand, A., Piacsek, M., Donohoe, D. L., Duffin, A. T., Riddell, G. T., Sun, C., . . . Yin, J. (2020). WEE1 inhibitor, AZD1775, overcomes trastuzumab resistance by targeting cancer stem-like properties in HER2-positive breast cancer. *Cancer letters*, 472, 119-131.
- Sanderson, B. J., Ferguson, L. R., & Denny, W. A. (1996). Mutagenic and carcinogenic properties of platinum-based anticancer drugs. *Mutation research*, 355(1-2), 59-70.
- Sang, W., Zhang, Z., Dai, Y., & Chen, X. (2019). Recent advances in nanomaterial-based synergistic combination cancer immunotherapy. *Chemical Society Reviews*, 48(14), 3771-3810.
- Sangster, J. (1997). *Octanol-water partition coefficients: fundamentals and physical chemistry* (Vol. 1): John Wiley & Sons.
- Sanmamed, M. F., & Chen, L. (2018). A Paradigm Shift in Cancer Immunotherapy: From Enhancement to Normalization. *Cell*, 175(2), 313-326. doi: 10.1016/j.cell.2018.09.035
- Sansook, S., Lineham, E., Hassell-Hart, S., Tizzard, G. J., Coles, S. J., Spencer, J., & Morley, S. J. (2018). Probing the anticancer action of novel ferrocene analogues of MNK inhibitors. *Molecules*, 23(9), 2126.
- Sari, Y., Gürses, C., Celepci, D. B., Keleştemur, Ü., Aktaş, A., Yüksel, Ş., . . . Gök, Y. (2020). 4-Vinylbenzyl and 2-morpholinoethyl substituted ruthenium (II) complexes: Design, synthesis, and biological evaluation. *Journal of Molecular Structure*, 1202, 127355.
- Sartorelli, A. C., & Booth, B. A. (1967). Inhibition of the growth of sarcoma 180 ascites cells by combinations of inhibitors of nucleic acid biosynthesis and the cupric chelate of kethoxal bis-(thiosemicarbazone). *Cancer research*, 27(9), 1614-1619.
- Sawama, Y., Park, K., Yamada, T., & Sajiki, H. (2018). New Gateways to the Platinum Group Metal-Catalyzed Direct Deuterium-Labeling Method Utilizing Hydrogen as a Catalyst Activator. *Chemical and Pharmaceutical Bulletin*, 66(1), 21-28.
- Scalbert, A., & Williamson, G. (2000). Dietary intake and bioavailability of polyphenols. *The Journal of nutrition*, 130(8), 2073S-2085S.
- Scavo, M. P., Depalo, N., Tutino, V., De Nunzio, V., Ingrosso, C., Rizzi, F., . . . Giannelli, G. (2020). Exosomes for Diagnosis and Therapy in Gastrointestinal Cancers. *International journal of molecular sciences*, 21(1), 367.
- Schaaf, M. B., Garg, A. D., & Agostinis, P. (2018). Defining the role of the tumor vasculature in antitumor immunity and immunotherapy. *Cell Death & Disease*, 9(2), 1-14.

- Schafer, F. Q., & Buettner, G. R. (2001). Redox environment of the cell as viewed through the redox state of the glutathione disulfide/glutathione couple. *Free Radical Biology and Medicine*, 30(11), 1191-1212.
- Schep, S., Schutgens, R., Fischer, K., & Boes, M. (2018). Review of immune tolerance induction in hemophilia A. *Blood reviews*, 32(4), 326-338.
- Seago, M., Shumaker, P. R., Spring, L. K., Alam, M., Al-Niaimi, F., Rox Anderson, R., . . . Chan, H. H. (2019). Laser treatment of traumatic scars and contractures: 2020 international consensus recommendations. *Lasers in Surgery and Medicine*.
- Selvamurugan, S., Ramachandran, R., Prakash, G., Nirmala, M., Viswanathamurthi, P., Fujiwara, S., & Endo, A. (2017). Ruthenium (II) complexes encompassing 2-oxo-1, 2-dihydroquinoline-3-carbaldehyde thiosemicarbazone hybrid ligand: A new versatile potential catalyst for dehydrogenative amide synthesis. *Inorganica chimica acta*, 454, 46-53.
- Shadap, L., Tyagi, J. L., Poluri, K. M., Pinder, E., Phillips, R. M., Kaminsky, W., & Kollipara, M. R. (2020). Synthesis, structural and in-vitro functional studies of half-sandwich platinum group metal complexes having various bonding modes of benzhydrazone derivative ligands. *Polyhedron*, 176, 114293.
- Shao, J., Zhou, B., Di Bilio, A. J., Zhu, L., Wang, T., Qi, C., . . . Yen, Y. (2006). A Ferrous-Triapine complex mediates formation of reactive oxygen species that inactivate human ribonucleotide reductase. *Molecular cancer therapeutics*, 5(3), 586-592.
- Sharninghausen, L. S., Sinha, S. B., Shopov, D. Y., Choi, B., Mercado, B. Q., Roy, X., . . . Crabtree, R. H. (2016). High oxidation state iridium mono- μ -oxo dimers related to water oxidation catalysis. *Journal of the American Chemical Society*, 138(49), 15917-15926.
- Shastri, M. D., Shukla, S. D., Chong, W. C., Dua, K., Peterson, G. M., Patel, R. P., . . . O'Toole, R. F. (2018). Role of oxidative stress in the pathology and management of human tuberculosis. *Oxidative medicine and cellular longevity*, 2018.
- Sheldrick, G. M. (2015). Crystal structure refinement with SHELXL. *Acta Crystallographica Section C: Structural Chemistry*, 71(1), 3-8.
- Shih, W.-C., & Ozerov, O. V. (2017). Synthesis and characterization of PBP pincer iridium complexes and their application in alkane transfer dehydrogenation. *Organometallics*, 36(1), 228-233.
- Shirakawa, N., Iwata, T., Miyake, S., Otsuka, T., Koizumi, S., Usui, T., & Kawata, T. (2017). Development of the aesthetic orthodontic appliances using a silver plating process: the report on peel resistance.
- Shtemenko, A. V., Chifotides, H. T., Yegorova, D. E., Shtemenko, N. I., & Dunbar, K. R. (2015). Synthesis and X-ray crystal structure of the dirhenium complex $\text{Re}_2(\text{i-C}_3\text{H}_7\text{COO})_4\text{Cl}_2$ and its interactions with the DNA purine nucleobases. *Journal of inorganic biochemistry*, 153, 114-120.
- Sicklick, J. K., Kato, S., Okamura, R., Schwaederle, M., Hahn, M. E., Williams, C. B., . . . Miller, V. A. (2019). Molecular profiling of cancer patients enables personalized combination therapy: the I-PREDICT study. *Nature medicine*, 25(5), 744-750.
- Singh, M., Prasad, C. P., Singh, T. D., & Kumar, L. (2018). Cancer research in India: Challenges & opportunities. *The Indian journal of medical research*, 148(4), 362.

- Sinniah, S. K., Sim, K. S., Ng, S. W., & Tan, K. W. (2017). Structural and cytotoxic studies of cationic thiosemicarbazones. *Journal of Molecular Structure*, *1137*, 253-259.
- Smitten, K. L., Fairbanks, S. D., Robertson, C. C., de la Serna, J. B., Foster, S. J., & Thomas, J. A. (2020). Ruthenium based antimicrobial theranostics—using nanoscopy to identify therapeutic targets and resistance mechanisms in *Staphylococcus aureus*. *Chemical Science*, *11*(1), 70-79.
- Souza-Fonseca-Guimaraes, F., Cursons, J., & Huntington, N. D. (2019). The emergence of natural killer cells as a major target in cancer immunotherapy. *Trends in immunology*, *40*(2), 142-158.
- Spingler, B., Whittington, D. A., & Lippard, S. J. (2001). 2.4 Å crystal structure of an oxaliplatin 1,2-d(GpG) intrastrand cross-link in a DNA dodecamer duplex. *Inorganic Chemistry*, *40*(22), 5596-5602.
- Spugnini, E. P., Logozzi, M., Di Raimo, R., Mizzoni, D., & Fais, S. (2018). A role of tumor-released exosomes in paracrine dissemination and metastasis. *International journal of molecular sciences*, *19*(12), 3968.
- Storr, T. (2014). *Ligand design in medicinal inorganic chemistry*: Wiley Online Library.
- Strieth, S., Hagemann, J., & Hess, M. (2020). Angiolytic laser applications for the larynx: Phonosurgical concepts for transoral laser microsurgery. *HNO*, *68*(1), 59.
- Su, M.-D., & Chu, S.-Y. (2001). Theoretical Study of the Oxidative Addition of 16-Electron d⁴ [n]-Metalocenophane Complexes with Methane. *The Journal of Physical Chemistry A*, *105*(14), 3591-3597.
- Su, Q.-Q., Fan, K., Huang, X.-D., Xiang, J., Cheng, S.-C., Ko, C.-C., . . . Lau, T.-C. (2020). Field-Induced Slow Magnetic Relaxation in Low-Spin S = ½ Mononuclear Osmium (V) Complexes. *Dalton Transactions*.
- Sugiyama, H., Lian, C., Isomura, M., Saito, I., & Wang, A. H.-J. (1996). Distamycin A modulates the sequence specificity of DNA alkylation by duocarmycin A. *Proceedings of the National Academy of Sciences*, *93*(25), 14405-14410.
- Sun, Y. d., Zhang, H., Liu, J. z., Xu, H. r., Wu, H. y., Zhai, H. z., . . . Zhou, L. l. (2019). Efficacy of radiofrequency ablation and microwave ablation in the treatment of thoracic cancer: A systematic review and meta-analysis. *Thoracic cancer*, *10*(3), 543-550.
- Suntharalingam, K., Mendoza, O., Duarte, A. A., Mann, D. J., & Vilar, R. (2013). A platinum complex that binds non-covalently to DNA and induces cell death via a different mechanism than cisplatin. *Metallomics*, *5*(5), 514-523.
- Suter, V., Altermatt, H., & Bornstein, M. (2020). A randomized controlled trial comparing surgical excisional biopsies using CO₂ laser, Er: YAG laser and scalpel. *International journal of oral and maxillofacial surgery*, *49*(1), 99-106.
- Taheri, O., Behzad, M., Ghaffari, A., Kubicki, M., Dutkiewicz, G., Bezaatpour, A., . . . Salehi, M. (2014). Synthesis, crystal structures and antibacterial studies of oxidovanadium (IV) complexes of salen-type Schiff base ligands derived from meso-1, 2-diphenyl-1, 2-ethylenediamine. *Transition Metal Chemistry*, *39*(2), 253-259.

- Tan, W., Deng, Q., Lin, S., Wang, Y., & Xu, G. (2019). Comparison of microwave ablation and radiofrequency ablation for hepatocellular carcinoma: a systematic review and meta-analysis. *International Journal of Hyperthermia*, 36(1), 264-272.
- Tang, J., Shalabi, A., & Hubbard-Lucey, V. (2018). Comprehensive analysis of the clinical immunology landscape. *Annals of Oncology*, 29(1), 84-91.
- Tanyi, J. L., Bobisse, S., Ophir, E., Tuyaeerts, S., Roberti, A., Genolet, R., . . . Dangaj, D. (2018). Personalized cancer vaccine effectively mobilizes antitumor T cell immunity in ovarian cancer. *Science translational medicine*, 10(436), eaao5931.
- Taylor, E. M., Koss, B., Davis, L. E., & Tackett, A. J. (2020). Histone Modifications as Biomarkers for Immunotherapy *Biomarkers for Immunotherapy of Cancer* (pp. 213-228): Springer.
- Temburnikar, K. W., Ross, C. R., Wilson, G. M., Balzarini, J., Cawrse, B. M., & Seley-Radtke, K. L. (2015). Antiproliferative activities of halogenated pyrrolo [3, 2-d] pyrimidines. *Bioorganic & medicinal chemistry*, 23(15), 4354-4363.
- Todd, R. C., & Lippard, S. J. (2010). Structure of duplex DNA containing the cisplatin 1, 2-{Pt (NH₃)₂} 2+-d (GpG) cross-link at 1.77 Å resolution. *Journal of inorganic biochemistry*, 104(9), 902-908.
- Tognetti, V., Guégan, F., Luneau, D., Chermette, H., Morell, C., & Joubert, L. (2017). Structural effects in octahedral carbonyl complexes: an atoms-in-molecules study. *Theoretical Chemistry Accounts*, 136(7), 85.
- Tolman, C. A. (1970). Phosphorus ligand exchange equilibria on zerovalent nickel. Dominant role for steric effects. *Journal of the American Chemical Society*, 92(10), 2956-2965.
- Topazian, H., Cira, M., Dawsey, S. M., Kibachio, J., Kocholla, L., Wangai, M., . . . Galassi, A. (2016). Joining forces to overcome cancer: the Kenya cancer research and control stakeholder program. *Journal of cancer policy*, 7, 36-41.
- Tran, W. T., Jerzak, K., Lu, F.-I., Klein, J., Tabbarah, S., Lagree, A., . . . Saednia, K. (2019). Personalized breast cancer treatments using artificial intelligence in radiomics and pathomics. *Journal of medical imaging and radiation sciences*, 50(4), S32-S41.
- Trondl, R., Heffeter, P., Kowol, C. R., Jakupec, M. A., Berger, W., & Keppler, B. K. (2014). NKP-1339, the first ruthenium-based anticancer drug on the edge to clinical application. *Chemical Science*, 5(8), 2925-2932.
- Turan, N., & Buldurun, K. (2018). Synthesis, characterization and antioxidant activity of Schiff base and its metal complexes with Fe (II), Mn (II), Zn (II), and Ru(II) ions: Catalytic activity of ruthenium (II) complex. *European Journal of Chemistry*, 9(1), 22-29.
- Ünver, H., & Hayvali, Z. (2010). Synthesis, spectroscopic studies and structures of square-planar nickel (II) and copper (II) complexes derived from 2-{(Z)-[furan-2-ylmethyl] imino} methyl}-6-methoxyphenol. *Spectrochimica Acta Part A: Molecular and Biomolecular Spectroscopy*, 75(2), 782-788.
- V Kouznetsov, V., A Rojas Ruiz, F., Y Vargas Mendez, L., & P Gupta, M. (2012). Simple C-2-substituted quinolines and their anticancer activity. *Letters in Drug Design & Discovery*, 9(7), 680-686.

- Vaidya, A., Jain, A. K., Kumar, P., Kashaw, S. K., & Agrawal, R. K. (2011). Predicting anti-cancer activity of quinoline derivatives: CoMFA and CoMSIA approach. *Journal of enzyme inhibition and medicinal chemistry*, 26(6), 854-861.
- Vaidya, P., Wang, X., Bera, K., Khunger, A., Choi, H., Patil, P., . . . Madabhushi, A. (2018). *RaPtomics: integrating radiomic and pathomic features for predicting recurrence in early stage lung cancer*. Paper presented at the Medical Imaging 2018: Digital Pathology.
- Vander Zanden, C. M., & Chi, E. Y. (2020). Passive immunotherapies targeting amyloid beta and tau oligomers in Alzheimer's disease. *Journal of pharmaceutical sciences*, 109(1), 68-73.
- Vekariya, P. A., Karia, P. S., Bhatt, B. S., & Patel, M. N. (2019). Half sandwich rhodium (III) and iridium (III) complexes as cytotoxic and metallonuclease agents. *Applied biochemistry and biotechnology*, 187(2), 556-569.
- Velásquez, A., Souza, R. A. d., Passalacqua, T. G., Ribeiro, A. R., Scontri, M., Chin, C. M., . . . Mauro, A. E. (2016). Antiprotozoal activity of the cyclopalladated complexes against *Leishmania amazonensis* and *Trypanosoma cruzi*. *Journal of the Brazilian Chemical Society*, 27(6), 1032-1039.
- Venter, K. (2011). Cisplatin-induced ototoxicity: the current state of ototoxicity monitoring in New Zealand.
- Vessieres, A., Top, S., Pigeon, P., Hillard, E., Boubeker, L., Spera, D., & Jaouen, G. (2005). Modification of the estrogenic properties of diphenols by the incorporation of ferrocene. Generation of antiproliferative effects in vitro. *Journal of medicinal chemistry*, 48(12), 3937-3940.
- Vezzu, D. A., Lu, Q., Chen, Y.-H., & Huo, S. (2014). Cytotoxicity of cyclometalated platinum complexes based on tridentate NCN and CNN-coordinating ligands: Remarkable coordination dependence. *Journal of inorganic biochemistry*, 134, 49-56.
- Vidimar, V., Meng, X., Klajner, M., Licon, C., Fetzer, L., Harlepp, S., ... & Mellitzer, G. . . (2012). Induction of caspase 8 and reactive oxygen species by ruthenium-derived anticancer compounds with improved water solubility and cytotoxicity. *Biochemical pharmacology*, 84(11), 1428-1436.
- Wagner, S., Mullins, C. S., & Linnebacher, M. (2018). Colorectal cancer vaccines: Tumor-associated antigens vs neoantigens. *World journal of gastroenterology*, 24(48), 5418.
- Wallis, C. J., Butaney, M., Satkunasivam, R., Freedland, S. J., Patel, S. P., Hamid, O., . . . Klaassen, Z. (2019). Association of patient sex with efficacy of immune checkpoint inhibitors and overall survival in advanced cancers: a systematic review and meta-analysis. *JAMA oncology*, 5(4), 529-536.
- Walton, J. W., & Wilkinson, L. A. (2018). π -Coordinated arene metal complexes and catalysis. *Organometallic Chemistry*, 42, 125-171.
- Wan, X., Beaudoin, J. J., Vinod, N., Min, Y., Makita, N., Bludau, H., . . . Kabanov, A. V. (2019). Co-delivery of paclitaxel and cisplatin in poly (2-oxazoline) polymeric micelles: Implications for drug loading, release, pharmacokinetics and outcome of ovarian and breast cancer treatments. *Biomaterials*, 192, 1-14.
- Wang, D., & Lippard, S. J. (2005). Cellular processing of platinum anticancer drugs. *Nature reviews Drug discovery*, 4(4), 307.

- Wang, D., Liu, T., Wang, J., & Wu, Z. (2018). N, P (S) Co-doped Mo₂C/C hybrid electrocatalysts for improved hydrogen generation. *Carbon*, *139*, 845-852.
- Wang, F., Bella, J., Parkinson, J. A., & Sadler, P. J. (2005). Competitive reactions of a ruthenium arene anticancer complex with histidine, cytochrome c and an oligonucleotide. *Journal of biological inorganic chemistry : JBIC : a publication of the Society of Biological Inorganic Chemistry*, *10*(2), 147-155.
- Wang, J., Liu, Y., Jiang, M., Li, Y., Xia, L., & Wu, P. (2018). Aldehyde-functionalized metal-organic frameworks for selective sensing of homocysteine over Cys, GSH and other natural amino acids. *Chemical communications*, *54*(8), 1004-1007.
- Wang, X., Van Bokhoven, J. A., & Palagin, D. (2020). Atomically dispersed platinum on low index and stepped ceria surfaces: phase diagrams and stability analysis. *Physical Chemistry Chemical Physics*, *22*(1), 28-38.
- Wang, Y., Bao, Y., Zhang, S., & Wang, Z. (2020). Splicing dysregulation in cancer: from mechanistic understanding to a new class of therapeutic targets. *Science China Life Sciences*, 1-16.
- Wang, Y., Deng, W., Li, N., Neri, S., Sharma, A., Jiang, W., & Lin, S. H. (2018). Combining immunotherapy and radiotherapy for cancer treatment: current challenges and future directions. *Frontiers in pharmacology*, *9*, 185.
- Wang, Y., Du, Z., Zheng, W., Wu, K., Xu, D., Luo, Q., . . . Wang, F. (2017). Deciphering of interactions between platinated DNA and HMGB1 by hydrogen/deuterium exchange mass spectrometry. *Dalton Transactions*, *46*(19), 6187-6195.
- Ward, R. C., Lourenco, A. P., & Mainiero, M. B. (2020). Implementing breast cryoablation in practice. *Journal of Breast Imaging*, *2*(1), 61-66.
- West, D. X., Liberta, A. E., Padhye, S. B., Chikate, R. C., Sonawane, P. B., Kumbhar, A. S., & Yerande, R. G. (1993). Thiosemicarbazone complexes of copper (II): structural and biological studies. *Coordination Chemistry Reviews*, *123*(1-2), 49-71.
- West, D. X., Nassar, A. A., El-Saied, F. A., & Ayad, M. I. (1999). Cobalt (II) complexes with 2-aminoacetophenone N (4)-substituted thiosemicarbazones. *Transition Metal Chemistry*, *24*(6), 617-621.
- White, P. B., Jaworski, J. N., Fry, C. G., Dolinar, B. S., Guzei, I. A., & Stahl, S. S. (2016). Structurally Diverse Diazafluorene-Ligated Palladium(II) Complexes and Their Implications for Aerobic Oxidation Reactions. *Journal of the American Chemical Society*, *138*(14), 4869-4880.
- White, S., Baird, E. E., & Dervan, P. B. (1997). Orientation Preferences of Pyrrole- Imidazole Polyamides in the Minor Groove of DNA. *Journal of the American Chemical Society*, *119*(38), 8756-8765.
- Whiteside, T. L. (2018). *Exosome and mesenchymal stem cell cross-talk in the tumor microenvironment*. Paper presented at the Seminars in immunology.
- Wilson, J. J., & Lippard, S. J. (2011). Synthesis, characterization, and cytotoxicity of platinum (IV) carbamate complexes. *Inorganic Chemistry*, *50*(7), 3103-3115.

- Wilson, J. J., & Lippard, S. J. (2012). Acetate-bridged platinum (III) complexes derived from cisplatin. *Inorganic Chemistry*, 51(18), 9852-9864.
- Wolff, J., & Sheldrick, W. (1997). Bis (arene) ruthenium (II) complexes containing η^6 -coordinated phenylalanine derivatives. *Journal of organometallic chemistry*, 531(1-2), 141-149.
- Wolfson, A., & Levy-Ontman, O. (2020). Recent Developments in the Immobilization of Palladium Complexes on Renewable Polysaccharides for Suzuki–Miyaura Cross-Coupling of Halobenzenes and Phenylboronic Acids. *Catalysts*, 10(1), 136.
- Wong, E., & Giandomenico, C. M. (1999). Current status of platinum-based antitumor drugs. *Chemical reviews*, 99(9), 2451-2466.
- Wong, W. Y., & Harvey, P. D. (2010). Recent Progress on the Photonic Properties of Conjugated Organometallic Polymers Built Upon the trans-Bis (para-ethynylbenzene) bis (phosphine) Platinum(II) Chromophore and Related Derivatives. *Macromolecular rapid communications*, 31(8), 671-713.
- Xavier, T., de Gois, E., Sarto, L., & de Almeida, E. (2018). Thermal behavior study of Palladium(II) complexes containing the iminic ligand N, N'-bis (3, 4-dimethoxybenzaldehyde) ethane-1, 2-diamine. *Journal of Thermal Analysis and Calorimetry*, 134(3), 1829-1837.
- Xiao, X., Oswald, J. T., Wang, T., Zhang, W., & Li, W. (2020). Use of anticancer platinum compounds in combination therapies and challenges in drug delivery. *Current medicinal chemistry*.
- Xie, W., Xu, J., Hu, S., Li, S., Wang, W., Yin, C. C., . . . Tang, G. (2020). iAMP21 in acute myeloid leukemia is associated with complex karyotype, TP53 mutation and dismal outcome. *Modern Pathology*, 1-9.
- Xie, Y., Dang, W., Zhang, S., Yue, W., Yang, L., Zhai, X., . . . Lu, J. (2019). The role of exosomal noncoding RNAs in cancer. *Molecular cancer*, 18(1), 37.
- Xu, Z., Xie, H., Zhou, L., Chen, X., & Zheng, S. (2019). The Combination Strategy of Transarterial Chemoembolization and Radiofrequency Ablation or Microwave Ablation against Hepatocellular Carcinoma. *Analytical Cellular Pathology*, 2019.
- Yang, G.-J., Zhong, H.-J., Ko, C.-N., Wong, S.-Y., Vellaisamy, K., Ye, M., . . . Leung, C.-H. (2018). Identification of a rhodium (iii) complex as a Wee1 inhibitor against TP53-mutated triple-negative breast cancer cells. *Chemical communications*, 54(20), 2463-2466.
- Yimer, A. M. (2015). Review on preparation and description of some first series divalent transition metal complexes with novel Schiff's base ligands. *Rev. Catal*, 2, 14-25.
- Young, K. J., Mironov, O. A., & Periana, R. A. (2007). Stoichiometric Oxy Functionalization and CH Activation Studies of Cyclometalated Iridium (III) 6-Phenyl-2, 2 '-Bipyridine Hydrocarbyl Complexes. *Organometallics*, 26(9), 2137-2140.
- Zaidi, N., & Jaffee, E. M. (2019). Immunotherapy transforms cancer treatment. *J Clin Invest*, 129(1), 46-47. doi: 10.1172/jci126046
- Zaki, M., Hairat, S., & Aazam, E. S. (2019). Scope of organometallic compounds based on transition metal-arene systems as anticancer agents: starting from the classical paradigm to targeting multiple strategies. *RSC Advances*, 9(6), 3239-3278.

- Zang, J., Lu, D., & Xu, A. (2020). The interaction of circRNAs and RNA binding proteins: An important part of circRNA maintenance and function. *Journal of neuroscience research*, 98(1), 87-97.
- Zeman, E. M., Schreiber, E. C., & Tepper, J. E. (2020). Basics of radiation therapy *Abeloff's Clinical Oncology* (pp. 431-460. e433): Elsevier.
- Zeng, Z., Li, Y., Pan, Y., Lan, X., Song, F., Sun, J., . . . Wang, F. (2018). Cancer-derived exosomal miR-25-3p promotes pre-metastatic niche formation by inducing vascular permeability and angiogenesis. *Nature communications*, 9(1), 1-14.
- Zhang, J., Xu, L., & Wong, W.-Y. (2018). Energy materials based on metal Schiff base complexes. *Coordination Chemistry Reviews*, 355, 180-198.
- Zhang, K., Yuan, C., Guo, F.-S., Zhang, Y.-Q., & Wang, Y.-Y. (2017). Fine-tuning terminal solvent ligands to rationally enhance the energy barrier in dinuclear dysprosium single-molecule magnets. *Dalton Transactions*, 46(1), 186-192.
- Zhang, L., Tan, M., Zhou, L., & Zeng, Q. (2018). A novel, C₂-symmetric, chiral bis-cyclo-sulfonamide-olefin tridentate ligand in Rh-catalyzed asymmetric 1, 4-additions. *Tetrahedron Letters*, 59(29), 2778-2783.
- Zhang, P., & Sadler, P. J. (2017). Redox-Active Metal Complexes for Anticancer Therapy. *European Journal of Inorganic Chemistry*, 2017(12), 1541-1548.
- Zhang, X., Ma, X., Zhang, T., Li, B., Jiang, S., Zhang, G., . . . Shao, X. (2018). The influence of phosphine ligand substituted [2Fe2S] model complexes as electro-catalyst on proton reduction. *RSC Advances*, 8(74), 42262-42268.
- Zhang, X., Yao, T., Campo, M. A., & Larock, R. C. (2010). Synthesis of substituted quinolines by the electrophilic cyclization of n-(2-alkynyl) anilines. *Tetrahedron*, 66(6), 1177-1187.
- Zhang, Y., Chen, X., Gueydan, C., & Han, J. (2018). Plasma membrane changes during programmed cell deaths. *Cell research*, 28(1), 9-21.
- Zhang, Y., Zheng, S., Zheng, J.-S., Wong, K.-H., Huang, Z., Ngai, S.-M., . . . Chen, T. (2014). Synergistic induction of apoptosis by methylseleninic acid and cisplatin, the role of ROS-ERK/AKT-p53 pathway. *Molecular pharmaceutics*, 11(4), 1282-1293.
- Zhao, G., Lin, H., Yu, P., Sun, H., Zhu, S., Su, X., & Chen, Y. (1999). Ethylenediamine-palladium(II) complexes with pyridine and its derivatives: synthesis, molecular structure and initial antitumor studies. *J Inorg Biochem*, 73(3), 145-149.
- Zhou, W., Almeqdadi, M., Xifaras, M. E., Riddell, I. A., Yilmaz, Ö. H., & Lippard, S. J. (2018). The effect of geometric isomerism on the anticancer activity of the monofunctional platinum complex trans-[Pt (NH₃)₂ (phenanthridine) Cl] NO₃. *Chemical communications*, 54(22), 2788-2791.
- Zins, K., & Abraham, D. (2020). Cancer Immunotherapy: Targeting Tumor-Associated Macrophages by Gene Silencing *RNA Interference and CRISPR Technologies* (pp. 289-325): Springer.

APPENDICES

SPECTRA PEAKS FOR THE LIGANDS AND COMPLEXES

FTIR Spectra Data

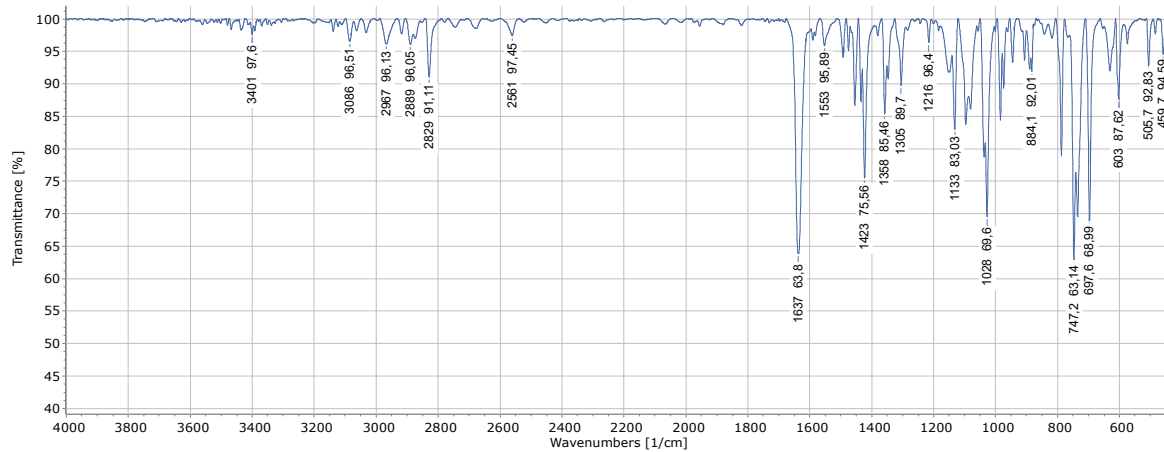


Figure 54 FTIR Spectra for L1

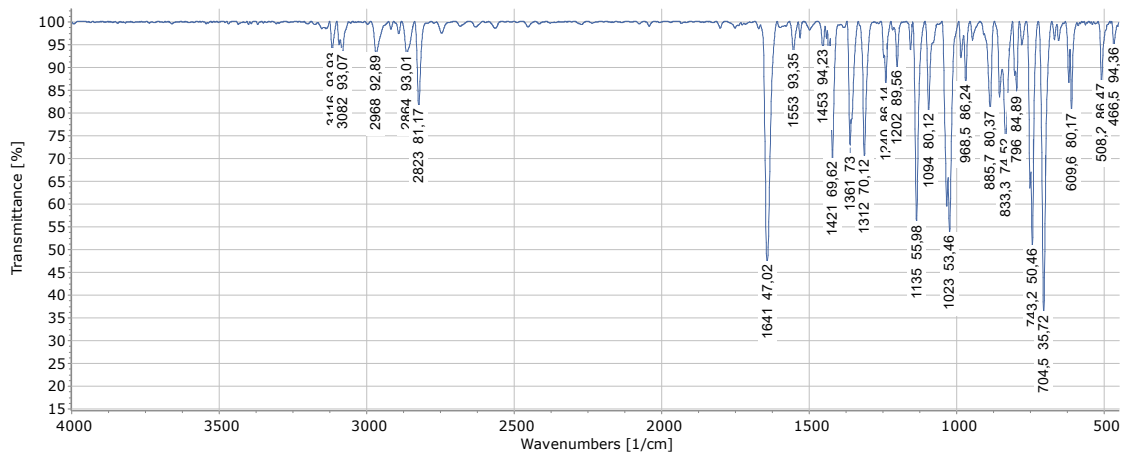


Figure 55 FTIR Spectra for L2

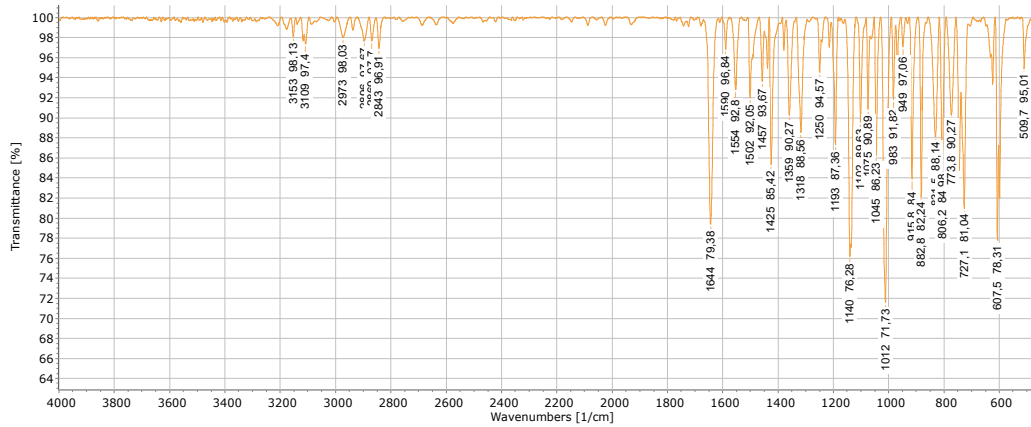


Figure 56 FTIR Spectra for L3

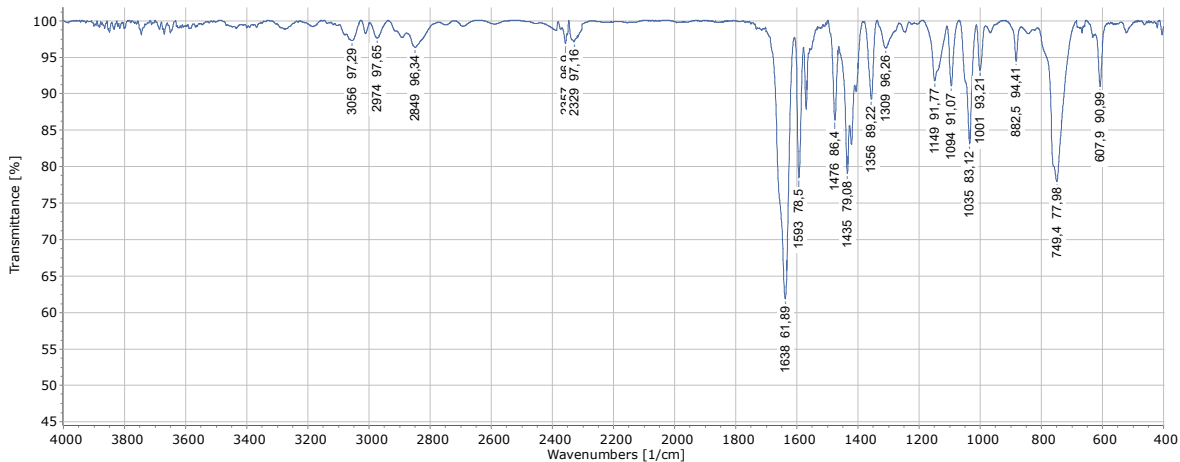


Figure 57 FTIR Spectra for L4

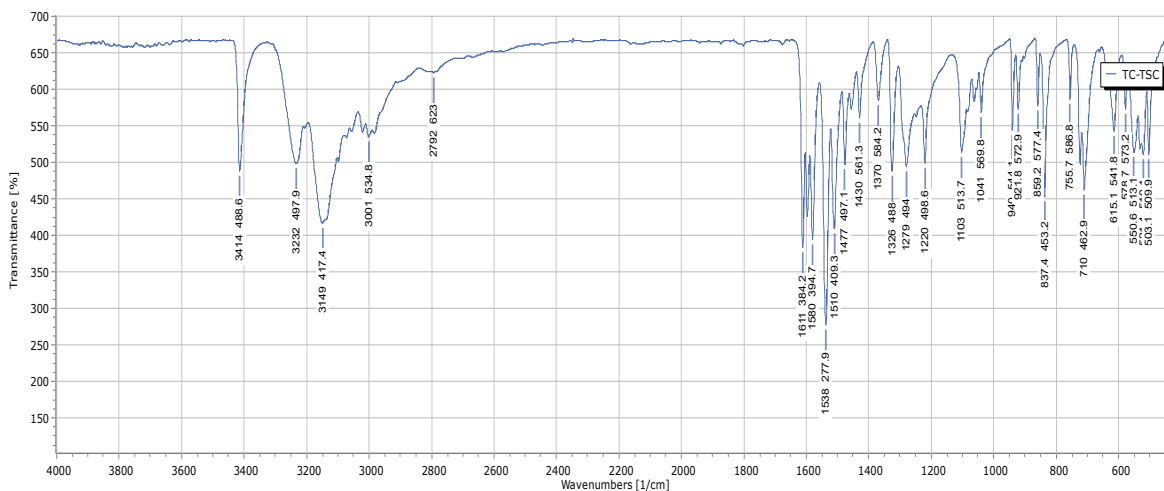


Figure 58 FTIR Spectra for L5

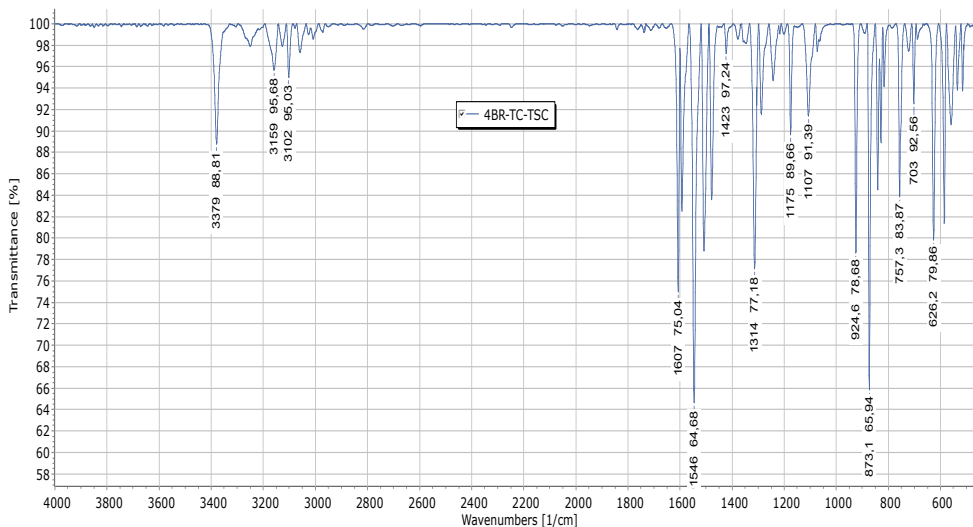


Figure 59 FTIR Spectra for L7

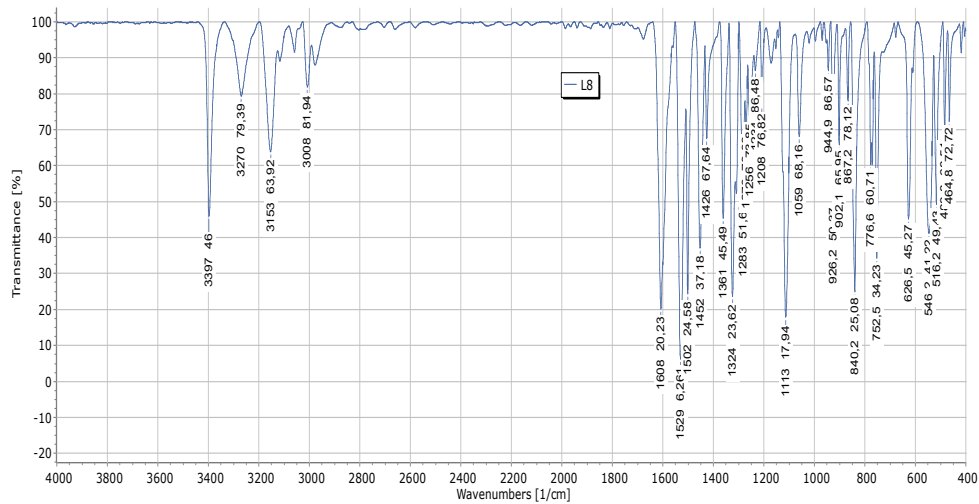


Figure 60 FTIR Spectra for L8

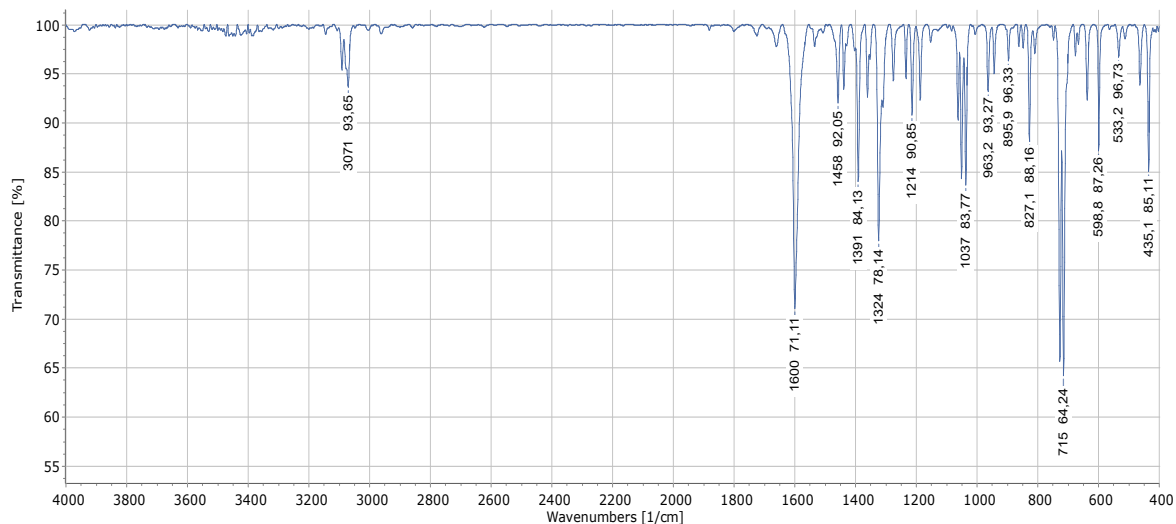


Figure 61 FTIR Spectra for C2

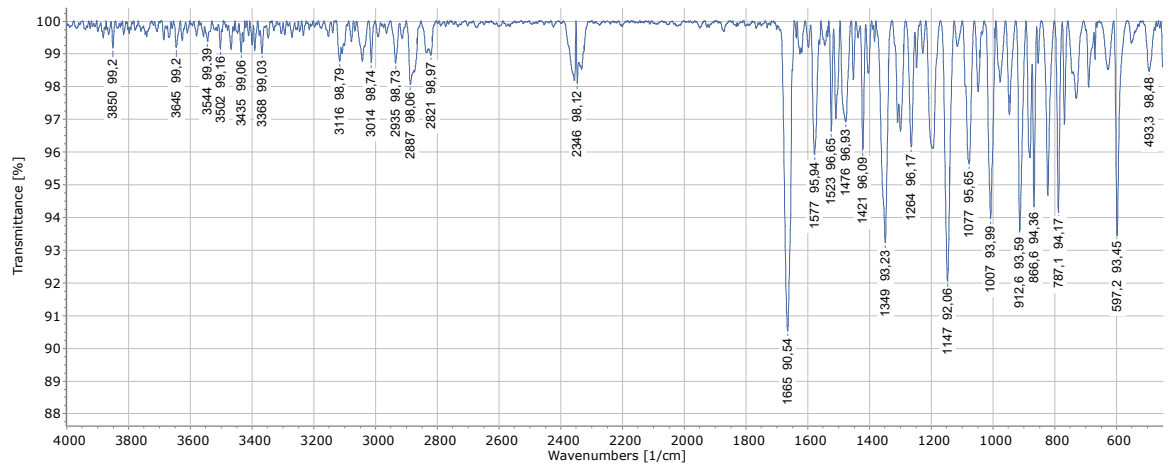


Figure 62 FTIR Spectra for C3

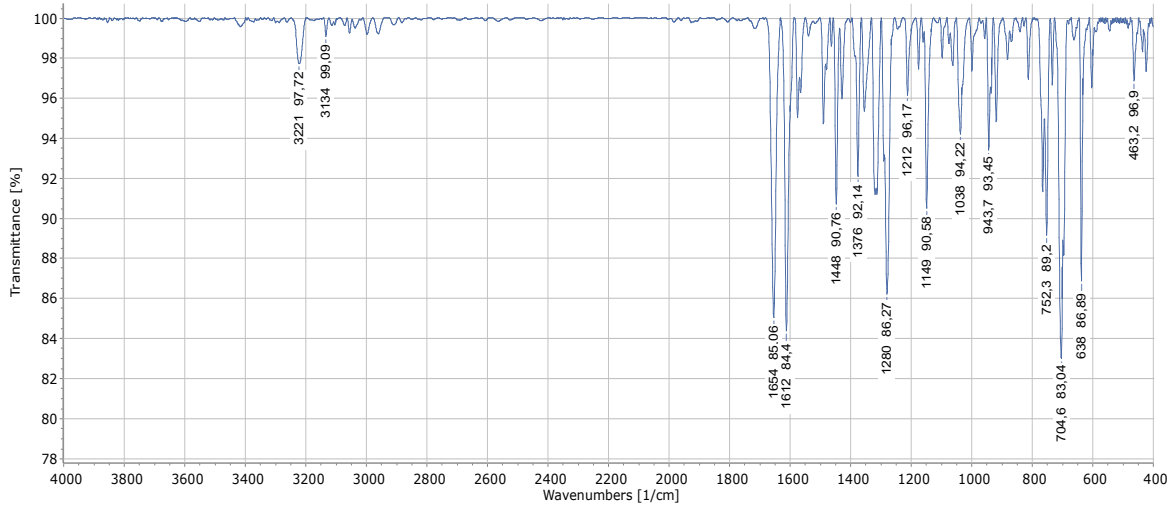


Figure 63 FTIR Spectra for C4

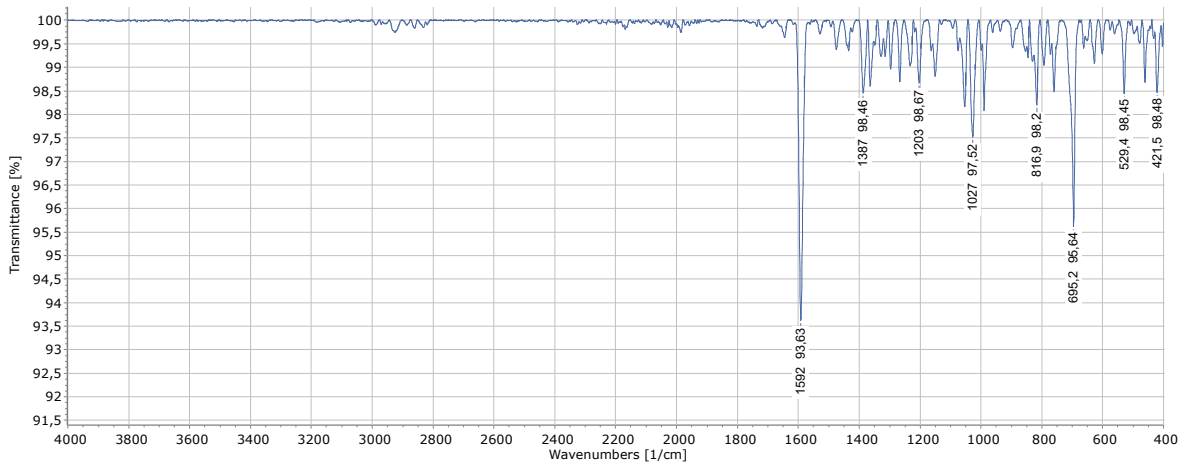


Figure 64 FTIR Spectra for C5

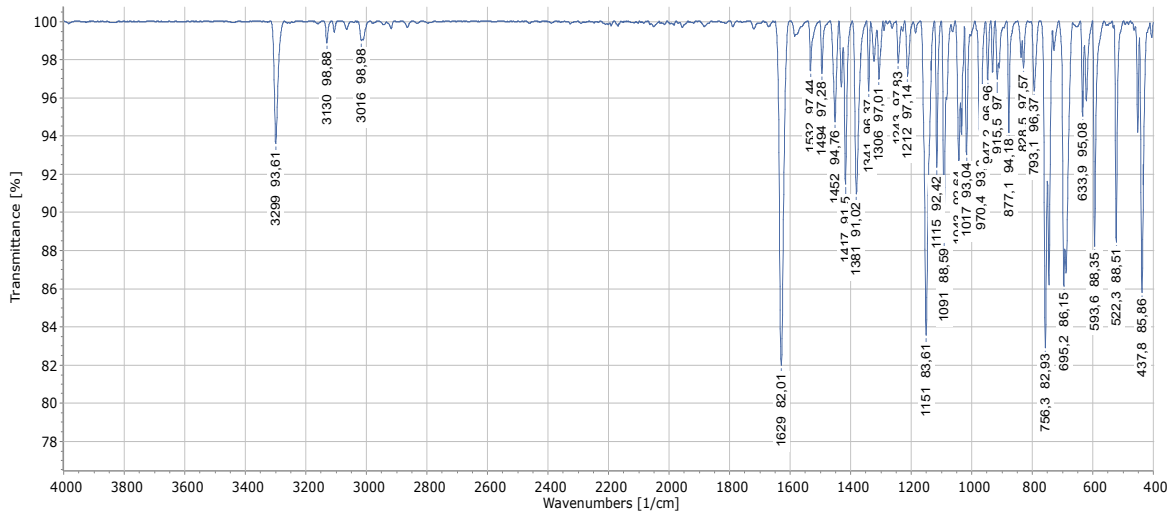


Figure 65. FTIR Spectra for C6

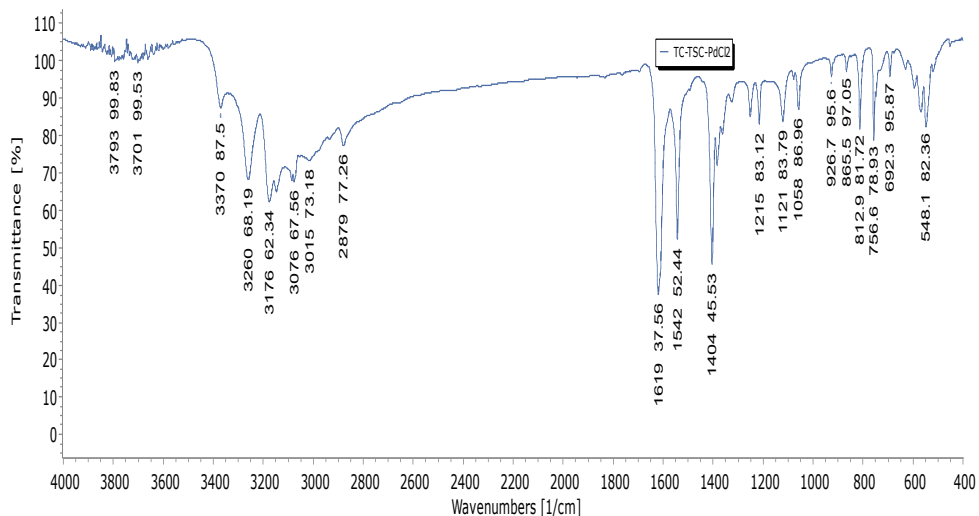


Figure 66 FTIR Spectra for C7

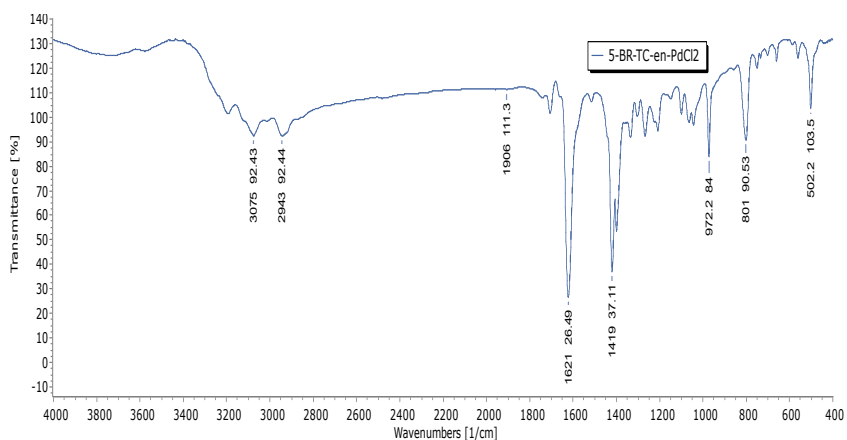


Figure 67 FTIR Spectra for C8

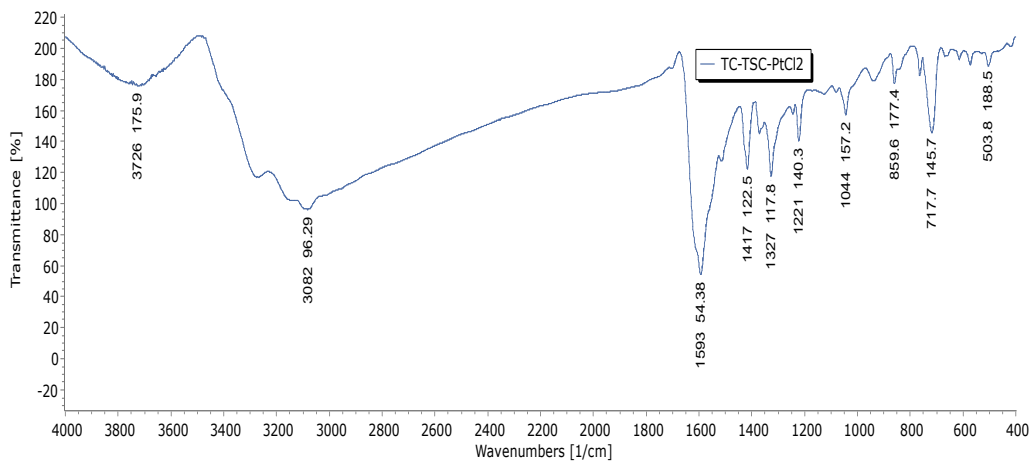


Figure 68 FTIR Spectra for C10

Proton Nuclear Magnetic Resonance spectra for the Ligands

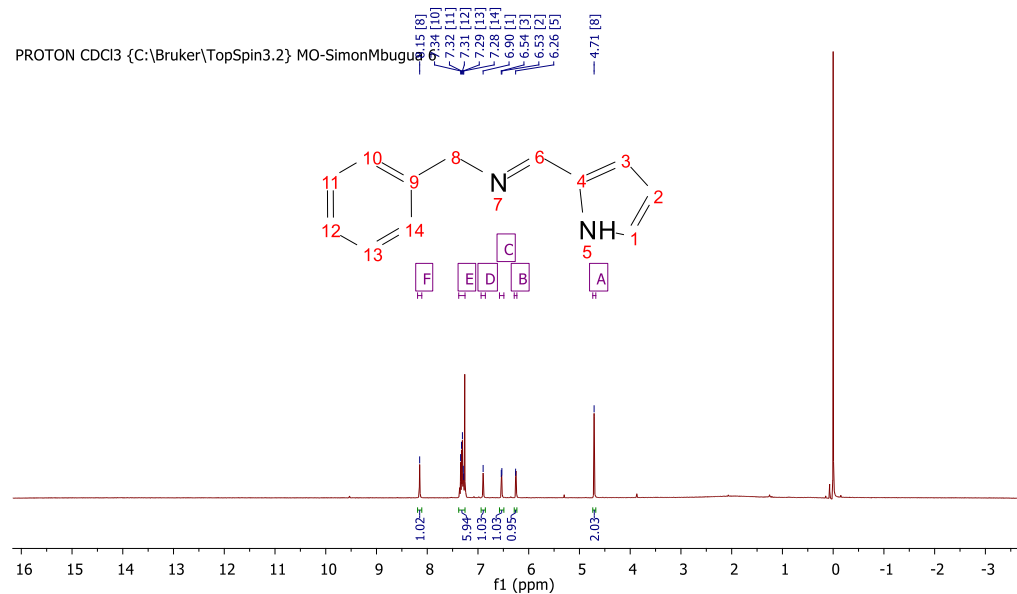


Figure 69 ¹H NMR for L1

PROTON CDCl₃ {C:\Bruker\TopSpin3.2} MO-SimonMbugua 4

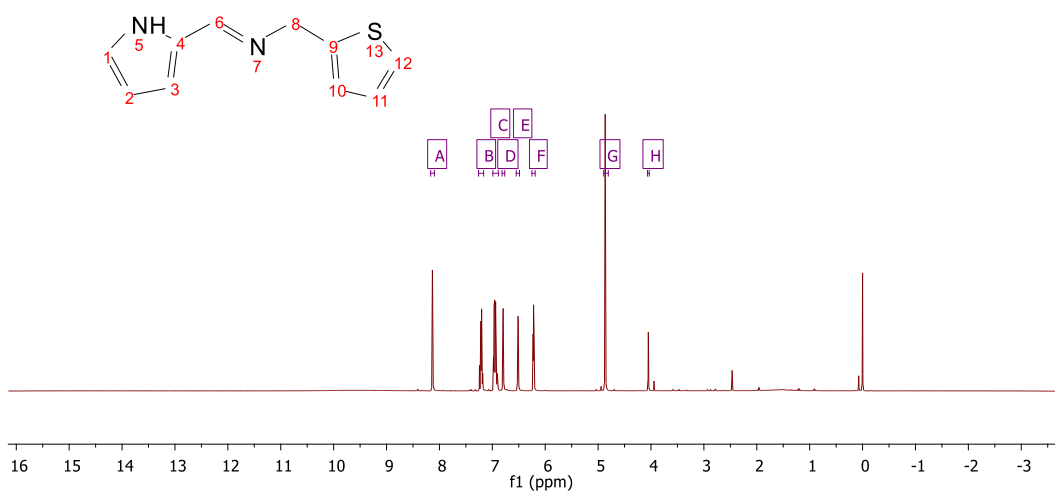
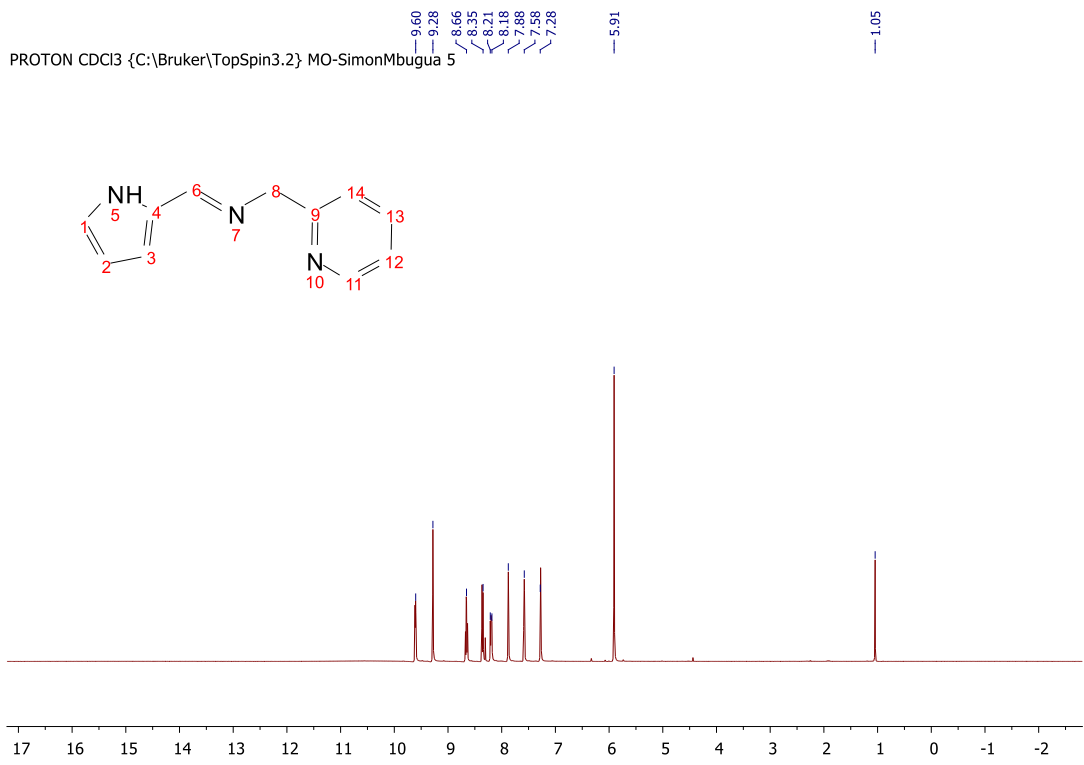
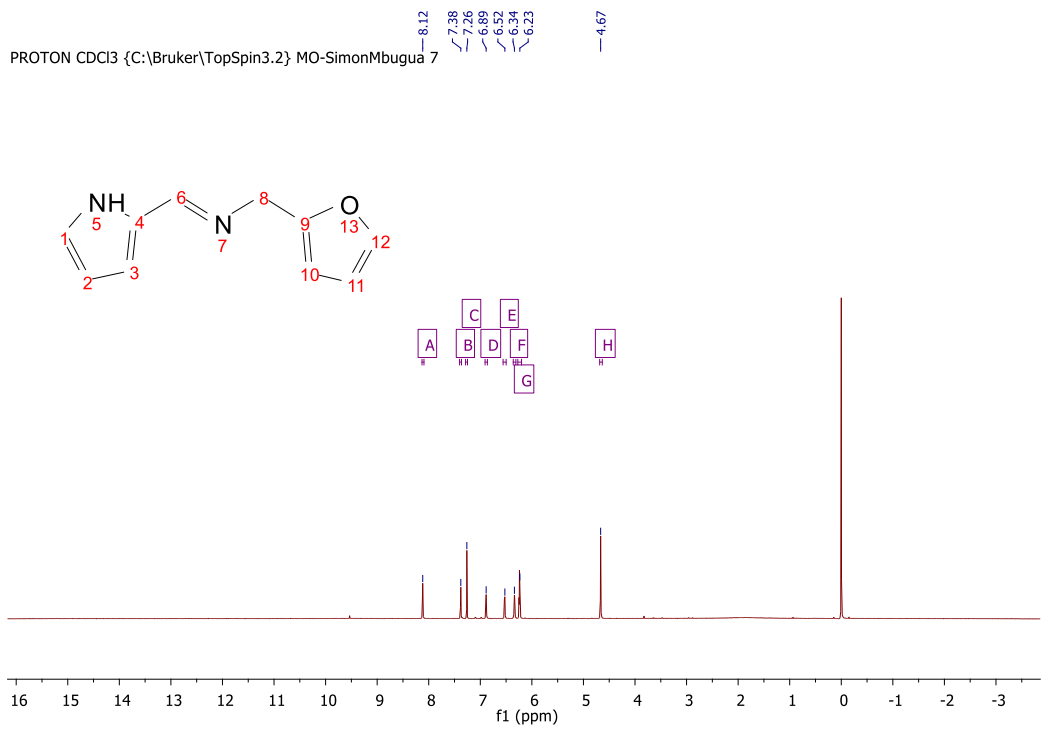


Figure 70 ¹H NMR for L2



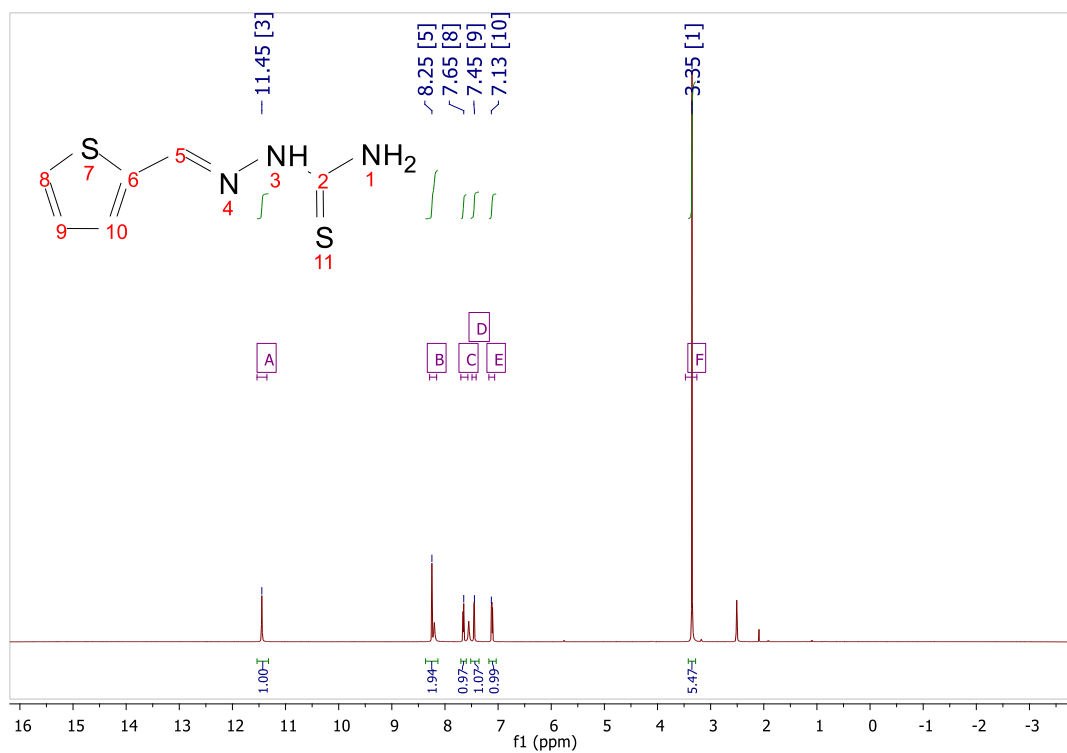


Figure 73 ¹H NMR for L5

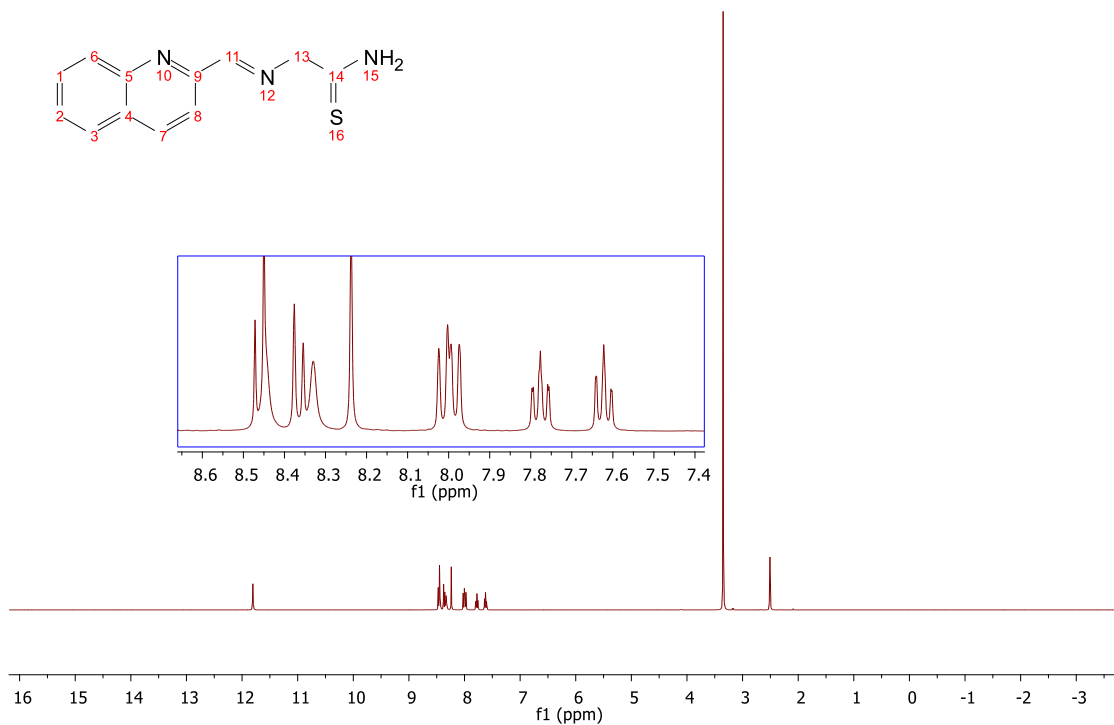


Figure 74 ¹H NMR for L8

Proton Nuclear Magnetic Resonance Spectra for the Complexes

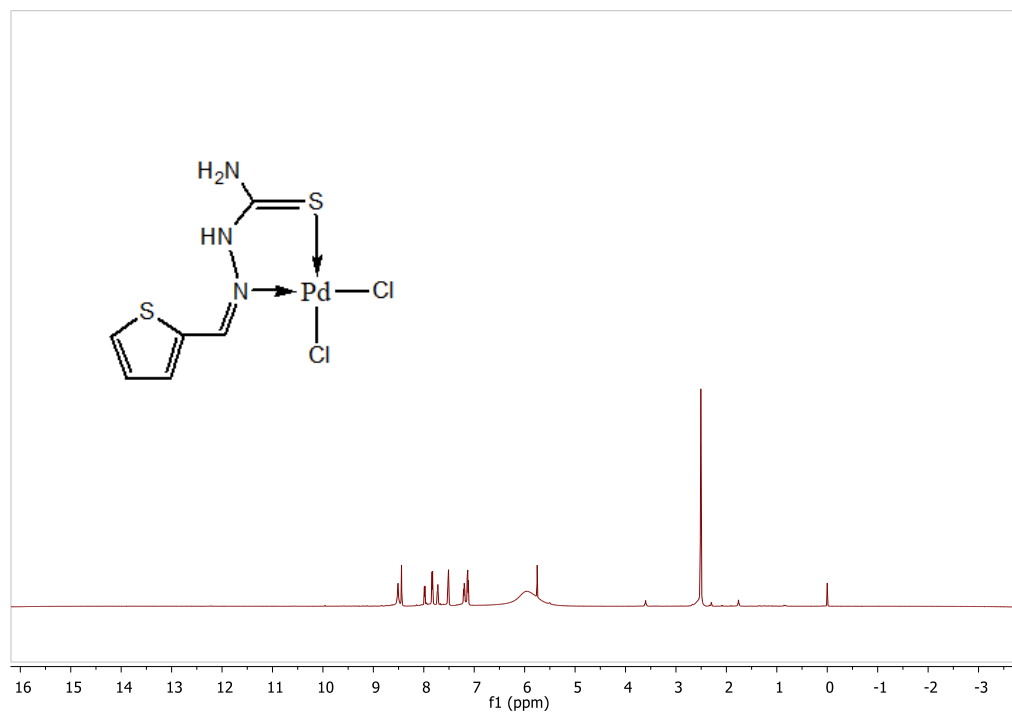


Figure 75 ¹H NMR for C7

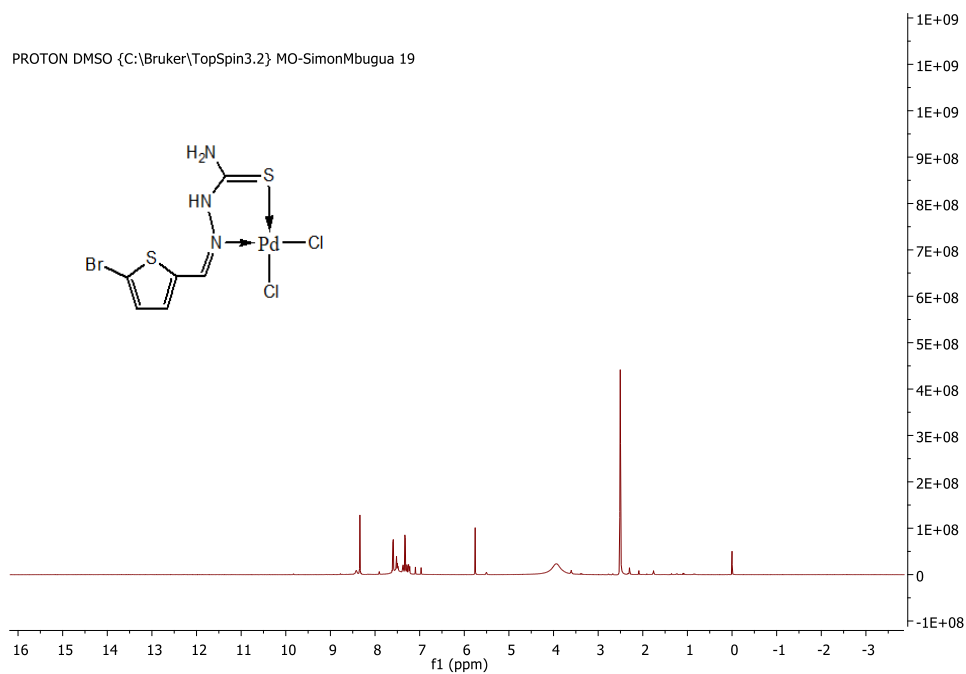


Figure 76 ¹H NMR for C8

QC- TSC- Me

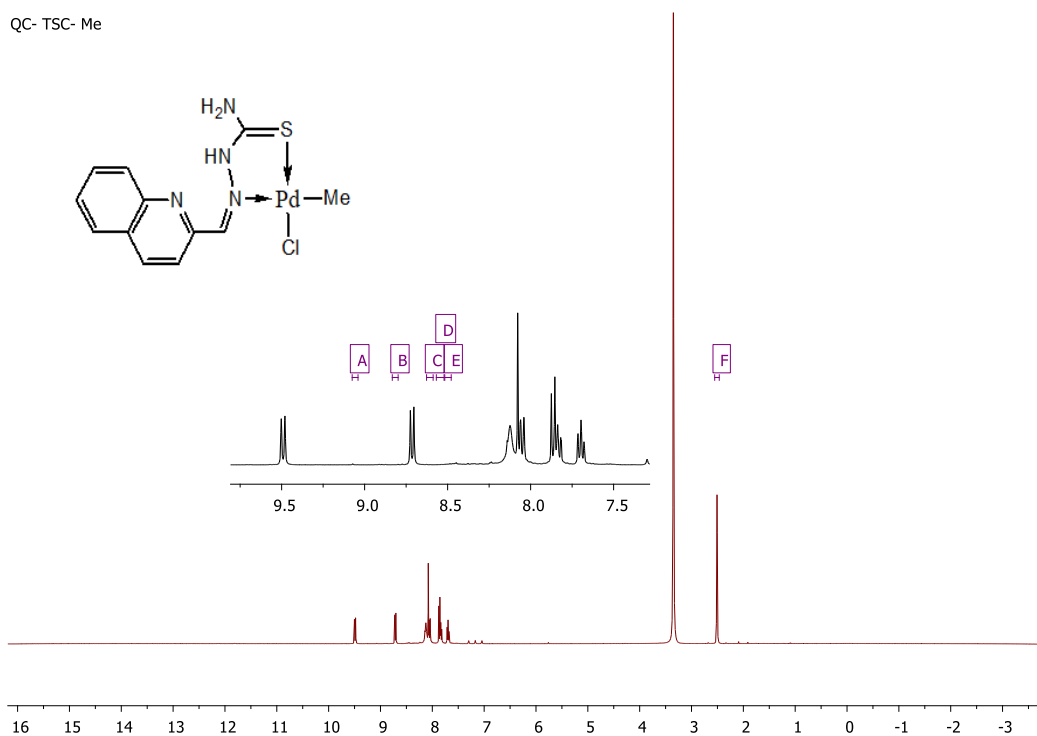


Figure 77 ¹H NMR for C9

PROTON DMSO PC-BA-Pt

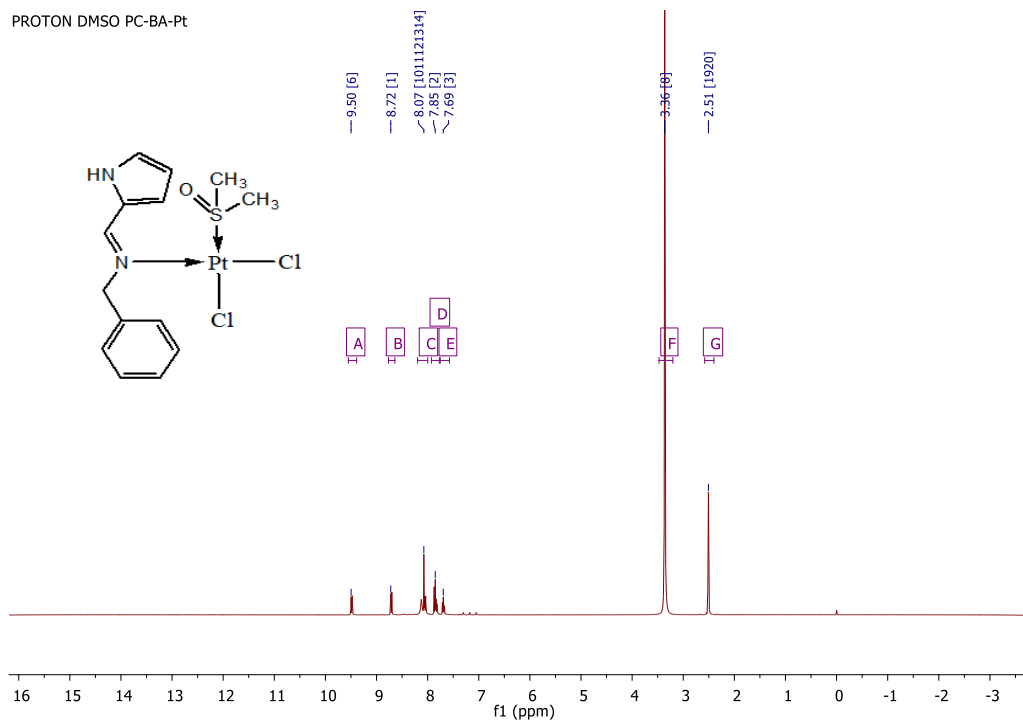


Figure 78 ¹H NMR for C6

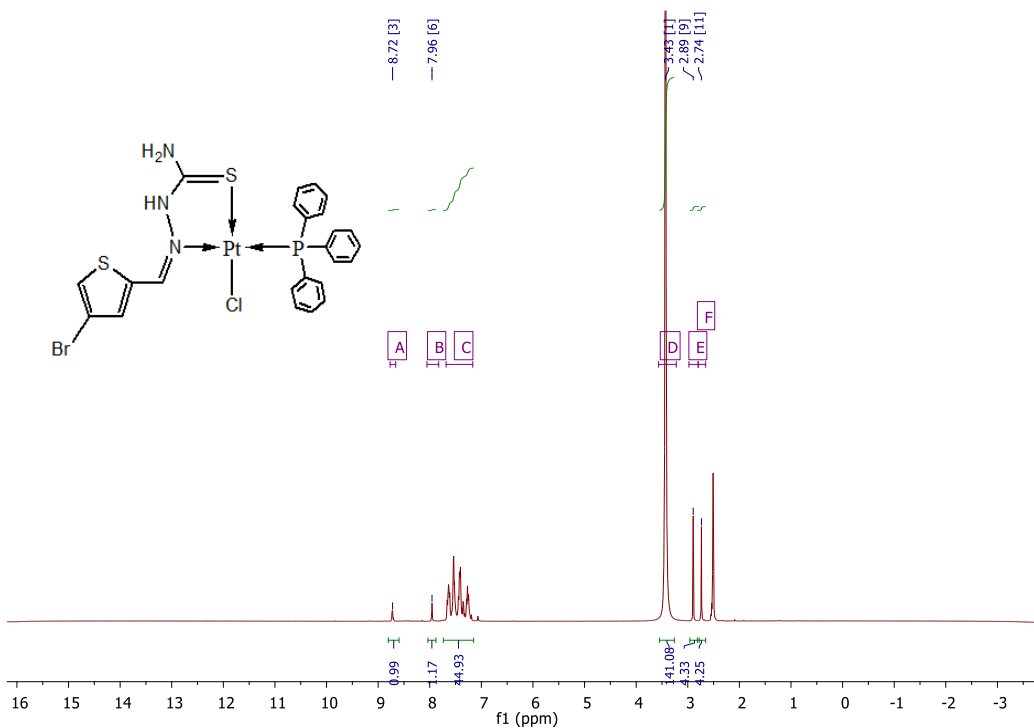


Figure 79 ¹H NMR for C11

Carbon-13 Nuclear Magnetic Resonance Spectra for the Ligands

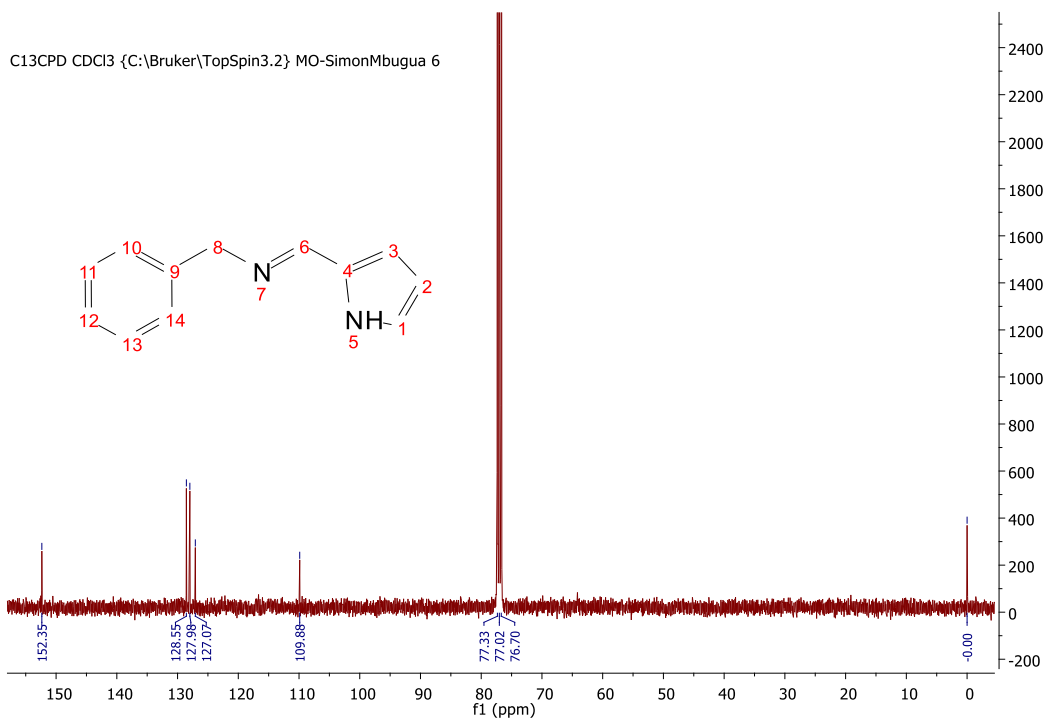


Figure 80 ¹³C NMR for L1

C13CPD CDCl3 {C:\Bruker\TopSpin3.2} MO-SimonMbugua 4

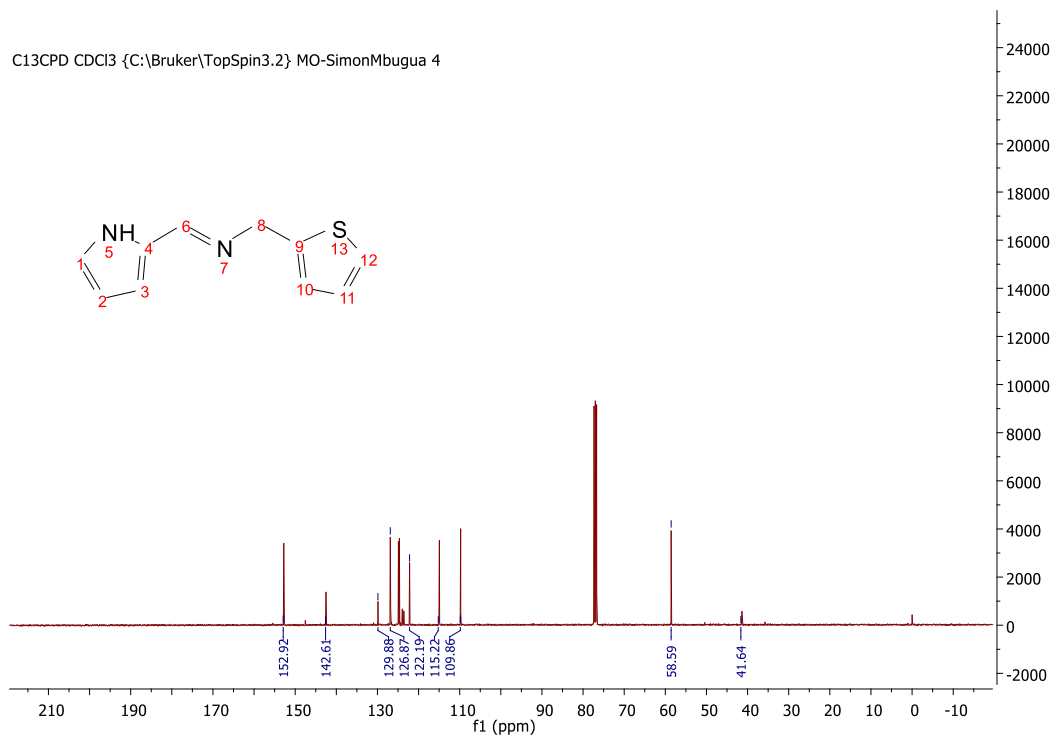


Figure 81 ¹³C NMR for L2

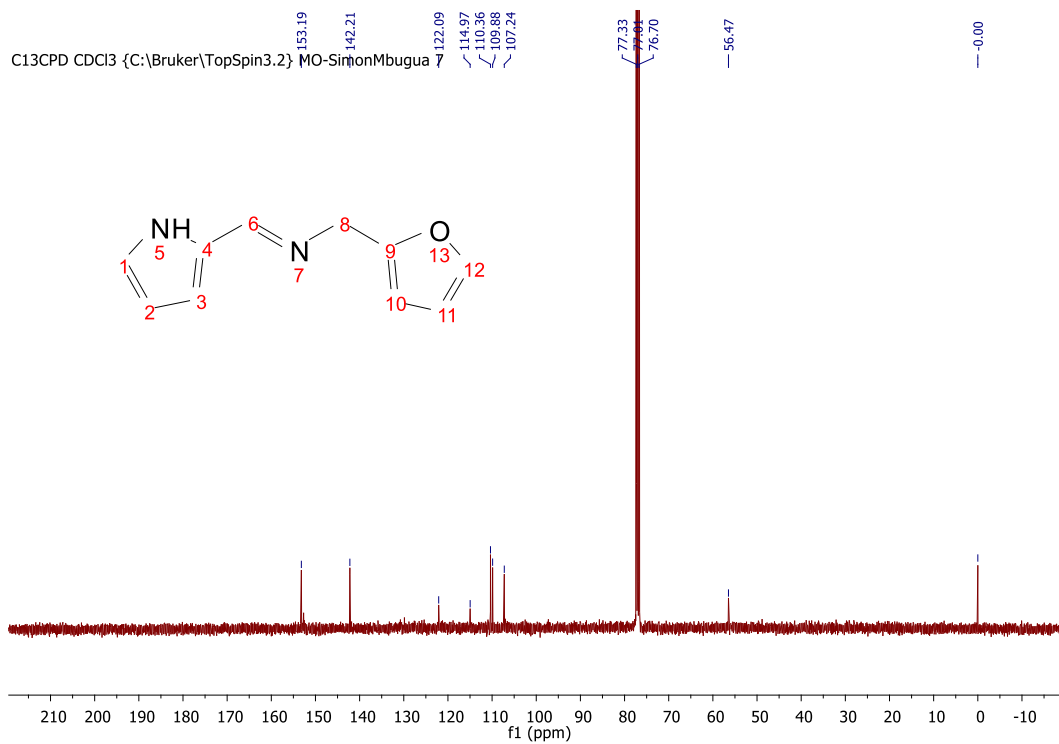


Figure 82 ¹³C-NMR for L3

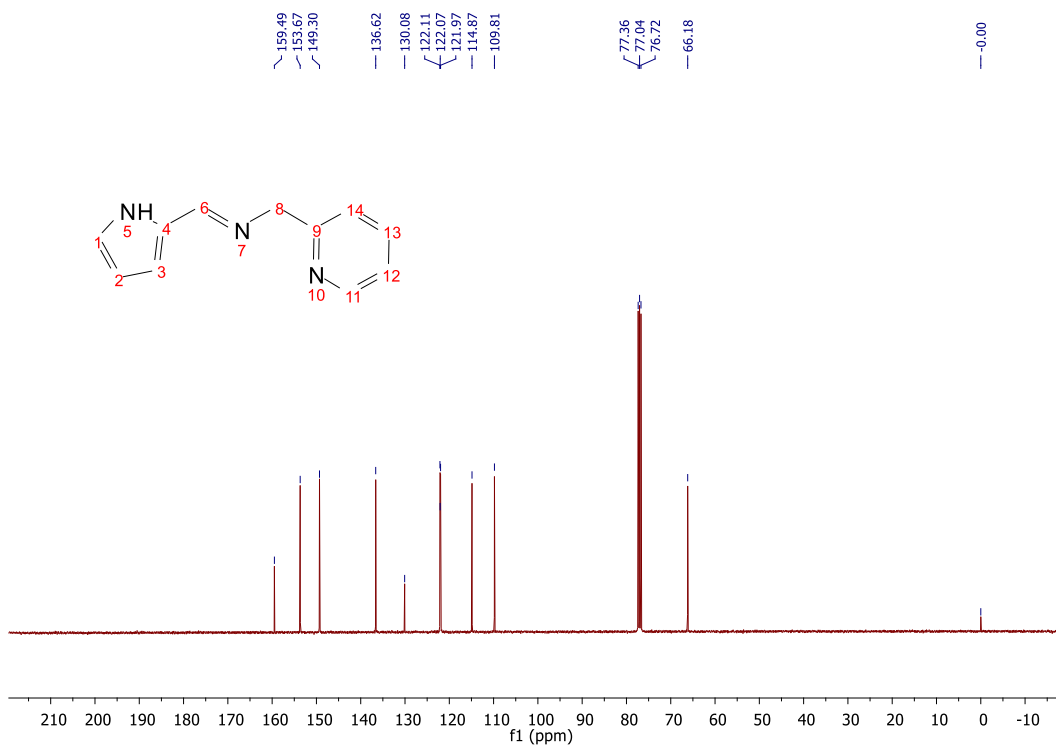


Figure 83 ^{13}C NMR for L4

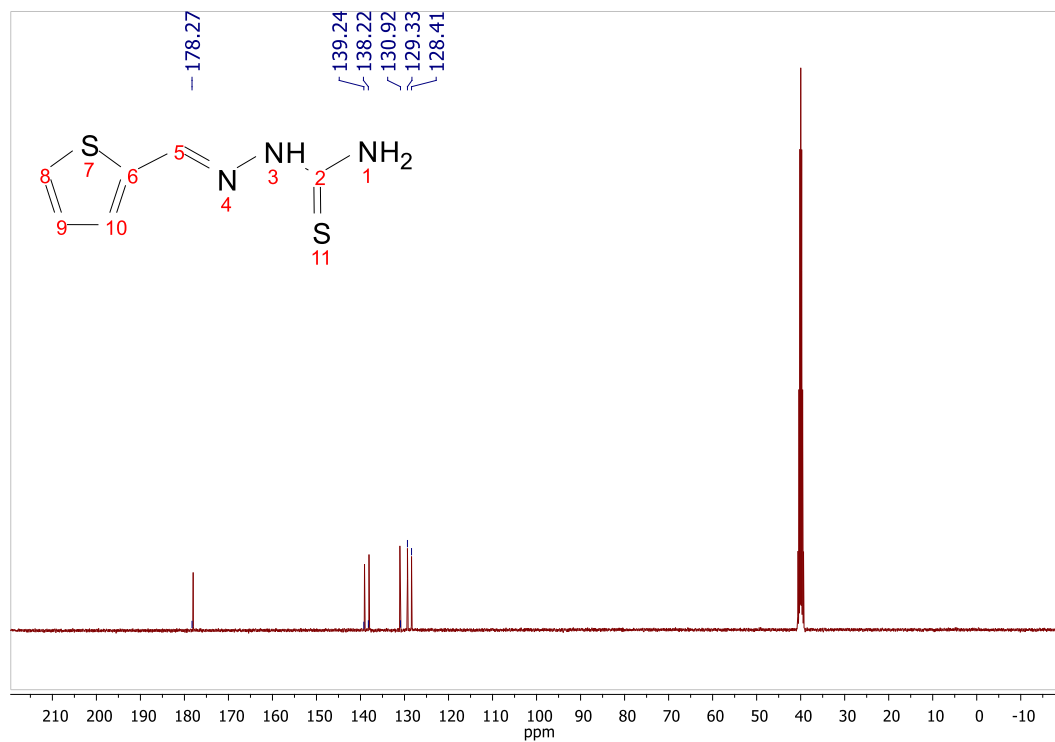


Figure 84 ^{13}C NMR for L5

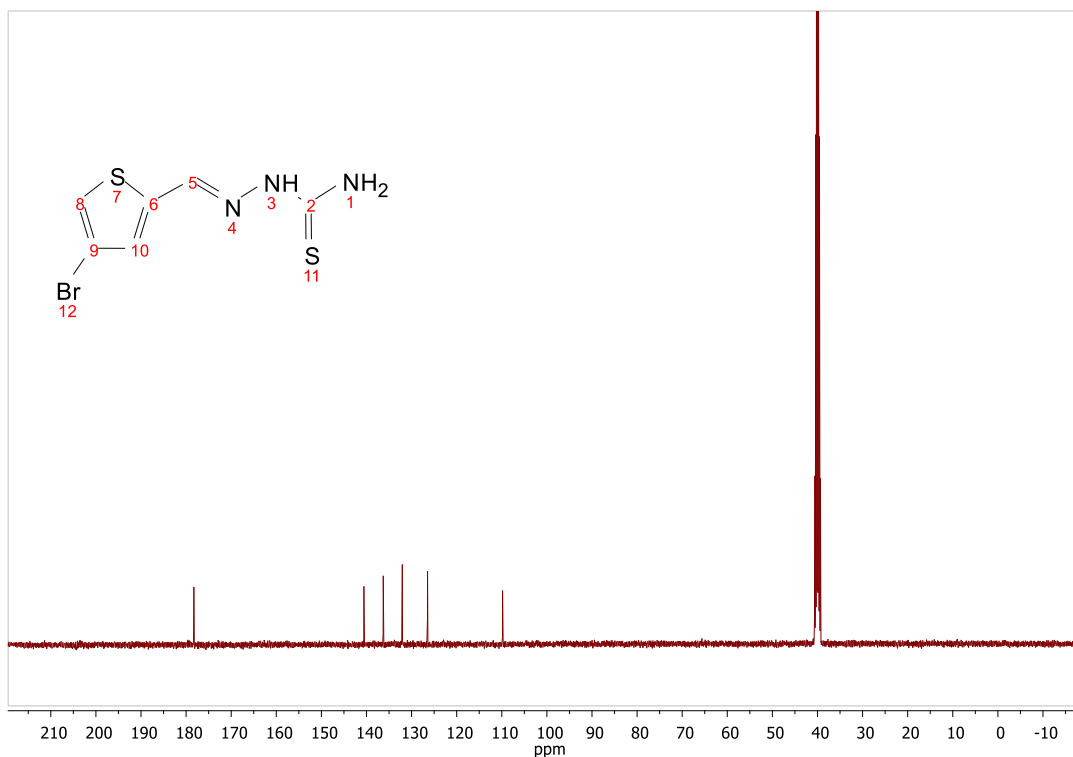


Figure 85 ¹³C NMR for L7

QC-TSC C13

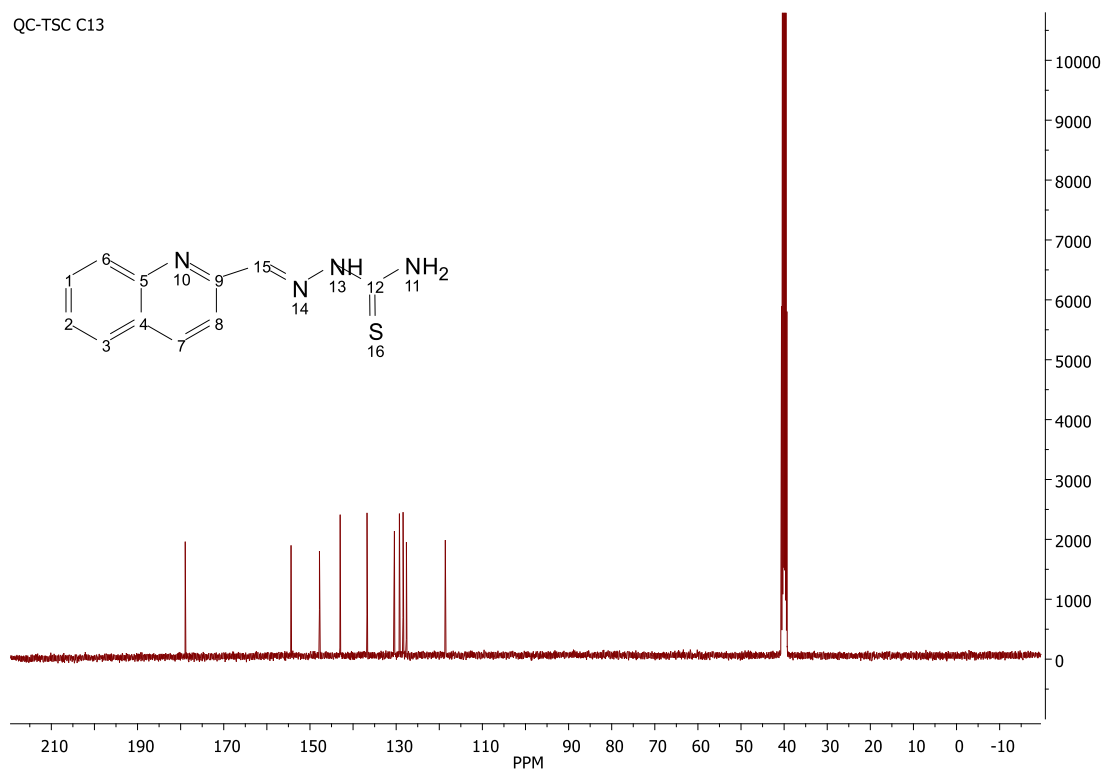
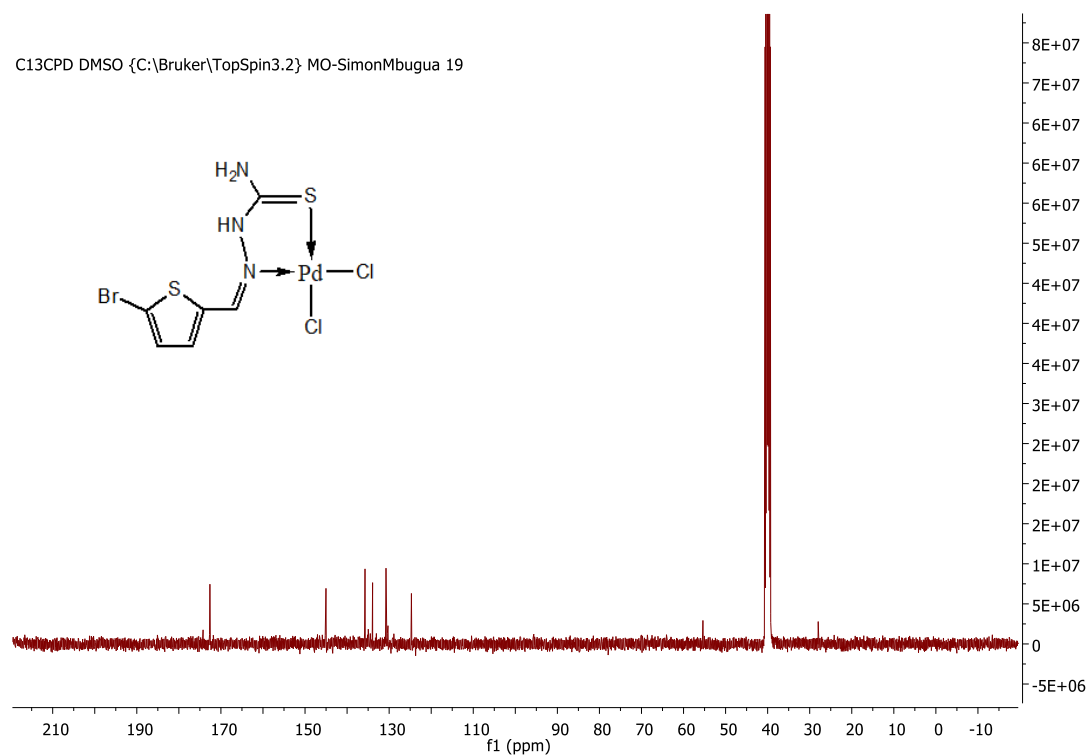
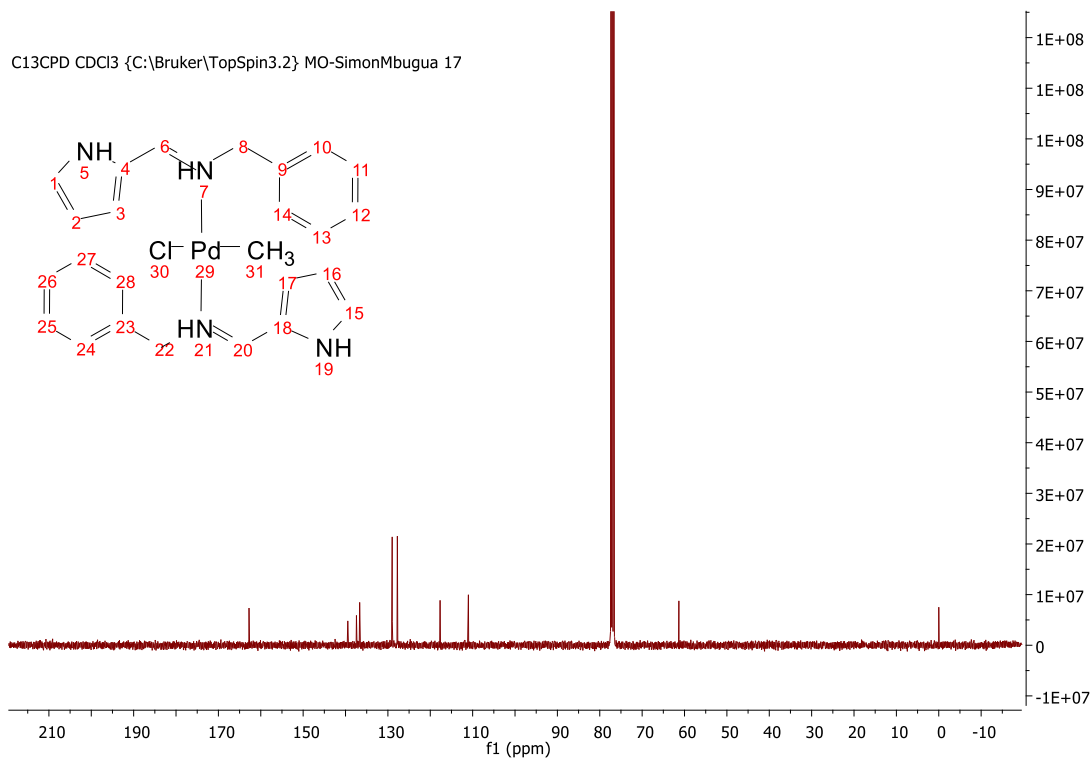


Figure 86 ¹³C NMR for L8

Carbon-13 Nuclear Magnetic Resonance Spectra for the Complexes



QC- TSC- Me C13

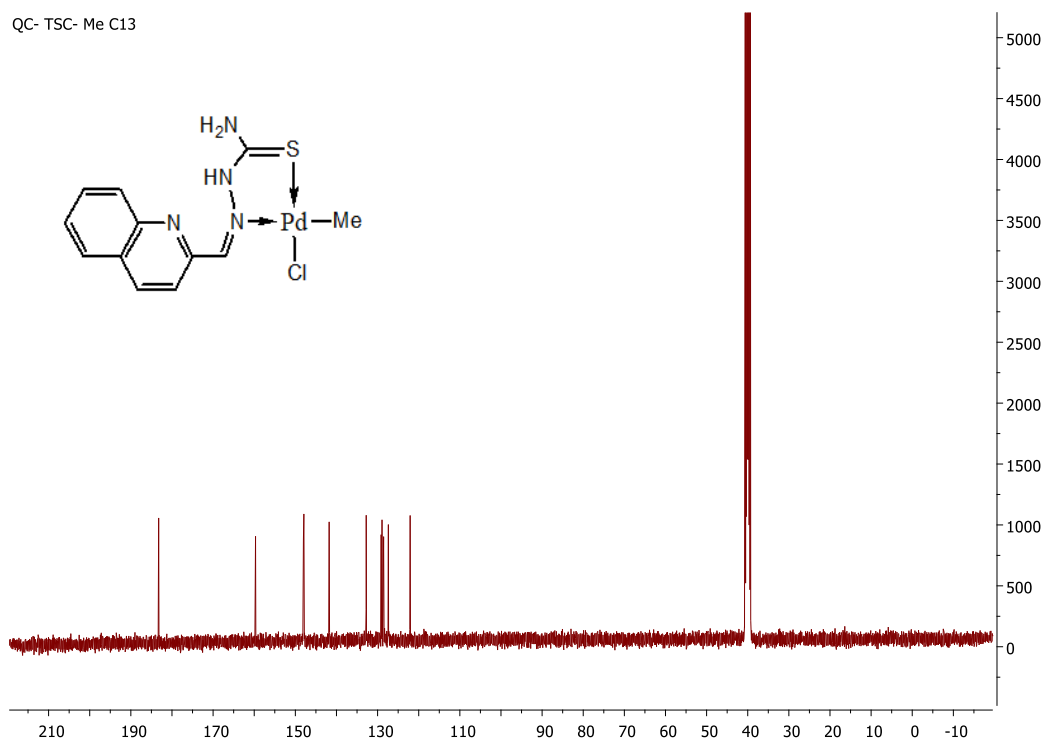


Figure 89 ¹³C-NMR for C9

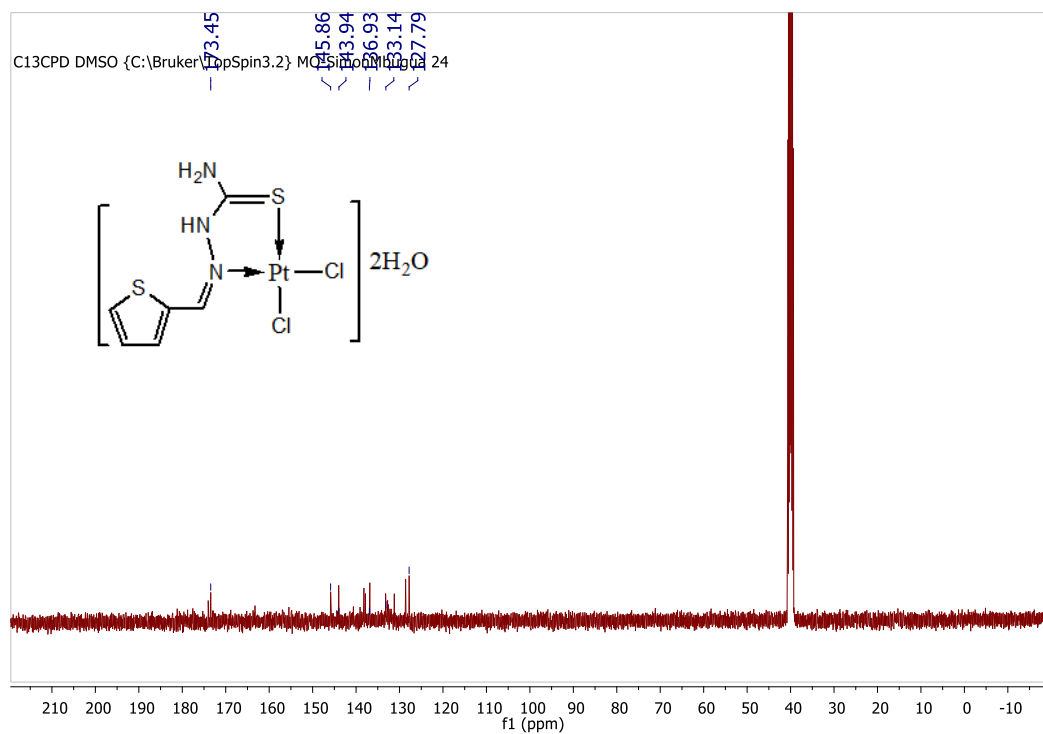


Figure 90 ¹³C-NMR for C10

UV/Vis Spectra for selected Ligands and Complexes

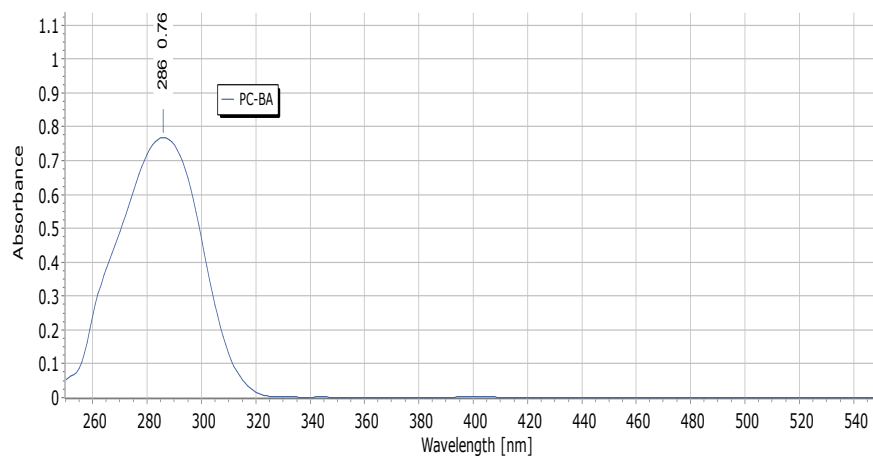


Figure 91 UV-Vis for L1

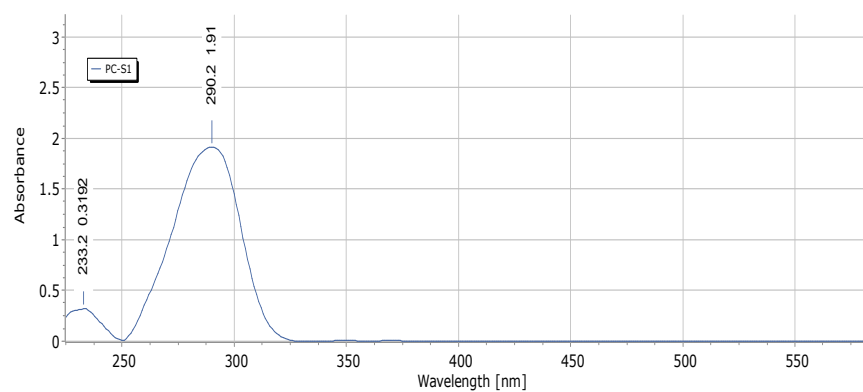


Figure 92 UV-Vis for L2

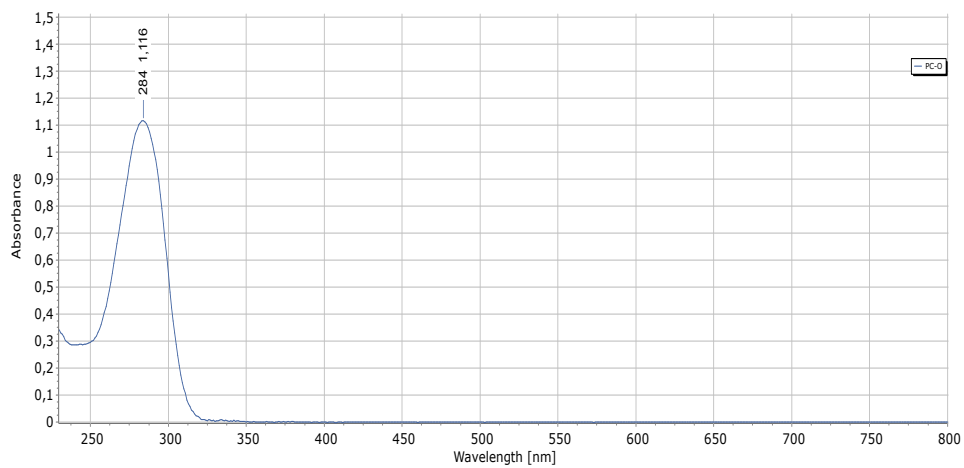


Figure 93 UV-Vis for L3

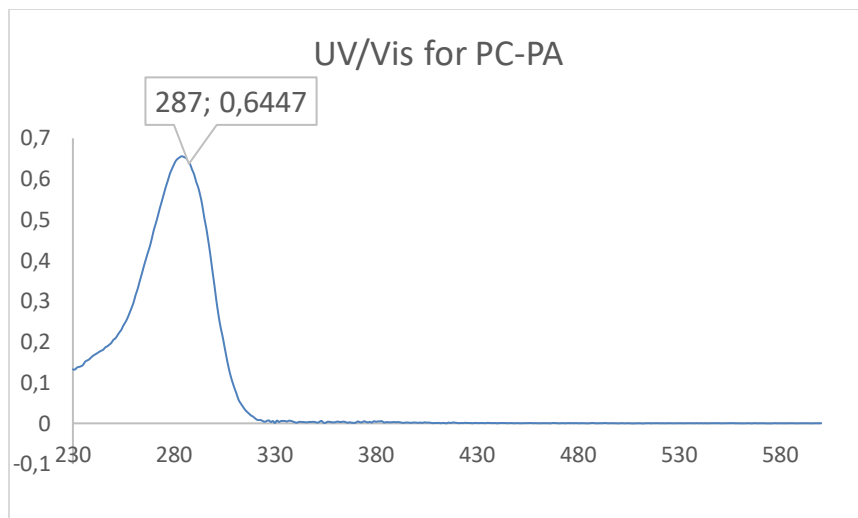


Figure 94 UV-Vis for L4

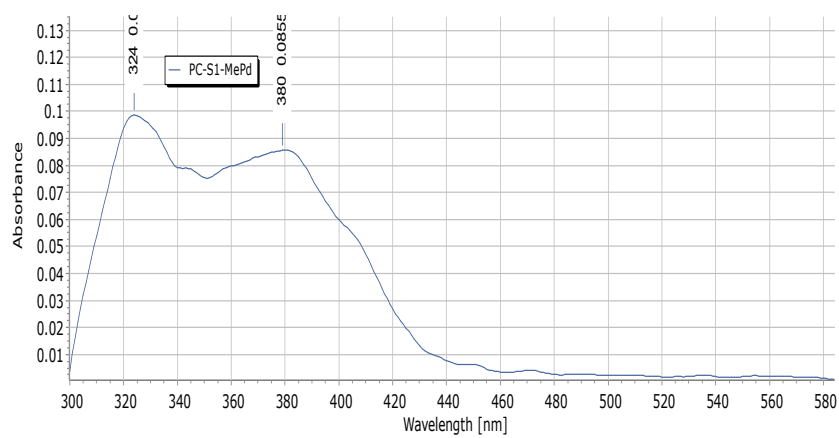


Figure 95 UV-Vis Spectra for C2

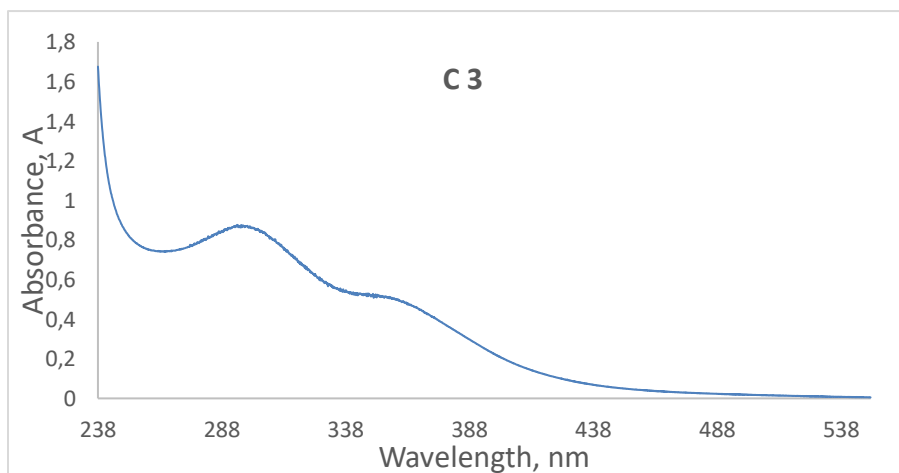


Figure 96 UV-Vis Spectra for C3

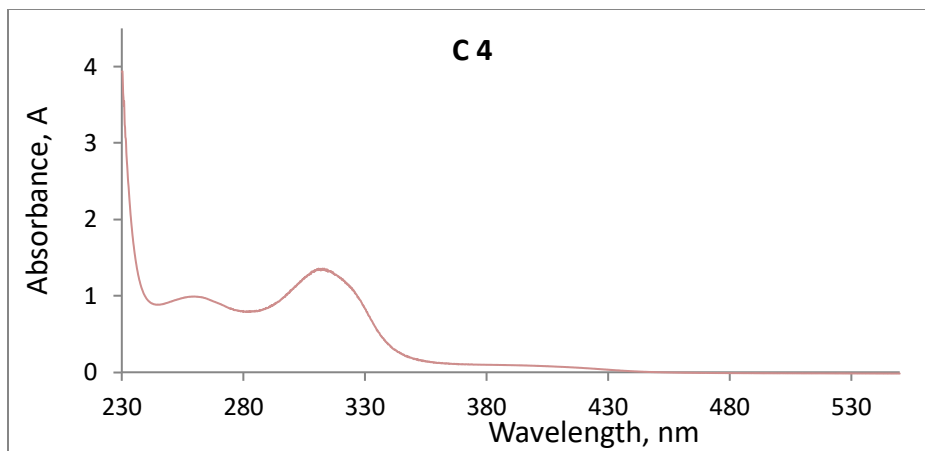


Figure 97 UV-Vis Spectra for C4

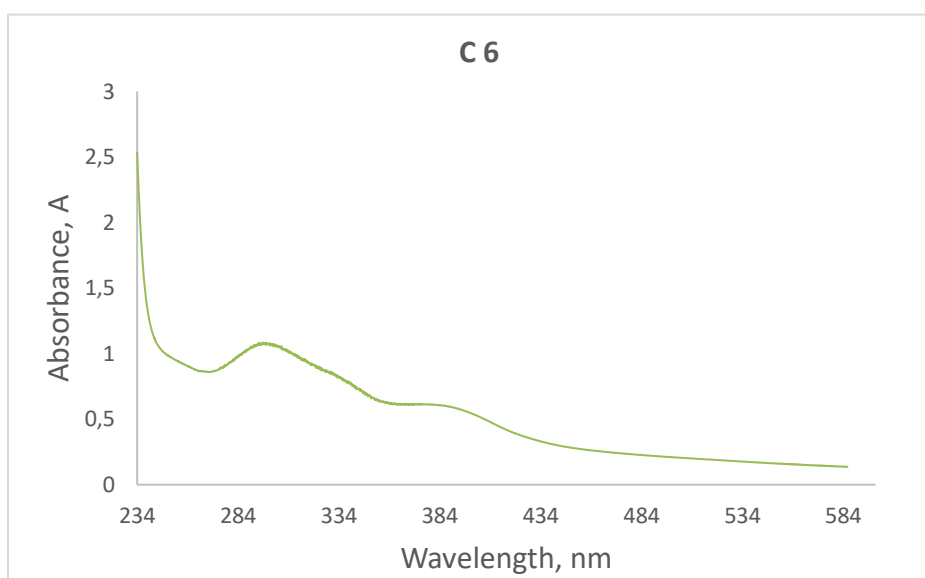


Figure 98 UV-Vis Spectra for C6

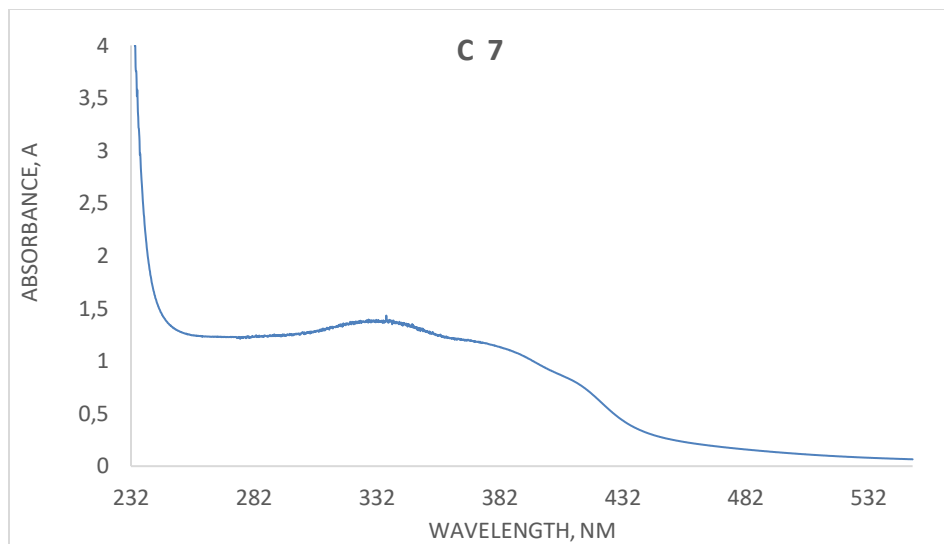


Figure 99 UV-Vis Spectra for C7

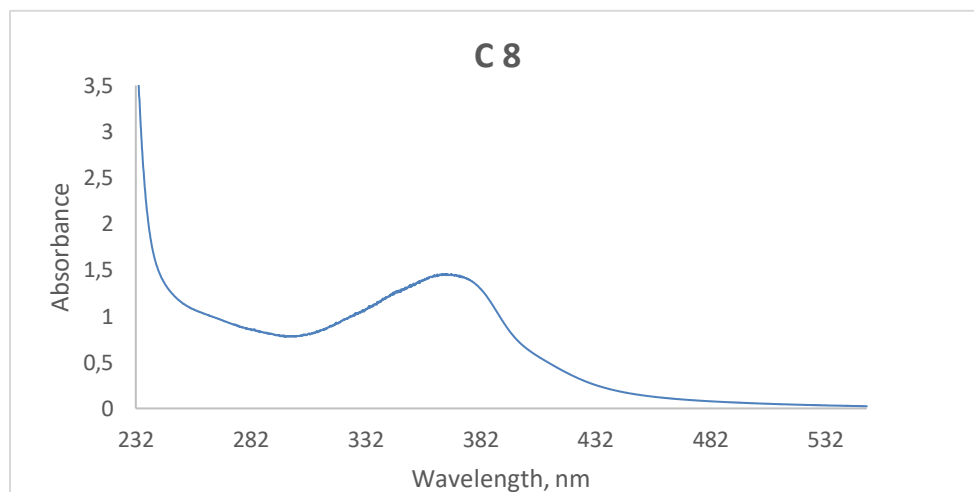


Figure 100 UV-Vis Spectra for C8

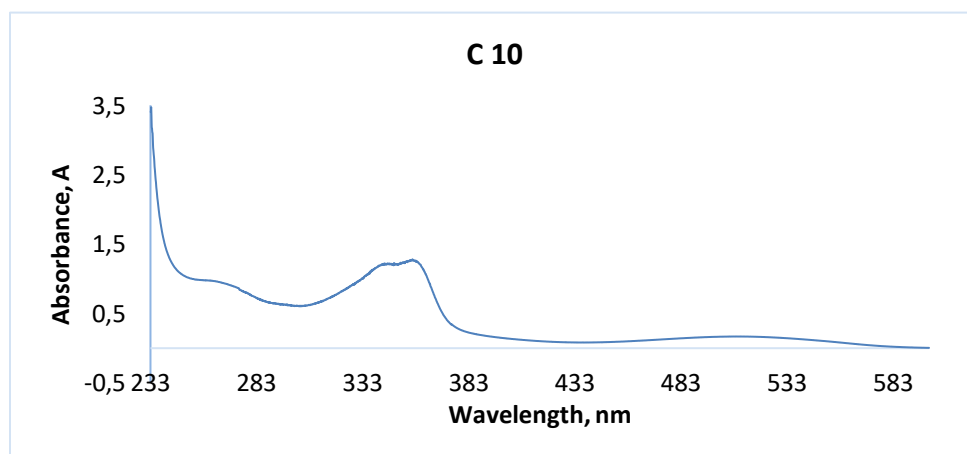


Figure 101 UV-Vis Spectra for C10

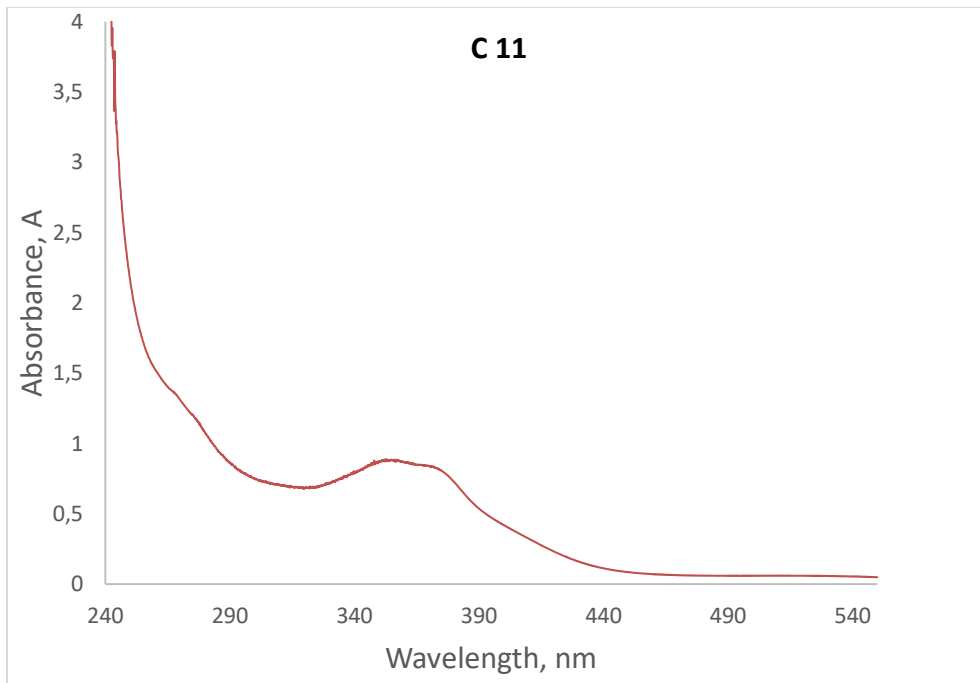


Figure 102 UV-Vis Spectra for C11

Publications

New Palladium(II) and Platinum(II) Complexes Based on Pyrrole Schiff Bases: Synthesis, Characterization, X-ray Structure, and Anticancer Activity

Simon N. Mbugua, Nicole R. S. Sibuyi, Lydia W. Njenga, Ruth A. Odhiambo, Shem O. Wandiga, Mervin Meyer, Roger A. Lalancette, and Martin O. Onani*



Cite This: <https://dx.doi.org/10.1021/acsomega.0c00360>



Read Online

ACCESS |



Metrics & More

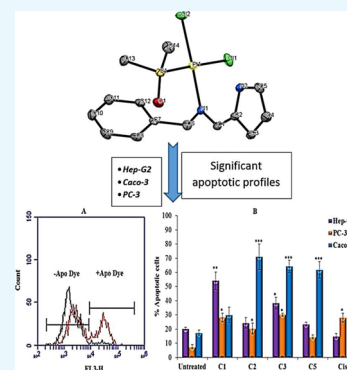


Article Recommendations



Supporting Information

ABSTRACT: New palladium (Pd)II and platinum (Pt)II complexes (C1–C5) from the Schiff base ligands, R-(phenyl)methanamine (L1), R-(pyridin-2-yl)methanamine (L2), and R-(furan-2-yl)methanamine (L3) (R-(*E*)-N-((1*H*-pyrrol-2-yl) methylene)) are herein reported. The complexes (C1–C5) were characterized by FTIR, ¹H and ¹³C NMR, UV–vis, and microanalyses. Single-crystal X-ray crystallographic analysis was performed for the two ligands (L1–L2) and a Pt complex. Both L1 and L2 belong to P₂₁/*n* monoclinic and P-1 triclinic space systems, respectively. The complex C5 belongs to the P2₁/*c* monoclinic space group. The investigated molar conductivity of the complexes in DMSO gave the range 4.0–8.8 μS/cm, suggesting neutrality, with log *P* values ≥ 1.2692 ± 0.004, suggesting lipophilicity. The anticancer activity and mechanism of the complexes were investigated against various human cancerous (Caco-2, HeLa, HepG2, MCF-7, and PC-3) and noncancerous (MCF-12A) cell lines using 3-(4,5-dimethylthiazol-2-yl)-2,5-diphenyltetrazolium bromide (MTT) and Apopercantage assays, respectively. C5 demonstrated strong DNA-binding affinity for calf thymus DNA (CT-DNA) with a binding constant of 8.049 × 10⁴ M⁻¹. C3 reduced cell viability of all the six cell lines, which included five cancerous cell lines, by more than 80%. The C5 complex also demonstrated remarkably high selectivity with no cytotoxic activity toward the noncancerous breast cell line but reduced the viability of the five cancerous cell lines, which included one breast cancer cell line, by more than 60%. Further studies are required to evaluate the selective toxicity of these two complexes and to fully understand their mechanism of action.



INTRODUCTION

According to WHO, Cancer is the second leading cause of death globally and is responsible for an estimated 9.6 million deaths in 2018.¹ Globally, about 1 in 6 deaths is due to cancer.² New anticancer agents, which can effectively treat this disease with minimal side effects, remain of primary importance to the world research community.^{3–5}

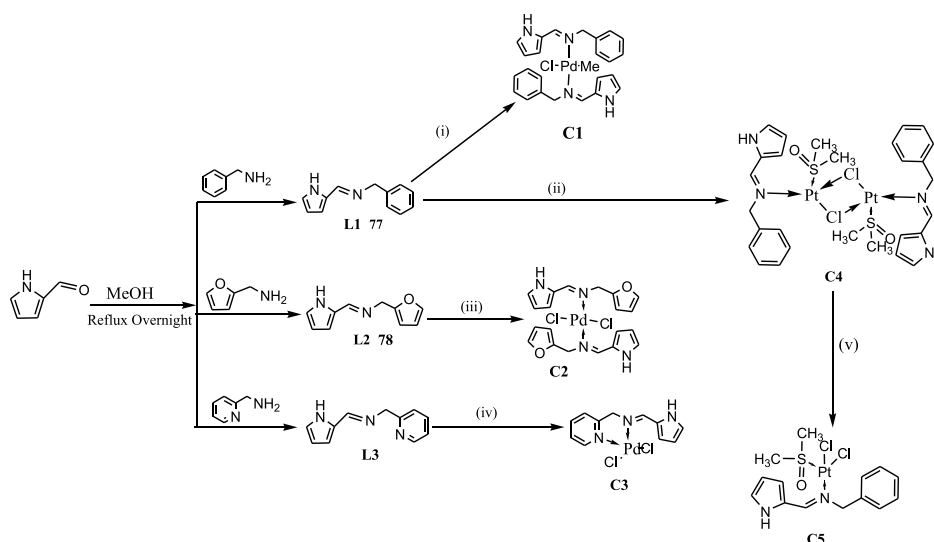
The development of drug resistance and disease relapse are major challenges in anticancer drug development.⁶ This factor is of crucial significance in the world where this disease continues to burden global health care systems and escalate the mortality rates.⁷ Metals have long been useful in treatment of various ailments known to man.⁸ Because of their unique properties, metal complexes, especially those containing transition metals have gained tremendous attention as anticancer agents.⁹ Most recently, the metal complexes derived from pyrrole moieties have shown good antiproliferative activity against lymphocytic, cervical, and breast cancer cells.^{10–12} A series of pyrrole-based ferrocene complexes were also reported to be cytotoxic against breast cancer (MCF-7),¹³ colon cancer (HT-29) cell lines, and non-cancerous breast cells (MCF-10A).¹⁴ Equally, the known cancer drug to date, cisplatin has undergone various

derivatization. The analogues containing bulky groups have displayed enhanced cytotoxicity profiles against cisplatin-resistant cells. This led to a conclusion that the steric shielding of the metal center can regulate ligand substitution and consequently increase an efficiency to DNA binding.¹⁵ The binding interactions is best followed by spectroscopy studies, where an observation of the alterations in the λ_{max} absorption values appear as a result of π–π* intraligand transitions, ligand → metal/metal → ligand charge transfers, or on the d–d transitions.¹⁶ During any of these mentioned processes, the DNA concentration is serially increased to the metal complex. Various modes of binding are then deduced from the spectral response, whereby an intercalative manner of interaction is specified by a hypochromic shift, bathochromic shift, or hypsochromism.¹⁷ Intercalation of a complex with the base

Received: January 25, 2020

Accepted: May 14, 2020

Scheme 1. Synthetic Routes for the Ligands and Their Corresponding Complexes; (i) Pd(cod)ClMe, DCM, Room Temperature, 12 h; (ii) Pt(DMSO)₂Cl₂, DCM, Room Temperature; (iii) and (iv) Pd(cod)Cl₂, DCM, Room Temperature, 12 h; (v) Crystals Grown by Slow Evaporation of a DCM Solution of C4



pairs of DNAs is as a result of overlaps of π^* -antibonding orbitals of the ligands bound to the complex with π -bonding orbitals of the DNA base pairs.¹⁸ This decreases the probable transitions, and the effect is observed as a hypochromic shift.¹⁹ On the other hand, a hyperchromic shift suggests electrostatic mode of binding. The spectral shift in the metal complex absorption is correlated to the binding strength from which the kinetics can then be determined.²⁰ The investigation of drug–DNA interaction is important in understanding the molecular mechanism of drug action and for the design of the specific DNA-targeted drug.

Although the Schiff base ligands are reported in literature for C–C coupling reactions,²¹ their use in Pt or Pd complexes in anticancer studies has been limitedly studied, particularly, the pyrrole based Schiff bases. In this regard, the ligands and their corresponding Pd(II) and Pt(II) complexes were synthesized and characterized followed by investigation of their DNA binding and anticancer activities. The motivation behind this study was two-fold. First, these complexes have square planar geometry analogous to the common anticancer drug, cisplatin, but bears sterically bulky substituents around the metal center. This is a strategy reported in literature for prevention of an axial approach to the metal atom from the z^2 direction, thus hindering the formation of a trigonal bipyramidal intermediate, which leads to ligand substitution.²² In this way, the sterically bulky groups shield the labile ligands, therefore reducing the rate of hydrolysis and substitution long enough for the complexes to bind to the desired target. Second, the trans-geometry complexes have not been widely explored as anticancer agents despite literature reports that they could exhibit cytotoxicity equivalent to or greater than that of cisplatin.^{23–25}

RESULTS AND DISCUSSION

Synthesis of Organometallic Complexes. A series of pyrrole-based ligands and their corresponding Pd(II) and Pt(II) complexes are synthesized, as shown in Scheme 1. The ligands (L1–L3) were synthesized by standard Schiff base condensation reaction of pyrrole-2-carboxaldehyde either with benzyl amine (L1), 2-furanmethyl amine (L2), or 2-picoly-

amine (L3), under reflux overnight. To the best of our knowledge, this is the first time that the crystal structures of L1 and L2 are reported. The metal complexes (C1–C5) were obtained through the reaction of Pd(cod)Cl₂, Pd(cod)ClMe, or Pt(DMSO)₂Cl₂ precursors with a solution of ligand in DCM at room temperature. The complexes (C1 and C2) were formed through a reaction of 1:2 (metal/ligand) molar ratios using ligands L1 and L2, while C3 and C4 were formed from a 1:1 M ratio using L3 and L1, respectively, as shown in Error! Reference source not found.. Because of steric factors, the Pd complexes binding at 1:2 ratio (metal/ligand) are believed to be of trans-geometry. Similar work was reported on the bis-ferrocenyl Schiff base complexed with Pd which confirmed a monodentate binding of the Schiff bases to the metal center through the imine-N without involving the heteroatoms on the rings.²⁶ This resulted in a square planar geometry at the Pd center. These ratios were confirmed by elemental analysis.

The elemental analysis showed close agreement with the theoretical calculations confirming the proposed structures of the compounds. An interesting observation was made for the Pt complex which was shown to exist either as a monomer or a chlorobridged dimer. A chlorobridged dimer (C4) was confirmed by elemental analysis but the structure obtained after growing single crystals corresponded to a monomer (C5). This suggests that the existence of the compound in the amorphous form differed from the crystalline state, whereby the crystal lattice constraints affect a major conformational rearrangement of the individual molecules favoring the free monomer.²⁷

Characterization of the Complexes. Fourier Transform Infrared Spectra. The Fourier transform infrared (FTIR) analysis for the compounds was performed using potassium bromide (KBr) pellets. Comparisons were drawn between the transmission frequencies for the azomethine functional groups and those of free ligands. The IR spectrum for the ligands showed clear imine C=N (stretch) vibration band which occurred between 1636 and 1644 cm^{-1} . Similar azomethine bands for the complexes occurred between 1592 and 1628 cm^{-1} . The shift was an indication of chelation of Pd or Pt through the imine nitrogen, and the magnitude could be

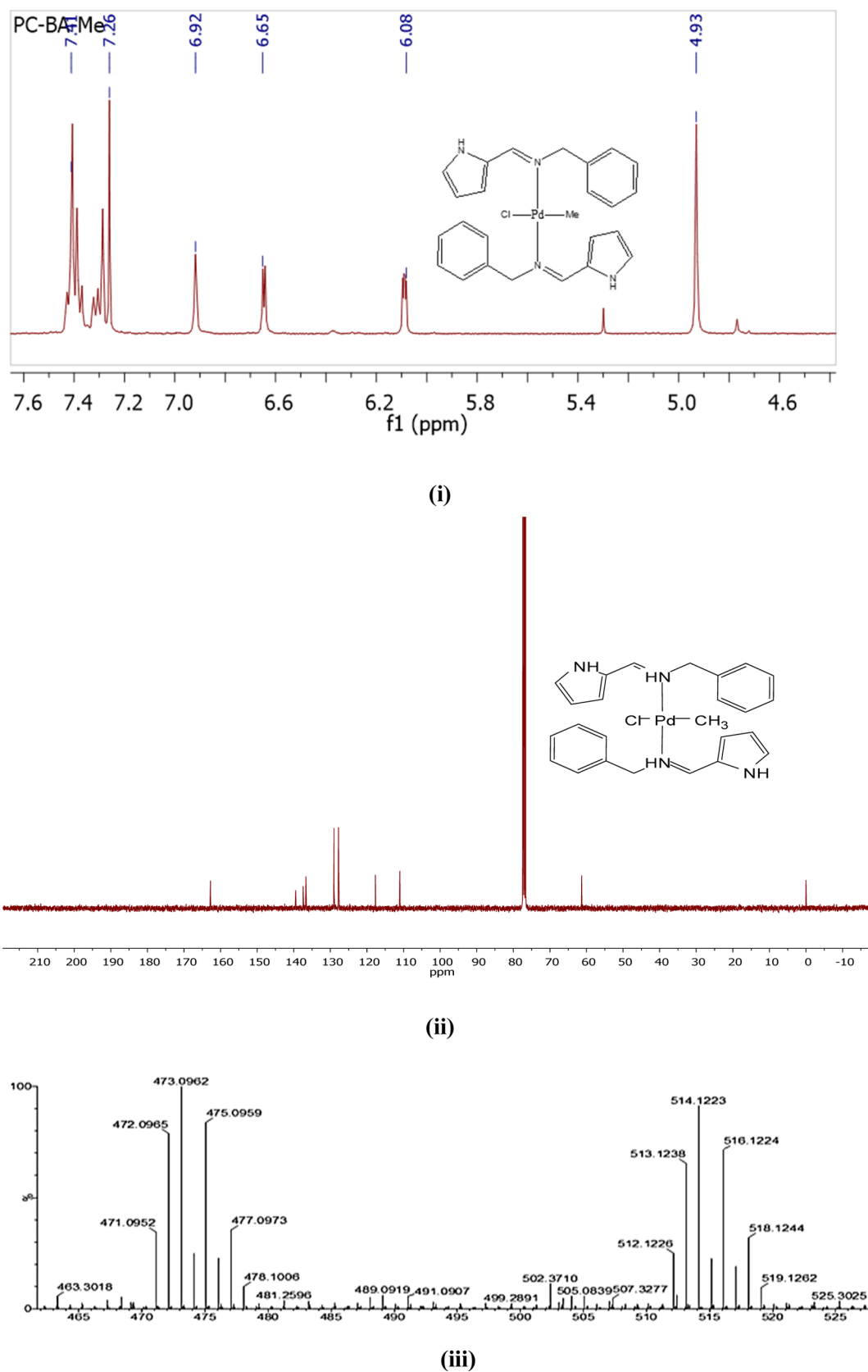


Figure 1. Representative spectra; (i) ^1H NMR for C1, (ii), ^{13}C -NMR for C1, and (iii) LC-MS for Complex C1.

attributed to the different ligands attached to the metal center and to the groups attached to the azomethine region. In general, the shifting to lower frequencies is ascribed to the pi-

back donation from metal d -orbitals to empty pi-antibonding orbitals of $\text{CH}=\text{N}$.²⁸ A characteristic peak at 696 cm^{-1} for platinum complexes and at 598 cm^{-1} for Pd complexes

appeared and was ascribed to the $\nu[M - N]$ coordination. The FTIR spectra are shown in Figures S1–S7 in the Supporting Information.

¹H-NMR Spectra. The ¹H NMR spectra for the complexes also showed a similar trend in the shifts in frequency of the methylene protons compared to the free ligands. The peak because of CH=N– in C1 and C4 occurred at 7.41 and 7.81 ppm, respectively, compared to 8.15 ppm in the parent ligand L1. In complex C2, the peak occurred at 7.69 ppm compared to 8.12 ppm in the parent ligand, L2. In complex C3, the methylene peak appeared at 7.69 ppm compared to 8.57 ppm in the parent ligand L3. This up-field shifts of 0.74, 0.34, and 1.04 ppm in C1, C3, and C4, respectively, to lower frequencies is because of pi-electrons of the azomethine group shifting toward the *d*-orbitals of metal leading to deshielding of the azomethine proton^{29,30} as a result of coordination to the azomethine nitrogen. The ¹H-NMR spectra are shown in Figures S8–S13 in the Supporting Information.

¹³C-NMR Spectra. Similar trends in shifts to higher frequencies were observed in the ¹³C-NMR peaks for the compounds. The ¹³C-NMR spectra are shown in Figures S14–S18 in the Supporting Information.

Electronic Spectra. The UV–vis spectra of the ligands and the Pd complexes in dimethyl sulfoxide (DMSO) were measured at the 200–800 nm range. The molar absorptivity for all the compounds was determined using UV titrations. Ligand spectra showed peaks corresponding to intraligand, spin-allowed $\pi \rightarrow \pi^*$ centered on the aromatic units in addition to $n \rightarrow \pi^*$. These transitions had molar extinction coefficients ranging from 103 to 104 L mol⁻¹ cm⁻¹. On the other hand, the UV–vis spectra for all the complexes showed two peaks corresponding to a combination of the spin allowed ¹A_{1g} → ¹B_{1g} transitions and $d\pi-\pi^*$ ligand transitions with molar extinction coefficients ranging from 10³ to 10⁴ L mol⁻¹ cm⁻¹. This transition is characteristic of square planar geometry. The UV–vis spectra are shown in Figures S26–S32 in the Supporting Information. Representative spectra for complex C1 are shown in Figure 1.

Molar Conductance. The molar conductance was measured for the complexes in DMSO and showed values ranging from 4.0 to 8.2 S cm² mol⁻¹. This is in agreement with other reports in the literature, which indicates a less than 30 S cm² mol⁻¹ as an indication of nonconductance. This confirms that these types of complexes are nonelectrolytic in solution.³¹

Partition Coefficient. The partition coefficient was determined as log *P* values by the UV–vis method. The values were 1.3953 ± 0.0065 for C1, 1.3816 ± 0.0032 for C2, 1.2692 ± 0.004 for C3, and 1.3072 ± 0.0082 for C5, indicating a more than 20-times partitioning of the compounds in the oil layer compared to the water layer. This implies that the compounds can be suitable for oral administration.³²

Electrochemical Properties of the Pd and Pt Complexes. Electrochemical studies were performed on C2, C3, and C5. The cyclic voltammograms are shown in Figure 2 below.

Complex C2 exhibits two irreversible reduction peaks at –0.57 V and at –1.7 V, while C3 showed reduction peaks with no anodic peaks present at –0.57 V and at –1.47 V (Figure 2). The observed processes most likely correspond to a metal-centered one-electron reduction process for the two peaks as shown in eqs 1 and 2.

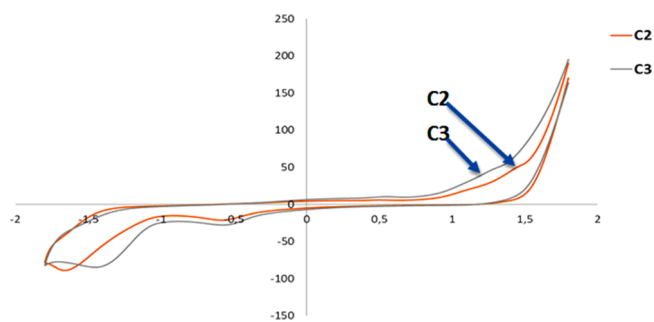
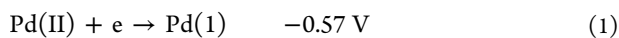
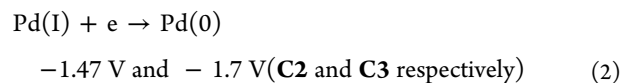


Figure 2. Cyclic voltammograms for C2 and C3 showing irreversible reduction peaks.



The cyclic voltammetry for the Pt complexes was performed at a scan rate of 200 mV/s at pH 7.0 versus Ag/AgCl, glassy carbon working electrode, and Pt wire counter electrode. As shown in Figure 3, one peak was observed at –0.5 V which was credited to the diffusion-controlled H⁺ reduction to H₂ which occurs around –0.41 V at pH 7 versus Ag/AgCl.³³

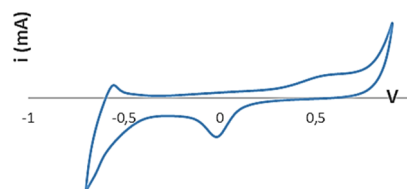


Figure 3. Cyclic voltammograms for C5 showing diffusion-controlled H-reduction.

In physiological systems, the redox stability appears within an accessible window of potential ranging between –0.4 and +0.8 V versus normal hydrogen electrode (NHE).³⁴ These values correspond to the potentials for the main reducing agents in biological systems; NADPH with approximately –0.38 V and oxygen at around +0.815 V, at pH 7.0 versus NHE.²³ Typically, all redox processes with a bigger or lesser value of potential compared to this physiological range cannot happen in the biological setting. However, there are other routes by which metal complexes interfere with cellular redox reactions through interaction via their redox centers either on the metal or ligand or through coordinating to biomolecules which facilitate cellular redox mechanisms.³⁵

Stability Studies. Stability tests were performed for C1 and C5 in DMSO-*d*₆ over a 72 h period in the presence of 200 μL D₂O. ¹H-NMR scans were conducted at 6 h intervals to monitor any changes in proton environments. There were no shifts in peaks or any other change in spectra over the 72 h period. This indicated that the compounds were stable in solution as shown in the ¹H-NMR plots and could be biocompatible.²⁶ The spectra are shown in Figure S33a–c in the Supporting Information.

X-ray Crystal Structure Analysis for Ligands L1 and L2 and C5 Complex. Crystals suitable for X-ray crystallography were grown for L1 and L2 and for the C5 Pt complex. The compounds crystallize in the monoclinic *P*₂₁/*n* space system for L1, *P*-1 for L3, and *P*₂₁/*c* for C5.

The crystal data for the four compounds are shown in Table 1.

Table 1. Single-Crystal Data and Structure Refinement Parameters for L1, L2, and C5

compound	L1	L2	C5
formula	C ₁₂ H ₁₂ N ₂	C ₁₀ H ₁₀ N ₂ O	C ₁₄ H ₁₈ Cl ₂ N ₂ OPtS
space group	P2 ₁ /n	P-1	P2 ₁ /c
cell lengths	<i>a</i> = 9.8330(3) <i>b</i> = 17.3251(7) <i>c</i> = 11.7851(4)	<i>a</i> = 4.8147(1) <i>b</i> = 9.1561(3) <i>c</i> = 10.0726(3)	<i>a</i> = 8.0734(1) <i>b</i> = 18.0661(3) <i>c</i> = 11.5367(2)
cell angles	α 90 β 94.219(2) γ 90	α 96.269(1) β 97.570(2) γ 94.171(1)	α = 90 β = 94.229(1) γ = 90
cell volume	2002.24	435.82(2)	1678.10(5)
Z	8	2	4
temperature	100 K	100 K	100 K

The structure and ORTEP ellipsoid diagram for L1 is shown in Figure 4. The ligand exists as a molecular pair. Stabilization

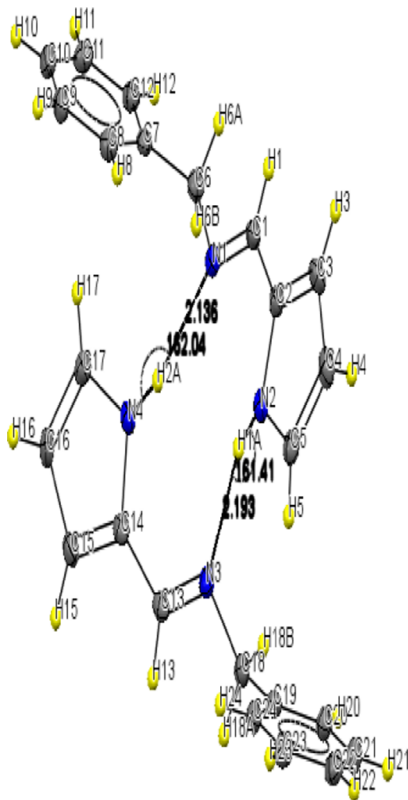


Figure 4. ORTEP Ellipsoids for L1 at 50% probability showing the intramolecular stabilization through H-bonding.

within the molecule is through intermolecular hydrogen bonding, between the imine nitrogen of one molecule and the hydrogen attached to the pyrrole nitrogen of the second molecule. The intermolecular bond distances are 2.136 and 2.193 Å. The intermolecular bond angles subtended by the H-bonded hydrogens are 161.41° for N2–H1–N3 and 162.04° for N1–H2–N4. The pyrrole and the benzyl rings lie at a torsion angle of 123.57° for one molecule and 118.97° for the second molecule.

The ORTEP plot for L2 is shown in Figure 5a,b. The crystal is stabilized by intermolecular hydrogen bonding of the

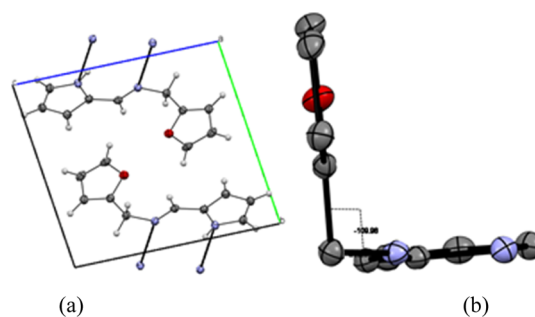


Figure 5. Unit cell for L2 viewed along the crystallographic *a*-axis showing hydrogen bonding in the unit cell (a) and the near perpendicular (109.98°) molecular planes (b).

hydrogens attached to imine and pyrrole nitrogen of adjacent molecules but facing away from the center of the molecule to the adjacent crystal units in opposite directions. The pyrrole and furan moieties making up one molecule exist at an almost perpendicular planes to each other, at an angle of 109.98°.

The ORTEP plot for the Pt complex (C5) is shown in Figure 6a,b with the unit cell consisting of four molecules. The

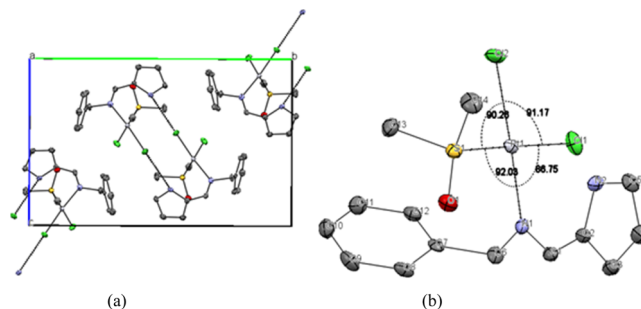


Figure 6. Unit cell packing showing hydrogen bonding, (a), and bond angles around the Pt center (b) for C5. Hydrogen atoms are omitted for clarity.

angles subtended around the Pt center are approximately right angles confirming the square planar geometry of a Pt(II) metal oxidation state.

The crystal is stabilized through intermolecular hydrogen bonding (3.198 Å) between the pyrrole hydrogen and chloride atom para to the imine nitrogen of adjacent molecules. A notable property of this complex is the unequal bond distances between the Pt metal center and the two chloride atoms attached to it. The bond length between the Pt and chloride para to the imine nitrogen is 2.302 Å, while the distance between the Pt center and chloride atom para to the sulfur atom of DMSO is 2.317 Å. This is credited to the stronger ground state trans-influence of sulfur compared to nitrogen, leading to a lengthening (and weakening) of interatomic bonds.

These observations are similar to what was reported by Murray and Hartley on N- and S-bonded PdCl₂ on amino acid backbones. In their work, a bond length of 2.305 Å for Pd–Cl trans to N-atom and 2.324 Å for Pd–Cl trans to S was observed.³⁶ It is observed that coordination occurs preferentially between Pt and sulfur of DMSO rather than with the oxygen atom despite the latter being less sterically hindered. This is expected because Pt, being a soft acid, prefers to coordinate with soft donors such as sulfur as opposed to nitrogen.

Bioactivity of the Organometallic Complexes. *DNA Binding Studies.* Observation on the spectral changes of metal complexes in the UV–vis range after addition of increasing concentrations of DNA is a generally accepted technique to assess the mode of binding and the kinetics of DNA–metal complex interaction.³⁷ In this study, calf thymus DNA (CT-DNA) was used to simulate how the complexes bind to DNA. The metal complex–DNA mixture was allowed to equilibrate for 10 min prior to taking UV–vis measurements. With continued addition of DNA, the peaks of the complexes decreased up to a point where they disappeared, and a peak at 260 nm corresponding to DNA appeared. The appearance of the DNA peak at λ_{260} nm was used as an indication of the interaction with the complexes. DNA concentration was calculated using the molar absorptivity of the CT-DNA, $\epsilon = 6600 \text{ M}^{-1}$, as shown in Figure S34 in the [Supporting Information](#).

The binding kinetics for the complex–DNA interaction was then determined from the intrinsic binding constant, K_b , by plots of the Benesi–Hildebrand host–guest equation,³⁸ (eq 3), where the strength of the interaction is reflected by the value of the binding constant.

$$\frac{A_0}{A - A_0} = \frac{\epsilon_G}{\epsilon_{H-G} - \epsilon_G} + \frac{\epsilon_G}{\epsilon_{H-G} - \epsilon_G} \frac{1}{K_b[\text{DNA}]} \quad (3)$$

A_0 and A are the absorbance of the blank sample without DNA, and absorbance of complex–DNA after addition of DNA, respectively, ϵ_G and ϵ_{H-G} are the molar extinction coefficients of complex only and complex–DNA, respectively. The binding constant is determined by plotting $A_0/(A - A_0)$ versus $1/[\text{DNA}]$ to give a straight–line graph. The equation of the straight line gives the slope and intercept, where the K_b value was calculated from the ratio of the intercept to the slope. From the K_b values, Gibbs free energy changes, ΔG , for the complex–DNA interactions were calculated using eq 4.

$$\Delta G = -RT \ln K_b \text{ kJ mol}^{-1} \quad (4)$$

where R is the gas constant and T is the absolute temperature.

The absorption spectra of the interaction of CT-DNA with the complexes together with the Benesi–Hildebrand plots are shown in Figures 7–10. The arrows show the intensity changes upon increasing concentration of CT DNA. Inset is the Benesi–Hildebrand plots for the determination of the binding constant.

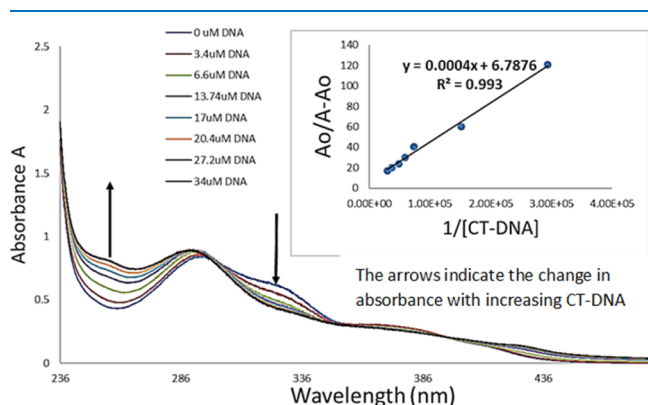


Figure 7. UV–vis absorption spectra for the CT-DNA Interactions with C1.

The spectra for C1 (Figure 6) showed a 5% hyperchromism at 294 nm. The observed hyperchromism is attributed to external associations by electrostatic interactions of the complex with the groove bases in the DNA possibly through the planar aromatic phenyl and pyrrole moieties and from hydrogen bonding with the negatively charged phosphate backbone.³⁹ This is further supported by the hypsochromic shift of 6 nm because a decrease in electron density in pi-orbitals stabilizes the orbitals, which causes an increase in the energy gap between pi and pi* orbitals, shifting the absorption to a lower wavelength.

On the other hand, the spectra for C2 (Figure 7), C3 (Figure 8), and C5 (Figure 9) showed hypochromic shifts with no shift in wavelength. The hypochromism is explained by the probability of intercalative interactions of the chromophores in the complexes with the DNA base pairs.⁴⁰ Furthermore, distinct isosbestic points appeared at 300 nm in the spectrum of C1 and 285 nm in the spectra of C2, C3, and C5. This is a clear indication of equilibrium between bound DNA and the free form of the compounds and that no other species apart from the free and the intercalated forms were present in the mixture.⁴¹ The mode of binding, K_b values, and Gibbs free energy for the complexes are shown in Table 2.

These values indicate a comparatively strong interaction between the complexes and CT-DNA. Complexes C1, C2, and C3 had lower binding constants which are comparable to the values of the known DNA intercalators: Lumazine, Epirubicin, and Proflavine ($2.32 \times 10^4 \text{ M}^{-1}$).⁴² The Pt complex C5 showed higher K_b values than those of Lumazine, Epirubicin ($3.4 \times 10^4 \text{ M}^{-1}$),⁴² and Proflavine ($1.74 \times 10^4 \text{ M}^{-1}$)⁴³ but lower than that of ethidium bromide ($1.4 \times 10^6 \text{ M}^{-1}$).⁴⁴ This strong affinity to bind to the DNA indicates its significance as a possible candidate in the line of potential anticancer drug candidates. The high binding constant for C5 suggests that it can also be a viable candidate for new intercalator compounds. The ΔG values for all the complexes were negative which specified the spontaneity of interaction during the complex–DNA formation process.⁴²

Anticancer Activity of the Organometallic Complexes. The main objective of the study was to demonstrate that stabilizing Pt and Pd by complexing with sterically bulky substituents around the metal center can block the attack from the axial z^2 -direction of the square planar complexes, thereby reducing ligand substitution reactions when in solution⁸ and improving their activities. Cytotoxicity of the compounds was assessed by MTT assay on selected cancerous (Caco-2, HeLa, Hep-G2, MCF-7, and PC-3), and noncancerous (MCF-12A) cell lines. The cells were initially treated with a single dose (100 $\mu\text{g}/\text{mL}$) of the ligands (L1–3) and their respective complexes (C1–5) to evaluate their potential anticancer activity. The ligands did not show any substantial activity at this dose (data not shown) compared to their corresponding complexes, and therefore, the reduced cell proliferation shown in Figure 11 could be accredited to the complexed compounds.

Two complexes (C3 and C5) were highly toxic to the cancer cells. C3 reduced cell viability by more than 80% in the six cell lines evaluated in this study and was the most cytotoxic complex. C5 demonstrated remarkable selective toxicity. It reduced viability of all the cancer cell lines by 60% or more but did not affect the viability of the noncancerous KMST6/MCF-12A cells. In general, C1 and C2 was less toxic but also demonstrated some level of selective toxicity. C2, for example, did not significantly reduce the viability of Caco-2 and MCF-7

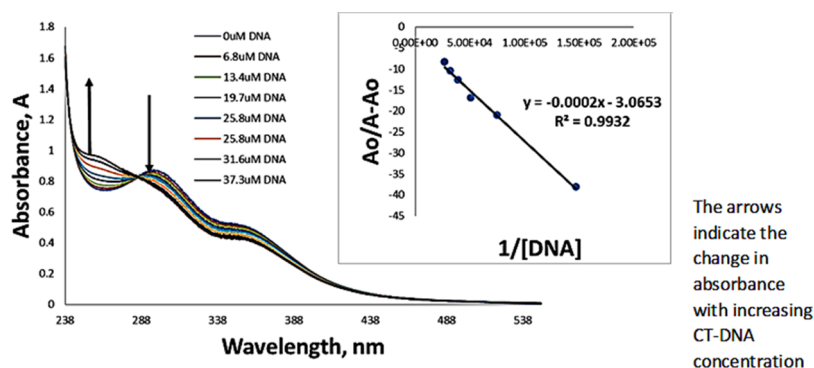


Figure 8. UV-vis absorption spectra for the CT-DNA interactions with C2.

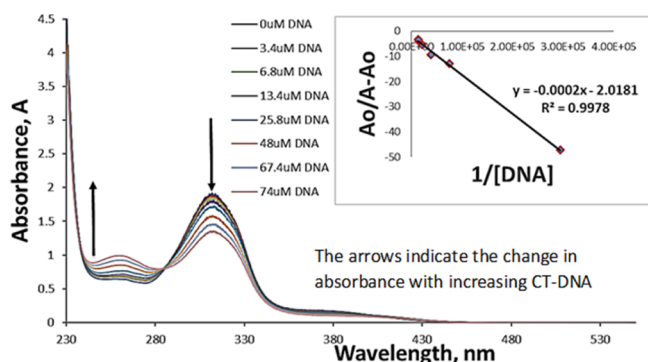


Figure 9. UV-vis absorption spectra for the CT-DNA interactions with C3.

cells but was highly toxic to the other four cell lines (HeLa, Hep-G2, PC-3, and MCF-12A). The different responses observed for the different cell lines may be attributed to genetic and transcriptional heterogeneity between the cell lines. Specific genetic mutations in these cells may have resulted increased susceptibility or conversely may result in increased resistance to the complexes. Further testing using whole proteome or genome analysis is needed to fully understand why the different cell lines responded in the way they did.

C1 and C2 only differ in structure by a CH_3^- in C1 and a Cl^- in C2 around the metal center. Because the CH_3 group is a strong σ -bonding ligand with a stronger trans-influence compared to Cl^- , it causes the σ -bonding character of the Pd-Cl bond in C1 to decrease. This means a better lability of the Cl-trans to CH_3^- in C1 compared to C2, which led to the

Table 2. Binding Constants and Gibbs Free Energy Values for the Complex-DNA Interactions

complex	mode of binding	binding constant K_b (M^{-1})	gibbs free energy (ΔG) (kJ mol^{-1})
C1	electrostatic	1.6969×10^4	-24.13
C2	intercalative	1.5327×10^4	-23.88
C3	intercalative	1.0091×10^4	-22.84
C5	intercalative	8.049×10^4	-27.99

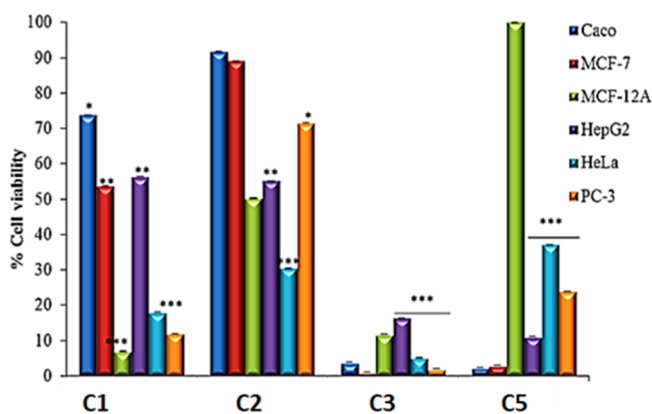


Figure 11. Screening of anticancer activity of Pd and Pt complexes (C1, C2, C3, and C5) against selected human cell lines. The cells were exposed to $100 \mu\text{g/mL}$ of compounds for 24 h; cell viability was assessed by MTT assay. *indicates statistical significance at $p < 0.05$ when compared to untreated cells, while ** indicates $p < 0.01$ and *** $p < 0.001$.

observed differences in their cytotoxicity profile. The IC_{50} values for the complexes (C1, C2, C3, and C5) are shown in

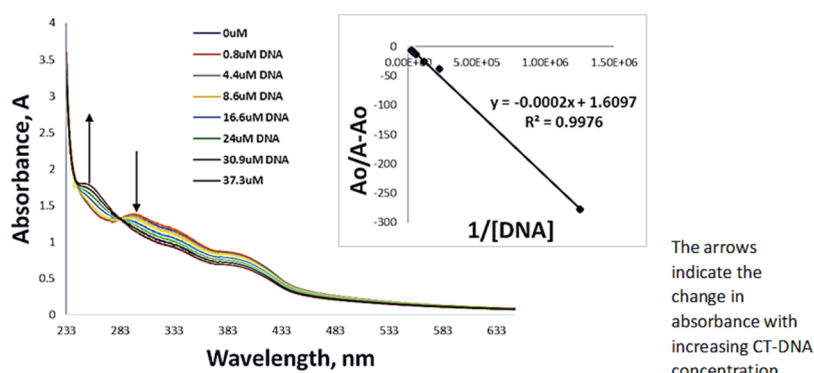


Figure 10. UV-vis absorption spectra for the CT-DNA Interactions with C5.

Table 3. IC₅₀ Values for the Ligands and Their Respective Complexes

	[complex] (μg/mL)				
	L1–3 Ligands	C1	C2	C3	C5
Caco-2	>100	>100	>100	15.81 ± 0.039	16.63 ± 0.006
MCF-7	>100	>100	>100	64.5 ± 0.0171	23.3 ± 0.0031
MCF-12A	>100	22.95 ± 0.014	53.5 ± 0.0753	24.9 ± 0.0199	>100
HeLa	>100	66.62 ± 0.051	86.4 ± 0.0286	45.5 ± 0.1665	84.86 ± 0.087
Hep-G2	>100	>100	>100	13.0 ± 0.0294	0.3 ± 0.0054
PC-3	>100	25.1 ± 0.0161	>100	20.9 ± 0.0179	29.5 ± 0.0961

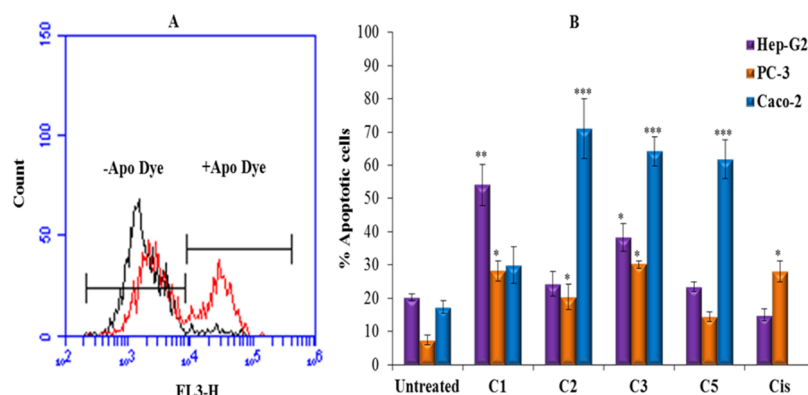


Figure 12. Apoptotic effects of organometallic complexes on human cancer cells.

Table 3. The ligands (L1–3) were not cytotoxic at the highest concentration (100 μg/mL) tested. The complexes with cis geometry, C3 and C5, showed enhanced cytotoxicity compared to the trans-geometry complexes C1 and C2. The IC₅₀ values varied significantly depending on the cell line and complex used. The IC₅₀ value for C5 (0.3 ± 0.0054 μg/mL) on the Hep-G2 cell line was the lowest IC₅₀ value obtained. The IC₅₀ values also demonstrate the selective toxicity of some of the complexes. While the IC₅₀ values for C1 and C2 varied between 22 and 86 μg/mL for MCF-12A, HeLa, and PC-3 cells, the IC₅₀ values for C1 and C2 were more than 100 μg/mL for Caco-2, MCF-7, and Hep-G2 cells. Interestingly, C5 was highly toxic to MCF-7 cells with an IC₅₀ value of 23.3 ± 0.0031 μg/mL, while the IC₅₀ value for MCF-12A cells was more than 100 μg/mL. This is significant because MCF-7 and MCF-12A are, respectively, cancerous and noncancerous cell lines from breast tissue. This demonstrates the selective toxicity of C5 toward MCF-7 breast cancer cells compared to the noncancerous breast cells.

The cells treated with these complexes demonstrated morphological changes, as shown in Figure S35, such as cell shrinking, loss of cell contact (detachment), membrane blebbing, and formation of apoptotic bodies, which are features that can be associated with apoptosis.^{45,46} To further confirm if the cytotoxic effects of the complexes are exerted through apoptosis, phosphatidyl serine (PS) externalization as one of the molecular markers of apoptosis was investigated using APOPercentage dye. PS is localized in the inner membrane of viable intact cells. Transmembrane lipid translocation during apoptosis results in the translocation of PS to the outside of the membrane. At this stage of apoptosis, apoptotic cells can be detected with the APOPercentage dye, which become entrapped within apoptotic cells.⁴⁷

APOPercentage dye uptake was studied in selected cells (Hep-G2, PC-3, and Caco-2) treated with the complexes for 24 h, and the number of apoptotic cells was quantified using a

flow cytometer as described by Meyer et al. (2008);⁴⁸ Figure 12 shows that the cell lines differed in their response to the complexes. Significantly higher levels of apoptosis were observed for the Caco-2 cell line when the cells were treated with C2, C3, and C5. Interestingly, C1 did not induce significant levels of apoptosis in Caco-2 cells. The Caco-2 cell line was the only cell line that showed a significant increase in the percentage of apoptotic cells when treated with C5. Only C1 and C3 were able to induce significant levels of apoptosis in Hep-G2 cells, while C1, C2, and C3 induced significant levels of apoptosis in Hep-G2 cells PC3 cells. Cisplatin, which was used as a positive control, induced significant levels of apoptosis in PC3 cells but not Hep-G2 cells. The Caco-2 cell line was not treated with cisplatin.

The cells were exposed to IC₅₀ of complexes (100 μg/mL) for 24 h; apoptosis was assessed by the APOPercentage assay. Representative histograms (A) depict untreated (in black) and C3-treated (in red) Caco-2 cells. The cell population that is stained with the APOPercentage is labeled as +Apo Dye, and the cell population that are not stained is labeled as -Apo Dye. The bar graph in (B) shows the percentage apoptotic cells when Hep-G2, PC3, and Caco-2 cells are treated with the complexes. Treatment with Cisplatin (Cis) was used as a positive control. *indicates statistical significance at $p < 0.05$ when compared to untreated cells, while ** indicates $p < 0.01$ and *** $p < 0.001$

CONCLUSIONS

New complexes based on pyrrole were synthesized and fully characterized. The structures were confirmed by elemental analysis, and the molecular structure and geometry of the Pt complex were confirmed by single-crystal X-ray crystallography.

Despite literature reports that the use of bulky ligands in trans-Pd complexes may confer increased cytotoxic activity, this was not observed in this study. This shows that bulky

ligands, which shield the metal center to a point where it is not accessible for ligand substitution, may in fact reduce the efficacy of these compounds. The challenge is to balance the extent of shielding and the extent of accessibility of the metal center to bioligands. This conclusion is based on the bioactivity of **C2** (trans-geometry with bulky ligands) compared to **C3** (cis-geometry with unshielded metal centre). **C2** showed selective cytotoxicity, while **C3** displayed high cytotoxicity to all six cell lines tested in this study.

The Pt complex (**C5**), also of cis-conformation, showed enhanced and selective cytotoxicity and selectivity to cancer cells. This compound also demonstrated strong DNA intercalation activity. This suggests that **C5** can be a viable candidate for cancer treatment and requires further *in vivo* tests.

EXPERIMENTAL SECTION

Standard inert atmosphere Schlenk line techniques under nitrogen or argon in the Laminar flow were used for all the synthetic procedures employed in this study. Reaction progress was monitored on a silica gel thin layer chromatography (Fluka) plates of 15 μm particle size. Solvent was removed under vacuum via a liquid nitrogen trap, and samples are stored and dried as recommended and distilled prior to use. All reagents utilized in synthesis were of analytical grade; they were purchased from Sigma-Aldrich or Merck and used without further modifications.

Determination of melting points was performed on open glass capillaries using the SMP-10 instrument. FTIR spectra were run using a PerkinElmer Spectrum 100 Series FTIR instrument on the range 4000–400 cm^{-1} using KBr pellets. Proton nuclear magnetic resonance (^1H NMR) spectra were run on a Bruker 400 MHz spectrometer available at the University of Western Cape, South Africa. The chemical shifts were measured in ppm relative to TMS standard. Elemental analysis was performed on Server 1112 series Elemental Analyzer at Stellenbosch University. UV–vis spectra were recorded in DMSO at a range of 200–800 nm using Nicolet evolution 100 spectrophotometer from Thermo Electron Corporation, and the data were analyzed using VisionPro software. Cyclic voltammetry studies were performed using the PalmerScan3 instrument equipped with glassy carbon electrodes as working electrodes, Ag/AgCl as the reference electrode, and platinum wire as the counter electrode, scan range of -1.8 to $+1.8$, and a scan rate of 200 mV/s. The supporting electrolyte was 5 mL of 10 mMol phosphate-buffered saline (PBS) buffer at pH 7. Single-crystal X-ray crystallography was performed on Bruker SMART CCD APEXII area-detector diffractometer available at Rutgers University, USA.

Synthesis of the Ligands and Complexes. (*E*)-*N*-((1*H*-Pyrrol-2-yl)methylene) (Phenyl) Methanamine (**L1**). The ligand was synthesized using 0.3882 g (4 mmol) Pyrrole-2-carbaldehyde and 440 μL (4 mmol) benzylamine in dry methanol and refluxed overnight. The solvent was rotavaped to dryness, and the product was obtained as orange powder. It was recrystallized in DCM/Et₂O and kept in fridge overnight for complete precipitation. The mother liquor was filtered off, and the product dried under vacuum. Crystals suitable for X-ray crystallography were grown by slow diffusion of hexane into DCM, yielding light brown crystals. Yield: 95% mp 110–112 $^{\circ}\text{C}$. FTIR (KBr cm^{-1}): 1636, (C=N); 2829 (sp^3 C–H); 2888 (C–H benzene), 3369, (N–H). ^1H NMR (400 MHz, CDCl_3 , δ -ppm): δ 8.15 (s, 1H), 7.24–7.37 (m, 5H),

6.90 (s, 1H), 6.53 (dd, $J = 1.22, 3.55$ Hz, 1H), 6.22–6.27 (m, 1H), 4.71 (s, 2H). ^{13}C NMR (400 MHz, CDCl_3): δ 152.35 (imine C=N), 137.04 (C₂C–N pyrrole), 128.55, 128.19, 127.98, 127.56, 127.07, 120.23 (C₂C–N pyrrole), 109.88, 88.93, 55.29 (CH₂). Molecular weight (Calcd); 184.2371, ESI–MS (m/z): $[\text{M} + \text{H}]^+$ (obtained); 184.2. Molecular formula; C₁₂H₁₂N₂, elemental analysis; Calcd (obtained) N, 15.21 (15.63); C, 74.2 (74.46); H, 6.8 (7.0)

(*E*)-*N*-((1*H*-Pyrrol-2-yl)methylene) (Furan-2-yl) Methanamine (**L2**). The ligand was synthesized as for the previous ligand using 0.4853 g (5 mmol) pyrrole-2-carbaldehyde and 450 μL (5 mmol) furfurylamine with MgSO₄ and stirred in room temperature for 18 h. Orange powder turned to brown. It was recrystallized from DCM with ether. Yield: 0.8166 g (94%). mp 86–89 $^{\circ}\text{C}$. Soluble in methanol, chloroform, DCM, Et₂O.

FTIR (KBr ν^{-1}); 1644, C=N (stretch); 2868 sp^3 C–H stretch; 2975 C–H (aromatic) stretch, 3177; N–H stretch. ^1H NMR (400 MHz, CDCl_3): δ 8.12 (s, 1H), 7.38 (s, 1H), 6.89 (s, 1H), 6.53 (br s, 1H), 6.34 (d, $J = 3.06$ Hz, 1H), 6.24 (s, 2H), 4.67 (s, 2H). ^{13}C NMR (400 MHz, Chloroform-*d*): δ 153.19 (C \equiv N imine), 153.09 (C₂C–O furan), 152.68 (C–C–O furan), 149.24 (C₂C=N pyrrole), 142.21 (C₂C–N pyrrole), 124.79, 122.09, 120.07, 114.97, 56.47 (CH₂)

Molecular weight (Calcd); 174.1992, ESI–MS (m/z): $[\text{M} + \text{H}]^+$ (obtained); 174. Molecular formula; C₁₀H₁₀N₂O, elemental analysis; Calcd (obtained) C, 68.95(68.61); H, 5.79(6.2); N, 16.08(16.47).

(*E*)-*N*-((1*H*-Pyrrol-2-yl)methylene) (Pyridin-2-yl) Methanamine (**L3**). The ligand was synthesized as for the previous ligands using 0.3882 g (4 mmol) pyrrole-2-carbaldehyde and 4 mmol (420 μL) 2-methylamino pyridine (picolyamine). The reaction mixture turned yellow during reflux. The solvent was evaporated to dryness under rotavap, and the product was isolated as a paste. It was recrystallized in DCM/Et₂O and kept in fridge overnight to complete precipitation; mother liquor was filtered off, and the product dried under vacuum. Yield: 94%. mp 96–99 $^{\circ}\text{C}$. Soluble in methanol, chloroform, DCM, Et₂O.

FTIR (KBr ν^{-1}); 1632, C=N (stretch); 2962 sp^3 C–H stretch; 2847 C–H (aromatic) stretch, 3080; N–H stretch. ^1H NMR (400 MHz, CDCl_3): δ 8.56 (d, $J = 4.16$ Hz, 1H), 8.24 (s, 1H), 7.61 (dt, $J = 1.71, 7.64$ Hz, 1H), 7.31 (d, $J = 7.82$ Hz, 1H), 7.15 (dd, $J = 5.32, 6.91$ Hz, 1H), 6.83 (s, 1H), 6.54 (dd, $J = 1.10, 3.55$ Hz, 2H), 6.23 (dd, $J = 2.81, 3.42$ Hz, 1H), 4.86 (s, 2H). ^{13}C NMR (400 MHz, CDCl_3): δ 160.03 (C₂C=N pyridine), 153.67 (C=N imine), 150.50, 149.30, 142.99, 136.62 (C₂C–N pyrrole), 131.59, 130.08, 119.80 (C₂C–N pyrrole), 114.87, 111.11, 66.18 (CH₂).

Molecular weight (Calcd); 185.2251, ESI–MS (m/z) $[\text{M} + \text{H}]^+$ 183.1. Molecular formula; C₁₁H₁₁N₃. Elemental analysis Calcd (obtained); N, 22.69(22.45); C, 70.33(69.38); H, 5.99(5.6).

Trans-Chloridobis[(pyrrolylmethylidene) (Benz-2-yl-methyl) Amine- κN] Methylpalladium(II) (**C1**). To a stirring solution of 92 mg (0.5 mmol) **L1** in CH₂Cl₂ under nitrogen was added dropwise a solution of 0.25 mmol (66 mg) Pd(COD)ClMe in CH₂Cl₂. The solution turned green, and stirring was sustained overnight at room temperature conditions. The solution was reduced under vacuum to about 1 mL, and hexane was added in excess to precipitate out the product. The mixture was kept in fridge overnight to allow complete precipitation; liquor was filtered off, and the precipitate was washed with more hexane,

filtered, and dried in inert conditions under vacuum. Yield: 52%, mp 216 °C (decompose). FTIR (KBr cm^{-1}): 3025, (aromatic C–H); 2937, (aliphatic C–H); 1602, (C=N). ^1H NMR (400 MHz, CDCl_3): δ 7.78 (s, 2H), 7.41 (m, 5H), 7.29 (m, 5H), 6.92 (s, 2H), 6.64 (s, 4H), 6.09 (br. s., 2H), 4.93 (s, 4H), 1.58 (br. s., 3H). ^{13}C NMR (101 MHz, CDCl_3): δ = 162.8, 139.5, 137.5, 136.7, 129.0, 127.8, 117.7, 111.0, 61.3. Molecular weight (Calcd); 525.38, molecular formula; liquid chromatography–mass spectrometry (LC–MS) (m/z): $[\text{M} + \text{H}]^+$ (obtained) 525.30; $\text{C}_{25}\text{H}_{27}\text{ClN}_4\text{Pd}$, elemental analysis; Calcd (obtained); N, 110.7 (11.3); C, 55.2 (55.79); H, 5.2 (5.1).

Trans-Dichloridobis[(pyrrolylmethylidene) (furan-2-yl-methyl) Amine- κN] Methylpalladium(II) (C2). The complex was synthesized for the previous one using 174 mg (1 mmol) of L3 and 144 mg (0.5 mmol) $\text{Pd}(\text{COD})\text{Cl}_2$. The mixture formed an orange solution which was reduced to about 1 mL by vacuum, and the product was recrystallized with diethyl ether. It was filtered, washed with 5 mL Et_2O and further with 2×5 mL hexane, and dried under vacuum to afford an orange product. Yield: 60 mg, 23%. The complex was analyzed by FTIR, UV–vis, and elemental analysis. FTIR (KBr cm^{-1}) 3117, (aromatic C–H); 3015, (aliphatic C–H); 1662, (C=N). ^1H NMR (400 MHz, CDCl_3): δ 7.69 (s, 1H), 7.54 (br s, 2H), 7.13 (br s, 1H), 6.46 (br s, 3H), 4.81 (br s, 2H), 3.49 (s, 2H), 1.59 (s, 3H), 1.21 (s, 3H). Molecular formula; $\text{C}_{20}\text{H}_{20}\text{Cl}_2\text{N}_4\text{O}_2\text{Pd}$, molecular weight (Calcd); 525.72, LC–MS (m/z): $[\text{M} + \text{H}]^+$ (obtained) 525.29. Elemental analysis; Calcd (obtained); C, 45.69(45.84); H, 2.84(2.79); N, 5.30(5.65).

cis-Dichlorido[(pyrrolylmethylidene) (Pyridyl-2-yl-methyl) Amine N,N] Pd(II) (C3). The complex was synthesized as for the previous one using 93 mg (0.5 mmol) L3 and 0.5 mmol (144 mg) $\text{Pd}(\text{COD})\text{Cl}_2$. The product precipitated immediately, and the mixture was stirred overnight after which the precipitation was deemed complete. It was filtered, washed with 5 mL Et_2O and further with 2×5 mL hexane, and dried under vacuum to afford a gray product. The compound was analyzed by FTIR, UV–vis, and elemental analysis. Yield: 90%. mp 250 °C (decompose). FTIR (KBr cm^{-1}) 1610, C=N (stretch); 1576, C=N (aromatic). ^1H NMR (400 MHz, CDCl_3): δ 7.44 (d, 1H), 7.26 (s, 1H), 6.44 (m, 1H), 6.31 (m, 2H), 5.30 (m, 1H), 4.81 (m, 1H), 3.49 (m, 1H), 1.57 (d, 1H), 1.21 (s, 2H). Molecular formula; $\text{C}_{11}\text{H}_{11}\text{Cl}_2\text{N}_3\text{Pd}$, Molecular weight (Calcd); 362.55; LC–MS (m/z): $[\text{M} + \text{H}]^+$ (obtained) 362.04. Elemental analysis Calcd (obtained); C, 36.4(36.5); H, 3.1(3.5); N, 11.6(11.2).

Pt Complex [Pt₂(μ -Cl)₂(dmsol)₂(L1)₂] (C5) and PtCl₂dmsol1 (C5). The platinum complex C5 was obtained by reaction of L1 with $\text{Pt}(\text{DMSO})_2\text{Cl}_2$ at room temperature. Into a stirring solution of 42 mg (0.125 mmol) $\text{Pt}(\text{DMSO})_2\text{Cl}_2$ in 15 mL DCM, 0.125 mmol (23 mg) L1 in 5 mL DCM was added dropwise using a nitrogen-filled syringe. Stirring was continued overnight, evaporated under vacuum to yield a yellow precipitate of C5 which was filtered and dried under vacuum. Yield: 65%. FTIR (KBr cm^{-1}) 3300, (2° amine N–H for pyrrole); 3130, (aromatic C–H); 3016, (aliphatic C–H); 1631, (C=N). ^1H NMR (400 MHz, CDCl_3): δ 7.78–7.85 (m, 2H), 7.26 (s, 10H), 6.90–7.01 (m, 4H), 6.55–6.61 (m, 2H), 3.43–3.52 (m, 2H), 2.17 (s, 4H), 1.56 (s, 12H). Elemental analysis; Calcd (obtained); C, 34.11 (34.15); H, 3.68 (3.70); N, 5.68 (5.69); S, 6.51 (6.50). Crystals suitable for X-ray crystallography were obtained by slow evaporation of the

DCM solution and were obtained as light-yellow crystals of C5. ^1H NMR (400 MHz, $\text{DMSO}-d_6$): δ 8.72 (br. s., 1H), 8.44 (s, 1H), 7.45 (s, 5H), 6.45 (br. s., 1H), 5.11 (s, 1H), 4.92 (s, 1H), 3.35 (s, 2H), 2.54 (s, 6H). Molecular weight (Calcd); 528.3 LC–MS (m/z): $[\text{M} + \text{H}]^+$ (obtained), 530.07.

Partition Coefficient. The partition coefficient as the log P value was determined for C1–C5 by the shake-flask method. The values were determined by partitioning the complexes between 10 mL of deionized water (the medium inside and outside the cells) and 10 mL of 99% n -octanol (a model of the lipid bilayer of the cell membrane) and stirring for 48 h. The two layers were first presaturated with each other to avoid solubility-induced volume changes during the extraction step.⁴⁹ Before extraction, the absorbance of the initial stock was determined after appropriate dilutions.

The mixture was then left to settle for 24 h after which 3 mL aliquots were taken from each layer and centrifuged for 2 h at 7000 rpm using the Minispin Eppendorf centrifuge. The UV–vis absorbance for the two layers was taken after appropriately diluting the layers.⁵⁰ Absorbance was read using a 96-well microplate on a POLARstar Omega microplate reader instrument from BMG Labtech. The partition coefficient was calculated as $\log(C_o/C_w)$, where C_o is the concentration in the oil layer, and C_w is the concentration in the water layer.

Electrochemical Properties of the Pd Complexes. Electrochemical studies in solution were performed on two of the complexes (C3 and C4) using the PalmerScan3 instrument equipped with glassy carbon electrodes as working electrodes, Ag/AgCl as the reference electrode and platinum wire as the counter electrode. A scan range of -1.8 to $+1.8$ and a scan rate of 200 mV/s were used. The supporting electrolyte was 5 mL of 10 mMol PBS buffer at pH 7.0.

Single-Crystal X-ray Analysis. Crystals suitable for X-ray crystallography were grown by slow diffusion of hexane into DCM which gave crystal for L1 or by slow evaporation of a DCM solution of the ligand for L2 and the platinum complex, C5. X-ray crystallography was performed on a Bruker SMART CCD APEXII area-detector diffractometer and was kept at 100.03 K during data collection. Using Olex2 software,⁵¹ the structure was solved with the ShelXS-1997⁵² structure solution program using Direct Methods and refined with the Olex2 refinement package.⁵³

Evaluation of the Bioactivity of the Organometallic Compounds. DNA Binding Studies. This was done by UV–vis spectroscopy by serial titrations of CT-DNA into a fixed concentration of the complexes in a quartz cuvette. UV–vis readings were taken at increasing amounts of DNA and allowing for 10 min equilibration time after each addition. The binding kinetics for the complex–DNA interaction was then determined from the intrinsic binding constant, K_b , by plots of the Benesi–Hildebrand host–guest equation.⁵⁴ From the K_b values, Gibbs free energy changes (ΔG) for the complex–DNA interactions were then calculated and compared with known DNA intercalators.

Effect of Compounds on Cancer Cells. Cytotoxicity of the compounds was tested against human cell lines: Caco-2 (colon), HeLa (Cervical), Hep-G2 (Hepatocellular Carcinoma/liver cancer), MCF-7 (breast cancer), PC-3 (prostate), and MCF-12A (non-cancer breast) cells. The cells were cultured in their respective media supplemented with 10% foetal bovine serum (FBS) and 1% pen-strep cocktail comprised of streptomycin (100 $\mu\text{g}/\text{mL}$) and penicillin (100 U/mL). Caco-2, HeLa, Hep-G2, and MCF-7 cell lines were cultured

in Dulbecco's modified Eagle medium (DMEM); MCF-12A in DMEM-F12 containing insulin, EGF, and hydrocortisone, while PC-3 cells were cultured RPMI-1640 media. The cells were incubated at 37 °C in a 5% humidified CO₂ incubator (Labotech, South Africa).

The cells were seeded at 1 × 10⁵ cells/mL density in a 96-well plate and incubated at 37 °C for 24 h. The cells were treated with varying concentrations of extracts (0–100 μg/mL) for 24 h. Cytotoxicity of the compounds was assessed by MTT assay following manufacturer's instructions. After treatment, 10 μL of 5 mg/mL MTT (Sigma, USA) was added to each well and the plates were incubated at 37 °C for 3 h. The insoluble formazan crystals were solubilized by adding 100 μL of DMSO. The reduction of MTT was read at 570 nm using the POLARStar Omega plate reader. Cell viability was calculated using eq 5 given below

$$\% \text{ cell viability} = \frac{\text{average absorbance of treated cells}}{\text{average absorbance of control}} \times 100 \quad (5)$$

The half-maximal cytotoxic concentration (IC₅₀) on each cell line was estimated using GraphPad Prism software version 5 (GraphPad Software, California, USA).

APOPercentage Apoptosis Assay. APOPercentage assay (Biocolor Ltd.) was performed following a protocol described by Alpuche-Aviles et al. (2018).³³ Briefly, selected cell lines (Hep-G2, PC-3, and Caco-2) were seeded in 12 well cell culture plates at a density of 1 × 10⁵ cells/mL and treated using concentrations equivalent to the IC₅₀ values obtained using the MTT assay. After treatment, the morphological changes in the cells were observed under inverted contrast microscope (EVOS XL Core microscope; Thermo Fisher Scientific, Germany) at 10× magnification. The cells were then trypsinized and stained with APOPercentage dye. The cells staining positive for the APOPercentage dye were quantified using a Becton Dickinson (BD) Accuri C6 Flow cytometer (BD Biosciences Pharmingen, San Diego, CA, USA). A minimum of 10,000 events per sample was acquired, and the data were analyzed using the BD Accuri software (BD Biosciences).

Statistical Analyses. Statistical analyses for MTT and APOPercentage Apoptosis data were analyzed using GraphPad Prism 6.0. The data were presented as means ± S according to the one-way ANOVA test and student *t*-test. A *p* value of <0.05 was considered to be of statistical significance and represented by an asterisk (*). **p* < 0.05, ***p* < 0.01, and ****p* < 0.001.

■ ASSOCIATED CONTENT

SI Supporting Information

The Supporting Information is available free of charge at <https://pubs.acs.org/doi/10.1021/acsomega.0c00360>.

FTIR spectra (Figures S1-S7); ¹H NMR spectra (Figures S8-S13); ¹³C NMR spectra (Figures S14-S18); mass spectra supplementary data (Figures S19-25); UV/Vis spectra (Figures S26-S32); and check CIF data for L1 (labelled PC-BA), L2 (labelled PC-O), and C5 (labelled PC-BA-Pt) (PDF)

CheckCIF report for Ligand L1 (CIF)

CheckCIF report for Ligand L2: Alert levels A and B explained (CIF)

CheckCIF report for Complex C5 (CIF)

■ AUTHOR INFORMATION

Corresponding Author

Martin O. Onani – *Organometallics and Nanomaterials, Department of Chemistry, University of the Western Cape, Bellville 7535, South Africa*; orcid.org/0000-0002-4735-3669; Email: monani@uwc.ac.za

Authors

Simon N. Mbugua – *Organometallics and Nanomaterials, Department of Chemistry, University of the Western Cape, Bellville 7535, South Africa*; *Department of Chemistry, University of Nairobi, Nairobi 00100, Kenya*

Nicole R. S. Sibuyi – *Department of Science and Technology/Mintek Nanotechnology Innovation Centre (DST/Mintek NIC), Biolabels Node, Department of Biotechnology, University of the Western Cape, Bellville 7535, South Africa*; orcid.org/0000-0001-7175-5388

Lydia W. Njenga – *Department of Chemistry, University of Nairobi, Nairobi 00100, Kenya*

Ruth A. Odhiambo – *Department of Chemistry, University of Nairobi, Nairobi 00100, Kenya*

Shem O. Wandiga – *Department of Chemistry, University of Nairobi, Nairobi 00100, Kenya*

Mervin Meyer – *Department of Science and Technology/Mintek Nanotechnology Innovation Centre (DST/Mintek NIC), Biolabels Node, Department of Biotechnology, University of the Western Cape, Bellville 7535, South Africa*

Roger A. Lalancette – *Rutgers, Department of Chemistry, Rutgers State University, Newark, New Jersey 07102, United States*; orcid.org/0000-0002-3470-532X

Complete contact information is available at: <https://pubs.acs.org/10.1021/acsomega.0c00360>

Notes

The authors declare no competing financial interest.

■ ACKNOWLEDGMENTS

The authors gratefully acknowledge the International Science Program (ISP) Uppsala, Sweden under the KEN-01 project, and the NRF South Africa (CSUR160323161066) for funding this research; NIC Biolabels Node (Department of Biotechnology, UWC), University of Nairobi, for support and guidance in this work; and the Organometallics and Nanomaterials group (Department of Chemical Sciences, UWC), South Africa, where this work was carried out.

■ REFERENCES

- (1) Siegel, R. L.; Miller, K.; Jemal, A. *Cancer Statistics*, 2018. *Ca—Cancer J. Clin.* **2018**, *68*, 7–30.
- (2) Ferlay, J.; Colombet, M.; Soerjomataram, I.; Mathers, C.; Parkin, D. M.; Piñeros, M.; Znaor, A.; Bray, F. : Estimating The Global Cancer Incidence And Mortality In 2018: Globocan Sources And Methods. *Int. J. Canc.* **2019**, *144*, 1941–1953.
- (3) Nagaraju, G. P.; Srivani, G.; Dariya, B.; Chalikonda, G.; Farran, B.; Behera, S. K.; Alam, A.; Kamal, M. A. Nanoparticles Guided Drug Delivery and Imaging in Gastric Cancer. *Semin. Cancer Biol.* **2020**, DOI: 10.1016/j.semcancer.2020.01.006.
- (4) Misirlic-Dencic, S.; Poljarevic, J.; Isakovic, A. M.; Sabo, T.; Markovic, I.; Trajkovic, V. Current Development Of Metal Complexes With Diamine Ligands As Potential Anticancer Agents. *Curr. Med. Chem.* **2020**, *27*, 380–410.
- (5) El-Razek, S. E. A.; El-Gamasy, S. M.; Hassan, M.; Abdel-Aziz, M. S.; Nasr, S. M. Transition Metal Complexes Of A Multidentate Schiff Base Ligand Containing Guanidine Moiety: Synthesis, Character-

- ization, Anti-Cancer Effect, And Anti-Microbial Activity. *J. Mol. Struct.* **2020**, *1203*, 127381.
- (6) Hallek, M. Chronic Lymphocytic Leukemia: 2020 Update On Diagnosis, Risk Stratification And Treatment. *Am. J. Hematol.* **2019**, *94*, 1266–1287.
- (7) Ginsburg, O.; Bray, F.; Coleman, M. P.; Vanderpuye, V.; Eniu, A.; Kotha, S. R.; Sarker, M.; Huong, T. T.; Allemanni, C.; Dvaladze, A.; Gralow, J.; Yeates, K.; Taylor, C.; Oomman, N.; Krishnan, S.; Sullivan, R.; Kombe, D.; Blas, M. M.; Parham, G.; Kassami, N.; Conteh, L. The Global Burden Of Women's Cancers: A Grand Challenge In Global Health. *Lancet* **2017**, *389*, 847–860.
- (8) Ward, R. J.; Crichton, R. R. Essential Metals In Medicine: Therapeutic Use And Toxicity Of Metal Ions In The Clinic. *Met. Ions Life Sci.* **2019**, *19*, 87–122.
- (9) Sánchez-López, E.; Gomes, D.; Esteruelas, G.; Bonilla, L.; Lopez-Machado, A. L.; Galindo, R.; Cano, A.; Espina, M.; Ettchet, M.; Camins, A.; Silva, A. M.; Durazzo, A.; Santini, A.; Garcia, M. L.; Souto, E. B. Metal-Based Nanoparticles As Antimicrobial Agents: An Overview. *Nanomaterials* **2020**, *10*, 292.
- (10) Ali, I.; Lone, M.; Al-Othman, Z.; Al-Warthan, A.; Sanagi, M. Heterocyclic Scaffolds: Centrality In Anticancer Drug Development. *Curr. Drug Targets* **2015**, *16*, 711–734.
- (11) Özdemir, İ.; Çiftçi, O.; Evren, E.; Gürbüz, N.; Kaloglu, N.; Başak Türkmen, N.; Yaşar, Ş.; Üstün, E.; Hamdi, N.; Mansour, L.; Özdemir, İ. Synthesis, Characterization And Antitumor Properties Of Novel Silver (I) And Gold (I) N-Heterocyclic Carbene Complexes. *Inorg. Chim. Acta* **2020**, *506*, 119530.
- (12) Sreenivasulu, R.; Tej, M. B.; Jadav, S. S.; Sujitha, P.; Kumar, C. G.; Raju, R. R. Synthesis, Anticancer Evaluation And Molecular Docking Studies Of 2, 5-Bis (Indolyl)-1, 3, 4-Oxadiazoles, Nortopsentin Analogues. *J. Mol. Struct.* **2020**, *1208*, 127875.
- (13) Apetrei, R.-M.; Camurlu, P. Functional Platforms For (Bio) Sensing: Thiophene-Pyrrole Hybrid Polymers. *J. Electrochem. Soc.* **2020**, *167*, 037557.
- (14) Bavadi, M.; Niknam, K.; Shahraki, O. Novel Pyrrole Derivatives Bearing Sulfonamide Groups: Synthesis In Vitro Cytotoxicity Evaluation, Molecular Docking And Dft Study. *J. Mol. Struct.* **2017**, *1146*, 242–253.
- (15) Saeed, H.; Sreedharan, S.; Thomas, J. A. Photoactive Metal Complexes That Bind Dna And Other Biomolecules As Cell Probes, Therapeutics, And Theranostics. *Chem. Commun.* **2020**, *56*, 1464.
- (16) Martinez-Gonzalez, A. I.; Diaz-Sánchez, A. G.; De La Rosa, L. A.; Bustos-Jaimes, I.; Alvarez-Parrilla, E.; Alvarez-Parrilla, E.: Inhibition Of α -Amylase By Flavonoids: Structure Activity Relationship (Sar). *Spectrochim. Acta, Part A* **2019**, *206*, 437–447.
- (17) Ren, C.; Xiong, W.; Li, J.; Li, B. Comparison Of Binding Interactions Of Cyanidin-3-O-Glucoside To B-Conglycinin And Glycinin Using Multi-Spectroscopic And Thermodynamic Methods. *Food Hydrocolloids* **2019**, *92*, 155–162.
- (18) Fairbanks, S. D.; Robertson, C. C.; Keene, F. R.; Thomas, J. A.; Williamson, M. P. Structural Investigation Into The Threading Intercalation Of A Chiral Dinuclear Ruthenium (Ii) Polypyridyl Complex Through A B-Dna Oligonucleotide. *J. Am. Chem. Soc.* **2019**, *141*, 4644–4652.
- (19) Zhang, Y.-P.; Li, Y.; Xu, G.-C.; Li, J.-Y.; Luo, H.-Y.; Li, J.-Y.; Zhang, L.; Jia, D.-Z. Synthesis, Crystal Structure, Dna/Bovine Serum Albumin Binding And Antitumor Activity Of Two Transition Metal Complexes With 4-Acylpyrazolone Derivative. *Appl. Organomet. Chem.* **2019**, *33*, No. E4668.
- (20) Morgan, S. M.; El-Sonbati, A. Z.; Eissa, H. R. Geometrical Structures, Thermal Properties And Spectroscopic Studies Of Schiff Base Complexes: Correlation Between Ionic Radius Of Metal Complexes And Dna Binding. *J. Mol. Liq.* **2017**, *240*, 752–776.
- (21) Layek, S.; Anuradha, B.; Agrahari, B.; Pathak, D. D. Synthesis And Characterization Of A New Pd (Ii)-Schiff Base Complex [Pd (Apd) 2]: An Efficient And Recyclable Catalyst For Heck-Mizoroki And Suzuki-Miyaura Reactions. *J. Organomet. Chem.* **2017**, *846*, 105–112.
- (22) Janssen-Müller, D.; Schleppehorst, C.; Glorius, F. Privileged Chiral N-Heterocyclic Carbene Ligands For Asymmetric Transition-Metal Catalysis. *Chem. Soc. Rev.* **2017**, *46*, 4845–4854.
- (23) Popova, E. A.; Protas, A. V.; Trifonov, R. E. Tetrazole Derivatives As Promising Anticancer Agents. *Anti Canc. Agents Med. Chem.* **2017**, *17*, 1856–1868.
- (24) Zhang, B.; Luo, H.; Xu, Q.; Lin, L.; Zhang, B. Antitumor Activity Of A Trans-Thiosemicarbazone Schiff Base Palladium (Ii) Complex On Human Gastric Adenocarcinoma Cells. *Oncotarget* **2017**, *8*, 13620.
- (25) Gaspari, R.; Prota, A. E.; Bargsten, K.; Cavalli, A.; Steinmetz, M. O. Structural Basis Of Cis-And Trans-Combretastatin Binding To Tubulin. *Chem* **2017**, *2*, 102–113.
- (26) Motswainyana, W. M.; Onani, M. O.; Madiehe, A. M. Bis (Ferrocenylimine) Palladium (Ii) And Platinum (Ii) Complexes: Synthesis, Molecular Structures And Evaluation As Antitumor Agents. *Polyhedron* **2012**, *41*, 44–51.
- (27) Ehrmann, F. R.; Stojko, J.; Metz, A.; Debaene, F.; Barandun, L. J.; Heine, A.; Diederich, F.; Cianferani, S.; Reuter, K.; Klebe, G. Soaking Suggests "Alternative Facts": Only Co-Crystallization Discloses Major Ligand-Induced Interface Rearrangements Of A Homodimeric Trna-Binding Protein Indicating A Novel Mode-Of-Inhibition. *PLoS One* **2017**, *12*, No. e0175723.
- (28) Manjunath, M.; Kulkarni, A. D.; Bagihalli, G. B.; Malladi, S.; Patil, S. A. Bio-Important Antipyrine Derived Schiff Bases And Their Transition Metal Complexes: Synthesis, Spectroscopic Characterization, Antimicrobial, Anthelmintic And Dna Cleavage Investigation. *J. Mol. Struct.* **2017**, *1127*, 314–321.
- (29) Tyagi, P.; Tyagi, M.; Agrawal, S.; Chandra, S.; Ojha, H.; Pathak, M. Synthesis, Characterization Of 1, 2, 4-Triazole Schiff Base Derived 3d-Metal Complexes: Induces Cytotoxicity In Hepg2, MCF-7 Cell Line, Bsa Binding Fluorescence And Dft Study. *Spectrochim. Acta, Part A* **2017**, *171*, 246–257.
- (30) Ekenia, A. C.; Osowole, A. A.; Olasunkanmi, L. O.; Onwudiwe, D. C.; Ebenso, E. E. Coordination Behaviours Of New (Bidentate N, O-Chelating) Schiff Bases Towards Copper (Ii) And Nickel (Ii) Metal Ions: Synthesis, Characterization, Antimicrobial, Antioxidant, And Dft Studies. *Res. Chem. Intermed.* **2017**, *43*, 3787–3811.
- (31) Al-Fregi, A. A. Synthesis, Characterization And Molar Conductivity Study Of Some New Palladium (Ii) And Platinum (Ii) Complexes Containing Heterocyclic Tellurium-Dicarboxylate Ligands. *Int. J.* **2015**, *3*, 637–647.
- (32) Bhal, S. K. Logp—Making Sense Of The Value. *Adv. Chem. Dev.* **2007**, *1–4*.
- (33) Alpuche-Aviles, M. A.; Farina, F.; Ercolano, G.; Subedi, P.; Cavaliere, S.; Jones, D. J.; Rozière, J. Electrodeposition Of Two-Dimensional Pt Nanostructures On Highly Oriented Pyrolytic Graphite (Hogp): The Effect Of Evolved Hydrogen And Chloride Ions. *Nanomaterials* **2018**, *8*, 668.
- (34) Janssen-Müller, D.; Schleppehorst, C.; Glorius, F. Correction: Privileged Chiral N-Heterocyclic Carbene Ligands For Asymmetric Transition-Metal Catalysis. *Chem. Soc. Rev.* **2017**, *46*, 5463.
- (35) Zhang, P.; Sadler, P. J. Redox-Active Metal Complexes For Anticancer Therapy. *Eur. J. Inorg. Chem.* **2017**, *2017*, 1541–1548.
- (36) Murray, S. G.; Hartley, F. R. Coordination Chemistry Of Thioethers, Selenoethers, And Telluroethers In Transition-Metal Complexes. *Chem. Rev.* **1981**, *81*, 365–414.
- (37) Olsztynska, S.; Komorowska, M. *Biomedical Engineering: Trends, Research and Technologies*; Bod—Books on Demand, 2011.
- (38) Kuntz, I., Jr; Gasparro, F.; Johnston, M., Jr; Taylor, R. Molecular Interactions And The Benesi-Hildebrand Equation. *J. Am. Chem. Soc.* **1968**, *90*, 4778–4781.
- (39) Suntharalingam, K.; Mendoza, O.; Duarte, A. A.; Mann, D. J.; Vilar, R. A Platinum Complex That Binds Non-Covalently To Dna And Induces Cell Death Via A Different Mechanism Than Cisplatin. *Metallomics* **2013**, *5*, 514–523.
- (40) Pyle, A. M.; Rehmann, J. P.; Meshoyrer, R.; Kumar, C. V.; Turro, N. J.; Barton, J. K. Mixed-Ligand Complexes Of Ruthenium

(li): Factors Governing Binding To Dna. *J. Am. Chem. Soc.* **1989**, *111*, 3051–3058.

(41) Arshad, N.; Bhatti, M. H.; Farooqi, S. I.; Saleem, S.; Mirza, B. Synthesis, Photochemical And Electrochemical Studies On Triphenyltin (Iv) Derivative Of (Z)-4-(4-Cyanophenylamino)-4-Oxobut-2-Enoic Acid For Its Binding With Dna: Biological Interpretation. *Arabian J. Chem.* **2016**, *9*, 451–462.

(42) Aslanoglu, M. Electrochemical And Spectroscopic Studies Of The Interaction Of Proflavine With Dna. *Anal. Sci.* **2006**, *22*, 439–443.

(43) Ibrahim, M. S.; Shehata, I. S.; Al-Nayeli, A. A. Voltammetric Studies Of The Interaction Of Lumazine With Cyclodextrins And Dna. *J. Pharmaceut. Biomed. Anal.* **2002**, *28*, 217–225.

(44) Lepecq, J.-B.; Paoletti, C. A Fluorescent Complex Between Ethidium Bromide And Nucleic Acids: Physical—Chemical Characterization. *J. Mol. Biol.* **1967**, *27*, 87–106.

(45) Zhang, Y.; Chen, X.; Gueydan, C.; Han, J. Plasma Membrane Changes During Programmed Cell Deaths. *Cell Res.* **2018**, *28*, 9–21.

(46) Meyer, M.; Essack, M.; Kanyanda, S.; Rees, J. G. A Low-Cost Flow Cytometric Assay For The Detection And Quantification Of Apoptosis Using An Anionic Halogenated Fluorescein Dye. *Biotechniques* **2008**, *45*, 317–320.

(47) Park, S.-Y.; Kim, I.-S. Engulfment Signals And The Phagocytic Machinery For Apoptotic Cell Clearance. *Exp. Mol. Med.* **2017**, *49*, No. E331.

(48) Meyer, M.; Essack, M.; Kanyanda, S.; Rees, J. G. A low-cost flow cytometric assay for the detection and quantification of apoptosis using an anionic halogenated fluorescein dye. *BioTechniques* **2008**, *45*, 317–320.

(49) Sangster, J. Octanol–Water Partition Coefficients: Fundamentals And Physical Chemistry. *Eur. J. Med. Chem.* **1997**, *32*, 842.

(50) Minick, D. J.; Frenz, J. H.; Patrick, M. A.; Brent, D. A. A Comprehensive Method For Determining Hydrophobicity Constants By Reversed-Phase High-Performance Liquid Chromatography. *J. Med. Chem.* **1988**, *31*, 1923–1933.

(51) Liao, B.-L.; Yin, X.-J. Synthesis, Structure And High Photocatalytic Performance Of A Novel Vanadium (V) Complex Based On Pyridine-2, 4, 6-Tricarboxylic Acid. *Inorg. Nano-Met. Chem.* **2018**, *48*, 427–433.

(52) Sheldrick, G. M. Crystal Structure Refinement With Shelxl. *Acta Crystallogr., Sect. C: Struct. Chem.* **2015**, *71*, 3–8.

(53) Bourhis, L. J.; Dolomanov, O. V.; Gildea, R. J.; Howard, J. A. K.; Puschmann, H. The Anatomy Of A Comprehensive Constrained, Restrained Refinement Program For The Modern Computing Environment—Olex2 Dissected. *Acta Crystallogr., Sect. A: Found. Adv.* **2015**, *71*, 59–75.

(54) Wang, F.; Gao, L.; Zhao, Q.; Zhang, Y.; Dong, W.-K.; Ding, Y.-J. A Highly Selective Fluorescent Chemosensor For Cn– Based On A Novel Bis (Salamo)-Type Tetraoxime Ligand. *Spectrochim. Acta, Part A* **2018**, *190*, 111–115.

Research Article

Synthesis, Characterization, and DNA-Binding Kinetics of New Pd(II) and Pt(II) Thiosemicarbazone Complexes: Spectral, Structural, and Anticancer Evaluation

Simon N. Mbugua ¹, Lydia W. Njenga,¹ Ruth A. Odhiambo,¹ Shem O. Wandiga,¹ Mervin Meyer ², Nicole Sibuyi ², Roger A. Lalancette,³ and Martin O. Onani ⁴

¹Department of Chemistry, University of Nairobi, P.O. Box 30197-00100, Nairobi, Kenya

²Department of Biotechnology, University of the Western Cape, Private Bag X17, Belville 7535, South Africa

³Department of Chemistry, Rutgers University, 73 Warren St., Newark, NJ 07102, USA

⁴Department of Chemical Sciences, University of the Western Cape, Private Bag X17, Belville 7535, South Africa

Correspondence should be addressed to Simon N. Mbugua; mbuguasn@students.uonbi.ac.ke

Received 2 December 2019; Revised 22 April 2020; Accepted 22 May 2020; Published 27 June 2020

Academic Editor: Michele Benedetti

Copyright © 2020 Simon N. Mbugua et al. This is an open access article distributed under the Creative Commons Attribution License, which permits unrestricted use, distribution, and reproduction in any medium, provided the original work is properly cited.

In a bid to come up with potential anticancer agents, a class of thiosemicarbazone ligands bearing substituted thiophene were synthesized followed by complexation with various Pd(II) and Pt(II) metal precursors. The ligands (E)-1-((thiophen-2-yl)methylene)thiosemicarbazide (**L1**), (E)-1-((4-bromothiophen-2-yl)methylene)thiosemicarbazide (**L2**), and (E)-1-((5-bromothiophen-2-yl)methylene)thiosemicarbazide (**L3**) were synthesized by condensation reactions and obtained in good yields. Complexation of **L1** and **L2** with Pd(cod)Cl₂ gave **C1** (C₆H₇Cl₂N₃PdS₂) and **C2** (C₆H₆BrCl₂N₃PdS₂), respectively. Complexation of **L1** with K₂PtCl₄ gave **C3** (C₆H₇Cl₂N₃PtS₂), while **L3** with K₂PtCl₂[(PPh)₃]₂ gave **C4** (C₂₄H₂₁BrClN₃PPtS₂). The structures and coordination for all compounds were established by FTIR, ¹H-NMR, ¹³C-NMR, UV-Vis, elemental analysis, and single-crystal X-ray diffraction studies for ligand **L1**. Tuning of the spectral and anticancer activity of the compounds was investigated by changing the position of the bromide substituent, metal center, and the σ or π-donor/acceptor strength of the groups surrounding the metal center. The compounds had low to moderate anticancer potency with their spectral and structural properties correlating with the corresponding anticancer activity profiles. DNA binding modes were studied by spectroscopy and were comparable to known DNA intercalators. Structure-activity profiles were evident especially between **C1** and **C2** differing by the presence of a Br in position 5 of thiophene ring, which caused a remarkable increase in IC₅₀ values, from 14.71 ± 0.016 (**C1**) to 43.08 ± 0.001 (**C2**) in Caco-2 cells, 1.973 ± 0.048 (**C1**) to 59.56 ± 0.010 (**C2**) in MCF-7 cells, 16.65 ± 0.051 (**C1**) to 72.25 ± 0.003 (**C2**) in HeLa cells, 14.64 ± 0.037 (**C1**) to 94.34 ± 0.003 (**C2**) in HepG2, and 14.05 ± 0.042 (**C1**) to >100(**C2**) in PC-3 cells.

1. Introduction

Cancer is the second leading cause of death globally, with an estimated 1 in 6 deaths, and is responsible for an estimated 9.6 million deaths in 2018 [1]. It is estimated that approximately 70% of all deaths are cancer-related and occur in low- and middle-income countries [1]. The economic impact of cancer is significant and is increasing with a total annual economic cost of cancer in 2010 estimated at approximately US\$ 1.16 trillion. Only 1 in 5

low- and middle-income countries have the necessary data to drive cancer policy [1]. Although major steps have been made in medicine, many difficulties still need to be resolved in order to boost cancer therapy. In line with this, research is putting a great deal of effort into discovering new and effective therapeutics that can mitigate the pertinent adverse effects. Many research reports have focused on creating alternative treatments to minimize the side effects of traditional medicines over the past decade [2–4].

The most practiced efforts to combat cancer include surgery, chemotherapy using chemical drugs, and radiotherapy using electromagnetic radiation like X-rays to kill cancerous cells. New strategies like gene therapy are still being developed where genes from donors are inserted into the DNA of a patient to boost recognition of cancerous cells by the body's diseases fighting mechanisms. Some of the most successful chemotherapeutic drugs include those derived from metals like platinum, ruthenium, titanium, and palladium, among others.

Research on thiosemicarbazone compounds for medical applications appeared as early as 1950s when they were used against TB and leprosy [5]. The following decade saw these compounds tested for antiviral properties which were confirmed, leading to intense research which eventually culminated to the commercialization of some thiosemicarbazone products under trade names methisazone and Marboran®, in the treatment of smallpox [6]. Another major step in utilization of these compounds was the publication of the first antitumor tests [7]. Finch and coworkers explored the broad areas of application where thiosemicarbazones have received most attention, classifying them in relation to their activities against cancerous cells, protozoa, bacteria, or viruses. Their activity is found to correlate to the type of metal center [8]. As anticancer agents, the activity is shown to substantially increase for the complexed product as compared to the free ligand, and also, the undesirable cytotoxicity as side effects was shown to be minimized in the complexes [8].

This work reports the anticancer activity of newly synthesized Pd(II) and Pt(II) complexes bearing thiosemicarbazone ligands. The main objectives were to evaluate the tuning of structure-activity relationships vis-à-vis different σ and/or π -donor/acceptor properties of the groups attached to the metal center, their anticancer activities, and their binding modes to DNA.

Anticancer and apoptotic properties were performed *in vitro* using human colon (Caco-2), human cervical (HeLa), human hepatocellular carcinoma (HepG2), breast cancer (MCF-7), human prostate (PC-3), and noncancer human breast (MCF-12A) cells. Binding modes to DNA were studied by use of calf thymus DNA (CT-DNA). A crystal structure of one of the ligands, L1, is also reported here for the first time according to the CSD database.

2. Materials and Methods

All synthetic manipulations were performed under the fume hood under inert conditions. The solvents were of analytical grade, and each was dried with the recommended drying agent and distilled prior to use. All reagents used in the syntheses were of analytical grade procured from Sigma-Aldrich or Merck Chemicals and used without further modifications.

The melting points were determined on open capillaries using SMP-10 melting point apparatus. FTIR spectra were recorded using PerkinElmer Spectrum 100 Series ATR or FT-IR instrument on KBr pellets in the range

4000–400 cm^{-1} . Proton and carbon-13 nuclear magnetic resonance spectra were obtained from the Bruker 400 MHz spectrometer. The chemical shifts were measured in ppm relative to a TMS standard. UV-Vis spectra were recorded in DMSO solvent at a range of 200–800 nm. Bioassays on the anticancer efficacy were performed at the Department of Biotechnology at the University of the Western Cape. The elemental microanalysis was performed on Server 112 series Elemental Analyzer at the University of Stellenbosch. The single crystal X-ray crystallography was performed at Rutgers University, USA, using a Bruker SMART CCD Apex-II area-detector.

The complexes (C1–C4) were tested against human cell lines: Caco-2 (human colon), HeLa (human cervical), HepG2 (human hepatocellular), MCF-7 (breast cancer), PC-3 (human prostate), and MCF-12A (noncancer human breast) cells. The cells were cultured in their respective media supplemented with 10% fetal bovine serum (FBS) and 1% pen-strep cocktail (100 U/mL penicillin and 100 g/mL streptomycin). Caco-2, HeLa, HepG2, and MCF-7 cells were grown in Dulbecco's Modified Eagle Medium and MCF-12A in DMEM-F12 containing insulin, EGF, and hydrocortisone, while PC-3 cells were cultured in RPMI-1640 media. The cells were grown at 37°C in a 5% CO_2 humidified incubator (Labotec, South Africa) and seeded at 1×10^5 cells/mL density in a 96-well plate for 24 h. The cells were treated with 100 $\mu\text{g}/\text{mL}$ of the test compound for 24 h period. Cytotoxicity of the compounds was assessed by MTT assay following manufacturer's instructions. After treatment, 10 μL of 5 mg/mL MTT (Sigma, USA) was added to each well, and the plates were incubated at 37°C for 3 h. The insoluble formazan crystals were solubilised by adding 100 μL of DMSO. The reduction of MTT was read at 570 nm using POLARStar Omega plate reader.

2.1. Synthesis of the Ligands

2.1.1. (E)-1-((Thiophen-2-yl)methylene)thiosemicarbazide (L1). The ligand was synthesized using the method described by Channar et al. [9] with some modifications. Thiophene-2-carbaldehyde (475 μL (5 mmol)) and thiosemicarbazide (0.4558 g (5 mmol)) were refluxed under inert conditions in 20 ml dry methanol for 12 hours. On cooling, a light brown precipitate was formed which was redissolved in diethyl ether, filtered on activated carbon, and kept in the fridge for slow evaporation where shiny brown crystals were obtained.

Yield: 54%. FTIR (KBr ν^{-1}): (3414–3149 N-H stretch) 3000 (sp^2 C-H bend), 1611 CH=N stretch, and 1538 C=S stretch.

$^1\text{H-NMR}$ (400 MHz, DMSO- d_6) δ 11.45 (s, 1H), 8.09–8.33 (m, 1H), 7.65 (d, J = 5.01 Hz, 1H), 7.45 (dd, J = 0.73, 3.55 Hz, 1H), 7.12 (dd, J = 3.67, 5.01 Hz, 1H), and 3.35 (s, 2H).

$^{13}\text{C-NMR}$ (400 MHz, DMSO- d_6) δ 178.27 (C=N imine), 139.24, 138.22, 130.92, 129.33, and 128.41.

Molecular weight: 185.27. Elemental analysis; molecular formula; $\text{C}_6\text{H}_7\text{N}_3\text{S}_2$. Calculated (obtained); C, 38.90(38.83); H, 3.81(3.87); N, 22.68(22.63); and S, 34.61(34.63).

2.1.2. (*E*)-1-((5-Bromothiophen-2-yl)methylene)thiosemicarbazide (L2). The ligand was synthesized with a synthetic procedure similar for L1 using 4-bromothiophene-2-carbaldehyde (625 μ l (5 mmol)) and thiosemicarbazide (0.4558 g (5 mmol)). The ligand was isolated as a light brown precipitate.

Yield 68%. FTIR (KBr ν^{-1}); (3429–3276 N-H stretch), 3155–2999 (sp^2 C-H bend), 1608 CH = N stretch, and 1543 C = S stretch. $^1\text{H-NMR}$ (400 MHz, DMSO- d_6) δ 11.50 (s, 1H), 8.14 (s, 1H), 7.64 (br. s., 1H), 7.24 (s, 1H), and 3.35 (s, 2H).

$^{13}\text{C-NMR}$ (400 MHz, DMSO- d_6) δ 184.27 (C = N imine), 178.25 141.07, 137.29, 131.58, and 115.03.

Molecular weight: 264.17. Elemental analysis; molecular formula; $\text{C}_6\text{H}_6\text{BrN}_3\text{S}_2$. Calculated (obtained); C, 27.28(27.26); H, 2.29(2.27); N, 15.91(15.96); and S, 24.28(25.27).

2.1.3. (*E*)-1-((4-Bromothiophen-2-yl)methylene)thiosemicarbazide (L3). The ligand was synthesized with a synthetic procedure similar to L1 using 4-bromothiophene-2-carbaldehyde (1.061 g (5 mmol)) and thiosemicarbazide (0.4558 g (5 mmol)). The ligand was isolated as a light brown powder.

Yield 58%. FTIR (KBr ν^{-1}); (3378–3246 N-H stretch), 3155–3008 (sp^2 C-H bend), 1605 CH = N stretch, and 1545 C = S stretch. $^1\text{H-NMR}$ (400 MHz, DMSO- d_6) δ 11.54 (s, 1H), 8.16 (s, 1H), 7.75 (s, 1H), 7.53 (s, 1H), and 3.34 (s, 2H). $^{13}\text{C-NMR}$ (400 MHz, DMSO- d_6) δ 178.27 (C = N imine), 140.80, 136.35, 132.21, 126.46, and 109.97.

Molecular weight: 264.17. Elemental analysis; molecular formula; $\text{C}_6\text{H}_6\text{BrN}_3\text{S}_2$. Calculated (obtained); C, 27.28 (27.22); H, 2.29 (2.24); N, 15.91 (15.87); and S, 24.28 (24.27).

2.2. Synthesis of Pd(II) Complexes

2.2.1. Synthesis of Pd(II) Complex (C1). The ligand L1 92 mg (0.25 mmol) was dissolved in THF (2 ml) and was added dropwise into a stirring solution of Pd(cod)Cl₂ (72 mg (0.25 mmol)) dissolved in DCM (15 ml) under argon. A red precipitate was formed, and stirring was continued at room temperature for 6 hours while monitoring the reaction with TLC until completion. The solvent was reduced under pressure to about 1 ml. Excess hexane was added followed by filtration and washing of the red powder product with more hexane (3 \times 5 ml) followed by filtration and drying under vacuum.

Yield 71%. FTIR (KBr ν^{-1}); 3370, NH stretch; 3176–3076, CH stretch, 1619, C = N, 1542; C = S stretch. $^1\text{H-NMR}$ (400 MHz, DMSO- d_6) δ 8.35–8.60 (m, 1H), 7.98 (s, 1H), 7.84 (s, 1H), 7.51 (br. s., 1H), 7.13 (d, J = 4.89 Hz, 1H), and 3.60 (s, 2H). $^{13}\text{C-NMR}$ (400 MHz, DMSO- d_6) δ 177.24 (C = N imine), 172.16, 146.15, 135.36, 133.53, and 127.13.

Molecular weight: 362.6. Elemental analysis; molecular formula; $\text{C}_6\text{H}_7\text{Cl}_2\text{N}_3\text{PdS}_2$. Calculated (obtained); C, 19.87 (19.77); H, 1.95 (1.96); and N, 11.59 (11.52).

2.2.2. Synthesis of Pd(II) Complex (C2). The complex was synthesized with a procedure similar to C1 using L2 (66 mg(0.25 mmol)). The complex was isolated as a brown powder.

Yield 74%. FTIR (KBr ν^{-1}); 3075, NH stretch; 2943 CH stretch; 1621 C = N; and 1419 C = S stretch. $^1\text{H-NMR}$ (400 MHz, DMSO- d_6) δ 8.34 (s, 1H), 7.59 (s, 1H), 7.32 (s, 1H), 6.97 (s, 1H), 5.76 (s, 1H), and 3.60 (br. s., 2H). $^{13}\text{C-NMR}$ (400 MHz, DMSO- d_6) δ 172.83 (C = N imine), 144.86, 136.01, 134.09, 130.64, and 124.92.

Molecular weight: 441.49. Elemental analysis; molecular formula; $\text{C}_6\text{H}_6\text{BrCl}_2\text{N}_3\text{PdS}_2$. Calculated (obtained); C, 16.32 (16.36); H, 1.37 (1.31); N, 9.52 (9.45); and S, 14.53 (14.57).

Molecular weight: 387.2. Elemental analysis; molecular formula; $\text{C}_{12}\text{H}_{13}\text{ClN}_4\text{PdS}$. Calculated (obtained); C, 37.22 (37.27); H, 3.38 (2.33); N, 14.47 (14.42); and S, 8.28 (8.27).

2.3. Synthesis of Pt(II) Complexes

2.3.1. Synthesis of Pt(II) Complex (C3). The complex was synthesized by dropwise addition of a solution of K₂PtCl₄ (104 mg (0.25 mmol)) dissolved in MeOH/H₂O (2 : 1) (3 ml), into a stirring solution of L1 (46 mg (0.25 mmol)) in THF (2 ml). A yellow precipitate was formed immediately, and stirring was continued for one and half hours at room temperature, filtered followed by washing with diethyl ether (3 \times 5 ml) and dried under vacuum.

Yield 98%. FTIR (KBr ν^{-1}); 3268, NH stretch; 3082, CH stretch; 1593, C = N; 1515, C = S stretch. $^1\text{H-NMR}$ (400 MHz, DMSO- d_6) δ 12.34 (br. s., 1H), 8.55 (s, 1H), 7.60 (br. s., 1H), 7.16 (br. s., 1H), 6.95 (s, 1H), and 3.46 (br. s., 2H). $^{13}\text{C-NMR}$ (400 MHz, DMSO- d_6) δ 173.45 (C = N imine), 145.86, 143.94, 136.93, 133.14, and 127.79.

Molecular weight: 451.25. Elemental analysis; molecular formula; $\text{C}_6\text{H}_7\text{Cl}_2\text{N}_3\text{PtS}_2$. Calculated (obtained); C, 15.97 (15.91); H, 1.56 (1.51); N, 9.31 (9.38); and S, 14.21 (14.26).

2.3.2. Synthesis of Pt(II) Complex (C4). The complex was synthesized following the procedure for the previous one by adding of PtCl₂[(PPh₃)₂]₂ (198 mg(0.25 mmol)) in DCM (5 ml) into a stirring solution of L2 (66 mg (0.25 mmol)) in benzene (20 ml) at room temperature and stirred for 24 h. The complex was isolated as a yellow powder.

Yield 36%. FTIR (KBr ν^{-1}); (3287–3166 N-H stretch), 3076–2958 (sp^2 C-H bend), 1608 CH = N stretch, 1582 C = S stretch. $^1\text{H-NMR}$ (400 MHz, DMSO- d_6) δ 8.72 (s, 1H), 7.96 (s, 1H), 7.43 (m, 15H), 3.43 (s, 1H), 2.89 (s, 1H), and 2.74 (s, 2H).

Molecular weight: 756.98. Elemental analysis; molecular formula; $\text{C}_{24}\text{H}_{21}\text{BrClN}_3\text{PPtS}_2$. Calculated (obtained); C, 38.08 (38.0); H, 2.80 (2.79); N, 5.55 (5.53); and S, 8.90 (8.87).

2.4. Crystal Structure for L1. The single crystal X-ray crystallography experiment was performed using a Bruker SMART CCD Apex-II area-detector. The crystal structure was solved and refined using the full-matrix least-square

method based on F^2 [10] and the graphics interface program ORTEP-3 for Windows [11].

2.5. Anticancer Activity. This was performed using human colon (Caco-2), human cervical (HeLa), human hepatocellular carcinoma (HepG2), breast cancer (MCF-7), human prostate (PC-3), and noncancer human breast (MCF-12A) cancer cells *in vitro* by incubating the particular cancer cells with 2.2×10^{-4} M of the various compounds. Cell viability was determined after a 24 h period.

Attempts to complex **L2** with K_2PtCl_4 and **L3** with either $Pd(cod)Cl_2$ or K_2PtCl_4 did not give a product. Similar attempts to complex **L1** with $PtCl_2[(PPh_3)_2]$ did not yield a product.

3. Results and Discussion

3.1. Synthesis. The ligands **L1–L3** were synthesized via Schiff base condensation reaction of thiosemicarbazide compound with an appropriate thiophene-2-carbaldehyde under reflux for 12 hours. The complexes were then formed through a reaction of the ligands with metal precursors $Pd(cod)Cl_2$ (**C1** and **C2**), K_2PtCl_4 (**C3**), and $PdCl_2(PPh_3)_2$ (**C4**). These reactions are summarized under Scheme 1.

3.2. Infrared Spectra. The FTIR for the compounds were recorded in either KBr pellets or ATR. The IR spectrum for the ligands displayed a clear stretching vibration bands between 1605 and 1611 cm^{-1} which were assigned to the imine C=N moiety. The ligand **L1** has an unsubstituted thiophene and shows the highest energy for the imine bond at 1611 cm^{-1} . On introducing a bromide at position 4 on the thiophene ring (**L3**), there is a hypsochromic shift of 6 cm^{-1} to 1605 cm^{-1} . This is because of the electron withdrawing effect of the electronegative bromide which draws electron density away from the thiophene ring and consequently from the imine region thereby raising the single bond character of the imine bond resulting in the observed lower shift in the frequency.

The ligand **L2** with a -Br introduced at position 5 on the thiophene ring showed a lesser shift in frequency (3 cm^{-1}) from 1611 cm^{-1} to 1608 cm^{-1} . Compared to **L3**, the -Br at position 5 has a possible resonance donation from its lone pair of nonbonding electrons which contribute to an increased electron density to the thiophene ring and consequently to the imine region. However, the electronegativity dipole is dominant compared to the resonance dipole due to the poor overlap of $4p-2p$ orbitals with carbon. The FTIR spectra for the ligands are shown in Table 1.

The azomethine peaks were observed in the complexes where they were found to have shifted to between 1593 and 1637 cm^{-1} . It was observed that, in all the Pd complexes, the azomethine peak shifted to higher energy, while for Pt(II) complexes, it shifted to lower energy in the IR spectra. For the ligands, a possible explanation to this can be deduced from a consideration of the different groups and substituents attached to the imine bond. Complexes **C1** and **C3** were compared to the parent ligand **L1** after the introduction of

$PdCl_2$ and $PtCl_2$ salts, respectively. As mentioned earlier, complexation with Pd(II) caused a shift to higher energy by 8 cm^{-1} (1611 cm^{-1} to 1619 cm^{-1} for **C1**) while complexation with Pt(II) shifted the energy to a lower wavenumber by 18 cm^{-1} (1593 cm^{-1} to 1611 cm^{-1} for **C3**). This can be explained in terms of nuclear charge for the two metals. Pt(II) has a higher nuclear charge inferring that the incoming ligand will be attracted more to Pt than to Pd. This leaves the azomethine region with less electron density and more single bond character for the Pt(II) complex compared to the Pd(II) complex. Bond dissociation energies for M-L bond is also greater for Pt than Pd due to less steric crowding around the Pt metal center. These factors raise the overall reactivity of Pd(II) complexes compared to Pt(II), a reason why Pd-Cl bond dissociates 10^4-10^5 times faster in Pd(II) complexes [12].

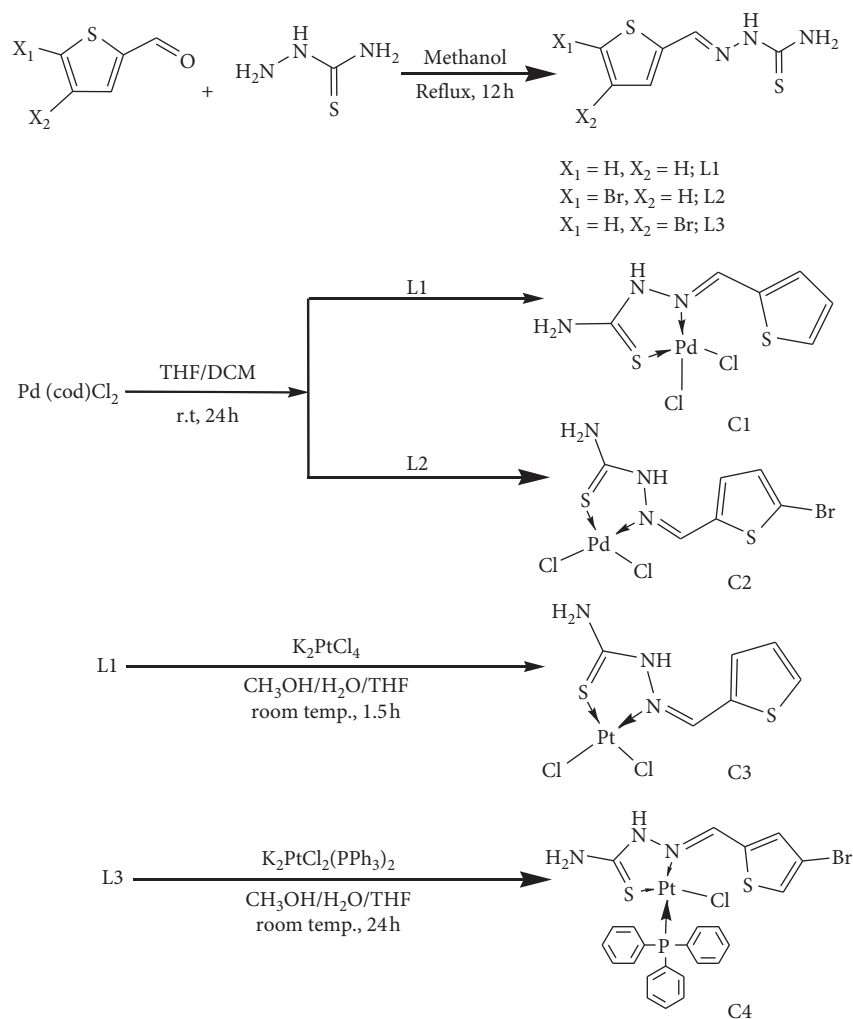
Complex **C4** was a modification of **C3**, where one -Cl was substituted for -PPh₃ and a -Br introduced at position 4 on the thiophene ring. The -PPh₃ group is a much better σ donor and π acceptor which effectively weakens the Pt-N bond *trans* to itself in **C4** through ground state *trans*-influence. This in turn means that electron density is not drawn from the imine region, and therefore, the imine bond in **C4** retains more π character compared to that in **C3**. However, the -Br in position 4 has minimal influence since there is no resonance donation for the nonbonding electrons. These factors resulted in the observed difference in energy for the imine bonds, 1608 cm^{-1} versus 1593 cm^{-1} for **C4** and **C3**, respectively.

Complex **C2** was a modification of **C1**, where a -Br was introduced at position 5 on the thiophene ring. At position 5, there is a possible resonance donation from the halide lone pair implying that the imine bond retains more π character in **C4** compared to **C1**, reflected in the hypsochromic shift observed in **C2** (1621 cm^{-1} from 1608 cm^{-1} (**L2**)). The FTIR spectra data for the complexes are shown in Table 1.

3.2.1. 1H -NMR Spectra. The azomethine protons together with the protons attached to the thiophene ring were observed and compared for the three ligands after introduction of the bromide substituent, as shown in Figure 1.

For **L1**, H_a , H_b , and H_c occurred at 7.13, 7.45, and 7.65 ppm, respectively, while the azomethine proton occurred at 8.25 ppm. Upon introduction of a Br at position 4 (**L3**), the remaining protons H_a and H_c appeared further downfield (7.53 and 7.75 ppm, respectively), as a result of deshielding by the Br substituent. Similar trend is observed when the Br is introduced at position 5 (**L2**). The peaks for H_a and H_b now appear at 7.27 and 8.14 ppm, respectively. Together with the electronegativity of the -Br, the protons at orthoposition to -Br experience steric deshielding as the hydrogen s-orbitals are disrupted from the normal spherical symmetry.

The azomethine proton for **L1** appeared at 8.25 ppm. On introduction of a Br at position 4 (**L3**) and position 5 (**L2**) of the thiophene ring, an upfield shift of 0.10 ppm (to 8.16 ppm, **L3**) and 0.11 ppm (to 8.14 ppm, **L2**) was observed. This trend is expected because, at position 5, there is resonance



SCHEME 1: Synthesis of Pd (II) and Pt (II) complexes.

TABLE 1: Photophysical data for ligands (L1–L3) and complexes (C1–C4).

	FTIR Imine (C=N)	¹ H-NMR Imine (CH=N)	¹³ C-NMR Imine (C=N)	Absorption ($\epsilon \times 10^4$ LMol ⁻¹ cm ⁻¹) λ_{max} (nm)
L1	1611	8.25	139.09	340 (0.53)
L2	1608	8.14	141.16	347 (0.64)
L3	1605	8.16	140.58	343 (0.61)
C1	1619	8.41	146.04	364, 382 (1.51, 1.34)
C2	1621	7.59	145.02	371, 390 (1.16, 1.09, 0.0557)
C3	1593	8.55	145.86	348, 363, 540 (1.30, 0.86, 0.0087)
C4	1608	7.96	142.98	348, 401, 555 (1.41, 1.31)

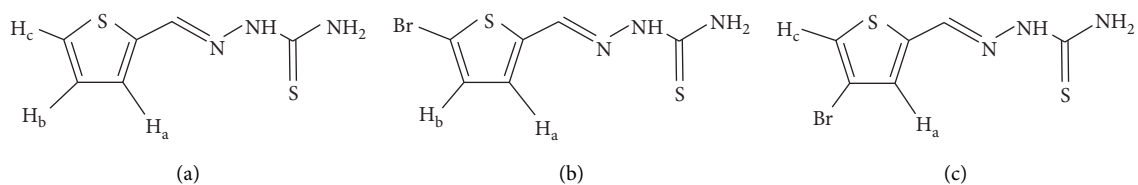


FIGURE 1: Ligands (a) L1, (b) L2, and (c) L3.

donation of Br lone pair electrons; thus, the azomethine proton for **L2** experiences a higher shielding effect and resonates further upfield compared to **L3**. The ^1H -NMR spectra data are shown in Table 1. A representative ^1H -NMR spectrum for ligand **L3** is shown in Figure 2.

Upon complexation, the resonance frequencies of the azomethine protons were observed and compared to those of the free ligands. Complexes **C1** and **C3** were compared to the parent ligand **L1**, where a downfield shift was observed in both complexes. The Pd(II) complex (**C1**) showed a lesser shift of 0.16 ppm compared to 0.30 ppm observed in the Pt(II) complex **C3**. As discussed above, this can be attributed to the higher nuclear charge of Pt(II) compared to Pd(II), which causes a higher deshielding of the azomethine region in the Pt(II) complex leading to a more downfield shift for the azomethine proton. A representative ^1H -NMR spectrum for complex **C1** is shown in Figure 3.

Complexes **C3** and **C4** differed in that there was a Br substituent attached to the thiophene ring, and the PPh_3 group coordinated to the metal center in **C4**, while no substituent was present in **C3**, and coordination to the metal was by Cl ligands. Considering **C4** with a Br at position 4 and a PPh_3 directly coordinated to the metal center, the Br at position 4 has minimal resonance influence to the complex, but PPh_3 is both a good s donor and a π acceptor. The s donation is through a hybrid orbital containing a lone pair located on phosphorus, which is enhanced by the electron-rich phenyl rings attached to the phosphorus. The steric bulk of the PPh_3 group and the resultant crowding around the metal center is a determinant in the rate at which the group dissociates from a metal, where the bulkier the R group, the faster the rate of dissociation [13]. These factors together with the higher *trans*-influence of PPh_3 compared to Cl make **C4** to be more shielded at the azomethine region compared to **C3**. This resulted in the observed difference of 0.59 ppm between the azomethine protons of the two complexes.

Complexes **C2** and **C1** differed only on the Br substituent at position 5 of the thiophene ring of **C2**. At position 5, the Br substituent has possible resonance donation to the adjacent π system. This increases the shielding of the azomethine proton making it to resonate at a higher field region compared to that of **C1**. The ^1H -NMR spectra for the complexes are shown in Table 1.

3.2.2. ^{13}C -NMR Spectra. The ^{13}C -NMR spectra for the ligands were compared with those of their corresponding complexes for carbons at the imine regions. The ligand imine carbons shifts occurred at 139.24 ppm, 141.07 ppm, and 140.80 ppm for **L1**, **L2**, and **L3**, respectively. Introduction of a -Br at position 5 (**L2**) had an incremental effect on the chemical shift (by 1.83 ppm) on the imine carbon compared to the -Br at position 4 (**L3**) which caused a shift of 1.56 ppm. At position 5, the -Br has a higher inductive effect on the ligand via the π system, which deshields the imine carbon more causing it to resonate at a higher frequency (low field). The ^{13}C -NMR spectra for the ligands are shown in Table 1. A representative ^{13}C -NMR spectrum for ligand **L3** is shown in Figure 4.

After complexation, the shifts for the imine carbon of complexes **C1** and **C3** occurred further downfield (146.04 ppm and 145.86 ppm, respectively) compared to the parent ligand **L1**. This increase in shift by 6.95 ppm and 5.28 ppm is as a result of coordination to the metal as electron density is pulled away from the azomethine bond deshielding the carbon nucleus. This means that only a smaller external magnetic field is necessary to bring the nucleus into resonance, resulting in the observed higher chemical shifts in ^{13}C -NMR. Similar trend is observed for complexes **C4** and **C2** compared to the parent ligands. A representative ^{13}C -NMR spectrum for complex **C2** is shown in Figure 5.

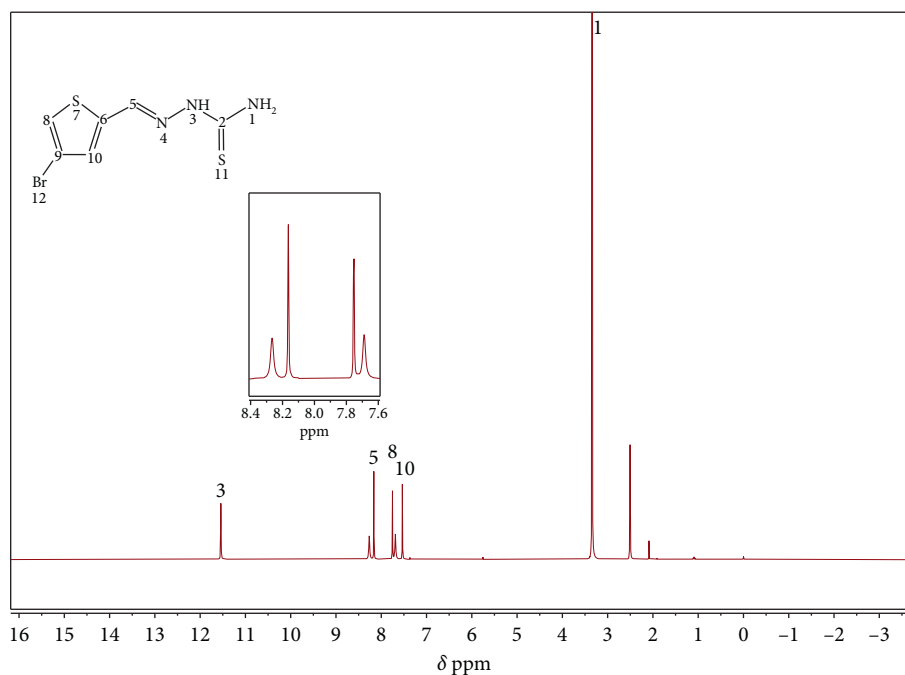
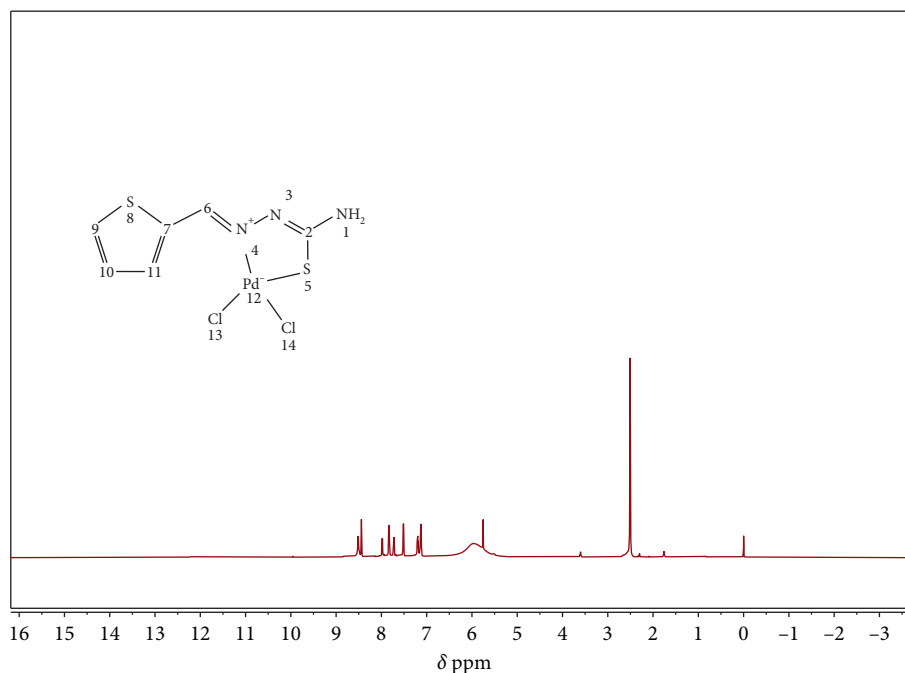
3.2.3. Electronic Spectra. UV-visible spectra for the compounds were recorded in DMSO at range 200–800 nm using quartz cells at a concentration of 1.0×10^{-3} M. The results for the photophysical data are summarized in Table 1.

As shown in Table 1, a higher bathochromic shift (7 nm) was observed in **L2** after introducing Br at position 5 of the thiophene ring than in **L3** (3 nm) with the -Br at position 4. An auxochrome at position 5, as opposed to position 4, has better p - π conjugation with the rest of the π system from the possible resonance donation of the lone pair on -Br. This increased conjugation led to the observed hyperchromic effect in **L2**.

The complexes had different metal centers and ligands coordinated to the metal. **C1** and **C3** differed only by the type of metal center. The absorbance for **C3** with a Pt (II) metal center occurred at a shorter wavelength (348 nm) compared to **C1** (364 nm) with a Pd(II) metal center. A possible reason for this is the higher nuclear charge of Pt(II) which draws electron density away from the π system effectively lowering the energy of π orbitals thereby increasing the ΔE between π - π^* levels in **C3**. **C1** and **C2** differed only by the presence of a -Br in position 5 of **C2**. The presence of the auxochrome increased the electron density of the π bonding orbitals resulting in raised energy level through electron-electron repulsion, leading to the observed longer wavelength in **C2**.

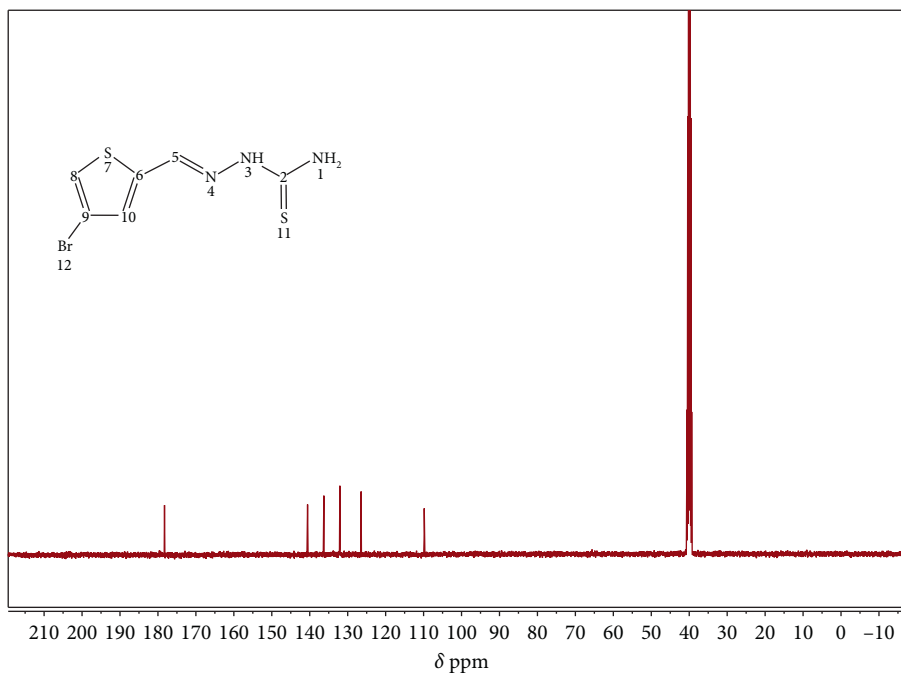
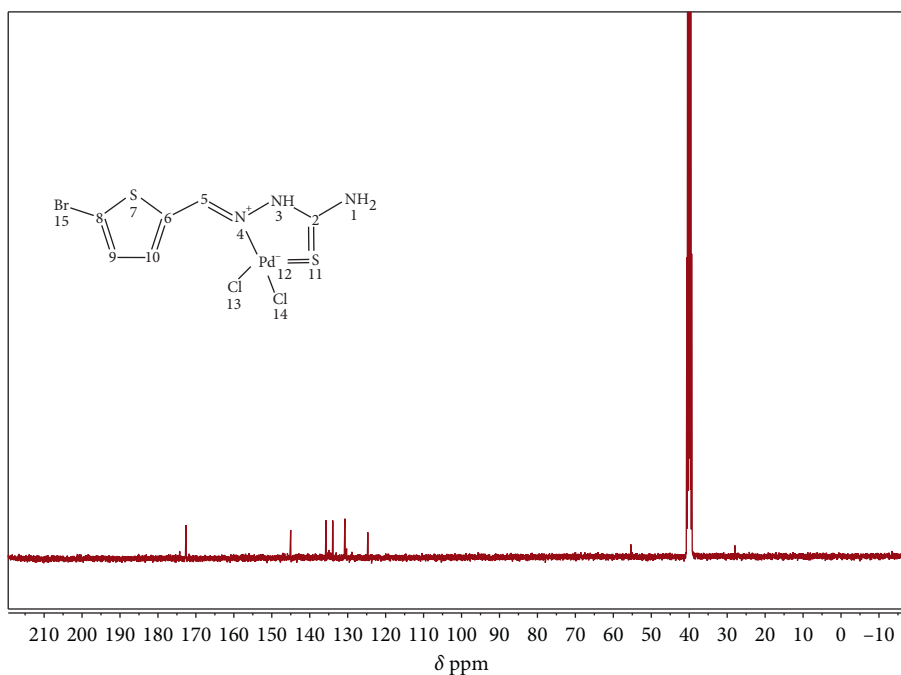
C4 and **C3** differed in that there was a -Br substituent in position 4 of the thiophene ring, and a bulky - PPh_3 coordinated to the metal center of **C4**. PPh_3 is a better s donor- π acceptor compared to Cl, and the electron-rich phenyl rings impart it with better ligand to metal charge transfer properties causing the observed red shift in **C4**. The UV-Vis spectra for the complexes are displayed in Table 1.

In general, ligand spectra showed peaks corresponding to $\pi \rightarrow \pi^*$ transitions with molar extinction coefficients of 10^3 $\text{LMol}^{-1} \text{cm}^{-1}$, while the complexes exhibited an extra broad and weak absorptions at around 550–570 nm assigned to d-d transitions, with molar extinction coefficients of 10^1 – 10^2 $\text{LMol}^{-1} \text{cm}^{-1}$. In contrast, the spectra for all the complexes displayed two peaks for **C1** and **C2** and three peaks for **C3** and **C4**. Similar observations are reported in literature and are attributed to a combination of the ligand based π - π^* and MLCT [$(d\pi_{(\text{metal})} - \pi^*_{(\text{ligand})})$] [14]. The UV-Vis spectra for complex **C3** is shown in Figure 6.

FIGURE 2: $^1\text{H-NMR}$ spectra for ligand **L3**.FIGURE 3: $^1\text{H-NMR}$ spectra for complex **C1**.

3.2.4. *Crystal Structure for Ligand L1*. Crystals suitable for X-ray crystallography were grown for ligand **L1** by slow diffusion of hexane into a THF solution of **L1**. The ligand belongs to the monoclinic $P21/n$ space system with 8-unit molecules packed into the crystal unit. The structure data and refinement parameters are shown in Table 2. The structure showed the thiosemicarbazone existing in the thione form.

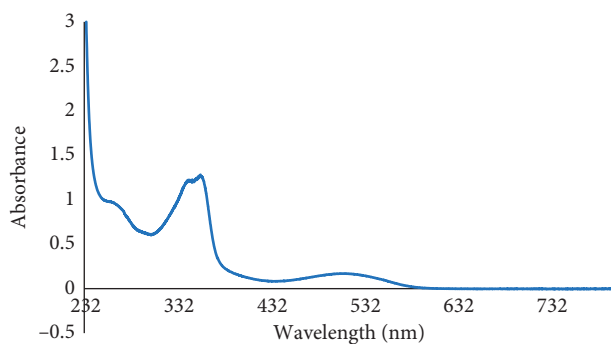
The molecular pair adopts a different conformation for each unit molecule with one molecule lying on a perfect plane but the other having a torsion angle of about 17° (Figure 7(a)). The molecule is stabilized through intermolecular hydrogen bonding between the hydrogen attached to N-5 of one molecule and thiosemicarbazide sulphur of the other molecules. Furthermore, hydrogen bonding extends towards the adjacent molecular pair, as shown in Figure 7(b).

FIGURE 4: ¹³C-NMR for L3.FIGURE 5: ¹³C-NMR for C2.

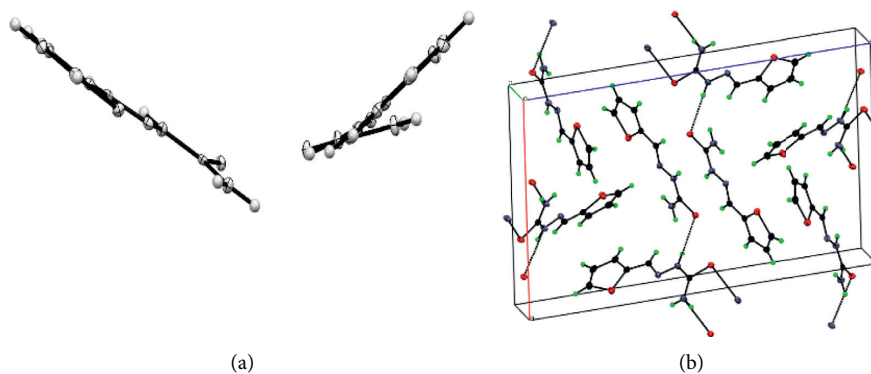
Proton scans over a 72 h period were conducted to establish stability in solution, as shown in Figure 8. Lack of any changes in peaks over the test period indicated that the compounds were stable in solution and therefore could be studied for bioassay.

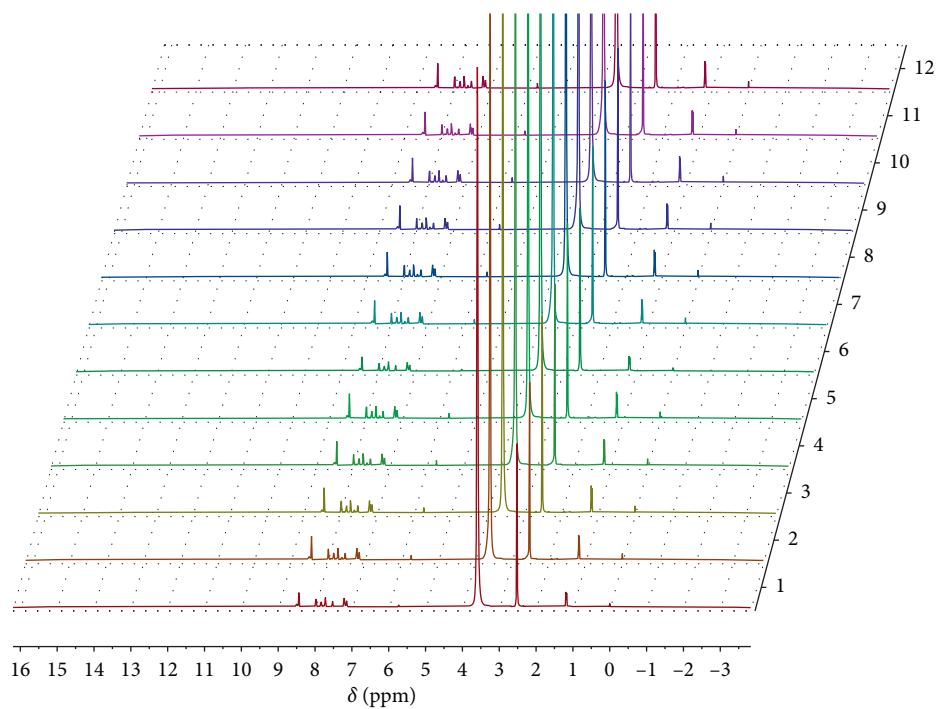
The complexes were then subjected for bioassays to assess their anticancer activities.

3.3. Bioassays on Cytotoxicity. The main objective of this work was to evaluate thiosemicarbazone-based Pd(II) and Pt(II) complexes for possible anticancer properties. The motivation behind this study was two-fold. First, the sterically bulky substituents around the metal center are a strategy appearing in literature for prevention of axial approach to the metal atom from the z^2 -direction. This hinders

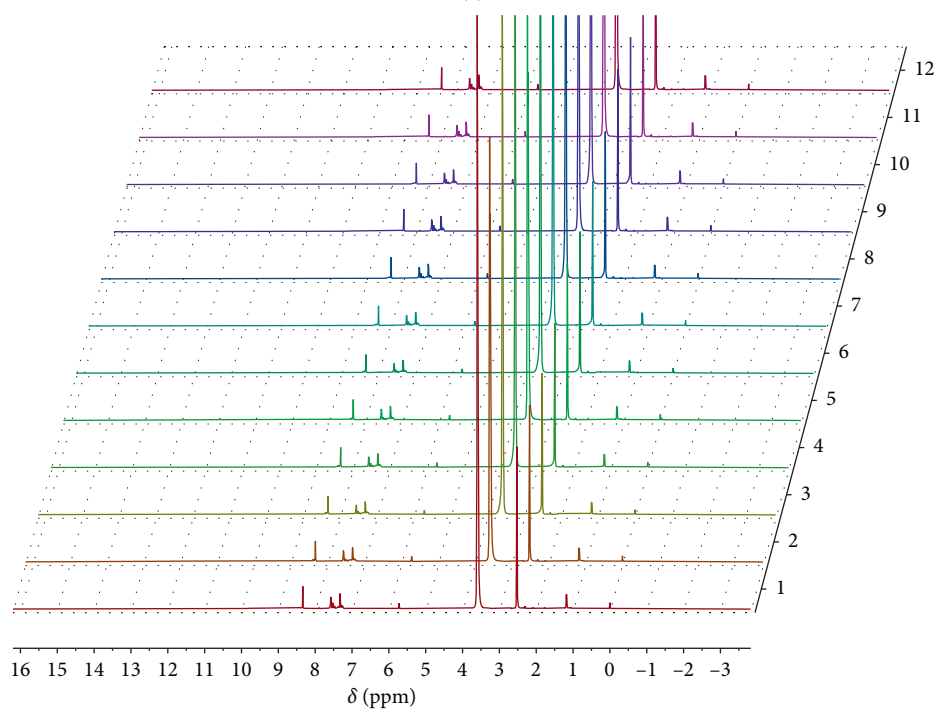
FIGURE 6: UV-Vis spectra for complex **C3**.TABLE 2: Crystal data for **L1**.

Chemical formula	$C_6H_7N_3S_2$
Mr	185.27
Crystal system, space group	Monoclinic, $P21/n$
Temperature (K)	100
a, b, c (\AA)	13.4381 (2), 5.7728 (1), 21.2683 (4)
β ($^\circ$)	96.302 (1)
V (\AA^3)	1639.93 (5)
Z	8
Radiation type	Cu $K\alpha$
μ (mm^{-1})	5.37
Crystal size (mm)	$0.37 \times 0.23 \times 0.19$
<i>Data collection</i>	
Diffractometer	Bruker SMART CCD Apex-II area-detector
T_{\min} , T_{\max}	0.272, 0.496
No. of measured, independent, and observed ($I > 2\sigma(I)$) reflections	21136, 2897, 2744
R int	0.041
$(\sin \theta/\lambda)_{\max}$ (\AA^{-1})	0.596
<i>Refinement</i>	
$R[F^2 > 2\sigma(F^2)]$, $wR(F^2)$, S	0.026, 0.067, 1.04
No. of reflections	2897
No. of parameters	200
H-atom treatment	H-atom parameters constrained
$\Delta\rho_{\max}$, $\Delta\rho_{\min}$ ($e \text{\AA}^{-3}$)	0.37, -0.27

FIGURE 7: (a) ORTEP view for the molecular pair for ligand **L1** showing the torsion in one molecule; (b) the crystal packing and H-bonding.



(a)



(b)

FIGURE 8: Continued.

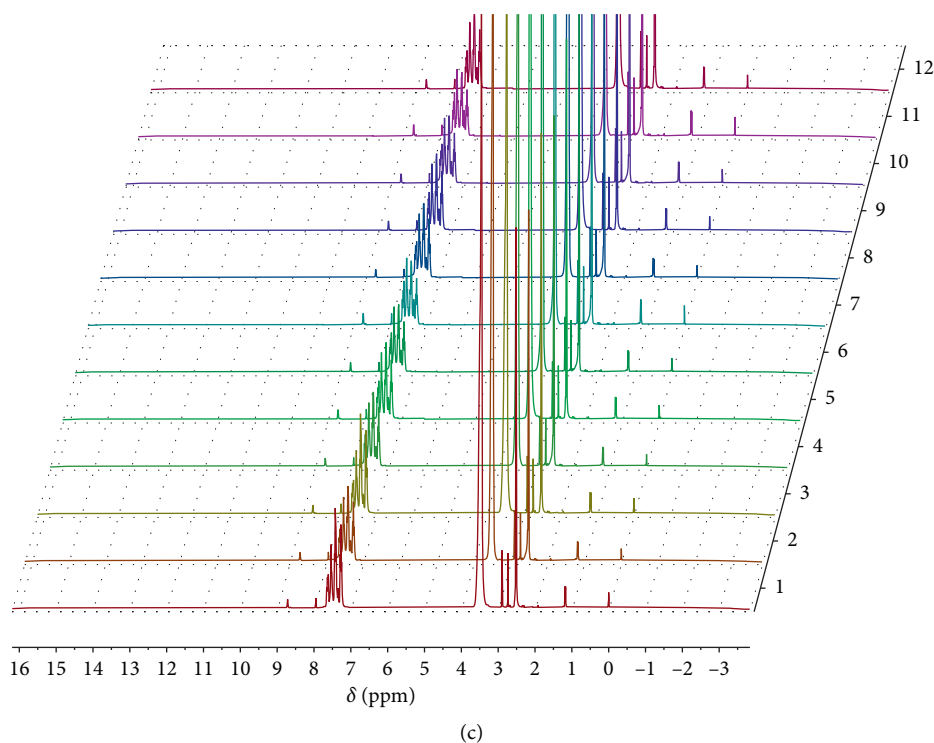


FIGURE 8: ^1H -NMR scans for (a) **C1**, (b) **C2**, and (c) **C4** at 6 h intervals for 72 h in the presence of D_2O .

the formation of a trigonal bipyramid (TBP) intermediate which would lead to a ligand substitution [15] and thereby lead to high binding selectivity to DNA *in vitro* and *in vivo* [16]

Secondly, it has been shown that bidentate chelation plays a significant role in preventing *trans*-labilization and unwanted dislodgment of ligands *in vivo* [17, 18]. Preliminary results with the free ligands did not show any substantial activity either as anticancer agents, and therefore, the detected activity could be accredited to the complexed forms.

The anticancer activity was calculated according to the following equation:

$$\% \text{ cell viability} = \left(\frac{\text{average absorbances of treated cells}}{\text{average absorbances of control}} \right) \times 100\% \quad (1)$$

The results obtained against a control under similar test conditions with no test compound added are shown in Figure 9.

Structure-activity correlations were drawn on the different trends in cytotoxicity of these complexes. Complex **C1** was similar to **C2** differing only by a -Br substituent on position 5 of the thiophene moiety of **C2**. Comparing the results for these two complexes, the introduction of the -Br (**C2**) resulted in remarkable difference in activity, where cell viability in all cell lines Caco-2 (8%), HepG2 (5%), HeLa (38%), MCF-7 (6%), MCF-12A (5%), and PC-3 (49%) increased remarkably. The difference in the results for **C1** and **C2** could be attributed to the presence

of -Br in **C2** which decreased the electron density around the metal center. This caused the -Cl ligands to be held more firmly, which in turn decreased the rate of -Cl substitution reducing the cytotoxicity of **C2**. Similar observations are reported in literature where it is observed that an increase in donor properties of the coordinated groups directly leads to increased cytotoxicity for Pd drugs [19].

Complexes **C1** and **C3** had similar structures differing only by the metal center, Pd(II) for **C1** and Pt(II) for **C3**. Complex **C1** was found to be more cytotoxic than **C3** in all the tested cells. Since Pd(II) has a lower nuclear charge compared to Pt(II), the ligands are less strongly held in **C1**. The smaller spatial size of 4d-orbitals in Pd (II) compared to 5d-orbitals in Pt (II) also led to more steric crowding in the Pd (II) centre which probably resulted in higher rates of ligand substitution, raising the cytotoxicity in **C1**.

The observed higher cytotoxicity in **C4** in comparison to **C3** could be attributed to the steric crowding effects of the bulky PPh_3 group in **C4** since the steric bulk of a PR_3 group and the resultant crowding around the metal center is a determinant in the rate at which the group dissociates from the metal. Tolman [13] working on nickel complexes made similar observations where steric hindrance played a bigger role than electronic effects in influencing the rate of attaining equilibrium in a number of phosphorus ligands on nickel(0) [13]. The expected higher ligand dissociation determined the observed higher cytotoxicity for **C4** compared to **C3** with a Cl group. The plain ligands did not show any substantial activity at the tested dose (data not shown) compared to their corresponding complexes, and therefore, the reduced cell proliferation shown could be accredited to the complex compounds.

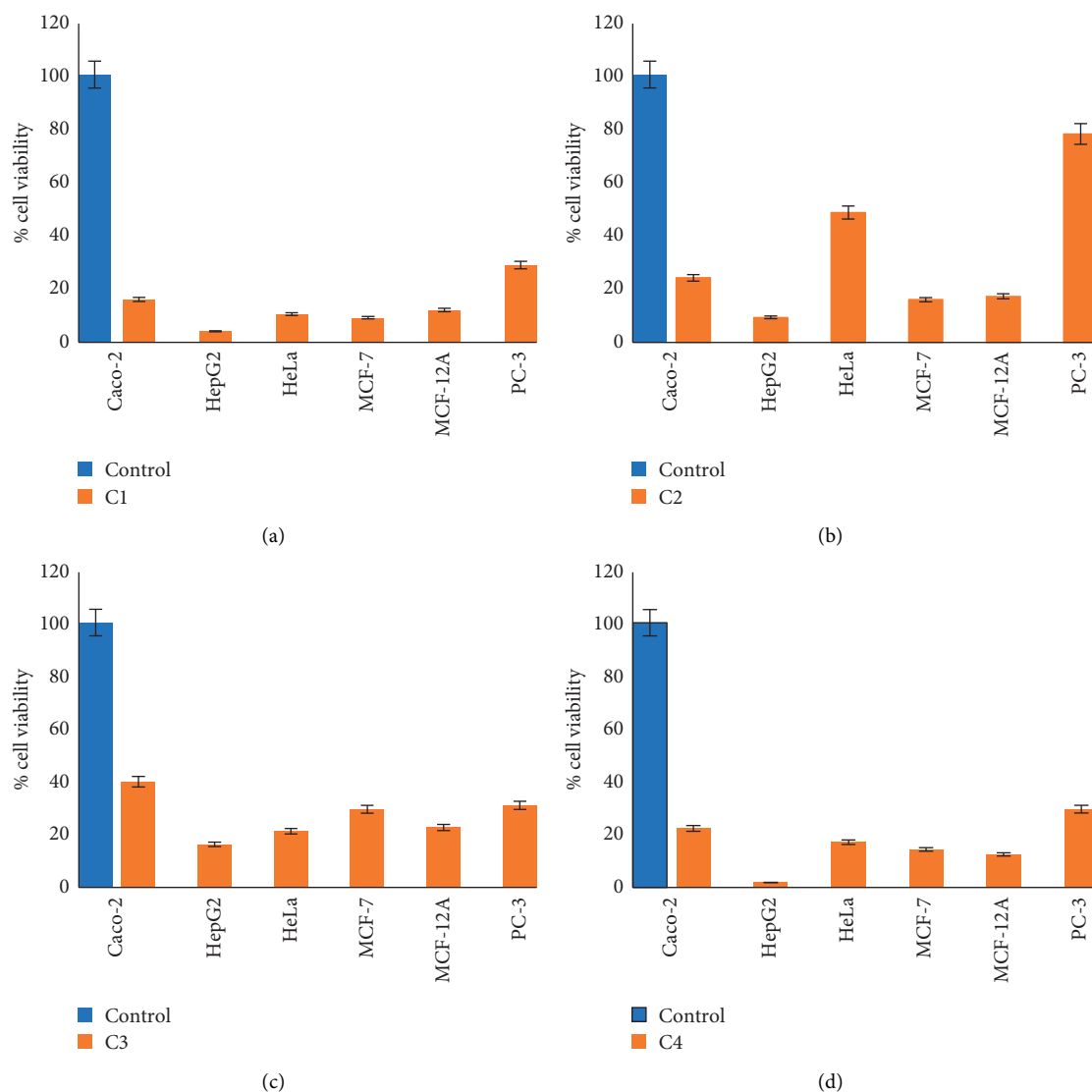


FIGURE 9: Percent cell viability for the different compounds (C1–C4) after 24 h of treatment assessed by the colorimetric MTT assay: (a) C1; (b) C2; (c) C3; (d) C4.

TABLE 3: The IC_{50} values for ligands and complexes C1–C4.

	Complex (μM)				Ligands
	C1	C2	C3	C4	
Caco-2	14.71 ± 0.016	43.08 ± 0.001	17.52 ± 0.005	31.14 ± 0.002	>100 (L1–L4)
MCF-7	1.973 ± 0.048	59.56 ± 0.010	12.52 ± 0.011	70.09 ± 0.006	>100 (L1–L4)
HeLa	16.65 ± 0.051	72.25 ± 0.003	19.2 ± 0.003	46.25 ± 0.011	>100 (L1–L4)
HepG2	14.64 ± 0.037	94.34 ± 0.003	29 ± 0.003	48.03 ± 0.006	>100 (L1–L4)
PC-3	14.05 ± 0.042	>100	6.98 ± 0.008	12.63 ± 0.036	>100 (L1–L4)

The IC_{50} values for the complexes are tabulated in Table 3.

3.4. DNA-Binding Studies. Spectroscopy is widely used in the study of binding modes for metal complexes by observing the alterations that appear in the λ_{max} absorption values of π - π^* intraligand transitions, ligand \rightarrow metal charge transfers, or

on the d - d transitions, as the DNA concentration is serially increased to a solution of a metal complex. Binding modes are then inferred from the spectra, whereby an intercalative mode results in a hypochromic shift and bathochromic shift or hypsochromism. Intercalation is as a result of overlap of π^* antibonding orbitals of the ligands bound to the complex with π bonding orbitals of the DNA base pairs. This decreases the probable transitions, and the effect is observed as

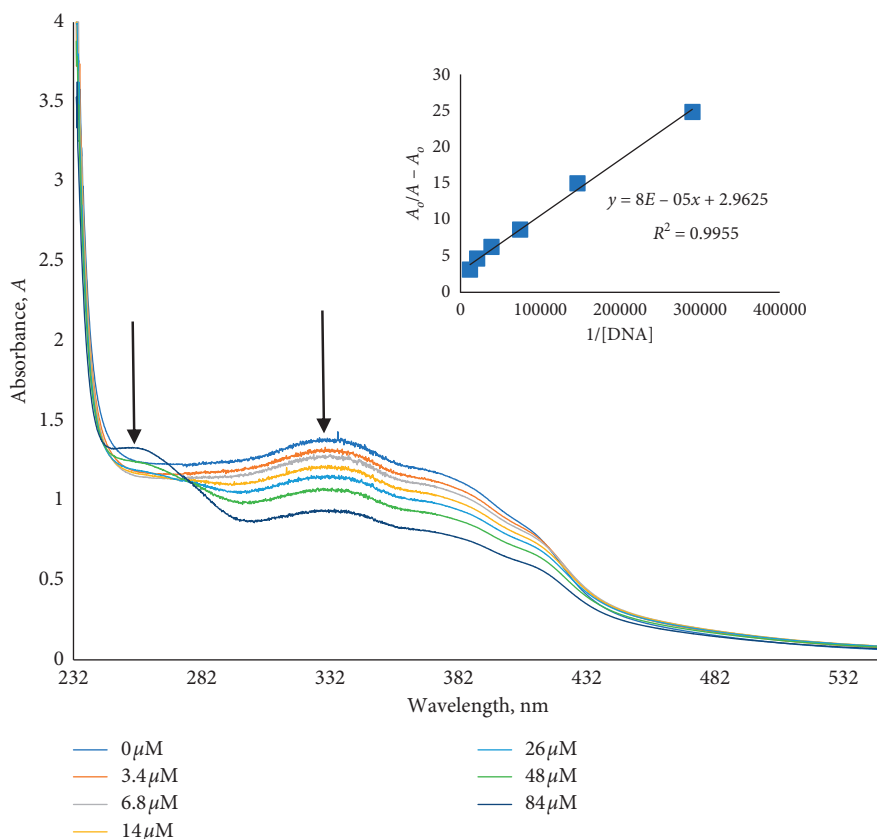


FIGURE 10: UV-visible absorption spectra for the C1 at $18 \mu\text{M}$ without CT-DNA and with serial addition of DNA. Inset is the Benesi-Hildebrand plots for the determination of binding constant.

hypochromic response [20]. On the contrary, a hyperchromic shift suggests electrostatic mode of binding. The spectral shift in the metal complex absorption is correlated to the binding strength from which the kinetics can then be determined [21].

Observations on the changes occurring in the UV-Vis spectra of a compound during serial additions of DNA is an accepted procedure in studying the binding modes and kinetics of DNA-complex interactions [22]. In this study, we used calf thymus-DNA (CT-DNA) prepared in 10 mM Tris-HCl buffer at pH 7.29. The DNA concentration was calculated from the λ_{max} of 260 nm using the molar absorptivity of the CT-DNA and $\epsilon = 6600 \text{ M}^{-1}$. The ratio of the absorbance (A_{260}/A_{280}) was found to be 1.918 which assured that DNA was free of protein [23].

Serial concentrations of calf thymus DNA (CT-DNA) were titrated to a fixed concentration of the complexes in the cuvette and scanned from 200–800 nm. The mixture was allowed to incubate for 5 minutes prior to taking UV-Vis measurements. With continued addition of DNA, the peaks of interest eventually decreased up to a point where they disappeared, and at the same time, there appeared a peak at 260 nm. This clearly showed that all the complex had been bound to DNA and further additions resulted in excess free DNA in the mixture which was indicated by the appearance of a characteristic DNA peak at 260 nm.

The binding kinetics for the complex-DNA interaction was then determined by the intrinsic binding constant, K_b , by plots of the Benesi-Hildebrand equation [24] and shown as follows:

$$\frac{A_0}{A - A_0} = \frac{\epsilon_G}{\epsilon_{H-G}} + \frac{\epsilon_G}{\epsilon_{H-G}} \frac{1}{K_b [\text{DNA}]}, \quad (2)$$

where A_0 and A are the absorbances of the blank sample without DNA and absorbance of complex DNA after addition of serial concentrations of DNA, respectively, while ϵ_G and ϵ_{H-G} are the molar extinction coefficients of complex only and complex DNA, respectively. The binding constant is determined by plotting $A_0/(A - A_0)$ vs $1/[\text{DNA}]$ to give a straight line graph. The equation of the straight line gives the slope and intercept where the K_b value was calculated from the ratio of the intercept to the slope. The strength of the interaction is reflected by the value of the binding constant.

From the binding constant values, Gibbs free energy changes, ΔG , for the complex DNA interactions were calculated using the following equation:

$$\Delta G = -RT \ln K_b k \text{ mol}^{-1}, \quad (3)$$

where R is the gas constant and T is the absolute temperature.

The absorption spectra of the interaction of CT-DNA with the complexes together with the Benesi-Hildebrand plots are shown in Figures 10–13.

All the complexes exhibited hypochromic shifts at λ_{max} . The hypochromism is probably the result of intercalative mode of binding as a result of the overlap of π^* antibonding orbitals of the ligands bound to the complex, with π bonding

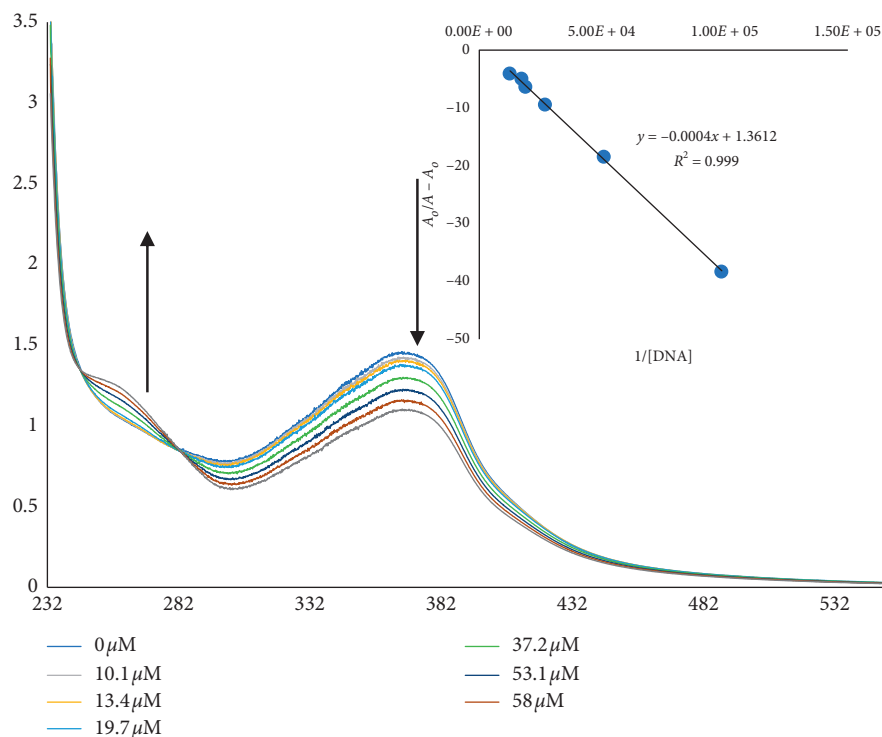


FIGURE 11: UV-visible absorption spectra for the C2 at 18 μM without CT-DNA and with serial addition of DNA. Inset is the Benesi-Hildebrand plots for the determination of binding constant.

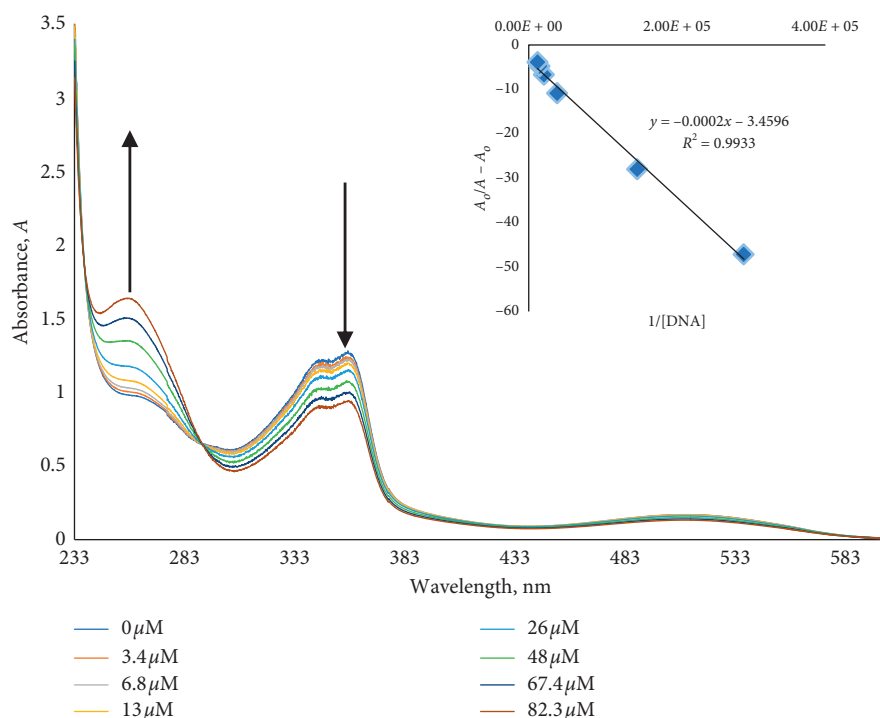


FIGURE 12: UV-visible absorption spectra for the C3 at 18 μM without CT-DNA and with serial addition of DNA. Inset is the Benesi-Hildebrand plots for the determination of binding constant.

orbitals of the DNA base pairs [25]. This decreases the probable transitions, and the effect is observed as a hypochromic shift [20].

Furthermore, distinct isosbestic points appeared at 283 nm in the spectra of C2 and C4 and 292 nm for C3. This is as a result of equilibrium between bound and free

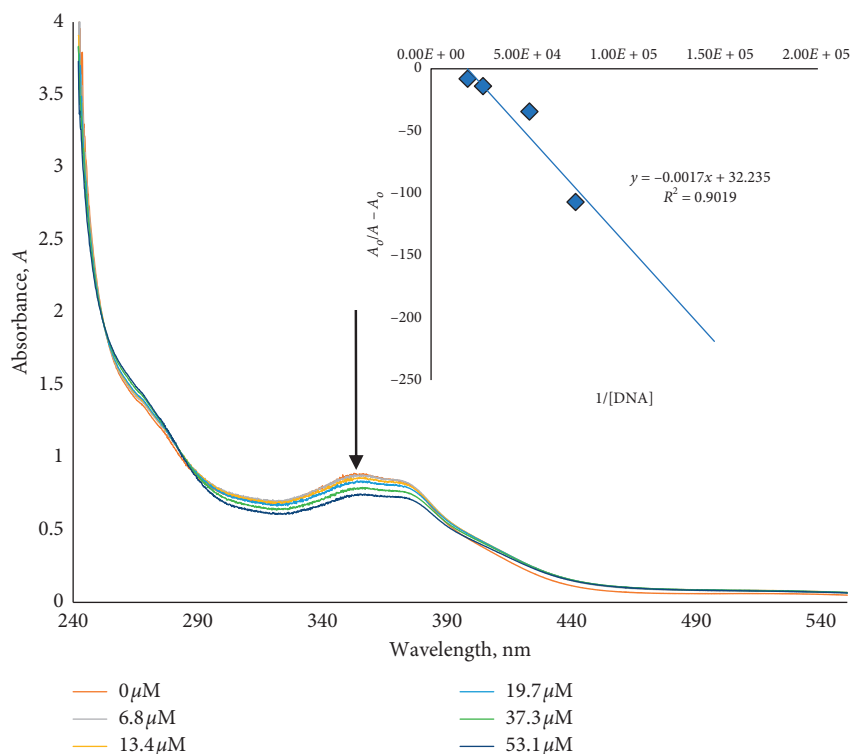


FIGURE 13: UV-visible absorption spectra for the **C4** at $18\ \mu\text{M}$ without CT-DNA and with serial addition of DNA. Inset is the Benesi-Hildebrand plots for the determination of binding constant.

TABLE 4: Comparison of binding constants (K_b) and Gibbs free energy values for the complexes-DNA interactions derived from UV spectrophotometric data at pH 7.21 with other reported intercalators.

Complex	Mode of binding	Binding constant, K_b (M^{-1})	Gibbs free energy, ΔG (kJ mol^{-1})	References
C1	Intercalative	3.7031×10^4	-26.03	CW
C2	Intercalative	3.403×10^3	-20.15	CW
C3	Intercalative	1.7298×10^4	-24.18	CW
C4	Intercalative	1.8962×10^4	-24.04	CW
Ethidium bromide	Intercalative	1.4×10^6	-35.06	[27]
Lumazine	Intercalative	1.74×10^4	-24.19	[28]
Epirubicin	Intercalative	3.4×10^4	-25.85	[29]
Proflavine	Intercalative	2.32×10^4	-24.90	[29]

CW = current work.

form of DNA and indicates that there are no other species in the mixture [26]. Binding constant and Gibbs free energy values were then evaluated and compared to those of common DNA intercalators, as shown in Table 4.

Complex **C1** showed higher values compared to those of the known DNA intercalators lumazine, epirubicin, and proflavine, indicating a strong binding between these complexes and DNA. Complex **C3** showed a lower binding constant probably due to the presence of the Br substituent. Since intercalation generally arises from the overlap of π^* -orbitals of intercalator with the π -orbitals DNA base pairs [30], the presence of an electronegative substituent conjugated to the π -system of an intercalator will remove electron density, thereby reducing the reactivity of the

system. This may have contributed to the low binding profile of **C2**.

As shown in Table 4, all the ΔG values were negative, an indication of the spontaneity of interaction during the complex-DNA formation process [28].

4. Conclusion

This work produced new complexes of Pd(II) and Pt(II) with insights into tuning the physical-chemical properties and the resultant biological effects. Synthesis, isolation, and purification were all performed under mild laboratory conditions. The suggested structures were confirmed by elemental microanalysis and X-ray crystallography for one of the ligands.

Binding profiles with DNA were studied using CT-DNA and UV-Vis spectroscopy, where they exhibited hypochromic shifts at λ_{max} which indicated an intercalative binding mode. Furthermore, the intrinsic DNA-binding constants, k_b , (M^{-1}) of 3.7031×10^4 (C1), 1.7298×10^4 (C3), and 1.8962×10^4 (C4) and Gibbs free energy (ΔG kJ mol^{-1}) values ranging from 24.04 to 26.03 are compared to some of the available well-known intercalators further suggesting this mode of binding. Anticancer tests against selected cancer cells *in vitro* showed that their activities correlated with their corresponding structures, where the different ligands around the metal center effected different rates of ligand substitution, which reflected on the observed cytotoxicity profiles. This was most notable on C2, which was a modification of C1 after introduction of -Br to position 5 of thiophene ring. This caused a remarkable increase in cell viability from 11% to 48% in HeLa cells and 28% to 78% in PC-3 cells and a difference of 37% and 50%, respectively.

Data Availability

The data used to support these findings, i.e., FTIR peaks, ^1H -NMR peaks, ^{13}C -NMR peaks, and UV-Vis peaks, for all the compounds together with the calibration curve used to determine the CT-DNA concentration are included within the supplementary information file which has been attached as a separate PDF document. The figures are arranged as follows: (1) FTIR spectra; Figures ESI 1–7. (2) ^1H -NMR spectra; Figures ESI 8–12. (3) ^{13}C -NMR spectra; Figures ESI 13–17. (4) UV/Vis spectra; Figures ESI 18–23. (5) Calibration curve for determination of DNA concentration; Figure ESI 24. (6) CIF file for L1. The crystallographic structure for ligand L1 has been deposited with Cambridge Crystallographic Data Centre, CCDC 1885726. A Copy of this data may be found from CCDC, 12 Union Road, Cambridge, CB2 1EZ, UK (fax: +44-1223-336033 or by e-mailing deposit@ccdc.cam.ac.uk or going to the website <http://www.ccdc.cam.ac.uk>).

Conflicts of Interest

The authors declare that they have no conflicts of interest.

Acknowledgments

The authors acknowledge the support of the International Science Program (ISP) under KEN-01 Project for the funding and NRF, South Africa. The authors thank the Department of Chemistry, University of Nairobi, for support and guidance in this work and the Department of Chemistry and the Department of Biotechnology, University of the Western Cape (UWC), South Africa, where most of this work was carried out.

Supplementary Materials

Figures of (1) FTIR spectral data, (2) ^1H -NMR spectra, (3) ^{13}C -NMR spectra, (4) UV-Vis spectra, and (5) crystal CIF file for ligand L1. (*Supplementary Materials*)

References

- [1] J. Ferlay, M. Colombet, I. Soerjomataram et al., “Estimating the global cancer incidence and mortality in 2018: GLOBOCAN sources and methods,” *International Journal of Cancer*, vol. 144, no. 8, pp. 1941–1953, 2019.
- [2] Y. Dai, J. Su, K. Wu et al., “Multifunctional thermosensitive liposomes based on natural phase-change material: near-infrared light-triggered drug release and multimodal imaging-guided cancer combination therapy,” *ACS Applied Materials & Interfaces*, vol. 11, no. 11, pp. 10540–10553, 2019.
- [3] J. Galon and D. Bruni, “Approaches to treat immune hot, altered and cold tumours with combination immunotherapies,” *Nature Reviews Drug Discovery*, vol. 18, no. 3, pp. 197–218, 2019.
- [4] R. S. Riley, C. H. June, R. Langer, and M. J. Mitchell, “Delivery technologies for cancer immunotherapy,” *Nature Reviews Drug Discovery*, vol. 18, no. 3, pp. 175–196, 2019.
- [5] E. M. Bavin, R. J. W. Rees, J. M. Robson, M. Seiler, D. E. Seymour, and D. Suddaby, “The tuberculostatic activity of some thiosemicarbazones,” *Journal of Pharmacy and Pharmacology*, vol. 3, no. 1, p. 46, 1951.
- [6] G. A. Kune, “To-day’s drugs: methisazone,” *British Medical Journal*, vol. 2, no. 5409, p. 621, 1964.
- [7] A. C. Sartorelli and B. A. Booth, “Inhibition of the growth of sarcoma 180 ascites cells by combinations of inhibitors of nucleic acid biosynthesis and the cupric chelate of kethoxal bis-(thiosemicarbazone),” *Cancer Research*, vol. 27, no. 9, pp. 1614–1619, 1967.
- [8] R. A. Finch, M.-C. Liu, A. H. Cory, J. G. Cory, and A. C. Sartorelli, “Triapine (3-aminopyridine-2-carboxaldehyde thiosemicarbazone; 3-AP): an inhibitor of ribonucleotide reductase with antineoplastic activity,” *Advances in Enzyme Regulation*, vol. 39, no. 1, pp. 3–12, 1999.
- [9] P. A. Channar, A. Saeed, F. A. Larik et al., “Synthesis, computational studies and enzyme inhibitory kinetics of substituted methyl [2-(4-dimethylamino-benzylidene)-hydrazono]-4-oxo-thiazolidin-5-ylidene]acetates as mushroom tyrosinase inhibitors,” *Bioorganic & Medicinal Chemistry*, vol. 25, no. 21, pp. 5929–5938, 2017.
- [10] G. M. Sheldrick, “Crystal structure refinement with SHELXL,” *Acta Crystallographica Section C Structural Chemistry*, vol. 71, no. 1, pp. 3–8, 2015.
- [11] L. J. Farrugia, “WinGX and ORTEP for windows: an update,” *Journal of Applied Crystallography*, vol. 45, no. 4, pp. 849–854, 2012.
- [12] M. D. Coskun, F. Ari, A. Y. Oral et al., “Promising anti-growth effects of palladium (II) saccharinate complex of terpyridine by inducing apoptosis on transformed fibroblasts *in vitro*,” *Bioorganic & Medicinal Chemistry*, vol. 21, no. 15, pp. 4698–4705, 2013.
- [13] C. A. Tolman, “Phosphorus ligand exchange equilibria on zerovalent nickel. Dominant role for steric effects,” *Journal of the American Chemical Society*, vol. 92, no. 10, pp. 2956–2965, 1970.
- [14] Ö. Şahin, Ü. Ö. Özdemir, N. Seferoğlu et al., “A highly selective and sensitive chemosensor derived coumarin–thiazole for colorimetric and fluorimetric detection of CN⁻ ion in DMSO and aqueous solution: synthesis, sensing ability, Pd (II)/Pt (II) complexes and theoretical studies,” *Tetrahedron*, vol. 72, no. 39, pp. 5843–5852, 2016.
- [15] A. C. G. Hotze, Y. Chen, T. W. Hambley et al., “cis-[PtCl₂(NH₃){2-(2-hydroxyethyl)pyridine}]—an analogue of the anticancer drug AMD473: unusual hydrolysis rates and

- pKa values for the diaqua adduct," *European Journal of Inorganic Chemistry*, vol. 2002, no. 5, pp. 1035–1039, 2002.
- [16] E. Ulukaya, F. Ari, K. Dimas, E. I. Ikitimur, E. Guney, and V. T. Yilmaz, "Anti-cancer activity of a novel palladium (II) complex on human breast cancer cells in vitro and in vivo," *European Journal of Medicinal Chemistry*, vol. 46, no. 10, pp. 4957–4963, 2011.
- [17] W. M. Motswainyana, M. O. Onani, A. M. Madiehe, M. Saibu, J. Jacobs, and L. Van Meervelt, "Imino-quinolyl palladium(II) and platinum(II) complexes: synthesis, characterization, molecular structures and cytotoxic effect," *Inorganica Chimica Acta*, vol. 400, pp. 197–202, 2013.
- [18] J. W. Williams, Y. Qu, G. H. Bulluss, E. Alvorado, and N. P. Farrell, "Dinuclear platinum complexes with biological relevance based on the 1,2-diaminocyclohexane carrier ligand," *Inorganic Chemistry*, vol. 46, no. 15, pp. 5820–5822, 2007.
- [19] A. S. Abu-Surrah, H. H. Al-Sa'doni, and M. Y. Abdalla, "Palladium-based chemotherapeutic agents: routes toward complexes with good antitumor activity," *Cancer Therapy*, vol. 6, no. 6, pp. 1–10, 2008.
- [20] N. Raman and S. Sobha, "Exploring the DNA binding mode of transition metal based biologically active compounds," *Spectrochimica Acta Part A: Molecular and Biomolecular Spectroscopy*, vol. 85, no. 1, pp. 223–234, 2012.
- [21] M. Ashfaq, T. Najam, S. S. A. Shah et al., "DNA binding mode of transition metal complexes, a relationship to tumor cell toxicity," *Current Medicinal Chemistry*, vol. 21, no. 26, pp. 3081–3094, 2014.
- [22] S. Olsztynska and M. Komorowska, *Biomedical Engineering: Trends, Research and Technologies*, IntechOpen, London, UK, 2011.
- [23] S. S. Babkina and N. A. Ulakhovich, "Complexing of heavy metals with DNA and new bioaffinity method of their determination based on amperometric DNA-based biosensor," *Analytical Chemistry*, vol. 77, no. 17, pp. 5678–5685, 2005.
- [24] I. D. Kuntz Jr, F. P. Gasparro, M. D. Johnston Jr, and R. P. Taylor, "Molecular interactions and the Benesi-Hildebrand equation," *Journal of the American Chemical Society*, vol. 90, no. 18, pp. 4778–4781, 1968.
- [25] A. M. Pyle, J. P. Rehmann, R. Meshoyrer, C. V. Kumar, N. J. Turro, and J. K. Barton, "Mixed-ligand complexes of ruthenium (II): factors governing binding to DNA," *Journal of the American Chemical Society*, vol. 111, no. 8, pp. 3051–3058, 1989.
- [26] N. Arshad, M. H. Bhatti, S. I. Farooqi, S. Saleem, and B. Mirza, "Synthesis, photochemical and electrochemical studies on triphenyltin(IV) derivative of (Z)-4-(4-cyanophenylamino)-4-oxobut-2-enoic acid for its binding with DNA: biological interpretation," *Arabian Journal of Chemistry*, vol. 9, no. 3, pp. 451–462, 2016.
- [27] J.-B. LePecq and C. Paoletti, "A fluorescent complex between ethidium bromide and nucleic acids," *Journal of Molecular Biology*, vol. 27, no. 1, pp. 87–106, 1967.
- [28] M. S. Ibrahim, I. S. Shehatta, and A. A. Al-Nayeli, "Voltammetric studies of the interaction of lumazine with cyclodextrins and DNA," *Journal of Pharmaceutical and Biomedical Analysis*, vol. 28, no. 2, pp. 217–225, 2002.
- [29] M. Aslanoglu, "Electrochemical and spectroscopic studies of the interaction of proflavine with DNA," *Analytical Sciences*, vol. 22, no. 3, pp. 439–443, 2006.
- [30] Z.-H. Xu, F.-J. Chen, P.-X. Xi, X.-H. Liu, and Z.-Z. Zeng, "Synthesis, characterization, and DNA-binding properties of the cobalt(II) and nickel(II) complexes with salicylaldehyde 2-phenylquinoline-4-carboylhydrazone," *Journal of Photochemistry and Photobiology A: Chemistry*, vol. 196, no. 1, pp. 77–83, 2008.

REVIEW ARTICLE

Beyond DNA-targeting in Cancer Chemotherapy. Emerging Frontiers - A Review

S.N. Mbugua¹, L.W. Njenga¹, R.A. Odhiambo¹, S.O. Wandiga¹ and M.O. Onani^{2,*}

¹Department of Chemistry, University of Nairobi, P.O. Box 30197-00100, Nairobi, Kenya; ²Organometallics and Nanomaterials, Department of Chemical Sciences, University of the Western Cape, Private Bag X17, Bellville, 7535, Zambia

Abstract: Modern anti-cancer drugs target DNA specifically for rapid division of malignant cells. One downside of this approach is that they also target other rapidly dividing healthy cells, such as those involved in hair growth leading to serious toxic side effects and hair loss. Therefore, it would be better to develop novel agents that address cellular signaling mechanisms unique to cancerous cells, and new research is now focussing on such approaches. Although the classical chemotherapy area involving DNA as the set target continues to produce important findings, nevertheless, a distinctly discernible emerging trend is the divergence from the cisplatin operation model that uses the metal as the primary active center of the drug. Many successful anti-cancer drugs present are associated with elevated toxicity levels. Cancers also develop immunity against most therapies and the area of cancer research can, therefore, be seen as an area with a high unaddressed need. Hence, ongoing work into cancer pathogenesis is important to create accurate preclinical tests that can contribute to the development of innovative drugs to manage and treat cancer.

Some of the emergent frontiers utilizing different approaches include nanoparticles delivery, use of quantum dots, metal complexes, tumor ablation, magnetic hypothermia and hyperthermia by use of Superparamagnetic Iron oxide Nanostructures, pathomics and radiomics, laser surgery and exosomes.

This review summarizes these new approaches in good detail, giving critical views with necessary comparisons. It also delves into what they carry for the future, including their advantages and disadvantages.

ARTICLE HISTORY

Received: May 18, 2020

Revised: July 07, 2020

Accepted: July 08, 2020

DOI:

10.2174/1568026620666200819160213

Keywords: Cancer, immunotherapy, liposomes, gene therapy, exosomes, tumour ablation.

1. INTRODUCTION

Cancer is the second leading cause of death globally, with an estimated 1 in 6 deaths, and is responsible for approximately 9.6 million deaths in 2018 [1]. It is estimated that approximately 70% of all deaths are cancer-related and occur in low and middle-income countries [2]. The economic impact of cancer is significant and is increasing with a total annual cost, in 2010, estimated at approximately US\$ 1.16 trillion. Only 1 in 5 low- and middle-income countries have the necessary data to drive cancer policy [1]. Fortunately, it is not a contagious disease like the most recent, deadly covid-19, which has brought the world to a standstill.

Although major steps have been made in medicine, many difficulties still need to be resolved in order to boost cancer therapy. In line with this, research is putting a great deal of effort into discovering new and effective therapies that can mitigate the pertinent adverse effects of therapies. Many research reports have focused on creating alternative treat-

ments to minimize the side effects of traditional medicines over the past decade [2].

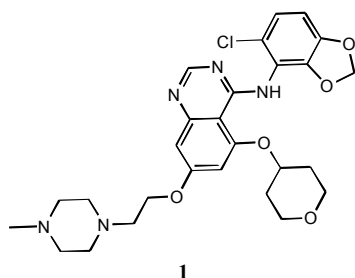
Various technologies are now being tested in clinical trials, with some already implemented in the clinical practice [3]. These include targeting overexpressed proteins and antigens on tumor cell surfaces, targeted drug delivery, nanoparticle delivery, among others. In the last 70 years or so, cancer treatment has progressed exponentially, from cytotoxic drugs that reduce tumors but with severe systemic side effects, to specific treatments that can cause cancer-cell death while leaving healthy tissues unchanged. This article describes some of the successful strategies and many others that are in the early stages of development.

The origins of many tumors are not fully understood, which makes it difficult to establish effective therapies, as is evident in the high cancer drug failure rate during clinical trials [1]. In this review, a detailed study of the most ground breaking developments in the fundamental and advanced cancer research, was carried out. A broad overview of a combination of the most effective, specific, and applicable cancer treatments, together with the new approaches that are currently under investigation at the research phase, which

*Address correspondence to this author at the Organometallics and Nanomaterials, Department of Chemical Sciences, University of the Western Cape, Private Bag X17, Bellville, 7535, Zambia;
E-mail: monani@uwc.ac.za

should transcend the weakness of traditional therapeutics, is presented.

Directed or not, resistance to chemotherapy drugs is an endemic problem, and scientists are trying to find ways to circumvent the resistance. The easiest solution is to switch the treatment of an individual from one treatment to another via a different target or mechanism or to introduce another medication to the protocol [3]. Scientists are studying cellular mechanisms and genes that might cause resistance and using them as targets [4]. Through inserting an agent that prevents or creates another route, this resistance can be partly solved, raising the response rate from 40 to 60% [5]. In a preclinical study, the application of saracatinib [6] to trastuzumab, a monoclonal antibody used to treat breast cancer and stomach cancer, demonstrated a decrease of 90 percent in tumor volume in previously trastuzumab-resistant mice [6].



Trastuzumab is normally overexpressed in chronic myeloid leukemia cells [7]. It is a dual-specific protein tyrosine kinase inhibitor that binds and inhibits these tyrosine kinases, thus affecting cell motility, cell migration, adhesion, invasion, proliferation, differentiation, and survival [8].

Patients vaccinated against cancer may still develop resistance from chemicals released by tumors, which inhibit an immune response to the tumor or from genetic changes in the tumor itself [9]. Scientists search for ways of reducing this tolerance through the use of vaccines that combine various antigens in one vaccination or through targeting of T-cells that can diminish the immune system response [10, 11].

Different options for the diagnosis and treatment of cancer are discussed in this study, as well as their current position in the clinical stage, emphasizing their anticipated impacts as revolutionary approaches to anti-cancer studies.

2. CLASSIFICATION OF THE REVIEWED AREAS

This review falls under four broad areas of the most recent fields of cancer therapy that target non-DNA targets in cells. These include diagnostics, therapeutics, targeted nanocomposites, and NanoPlatforms [4], which are nanoparticles combined with drugs and theragnostics, which combine diagnostic and therapeutic approaches to achieve better outcomes. Theranostic combinations appear in the discussions section showing the various combinations used synergistically to achieve better anti-cancer results. These various classification areas are discussed below.

3. DIAGNOSTICS

Screening of diseases always have huge benefits in determining the status of sickness. Cancer diagnosis is advan-

tageous in that it may reveal changes in the body, which may lead to possible prevention of cancer. Earlier diagnosis of cancer may lead to easier treatment because it may be found confined in a smaller area before a widespread. The diagnosis gives a chance of early detection, which means a patient will spend less time in treatment and recovery. An individual will also have a better chance of survival.

3.1. Radiomics and Pathomics

Radiomics and pathomics are two exciting and groundbreaking areas focused on the accumulation of radiology and pathology imaging, whose quantitative picture features as medicinal and prognostic markers of disease outcome [11]. Radiomics is designed to measure high-throughput tumor properties derived via diagnostic image data analysis [12-14]. Pathomics, on the other hand, is focused on producing and characterizing high-resolution images of the tissue [15]. Most works focus on developing new image analytical methodologies to deduce details through quantitative analysis and classification of the disease [16].

Although surgery still remains one of the main procedures for cancer treatment, about 50 percent of patients undergo radiation therapy. Radiation therapy is administered by the use of an external source of light beam or by adding a radioactive source locally [17] to achieve intense irradiation [18]. Localization of the pulse is now enabled by image-guided radiation therapy, in which the patient's images are obtained during treatment, enabling the correct amount of radiation to be determined [18]. Through the emergence of intensity-modulated radiotherapy [19], varying strengths of radiation fields can be generated, significantly reducing the doses reaching healthy tissues and therefore limiting negative side effects [19, 20].

Finally, it is possible, by stereotactic ablative radiation therapy [21], to deliver an ablative radiation dose only to a specific target range, greatly reducing unwanted side effects [17]. Cancer is a complex ailment and its successful treatment requires enormous efforts to combine the amount of information gained through testing and therapy procedures. The ability to connect data gathered from diagnostic images and molecular analyses has enabled non-invasive imaging techniques to achieve an analysis of the entire three-dimensional structure of the tumor. This is in accordance with the main objective of precision therapy, which is to reduce adverse effects linked to treatment while maximizing its success in order to obtain the best individualized therapy [22].

Radiomics has the advantage that a whole three-dimensional image of the tumor can be created by non-invasive imaging techniques. However, standardization of procedures to facilitate clinical translation still remains a challenge [16].

3.2. Exosomes

Exosomes serve as an essential regulatory factor during metastasis [23]. These include the initiation, development, and colonizing of metastases in surrounding regions by transmitting functional molecules, thereby directly affecting targeted cells [24]. Exosomes are secreted by practically all

types of cells and can deliver proteins, lipids, DNA, and RNA into the receiver cells [25]. This happens in three pathways namely; attachment of the surface receptor, binding to the target cells, or internalization of the vesicle, thereby controlling the functional state of the cells [26].

The structure and contents of the cancer derived-exosome are as shown in Fig. (1). As indicated in the figure, exosomes contain lipid bilayer membranes with characteristic transmembrane proteins and receptors depending on the nature of tumor cells. These include adhesion molecules, lipid raft-associated proteins for signaling and/or intra-cellular transport in epithelial cells, immune regulator molecules, and tetraspanins, which are proteins capable of arresting tumor development.

The proteins include many of the major raft lipids present in cell membranes, such as ceramides, sphingolipids, cholesterol, and glycerophospholipids [27]. Exosomes' primary RNA is miRNA, but they also contain long non-coding RNAs, which in many respects, control gene expression [28].

Organs prone to metastasis may be modified to be optimal for tumor colonization prior to the arrival of cancer cells, i.e., premetastatic niche formation [29]. In the physiological system, *green fluorescent protein* exosomes are secreted into the neighboring tumor tissues and are distributed from primary to metastatic niche tumors [26].

Studies show that exosomes play a critical part in cancer metastasis [30]. This includes taking part in the formation of the premetastatic niche, microenvironment of tumor cells, and in the determination of specific organotropic metastasis [31, 32]. Upon drug treatment, exosomes originating from drug resistance cells may also transfer the resistant characteristics to the recipient cells for induction of resistance [27]. In fact, exosomes will usually activate the immune response to suppress the activity of the immune cells, thus growing immunogenicity to enhance the anti-tumor activity under certain stress conditions [25, 27]. Attacking metastasis-related

exosomes offers a new strategy for designing innovative, effective anti-tumor treatment agents [33]. Increasing evidence indicates that exosomes and their contents lead to pre-metastatic microenvironment development and trends of non-random metastasis [26, 34].

There is, however, still a shortage of preclinical data and further clinical treatment trials of antimetastatic-active agents [35]. Hence, explicitly designing antimetastatic medication for clinical use will be necessary to allow researchers to concentrate on the dynamics of cancer metastasis.

4. THERAPEUTICS

The cancer treatment is highly variable and dependent on many factors such as the type, location, stage of the disease, and the health status of the patient. Most of the cancer therapeutics are aimed at either directly destroying the cancer cells or inducing their apoptosis by depriving them of signals needed for survival. The other cancer therapies work by stimulating the body's own defenses against the cancer cells. There are a number of cancer treatments and some of the latest types are discussed below.

4.1. Immunotherapies

The aim of immunotherapy treatment is to boost a patient's immune system for it to fight against any tumor invasion. Immunotherapies, which are also regarded as cancer vaccines, induce the immune function of a patient to kill cancerous cells [36]. By either enhancing the host's immune responses against cancers or countering the signals generated by cancer cells that inhibit immune response, immunotherapy has become a successful procedure alone, or paired with other therapies such as surgery, chemotherapy, and radiation therapy [37].

Additionally, immunotherapy interventions can be categorized into two broad categories: active and passive [38]. The active approach entails channeling the host immune response toward tumor-associated antigens [39] on the tumor

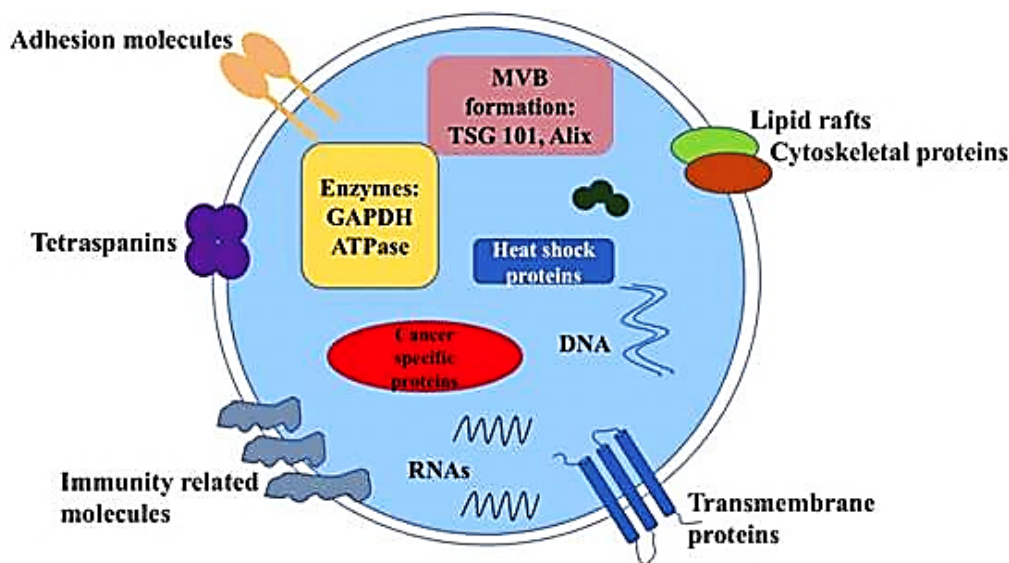


Fig. (1). Structure and Composition of exosomes derived from cancerous Cells [26]. (A higher resolution / colour version of this figure is available in the electronic copy of the article).

surface [40]. These antibodies can be particular proteins or carbohydrates, which are expressed exclusively or excessively in tumor cells [41]. The passive immunotherapy, by contrast, entails strengthening the immune system's generic anti-cancer approach using monoclonal antibodies, lymphocytes, and cytokines [41]. A drug combination therapy would, by extension, constitute one or several elements of these two types of immunotherapies [42]. It is notable that immunotherapy distribution and efficacy are heavily reliant on the version, grade, predictive response rate, and relevant biomarker expression of cancer, although response rates from patients may still vary [39, 43-45].

The opposite **approach** is to decrease the immunosuppressive effects that promote the growth of cancer cells. Food and Drug Administration [46] approved the first vaccine of its kind, in 2010, for the treatment of advanced hormone refractory prostate cancer [47-49]. The main advantage associated with immunotherapy is that since vaccines induce an immune response, patients can be protected from metastasis and relapsing. Their side-effects profiles are relatively mild, restricted mainly to inflammatory irritation at the injection site [39, 40, 50].

Some of the challenges are that, although it has been shown that immunotherapy is effective, patient success rates differ and, most often, only a small percentage of patients within a broad subset respond positively to the therapy [51]. This problem is a hurdle to immunotherapy efficacy and rates of response from patients. A major factor contributing to discrepancies in the rates of response to cancer vaccinations is the specific nature of the vaccination as well as whether off-the-shelf forms of the vaccination is manufactured with similar antigen existing in the client's tumor in order for their immune system to recognize its presence in the system [52].

Genetic mutations may also contribute to the activation of neo-antigens [53], which are recognized by the immune system during tumor growth [53]. Nevertheless, once cancerous cells are formed, they are able to evade this immunity protection by shutting these antibodies off through immune tolerance induction [54]. Another immune avoidance method may arise when a tumor associates with its microenvironment to prevent antitumor responses [55]. Several methods exist to improve response levels, such as the identification of more specialized genetic markers and agonists of immune control points [56]. Better predictive tools and assays are also capable of identifying patients who will react well to immunotherapy [57].

Cancerous cells have evolved specific cellular processes to aid tumor microenvironment development [58]. One technique employed by cancer cells to ensure survival and advancement is to avoid checkpoints on the immune system [44]. Immune system check points operate to track autoimmunity and alleviate damage to tissue caused by immune responses through modulation of costimulatory and inhibitory signals [59]. During carcinogenesis, however, the dysregulation of protein expression at the checkpoint may lead to aberrant activation of inhibitory checkpoint receptors, thus, hindering T cells from identifying and eradicating tumorigenic cells [60, 61].

The development of the tumor microenvironment [62] not only enables the tumor to evolve but also causes it to recruit host immune system components [63]. In addition to fostering tumor growth, these TME components principally act as cellular obstacles to avoid any intrusion by antitumor immune cells [63]. The growth of a thick epithelial layer enveloping the malignant mass produces a protective barrier marked by several traits known to enhance tumor growth, such as hypoxic conditions and anomalous neovascularization of tumors [64]. Not only does this deter prospective immune system cells from entering the tumor but it also establishes blood vessels to enable cells to metastasize into remote tissues [65]. Until such time as these processes are eliminated, tumors will continue to evade the body's immune defenses [66].

Currently, immunotherapy treatments are obtainable as cancer vaccinations. Immunotherapy works similarly to standard methods of vaccination, where the goal is to stimulate an immune response. In short, cancer vaccinations, containing whole or fragments of antibodies, are intended to induce an immune reaction [40]. As shown in Fig. (2). The mode of action for the vaccines is illustrated. The vaccines are applied by injection through the dermis with an immune booster that helps in activating the dendritic cells [67]. The cells then pick antigens developed on cancerous cells and convey them to CD4 cell sites and CD8 cells [67]. This then prompts the CD8 cells to bind to the antigen expressed on the tumor surface [40].

Since many antigens, reflected on cancer cells, are also present on normal cells, treatment with a non-tumor-specific antigen will also be cytotoxic to healthy cells. This means that although immunotherapy **has** transformed the **treatment** of multiple advanced-stage malignancies, it has not been beneficial to many patients for whom immune functions have been jeopardized by traditional treatments [52]. In order for immunotherapies to be administered to wider patient demography, more diverse biomarkers that are expressed on the tumor cell surface need to be discovered. This will establish particular patterns that are displayed solely on cancer cells, the so-called neoantigens or tumor-specific antigens, allowing for better immunotherapy targets [68]. Determining a proper target for TSA will certainly lead to higher efficacy of immunotherapy treatment results in terms of reduced adverse effects to normal cells [69, 70].

One of the proposed approaches in overcoming immunotherapy resistance from cancer cells is the use of combined immunotherapy or multi-modal strategies [71]. This method could efficiently raise the likelihood of antigens being targeted by immunotherapies and, therefore, overcome the cancer cells' compensatory nature [72, 73].

4.2. Gene Therapy for Cancer Treatment

Gene therapy is designed to insert a healthy copy of a deformed gene into the genome for the purpose of treating particular diseases [74]. The 1990s marks the first reported cases when a retroviral vector was used in patients with severe combined immunodeficiency [75] to transmit the gene adenosine deaminase to T-cells [75]. Further work has shown that genetic engineering can be incorporated in many unusual and recurrent human diseases and, most notably, in

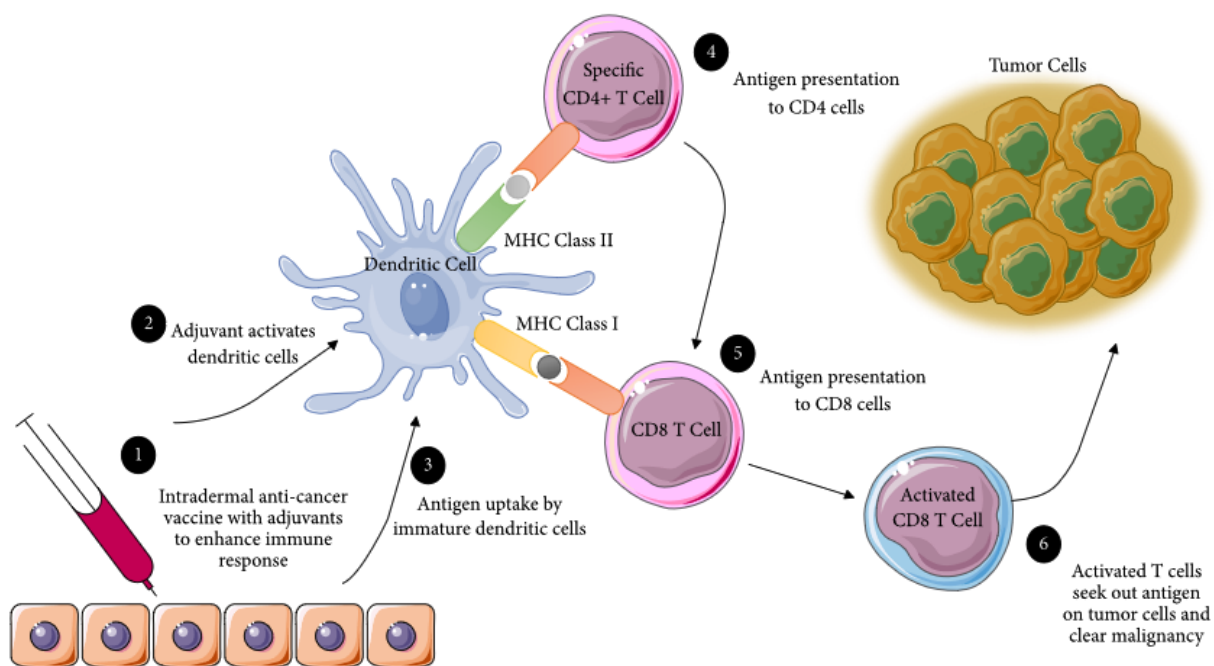


Fig. (2). Mechanism of Action of Cancer Vaccines. Administered through injection with adjuvants that activate dendritic cells. (Adapted from [40]). (A higher resolution / colour version of this figure is available in the electronic copy of the article).

treating cancer [76]. More than two-thirds of clinical trials currently being studied for gene therapy are cancer-related [76, 77].

Different strategies are under evaluation for cancer gene therapy. These include expression of pro-apoptotic and chemo-sensitizing genes [78], expression of wild type tumor suppressor genes [77, 79], expression of genes able to solicit specific antitumor immune responses, and targeted silencing of oncogenes [80, 81]. Despite many achievements in this area, there are still some challenges to face when dealing with gene therapy. These include the selection of the right conditions for optimal expression levels and the choice of the best delivery system to unequivocally target cancer cells [82]. Gene therapy also presents some drawbacks linked to genome integration, limited efficacy in specific subsets of patients, and high chances of being neutralized by the immune system [83]. Other issues include limited efficacy in specific subsets of patients [84], high chances of being neutralized by natural body immune defenses [85], off-target effects in terms of side effects, need of *ad hoc* delivery systems with the set-up of doses and suitable conditions for controlled release, remain a challenge [86].

4.3. Tumour Ablation and Magnetic Hyperthermia

Use of heat for tumor ablation, i.e heating or cooling cells to cytotoxic levels from about -40°C or above 60°C , opens up new possibilities for precision therapy, rendering the medication to be focussed in very tight and precise regions [87]. These techniques could also be a suitable replacement for more intrusive methods like surgery. Tumor thermal ablation requires a set of procedures utilizing heat [88] or cold [89] to kill metastatic cells [90]. Cell necrosis is known to occur at temperatures below -40°C or above 60°C

[89, 91]. Long temperature periods between 41°C and 55°C are also successful in damaging tumor cells [91]. The complementary use of the hyperthermia process with other treatment options is portrayed in Fig. (3). The combined therapies work synergistically to achieve better outcomes in effecting tumor cell death.

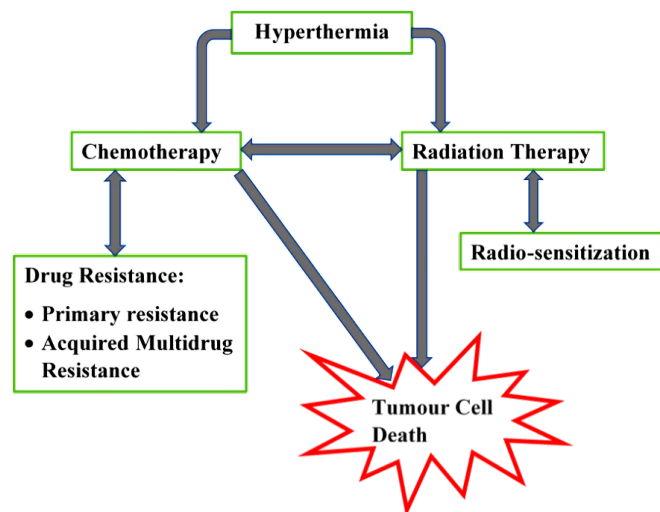


Fig. (3). Process of hyperthermia complementing traditional cancer therapy. (A higher resolution / colour version of this figure is available in the electronic copy of the article).

Furthermore, cancer cells are known to be more temperature sensitive at higher temperatures than normal cells [92]. Upon cooling, hypothermic ablation takes place whereby ice crystals form and break cell membranes, which eventually kills cells [88, 93]. Argon gas is the ideal coolant in these studies because it can disinfect the surrounding tissues to as low as -160°C [93].

Gasses, such as ammonia, can also be used at their critical point because they have a higher heat capacity compared to argon [88]. Yet the technologies for manipulating and controlling them is still not well developed. Ablation through hyperthermia currently utilizes microwave radiofrequencies [17] and laser [94]. Microwave ablation is based on the electromagnetic interaction between microwaves and polar molecules in fluids, such as liquids, which induces oscillation and, therefore, temperature changes. The more conductive the medium, the more effective the process. For this reason, Radiofrequency ablation works very well in the liver and in other areas with a high content of water and ions, whereas it has a poor effect in the lungs [95]. Radiofrequency ablation has been the most widely used in hospitals, since it is efficient and safe [96]. An alternated current of radiofrequency waves is applied to a target zone by an insulated electrode tip, while a second electrode, needed to close the circuit, is placed on the skin surface [97]. The interaction with the current causes the oscillation of ions in the extracellular fluid, which, in turn, produces heat⁹⁶.

In contrast to the electrical current in radiofrequency ablation, microwaves will spread through any type of tissue allowing high temperatures to be achieved in a short time, greater infiltration, and treatment of wider tumor areas^{108,109}.

Other advantages associated with these strategies include precise treatment of the interested area and the possibility of performing the treatment along with MRI imaging [91]. Challenges include low penetration power and the need for a skilled operator to perform the treatment [98].

4.4. Laser Therapy

Laser therapy uses the characteristics of laser beams, which are very small and of a specific wavelength and are extremely focused [99]. This makes the procedure very effective and precise, making it a viable alternative to traditional surgery [100]. The laser-emitted absorption of the light results in heating and eventual damages to the affected area [101]. Different types of lasers may be used according to the specific application. Neodymium: yttrium-aluminum-garnet (Nd: YAG) lasers (1064 nm wavelength) and diode lasers (800–900 nm wavelength), with a penetration range of up to 10 cm, are used for the treatment of internal organs. Conversely, for superficial therapies, CO₂ lasers [44] with a penetration depth of 10 μm up to 1 mm are used [102].

Laser therapy is receiving a lot of interest in science over other ablation methods because of its benefits, such as higher effectiveness, safety and accuracy, and a shorter treatment session required to achieve similar results [103]. In fact, the fibers to relay laser light are compliant with magnetic resonance imaging so that the temperature and thermal dosage can be calculated accurately [103]. However, certain drawbacks still need to be addressed, such as the need for a highly-skilled operator to bring the fiber in the right position [104]. Ultimately, despite new methods of heating tumor tissues via electromagnetic hyperthermia (as discussed above) showing better advantages by using superparamagnetic or ferromagnetic nanoparticles to generate heat through alternating magnetic fields, laser surgery still remains one of the most precise in tumor ablation.

5. NANOPLATFORMS/ NANOPARTICLE CARRIERS

The use of nanoscale materials and the advances in nanotechnology has brought about a new platform which has positively impacted on current cancer handling techniques. The developed smart activated nanosystems for cancer treatment carry the advantages of target specificity [105]. The disease-specific receptors on the surface of cells provide useful targets for nanoparticles. These nanoparticles can be engineered from disease recognizing components at the cellular level. They are visible on imaging studies and deliver therapeutic compounds on targets and in the lethally but minute quantities.

5.1. Drug Delivery by Liposomes

Liposomes are vesicles for drug delivery, with a lipid membrane bilayer containing an aqueous media, as shown in (Fig. 4) [106].

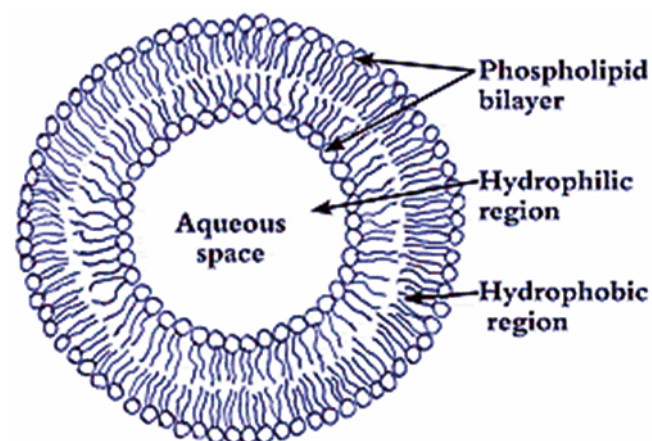


Fig. (4). Liposome showing a lipid bilayer enclosing a central aqueous space [106]. (A higher resolution / colour version of this figure is available in the electronic copy of the article).

Their mode of drug delivery is by connecting with the cell lipid membrane, which immediately transfers the drug dosage to the cells [107]. Due to differences in the permeability of normal blood vessels, selective accumulation of liposomes and other macromolecules occurs preferentially in cancer tissue [108]. The addition of polyethylene glycol to the liposome surface (PEGylation) [109] also reduces systemic adverse effects; it eliminates, for example, doxorubicin-related cardiotoxicity. Several liposomal therapeutic formulations for cancer exist, comprising of liposomal cytarabine (Depocyte), liposomal daunorubicin (DaunoXome), liposomal doxorubicin (Myocet), and liposome-PEG doxorubicin (Doxil / Caelyx) [110, 111]. Scientists are creating liposomes which have increased stability, encapsulation ability, can be metabolized *in vivo*, can hold a broader spectrum of medications, or kill cancer cells while enhancing safety and efficacy [112]. *In vitro* trials of monoclonal antibodies (mAbs) labeled doxorubicin liposomes demonstrated an increased efficacy relative to the untagged drug [113]. Organic nanoparticles are commonly used as drug delivery devices [114, 115]. They are principally used to encapsulate lipophobic substances in their aqueous core, but hydrophobic substances can also be stored in the bilayer or chemically linked to the particles [116]. Doxil, PEG-ylated liposomes

(Fig. 5) packed with doxorubicin, were the pioneer nanoparticles endorsed by the FDA, in 1995, to treat Kaposi's AIDS-associated sarcoma [117, 118].

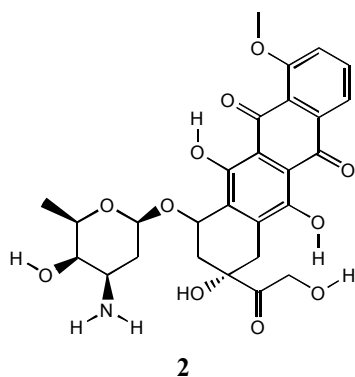


Fig. (5). Doxorubicin (2) and PEGylated liposomal DOX (Doxil®) enclosed in the liposome.

This approach significantly decreases the adverse effects of doxorubicin. Other liposomal formulas, such as Myocet and DaunoXome, have now been endorsed by the FDA for the treatment of cancer [2, 119]. Polymeric nanoparticles are produced from bio-compatible or natural polymers, like poly(lactide-co-glycolide), poly(γ -caprolactone), chitosan, alginate, and albumin [120]. New nanoparticles are currently being taken through research testing, which would increase the efficiency of treatments. For example, solid lipid nanoparticles made from solid fats at body temperature [121] and manufactured to load hydrophobic drugs have been shown to provide increased drug stability and extended release, particularly in comparison to hydrophobic substances [122, 123].

To resolve this problem, one or several lipids, liquid at ambient temperature (such as oleic acid, for instance), are included in the formula. Lipid nanoparticles are viable candidates for brain tumor therapy as they can pass the blood-brain barrier (BBB) [124-126].

5.2. Nanoparticles Therapy Systems

Systems used for drug-delivery can be utilized to alter the release of active compounds, allowing them to stay for longer periods *in vivo*, thereby allowing them to reach target sites [127]. The overall effect is increased effectiveness and reduced systemic cytotoxicity. This approach reduces the adverse effects and medical costs by reducing the quantity of the drug to be given. Scientists are searching for a broad range of strategies for the direct delivery of drugs to tumors. One of the areas under investigation is the coupling of magnetic nanoparticles with drugs [128, 129]. This will allow an external magnet to draw the medication conjugate to a target area where the drug exerts its biochemical effects. This magnetic targeting is also aimed at minimizing side effects [130].

A major problem with modern cancer treatment is the poor sensitivity of cancer cells to chemotherapeutic drugs [131]. Some drugs actually function on both normal and cancerous organs, causing serious adverse effects. Scientists are making significant efforts to find ways to target just the appropriate tumor location. Nanoparticles are miniature structures with unusual physical and chemical characteristics,

owing to their scale and large surface-to-volume ratio (1–1,000 nm in size) [132]. In chemotherapy, biocompatible nanoparticles are utilized to overcome several of the tissues surrounding traditional treatments, like the low selectivity and bio-availability of medicines or contrast agents [133]. Accordingly, the encapsulation of the active ingredients in nanoparticles will boost their solubility/ biocompatibility, their stability in body fluids, and tumor vasculature retention time [134]. Nanoparticles may also be designed to be highly selective for a specific target and release of the drug in a controlled manner by responding to a particular stimulus [135, 136]. This is the case with ThermoDox, a liposomal formulation that can release doxorubicin as a reaction to temperature increment [137].

Due to the improved permeability and retention potential, nanoparticles have generated considerable interest due to their propensity to accumulate more in tumor tissues [138]. This method, known as passive targeting, is focused on the small size of nanoparticles and leaky vasculature and compromised neoplastic tissue's lymphatic drainage [139]. Nonetheless, passive targeting is hard to manage and can trigger multidrug resistance (MDR) [140]. In an active targeting process, various types of small peptides and proteins have also been successful [141]. The Angiopep-2 peptide has generated considerable interest in the treatment of brain cancer. It attaches to the low-density lipoprotein-related protein-1 (LRP1) of endothelial cells in the blood brain barrier and is also overexpressed in cancerous cells of glioblastoma [142]. Coupling bombesin peptide with poly(lactic-co-glycolic acid) (PLGA) nanoparticles loaded with docetaxel has been used to target the gastrin-releasing peptide receptor on ovarian, pancreatic, and colorectal cancer cells [143].

Comparing active and passive targeting, active targeting increases tumor cell absorption by focusing on specific targets that are overexpressed on them [144]. For instance, nanoparticles can be activated with ligand molecules that bind to specific cells or subcellular sites. Many forms of ligands, like organic compounds, peptides, hormones, aptamers, and antibodies, may be used [145]. Aptamers are a class of small molecules which are lightweight, single-stranded synthetic RNA or DNA oligonucleotides folding into unique shapes that allow them to attach to particular sites [146]. Recent studies have shown that *in vitro* cytotoxicity is greatly enhanced by the use of aptamers linked to nanoparticles, which enhances cytotoxicity [147]. Furthermore, aptamers are reported to have been used for the preparation of quantum dot-doxorubicin conjugates [147, 148], which falls into the same category.

Also, biotin and folic acid are other examples of small molecules with overexpressed receptors in tumor cells. Further studies have been performed on folic acid functionalized nanocarriers to treat cancers of the ovaries and endometrium [149]. Small ligands are cheap, making them suitable for linkage to nanoparticles using simple conjugation chemistry. Polyethylene glycol-poly(lactic-co-glycolic acid) nanoparticles conjugated to folic acid have been used to deliver docetaxel to cervical cancer cells where the cellular uptake has been noted to increase considerably [150, 151]. Other examples include transferrin, which is a serum glycoprotein [152] overexpressed on several solid tumors, especially on multi-

form glioblastoma cells and on blood brain barrier epithelial cells [153, 154]. Transferrin-conjugated chitosan-polyethylene glycol nanoparticles loaded with paclitaxel demonstrate higher cytotoxicity against human non-small cell lung cancer cells (NSCLCs), as well as the transferrin-over-expressing HOP-62 [155].

Inorganic nanoparticles are non-toxic, hydrophilic, bio-compatible, and highly stable compared to organic materials. There reduced adverse effects and drug delivery abilities have made them suitable as diagnostic contrast agents [156]. Amongst these nanoparticles, quantum dots are tiny light-emitting semiconductor nanocrystals with unusual electronic and optical properties that make them extremely fluorescent, photo-bleaching resistant, and prone to observation and bio-imaging purposes [157]. Alternatively, when they are conjugated to active ligands, they become effective methods for theranostic applications. In a recent example, a poly(ethylene glycol) [158]-coated quantum dots (Fig. 6) were attached to anti-HER2 antigen and targeted in specific tumor cells [159]. This technique showed a new route towards the preparation of biocompatible, non-toxic QDs, which may be used for both *in vitro* and *in vivo* diagnostic and therapeutic applications.

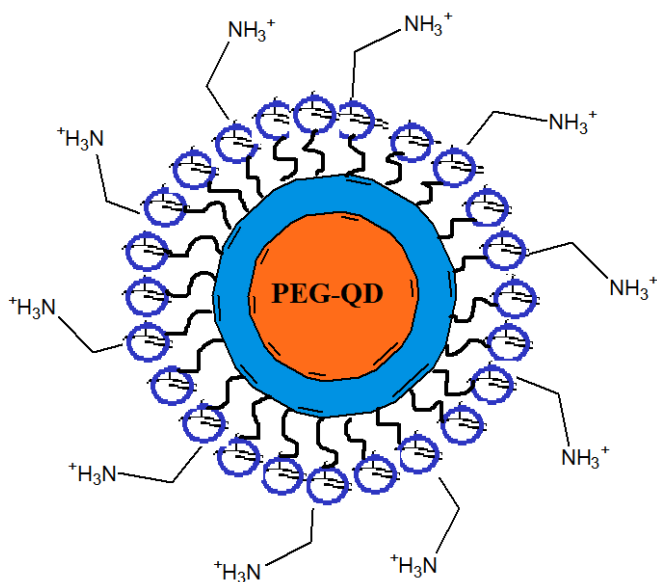


Fig. (6). Schematic diagram of quantum dots-polyethylene glycol (QD-PEG). (A higher resolution / colour version of this figure is available in the electronic copy of the article).

Nanoparticles based on gold have sparked interest due to their low toxicity and optical and electrical properties [160]. They are being used primarily as bio-imaging agents for X-rays, computed tomography, photoacoustic imaging, and photodynamic therapy [161, 162]. The Food and Drug Administration [46] approved a nanoshell developed from a silica core and a gold shell covered with PEG and marketed as AuroShell (Nanospectra) for the diagnosis of cancerous breast cells by photodynamic therapy [163].

The most researched nanomedicine structures are superparamagnetic iron oxide nanostructures (SPIONs), employed in magnetic hyperthermia [164]. In magnetic hyperthermia

therapy, the magnetic field is used to cause heat changes around cancerous cells, thereby inducing apoptosis. The heat is attributed to the interaction of magnetic fields in the particles once it is introduced, and the resulting relaxation cycles (Brownian and/or Neel relaxation) at which heat is emitted, when the magnetic field is withdrawn and the particle magnetization goes back to zero [165]. Magnetic hyperthermia can penetrate any area of the body and SPIONs can serve as MRI bioimaging agents to monitor their correct localization before exposure and stimulation [166]. To impart targeting properties, the particles can be filled with biocompatible polymers and/or lipids and functionalized with different ligands. Iron oxide nanoparticles capped with aminosilane (Nanotherm) have received approval for glioblastoma treatment [167]. SPIONs have been directly embedded with an anti-cancer drug in lipid nanocarriers, thereby coupling chemotherapy with hyperthermia [168, 169].

Recent study reports have shown that lipid nanoparticles coupled with superparamagnetic iron oxide nanostructures (SPIONs) [170] and temozolomide are successful in the treatment of glioblastoma as they integrate traditional chemotherapy and hyperthermia [171]. As shown in (Fig. 7), they comprise of core-shell super-paramagnetic nanofluids and consist of surface-functionalized magnetic iron oxide nanoparticles with a coat of carboxymethyl cellulose groups. These behave as magnetic nano-heaters that destroy cancer cells by hyperthermia through the heat generated by applying an alternating magnetic field.

Dendrimers are yet another sub-group of nanoparticles made up of polymers with a repetitive branching structure characterized by a spherical morphology [172]. Its design can be managed quickly, rendering its layout highly scalable for several uses. Moreover, several recent research studies show that *in vivo* tumor variants, poly-L-lysine (PLL) dendrimers, packed with doxorubicin induce anti-angiogenic responses [173]. There are current clinical studies for the diagnosis of inoperable liver cancers which does not react to traditional treatments for a formulation based on a dendrimer and a rhenium complex combined with an imidazolium ligand [174]

Nano-delivery systems provide a flexible framework of bio-compatible and bio-degradable systems capable of delivering traditional anti-cancer medications *in vivo*, boosting their bio-availability and tumor tissue concentration, and enhancing their release characteristics. They can be used for various applications, ranging from treatment to therapy. An area recently explored as efficient drug delivery vehicles is the extracellular vesicles (EVs), which are known to be responsible for cancer growth, micro-environmental alteration, and are needed for tumors progression [175, 176]. Exploiting these qualities opens up possibilities for targeting drugs to tumor sites using extracellular vesicles targeted therapy and immunotherapy.

Furthermore, the extracellular vesicles have the advantage that they are physiologically secreted. They exhibit good molecular characterization, have shown high biocompatibility, and are easily modifiable/loadable *in vitro* [176, 177]. However, these depend on the particular nanoparticles used.

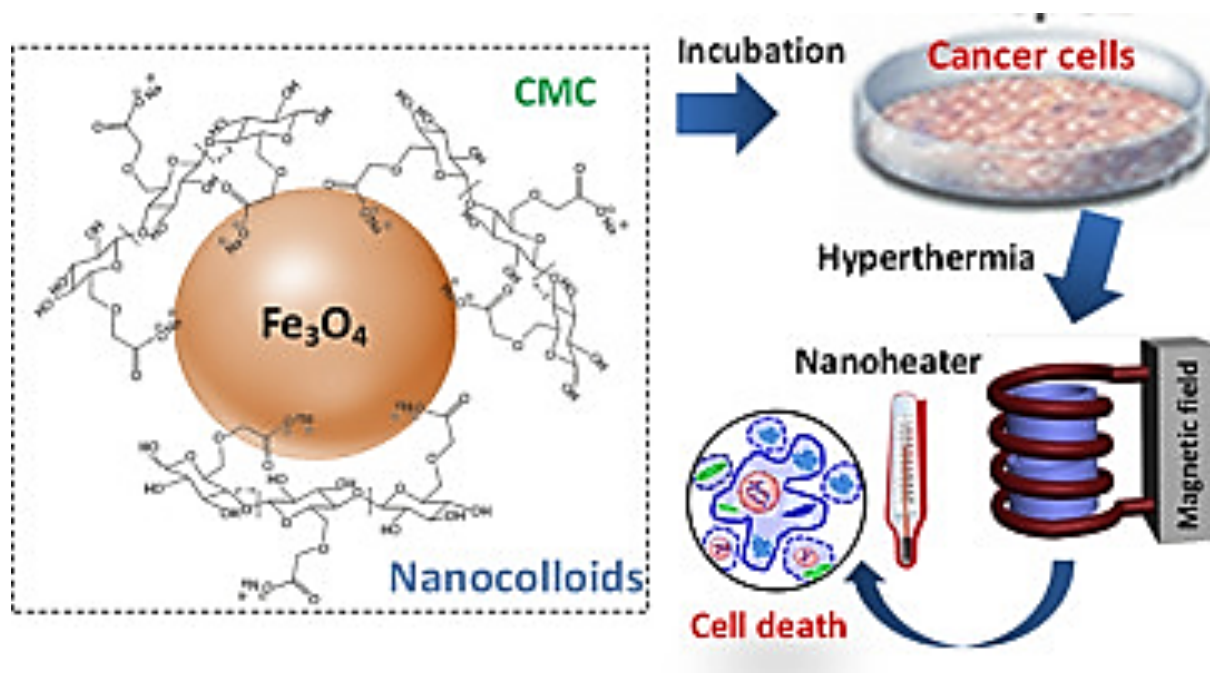


Fig. (7). SPIONs for hyperthermia therapy of cancer cells. (Adapted from ¹⁸⁸). (A higher resolution / colour version of this figure is available in the electronic copy of the article).

6. PREVENTIVE/ THERAPEUTIC

A worldwide cancer mortality projection of 19.3 million cases per year until 2025 is alarming. More than half of cancer cases and mortality occur in low- and middle-income countries, and these proportions are expected to increase by the year 2025 [178]. The cancer diagnoses and subsequent targeted therapies have achieved notable successes in some cancers. However, this approach is known to hold a significant number of negative properties, such as toxicity, high costs, and relapse of patients after a few disease-free months. For these reasons, prevention is still and will always be the best alternative.

6.1. Natural Anti-oxidants

The human body faces various exogenous assaults on a daily basis, such as ultraviolet (UV) radiation, air pollution, and tobacco smoke, culminating in the development of reactive species, particularly oxidants and free radicals, blamed for the emergence of many diseases such as cancer [179]. These molecules could also be formed as a result of medicinal drug treatment, but they are also spontaneously generated by mitochondria and peroxisomes within the cells and tissues, and by metabolism from macrophages, during regular aerobic physiological activities. Oxidative stress from reactive oxygen species are capable of destroying DNA (genetic changes, DNA double-strand splits and chromosomal aberrations) [180], and other bio-macromolecules, such as lipids (membrane peroxidation and necrosis and proteins) [181], significantly altering the function of transcription factors and, ultimately, important metabolic pathways [182, 183]. The body's defenses against these molecules often show inadequacies in overcoming the tremendous losses that have been created.

Together with studies into the functions of the superoxide dismutase (SOD), catalase [12] and glutathione peroxidase (GP) biological enzymes, natural anti-oxidants, such as vitamins, polyphenols and bioactive compounds derived from plants are being researched for protective agents and possible medicinal drugs [184, 185]. The anti-inflammatory and anti-oxidant effects of these molecules are present in many foods and spices [186]. The vitamins, alkaloids, flavonoids, carotenoids, curcumin, berberin, quercetin, and many other substances have been tested *in vitro* and checked *in vivo*, exhibiting strong antiproliferative and pro-apoptotic effects, and have been fronted to complement existing cancer treatments [187, 188]. The advantages associated with this approach include the fact that they are available easily and in large quantities. However, due to their limited bioavailability, their integration through clinical practice remains difficult [189, 190].

7. DISCUSSIONS

Today, the most common reports on chemotherapy treatments in the clinical research database (www.clinicaltrials.gov) refer to the words precision therapy, immunotherapy, and gene therapy, demonstrating that these are the most prevalent techniques (Fig. 8) under study, especially when they have displayed success and effectiveness as already stated. The rising number of these new technologies demonstrates how the potential and applicability are increasing rapidly to substitute and/or strengthen traditional therapeutics. Radiomics, immunotherapy, and exosomes can be seen as the categories whose numbers have risen most in the last decade.

The current situation for cancer research is broad, providing several opportunities for innovation, taking into account not just the rehabilitation of patients but rather their well-

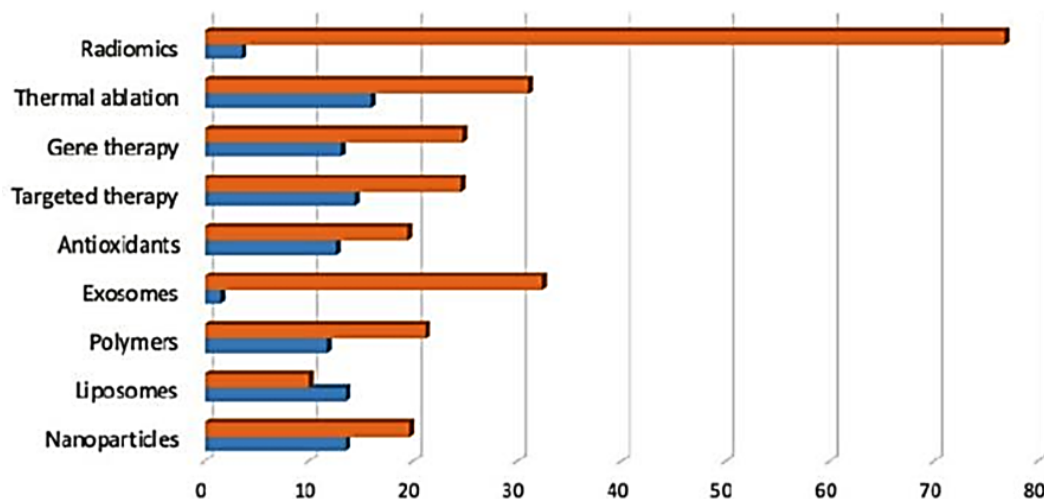


Fig. (8). Summary of the number of clinical trials started during the years 2008–2010 (blue) and from 2017 until today (orange). Date accessed: 01/08/19. (A higher resolution / colour version of this figure is available in the electronic copy of the article).

being during treatment [191]. Such new techniques offer several benefits in comparison to conventional treatments. Nonetheless, to boost their performance, several drawbacks have yet to be resolved [192–195]. Great advances have been made, but even more are likely to emerge in the coming years, creating more *ad hoc* customized treatment.

Due to the possibility of targeting several signaling pathways in combination therapy, there are possibilities of utilizing the various pathway mechanisms by a combination of the different therapies to lessen the progress of resistance in cancer cells. Literature reports on the combination of different therapies indicate that a combination of radiation and immunotherapy could increase the therapeutic response to immunotherapy. This is through several synergistic mechanisms that enhance tumor antigens visibility and activation of the various pathways through the modulation of the tumor microenvironment [196]. Results from preclinical and clinical studies show potential in the efficacy of combined therapy of the two but it requires further investigation [196]. It has, however, not yet been proved whether immunotherapy could conversely improve a tumor's sensitivity to radiation.

Earlier studies determining the synergistic effects of a combined model of liposomal drug delivery and radiofrequency (RF) ablation using animal tumor model by Goldberg and the group, indicated that the combined therapy had enhanced anti-tumor effects compared to RF ablation alone [197]. This established that the use of a combination of liposomes in drug delivery improved tumor ablation by radiofrequency. Another *in vitro* study used melanoma cells from mice to explore the effects of a combinatorial therapy, using gene transfer combined with magnetic hyperthermia. Another group of Ito Akira reported that the combined therapy, to a greater extent, halted tumor progression over a period of 30-days. They observed a total reversion of tumors in 30% of the test sample [198]. The mice that recovered were the ones from the combined therapy tests only. Their work established that the strategy of merging the use of gene therapy and magnetic hyperthermia could be applied clinically to advanced tumors [198].

The aim of using a combinatorial therapy is mainly to utilize one method to enhance a tumor's sensitivity to another. This may have the advantage of achieving better cytotoxicity profiles by using reduced dosages. Challenges arise, especially in predicting the response to combined therapy, keeping in mind that identification of biomarkers to predict the response of one treatment method is itself a challenge [199]. Moreover, the combination itself may produce new tumor signaling pathways, or affect the known pathways to the extent of altering the behavior and response of the treatment [200]. Also, a response(s) from one therapy may develop at a later point in time than the responses from others since each follows a distinct and different pathway.

In the light of these challenges, identifying a common bio-marker that elicits a predictable “universal response” may not be feasible.

A major challenge in immunotherapy is the difficulty of efficiently delivering enough loads of antigens into dendritic cells for the subsequent activation of a sufficient number of T cells and CD4⁺ helper T cells to attack cancerous cells [201]. Literature reports on the applications of Iron oxide nanoparticles, in combination with immunotherapy, show iron oxide nanoparticles as plausible transporters for sufficient antigens into dendritic cells [201].

Natural compounds combined with conventional treatments may help in overcoming some resistance by altering regulatory cell pathways that are accountable for drug resistance in cancer cells [202]. The use of anti-oxidants in combination with exosomes has been shown to improve the stability, solubility *in vitro*, and anti-inflammatory effects of the anti-oxidants, resulting in better outcomes compared to either one alone. This has been reported by a group working with curcumin encapsulated with exosomes. They found that the stability and systemic bioavailability of the exosomal-curcumin resulted in a five- to ten-fold better accumulation of curcumin in the blood, compared to curcumin alone *in vivo* [203].

The capability to culture liposomes with cancer cells to yield exosomes with precise proteins may result in enhanced

treatment profiles. To improve the solubility of hydrophobic drugs, it has been demonstrated that the effectiveness of pre-loaded anti-cancer exosomes is higher by the use of liposome-delivery in cells. Compared to control liposomes, the liposome-functionalized exosomes displayed greater retention of exosomes in circulation and a subsequently enhanced efficacy [204]. Since exosomes are known to be unstable *in vivo*, this could point to the stability-enhancing properties of the combined therapy. The combined treatment was shown to suppress cancer progression in multiple mouse models of pancreatic cancer, significantly improving their general survival rates [204].

This may result in enhanced susceptibility of cancer cells to other therapies, thereby mutually strengthening the overall outcomes for both therapeutics. For the treatment of Triple Negative Breast Cancer (TNBC), Chalakur-Ramireddy and co-workers suggested that a better treatment outcome could be achieved by selecting suitable combination treatment by studying patient-specific molecular features, biomarkers, clinical and pathological characteristics [205]. This is affirmed by the large number of clinical trials (almost 80%) currently utilizing combination treatments to study new therapeutic approaches for the treatment of TNBC.

The summarized synergistic combinations for the therapies, as reported in the literature are as summarized in Fig. (9).

Although this is not an exhaustive interrelationship, it clearly shows the possibilities and opportunities that exist in exploring combinations of different therapeutic procedures in efforts to synergistically optimize the already tested treatments.

CONCLUSION

Even though there are quite a variety of plausible hypotheses on how to manage cancer, there are still some inherent issues **that** cannot be overlooked in finding a cure,

especially for solid tumors. First, tumors are not just a single disease but a number of diseases that have selective responses to different anti-cancer agents. In order to detect disease genotypes, robust repositories are needed to manage vast volumes of data from the expression of genes, histology, 3D tissue modeling (MRI), and metabolism characteristics (positron emission tomography, PET) [206-208].

Progress into cancer therapy has taken significant strides in recent years toward more reliable, accurate, and less intrusive therapies. While nanomedicine, along with targeted therapy, has continued to enhance the biodistribution of emerging or already approved therapeutic drugs around the particular tissue to be handled, other methods, such as gene therapy, nanoparticle delivery, immunotherapy, and antioxidant molecules, offer new opportunities to cancer victims [209-211]. Thermal ablation and electrical hyperthermia, on the other side, offer solutions for resection of tumors [212, 213]. Not only can tumors from the same population be distinct, but not all cells are identical even from the same tumor in that same individual. Genotyping **has** shown that, when analyzed using the standard histological staining method, what appears as a single disease could possibly be multiple cancers, with separate prognoses, that could require different treatments [214].

Ultimately, approaches to radiomics and pathomics help enhance diagnosis and result in the handling of large data collections from cancer victims [215-218].

Taken collectively, these approaches would be able to provide people with cancer with the most tailored treatments, emphasizing the importance of combining different fields to achieve the best results [58].

Cells can develop inhibitors in the form of enzymes to render drugs inactive [219, 220]. They may also develop various pathways to eject cell-based anti-cancer agents through specific proteins, such as P-glycoprotein 1, also known as multidrug resistance protein 1 (PgP) [221, 222].

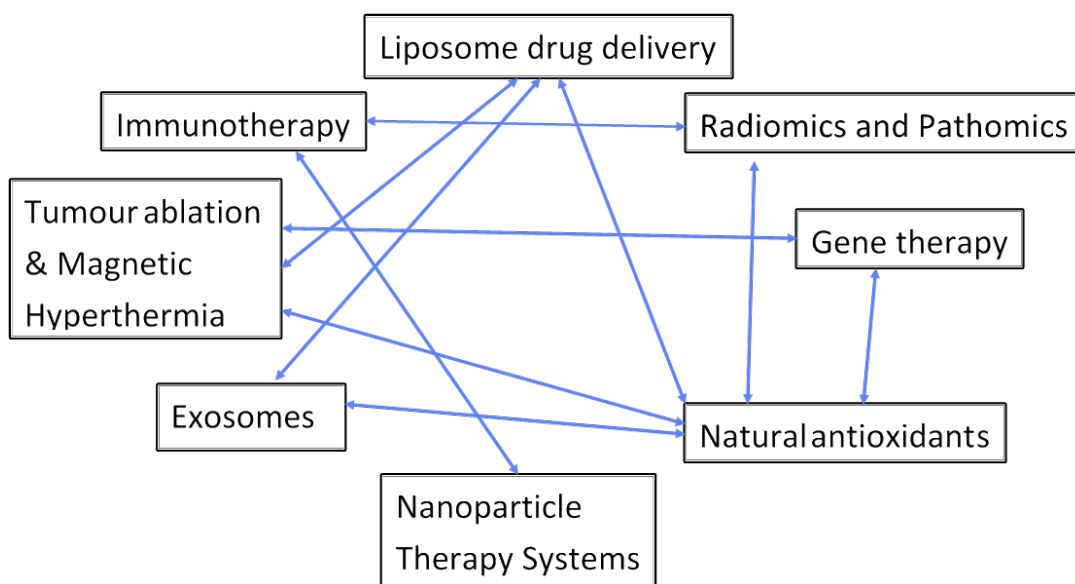


Fig. (9). Combination therapies and their corresponding synergistic summary. (A higher resolution / colour version of this figure is available in the electronic copy of the article).

While cancerous cells vary from healthy cells in many ways, the distinction has so far been difficult to analyze and exploit [223]. Chemotherapeutic medications are, thus, expected to also impose adverse effects on healthy cells, despite their innermost modes of action [224]. This is demonstrated by the cardiotoxicity of trastuzumab, a medication that directly binds to HER-2 receptors [225]. The use of different drug combinations is undoubtedly quite relevant, though it has not proven to be the final solution so far. Since cancer contributes to the breakdown of many complicated cellular functions, the most effective path may be to combine multiple strategies [2, 196]. This may include focusing on specific targets in cancer cells and several other rapidly-growing cells and triggering an immune response by increasing the normal immune response of the specific cancer cells [226].

CONSENT FOR PUBLICATION

Not applicable.

FUNDING

This project was financially supported by the International Science Program, ISP under the KEN-01 project, and the National Research Foundation NRF, South Africa, under grant no. CSUR160323161066.

CONFLICT OF INTEREST

The authors declare no conflict of interest, financial or otherwise.

ACKNOWLEDGEMENTS

Simon Mbugua gratefully acknowledges the University of Nairobi and the Organometallics and Nanomaterials group (Department of Chemical Sciences), UWC - South Africa, for providing a research platform.

REFERENCES

- [1] Ferlay, J.; Colombet, M.; Soerjomataram, I.; Mathers, C.; Parkin, D.M.; Piñeros, M.; Znaor, A.; Bray, F. Estimating the global cancer incidence and mortality in 2018: GLOBOCAN sources and methods. *Int. J. Cancer*, **2019**, *144*(8), 1941-1953. <http://dx.doi.org/10.1002/ijc.31937> PMID: 30350310
- [2] Riley, R.S.; June, C.H.; Langer, R.; Mitchell, M.J. Delivery technologies for cancer immunotherapy. *Nat. Rev. Drug Discov.*, **2019**, *18*(3), 175-196. <http://dx.doi.org/10.1038/s41573-018-0006-z> PMID: 30622344
- [3] Sanmamed, M.F.; Chen, L. A paradigm shift in cancer immunotherapy: from enhancement to normalization. *Cell*, **2018**, *175*(2), 313-326. <http://dx.doi.org/10.1016/j.cell.2018.09.035> PMID: 30290139
- [4] Gurunathan, S.; Kang, M.H.; Qasim, M.; Kim, J.H. Nanoparticle-mediated combination therapy: two-in-one approach for cancer. *Int. J. Mol. Sci.*, **2018**, *19*(10), E3264. <http://dx.doi.org/10.3390/ijms19103264> PMID: 30347840
- [5] Ribas, A.; Wolchok, J.D. Cancer immunotherapy using checkpoint blockade. *Science*, **2018**, *359*(6382), 1350-1355. <http://dx.doi.org/10.1126/science.aar4060> PMID: 29567705
- [6] McGivern, N.; El-Helali, A.; Mullan, P.; McNeish, I.A.; Paul Harkin, D.; Kennedy, R.D.; McCabe, N. Activation of MAPK signalling results in resistance to saracatinib (AZD0530) in ovarian cancer. *Oncotarget*, **2017**, *9*(4), 4722-4736. <http://dx.doi.org/10.18632/oncotarget.23524> PMID: 29435137
- [7] Laengle, J.; Kabiljo, J.; Hunter, L.; Homola, J.; Proding, S.; Egger, G.; Bergmann, M. Histone deacetylase inhibitors valproic acid and vorinostat enhance trastuzumab-mediated antibody-dependent cell-mediated phagocytosis. *J. Immunother. Cancer*, **2020**, *8*(1), e000195. <http://dx.doi.org/10.1136/jitc-2019-000195> PMID: 31940587
- [8] Feng, W.W.; Bang, S.; Kurokawa, M. CD36: a key mediator of resistance to HER2 inhibitors in breast cancer. *Mol. Cell. Oncol.*, **2020**, *7*(2), 1715766. <http://dx.doi.org/10.1080/23723556.2020.1715766> PMID: 32158927
- [9] Trujillo, J.A.; Sweis, R.F.; Bao, R.; Luke, J.J. T Cell-inflamed versus non-t cell-inflamed tumors: A conceptual framework for cancer immunotherapy drug development and combination therapy selection. *Cancer Immunol. Res.*, **2018**, *6*(9), 990-1000. <http://dx.doi.org/10.1158/2326-6066.CIR-18-0277> PMID: 30181337
- [10] Sahin, U.; Türeci, Ö. Personalized vaccines for cancer immunotherapy. *Science*, **2018**, *359*(6382), 1355-1360. <http://dx.doi.org/10.1126/science.aar7112> PMID: 29567706
- [11] Tanyi, J.L.; Bobisse, S.; Ophir, E.; Tuyvaerts, S.; Roberti, A.; Genolet, R.; Baumgartner, P.; Stevenson, B.J.; Iseli, C.; Dangaj, D.; Czerniecki, B.; Semilietof, A.; Racle, J.; Michel, A.; Xenarios, I.; Chiang, C.; Monos, D.S.; Torigian, D.A.; Nisenbaum, H.L.; Michielin, O.; June, C.H.; Levine, B.L.; Powell, D.J., Jr; Gfeller, D.; Mick, R.; Dafni, U.; Zoete, V.; Harari, A.; Coukos, G.; Kandalaf, L.E. Personalized cancer vaccine effectively mobilizes antitumor T cell immunity in ovarian cancer. *Sci. Transl. Med.*, **2018**, *10*(436), eaa05931. <http://dx.doi.org/10.1126/scitranslmed.aao5931> PMID: 29643231
- [12] Monti, S.; Brancato, V.; Di Costanzo, G.; Basso, L.; Puglia, M.; Ragozzino, A.; Salvatore, M.; Cavaliere, C. Multiparametric mri for prostate cancer detection: new insights into the combined use of a radiomic approach with advanced acquisition protocol. *Cancers (Basel)*, **2020**, *12*(2), E390. <http://dx.doi.org/10.3390/cancers12020390> PMID: 32046196
- [13] Derclé, L.; Lu, L.; Schwartz, L.H.; Qian, M.; Tejpar, S.; Eggleton, P.; Zhao, B.; Piessevaux, H. Radiomics response signature for identification of metastatic colorectal cancer sensitive to therapies targeting egfr pathway. *J. Natl. Cancer Inst.*, **2020**, dja017. <http://dx.doi.org/10.1093/jnci/djaa017> PMID: 32016387
- [14] Zhang, Q.; Peng, Y.; Liu, W.; Bai, J.; Zheng, J.; Yang, X.; Zhou, L. Radiomics based on multimodal mri for the differential diagnosis of benign and malignant breast lesions. *J. Magn. Reson. Imaging*, **2020**, *52*(2), 596-607. <http://dx.doi.org/10.1002/jmri.27098> PMID: 32061014
- [15] Moler, F.W.; Silverstein, F.S.; Holubkov, R.; Slomine, B.S.; Christensen, J.R.; Nadkarni, V.M.; Meert, K.L.; Browning, B.; Pemberton, V.L.; Page, K.; Gildea, M.R.; Scholefield, B.R.; Shankaran, S.; Hutchison, J.S.; Berger, J.T.; Ofori-Amanfo, G.; Newth, C.J.; Topjian, A.; Bennett, K.S.; Koch, J.D.; Pham, N.; Chanani, N.K.; Pineda, J.A.; Harrison, R.; Dalton, H.J.; Alten, J.; Schleien, C.L.; Goodman, D.M.; Zimmerman, J.J.; Bhalala, U.S.; Schwarz, A.J.; Porter, M.B.; Shah, S.; Fink, E.L.; McQuillen, P.; Wu, T.; Skellett, S.; Thomas, N.J.; Nowak, J.E.; Baines, P.B.; Pappachan, J.; Mathur, M.; Lloyd, E.; van der Jagt, E.W.; Dobyns, E.L.; Meyer, M.T.; Sanders, R.C., Jr; Clark, A.E.; Dean, J.M. THAPCA trial investigators. therapeutic hypothermia after in-hospital cardiac arrest in children. *N. Engl. J. Med.*, **2017**, *376*(4), 318-329. <http://dx.doi.org/10.1056/NEJMoa1610493> PMID: 28118559
- [16] Prior, F.; Almeida, J.; Kathiravelu, P.; Kurc, T.; Smith, K.; Fitzgerald, T.J.; Saltz, J. Open access image repositories: high-quality data to enable machine learning research. *Clin. Radiol.*, **2020**, *75*(1), 7-12. <http://dx.doi.org/10.1016/j.crad.2019.04.002> PMID: 31040006
- [17] Albuquerque, K.; Tuma, V.; Lea, J.; Ahn, C.; Richardson, D.; Miller, D.; Timmerman, R. A phase ii trial of stereotactic ablative radiation therapy as a boost for locally advanced cervical cancer. *Int. J. Radiat. Oncol. Biol. Phys.*, **2020**, *106*(3), 464-471. <http://dx.doi.org/10.1016/j.ijrobp.2019.10.042> PMID: 31697990
- [18] Kontaxis, C.; Bol, G.H.; Stemkens, B.; Glitzner, M.; Prins, F.M.; Kerkmeijer, L.G.W.; Lagendijk, J.J.W.; Raaymakers, B.W. Towards fast online intrafraction replanning for free-breathing

- stereotactic body radiation therapy with the MR-linac. *Phys. Med. Biol.*, **2017**, *62*(18), 7233-7248.
<http://dx.doi.org/10.1088/1361-6560/aa82ae> PMID: 28749375
- [19] Au, K.H.; Ngan, R.K.C.; Ng, A.W.Y.; Poon, D.M.C.; Ng, W.T.; Yuen, K.T.; Lee, V.H.F.; Tung, S.Y.; Chan, A.T.C.; Sze, H.C.K.; Cheng, A.C.K.; Lee, A.W.M.; Kwong, D.L.W.; Tam, A.H.P. Treatment outcomes of nasopharyngeal carcinoma in modern era after intensity modulated radiotherapy (IMRT) in Hong Kong: A report of 3328 patients (HKNPCSG 1301 study). *Oral Oncol.*, **2018**, *77*, 16-21.
<http://dx.doi.org/10.1016/j.oraloncology.2017.12.004> PMID: 29362121
- [20] Nguyen, T.K.; Senan, S.; Bradley, J.D.; Franks, K.; Giuliani, M.; Guckenberger, M.; Landis, M.; Loo, B.W., Jr; Louie, A.V.; Onishi, H.; Schmidt, H.; Timmerman, R.; Videtic, G.M.M.; Palma, D.A. Optimal imaging surveillance after stereotactic ablative radiation therapy for early-stage non-small cell lung cancer: Findings of an International Delphi Consensus Study. *Pract. Radiat. Oncol.*, **2018**, *8*(2), e71-e78.
<http://dx.doi.org/10.1016/j.prro.2017.10.008> PMID: 29291965
- [21] El-Razek, S.E.A. Transition metal complexes of a multidentate Schiff base ligand containing guanidine moiety: Synthesis, characterization, anti-cancer effect, and anti-microbial activity. *J. Mol. Struct.*, **2020**, *1203*, 127381.
<http://dx.doi.org/10.1016/j.molstruc.2019.127381>
- [22] Mi, P.; Cabral, H.; Kataoka, K. Ligand-installed nanocarriers toward precision therapy. *Adv. Mater.*, **2020**, *32*(13), e1902604.
<http://dx.doi.org/10.1002/adma.201902604> PMID: 31353770
- [23] Fang, T.; Lv, H.; Lv, G.; Li, T.; Wang, C.; Han, Q.; Yu, L.; Su, B.; Guo, L.; Huang, S.; Cao, D.; Tang, L.; Tang, S.; Wu, M.; Yang, W.; Wang, H. Tumor-derived exosomal miR-1247-3p induces cancer-associated fibroblast activation to foster lung metastasis of liver cancer. *Nat. Commun.*, **2018**, *9*(1), 191.
<http://dx.doi.org/10.1038/s41467-017-02583-0> PMID: 29335551
- [24] Zang, J.; Lu, D.; Xu, A. The interaction of circRNAs and RNA binding proteins: An important part of circRNA maintenance and function. *J. Neurosci. Res.*, **2020**, *98*(1), 87-97.
<http://dx.doi.org/10.1002/jnr.24356> PMID: 30575990
- [25] Pitarresi, J.R.; Rustgi, A.K. Mechanisms underlying metastatic pancreatic cancer. *Adv. Exp. Med. Biol.*, **2019**, *1164*, 3-10.
http://dx.doi.org/10.1007/978-3-030-22254-3_1 PMID: 31576536
- [26] Huang, T.; Deng, C.X. Current progresses of exosomes as cancer diagnostic and prognostic biomarkers. *Int. J. Biol. Sci.*, **2019**, *15*(1), 1-11.
<http://dx.doi.org/10.7150/ijbs.27796> PMID: 30662342
- [27] Scavo, M.P.; Depalo, N.; Tutino, V.; De Nunzio, V.; Ingrosso, C.; Rizzi, F.; Notarnicola, M.; Curri, M.L.; Giannelli, G. Exosomes for diagnosis and therapy in gastrointestinal cancers. *Int. J. Mol. Sci.*, **2020**, *21*(1), E367.
<http://dx.doi.org/10.3390/ijms21010367> PMID: 31935918
- [28] Xie, Y.; Dang, W.; Zhang, S.; Yue, W.; Yang, L.; Zhai, X.; Yan, Q.; Lu, J. The role of exosomal noncoding RNAs in cancer. *Mol. Cancer*, **2019**, *18*(1), 37.
<http://dx.doi.org/10.1186/s12943-019-0984-4> PMID: 30849983
- [29] Zeng, Z.; Li, Y.; Pan, Y.; Lan, X.; Song, F.; Sun, J.; Zhou, K.; Liu, X.; Ren, X.; Wang, F.; Hu, J.; Zhu, X.; Yang, W.; Liao, W.; Li, G.; Ding, Y.; Liang, L. Cancer-derived exosomal miR-25-3p promotes pre-metastatic niche formation by inducing vascular permeability and angiogenesis. *Nat. Commun.*, **2018**, *9*(1), 5395.
<http://dx.doi.org/10.1038/s41467-018-07810-w> PMID: 30568162
- [30] Whiteside, T.L. Exosome and mesenchymal stem cell cross-talk in the tumor microenvironment. *Semin. Immunol.*, **2018**, *35*, 69-79.
<http://dx.doi.org/10.1016/j.smim.2017.12.003> PMID: 29289420
- [31] Groza, M.; Zimta, A.A.; Irimie, A.; Achimas-Cadariu, P.; Cenariu, D.; Stanta, G.; Berindan-Neagoe, I. Recent advancements in the study of breast cancer exosomes as mediators of intratumoral communication. *J. Cell. Physiol.*, **2020**, *235*(2), 691-705.
<http://dx.doi.org/10.1002/jcp.29096> PMID: 31328284
- [32] Chicón-Bosch, M.; Tirado, O.M. Exosomes in bone sarcomas: Key players in metastasis. *Cells*, **2020**, *9*(1), E241.
<http://dx.doi.org/10.3390/cells9010241> PMID: 31963599
- [33] Jiang, S.; Hu, C.; Liu, P.; Lu, M. Tumor-derived exosomes in cancer metastasis risk diagnosis and metastasis therapy. *Clin. Transl. Oncol.*, **2019**, *21*(2), 152-159.
<http://dx.doi.org/10.1007/s12094-018-1918-0> PMID: 30051211
- [34] Do, H.T.T.; Lee, C.H.; Cho, J. Chemokines and their receptors: multifaceted roles in cancer progression and potential value as cancer prognostic markers. *Cancers (Basel)*, **2020**, *12*(2), E287.
<http://dx.doi.org/10.3390/cancers12020287> PMID: 31991604
- [35] Lu, D.Y.; Wu, F.G.; Zhen, Z.M.; Lu, T.R.; Wu, H.Y.; Che, J.Y.; Xu, B. Different spontaneous pulmonary metastasis inhibitions against lewis lung carcinoma in mice by bisdioxopiperazine compounds of different treatment schedules. *Sci. Pharm.*, **2010**, *78*(1), 13-20.
<http://dx.doi.org/10.3797/scipharm.0910-16> PMID: 21179367
- [36] Kruger, S.; Ilmer, M.; Kobold, S.; Cadilha, B.L.; Endres, S.; Ormanns, S.; Schuebbe, G.; Renz, B.W.; D'Haese, J.G.; Schloesser, H.; Heinemann, V.; Subklewe, M.; Boeck, S.; Werner, J.; von Bergwelt-Baildon, M. Advances in cancer immunotherapy 2019 - latest trends. *J. Exp. Clin. Cancer Res.*, **2019**, *38*(1), 268.
<http://dx.doi.org/10.1186/s13046-019-1266-0> PMID: 31217020
- [37] Souza-Fonseca-Guimaraes, F.; Cursors, J.; Huntington, N.D. The emergence of natural killer cells as a major target in cancer immunotherapy. *Trends Immunol.*, **2019**, *40*(2), 142-158.
<http://dx.doi.org/10.1016/j.it.2018.12.003> PMID: 30639050
- [38] Vander Zanden, C.M.; Chi, E.Y. Passive immunotherapies targeting amyloid beta and tau oligomers in alzheimer's disease. *J. Pharm. Sci.*, **2020**, *109*(1), 68-73.
<http://dx.doi.org/10.1016/j.xphs.2019.10.024> PMID: 31647950
- [39] Marra, A.; Viale, G.; Curigliano, G. Recent advances in triple negative breast cancer: the immunotherapy era. *BMC Med.*, **2019**, *17*(1), 90.
<http://dx.doi.org/10.1186/s12916-019-1326-5> PMID: 31068190
- [40] Sambhi, M.; Bagheri, L.; Szwczuk, M.R. Current challenges in cancer immunotherapy: multimodal approaches to improve efficacy and patient response rates. *J. Oncol.*, **2019**, *2019*, 4508794.
<http://dx.doi.org/10.1155/2019/4508794> PMID: 30941175
- [41] Rashidjahanabad, Z.; Huang, X. Recent advances in tumor associated carbohydrate antigen based chimeric antigen receptor T cells and bispecific antibodies for anti-cancer immunotherapy. *Semin. Immunol.*, **2020**, *47*, 101390.
<http://dx.doi.org/10.1016/j.smim.2020.101390> PMID: 31982247
- [42] Sicklick, J.K.; Kato, S.; Okamura, R.; Schwaederle, M.; Hahn, M.E.; Williams, C.B.; De, P.; Krie, A.; Piccioni, D.E.; Miller, V.A.; Ross, J.S.; Benson, A.; Webster, J.; Stephens, P.J.; Lee, J.J.; Fanta, P.T.; Lippman, S.M.; Leyland-Jones, B.; Kurzrock, R. Molecular profiling of cancer patients enables personalized combination therapy: the I-PREDICT study. *Nat. Med.*, **2019**, *25*(5), 744-750.
<http://dx.doi.org/10.1038/s41591-019-0407-5> PMID: 31011206
- [43] Camidge, D.R.; Doebele, R.C.; Kerr, K.M. Comparing and contrasting predictive biomarkers for immunotherapy and targeted therapy of NSCLC. *Nat. Rev. Clin. Oncol.*, **2019**, *16*(6), 341-355.
<http://dx.doi.org/10.1038/s41571-019-0173-9> PMID: 30718843
- [44] Havel, J.J.; Chowell, D.; Chan, T.A. The evolving landscape of biomarkers for checkpoint inhibitor immunotherapy. *Nat. Rev. Cancer*, **2019**, *19*(3), 133-150.
<http://dx.doi.org/10.1038/s41568-019-0116-x> PMID: 30755690
- [45] Otoshi, T.; Nagano, T.; Tachihara, M.; Nishimura, Y. Possible biomarkers for cancer immunotherapy. *Cancers (Basel)*, **2019**, *11*(7), E935.
<http://dx.doi.org/10.3390/cancers11070935> PMID: 31277279
- [46] Khailany, R.A.; Safdar, M.; Ozaslan, M. Genomic characterization of a novel SARS-CoV-2. *Gene Rep.*, **2020**, *19*, 100682.
<http://dx.doi.org/10.1016/j.genrep.2020.100682> PMID: 32300673
- [47] Golchin, A.; Farahany, T.Z. Biological products: cellular therapy and fda approved products. *Stem Cell Rev Rep*, **2019**, *15*(2), 166-175.
<http://dx.doi.org/10.1007/s12015-018-9866-1> PMID: 30623359
- [48] Zaidi, N.; Jaffee, E.M. Immunotherapy transforms cancer treatment. *J. Clin. Invest.*, **2019**, *129*(1), 46-47.
<http://dx.doi.org/10.1172/JCI126046> PMID: 30507614
- [49] Saito, H.; Kitagawa, K.; Yoneda, T.; Fukui, Y.; Fujisawa, M.; Bautista, D.; Shirakawa, T. Combination of p53-DC vaccine and rAd-p53 gene therapy induced CTLs cytotoxic against p53-deleted human prostate cancer cells *in vitro*. *Cancer Gene Ther.*, **2017**, *24*(7), 289-296.
<http://dx.doi.org/10.1038/cgt.2017.21> PMID: 28621316

- [50] Wallis, C.J.D.; Butaney, M.; Satkunasivam, R.; Freedland, S.J.; Patel, S.P.; Hamid, O.; Pal, S.K.; Klaassen, Z. Association of patient sex with efficacy of immune checkpoint inhibitors and overall survival in advanced cancers: a systematic review and meta-analysis. *JAMA Oncol.*, **2019**, *5*(4), 529-536. <http://dx.doi.org/10.1001/jamaoncol.2018.5904> PMID: 30605213
- [51] Hellmann, M.D. Genomic features of response to combination immunotherapy in patients with advanced non-small-cell lung cancer. *Cancer Cell*, **2018**, *35*(5), 843-852. <http://dx.doi.org/10.1016/j.ccell.2018.03.018>
- [52] Martin, J.D.; Cabral, H.; Stylianopoulos, T.; Jain, R.K. Improving cancer immunotherapy using nanomedicines: progress, opportunities and challenges. *Nat. Rev. Clin. Oncol.*, **2020**, *17*(4), 251-266. <http://dx.doi.org/10.1038/s41571-019-0308-z> PMID: 32034288
- [53] Malekzadeh, P.; Yossef, R.; Cafri, G.; Paria, B.C.; Lowery, F.J.; Jafferji, M.; Good, M.L.; Sachs, A.; Copeland, A.R.; Kim, S.P.; Kivitz, S.; Parkhurst, M.R.; Robbins, P.F.; Ray, S.; Xi, L.; Raffeld, M.; Yu, Z.; Restifo, N.P.; Somerville, R.P.T.; Rosenberg, S.A.; Deniger, D.C. Antigen experienced t cells from peripheral blood recognize p53 neoantigens. *Clin. Cancer Res.*, **2020**, *26*(6), 1267-1276. <http://dx.doi.org/10.1158/1078-0432.CCR-19-1874> PMID: 31996390
- [54] Schep, S.J.; Schutgens, R.E.G.; Fischer, K.; Boes, M.L. Review of immune tolerance induction in hemophilia A. *Blood Rev.*, **2018**, *32*(4), 326-338. <http://dx.doi.org/10.1016/j.blre.2018.02.003> PMID: 29482894
- [55] Binnewies, M.; Roberts, E.W.; Kersten, K.; Chan, V.; Fearon, D.F.; Merad, M.; Coussens, L.M.; Gabriilovich, D.I.; Ostrand-Rosenberg, S.; Hedrick, C.C.; Vonderheide, R.H.; Pittet, M.J.; Jain, R.K.; Zou, W.; Howcroft, T.K.; Woodhouse, E.C.; Weinberg, R.A.; Krummel, M.F. Understanding the tumor immune microenvironment (TIME) for effective therapy. *Nat. Med.*, **2018**, *24*(5), 541-550. <http://dx.doi.org/10.1038/s41591-018-0014-x> PMID: 29686425
- [56] Ren, D.; Hua, Y.; Yu, B.; Ye, X.; He, Z.; Li, C.; Wang, J.; Mo, Y.; Wei, X.; Chen, Y.; Zhou, Y.; Liao, Q.; Wang, H.; Xiang, B.; Zhou, M.; Li, X.; Li, G.; Li, Y.; Zeng, Z.; Xiong, W. Predictive biomarkers and mechanisms underlying resistance to PD1/PD-L1 blockade cancer immunotherapy. *Mol. Cancer*, **2020**, *19*(1), 19. <http://dx.doi.org/10.1186/s12943-020-1144-6> PMID: 32000802
- [57] Jiang, P.; Gu, S.; Pan, D.; Fu, J.; Sahu, A.; Hu, X.; Li, Z.; Traugh, N.; Bu, X.; Li, B.; Liu, J.; Freeman, G.J.; Brown, M.A.; Wucherpfennig, K.W.; Liu, X.S. Signatures of T cell dysfunction and exclusion predict cancer immunotherapy response. *Nat. Med.*, **2018**, *24*(10), 1550-1558. <http://dx.doi.org/10.1038/s41591-018-0136-1> PMID: 30127393
- [58] Roma-Rodrigues, C.; Mendes, R.; Baptista, P.V.; Fernandes, A.R. Targeting tumor microenvironment for cancer therapy. *Int. J. Mol. Sci.*, **2019**, *20*(4), E840. <http://dx.doi.org/10.3390/ijms20040840> PMID: 30781344
- [59] Sanchez-Correa, B.; Lopez-Sejas, N.; Duran, E.; Labella, F.; Alonso, C.; Solana, R.; Tarazona, R. Modulation of NK cells with checkpoint inhibitors in the context of cancer immunotherapy. *Cancer Immunol. Immunother.*, **2019**, *68*(5), 861-870. <http://dx.doi.org/10.1007/s00262-019-02336-6> PMID: 30953117
- [60] Taylor, E.M.; Koss, B.; Davis, L.E.; Tackett, A.J. Histone modifications as biomarkers for immunotherapy. *Methods Mol. Biol.*, **2020**, *2055*, 213-228. http://dx.doi.org/10.1007/978-1-4939-9773-2_10 PMID: 31502154
- [61] Wang, Y.; Bao, Y.; Zhang, S.; Wang, Z. Splicing dysregulation in cancer: from mechanistic understanding to a new class of therapeutic targets. *Sci. China Life Sci.*, **2020**, *63*(4), 469-484. <http://dx.doi.org/10.1007/s11427-019-1605-0> PMID: 32086672
- [62] Liu, J.; Zheng, X.; Tong, Q.; Li, W.; Wang, B.; Sutter, K.; Trilling, M.; Lu, M.; Dittmer, U.; Yang, D. Overlapping and discrete aspects of the pathology and pathogenesis of the emerging human pathogenic coronaviruses SARS-CoV, MERS-CoV, and 2019-nCoV. *J. Med. Virol.*, **2020**, *92*(5), 491-494. <http://dx.doi.org/10.1002/jmv.25709> PMID: 32056249
- [63] Corrales, L.; Matson, V.; Flood, B.; Spranger, S.; Gajewski, T.F. Innate immune signaling and regulation in cancer immunotherapy. *Cell Res.*, **2017**, *27*(1), 96-108. <http://dx.doi.org/10.1038/cr.2016.149> PMID: 27981969
- [64] Martin, J.D. Reengineering the tumor microenvironment to alleviate hypoxia and overcome cancer heterogeneity. *Cold Spring Harb. Perspect. Med.*, **2016**, *6*(12).
- [65] Samanta, D.; Semenza, G.L. Metabolic adaptation of cancer and immune cells mediated by hypoxia-inducible factors. *Biochim. Biophys. Acta Rev. Cancer*, **2018**, *1870*(1), 15-22. <http://dx.doi.org/10.1016/j.bbcan.2018.07.002> PMID: 30006019
- [66] Fleming, V.; Hu, X.; Weber, R.; Nagibin, V.; Groth, C.; Altevogt, P.; Utikal, J.; Umansky, V. Targeting myeloid-derived suppressor cells to bypass tumor-induced immunosuppression. *Front. Immunol.*, **2018**, *9*, 398. <http://dx.doi.org/10.3389/fimmu.2018.00398> PMID: 29552012
- [67] Xie, W.; Xu, J.; Hu, S.; Li, S.; Wang, W.; Cameron Yin, C.; Toruner, G.; Tang, Z.; Jeffrey Medeiros, L.; Tang, G. iAMP21 in acute myeloid leukemia is associated with complex karyotype, TP53 mutation and dismal outcome. *Mod. Pathol.*, **2020**, *33*(7), 1389-1397. <http://dx.doi.org/10.1038/s41379-020-0494-3> PMID: 32034282
- [68] Durgeau, A.; Virk, Y.; Corgnac, S.; Mami-Chouaib, F. Recent advances in targeting cd8 t-cell immunity for more effective cancer immunotherapy. *Front. Immunol.*, **2018**, *9*, 14. <http://dx.doi.org/10.3389/fimmu.2018.00014> PMID: 29403496
- [69] Wagner, S.; Mullins, C.S.; Linnebacher, M. Colorectal cancer vaccines: Tumor-associated antigens vs neoantigens. *World J. Gastroenterol.*, **2018**, *24*(48), 5418-5432. <http://dx.doi.org/10.3748/wjg.v24.i48.5418> PMID: 30622371
- [70] Conte, M.; De Palma, R.; Altucci, L. HDAC inhibitors as epigenetic regulators for cancer immunotherapy. *Int. J. Biochem. Cell Biol.*, **2018**, *98*, 65-74. <http://dx.doi.org/10.1016/j.biocel.2018.03.004> PMID: 29535070
- [71] Sang, W.; Zhang, Z.; Dai, Y.; Chen, X. Recent advances in nanomaterial-based synergistic combination cancer immunotherapy. *Chem. Soc. Rev.*, **2019**, *48*(14), 3771-3810. <http://dx.doi.org/10.1039/C8CS00896E> PMID: 31165801
- [72] Bolm, L.; Käsmann, L.; Paysen, A.; Karapetis, C.; Rades, D.; Wellner, U.F.; Keck, T.; Watson, D.I.; Hummel, R.; Hussey, D.J. Multimodal anti-tumor approaches combined with immunotherapy to overcome tumor resistance in esophageal and gastric cancer. *Anticancer Res.*, **2018**, *38*(6), 3231-3242. <http://dx.doi.org/10.21873/anticancer.12588> PMID: 29848670
- [73] Schaaf, M.B.; Garg, A.D.; Agostinis, P. Defining the role of the tumor vasculature in antitumor immunity and immunotherapy. *Cell Death Dis.*, **2018**, *9*(2), 115. <http://dx.doi.org/10.1038/s41419-017-0061-0> PMID: 29371595
- [74] Orkin, S.H.; Bauer, D.E. Emerging genetic therapy for sickle cell disease. *Annu. Rev. Med.*, **2019**, *70*, 257-271. <http://dx.doi.org/10.1146/annurev-med-041817-125507> PMID: 30355263
- [75] Ferrua, F.; Aiuti, A. Twenty-five years of gene therapy for ada-scid: from bubble babies to an approved Drug. *Hum. Gene Ther.*, **2017**, *28*(11), 972-981. <http://dx.doi.org/10.1089/hum.2017.175> PMID: 28847159
- [76] Hallek, M. Chronic lymphocytic leukemia: 2020 update on diagnosis, risk stratification and treatment. *Am. J. Hematol.*, **2019**, *94*(11), 1266-1287. <http://dx.doi.org/10.1002/ajh.25595> PMID: 31364186
- [77] Aubrey, B.J.; Kelly, G.L.; Janic, A.; Herold, M.J.; Strasser, A. How does p53 induce apoptosis and how does this relate to p53-mediated tumour suppression? *Cell Death Differ.*, **2018**, *25*(1), 104-113. <http://dx.doi.org/10.1038/cdd.2017.169> PMID: 29149101
- [78] Lewis, A.C.; Wallington-Beddoe, C.T.; Powell, J.A.; Pitson, S.M. Targeting sphingolipid metabolism as an approach for combination therapies in haematological malignancies. *Cell Death Discov.*, **2018**, *4*, 4. <http://dx.doi.org/10.1038/s41420-018-0075-0> PMID: 30062053
- [79] Lee, S.H.; Singh, I.; Tisdale, S.; Abdel-Wahab, O.; Leslie, C.S.; Mayr, C. Widespread intronic polyadenylation inactivates tumour suppressor genes in leukaemia. *Nature*, **2018**, *561*(7721), 127-131. <http://dx.doi.org/10.1038/s41586-018-0465-8> PMID: 30150773
- [80] Pucci, C.; Martinelli, C.; Ciofani, G. Innovative approaches for cancer treatment: current perspectives and new challenges. *Ecancermedicalscience*, **2019**, *13*, 961. <http://dx.doi.org/10.3332/ecancer.2019.961> PMID: 31537986

- [81] Rokudai, S. High-throughput rna interference screen targeting synthetic-lethal gain-of-function of oncogenic mutant tp53 in triple-negative breast cancer. *Methods Mol. Biol.*, **2020**, *2108*, 297-303. http://dx.doi.org/10.1007/978-1-0716-0247-8_25 PMID: 31939190
- [82] Rosik, J.; Szostak, B.; Machaj, F.; Pawlik, A. Potential targets of gene therapy in the treatment of heart failure. *Expert Opin. Ther. Targets*, **2018**, *22*(9), 811-816. <http://dx.doi.org/10.1080/14728222.2018.1514012> PMID: 30124081
- [83] Ohmori, T. Advances in gene therapy for hemophilia: basis, current status, and future perspectives. *Int. J. Hematol.*, **2020**, *111*(1), 31-41. <http://dx.doi.org/10.1007/s12185-018-2513-4> PMID: 30083852
- [84] Tzioufas, A.G.; Goules, A.V. Limited efficacy of targeted treatments in Sjögren's syndrome: why? *Clin Exp Rheumatol*, **2018**, *112*(3), 27-28.
- [85] Humbert, O.; Chan, F.; Rajawat, Y.S.; Torgerson, T.R.; Burtner, C.R.; Hubbard, N.W.; Humphrys, D.; Norgaard, Z.K.; O'Donnell, P.; Adair, J.E.; Trobridge, G.D.; Scharenberg, A.M.; Felsburg, P.J.; Rawlings, D.J.; Kiem, H.P. Rapid immune reconstitution of SCID-X1 canines after G-CSF/AMD3100 mobilization and *in vivo* gene therapy. *Blood Adv.*, **2018**, *2*(9), 987-999. <http://dx.doi.org/10.1182/bloodadvances.2018016451> PMID: 29720491
- [86] Lukashev, A.N.; Zamyatnin, A.A., Jr. Viral vectors for gene therapy: current state and clinical perspectives. *Biochemistry (Mosc.)*, **2016**, *81*(7), 700-708. <http://dx.doi.org/10.1134/S0006297916070063> PMID: 27449616
- [87] Mukalel, A.J.; Riley, R.S.; Zhang, R.; Mitchell, M.J. Nanoparticles for nucleic acid delivery: Applications in cancer immunotherapy. *Cancer Lett.*, **2019**, *458*, 102-112. <http://dx.doi.org/10.1016/j.canlet.2019.04.040> PMID: 31100411
- [88] Auloge, P.; Cazzato, R.L.; Koch, G.; Caudrelier, J.; De Marini, P.; Garnon, J.; Gangi, A. Percutaneous tumor ablation. *Presse Med.*, **2019**, *48*(10), 1146-1155. <http://dx.doi.org/10.1016/j.lpm.2019.10.011> PMID: 31676219
- [89] Kaija, H.; Pakanen, L.; Porvari, K. RNU6B, a frequent reference in miRNA expression studies, differentiates between deaths caused by hypothermia and chronic cardiac ischemia. *Int. J. Legal Med.*, **2020**, *134*(1), 159-162. <http://dx.doi.org/10.1007/s00414-019-02041-0> PMID: 30904931
- [90] Prasad, B.; Kim, S.; Cho, W.; Kim, S.; Kim, J.K. Effect of tumor properties on energy absorption, temperature mapping, and thermal dose in 13.56-MHz radiofrequency hyperthermia. *J. Therm. Biol.*, **2018**, *74*, 281-289. <http://dx.doi.org/10.1016/j.jtherbio.2018.04.007> PMID: 29801639
- [91] Mitxelena-Iribarren, O.; Campisi, J.; Martínez de Apellániz, I.; Lizarbe-Sancha, S.; Arana, S.; Zhukova, V.; Mujika, M.; Zhukov, A. Glass-coated ferromagnetic microwire-induced magnetic hyperthermia for *in vitro* cancer cell treatment. *Mater. Sci. Eng. C*, **2020**, *106*, 110261. <http://dx.doi.org/10.1016/j.msec.2019.110261> PMID: 31753330
- [92] Chen, J.; Ning, C.; Zhou, Z.; Yu, P.; Zhu, Y.; Tan, G.; Mao, C. Nanomaterials as photothermal therapeutic agents. *Prog. Mater. Sci.*, **2019**, *99*, 1-26. <http://dx.doi.org/10.1016/j.pmatsci.2018.07.005> PMID: 30568319
- [93] Testoni, S.G.G.; Healey, A.J.; Dietrich, C.F.; Arcidiacono, P.G. Systematic review of endoscopy ultrasound-guided thermal ablation treatment for pancreatic cancer. *Endosc. Ultrasound*, **2020**, *9*(2), 83-100. http://dx.doi.org/10.4103/eus.eus_74_19 PMID: 32295966
- [94] Izzo, F.; Granata, V.; Grassi, R.; Fusco, R.; Palaia, R.; Delrio, P.; Carrafiello, G.; Azoulay, D.; Petrillo, A.; Curley, S.A. Radiofrequency ablation and microwave ablation in liver tumors: an update. *Oncologist*, **2019**, *24*(10), e990-e1005. <http://dx.doi.org/10.1634/theoncologist.2018-0337> PMID: 31217342
- [95] Hsieh, Y.C.; Limquiao, J.L.; Lin, C.C.; Chen, W.T.; Lin, S.M. Radiofrequency ablation following artificial ascites and pleural effusion creation may improve outcomes for hepatocellular carcinoma in high-risk locations. *Abdom. Radiol. (N.Y.)*, **2019**, *44*(3), 1141-1151. <http://dx.doi.org/10.1007/s00261-018-1831-6> PMID: 30460530
- [96] Sun, Y.D.; Zhang, H.; Liu, J.Z.; Xu, H.R.; Wu, H.Y.; Zhai, H.Z.; Lu, C.Y.; Zhao, X.; Chen, Y.Q.; Zhou, L.L.; Han, J.J. Efficacy of radiofrequency ablation and microwave ablation in the treatment of thoracic cancer: A systematic review and meta-analysis. *Thorac. Cancer*, **2019**, *10*(3), 543-550. <http://dx.doi.org/10.1111/1759-7714.12973> PMID: 30677240
- [97] Boone, C.E.; Wojtasiewicz, T.; Moukheiber, E.; Butala, A.; Jordao, L.; Mills, K.A.; Sair, H.; Anderson, W.S. MR-guided functional neurosurgery: laser ablation and deep brain stimulation. *Top. Magn. Reson. Imaging*, **2018**, *27*(3), 171-177. <http://dx.doi.org/10.1097/RMR.000000000000152> PMID: 29870469
- [98] Meijerink, M.R.; Puijk, R.S.; van Tilborg, A.A.J.M.; Henningsen, K.H.; Fernandez, L.G.; Neyt, M.; Heymans, J.; Frankema, J.S.; de Jong, K.P.; Richel, D.J.; Prevoo, W.; Vlayen, J. Radiofrequency and microwave ablation compared to systemic chemotherapy and to partial hepatectomy in the treatment of colorectal liver metastases: a systematic review and meta-analysis. *Cardiovasc. Intervent. Radiol.*, **2018**, *41*(8), 1189-1204. <http://dx.doi.org/10.1007/s00270-018-1959-3> PMID: 29666906
- [99] Fincke, J.R.; Wynn, C.M.; Haupt, R.; Zhang, X.; Rivera, D.; Anthony, B. Characterization of laser ultrasound source signals in biological tissues for imaging applications. *J. Biomed. Opt.*, **2018**, *24*(2), 1-11. <http://dx.doi.org/10.1117/1.JBO.24.2.021206> PMID: 30550046
- [100] Seago, M.; Shumaker, P.R.; Spring, L.K.; Alam, M.; Al-Niaimi, F.; Rox Anderson, R.; Artzi, O.; Bayat, A.; Cassuto, D.; Chan, H.H.; Dierickx, C.; Donelan, M.; Gauglitz, G.G.; Leo Goo, B.; Goodman, G.J.; Gurtner, G.; Haedersdal, M.; Krakowski, A.C.; Manuskiatti, W.; Norbury, W.B.; Ogawa, R.; Ozog, D.M.; Paasch, U.; Victor Ross, E.; Tretti Clementoni, M.; Waibel, J. Laser treatment of traumatic scars and contractures: 2020 international consensus recommendations. *Lasers Surg. Med.*, **2020**, *52*(2), 96-116. <http://dx.doi.org/10.1002/lsm.23201> PMID: 31820478
- [101] Hong, C.S.; Cord, B.J.; Kundishora, A.J.; Elsamadicy, A.A.; Beckta, J.M.; Huttner, A.; Chiang, V.L.; Matouk, C.C. MRI-guided laser interstitial thermal therapy for radiation necrosis in previously irradiated brain arteriovenous malformations. *Pract. Radiat. Oncol.*, **2020**, *10*(4), e298-e303. <http://dx.doi.org/10.1016/j.pro.2020.02.003> PMID: 32068154
- [102] Strieth, S.; Hagemann, J.; Hess, M. Angiolytic laser applications for the larynx : Phonosurgical concepts for transoral laser microsurgery. *HNO*, **2020**, *68*(1), 59-68. <http://dx.doi.org/10.1007/s00106-019-00801-3> PMID: 31950226
- [103] Phadnis, A.; Kumar, S.; Srivastava, A. Numerical investigation of thermal response of laser-irradiated biological tissue phantoms embedded with gold nanoshells. *J. Therm. Biol.*, **2016**, *61*, 16-28. <http://dx.doi.org/10.1016/j.jtherbio.2016.08.002> PMID: 27712656
- [104] Suter, V.G.A.; Altermatt, H.J.; Bornstein, M.M. A randomized controlled trial comparing surgical excisional biopsies using CO₂ laser, Er:YAG laser and scalpel. *Int. J. Oral Maxillofac. Surg.*, **2020**, *49*(1), 99-106. <http://dx.doi.org/10.1016/j.ijom.2019.05.012> PMID: 31230766
- [105] Wierzbinski, K.R.; Szymanski, T.; Rozwadowska, N.; Rybka, J.D.; Zimna, A.; Zalewski, T.; Nowicka-Bauer, K.; Malcher, A.; Nowaczyk, M.; Krupinski, M.; Fiedorowicz, M.; Bogorodzki, P.; Grieb, P.; Giersig, M.; Kurpisz, M.K. Potential use of superparamagnetic iron oxide nanoparticles for *in vitro* and *in vivo* bioimaging of human myoblasts. *Sci. Rep.*, **2018**, *8*(1), 3682. <http://dx.doi.org/10.1038/s41598-018-22018-0> PMID: 29487326
- [106] El-Hammadi, M.M.; Arias, J.L. An update on liposomes in drug delivery: a patent review (2014-2018). *Expert Opin. Ther. Pat.*, **2019**, *29*(11), 891-907. <http://dx.doi.org/10.1080/13543776.2019.1679767> PMID: 31603360
- [107] Kauscher, U.; Holme, M.N.; Björnmalin, M.; Stevens, M.M. Physical stimuli-responsive vesicles in drug delivery: Beyond liposomes and polymersomes. *Adv. Drug Deliv. Rev.*, **2019**, *138*, 259-275. <http://dx.doi.org/10.1016/j.addr.2018.10.012> PMID: 30947810
- [108] Kang, J.H.; Ko, Y.T. Enhanced subcellular trafficking of resveratrol using mitochondriotropic liposomes in cancer cells. *Pharmaceutics*, **2019**, *11*(8), E423. <http://dx.doi.org/10.3390/pharmaceutics11080423> PMID: 31434345

- [109] Iinuma, H.; Maruyama, K.; Okinaga, K.; Sasaki, K.; Sekine, T.; Ishida, O.; Ogiwara, N.; Johkura, K.; Yonemura, Y. Intracellular targeting therapy of cisplatin-encapsulated transferrin-polyethylene glycol liposome on peritoneal dissemination of gastric cancer. *Int. J. Cancer*, **2002**, *99*(1), 130-137.
<http://dx.doi.org/10.1002/ijc.10242> PMID: 11948504
- [110] Yoon, H.J.; Lee, H.S.; Lim, J.Y.; Park, J.H. Liposomal indocyanine green for enhanced photothermal therapy. *ACS Appl. Mater. Interfaces*, **2017**, *9*(7), 5683-5691.
<http://dx.doi.org/10.1021/acsami.6b16801> PMID: 28152314
- [111] Belfiore, L.; Saunders, D.N.; Ranson, M.; Thurecht, K.J.; Storm, G.; Vine, K.L. Towards clinical translation of ligand-functionalized liposomes in targeted cancer therapy: Challenges and opportunities. *J. Control. Release*, **2018**, *277*, 1-13.
<http://dx.doi.org/10.1016/j.jconrel.2018.02.040> PMID: 29501721
- [112] Hamano, N.; Böttger, R.; Lee, S.E.; Yang, Y.; Kulkarni, J.A.; Ip, S.; Cullis, P.R.; Li, S.D. Robust microfluidic technology and new lipid composition for fabrication of curcumin-loaded liposomes: effect on the anticancer activity and safety of cisplatin. *Mol. Pharm.*, **2019**, *16*(9), 3957-3967.
<http://dx.doi.org/10.1021/acs.molpharmaceut.9b00583> PMID: 31381352
- [113] Du, Y.; Liang, X.; Li, Y.; Sun, T.; Jin, Z.; Xue, H.; Tian, J. Nuclear and fluorescent labeled pd-1-liposome-dox⁻⁶⁴cu/irdey800cw allows improved breast tumor targeted imaging and therapy. *Mol. Pharm.*, **2017**, *14*(11), 3978-3986.
<http://dx.doi.org/10.1021/acs.molpharmaceut.7b00649> PMID: 29016143
- [114] Xia, R.; Zheng, X.; Hu, X.; Liu, S.; Xie, Z. Photothermal-controlled generation of alkyl radical from organic nanoparticles for tumor treatment. *ACS Appl. Mater. Interfaces*, **2019**, *11*(6), 5782-5790.
<http://dx.doi.org/10.1021/acsami.8b18953> PMID: 30663874
- [115] Wu, F.; Chen, L.; Yue, L.; Wang, K.; Cheng, K.; Chen, J.; Luo, X.; Zhang, T. Small-molecule porphyrin-based organic nanoparticles with remarkable photothermal conversion efficiency for *in vivo* photoacoustic imaging and photothermal therapy. *ACS Appl. Mater. Interfaces*, **2019**, *11*(24), 21408-21416.
<http://dx.doi.org/10.1021/acsami.9b06866> PMID: 31120723
- [116] Ahmed, K.S.; Hussein, S.A.; Ali, A.H.; Korma, S.A.; Lipeng, Q.; Jinghua, C. Liposome: composition, characterisation, preparation, and recent innovation in clinical applications. *J. Drug Target.*, **2019**, *27*(7), 742-761.
<http://dx.doi.org/10.1080/1061186X.2018.1527337> PMID: 30239255
- [117] Lam, F.C.; Morton, S.W.; Wyckoff, J.; Vu Han, T.L.; Hwang, M.K.; Maffa, A.; Balkanska-Sinclair, E.; Yaffe, M.B.; Floyd, S.R.; Hammond, P.T. Enhanced efficacy of combined temozolomide and bromodomain inhibitor therapy for gliomas using targeted nanoparticles. *Nat. Commun.*, **2018**, *9*(1), 1991.
<http://dx.doi.org/10.1038/s41467-018-04315-4> PMID: 29777137
- [118] Pucci, C.; Martinelli, C.; Ciofani, G. What does the future hold for chemotherapy with the use of lipid-based nanocarriers? *Future Oncol.*, **2020**, *16*(5), 81-84.
<http://dx.doi.org/10.2217/fon-2019-0767> PMID: 31872773
- [119] Krauss, A.C.; Gao, X.; Li, L.; Manning, M.L.; Patel, P.; Fu, W.; Janoria, K.G.; Gieser, G.; Bateman, D.A.; Przepiorka, D.; Shen, Y.L.; Shord, S.S.; Sheth, C.M.; Banerjee, A.; Liu, J.; Goldberg, K.B.; Farrell, A.T.; Blumenthal, G.M.; Pazdur, R. FDA approval summary: (daunorubicin and cytarabine) liposome for injection for the treatment of adults with high-risk acute myeloid leukemia. *Clin. Cancer Res.*, **2019**, *25*(9), 2685-2690.
<http://dx.doi.org/10.1158/1078-0432.CCR-18-2990> PMID: 30541745
- [120] Atef, M.; Rezaei, M.; Behrooz, R. Preparation and characterization agar-based nanocomposite film reinforced by nanocrystalline cellulose. *Int. J. Biol. Macromol.*, **2014**, *70*, 537-544.
<http://dx.doi.org/10.1016/j.ijbiomac.2014.07.013> PMID: 25036597
- [121] Akhoond Zardini, A.; Mohebbi, M.; Farhoosh, R.; Bolurian, S. Production and characterization of nanostructured lipid carriers and solid lipid nanoparticles containing lycopene for food fortification. *J. Food Sci. Technol.*, **2018**, *55*(1), 287-298.
<http://dx.doi.org/10.1007/s13197-017-2937-5> PMID: 29358821
- [122] Ghasemiyeh, P.; Mohammadi-Samani, S. Solid lipid nanoparticles and nanostructured lipid carriers as novel drug delivery systems: applications, advantages and disadvantages. *Res. Pharm. Sci.*, **2018**, *13*(4), 288-303.
<http://dx.doi.org/10.4103/1735-5362.235156> PMID: 30065762
- [123] Mishra, V.; Bansal, K.K.; Verma, A.; Yadav, N.; Thakur, S.; Sudhakar, K.; Rosenholm, J.M. Solid lipid nanoparticles: emerging colloidal nano drug delivery systems. *Pharmaceutics*, **2018**, *10*(4), E191.
<http://dx.doi.org/10.3390/pharmaceutics10040191> PMID: 30340327
- [124] Erel-Akbaba, G.; Carvalho, L.A.; Tian, T.; Zinter, M.; Akbaba, H.; Obeid, P.J.; Chiocca, E.A.; Weissleder, R.; Kantarci, A.G.; Tannous, B.A. Radiation-induced targeted nanoparticle-based gene delivery for brain tumor therapy. *ACS Nano*, **2019**, *13*(4), 4028-4040.
<http://dx.doi.org/10.1021/acsnano.8b08177> PMID: 30916923
- [125] García-Pinel, B.; Porras-Alcalá, C.; Ortega-Rodríguez, A.; Sarabia, F.; Prados, J.; Melguizo, C.; López-Romero, J.M. Lipid-based nanoparticles: application and recent advances in cancer treatment. *Nanomaterials (Basel)*, **2019**, *9*(4), E638.
<http://dx.doi.org/10.3390/nano9040638> PMID: 31010180
- [126] Singh, I.; Swami, R.; Pooja, D.; Jeengar, M.K.; Khan, W.; Sista, R. Lactoferrin bioconjugated solid lipid nanoparticles: a new drug delivery system for potential brain targeting. *J. Drug Target.*, **2016**, *24*(3), 212-223.
<http://dx.doi.org/10.3109/1061186X.2015.1068320> PMID: 26219519
- [127] Patra, J.K.; Das, G.; Fraceto, L.F.; Campos, E.V.R.; Rodriguez-Torres, M.D.P.; Acosta-Torres, L.S.; Diaz-Torres, L.A.; Grillo, R.; Swamy, M.K.; Sharma, S.; Habtemariam, S.; Shin, H.S. Nano based drug delivery systems: recent developments and future prospects. *J. Nanobiotechnology*, **2018**, *16*(1), 71.
<http://dx.doi.org/10.1186/s12951-018-0392-8> PMID: 30231877
- [128] Ma, X.; Xiong, Y.; Lee, L.T.O. Application of nanoparticles for targeting g protein-coupled receptors. *Int. J. Mol. Sci.*, **2018**, *19*(7), E2006.
<http://dx.doi.org/10.3390/ijms19072006> PMID: 29996469
- [129] Jin, H.; Qian, Y.; Dai, Y.; Qiao, S.; Huang, C.; Lu, L.; Luo, Q.; Chen, J.; Zhang, Z. Magnetic enrichment of dendritic cell vaccine in lymph node with fluorescent-magnetic nanoparticles enhanced cancer immunotherapy. *Theranostics*, **2016**, *6*(11), 2000-2014.
<http://dx.doi.org/10.7150/thno.15102> PMID: 27698936
- [130] El-Boubbou, K. Magnetic iron oxide nanoparticles as drug carriers: preparation, conjugation and delivery. *Nanomedicine (Lond.)*, **2018**, *13*(8), 929-952.
<http://dx.doi.org/10.2217/nnm-2017-0320> PMID: 29546817
- [131] Senapati, S.; Mahanta, A.K.; Kumar, S.; Maiti, P. Controlled drug delivery vehicles for cancer treatment and their performance. *Signal Transduct. Target. Ther.*, **2018**, *3*, 7.
<http://dx.doi.org/10.1038/s41392-017-0004-3> PMID: 29560283
- [132] Akter, M.; Sikder, M.T.; Rahman, M.M.; Ullah, A.K.M.A.; Hossain, K.F.B.; Banik, S.; Hosokawa, T.; Saito, T.; Kurasaki, M. A systematic review on silver nanoparticles-induced cytotoxicity: Physicochemical properties and perspectives. *J. Adv. Res.*, **2017**, *9*, 1-16.
<http://dx.doi.org/10.1016/j.jare.2017.10.008> PMID: 30046482
- [133] Elzoghby, A.O.; Hemasa, A.L.; Freag, M.S. Hybrid protein-inorganic nanoparticles: From tumor-targeted drug delivery to cancer imaging. *J. Control. Release*, **2016**, *243*, 303-322.
<http://dx.doi.org/10.1016/j.jconrel.2016.10.023> PMID: 27794493
- [134] Jain, K.K. An overview of drug delivery systems. *Methods Mol. Biol.*, **2020**, *2059*, 1-54.
http://dx.doi.org/10.1007/978-1-4939-9798-5_1 PMID: 31435914
- [135] Sousa, F.; Cruz, A.; Fonte, P.; Pinto, I.M.; Neves-Petersen, M.T.; Sarmiento, B. A new paradigm for antiangiogenic therapy through controlled release of bevacizumab from PLGA nanoparticles. *Sci. Rep.*, **2017**, *7*(1), 3736.
<http://dx.doi.org/10.1038/s41598-017-03959-4> PMID: 28623267
- [136] Rizvi, S.A.A.; Saleh, A.M. Applications of nanoparticle systems in drug delivery technology. *Saudi Pharm. J.*, **2018**, *26*(1), 64-70.
<http://dx.doi.org/10.1016/j.jsps.2017.10.012> PMID: 29379334
- [137] Chen, S.; Huang, H.; Zhang, L.; Chen, Y.; Liu, X. Alternate release of different target species based on the same gold nanorods and monitored by cell imaging. *Colloids Surf. B Biointerfaces*, **2016**, *145*, 671-678.
<http://dx.doi.org/10.1016/j.colsurfb.2016.05.087> PMID: 27289308

- [138] Qian, K.; Chen, H.; Qu, C.; Qi, J.; Du, B.; Ko, T.; Xiang, Z.; Kandawa-Schulz, M.; Wang, Y.; Cheng, Z. Mitochondria-targeted delocalized lipophilic cation complexed with human serum albumin for tumor cell imaging and treatment. *Nanomedicine (Lond.)*, **2020**, *23*, 102087.
http://dx.doi.org/10.1016/j.nano.2019.102087 PMID: 31454551
- [139] Alavi, M.; Hamidi, M. Passive and active targeting in cancer therapy by liposomes and lipid nanoparticles. *Drug Metab. Pers. Ther.*, **2019**, *34*(1).
http://dx.doi.org/10.1515/dmpt-2018-0032 PMID: 30707682
- [140] Kankala, R.K.; Tsai, P.Y.; Kuthati, Y.; Wei, P.R.; Liu, C.L.; Lee, C.H. Overcoming multidrug resistance through co-delivery of ROS-generating nano-machinery in cancer therapeutics. *J. Mater. Chem. B Mater. Biol. Med.*, **2017**, *5*(7), 1507-1517.
http://dx.doi.org/10.1039/C6TB03146C PMID: 32264641
- [141] Yan, W.; Leung, S.S.; To, K.K. Updates on the use of liposomes for active tumor targeting in cancer therapy. *Nanomedicine (Lond.)*, **2020**, *15*(3), 303-318.
http://dx.doi.org/10.2217/nmm-2019-0308 PMID: 31802702
- [142] Kim, J.S.; Shin, D.H.; Kim, J.S. Dual-targeting immunoliposomes using angioprep-2 and CD133 antibody for glioblastoma stem cells. *J. Control. Release*, **2018**, *269*, 245-257.
http://dx.doi.org/10.1016/j.jconrel.2017.11.026 PMID: 29162480
- [143] Giorgakis, E.; Ramesh, B.; Kamali-Dashtarzheneh, A.; Fusai, G.K.; Imber, C.; Tsironis, D.; Loizidou, M. Demonstration of calreticulin expression in hamster pancreatic adenocarcinoma with the use of fluorescent gold quantum dots. *Anticancer Res.*, **2016**, *36*(3), 861-867.
PMID: 26976972
- [144] Rosenblum, D.; Joshi, N.; Tao, W.; Karp, J.M.; Peer, D. Progress and challenges towards targeted delivery of cancer therapeutics. *Nat. Commun.*, **2018**, *9*(1), 1410.
http://dx.doi.org/10.1038/s41467-018-03705-y PMID: 29650952
- [145] Panda, P.K.; Saraf, S.; Tiwari, A.; Verma, A.; Raikwar, S.; Jain, A.; Jain, S.K. Novel strategies for targeting prostate cancer. *Curr. Drug Deliv.*, **2019**, *16*(8), 712-727.
http://dx.doi.org/10.2174/1567201816666190821143805 PMID: 31433757
- [146] Kaur, H.; Bruno, J.G.; Kumar, A.; Sharma, T.K. Aptamers in the therapeutics and diagnostics pipelines. *Theranostics*, **2018**, *8*(15), 4016-4032.
http://dx.doi.org/10.7150/thno.25958 PMID: 30128033
- [147] Siminzar, P.; Omid, Y.; Golchin, A.; Aghanejad, A.; Barar, J. Targeted delivery of doxorubicin by magnetic mesoporous silica nanoparticles armed with mucin-1 aptamer. *J. Drug Target.*, **2020**, *28*(1), 92-101.
http://dx.doi.org/10.1080/1061186X.2019.1616745 PMID: 31062625
- [148] Xue, Q.; Zhang, Y.; Xu, S.; Li, H.; Wang, L.; Li, R.; Zhang, Y.; Yue, Q.; Gu, X.; Zhang, S.; Liu, J.; Wang, H. Magnetic nanoparticles-cooperated fluorescence sensor for sensitive and accurate detection of DNA methyltransferase activity coupled with exonuclease III-assisted target recycling. *Analyst (Lond.)*, **2015**, *140*(22), 7637-7644.
http://dx.doi.org/10.1039/C5AN01546D PMID: 26421322
- [149] Maiti, S.; Paira, P. Biotin conjugated organic molecules and proteins for cancer therapy: A review. *Eur. J. Med. Chem.*, **2018**, *145*, 206-223.
http://dx.doi.org/10.1016/j.ejmech.2018.01.001 PMID: 29324341
- [150] Huang, X.; Wu, W.; Yang, W.; Qing, X.; Shao, Z. Surface engineering of nanoparticles with ligands for targeted delivery to osteosarcoma. *Colloids Surf. B Biointerfaces*, **2020**, *190*, 110891.
http://dx.doi.org/10.1016/j.colsurfb.2020.110891 PMID: 32114271
- [151] Kim, K.T.; Lee, J.Y.; Kim, D.D.; Yoon, I.S.; Cho, H.J. Recent progress in the development of poly(lactic-co-glycolic acid)-based nanostructures for cancer imaging and therapy. *Pharmaceutics*, **2019**, *11*(6), E280.
http://dx.doi.org/10.3390/pharmaceutics11060280 PMID: 31197096
- [152] Li, S.; Zhao, H.; Fan, Y.; Zhao, G.; Wang, R.; Wen, F.; Wang, J.; Wang, X.; Wang, Y.; Gao, Y. Design, synthesis, and *in vitro* antitumor activity of a transferrin receptor-targeted peptide-doxorubicin conjugate. *Chem. Biol. Drug Des.*, **2020**, *95*(1), 58-65.
http://dx.doi.org/10.1111/cbdd.13613 PMID: 31452330
- [153] Jena, L.; McErlean, E.; McCarthy, H. Delivery across the blood-brain barrier: nanomedicine for glioblastoma multiforme. *Drug Deliv. Transl. Res.*, **2020**, *10*(2), 304-318.
http://dx.doi.org/10.1007/s13346-019-00679-2 PMID: 31728942
- [154] Mahmoud, B.S.; AlAmri, A.H.; McConville, C. Polymeric nanoparticles for the treatment of malignant gliomas. *Cancers (Basel)*, **2020**, *12*(1), E175.
http://dx.doi.org/10.3390/cancers12010175 PMID: 31936740
- [155] Dilnawaz, F.; Acharya, S.; Sahoo, S.K. Recent trends of nanomedical approaches in clinics. *Int. J. Pharm.*, **2018**, *538*(1-2), 263-278.
http://dx.doi.org/10.1016/j.ijpharm.2018.01.016 PMID: 29339248
- [156] Bayda, S.; Hadla, M.; Palazzolo, S.; Riello, P.; Corona, G.; Toffoli, G.; Rizzolio, F. Inorganic nanoparticles for cancer therapy: a transition from lab to clinic. *Curr. Med. Chem.*, **2018**, *25*(34), 4269-4303.
http://dx.doi.org/10.2174/0929867325666171229141156 PMID: 29284391
- [157] Mintz, K.J.; Zhou, Y.; Leblanc, R.M. Recent development of carbon quantum dots regarding their optical properties, photoluminescence mechanism, and core structure. *Nanoscale*, **2019**, *11*(11), 4634-4652.
http://dx.doi.org/10.1039/C8NR10059D PMID: 30834912
- [158] Li, S. Delivery of quantum dot-sirna nanoplexes in sk-n-sh cells for bace1 gene silencing and intracellular imaging. *Molecular Therapy–Nucleic Acids*, **2012**, *1*, e20.
- [159] Babu, L.T.; Paira, P. Current Application of Quantum Dots (QD) in Cancer Therapy: A Review. *Mini Rev. Med. Chem.*, **2017**, *17*(14), 1406-1415.
http://dx.doi.org/10.2174/1389557517666170315125504 PMID: 28320238
- [160] Kumar, A.; Das, N.; Satija, N.K.; Mandrah, K.; Roy, S.K.; Rayavarapu, R.G. A novel approach towards synthesis and characterization of non-cytotoxic gold nanoparticles using taurine as capping agent. *Nanomaterials (Basel)*, **2019**, *10*(1), E45.
http://dx.doi.org/10.3390/nano10010045 PMID: 31878144
- [161] Zhang, W.; Zhang, S.; Gao, P.; Lan, B.; Li, L.; Zhang, X.; Li, L.; Lu, H. The feasibility of NaGdF₄ nanoparticles as an x-ray fluorescence computed tomography imaging probe for the liver and lungs. *Med. Phys.*, **2020**, *47*(2), 662-671.
http://dx.doi.org/10.1002/mp.13930 PMID: 31742714
- [162] Shi, J.; Granger, B.; Xu, K.; Yang, Y. Quantitative X-ray fluorescence imaging of gold nanoparticles using joint L1 and total variation regularized reconstruction. *Quant. Imaging Med. Surg.*, **2020**, *10*(1), 184-196.
http://dx.doi.org/10.21037/qims.2019.10.15 PMID: 31956541
- [163] Pedrosa, P.; Corvo, M.L.; Ferreira-Silva, M.; Martins, P.; Carvalho, M.C.; Costa, P.M.; Martins, C.; Martins, L.M.D.R.S.; Baptista, P.V.; Fernandes, A.R. Targeting cancer resistance via multifunctional gold nanoparticles. *Int. J. Mol. Sci.*, **2019**, *20*(21), E5510.
http://dx.doi.org/10.3390/ijms20215510 PMID: 31694227
- [164] Zhao, X.F.; Wang, W.Y.; Li, X.D.; Li, S.P.; Song, F.G. Core-shell structure of Fe₃O₄@MTX-LDH/Au NPs for cancer therapy. *Mater. Sci. Eng. C*, **2018**, *89*, 422-428.
http://dx.doi.org/10.1016/j.msec.2018.04.024 PMID: 29752115
- [165] Nguyen, M.P.; Thuy, V.T.T.; Kim, D. Integration of iron oxide nanoparticles and polyaspartamide biopolymer for MRI image contrast enhancement and an efficient drug-delivery system in cancer therapy. *Nanotechnology*, **2020**, *31*(33), 335712.
http://dx.doi.org/10.1088/1361-6528/ab8f49 PMID: 32357358
- [166] Wu, K.; Su, D.; Liu, J.; Saha, R.; Wang, J.P. Magnetic nanoparticles in nanomedicine: a review of recent advances. *Nanotechnology*, **2019**, *30*(50), 502003.
http://dx.doi.org/10.1088/1361-6528/ab4241 PMID: 31491782
- [167] Grauer, O.; Jaber, M.; Hess, K.; Weckesser, M.; Schwindt, W.; Maring, S.; Wölfer, J.; Stummer, W. Combined intracavitary thermotherapy with iron oxide nanoparticles and radiotherapy as local treatment modality in recurrent glioblastoma patients. *J. Neurooncol.*, **2019**, *141*(1), 83-94.
http://dx.doi.org/10.1007/s11060-018-03005-x PMID: 30506500
- [168] Xiao, Y.; Du, J. Superparamagnetic nanoparticles for biomedical applications. *J. Mater. Chem. B Mater. Biol. Med.*, **2020**, *8*(3), 354-367.

- <http://dx.doi.org/10.1039/C9TB01955C> PMID: 31868197
- [169] Stiles, Z.E.; Murphy, A.J.; Anghelescu, D.L.; Brown, C.L.; Davidoff, A.M.; Dickson, P.V.; Glazer, E.S.; Bishop, M.W.; Furman, W.L.; Pappo, A.S.; Lucas, J.T., Jr; Deneve, J.L. Desmoplastic small round cell tumor: long-term complications after cytoreduction and hyperthermic intraperitoneal chemotherapy. *Ann. Surg. Oncol.*, **2020**, *27*(1), 171-178.
<http://dx.doi.org/10.1245/s10434-019-07339-2> PMID: 30963398
- [170] Leonel, A.G.; Mansur, H.S.; Mansur, A.A.P.; Caires, A.; Carvalho, S.M.; Krambrock, K.; Outon, L.E.F.; Ardisson, J.D. Synthesis and characterization of iron oxide nanoparticles/carboxymethyl cellulose core-shell nanohybrids for killing cancer cells *in vitro*. *Int. J. Biol. Macromol.*, **2019**, *132*, 677-691.
<http://dx.doi.org/10.1016/j.ijbiomac.2019.04.006> PMID: 30951776
- [171] Shaghghi, B.; Khoei, S.; Bonakdar, S. Preparation of multifunctional Janus nanoparticles on the basis of SPIONs as targeted drug delivery system. *Int. J. Pharm.*, **2019**, *559*, 1-12.
<http://dx.doi.org/10.1016/j.ijpharm.2019.01.020> PMID: 30664992
- [172] Hu, Y.; Mignani, S.; Majoral, J.P.; Shen, M.; Shi, X. Construction of iron oxide nanoparticle-based hybrid platforms for tumor imaging and therapy. *Chem. Soc. Rev.*, **2018**, *47*(5), 1874-1900.
<http://dx.doi.org/10.1039/C7CS00657H> PMID: 29376542
- [173] Bhattarai, P.; Hameed, S.; Dai, Z. Recent advances in anti-angiogenic nanomedicines for cancer therapy. *Nanoscale*, **2018**, *10*(12), 5393-5423.
<http://dx.doi.org/10.1039/C7NR09612G> PMID: 29528075
- [174] Ding, R.M.; He, H.; Li, J. Research progress of polyamidoamine dendrimer in targeting drug delivery system. *Yao Xue Xue Bao*, **2011**, *46*(5), 493-501.
PMID: 21800534
- [175] Bebelman, M.P.; Smit, M.J.; Pegtel, D.M.; Baglio, S.R. Biogenesis and function of extracellular vesicles in cancer. *Pharmacol. Ther.*, **2018**, *188*, 1-11.
<http://dx.doi.org/10.1016/j.pharmthera.2018.02.013> PMID: 29476772
- [176] Zhao, H.; Achreja, A.; Iessi, E.; Logozzi, M.; Mizzoni, D.; Di Raimo, R.; Nagrath, D.; Fais, S. The key role of extracellular vesicles in the metastatic process. *Biochim. Biophys. Acta Rev. Cancer*, **2018**, *1869*(1), 64-77.
<http://dx.doi.org/10.1016/j.bbcan.2017.11.005> PMID: 29175553
- [177] Jabalee, J.; Towle, R.; Garnis, C. The role of extracellular vesicles in cancer: cargo, function, and therapeutic implications. *Cells*, **2018**, *7*(8), E93.
<http://dx.doi.org/10.3390/cells7080093> PMID: 30071693
- [178] Cohen, P.A.; Jhingran, A.; Oaknin, A.; Denny, L. Cervical cancer. *Lancet*, **2019**, *393*(10167), 169-182.
[http://dx.doi.org/10.1016/S0140-6736\(18\)32470-X](http://dx.doi.org/10.1016/S0140-6736(18)32470-X) PMID: 30638582
- [179] Carrera, I.; Martinez, O.; Cacabelos, R. Neuroprotection with natural antioxidants and nutraceuticals in the context of brain cell degeneration: the epigenetic connection. *Curr. Top. Med. Chem.*, **2019**, *19*(32), 2999-3011.
<http://dx.doi.org/10.2174/1568026619666191202155738> PMID: 31789133
- [180] Kastan, M.B. Our cells get stressed too! Implications for human disease. *Blood Cells Mol. Dis.*, **2007**, *39*(2), 148-150.
<http://dx.doi.org/10.1016/j.bcmd.2007.04.002> PMID: 17537652
- [181] Shastri, M.D.; Shukla, S.D.; Chong, W.C.; Dua, K.; Peterson, G.M.; Patel, R.P.; Hansbro, P.M.; Eri, R.; O'Toole, R.F. Role of oxidative stress in the pathology and management of human tuberculosis. *Oxid. Med. Cell. Longev.*, **2018**, *2018*, 7695364.
<http://dx.doi.org/10.1155/2018/7695364> PMID: 30405878
- [182] Bhatti, J.S.; Bhatti, G.K.; Reddy, P.H. Mitochondrial dysfunction and oxidative stress in metabolic disorders - A step towards mitochondria based therapeutic strategies. *Biochim. Biophys. Acta Mol. Basis Dis.*, **2017**, *1863*(5), 1066-1077.
<http://dx.doi.org/10.1016/j.bbdis.2016.11.010> PMID: 27836629
- [183] Islam, M.T. Oxidative stress and mitochondrial dysfunction-linked neurodegenerative disorders. *Neurol. Res.*, **2017**, *39*(1), 73-82.
<http://dx.doi.org/10.1080/01616412.2016.1251711> PMID: 27809706
- [184] Altemimi, A. Phytochemicals: extraction, isolation, and identification of bioactive compounds from plant extracts. *Plants (Basel)*, **2017**, *6*(4).
- [185] Wasser, S.P. Medicinal mushrooms in human clinical studies. part i. anticancer, oncoimmunological, and immunomodulatory activities: a review. *Int. J. Med. Mushrooms*, **2017**, *19*(4), 279-317.
<http://dx.doi.org/10.1615/IntJMedMushrooms.v19.i4.10> PMID: 28605319
- [186] Baenas, N.; Belović, M.; Ilic, N.; Moreno, D.A.; Garcia-Viguera, C. Industrial use of pepper (*Capsicum annum* L.) derived products: Technological benefits and biological advantages. *Food Chem.*, **2019**, *274*, 872-885.
<http://dx.doi.org/10.1016/j.foodchem.2018.09.047> PMID: 30373022
- [187] Ijaz, S.; Akhtar, N.; Khan, M.S.; Hameed, A.; Irfan, M.; Arshad, M.A.; Ali, S.; Asrar, M. Plant derived anticancer agents: A green approach towards skin cancers. *Biomed. Pharmacother.*, **2018**, *103*, 1643-1651.
<http://dx.doi.org/10.1016/j.biopha.2018.04.113> PMID: 29864953
- [188] Bahall, M. Prevalence, patterns, and perceived value of complementary and alternative medicine among cancer patients: a cross-sectional, descriptive study. *BMC Complement. Altern. Med.*, **2017**, *17*(1), 345.
<http://dx.doi.org/10.1186/s12906-017-1853-6> PMID: 28666435
- [189] Pan, P.; Skaer, C.; Yu, J.; Zhao, H.; Ren, H.; Oshima, K.; Wang, L.S. Berries and other natural products in the pancreatic cancer chemoprevention in human clinical trials. *J. Berry Res.*, **2017**, *7*(3), 147-161.
<http://dx.doi.org/10.3233/JBR-170159> PMID: 29367867
- [190] Rezaei-amiri, E.; Bahramsoltani, R.; Rahimi, R. Plant-derived natural agents as dietary supplements for the regulation of glycosylated hemoglobin: A review of clinical trials. *Clin. Nutr.*, **2020**, *39*(2), 331-342.
<http://dx.doi.org/10.1016/j.clnu.2019.02.006> PMID: 30797623
- [191] Tang, J.; Shalabi, A.; Hubbard-Lucey, V.M. Comprehensive analysis of the clinical immuno-oncology landscape. *Ann. Oncol.*, **2018**, *29*(1), 84-91.
<http://dx.doi.org/10.1093/annonc/mdx755> PMID: 29228097
- [192] Cecchini, M.; Rubin, E.H.; Blumenthal, G.M.; Ayalew, K.; Burris, H.A.; Russell-Einhorn, M.; Dillon, H.; Lyster, H.K.; Reaman, G.H.; Boerner, S.; LoRusso, P.M. Challenges with novel clinical trial designs: master protocols. *Clin. Cancer Res.*, **2019**, *25*(7), 2049-2057.
<http://dx.doi.org/10.1158/1078-0432.CCR-18-3544> PMID: 30696689
- [193] Liu, J. An integrated TCGA pan-cancer clinical data resource to drive high-quality survival outcome analytics. *Cell*, **2018**, *173*(2), 400-416.
- [194] Singh, M.; Prasad, C.P.; Singh, T.D.; Kumar, L. Cancer research in India: Challenges & opportunities. *Indian J. Med. Res.*, **2018**, *148*(4), 362-365.
http://dx.doi.org/10.4103/ijmr.IJMR_1711_18 PMID: 30665997
- [195] McClure, J.J.; Li, X.; Chou, C.J. Advances and challenges of hdac inhibitors in cancer therapeutics. *Adv. Cancer Res.*, **2018**, *138*, 183-211.
<http://dx.doi.org/10.1016/bs.acr.2018.02.006> PMID: 29551127
- [196] Wang, Y.; Deng, W.; Li, N.; Neri, S.; Sharma, A.; Jiang, W.; Lin, S.H. Combining immunotherapy and radiotherapy for cancer treatment: current challenges and future directions. *Front. Pharmacol.*, **2018**, *9*, 185.
<http://dx.doi.org/10.3389/fphar.2018.00185> PMID: 29556198
- [197] Goldberg, S.N.; Girnan, G.D.; Lukyanov, A.N.; Ahmed, M.; Monsky, W.L.; Gazelle, G.S.; Huertas, J.C.; Stuart, K.E.; Jacobs, T.; Torchillin, V.P.; Halpern, E.F.; Kruskal, J.B. Percutaneous tumor ablation: increased necrosis with combined radio-frequency ablation and intravenous liposomal doxorubicin in a rat breast tumor model. *Radiology*, **2002**, *222*(3), 797-804.
<http://dx.doi.org/10.1148/radiol.2223010861> PMID: 11867804
- [198] Ito, A.; Matsuoka, F.; Honda, H.; Kobayashi, T. Heat shock protein 70 gene therapy combined with hyperthermia using magnetic nanoparticles. *Cancer Gene Ther.*, **2003**, *10*(12), 918-925.
<http://dx.doi.org/10.1038/sj.cgt.7700648> PMID: 14712318
- [199] Torphy, R.J.; Schulick, R.D.; Zhu, Y. Newly emerging immune checkpoints: promises for future cancer therapy. *Int. J. Mol. Sci.*, **2017**, *18*(12), E2642.
<http://dx.doi.org/10.3390/ijms18122642> PMID: 29211042
- [200] Wei, S.C. Distinct cellular mechanisms underlie anti-ctla-4 and anti-pd-1 checkpoint blockade. *Cell*, **2017**, *170*(6), 1120-1133.

- <http://dx.doi.org/10.1016/j.cell.2017.07.024>
- [201] Saeed, M.; Ren, W.; Wu, A. Therapeutic applications of iron oxide based nanoparticles in cancer: basic concepts and recent advances. *Biomater. Sci.*, **2018**, *6*(4), 708-725. <http://dx.doi.org/10.1039/C7BM00999B> PMID: 29363682
- [202] Rejhová, A.; Opatková, A.; Čumová, A.; Slíva, D.; Vodička, P. Natural compounds and combination therapy in colorectal cancer treatment. *Eur. J. Med. Chem.*, **2018**, *144*, 582-594. <http://dx.doi.org/10.1016/j.ejmech.2017.12.039> PMID: 29289883
- [203] Sun, D.; Zhuang, X.; Xiang, X.; Liu, Y.; Zhang, S.; Liu, C.; Barnes, S.; Grizzle, W.; Miller, D.; Zhang, H.G. A novel nanoparticle drug delivery system: the anti-inflammatory activity of curcumin is enhanced when encapsulated in exosomes. *Mol. Ther.*, **2010**, *18*(9), 1606-1614. <http://dx.doi.org/10.1038/mt.2010.105> PMID: 20571541
- [204] Zhang, Z.; Dombroski, J.A.; King, M.R. Engineering of Exosomes to Target Cancer Metastasis. *Cell. Mol. Bioeng.*, **2019**, *13*(1), 1-16. <http://dx.doi.org/10.1007/s12195-019-00607-x> PMID: 32030104
- [205] Chalukur-Ramireddy, N.K.R.; Pakala, S.B. Combined drug therapeutic strategies for the effective treatment of triple negative breast cancer. *Biosci. Rep.*, **2018**, *38*(1)BSR20171357 <http://dx.doi.org/10.1042/BSR20171357> PMID: 29298879
- [206] Lee, G.; Park, H.; Bak, S.H.; Lee, H.Y. Radiomics in lung cancer from basic to advanced: current status and future directions. *Korean J. Radiol.*, **2020**, *21*(2), 159-171. <http://dx.doi.org/10.3348/kjr.2019.0630> PMID: 31997591
- [207] Nadeem, M.W.; Ghamdi, M.A.A.; Hussain, M.; Khan, M.A.; Khan, K.M.; Almotiri, S.H.; Butt, S.A. Brain tumor analysis empowered with deep learning: a review, taxonomy, and future challenges. *Brain Sci.*, **2020**, *10*(2), E118. <http://dx.doi.org/10.3390/brainsci10020118> PMID: 32098333
- [208] Huang, H.Y.; Lin, Y.C.; Li, J.; Huang, K.Y.; Shrestha, S.; Hong, H.C.; Tang, Y.; Chen, Y.G.; Jin, C.N.; Yu, Y.; Xu, J.T.; Li, Y.M.; Cai, X.X.; Zhou, Z.Y.; Chen, X.H.; Pei, Y.Y.; Hu, L.; Su, J.J.; Cui, S.D.; Wang, F.; Xie, Y.Y.; Ding, S.Y.; Luo, M.F.; Chou, C.H.; Chang, N.W.; Chen, K.W.; Cheng, Y.H.; Wan, X.H.; Hsu, W.L.; Lee, T.Y.; Wei, F.X.; Huang, H.D. miRTarBase 2020: updates to the experimentally validated microRNA-target interaction database. *Nucleic Acids Res.*, **2020**, *48*(D1), D148-D154. PMID: 31647101
- [209] He, M.; Wang, Y.; Chen, X.; Zhao, Y.; Lou, K.; Wang, Y.; Huang, L.; Hou, X.; Xu, J.; Cai, X.; Cheng, Y.; Lan, M.; Yang, Y.; Gao, F. Spatiotemporally controllable diphtheria toxin expression using a light-switchable transgene system combining multifunctional nanoparticle delivery system for targeted melanoma therapy. *J. Control. Release*, **2020**, *319*, 1-14. <http://dx.doi.org/10.1016/j.jconrel.2019.12.015> PMID: 31838205
- [210] Zins, K.; Abraham, D. Cancer immunotherapy: targeting tumor-associated macrophages by gene silencing. *Methods Mol. Biol.*, **2020**, *2115*, 289-325. http://dx.doi.org/10.1007/978-1-0716-0290-4_17 PMID: 32006408
- [211] Nagaraju, G.P.; Srivani, G.; Dariya, B.; Chalikonda, G.; Farran, B.; Behera, S.K.; Alam, A.; Kamal, M.A. Nanoparticles guided drug delivery and imaging in gastric cancer. *Semin. Cancer Biol.*, **2020**. (In Press) <http://dx.doi.org/10.1016/j.semcancer.2020.01.006> PMID: 31954835
- [212] Anghileri, L.J.; Crone-Escanye, M.C.; Martin, J.A.; Robert, J. Modification of the ionic environment in the tumor cell by hyperthermia. *Neoplasma*, **1988**, *35*(5), 489-494. PMID: 3216927
- [213] Amini, S.M.; Kharrazi, S.; Rezayat, S.M.; Gilani, K. Radiofrequency electric field hyperthermia with gold nanostructures: role of particle shape and surface chemistry. *Artif. Cells Nanomed. Biotechnol.*, **2018**, *46*(7), 1452-1462. <http://dx.doi.org/10.1080/21691401.2017.1373656> PMID: 28891351
- [214] Nicolás, I.; Saco, A.; Barnadas, E.; Marimon, L.; Rakislova, N.; Fusté, P.; Rovirosa, A.; Gaba, L.; Buñesch, L.; Gil-Ibañez, B.; Pahisa, J.; Díaz-Feijoo, B.; Torne, A.; Ordi, J.; Del Pino, M. Prognostic implications of genotyping and p16 immunostaining in HPV-positive tumors of the uterine cervix. *Mod. Pathol.*, **2020**, *33*(1), 128-137. <http://dx.doi.org/10.1038/s41379-019-0360-3> PMID: 31492932
- [215] Tran, W.T.; Jerzak, K.; Lu, F.I.; Klein, J.; Tabbarah, S.; Lagree, A.; Wu, T.; Rosado-Mendez, I.; Law, E.; Saednia, K.; Sadeghi-Naimi, A. Personalized breast cancer treatments using artificial intelligence in radiomics and pathomics. *J. Med. Imaging Radiat. Sci.*, **2019**, *50*(4 Suppl. 2), S32-S41. <http://dx.doi.org/10.1016/j.jmir.2019.07.010> PMID: 31447230
- [216] Khorrami, M.; Bera, K.; Leo, P.; Vaidya, P.; Patil, P.; Thawani, R.; Velu, P.; Rajiah, P.; Alilou, M.; Choi, H.; Feldman, M.D.; Gilkeson, R.C.; Linden, P.; Fu, P.; Pass, H.; Velcheti, V.; Madabhushi, A. Stable and discriminating radiomic predictor of recurrence in early stage non-small cell lung cancer: Multi-site study. *Lung Cancer*, **2020**, *142*, 90-97. <http://dx.doi.org/10.1016/j.lungcan.2020.02.018> PMID: 32120229
- [217] Corredor, G.; Wang, X.; Zhou, Y.; Lu, C.; Fu, P.; Syrigos, K.; Kim, D.L.; Yang, M.; Romero, E.; Schalper, K.A.; Velcheti, V.; Madabhushi, A. Spatial architecture and arrangement of tumor-infiltrating lymphocytes for predicting likelihood of recurrence in early-stage non-small cell lung cancer. *Clin. Cancer Res.*, **2019**, *25*(5), 1526-1534. <http://dx.doi.org/10.1158/1078-0432.CCR-18-2013> PMID: 30201760
- [218] Vaidya, P.; Bera, K.; Gupta, A.; Wang, X.; Corredor, G.; Fu, P.; Beig, N.; Prasanna, P.; Patil, P.; Velu, P.; Rajiah, P.; Gilkeson, R.; Feldman, M.; Choi, H.; Velcheti, V.; Madabhushi, A. CT derived radiomic score for predicting the added benefit of adjuvant chemotherapy following surgery in Stage I, II resectable Non-Small Cell Lung Cancer: a retrospective multi-cohort study for outcome prediction. *Lancet Digit Health*, **2020**, *2*(3), e116-e128. [http://dx.doi.org/10.1016/S2589-7500\(20\)30002-9](http://dx.doi.org/10.1016/S2589-7500(20)30002-9) PMID: 32123864
- [219] Bandari, S.K.; Purushothaman, A.; Ramani, V.C.; Brinkley, G.J.; Chandrashekar, D.S.; Varambally, S.; Mobley, J.A.; Zhang, Y.; Brown, E.E.; Vlodaysky, I.; Sanderson, R.D. Chemotherapy induces secretion of exosomes loaded with heparanase that degrades extracellular matrix and impacts tumor and host cell behavior. *Matrix Biol.*, **2018**, *65*, 104-118. <http://dx.doi.org/10.1016/j.matbio.2017.09.001> PMID: 28888912
- [220] Luthra, S.; Rominski, A.; Sander, P. The role of antibiotic-target-modifying and antibiotic-modifying enzymes in *mycobacterium abscessus* drug resistance. *Front. Microbiol.*, **2018**, *9*, 2179. <http://dx.doi.org/10.3389/fmicb.2018.02179> PMID: 30258428
- [221] Macks, C.; Gwak, S.J.; Lynn, M.; Lee, J.S. Rolipram-loaded polymeric micelle nanoparticle reduces secondary injury after rat compression spinal cord injury. *J. Neurotrauma*, **2018**, *35*(3), 582-592. <http://dx.doi.org/10.1089/neu.2017.5092> PMID: 29065765
- [222] Park, J.K.; Coffey, N.J.; Bodine, S.P.; Zawatsky, C.N.; Jay, L.; Gahl, W.A.; Kunos, G.; Gochuico, B.R.; Malicdan, M.C.V.; Cinar, R. Bleomycin induces drug efflux in lungs: a pitfall for pharmacological studies of pulmonary fibrosis. *Am. J. Respir. Cell Mol. Biol.*, **2020**, *62*(2), 178-190. <http://dx.doi.org/10.1165/rmb.2018-0147OC> PMID: 31419911
- [223] Chen, D.S.; Mellman, I. Elements of cancer immunity and the cancer-immune set point. *Nature*, **2017**, *541*(7637), 321-330. <http://dx.doi.org/10.1038/nature21349> PMID: 28102259
- [224] Petrylak, D.P.; de Wit, R.; Chi, K.N.; Drakaki, A.; Sternberg, C.N.; Nishiyama, H.; Castellano, D.; Hussain, S.A.; Fléchon, A.; Bamias, A.; Yu, E.Y.; van der Heijden, M.S.; Matsubara, N.; Alekseev, B.; Necchi, A.; Géczi, L.; Ou, Y.C.; Coskun, H.S.; Su, W.P.; Bedke, J.; Gakis, G.; Percent, I.J.; Lee, J.L.; Tucci, M.; Semenov, A.; Laestadius, F.; Peer, A.; Tortora, G.; Safina, S.; Garcia Del Muro, X.; Rodriguez-Vida, A.; Cicin, I.; Harputluoglu, H.; Tagawa, S.T.; Vaishampayan, U.; Aragon-Ching, J.B.; Hamid, O.; Liepa, A.M.; Wijayawardana, S.; Russo, F.; Walgren, R.A.; Zimmermann, A.H.; Hozak, R.R.; Bell-McGuinn, K.M.; Powles, T. RANGE study investigators. Ramucirumab plus docetaxel versus placebo plus docetaxel in patients with locally advanced or metastatic urothelial carcinoma after platinum-based therapy (RANGE): overall survival and updated results of a randomised, double-blind, phase 3 trial. *Lancet Oncol.*, **2020**, *21*(1), 105-120. [http://dx.doi.org/10.1016/S1470-2045\(19\)30668-0](http://dx.doi.org/10.1016/S1470-2045(19)30668-0) PMID: 31753727
- [225] Han, M.; Hu, J.; Lu, P.; Cao, H.; Yu, C.; Li, X.; Qian, X.; Yang, X.; Yang, Y.; Han, N.; Dou, D.; Zhang, F.; Ye, M.; Yang, C.; Gu, Y.;

Dong, H. Exosome-transmitted miR-567 reverses trastuzumab resistance by inhibiting ATG5 in breast cancer. *Cell Death Dis.*, **2020**, *11*(1), 43.
<http://dx.doi.org/10.1038/s41419-020-2250-5> PMID: 31969559

[226] Galon, J.; Bruni, D. Approaches to treat immune hot, altered and cold tumours with combination immunotherapies. *Nat. Rev. Drug Discov.*, **2019**, *18*(3), 197-218.
<http://dx.doi.org/10.1038/s41573-018-0007-y> PMID: 30610226

DISCLAIMER: The above article has been published in Epub (ahead of print) on the basis of the materials provided by the author. The Editorial Department reserves the right to make minor modifications for further improvement of the manuscript.